ASME
SETTING THE STANDARD

Journal of Engineering for Gas Turbines and Power

Published Monthly by ASME

VOLUME 132 • NUMBER 2 • FEBRUARY 2010

Transactions of the ASME, Journal of Engineering for Gas Turbines and Power (ISSN 0742-4795) is published monthly by The American Society of Mechanical Engineers, Three Park Avenue, New York, NY 10016. Periodicals postage paid at New York, NY and additional mailing offices.
POSTMASTER: Send address changes to Transactions of the ASME, Journal of Engineering for Gas Turbines and Power, c/o THE AMERICAN SOCIETY OF MECHANICAL ENGINEERS, 22 Law Drive, Box 2300, Fairfield, NJ 07007-2300.
CHANGES OF ADDRESS must be received at Society headquarters seven weeks before they are to be effective. Please send old label and new address.
STATEMENT from By-Laws. The Society shall not be responsible for statements or opinions advanced in papers or ... printed in its publications (B7.1, par. 3).

RESEARCH PAPERS

(Contents continued on inside back cover)

This journal is printed on acid-free paper, which exceeds the ANSI Z39.48-1992 specification for permanence of paper and library materials. ♾™
♻ 85% recycled content, including 10% post-consumer fibers.

Journal of Engineering for Gas Turbines and Power FEBRUARY 2010

Volume 132, Number 2

The ASME Journal of Engineering for Gas Turbines and Power is abstracted and indexed in the following:

AESIS (Australia's Geoscience, Minerals, & Petroleum Database), Applied Science & Technology Index, Aquatic Sciences and Fisheries Abstracts, Civil Engineering Abstracts, Compendex (The electronic equivalent of Engineering Index), Computer & Information Systems Abstracts, Corrosion Abstracts, Current Contents, Engineered Materials Abstracts, Engineering Index, Enviroline (The electronic equivalent of Environment Abstracts), Environment Abstracts, Environmental Science and Pollution Management, Fluidex, INSPEC, Mechanical & Transportation Engineering Abstracts, Mechanical Engineering Abstracts, METADEX (The electronic equivalent of Metals Abstracts and Alloys Index), Pollution Abstracts, Referativnyi Zhurnal, Science Citation Index, SciSearch (The electronic equivalent of Science Citation Index), Shock and Vibration Digest

Spray in Crossflow: Dependence on Weber Number

Eugene Lubarsky
Senior Research Engineer
e-mail: eugene.lubarsky@aerospace.gatech.edu

Jonathan R. Reichel
Graduate Student
e-mail: jreichel3@mail.gatech.edu

Ben T. Zinn
Regents Professor
e-mail: ben.zinn@ae.gatech.edu

School of Aerospace Engineering,
Georgia Institute of Technology,
Atlanta, GA 30332

Rob McAmis
Arnold Engineering Development Center
Aerospace Testing Alliance,
Arnold Air Force Base, TN 37389

This paper describes an experimental investigation of the spray created by Jet A fuel injection from a plate containing sharp edged orifice 0.018 in. (457 μm) in diameter and L/D ratio of 10 into the crossflow of preheated air (555 K) at elevated pressure in the test section (4 atm) and liquid to air momentum flux ratio of 40. A two component phase Doppler particle analyzer was used for measuring the characteristics of the spray. The Weber number of the spray in crossflow was varied between 33 and 2020 and the effect of Weber number on spray properties was investigated. It was seen that the shear breakup mechanism dominates at Weber number greater than about 300. Droplets' diameters were found to be in the range of 15–30 μm for higher values of Weber numbers, while larger droplets (100–200 μm) were observed at Weber number of 33. Larger droplets were observed at the periphery of the spray. The droplet velocities and diameters were measured in a plane 30 mm downstream of the orifice along the centerline of the spray at an incoming airflow Mach number of 0.2. The droplets reach a maximum of 90% of the flow velocity at this location. The velocity of the droplets in the directions perpendicular to the airflow direction is higher at the periphery of the spray possibly due to the presence of larger droplets there. The rms values of the droplet velocities are highest slightly off the centerline of the spray due to the presence of vortices and shear layers around the liquid jet. The data presented here improve the understanding of spray formation processes, and provide benchmark data for computational fluid dynamics (CFD) code validation.
[DOI: 10.1115/1.2904892]

Introduction

Since cross flow fuel injection is widely used in gas turbine engines combustors, it is important to understand the mechanisms that control the spray breakup, penetration, and distribution within the crossflow. Such data are needed for validation of computational fluid dynamics (CFD) codes that will be incorporated into engine design tools. Additionally, this information is needed for understanding observed engine performance characteristics at different regimes of the flight envelope and development of approaches for solving problems such as combustion instabilities [1]. Consequently, there have been a number of experimental studies in this area that are briefly reviewed below.

Spray formation studies have identified two modes of liquid jet breakup; i.e., the column breakup and the shear breakup. During column breakup, the liquid "column" develops surface waves, which distort the liquid [2]. As the waves evolve downstream along the fuel jet, aerodynamic forces enhance the growth rate of the disturbances, leading to the formation of ligaments, which subsequently break up into droplets [3–6]. In shear breakup, aerodynamic forces on the surface of the liquid jet strip off droplets by shear. The domination of one mechanism over the other is dependent on liquid to air momentum flux ratio, q, and Weber number, We, which is a nondimensional ratio of aerodynamic to surface tension forces. The column breakup mechanism dominates the formation of droplets [6–8] at low We and low q. Transition from column breakup to shear breakup can be caused by increase in pressure or increase in shear velocity [9]. Shear breakup for turbulent liquid jets is enhanced by the internal liquid turbulence [6,10]. Wu et al. [11] proposed a breakup regime on a map of aerodynamic Weber number (We) and the momentum flux ratio (q). Rancher et al. [12] carried out studies at elevated pressures (1.5–15 bars) on Jet A fuel and found the breakup regimes of column and shear breakup to match those reported by Wu et al. [11]. Mazallon et al. [7] have found that for values of momentum flux ratio above 100, the dominant breakup mechanism is determined only by Weber number.

Jet penetration has received significant attention as well. Chen et al. [5] and Wu et al. [11,13] have carried out experiments at different momentum flux ratios of water jets and developed a correlation for the upper surface trajectory of jets in a crossflow with the liquid to air momentum flux ratio. Stenzler et al. [14] used Mie scattering images to find the effect of momentum flux ratio, Weber number, and liquid viscosity on jet penetration. Like other previous studies, they found that increasing momentum flux ratio increased penetration. Increasing the Weber number diminished the overall penetration by decreasing the average droplet size of the spray. Increasing the viscosity of the injected fluid decreased the penetration by increasing the drag force on the jet and causing it to bend more sharply. Various researchers have developed correlations for the trajectory of the liquid jet, which used exponential, logarithmic, and power laws.

Leong et al. [15] have studied Jet A in crossflow air at 38 m/s for different ambient pressures (1 atm, 3 atm, and 5 atm). They found that at a given jet to crossflow momentum flux ratio, an increase in ambient pressure decreases jet penetration and increases breakup. Aalburg et al. [16] have explored the effect of turbulent internal flow of the fuel flow. They used cavitations and hydraulic flip to change the orifice internal flow. They found that such spray characteristics as the liquid column trajectories follow the correlations obtained by Wu et al. [11] in the absence of cavitation and hydraulic flip and deviate from the correlations significantly in the presence of these phenomena. Thus, they concluded that the internal orifice flow has a significant effect on spray characteristics.

In spite of the considerable amount of work done in this field, very few studies have been carried out under conditions typical of aerospace applications. Becker and Hassa [9]. and Rancher et al. [12] carried out studies at elevated pressures at room temperature. This study aims at investigating the spray in crossflow close to conditions in gas turbine combustors. Consequently, the reported

Contributed by the International Gas Turbine Institute (IGTI) of ASME for publication in the JOURNAL OF ENGINEERING FOR GAS TURBINES AND POWER. Manuscript received October 11, 2007; final manuscript received February 1, 2008; published online October 15, 2009. Review conducted by Dilip R. Ballal.

experiments employed preheated air to allow investigation of the effect of higher air temperature on the spray formation process.

In this study, Jet A fuel was injected into a crossflow of preheated air (555 K) from a straight orifice with a length to diameter ratio of 10. Investigation of the spray was carried out for a momentum flux ratio of 40. Velocity of the airflow was varied to give flow Weber numbers between 33 and 2020. The pressure in the chamber was maintained at 4 atm. The main goal of this study is to collect experimental data to validate CFD codes used to compute flow characteristics in turbine engine liquid fuel spray systems [17].

Experimental Setup

Figure 1(*a*) shows a schematic of the experimental setup developed at Georgia Tech to study the injection of jet fuel from a flat surface into the crossflow of preheated air at elevated pressures. This setup consists of a plenum chamber, rectangular air supply channel, test section with the injector under investigation, and pressurized chamber with three windows for optical access to the spray. The plenum chamber is 6 in. in diameter and 18 in. (457.2 mm) long. The chamber is thermally insulated to reduce heat losses. Dimensions of the cross section of the rectangular supply channel are 2.43×2.43 in.^{2} (67.7×67.7 mm^2). The length of the channel is 12 in. (304.8 mm). The channel is equipped with a "bell-mouth" air intake, which is submerged by 1 in. into the bottom of the plenum chamber to smooth the airflow. The other end of the channel is submerged into the pressurized chamber. Two aerodynamically shaped plates are attached to the walls at this end of the channel thus creating a test section.

A sharp-edged fuel injection orifice 0.018 in. (457 μm) in diameter with an L/D ratio of 10 and a nozzle flow coefficient of 0.73 is located on the centerline of the plate 10 mm downstream of the supply channel termination (see Fig. 1(*b*)).

Three quartz windows 1/8 in. (3.18 mm) thick are inserted into the slots of the aerodynamically shaped plates using teflon gaskets (see Fig. 2). Such design of the test section provides full confinement of the airflow. The dimensions of the rectangular test section are 30×46 mm^2 (from the orifice plate to opposite window and from window to window, respectively). The length of the quartz windows is 3 in. (76.2 mm).

The pressure chamber is designed to withstand an internal pressure up to 200 psi. In the reported experiments, pressure in the chamber was typically 59 psi (absolute) (4 atm). A stainless steel flexible exhaust line, 4 in. in diameter, was connected to the pressurized chamber at its bottom through the throttle valve with maximum opening of 3 in. This line was connected to the laboratory ejection exhaust pipe via muffler.

The whole system is installed on a traversing table, which provides precise movement (minimal step is 0.001 in. (0.0254 mm)) in three mutually orthogonal directions using step motors and electronic drivers connected to the PDPA computer. The transmitter and receiver of the PDPA system are attached to the optical tables locked to the frame of the rig. In the current study, 1 mm increments of movement were typically used for characterization of the spray.

Preheated air was supplied to the test rig from a high pressure air system (P_{max}=720 psi, T_{max}=555 K), which automatically maintains constant pressure and temperature. Control of the Mach number and pressure was provided by variation of the pressure supplied to the test cell and by simultaneous variation of the opening of the throttle valve in the exhaust line. The Mach Number of the airflow was monitored using a combination of static and total pressure probes installed in the rectangular air supply channel about 6 in. upstream the fuel injection orifice (see Fig. 3).

Temperatures of the air, liquid fuel, and wall were measured using *K*-type thermocouples. Air temperature was measured at the center of the rectangular cross section 1.4 in. (35.56 mm) upstream of the fuel injection orifice. The temperature of the fuel was measured at the point of its injection. Fuel flow rate was measured with a turbine flow meter.

Coordinate System. The axes used to orient the measurements are centered at the orifice. The three mutually orthogonal directions (X, Y, and Z) are aligned, as shown in Fig. 4. The positive X-axis points in the direction of fuel injection, the Z-axis points in the direction of incoming air, and the positive Y-axis is on the plate having the orifice forming a left handed coordinate system. X-scans refer to the measurement of velocity components while moving in the X-direction. In the current study, X-scans are made for different Weber numbers at the centerline of the spray (Y=0) and Z=30 mm. For measuring the spray characteristics, X-scans were made for Z=30 mm and different Y locations.

Phase Doppler Particle Analyzer. A ⟨TSI⟩ two component PDPA was used to measure the diameter of fuel droplets and their velocities. The PDPA system consists of transmitting optics (Model 450500) with a focal length of 500 mm and receiving optics (Model 450300) with a focal length of 300 mm, both installed on stationary tables. Receiving optics are connected to the photodetector module (Model PDM 1000) using fiber-optic cables. Photomultiplier signals are processed using a multibit digital processor (Model FSA 3500). To generate the laser beams, which create the optical measuring volume of the PDPA, an ⟨Innova 90⟩ watercooled argon-ion laser, beam splitter, and Brag cell are used. The laser provides 0.8 W green (λ=514.5 nm) and 0.3 W blue (λ=496.5 nm) beams. To obtain all three velocity components, the velocity measurements are carried out twice in different configurations. For the measurement of Z- and X-components of velocity and diameter, the 150 deg scatter mode is used. Coincidence mode is used to obtain measurements of the droplet size and their corresponding velocities. For measuring the Y-component of the velocity, the 90 deg scatter mode is used.

Results and Discussion

This study of the spray in crossflow primarily consists of two parts: one investigates the effect of the Weber number upon spray characteristics measured along the spray's centerline, and the other obtained a data set of droplet velocities and diameters that could be used to validate CFD codes and to understand some of the physical phenomena occurring during the formation of droplets.

During setup, the observed rms velocity of the incoming air was found to be around 4% of the mean velocity. The boundary layer on the plate with the injection orifice was found to be about 3 mm across. The characteristics of the incoming airflow at a plane located 5 mm upstream of the orifice were found to be fairly independent of the spray and hence this plane can be treated as a boundary for CFD codes [18]. The flow was uniform and stable in the region of interest.

Effects of Weber Number. In the first part, the operating conditions were varied to obtain different Weber numbers ranging from 33 to 2020. The experiment was run at an elevated pressure of 4 atm (0.405 MPa) and temperature of 555 K. The liquid to air momentum flux ratio was maintained constant at 40 by varying the fuel flow rate. Table 1 summarizes the different operating conditions used for the current investigation [19].

Figures 5(*a*) and 5(*b*) show the arithmetic mean diameters and Sauter mean diameters (SMDs) along the centerline of the spray at a Z-location of 30 mm downstream of the orifice at various values of Weber number. It is seen that at values of We greater than about 800, droplets formed have a mean diameter value of about 15–35 μm. Larger droplets are observed at the periphery of the spray. For We=33, the arithmetic mean diameter (AMD) at the periphery of the spray is over 90 μm (SMD$>$140 μm). It is seen that the larger droplets found at lower Weber number penetrate farther away from the orifice plate. However, it is also seen that in

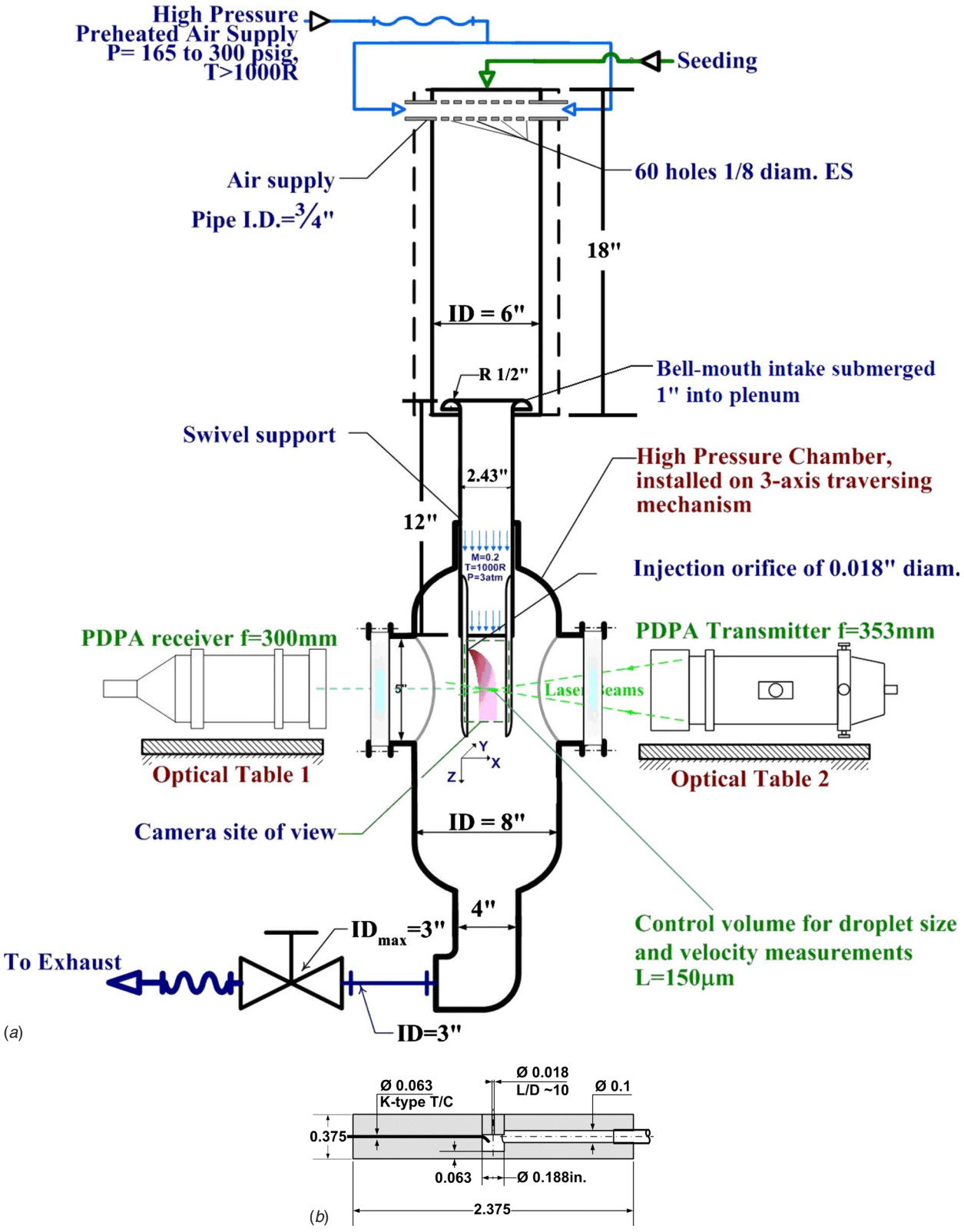

Fig. 1 Experimental setup: (*a*) schematic of test facility and (*b*) schematic of injector

the region of the spray close to the orifice plate, the droplets formed are much smaller. This indicates that the mechanism of formation of droplets in that region is shear breakup as is commonly seen in the case of higher Weber numbers. This evidence indicates that the spray is possibly formed by multimode breakup at lower Weber numbers (We=33).

To further investigate the matter of multimode breakup at low Weber number (We=33), diameter histograms at 16 mm from the orifice plate along the centerline in the periphery of the spray were plotted. Figures 6(*a*)–6(*d*) display histograms of the droplet diameter distribution at different Weber numbers. It is seen in the diameter histogram of Fig. 6(*a*), for We=33, that two "peaks" are

Fig. 2 Test section

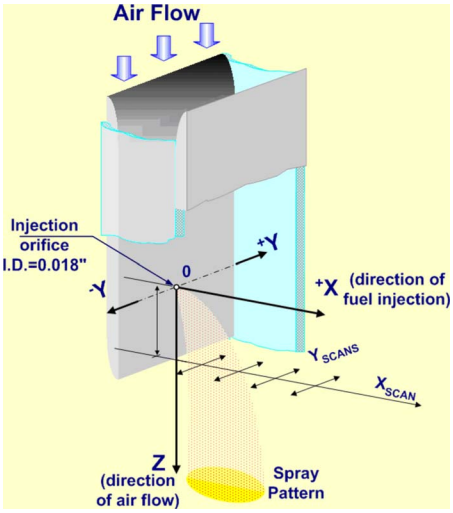

Fig. 4 Coordinate system

formed by the diameter distribution. The first peak occurs around 30 μm and the second peak occurs near 100 μm. This more clearly indicates that multimode column breakup occurs at We =33. As the Weber number increases (Figs. 6(*a*)–6(*c*)), the droplet diameter distribution is seen to become more narrow, and, thus, more uniform throughout the spray, which once again indicates that shear breakup dominates in this regime.

After analyzing the effect of Weber number upon diameter, its effect upon the droplet average *Z*-velocities was investigated. Figure 7 shows the mean *Z*-velocity components of droplet velocities normalized with the corresponding incoming airflow velocity for various Weber numbers measured on the centerline of the spray ($Y=0$) in the plane 30 mm downstream of the injection orifice. The droplet velocities at high Weber numbers seem to have significant lag with respect to the velocity of incoming airflow, especially in the core of the spray located 7–8 mm from the orifice plate. It is observed that in the core of the spray (2–7 mm from the orifice plate), droplets have the same normalized velocity lag of 20–30% for the entire investigated range of Weber numbers with an exception at We=33, which displays only 0%–10% velocity lag 2–12 mm from the orifice plate.

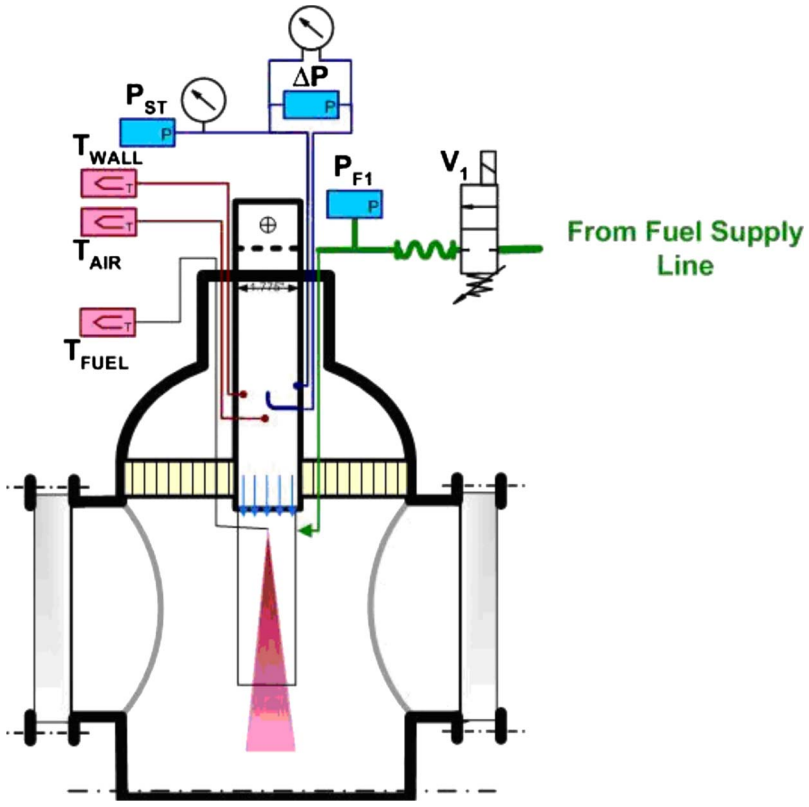

Fig. 3 Instrumentation of facility

Table 1 Air and fuel characteristics for different Weber

We	V_{air} (m/s)	V_f (m/s)	$\dot{m}_f$ (g/s)	T_f (K)
33	22.95	8.4	0.78	378
133	49.25	17.5	1.62	364
285	71.01	27.2	2.51	350
520	94.84	35.4	3.27	343
800	118.5	44.1	4.08	337
1140	142.28	52.1	4.81	333
1535	164.98	60.6	5.6	330
2020	190.64	70.1	6.48	326

Table 2 Operating conditions for spray characterization

Mach number	0.2
Pressure in the chamber	4 atm (0.405 MPa)
Temperature of air	555 K
Mass flow rate of air	0.665 kg/s
Velocity of air	94.7 m/s
Momentum flux ratio	40
Pressure of fuel	47 psi (0.324 MPa)
Mass flow rate of fuel	5.97 g/s
Temperature of fuel	323–328 K
Weber number	590

It is worth noting that at the periphery of the spray (10–25 mm from the orifice plate), the normalized velocity lag decreases with increase in Weber number within the range of We=133–2020. Thus, at a distance of about 14 mm from the orifice plate, droplet velocities attain 90% of the incoming airflow velocity at We =2020 while at We=133 droplet velocities attain only 76% of the incoming airflow velocity. This is due to the significant difference in mean droplet diameters, 20–40 μm for We=2020 and 133, respectively. It is worth noting that We=33 is the only exception from this trend, which reflects the fact that a different mechanism of jet disintegration dominates at We=33 (multimode instead of shear breakup).

The rms values of the Z-velocity components of droplets are plotted in Fig. 8. As expected, higher rms values were observed at higher Weber numbers. At We=2020, two maximum rms values of 22.5 m/s and 24.5 m/s were observed within the core of the spray at distances of 4.5 mm and 8 mm from the orifice plate, respectively. In the range We=133–1535, only one rms maximum in the core was typically observed.

Figure 9 shows the average X-component of droplet velocities normalized with respect to the corresponding jet velocities at different We numbers. The X-velocity is higher at the periphery of the spray. It is seen that droplet velocities in the X-direction typically retain 45% of the velocity of the jet on the outer border of the spray (~18–23 mm from the orifice plate) except that the spray with We=33 obtains a maximum velocity of droplets that is 65% of the jet velocity at a distance of ~26 mm from the plate. Higher velocities were observed at lower Weber numbers on the outer border of the spray. The average X-velocity of droplets near the orifice plate is negative, indicating the presence of vortices in the X-Z plane. Higher negative X-velocities exist near the orifice plate at higher Weber numbers. Both these trends in the X-velocity variation with Weber number can be explained by the droplet size dependence upon Weber number. Bigger droplets, which penetrate further from the orifice plate, have a higher X-velocity. Smaller droplets more closely follow the vortical flow and move in the negative direction toward the plate.

Rms values of droplet X-velocity components strongly depend upon Weber numbers (see Fig. 10). Their maximum values, observed in the core of the spray, vary from ~1.5 m/s to 12 m/s at We=33 and We=2020, respectively. Lower rms values (1–6 m/s) were observed on the periphery of the spray for the same range of We numbers.

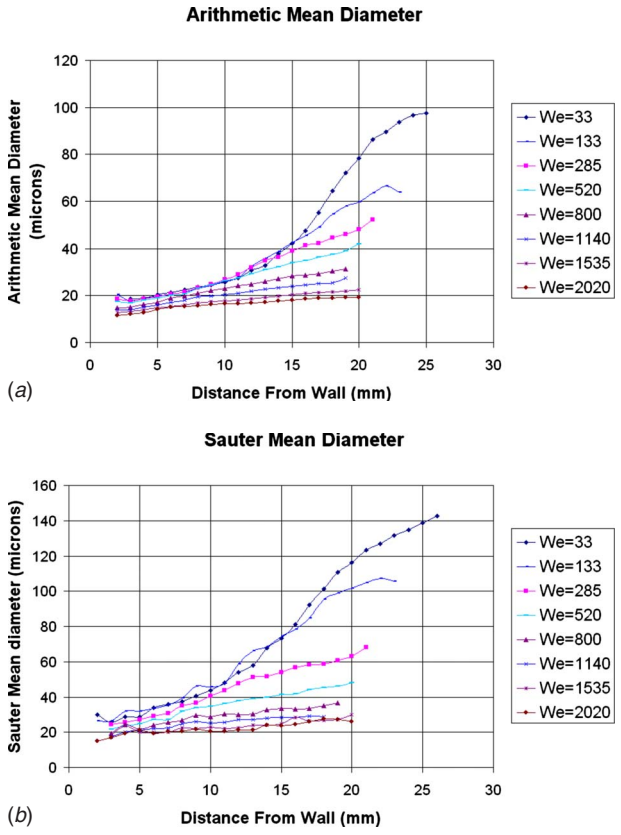

Fig. 5 (*a*) AMD for different Weber numbers and (*b*) SMD for different Weber numbers

Spray Characterization. Spray characteristics were measured using a two component PDPA system in a plane 30 mm downstream of the orifice. The droplet diameters and Z and X average droplet velocities and rms values were measured using the 150 deg scattering mode of the PDPA system. The test channel was then rotated 90 deg and the PDPA system was operated in laser Doppler velocimeter (LDV) mode (droplet velocities measured without diameters) to obtain the Y-velocity mean and rms values. X-scans were made with a step size of 1 mm at different Y-locations. The Y-locations are 2 mm apart. Table 2 summarizes the flow conditions involved in the experiment.

Figures 11(*a*) and 11(*b*) show AMDs and SMDs at different locations in the plane with Z=30 mm. The AMDs range from approximately 22 μm to 42 μm and the SMDs range from approximately 25 μm to 49 μm. It can be seen that both the AMDs and SMDs increase in a nearly linear fashion as one moves away from the wall. It is also interesting to note that the largest AMDs and SMDs can be found at the periphery of the spray while the centerline region of the spray displays the smallest diameter droplets.

Figures 11(*c*) and 11(*d*) display the average Z-velocity components and Z rms velocity components of the droplets at Z =30 mm and M=0.2. It can be seen in Fig. 11(*c*) that the average Z-velocities of the droplets are highest on the periphery of the spray and are lowest in the core of the spray. The spray velocities on the periphery have increased up to almost 90% of the incoming airflow velocity of 94.7 m/s. Meanwhile, within the core, the velocities are only about 67% of the incoming airflow velocity.

In Fig. 11(*d*), it is interesting to note that at ±2 mm, the Z rms values are the highest. Z rms velocities dip toward the core of the spray and decrease past ±2 mm from the center of the spray. This

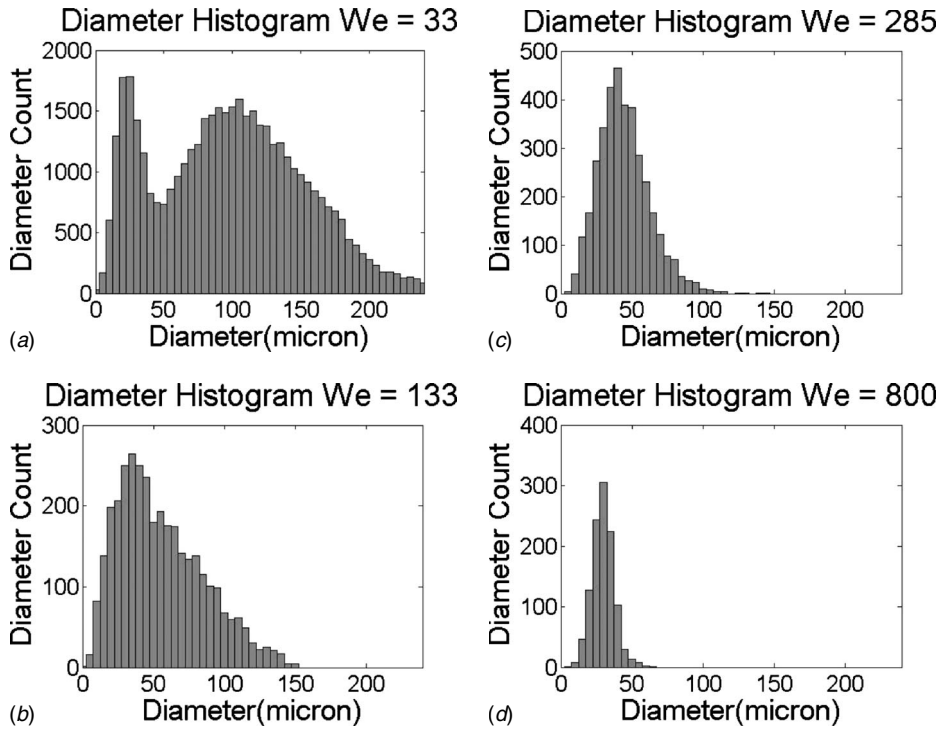

Fig. 6 Diameter histograms at various values of We number at 16 mm from injection wall: (*a*) We=33, (*b*) We=133, (*c*) We=285, and (*d*) We=800

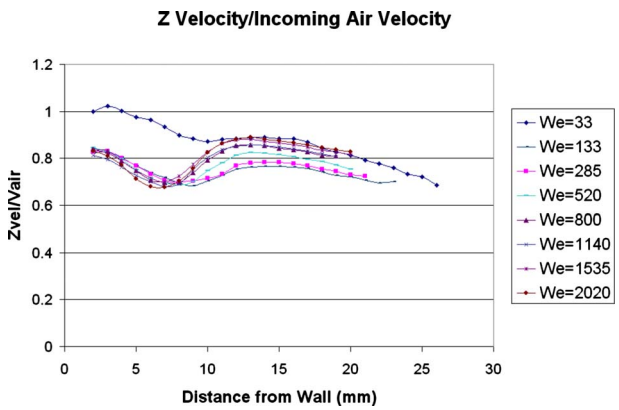

Fig. 7 *Z*-velocity normalized by velocity of incoming air

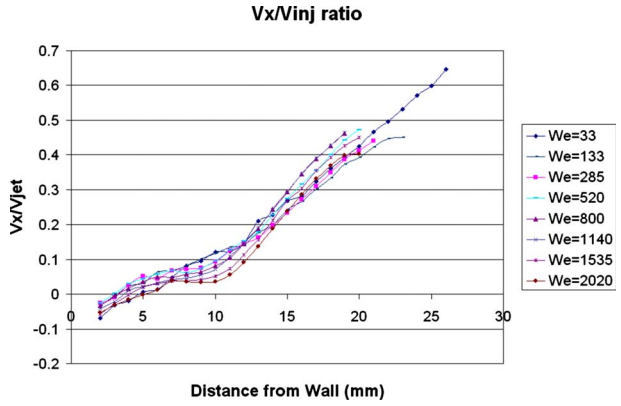

Fig. 9 Mean *X*-velocity of droplets normalized to liquid injection velocity

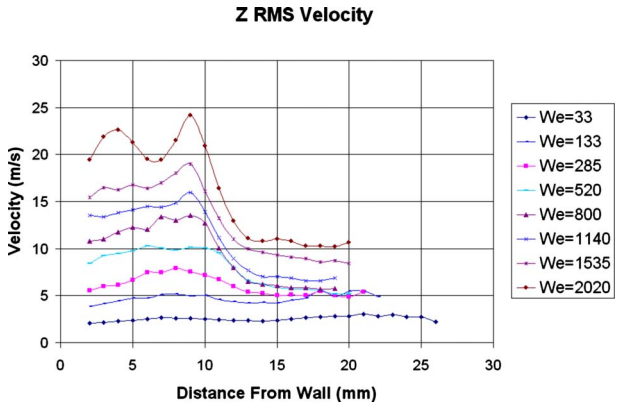

Fig. 8 *Z* rms velocities of droplets

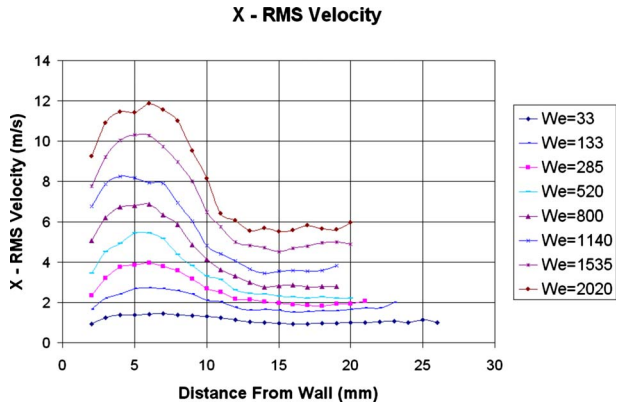

Fig. 10 *X* rms droplet velocities at different Weber numbers

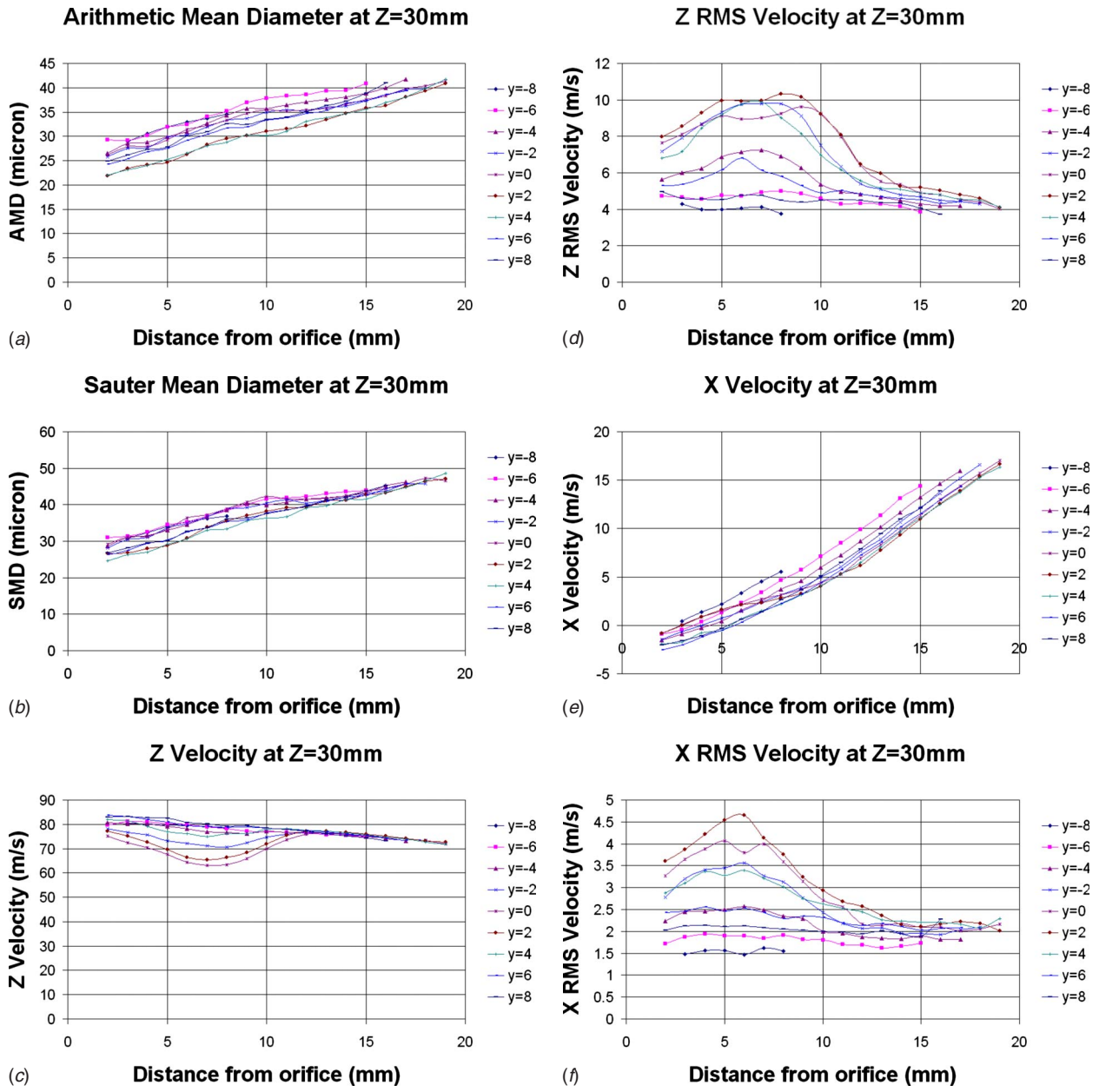

Fig. 11 Spray characteristics in the plane with *Z*=30 mm: (*a*) AMD, (*b*) SMD, (*c*) average *Z*-velocity component of droplets, (*d*) *Z* rms velocity of droplets, (*e*) average *X*-velocity component of droplets, and (*f*) *X* rms velocity of droplets

region of higher rms velocities at ±2 mm is approximately 11% higher than the rms at the core. The deviation can be attributed to a possible vortex flow that exists on the edge of the jet column. In this case, the column acts as a virtual cylinder within the flow and vortices are formed as the incoming airflow passes around this cylinder.

Figures 11(*e*) and 11(*f*) show the *X*-velocities and *X* rms values at $Z=30$ mm and $M=0.2$. In Fig. 11(*e*), it can be seen that the average velocities increase in a linear fashion away from the wall. A slight rise in the velocities is seen at the center of the spray. These higher *X*-velocities at the center are attributed to the higher momentum carried into the crossflow at the onset of fluid injection. This is the densest region of the spray. It is interesting to see that close to the wall, the average *X*-velocities measured were actually negative. This denotes a region of swirling flow where the spray actually curves back in on itself close to the boundary layer. Once again, the highest *X* rms values are found at the core of the spray as was true for the *Z* rms velocities. However, in the case of *X*-velocities, no deviation at ±2 mm is apparent as was seen in the *Z* rms plot (Fig. 11(*d*)).

Figures 12(*a*) and 12(*b*) display the average droplet *Y* velocities and rms values. At first glance, it appears that the *Y*-velocities become negative beyond the centerline; this is not the case. Droplets traveling away from the centerline toward the right are moving in the predesignated negative *Y*-direction and, therefore, their velocities are indicated as negative. An interesting phenomenon is seen in these measurements. Small negative values of *Y*-velocity are seen close to the center of the spray in Fig. 12(*a*). This indicates the presence of a vortex flow within the center of the spray (±2 mm) due to the liquid jet column itself. Though, overall the *Y*-velocities are symmetric and they decrease as the *Z*-location moves downstream of the injector. The *Y*-velocities decrease toward the center of the spray and are highest on the periphery. The

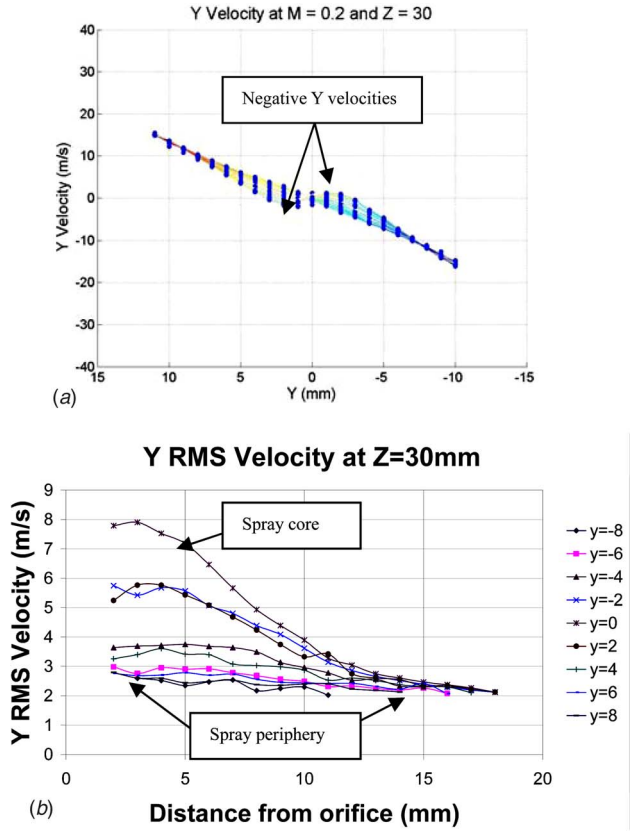

Fig. 12 ***Y*-velocity characteristics measured at *Z*=30 mm: (*a*) average *Y*-velocity component of droplets, 90 deg profile and (*b*) *Y* rms velocity of droplets**

symmetry of the spray is apparent in this view of the spray within the *Y*-*Z* plane. Figure 12(*b*) shows that the *Y* rms velocity component of the droplets is highest at the core of the spray and lowest on the periphery. As distance from the wall increases, the *Y* rms at the core decreases and begins to conform to the rest of the periphery rms values. This supports the theory of a vortex flow existing at the core of the spray, which bends the spray close to the wall.

Concluding Remarks

Spray formed by injection of Jet A into crossflowing air was investigated at elevated pressure (4 atm) and temperature (555 K, 1000 R) using PDPA. The influence of the flow Weber number upon spray characteristics was investigated within a range of We between 33 and 2020 while keeping the fuel to air momentum flux ratio constant at 40. The shear breakup mechanism dominates for We greater than about 300. Larger droplets (100–200 μm diameter) are observed at lower values of We (33, 133, and 285). Histograms of droplet diameter distribution were investigated to further clarify the dependence of the breakup mode upon We. It was seen that for low We (We$\sim$33), a double "peak" distribution occurred. This clearly indicates the domination of multimode breakup in this region. As We increases, the distribution of droplet diameters becomes narrower, indicating that the distribution is more uniform throughout the spray at higher We and shear breakup mechanism dominates.

The mean droplet *Z*-velocity components display considerable lag with respect to the incoming airflow velocity, especially within the core of the spray (7–8 mm from the orifice plate). The absolute value of the velocity lag seems to be directly proportional to the We number as it varies from 13 m/s to 60 m/s at We=133 and We=2020, respectively. It is seen that the velocity lag for each Weber number is approximately 20–30% with the exception of We=33, which displays a lag from 0% to 10% within the core. This is attributed to the presence of multimode breakup of the spray within the core at low Weber number.

The mean *X*-velocity close to the orifice plate is negative in magnitude indicating the presence of vortices, which are responsible for bending of the liquid jet. The negative velocities are higher in magnitude for higher values of Weber number. The mean *X*-velocities of the droplets were normalized with the velocity of the injected fuel. Typically, the droplets attained about 45% of the fuel jet velocity. However, at We=33, the droplets reached a maximum of 65% of the jet velocity. These findings support the previous finding that larger droplets are formed at low We and smaller droplets formed at high We. Specifically, larger droplets penetrate farther away from the orifice wall with a higher *X*-velocity while smaller droplets more closely follow the vortical flow within the core of the spray and move in the negative direction toward the orifice wall as the spray is bent by the vortex flow.

Acknowledgment

The authors thank the Arnold Engineering and Development Center for their financial support, which made this study possible.

Nomenclature

D = droplet diameter
D_{10}, AMD = arithmetic mean diameter, $\Sigma D_i n_i / \Sigma n_i$
D_{32}, SMD = Sauter mean diameter, $\Sigma D_i^3 n_i / \Sigma D_i^2 n_i$
M = Mach number, U_a / a
σ = surface tension
λ = laser wavelength
q = liquid to air momentum flux ratio, $\rho_l U_l^2 / \rho_a U_a^2$
Re = Reynolds number, $LU\rho/\mu$
ρ = density
P = pressure
U = speed
We = aerodynamic Weber number, $\rho_a U_a^2 D / \sigma$
d = diameter of the orifice, 457 μm for the current study

Subscripts

a = air
l = liquid

References

[1] Marmottant, P., and Villermaux, E., 2004, "On Spray Formation," J. Fluid Mech., **498**, pp. 73–111.
[2] Bonnell, J. M., Marchall, R. L., and Riecke, G. T., 1971, "Combustion Instability in Turbojet and Turbofan Augmentors," Seventh AIAA/SAE Propulsion Joint Specialist Conference Exhibit, Salt Lake City, UT, Paper No. AIAA 71-698.
[3] Sallam, K. A., Dai, Z., and Faeth, G. M., 2002, "Liquid Breakup at the Surface of Turbulent Round Liquid Jets in Still Gases," Int. J. Multiphase Flow, **28**(3), pp. 427–429.
[4] Tambe, S. B., Jeng, S. M., Mongia, H., and Hsiao, G., 2005, "Liquid Jets in Subsonic Flow," 43rd Aerospace Science Meeting & Exhibit, Reno, NV, Paper No. AIAA 2005-731.
[5] Chen, T. H., Smith, C. R., and Schommer, D. G., 1993, "Multi-Zone Behavior of Transverse Liquid Jet in High-Speed Flow," AIAA Paper No. 93-0453.
[6] Wu, P.-K., Hsiang, L.-P., and Faeth, G. M., 1995, "Aerodynamic Effects on Primary and Secondary Breakup," *Liquid Rocket Engine Combustion Instability*, Progress in Astronautics and Aeronautics, Vol. 169, V. Yang and W. Anderson, eds. (AIAA, Washington, DC), pp. 247–279.
[7] Mazallon, J., Dai, Z., and Faeth, G. M., 1998, "Aerodynamic Primary Breakup at the Surface of Nonturbulent Round Liquid Jets in Cross-Flows," 36th Aerospace Science Meeting & Exhibit, Reno, NV, Paper No. AIAA 1998-716.
[8] Ghosh, S., and Hunt, J. C. R., 1998, "Spray Jets in Cross-Flow," J. Fluid Mech., **365**, 109–136.
[9] Becker, J., and Hassa, C., 2002, "Breakup and Atomization of a Kerosene Jet in Crossflow at Elevated Pressure," Atomization Sprays, **11**, pp. 49–67.
[10] Wu, P.-K., Miranda, R. F., and Faeth, G. M., 1995, "Effects of Initial Flow Conditions on Primary Breakup of Nonturbulent and Turbulent Round Liquid Jets," Atomization Sprays, **5**(2), pp. 175–196.
[11] Wu, P.-K., Kirkendall, K. A., Fuller, R. P., and Nejad, A. S., 1998, "Spray Structures of Liquid Jets Atomized in Subsonic Cross-flows," J. Propul. Power,

14(2), pp. 173–182.
[12] Rancher, M., Becker, J., Hassa, C., and Doerr, T., 2002, "Modeling of the Atomization of a Plain Liquid Fuel Jet in Crossflow at Gas Turbine Conditions," Aerosp. Sci. Technol., **6**, pp. 495–506.
[13] Wu, P.-K., Kirkendall, K. A., Fuller, R. P., and Nejad, A. S., 1997, "Breakup Processes of Liquid Jets in Subsonic Cross-Flows," J. Propul. Power, **13**(1), pp. 64–73.
[14] Stenzler, J. N., Lee, J. G., and Santavicca, D. A., 2003, "Penetration of Liquid Jets in a Crossflow," 41st Aerospace Science Meeting & Exhibit, Reno, NV, Paper No. AIAA 2003-1327.
[15] Leong, M. Y., McDonell, V. G., and Samvelsen, G. S., 2001, "Effect of Ambient Pressure on an Airblast Spray Injected Into a Crossflow," J. Propul. Power, **17**(5), pp. 1076–1084.
[16] Aalburg, C., Sallam, K. A., and Faeth, G. M., 2004, "Properties of Nonturbulent Round Liquid Jets in Uniform Crossflows," Paper No. AIAA 2004-0969.
[17] Johnson, J. N., Lubarsky, E., and Zinn, B. T., 2005, "Experimental Investigation of Spray Dynamics Under Jet Engine Augmentor Conditions," AIAA/ASME/SAE/ASEE Joint Propulsion Conference & Exhibit, Tuscon, AZ, Paper No. AIAA 2005-4480.
[18] Lubarsky, E., Gopala, Y., Bibik, O., and Zinn, B. T., 2006, "Experimental Investigation of Spray Dynamics in Crossflow of Pre-Heated Air at Elevated Pressure," 44th Aerospace Science Meeting & Exhibit, Reno, NV, Paper No. AIAA 2006-1342.
[19] Gopala, Y., Lubarsky, E., Oleksandr, B., Zinn, B. T., and Dai, Z., 2006, "Experimental Investigation of Spray Dynamics in Cross-Flowing Air at High Weber Number," 42nd AIAA/ASME/SAE/ASEE Joint Propulsion Conference and Exhibit, Sacramento, CA, Jul. 9–12, Paper No. AIAA-2006-4568.

Effect of Flame Structure on the Flame Transfer Function in a Premixed Gas Turbine Combustor

Daesik Kim

Jong Guen Lee[1]

Bryan D. Quay

Domenic A. Santavicca

Department of Mechanical and Nuclear Engineering,
Penn State University,
University Park, PA 16802

Kwanwoo Kim

Shiva Srinivasan

GE Energy,
Greenville, SC 29615

The flame transfer function in a premixed gas turbine combustor is experimentally determined. The fuel (natural gas) is premixed with air upstream of a choked inlet to the combustor. Therefore, the input to the flame transfer function is the imposed velocity fluctuations of the fuel/air mixture without equivalence ratio fluctuations. The inlet-velocity fluctuations are achieved by a variable-speed siren over the forcing frequency of 75–280 Hz and measured using a hot-wire anemometer at the inlet to the combustor. The output function (heat release) is determined using chemiluminescence measurement from the whole flame. Flame images are recorded to understand how the flame structure plays a role in the global heat release response of flame to the inlet-velocity perturbation. The results show that the gain and phase of the flame transfer function depend on flame structure as well as the frequency and magnitude of inlet-velocity modulation and can be generalized in terms of the relative length scale of flame to convection length scale of inlet-velocity perturbation, which is represented by a Strouhal number. Nonlinear flame response is characterized by a periodic vortex shedding from shear layer, and the nonlinearity occurs at lower magnitude of inlet-velocity fluctuation as the modulation frequency increases. However, for a given modulation frequency, the flame structure does not affect the magnitude of inlet-velocity fluctuation at which the nonlinear flame response starts to appear. [DOI: 10.1115/1.3124664]

Keywords: combustion dynamics, gas turbine, combustion, flame transfer function, flame structure

1 Introduction

Lean premixed gas turbine combustors were successful in meeting current NO_x emissions regulations. However, these have been found to be susceptible to combustion instability, which is intimately related to the feedback coupling between unsteady heat release and acoustic pressure field [1,2].

A quantification of the heat release response of a flame to the unsteady inlet velocity and/or equivalence ratio, which are caused by the pressure waves in a combustor, is critical information in the theoretical description of combustion-induced oscillations. The flame transfer function describes its dynamic heat release response to inlet flow perturbations as a function of frequency (f) and with the inlet velocity as the input function it can be defined as

$$T(f) = \frac{Q'(f)/Q_{\text{mean}}}{V'(f)/V_{\text{mean}}}$$

where Q_{mean} is the temporal mean of heat release rate, V_{mean} is the mean bulk velocity of the mixture entering the combustor, and Q' and V' are their corresponding fluctuating components.

Flame transfer function may be obtained from an analytical description of flame response [3,4], from a computational fluid dynamics (CFD)-based study [5,6], and from an experiment [7–10]. However, both analytic and CFD-based approaches are limited in capturing the highly complex interaction between flow field and heat release precisely, and the experimental determination of the flame transfer function is still preferred. The measured flame transfer function can be used directly in the thermoacoustic network model where a gas turbine combustion system is modeled as a network of its elements such as air supply, plenum, premix duct, fuel injection, flame, combustor, etc. [11,12]. Both analytical and experimental works show that the gain of transfer function decreases as the perturbation frequency increases. And, for a given perturbation frequency, it is constant up to a certain level of perturbation but starts to decrease as the level increases further. The former and the latter behavior of flame response are often referred to as linear and nonlinear responses, respectively, and are known to be important to understand mechanism of combustion instability [13,14] in that linear response determines the frequency and the growth rate of combustion instability and the nonlinear process controls the amplitude of instability.

Analytical predictions based on a kinematic analysis of the flame front evolution show that the flame transfer function depends on flame angle [15] and flame length [14] in addition to the basic shape of undisturbed flame (i.e., conical, inverted wedge, V-flame, etc.). For example, the gain of transfer function is found not to be sensitive to the flame angle for a conical flame but quite sensitive for small flame-angle V-flame [15] (i.e., the gain increases as the flame angle decreases). Similarly, the ratio of the flame length to the width is found to affect the magnitude of velocity at which transfer function nonlinearities become significant [14]. However, there are little data available on detailed measurements of flame transfer function in highly turbulent, practical combustor. It will be interesting to see if the relatively simple kinematic analysis of flame dynamics can predict how flame responds to inlet-velocity distribution under practical operating conditions. Also, most flame transfer function measurements were made from the global heat release measurement where it is very difficult to understand why flame behaves in a certain way for given operating conditions.

The objective of this study is to experimentally determine the transfer function of turbulent premixed flames with main emphasis on the effect of flame structure on how the flames respond to inlet-velocity perturbation. Also, the nonlinear response of flame will be characterized, and controlling parameters of the nonlinearity will be identified.

[1]Corresponding author.

Manuscript received April 1, 2008; final manuscript received May 9, 2008; published online October 16, 2009. Review conducted by Dilip R. Ballal.

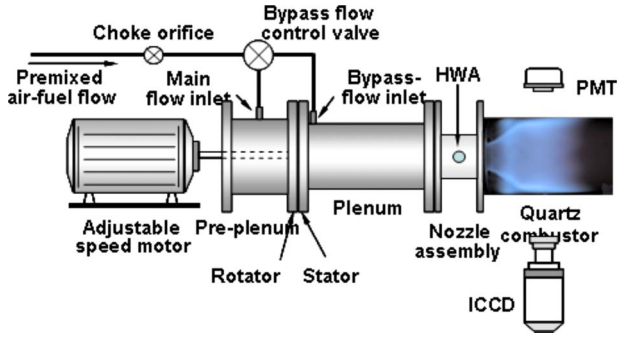

Fig. 1 Schematic diagram of experimental setup

2 Experimental Approach

The experimental setup consists of an optically-accessible combustor, a nozzle-assembly, and a device for modulating inlet velocity, as shown in Fig. 1.

The combustor is made of an optically accessible fused-silica combustor section (150 mm in diameter and 300 mm in length). The combustor exit is fully open without any restriction. The nozzle assembly consists of a center-bluff body (D=40 mm) whose end face is recessed by 20 mm from the dump plane and an annular mixing section where 45 deg swirl vanes are located. Figure 2 shows the schematic drawing of combustor and nozzle-assembly.

A siren type modulation device is used to impose the inlet-velocity fluctuation (V'). It consists of a variable-speed motor, a rotating plate, a preplenum, and a stator, and its modulation frequency range runs up to 400 Hz. The amount of inlet-velocity fluctuation (V'/V_{mean}) can be varied by controlling the relative amount of air flow through the modulating device. Natural gas is used as a fuel and is completely premixed with air at upstream of a choked inlet in order to avoid the fluctuation of equivalence ratio.

The velocity fluctuation in the annular mixing section is measured using a hot-wire anemometer (HWA) (TSI model 1210), which is located at 60 mm upstream of the dump plane. Chemiluminescence measurements are used to quantify the heat release response to inlet-velocity fluctuation. Photomultiplier tubes (PMTs) (Hamamatsu model 928A) are used to measure the global

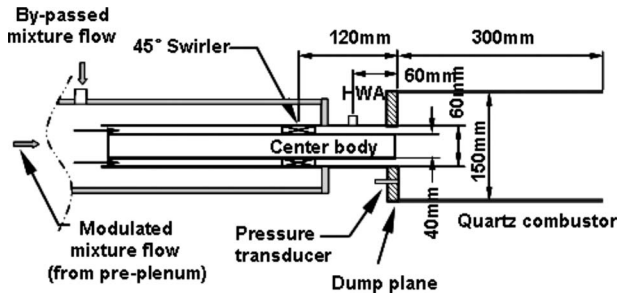

Fig. 2 Schematic drawing of the combustor and nozzle assembly

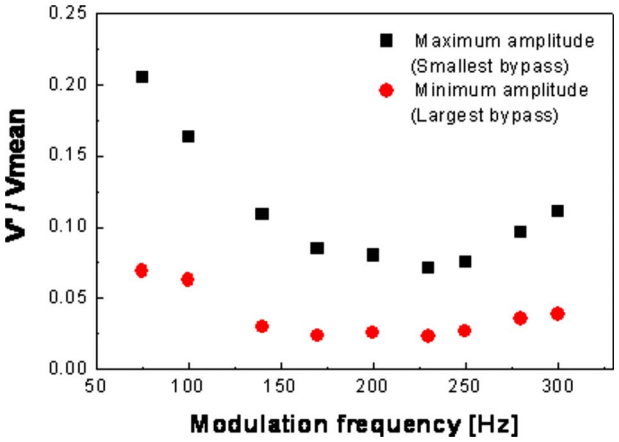

Fig. 3 Maximum and minimum amplitudes of velocity fluctuations at each modulation frequency ($V_{mean,nozzle}$=30 m/s)

CH* and OH* chemiluminescence intensities from the whole flame, which are collected using a narrow band-pass (±5 nm) filter centered at 430 nm and 307 nm, respectively. The calculated values of $(CH^*)'/(CH^*)_{mean}$ or $(OH^*)'/(OH^*)_{mean}$ through the fast Fourier transform (FFT) are used as the estimates for the heat release fluctuations. The signals from HWA and PMTs are digitized and recorded by a digital data acquisition system at a sampling rate of 16,384 Hz. A total of 16,384 data points is taken during each test.

Also, an intensifed charge coupled device (ICCD) camera (Princeton Instruments model 576 G) equipped with a band-pass filter ($\lambda=430\pm5$ nm) is used to capture the CH* chemiluminescence from the whole flame. Both time-averaged images over one period of inlet-velocity oscillation and phase-averaged images are taken for each condition. For all cases, 40 individual images are taken and averaged. For phase-averaged imaging, the camera is synchronized with the HWA signal, and 12 averaged images over one period of oscillation are taken with a phase interval of 30 deg. A three-point Abel deconvolution scheme is used to reconstruct the two-dimensional flame structure [16].

The operating conditions are summarized in Table 1. The experiments are conducted at room temperature and atmospheric-pressure conditions. Figure 3 shows the maximum and the minimum amplitude of inlet-velocity modulation that can be obtained over a range of frequency: The highest magnitude is found at the modulation frequency of 75 Hz and the lowest is found at around 230 Hz.

3 Results and Discussions

3.1 Global Characterization of Flame Response to Inlet-Velocity Fluctuation. Figure 4 shows typical time traces and frequency spectra of chemiluminescence intensity and inlet-velocity fluctuations measured for modulation frequency of 75 Hz, equivalence ratio of 0.7, and V'/V_{mean} of 0.07. Both CH*- and OH*-chemiluminescence intensities lag the inlet-velocity fluctuation, and the frequency spectra show that both inlet-velocity and chemiluminescence intensity fluctuations occur mainly at the

Table 1 Operating conditions

Mean velocity in the nozzle ($V_{mean,nozzle}$)	30 m/s
Equivalence ratio (ϕ)	0.65, 0.675, 0.7, 0.725, and 0.75
Inlet flow temperature	20°C
Modulation frequency (f)	75, 100, 140, 200, 250, and 280 (Hz)
Modulation amplitude (V'/V_{mean})	up to 21%
Reynolds number	35,600

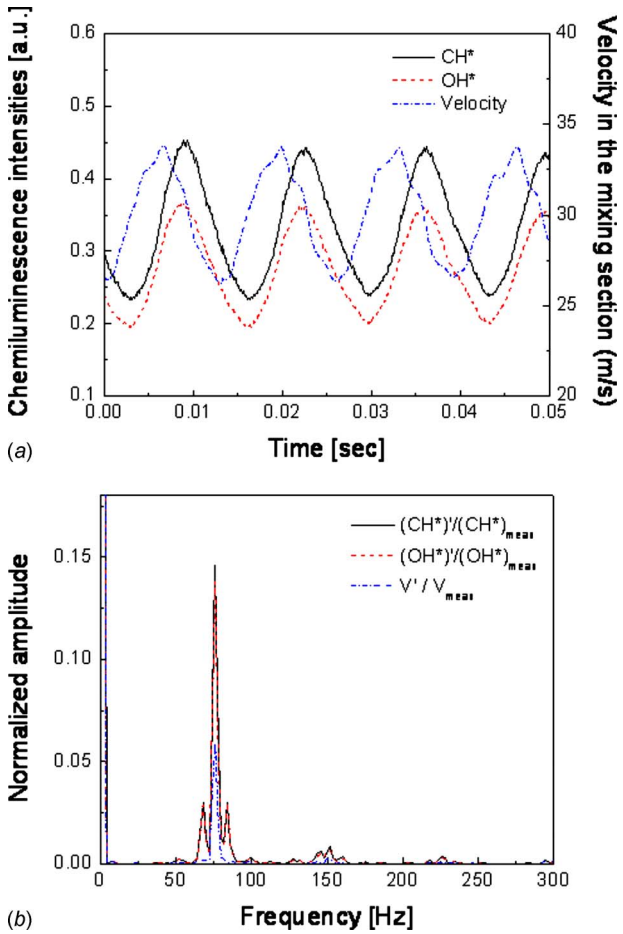

Fig. 4 (*a*) Time traces and (*b*) frequency spectra of CH* and OH* and inlet-velocity fluctuations ($V_{mean,nozzle}$=30 m/s, ϕ=0.7, f=75 Hz, and V'/V_{mean}=0.07)

modulation frequency with negligible amount of fluctuations at higher harmonic frequencies. Since the CH*- and OH*-chemiluminescence intensity fluctuations show similar behaviors both in amplitudes and in relative phases to the inlet-velocity perturbation over operating conditions listed in Table 1, only CH*-chemiluminescence results will be discussed hereafter.

Figure 5 shows averaged chemiluminescence images over 1 cycle of flow modulation at various modulation frequencies and equivalence ratios for a given mean velocity (V_{mean}=30 m/s). The modulation amplitude (V'/V_{mean}) was fixed at 0.07. In each

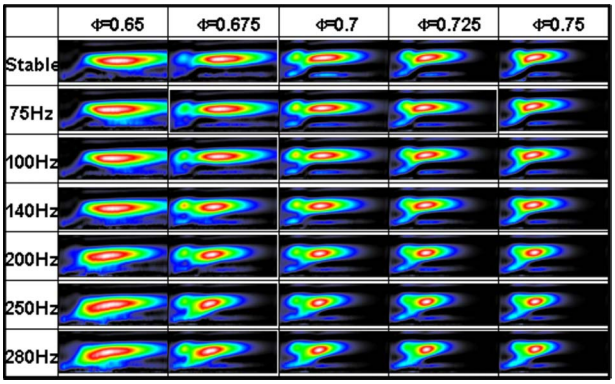

Fig. 5 Effects of modulation frequency and equivalence ratio on the flame structure ($V_{mean,nozzle}$=30 m/s and V'/V_{mean}=0.07)

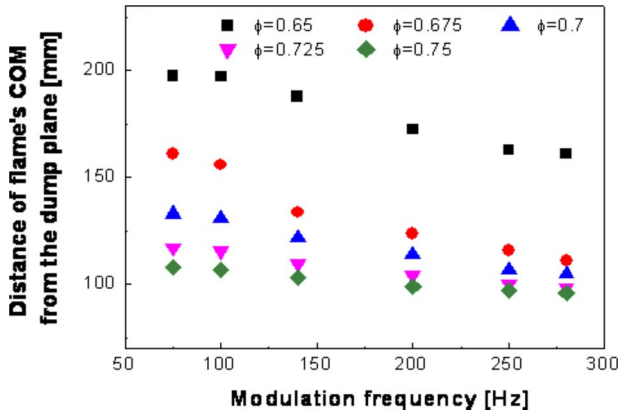

Fig. 6 Flame's COM location as a function of modulation frequency and equivalence ratio ($V_{mean,nozzle}$=30 m/s and V'/V_{mean}=0.07)

image, only the upper-half of the flame is shown because the deconvoluted images are axisymmetric. As mentioned in Sec. 2, the exposure time of the ICCD camera is set the same as the period of modulation so that each image represents an average of chemiluminescence images for one cycle of velocity fluctuation. These images show that the flame structure is affected by the modulation frequency as well as operating conditions (i.e., equivalence ratio): As the modulation frequency increases for a given equivalence ratio, the location for the maximum intensity region gets closer to the combustor inlet and the flame length decreases.

For more quantitative analysis of the change in flame structure, the location of center of mass (COM) from the dump plane is calculated for each image and plotted as a function of modulation frequency for various equivalence ratios, as shown in Fig. 6. It is evident that the distance of flame's COM from the dump plane decreases with increasing modulation frequency at a given equivalence ratio, and the trend is more obvious for the low equivalence ratio cases (say, ϕ=0.65 or 0.675) than the high equivalence ratio cases (say, ϕ=0.725 or 0.75). Since the location of COM can be interpreted as an effective flame location and/or the maximum heat release location, the results shown in Fig. 6 suggest that the actual convection time for the inlet-velocity perturbation to reach flame will change as the modulation frequency changes as well as inlet flow conditions. This will be further discussed in Secs. 3.2.

3.2 Transfer Function Measurement Results for a Fixed Amount of Inlet-Velocity Fluctuation. Since the effect of the magnitude of inlet-velocity fluctuation on transfer function measurement will be presented and discussed later, only cases for a fixed magnitude of input function (V'/V_{mean}=0.07) are presented in this section. Figure 7 shows the amplitude of CH* chemiluminescence fluctuation normalized by its mean value, which can be interpreted as the gain of transfer function (because the amplitude of velocity fluctuation is fixed) for different modulation frequencies and equivalence ratios. The gain of transfer function changes with respect to both inlet-velocity modulation frequency and inlet equivalence ratio. For a fixed equivalence ratio, the gain of transfer function decreases as the modulation frequency increases. Similar observations were made from analytical [14,15] and experimental works [7], where the global flame is found to behave as low-pass filter. Also, for a fixed modulation frequency, the gain increases as the equivalence ratio increases, indicating that the flame dynamics, which determines how flame responds to inlet-velocity fluctuation, depends on flame structure as well as on modulation frequency. As mentioned previously, analytical predictions have shown that the flame transfer function depends on flame angle [15] and flame length [14] for a given flame shape. In the present study, the flame structures such as flame length and the

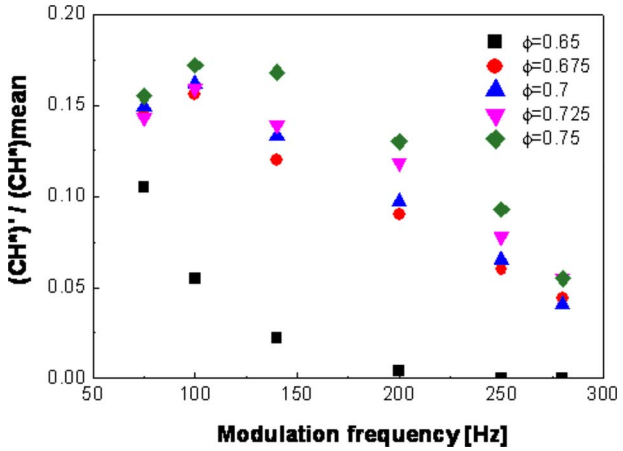

Fig. 7 Normalized CH* intensity fluctuation as a function of modulation frequency and equivalence ratio ($V_{mean,nozzle}$ =30 m/s and V'/V_{mean}=0.07)

existence of bright corner recirculation zone are changed with respect to the equivalence ratio, suggesting that the flame response to the same inlet-velocity fluctuation will change accordingly.

Figure 8 shows the phase-averaged CH* images taken for one cycle of inlet-velocity fluctuation for the equivalence ratio of 0.65 and modulation frequencies at 75 Hz and 280 Hz. The phase-averaging is synchronized with and referenced to the output signal from HWA. Low-frequency modulation (f=75 Hz) causes relatively larger amount of flame length change (as indicated by the variation in COM distance) as well as global chemiluminescence intensity (and hence heat release) than high-frequency modulation (f=280 Hz) does. For the 75 Hz case, the change in global heat release appears to be associated with the change in flame length even though they are not perfectly in phase, and the local heat release change occurs in the center part of the flame. However, for the 280 Hz case, the change in heat release in the center portion of the flame is minimal, and the flame front is more wrinkled, suggesting that the local flame stretch effect does not cause large variation in global heat release. For higher equivalence ratio case (ϕ=0.75) shown in Fig. 9, where the same amount of inlet-velocity modulation results in greater amount of fluctuations in heat release than ϕ=0.75 case, the heat release fluctuation seems to be associated with the change in flame length for both low- and high-frequency modulation cases. Also, the high-frequency modulation case (f=280 Hz) exhibits a periodic vortex-shedding process, which suggests that the flame response to inlet-velocity fluctuation may not be linear anymore at this condition, as suggested by Balachandran et al. [7].

Figure 10(a) shows the phase of transfer function between CH*-chemiluminescence intensity fluctuation, (CH*)', and V'. The absolute magnitude of the phase increases almost linearly as the modulation frequency increases for a given ϕ and decreases as ϕ increases for a fixed modulation frequency. Shown in Fig. 10(b) is the convection time delay (τ_{conv}) calculated from the phase. It shows that for a given ϕ, the higher the modulation frequency the shorter the delay between the heat release and inlet-velocity fluctuation, and for a given modulation frequency, the higher the equivalence ratio the shorter the delay. This is consistent with the effect of frequency and equivalence ratio on the flame's COM location shown in Fig. 6. This is because the closer the flame's COM location to the inlet of the combustor of the flame the shorter the delay.

From the data presented in Figs. 6 and 10, the effective convection velocity ($V_{eff}=L_{COM}/\tau_{conv}$) at which the inlet-velocity perturbation is convected in the combustor can be calculated. The results are shown in Fig. 11. The effective convection velocity is less than the mean inlet velocity to the combustor by a factor of 1.4–4 over the operating conditions and varies with respect to the modulation frequency as well as the equivalence ratio. For a given equivalence ratio, the effective convection velocity increases as the modulation frequency increases, seemingly suggesting that the effective convection velocity will increase as the flame becomes shorter. However, for a given modulation frequency, the effective convection velocity decreases as the equivalence ratio increases (as the flame length becomes shorter), suggesting that the effective convection velocity cannot be simply scaled with flame length but determined by the interaction of disturbance field with flame. One possible explanation for the reason why the effective convection velocity is not simply related to the flame length may have something to do with flame structures. Undisturbed flame

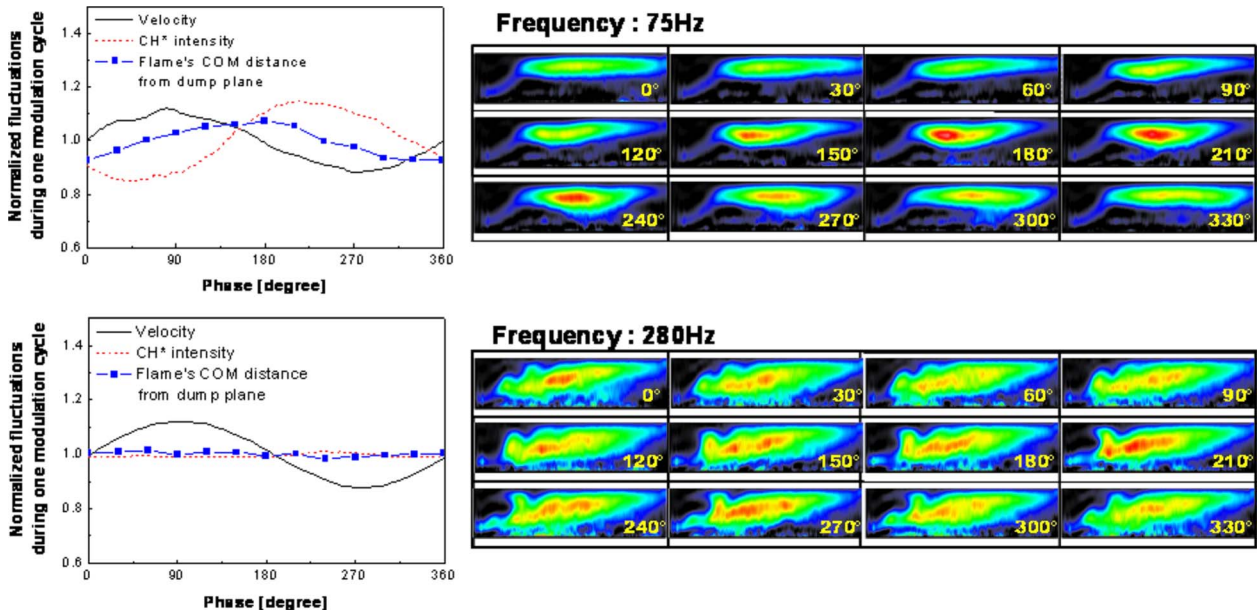

Fig. 8 Effects of modulation frequency on flame structure for one period of modulation ($V_{mean,nozzle}$=30 m/s, ϕ=0.65, and V'/V_{mean}=0.07)

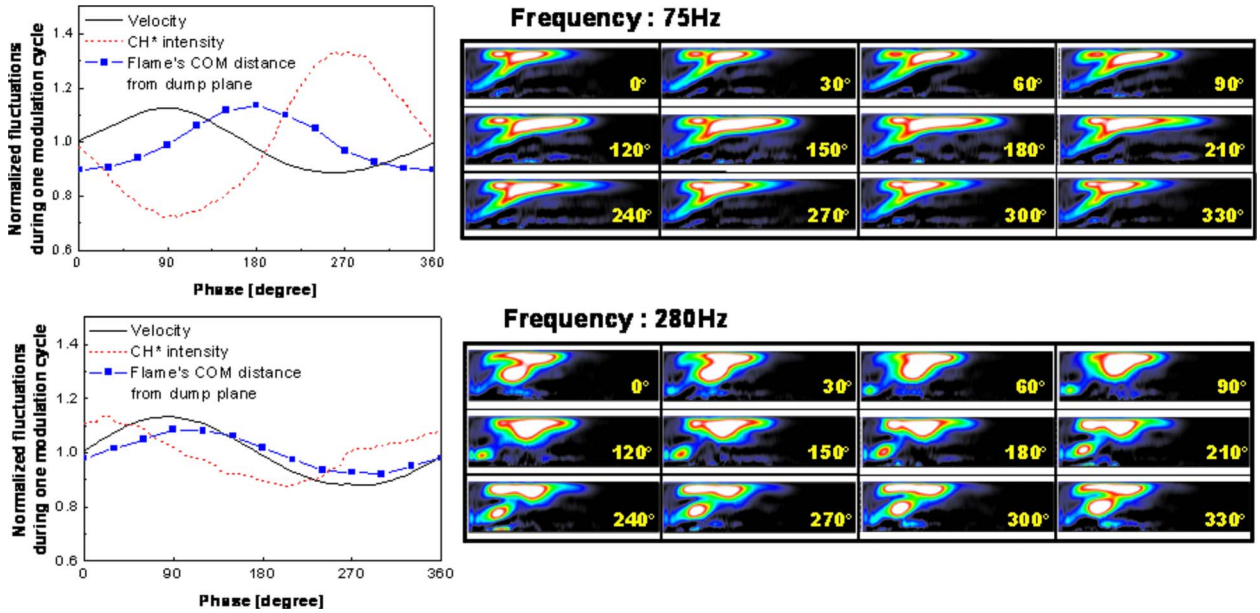

Fig. 9 Effects of modulation frequency on flame structure for one period of modulation ($V_{mean,nozzle}$=30 m/s, ϕ=0.75, and V'/V_{mean}=0.07)

image shows that for $\phi > 0.65$ cases, a bright heat release zone develops in the corner recirculation region, and this may cause the residence time of combustible mixture relatively longer for a given flame length than for $\phi = 0.65$ case.

Analytical studies [9,14,15] show that the dynamics of premixed flames submitted to harmonic flow perturbation with modulation frequency (f) can be characterized by the Strouhal number determined by

$$\mathrm{St} = \frac{L_{\mathrm{flame}}}{L_{\mathrm{conv}}} = \frac{L_{\mathrm{flame}}}{V_{\mathrm{eff}}/f}$$

which represents the ratio of flame length scale to the convective wavelength. Using the distance from the dump plane to the COM location shown in Fig. 6 as the flame length (L_{flame}) and the effective convection velocity shown in Fig. 11, the gain and phase of transfer function are plotted, as shown in Fig. 12. It shows that the flame length scale is always greater than the convection length scale (in other words St > 1) for the present operating conditions. Also, these results show that the gain and phase of transfer function for different equivalence ratios and frequencies are well represented by the Strouhal number, strongly suggesting that the flame dynamics over different equivalence ratios and modulation frequencies could be generalized in terms of the relative length scale of the flame to the convection length scale.

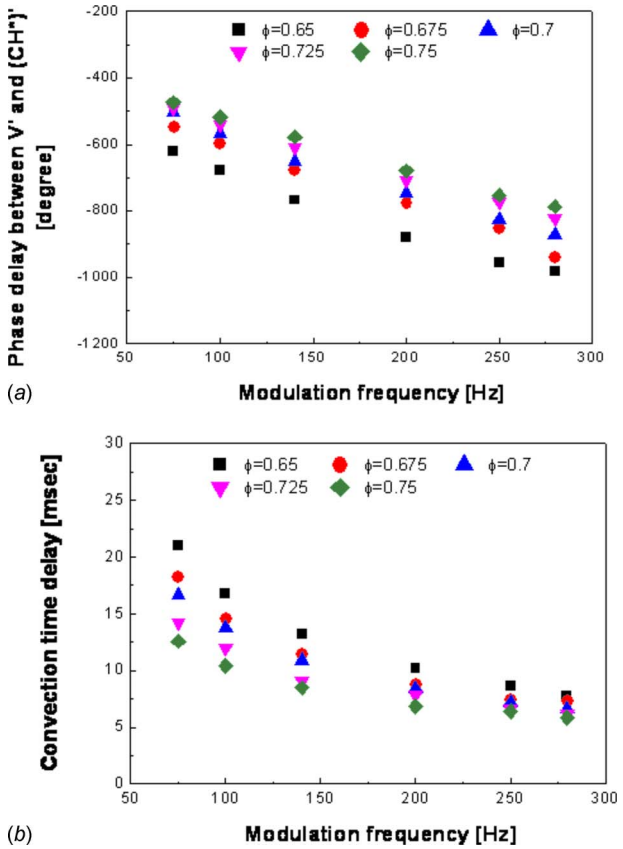

Fig. 10 (*a*) Phase of transfer function and (*b*) convection time delay as a function of modulation frequency and equivalence ratio ($V_{mean,nozzle}$=30 m/s and V'/V_{mean}=0.07)

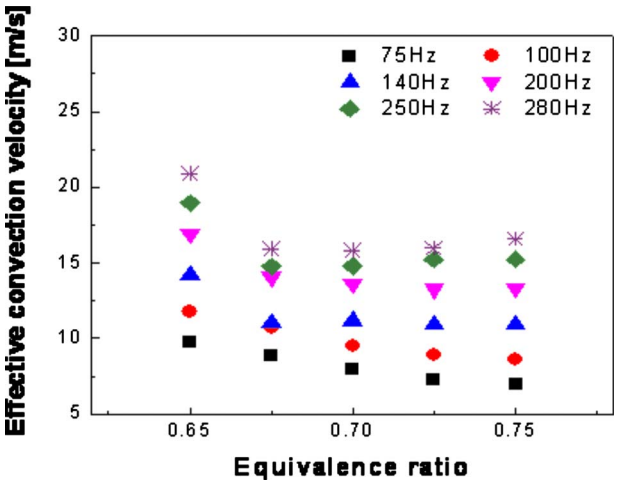

Fig. 11 Effective convection velocity as a function of modulation frequency and equivalence ratio ($V_{mean,nozzle}$=30 m/s and V'/V_{mean}=0.07)

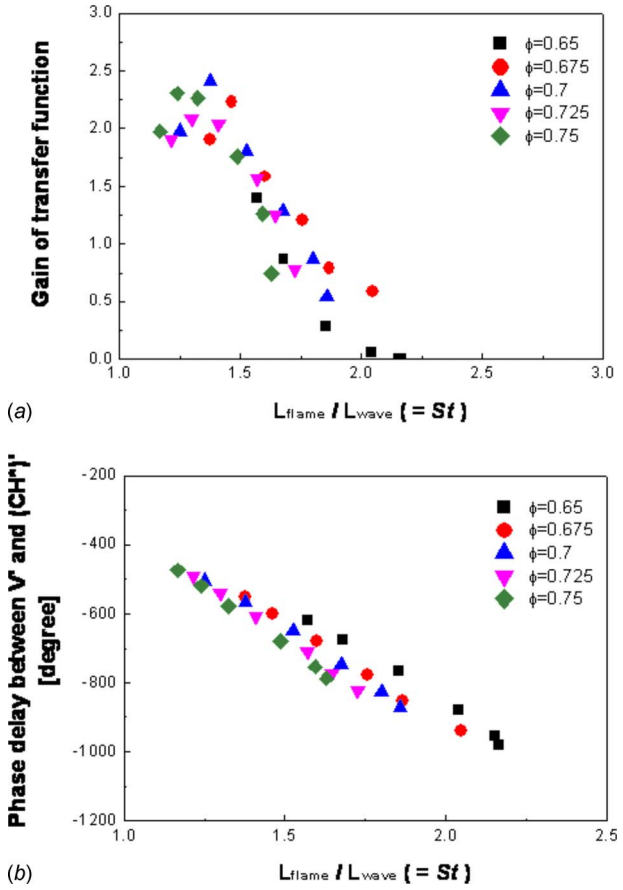

Fig. 12 (*a*) Gain and (*b*) phase of the transfer function versus Strouhal number ($V_{mean,nozzle}$=30 m/s and V'/V_{mean}=0.07)

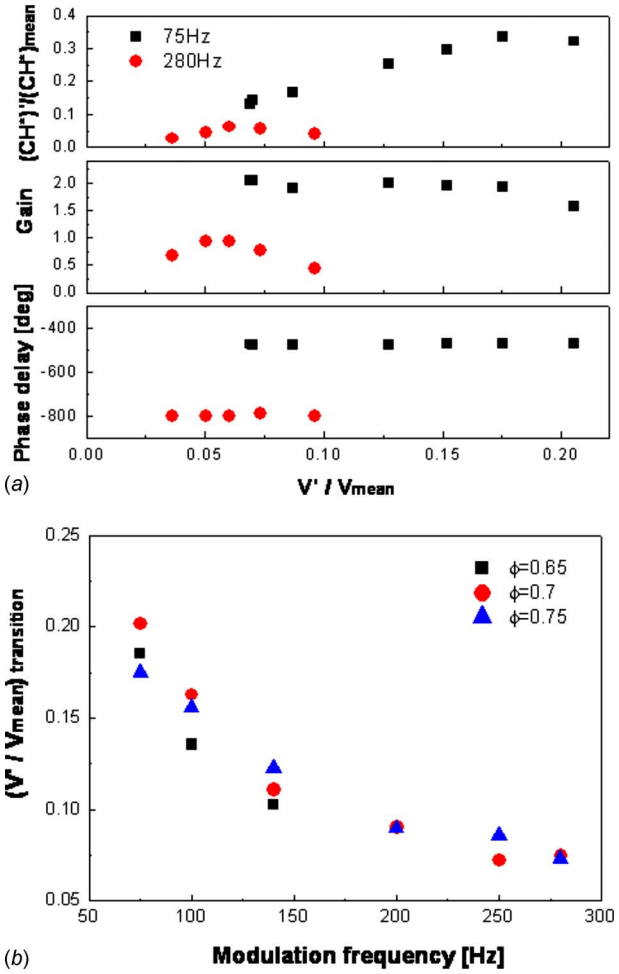

Fig. 13 (*a*) Normalized amplitude of CH^* fluctuation, gain, and phase of the transfer function as a function of modulation amplitude for $V_{mean,nozzle}$=30 m/s and ϕ=0.75 and (*b*) magnitude of V'/V_{mean} at which the flame response changes from linear to nonlinear as a function of modulation frequency

3.3 Effect of the Magnitude of Inlet-Velocity Fluctuation on the Flame Transfer Function: Nonlinear Flame Response. Nonlinear response of flame to inlet-velocity perturbation is another important subject to understand the mechanism of combustion-driven oscillation. Figure 13(*a*) shows the dependence of transfer function on the inlet-velocity fluctuation amplitude at two different modulation frequencies (f=75 Hz and 280 Hz). Normalized CH^*-chemiluminescence intensity increases and then start to saturate with increasing amplitude of inlet-velocity perturbation (V'/V_{mean}). The amplitude of inlet-velocity fluctuation at which the flame response becomes nonlinear for the 280 Hz modulation case is lower than that of the 75 Hz modulation case: For the latter the gain is almost constant up to V'/V_{mean} $\sim$17%, beyond which it slightly decreases but for the former, the gain starts to decrease when V'/V_{mean} becomes over 7%. Previous analytical work [15] predicts that nonlinearity is enhanced with increasing Strouhal number. Similar observations are reported by some experimental works [7,8] where the inception of nonlinear flame response is often manifested by the occurrence of the rollup of the shear layer into vortices or flame liftoff, which reduces the flame area. In the present study, the nonlinear response of the flame is related to the vortex shedding from the shear layer, as shown in Fig. 9. Even though the gain decreases as V'/V_{mean} increases, the phase is almost constant over the entire range of inlet-velocity fluctuation. Figure 13(*b*) shows a plot of $(V'/V_{mean})_{transition}$ (the magnitude of V'/V_{mean} at which the flame response changes from linear to nonlinear) as a function of modulation frequency. As the modulation frequency increases, the nonlinearity occurs at lower V'/V_{mean}. However, for a given modulation frequency, $(V'/V_{mean})_{transition}$ does not appear to be affected much by flame structure.

4 Conclusions

The transfer function of premixed flames submitted to inlet-velocity perturbation is measured experimentally for turbulent flames running in practical gas turbine combustor. Flame structure is characterized under inlet-velocity perturbation, and its effect on transfer function is investigated.

Flame images show that the effective flame location gets closer to the combustor inlet with increasing modulation frequency at a given equivalence ratio. For a fixed equivalence ratio, the gain of the transfer function decreases and the absolute magnitude of the phase increases as the modulation frequency increases. And, their detailed relationships are affected by flame structure: For a fixed modulation frequency, the gain increases and the absolute magnitude of the phase decreases as the equivalence ratio increases. The gain and phase of the transfer function are well represented by the Strouhal number, strongly suggesting that the flame dynamics for different operating conditions and modulation frequencies could be generalized in terms of the relative length scale of the flame to the convection length scale of the inlet-velocity perturbation.

As the magnitude of inlet-velocity fluctuation increases, the gain starts to decrease but the phase is almost constant over the entire range of inlet-velocity fluctuation. This nonlinear flame response is characterized by a periodic vortex shedding from the shear layer. As the modulation frequency increases, the nonlinearity occurs at lower magnitude of inlet-velocity fluctuation. How-

ever, for a given modulation frequency, the flame structure does not affect the magnitude of inlet-velocity fluctuation at which the nonlinearity starts.

References

[1] Candel, S. M., 1992, "Combustion Instabilities Coupled by Pressure Waves and Their Active Control," Proc. Combust. Inst., **24**, pp. 1277–1296.

[2] Keller, J. J., 1995, "Thermoacoustic Oscillations in Combustion Chambers of Gas Turbines," AIAA J., **33**(12), pp. 2280–2287.

[3] Dowling, A. P., 1999, "A Kinematic Model of a Ducted Flame," J. Fluid Mech., **394**, pp. 51–72.

[4] Lieuwen, T., 2003, "Modeling Premixed Combustion-Acoustic Wave Interactions: A Review," J. Propul. Power, **19**(5), pp. 765–781.

[5] Armitage, C. A., Balachandran, R., Mastorakos, E., and Cant, R. S., 2006, "Investigation of the Nonlinear Response of Turbulent Premixed Flames to Imposed Inlet Velocity Oscillations," Combust. Flame, **156**, pp. 419–436.

[6] Sengissen, A. X., Van Kampen, J. F., Huls, R. A., Stoffels, G. G. M., Kok, J. B. W., and Poinsot, T. J., 2007, "LES and Experimental Studies of Cold and Reacting Flow in a Swirled Partially Premixed Burner With and Without Fuel Modulation," Combust. Flame, **150**, pp. 40–53.

[7] Balachandran, R., Ayoola, B. O., Kaminski, C. F., Dowling, A. P., and Mastorakos, E., 2005, "Experimental Investigation of the Nonlinear Response of Turbulent Premixed Flames to Imposed Inlet Velocity Oscillations," Combust. Flame, **143**, pp. 37–55.

[8] Bellows, B. D., Bobba, M. K., Seitzman, J. M., and Lieuwen, T., 2007, "Nonlinear Flame Transfer Function Characteristics in a Swirl-Stabilized Combustor," ASME J. Eng. Gas Turbines Power, **129**(4), pp. 954–961.

[9] Birbaud, A. L., Durox, D., Ducruix, S., and Candel, S., 2007, "Dynamics of Confined Premixed Flames Submitted to Upstream Acoustic Modulations," Proc. Combust. Inst., **31**, pp. 1257–1265.

[10] Külsheimer, C., and Büchner, H., 2002, "Combustion Dynamics of Turbulent, Swirling Flows," Combust. Flame, **131**, pp. 70–84.

[11] Truffin, K., and Poinsot, T., 2005, "Comparison and Extension of Methods for Acoustic Identification of Burners," Combust. Flame, **142**, pp. 388–400.

[12] Bellucci, V., Schuermans, B., Nowak, D., Flohr, P., and Paschereit, C. O., 2005, "Thermoacoustic Modeling of a Gas Turbine Combustor Equipped With Acoustic Dampers," ASME J. Turbomach., **127**, pp. 372–379.

[13] Dowling, A. P., 1997, "Nonlinear Self-Excited Oscillations of a Ducted Flame," J. Fluid Mech., **346**, pp. 271–290.

[14] Lieuwen, T., 2005, "Nonlinear Kinematic Response of Premixed Flames to Harmonic Velocity Disturbances," Proc. Combust. Inst., **30**, pp. 1725–1732.

[15] Schuller, T., Durox, D., and Candel, S., 2003, "A Unified Model for the Prediction of Laminar Flame Transfer Functions: Comparisons Between Conical and V-Flame Dynamics," Combust. Flame, **134**, pp. 21–34.

[16] Dasch, C. J., 1992, "One-Dimensional Tomography: A Comparison of Abel, Onion-Peeling, and Filtered Backprojection Methods," Appl. Opt., **31**(8), pp. 1146–1152.

Determination of the Instantaneous Fuel Flow Rate Out of a Fuel Nozzle

Tongxun Yi[1]
e-mail: tzy1@psu.edu

Domenic A. Santavicca

Department of Mechanical and Nuclear Engineering,
Pennsylvania State University,
University Park, PA 16802

Reported is a practical method for accurate and fast determination of the instantaneous fuel flow rate out of a fuel injector. Both gaseous and liquid fuels are considered. Unsteady fuel flow rates introduced into a combustor can be caused by both self-excited pressure pulsations and fuel modulations. During combustion instability, the air flow rate into a combustor also varies in response to pressure pulsations. Accurate determination of the instantaneous fuel and air flow rates is important for both modeling and control of combustion instability. The developed method is based on the acoustic wave theory and pressure measurements at two locations upstream of a fuel injector. This method bypasses the complexities and nonlinearities of fuel actuators and fuel nozzles, and works for systems with slow-time-varying characteristics. Acoustic impedance of a gaseous fuel nozzle is found to be a function of multivariables, including the forcing frequency, the acoustic oscillation intensity, and the mean fuel flow rate. Thus, it is not an intrinsic property of the fuel injector alone. In the present study, sharp tubing bending with almost zero radii is found to have minimal effects on the distribution of 1D acoustic wave. This is probably because vortex shedding and recirculation at tubing corners do not alter the globally 1D characteristics of acoustic wave distribution. Different from the traditional two-microphone method, which determines the acoustic velocity at the middle locations of the two microphones, the present method allows the acoustic velocity, the acoustic mass flux, and the specific acoustic impedance to be determined along the fuel tubing or an air pipe. [DOI: 10.1115/1.3155784]

1 Introduction

Industrial gas turbines are typically fueled with natural gas and/or syngas, and the fuel injection ports are usually not choked. Acoustic oscillations in a combustor introduce unsteady fuel and air flow rates into the burner, resulting in heat release rate perturbations. During self-excited combustion instability, the instantaneous air flow rate into a combustor also varies in response to pressure pulsations. In some cases, feedback between pressure and heat release oscillations may become in phase, resulting in self-excited, large-amplitude, pressure pulsations. Accurate determination of the instantaneous fuel flow rate out of a fuel injector and the instantaneous air flow rate into a combustor is important for both root-cause analysis and active control of combustion instability. A literature review reveals that systematic investigations of this problem are rather scarce.

In this study, the gaseous fuel injector is simulated by an orifice plate. Local hydrodynamics and acoustical properties of a practical fuel injector may be somewhat different from those of an orifice plate. However, the dominant features of the discharge coefficient and acoustics/vortex interactions at the fuel injection ports are well kept. Many previous investigations focus on acoustic energy dissipation across an orifice at zero mean flow. During acoustic excitation, a finite dynamic vena contracta region is formed upstream and downstream of the orifice [1], and this region oscillates back and forth with the forcing cycle. This is particularly true if the amplitude of acoustic velocity exceeds the mean velocity. Across the orifice, a portion of acoustic energy is dissipated by the vortex ring formation. Hersh and Rogers [2] showed that, around the orifice, flow is spherical, unsteady, and incompressible (to a first approximation). At low sound intensity, the orifice reactance is directly related to the inertia of the oscillatory mass around the orifice. At high sound intensity, nonlinearity in acoustic impedance appears. A classical formula for acoustic energy dissipation caused by acoustics-excited vorticity generation is given by Howe [3]. The acoustic energy dissipation rate is proportional to the cross product of the acoustic particle velocity and the vorticity field. Different from previous investigations, the present paper focuses on the determination of the instantaneous fuel flow rate out of a fuel injector. Acoustic energy dissipation and reflection at the orifice are not the main interests of this study. However, they do affect the acoustic oscillation amplitude and the instantaneous fuel flow rate.

The unsteady velocity can be measured using hot wires or the two-microphone method [4]. But neither pressure sensors nor hot wires can be installed immediately upstream of a fuel nozzle because of the harsh environment, limited space, and flow interference. Acoustic mass flux measured at a location upstream of a fuel nozzle may differ substantially from that across the fuel nozzle. This is particularly true at higher frequency since the acoustic wavelength is shorter. Without knowing dynamic pressure immediately upstream of the fuel injector, even if acoustic impedance were known, one still could not determine the instantaneous fuel flow rate. Fluid dynamics within fuel tubing is mainly acoustical. However, near area discontinuities, such as around the fuel injectors, the fuel actuators, and sharp turning corners, hydrodynamics associated with flow inhomogeneities and acoustics/vortex interactions may not be negligible. Pressure within these regions may be still dominated by the acoustical mode, but the velocity field can be jointly determined by the acoustical and the vortical modes [5]. Density variations can be neglected if low Mach number and negligible heat transfer are assumed.

The instantaneous liquid fuel flow rate out of a fuel nozzle has been measured using a patternator consisting of a rotating disk, which is synchronized with the fuel modulation cycle [6,7]. This approach is not suitable for gas turbine applications and is semi-quantitative. Based on the pressure drop across an orifice plate upstream of the fuel injector, the instantaneous fuel flow rate can

[1]Corresponding author.

Manuscript received October 16, 2008; final manuscript received March 23, 2009; published online October 30, 2009. Review conducted by Nader Rizk.

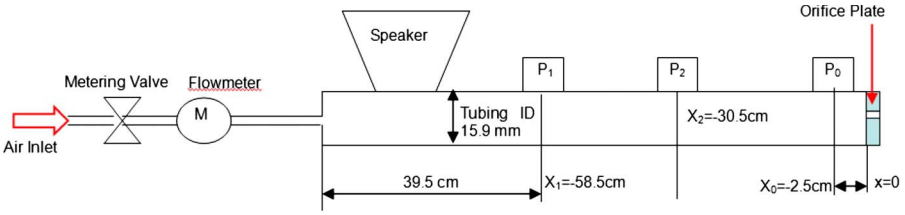

Fig. 1 Acoustic experiment setup

be determined, say, by treating the orifice as a purely resistive element [8,9]. However, the determined instantaneous liquid fuel flow rate is for the locations of pressure measurements, which is a good approximation to that across the fuel nozzle only for low-frequency fuel modulations and short tubing between the fuel injector and the fuel nozzle. In the case of high-frequency fuel modulations and long tubing between the fuel injector and the fuel nozzle, the determined instantaneous fuel flow rate across the orifice may differ considerably from that out of the fuel nozzle. In addition, in gas turbine engines, pressure cannot be measured immediately upstream of the fuel nozzle. The instantaneous velocity and the size of the droplets at a plane downstream of the fuel nozzle can be measured using phase-locked phase Doppler anemometry (PDA) measurements at a number of points. But the integrated instantaneous fuel flow rate may differ substantially from that across the fuel nozzle in both phases and amplitude, as it is known PDA measurements are not suitable for dense sprays.

This paper is organized as follows. First, the experimental setup is described. Second, methods for determining the acoustic wave distribution along the fuel tubing are developed, and accuracy is demonstrated. Third, methods for determining the instantaneous mass flux out of a fuel injector are presented. Fourth, acoustic impedance of a fuel injector at different forcing frequencies, acoustic oscillation intensities, and mean flows is reported. Lastly, extension of the present method to determine the instantaneous fuel flow rate out of a liquid fuel nozzle is discussed.

2 Experiment Setup

Figure 1 shows the experimental setup. Stainless steel tubing with an outside diamer (m) (OD) of 15.9 mm and a wall thickness of 1.6 mm is tightly fixed to a damping table from Newport Corp. (Irvine, CA), using six vibration-damping clamps. The fuel injector is simulated using an orifice plate with a thickness of 1.3 mm and a center hole with a diameter of 2.64 mm. Three high-sensitivity pressure sensors (PCB106B52, nominal sensitivity 5000 mV/psi) are used for pressure measurements. By measuring the same pressure field using the three pressure sensors, it is found that at some frequency, the measured amplitude can differ up to 3% and the phase can differ up to 4 deg. The differences in frequency responses have been considered during data analysis. Acoustic wave is generated using a 125 W speaker and a stereo amplifier. Input signals to the stereo amplifier are generated using a DS345 function generator from Stanford Research Systems (Sunnyvale, CA). A linear air flow meter (measurement uncertainty 5%) and metering valve are used to control the mean flow rate across the orifice. Here, compressed air from a constant-pressure reservoir is used. Acoustic data are sampled using a PCI-6221 DAQ board from National Instruments (Austin, TX), and the sampling frequency is 5 kHz. The data sampling time is 10 s. fast Fourier transform (FFT) analysis is performed for each 5000 samples, and acoustic impedance is obtained by averaging the results for the ten data segments. With the nonzero mean flow across the orifice, pressure signal is contaminated by broadband background noises, which is especially true at low forcing amplitude. But even at the lowest forcing amplitude, which is 0.8 V, the signal-to-noise ratio (SNR) of pressure at the three locations is still above 18 dB. In addition, variations in the measured pressure amplitude are within 1.0% during the same forcing experiment.

3 Determination of Acoustic Wave Distribution

1D linear acoustic wave within the fuel tubing is assumed, since the acoustic wavelength below 1 kHz is much larger than the tubing diameter. In the case of large-amplitude fuel modulations, particularly at high frequency, the 1D nonlinear wave equations accounting for nonlinear acoustics and viscous shear stress should be used. A simple method for validating linear acoustics is to compare measurements with linear prediction. Acoustic dissipation caused by viscous shear stress can be accounted for using the formula suggested in Ref. [10]. However, we find that there is almost no improvement in acoustic wave determination by considering viscous shear stress. This is probably because the thickness of the acoustic boundary layer is negligibly small compared with the tubing diameter. At the forcing frequency of 200 Hz, the acoustic boundary layer thickness is estimated as $O(\sqrt{\nu/F}) \approx 2.6 \times 10^{-4}$ m, which is a tiny fraction of the tubing diameter. Acoustic wave within fuel tubing can be expressed as follows:

$$\tilde{P}(x,t) = \hat{P}(x)e^{i\omega t} = Ae^{i(\omega t - kx/(1+M))} + Be^{i(\omega t + kx/(1-M))}$$
$$\tilde{U}(x,t) = \hat{U}(x)e^{i\omega t} = \frac{1}{\overline{\rho c}}[Ae^{i(\omega t - kx/(1+M))} - Be^{i(\omega t + kx/(1-M))}] \tag{1}$$

The complex amplitude of the downstream- and upstream-propagating waves can be uniquely determined from pressure measurements at two upstream locations:

$$A = \frac{\hat{P}_2 e^{ik(x_2/(1+M)+2x_1/(1-M^2))} - \hat{P}_1 e^{ik(x_1/(1+M)+2x_2/(1-M^2))}}{e^{ik[2x_1/(1-M^2)]} - e^{ik[2x_2/(1-M^2)]}}$$
$$B = \frac{\hat{P}_1 e^{ik[x_1/(1+M)]} - \hat{P}_2 e^{ik[x_2/(1+M)]}}{e^{ik[2x_1/(1-M^2)]} - e^{ik[2x_2/(1-M^2)]}} \tag{2}$$

As will be shown later in this paper, A and B change with the mean air flow rate, the fuel modulation frequency, the acoustic oscillations intensity, and the acoustic boundary conditions. The specific acoustic impedance along the fuel tubing is determined as

$$\tilde{R}(x) = \overline{\rho c}\frac{Ae^{-i[kx/(1+M)]} + Be^{i[kx/(1-M)]}}{Ae^{-i[kx/(1+M)]} - Be^{i[kx/(1-M)]}} \tag{3}$$

Equations (2) and (3) become singular if $x_1 \to x_2$ and $k(x_1 - x_2)/1-M^2 \to -m\pi$, where m is a positive integer. Sensor spacing should be carefully selected to avoid singularity within the interested frequency range. For acoustic measurements within a wide frequency range, multiple sensors should be installed, and a least-mean-square algorithm can be used to determine A and B.

Figure 2 shows the measured and predicted pressure 2.5 cm upstream of the fuel injector for both straight and bending tubings. For both tests, the average error is within 4% in pressure amplitude and within 5.5 deg in phases. The errors may be associated with the uncertainties of pressure sensors, sound speed, and measurement locations, but the major error source is believed to be

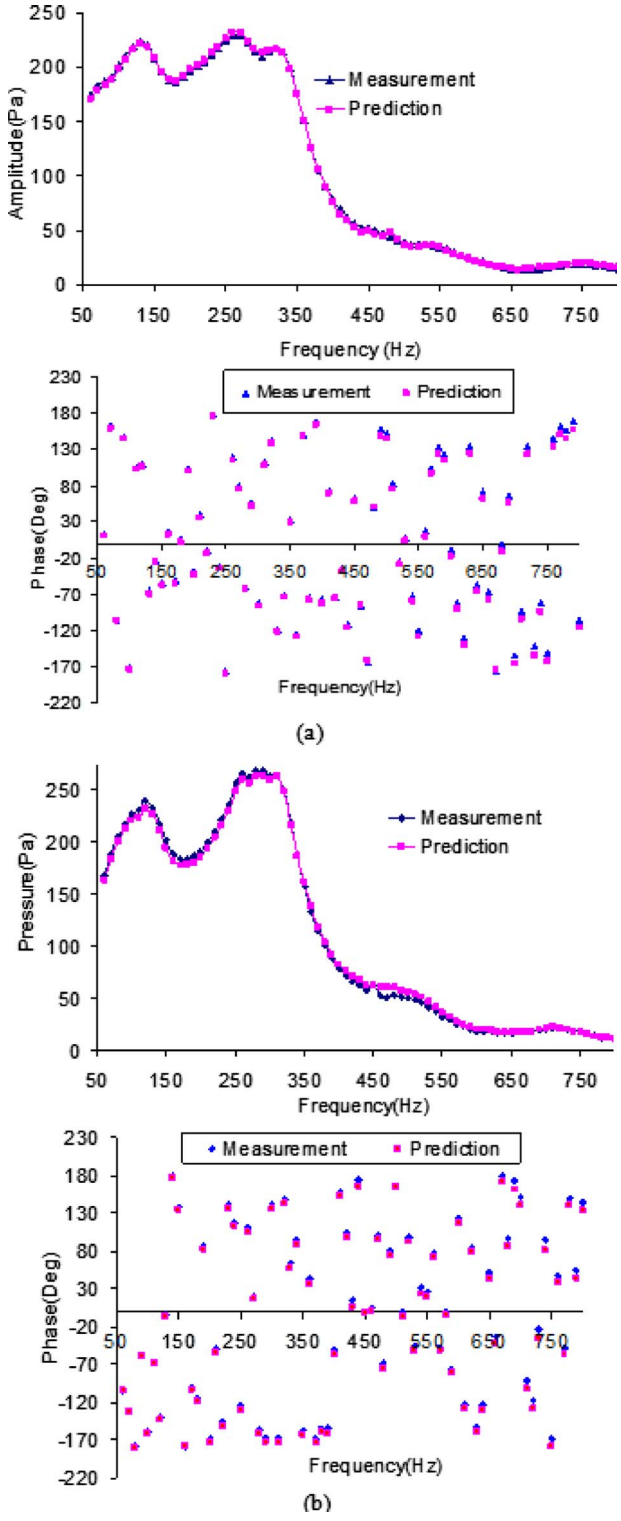

Fig. 2 Measured and predicted pressure 2.5 cm upstream of the fuel injector. (*a*) Straight tubing (0.98 m); (*b*) bending tubing with two 90 deg sharp turns with zero radii (1.02 m). For both tests, the air flow rate is 50.9 SLPM, and the forcing input amplitude is 1.8 V.

associated with sound distortion at sensor mounting locations. The tubing internal diameter (ID) is 12.7 mm, while the diaphragm diameter of pressure sensors is 15.7 mm. Around the sensor mounting locations, substantial sound diffraction exists. We have tried recess mounting to minimize sound distortion, but the gap between the sensor diaphragm and the recess hole makes acoustic correction at different frequencies and sound intensities even more challenging. In fact, the results are much worse than those shown in Fig. 2. We tend to believe that a 4% error in the predicted pressure amplitude and a 5.5 deg error in phases should be acceptable for engineering application. In gas turbine engines, fuel tubing bending is common; thus a reliable method for accurate determination of the instantaneous fuel flow rate should also be applicable to fuel modulations along bending tubings. Figure 2(*b*) shows that, without accounting for acoustic energy dissipation at tubing bending corners, pressure immediately upstream of the fuel nozzle can still be well determined. This is probably because acoustics/shear-layer/vortex interactions around tubing corners are highly localized and do not alter the global 1D characteristics of acoustic wave distribution. However, with tubing bending, some discernible differences in pressure amplitude below 350 Hz are observed. Note that the tubing length for Fig. 2(*b*) is 0.04 m longer than that for Fig. 2(*a*). To create tubing bending, we used two 90 deg elbow unions from Swagelok (Pittsburgh, PA), instead of directly bending the tubing using a tubing bender. The elbow unions have almost zero radii at the turning corners, while the minimum radius one can achieve using a tubing bender is 0.05 m. The two 90 deg bendings are installed between x_2 and x_0. The distance between x_1 and x_2 is shortened from 0.28–0.17 m, and that between x_2 and x_0 is increased from 0.28–0.43 m. Results reported in Fig. 2 are based on a sample length of 1 s.

4 Determination of the Instantaneous Fuel Flow Rate

Although the assumption of 1D acoustics within fuel tubing is generally valid, flow field immediately upstream of a fuel injector may considerably deviate from this assumption because of flow area discontinuities and possible vortex formation and shedding. Thus, the acoustic mass flux immediately upstream a fuel injector is not well defined. In addition, as will be shown later in this paper, acoustic impedance of a fuel injector is a function of multiple variables, including the forcing frequency, acoustic oscillation intensity, and mean flow. This implies that even if dynamic pressure immediately upstream of a fuel nozzle were known, it is still challenging to accurately determine the instantaneous fuel flow rate. Here, we bypass the concept of acoustic impedance and determine the instantaneous fuel flow rate based on acoustic wave prediction. The procedures are quite straightforward.

- Determine the acoustic mass flux $\dot{m}_i'(t)$ at a short distance, say, x_c upstream of the fuel injector. We recommend that the minimum x_c should be one internal diameter of the fuel tubing. It is conjectured that, at this location and further upstream, the effects of vortical motion and 3D hydrodynamics have decayed to be negligible. The acoustic mass flux at x_c is determined as $\dot{m}_i'(t)=\bar{\rho}A_t\,\mathrm{Re}(\tilde{U}_c(t))$, where $\tilde{U}_c(t)$ denotes the acoustic velocity at $x=x_c$.
- Determine the mass changing rate within the control volume from x_c to the fuel injector. We assume the internal flow passage of the fuel injector is negligibly small. According to Ref. [5], for low Mach number flow, density variations are mainly associated with the entropical and acoustical modes. By assuming a lump model and neglecting heat transfer, the mass changing rate within this control volume is determined as

$$\frac{dM_c}{dt}=A_t x_c\frac{d\rho_c'}{dt}=\frac{A_t x_c}{\bar{c}^2}\frac{dp_c'}{dt} \tag{4}$$

- Based on mass conservation, the instantaneous fuel flow rate out of the fuel injector $\dot{m}_e'(t)$ can be determined as

$$\dot{m}_e'(t)=\dot{m}_i'(t)-\frac{dM_c}{dt}=A_t\bar{\rho}\left[\mathrm{Re}(\tilde{U}_c(t))-\frac{x_c}{\bar{\rho}\bar{c}^2}\frac{dp_c'}{dt}\right] \tag{5}$$

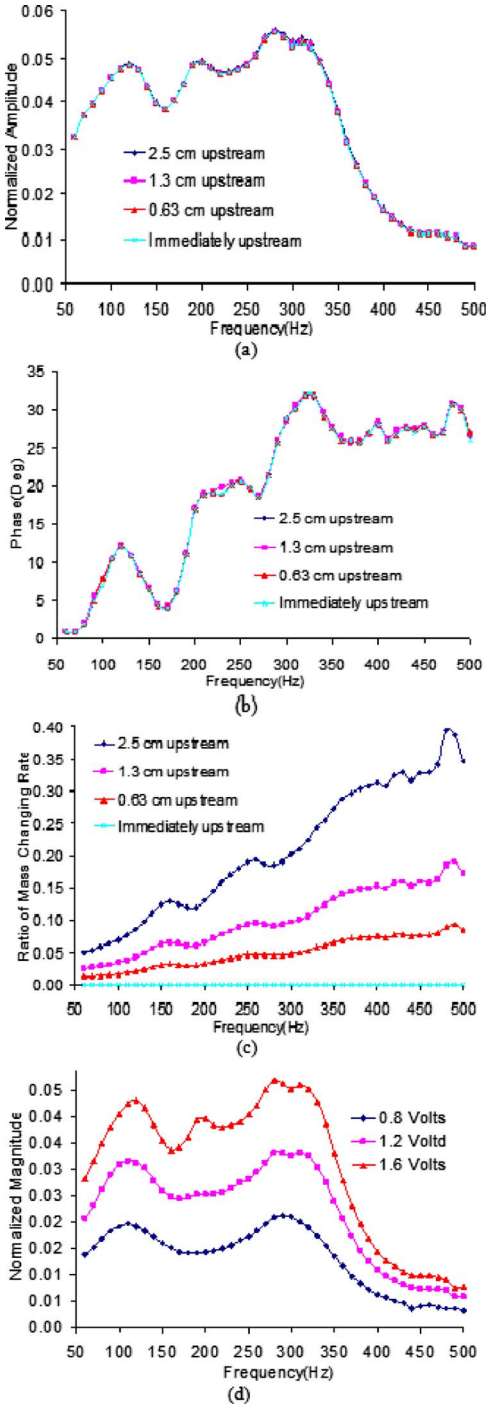

Fig. 3 (*a*) Normalized amplitude of the instantaneous mass flux; (*b*) phase lag between the instantaneous mass flux and pressure at $x_0=-2.5$ cm; (*c*) ratio of the mass changing rate to the inflow acoustic mass flux; and (*d*) normalized amplitude of the instantaneous mass flux at different forcing input amplitudes, namely, 0.8 V, 1.2 V, and 1.6 V

Figure 3 shows the amplitude of the instantaneous fuel flow rate oscillations and their phase lag from acoustic pressure measured at $x_0=-2.5$ cm. Here the mass flux is normalized by the mean flow, i.e., 50.9 SLPM. The forcing input amplitude is 1.8 V. We find that, with x_c at -2.5 cm, -1.3 cm, -0.63 cm, and immediately upstream of the fuel nozzle, the computed mass flux differs little in both amplitude and phases. Also shown in Fig. 3 is the ratio of the mass changing rate to the acoustic mass flux at the upstream boundary of the control volume. The mass changing rate

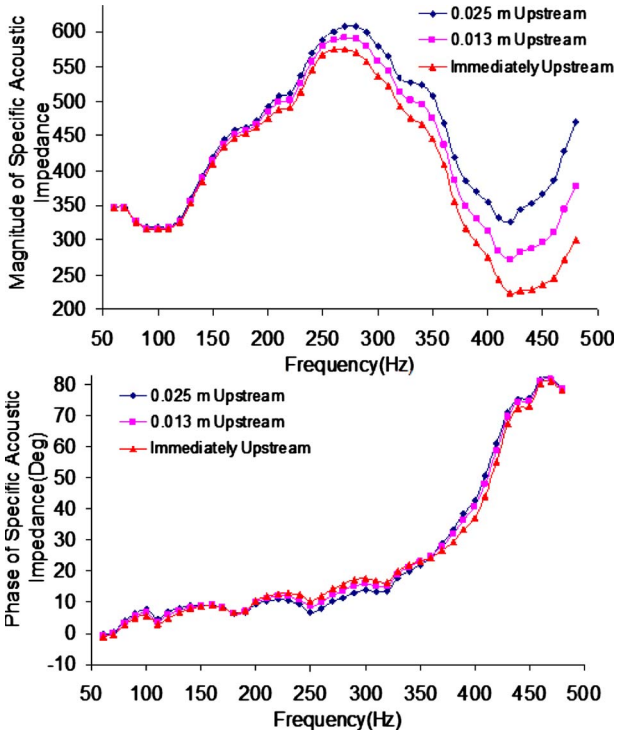

Fig. 4 Spatial distribution of specific acoustic impedance (forcing input amplitude of 1.8 V and zero mean flow)

is roughly proportional to the size of the control volume, and it increases almost linearly with frequency. At $x_0=-2.5$ cm, the mass changing rate can be more than 30% above 400 Hz. The phase lag between mass flux and pressure at $x_0=-2.5$ cm generally increases with frequency, which can be up to 30 deg above 350 Hz. Figure 3(*d*) shows the normalized amplitude of the instantaneous fuel flow rate at different input forcing amplitudes, namely, 0.8 V, 1.2 V, and 1.6 V. Here, $x_c=-1.3$ cm. With increasing acoustic oscillation intensity, the amplitude of the instantaneous mass flux increases. However, we can observe the nonlinearity between fuel modulation amplitude and the forcing input.

5 Characteristics of Specific Acoustic Impedance

Reported below are the characteristics of acoustic impedance of gaseous fuel nozzles. The specific acoustic impedance refers to the ratio of acoustic pressure to acoustic velocity. At the same forcing frequency, the acoustic impedance changes with axial locations. The real part of acoustic impedance represents the resistive nature of a fuel injector, such as that of an electrical resistor. The imaginary part represents the characteristics of a reactive element, such as an electrical inductor, a mass point, or a spring.

5.1 Special Distribution of Specific Acoustic Impedance. Figure 4 shows the specific acoustic impedance 2.5 cm, 1.3 cm, and immediately upstream of the fuel injector. There is no mean flow across the orifice. Differences in the magnitude of the specific acoustic impedance increase with frequency. This is due to the fact that for a fixed mass set into oscillation under acoustic forcing, the inertia increases roughly proportional to the frequency. Contrary to amplitude, the differences in phases among the three locations are rather small. This is due to the fact that within the frequency range under consideration, variations in acoustic pressure and velocity within a distance of 2.5 cm are just small. The phases of the specific impedance increase from 0 deg at 60 Hz to 80 deg above 450 Hz. This suggests that at zero mean flow, the fuel injector behaves like a purely resistive element at

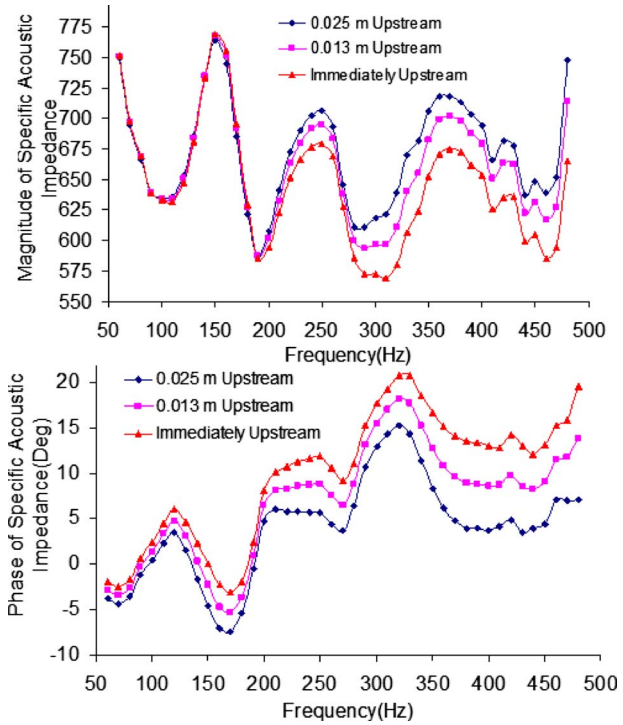

Fig. 5 Spatial distribution of specific acoustic impedance (forcing input amplitude of 1.8 V and mean flow of 50.9 SLPM)

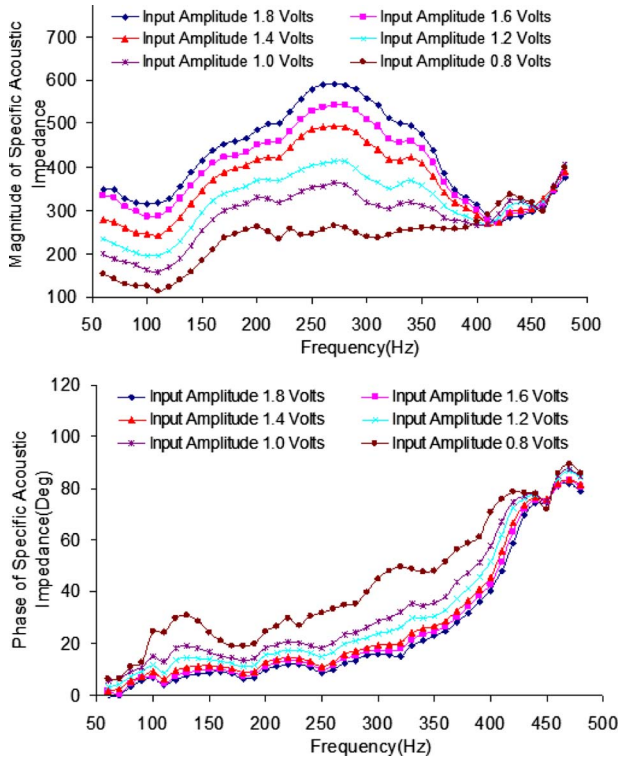

Fig. 6 Effects of forcing input on specific acoustic impedance (zero mean flow)

low frequency and a purely reactive element at high frequency.

However, the situation would be quite different if there is mean flow across the fuel injector, as shown in Fig. 5. The phases remain below 24 deg up to 450 Hz. This implies that in the presence of a relatively large pressure drop across a fuel injector, the dominant feature of the specific acoustic impedance is still resistive even at relatively high frequency. The differences in acoustic impedance at different fuel flow rates are associated with the hydrodynamic flow field, in particular, the size and pattern of the vena contracta region. At zero mean flow or very low flow rates, the dynamic vena contacta region is relatively large, since the amplitude of acoustic velocity can easily exceed the mean velocity. However, at relatively large mean flow rates, no flow reversal would occur, and the vena contracta region is smaller. In such cases, acoustic oscillations may just slightly deform the streamlines upstream of the orifice. By comparing Fig. 2(*a*) with Fig. 5, one can see that the peaks in the magnitude of the specific acoustic impedance correspond to the valleys in the acoustic oscillation amplitude, and vice versa. A tentative explanation will be given later. Note that except in Figs. 4 and 5, in other parts of this paper, the specific acoustic impedance refers to the location 2.5 cm upstream of the orifice plate.

5.2 Effects of Acoustic Oscillation Intensity. Figure 6 shows that at zero mean flow, the amplitude of the specific acoustic impedance increases with the acoustic intensity. This is due to the fact that at zero mean flow, in the presence of stronger acoustic oscillations, a larger vena contracta region is formed upstream and downstream of the orifice. The decrease in phases with acoustic intensity implies that, at zero mean flow, the growth rate of the resistive nature of fuel injectors with forcing amplitude somewhat outweighs that of the reactive nature. Probably this is due to the fact that with stronger acoustic oscillations across the orifice, acoustics-induced vorticity generation and acoustic energy dissipation are considerably enhanced. Note that acoustic energy losses are directly associated with the resistive nature of the acoustic impedance.

Figure 7 shows that, at a mean flow rate of 50.9 SLPM, the specific acoustic impedance is much higher than that at zero mean flow, while the phases are below 24 deg up to 500 Hz. Different from the case with zero mean flow, the magnitude of acoustic impedance decreases with acoustic intensity while the phase increases. The increase in phases with acoustic intensity can be explained by a larger mass set into oscillatory motion. But the

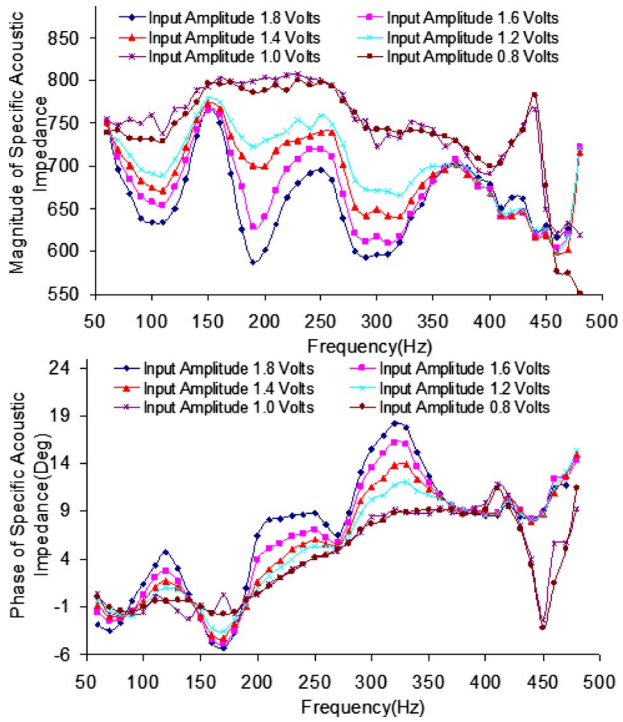

Fig. 7 Effects of forcing input on specific acoustic impedance (mean flow of 50.9 SLPM)

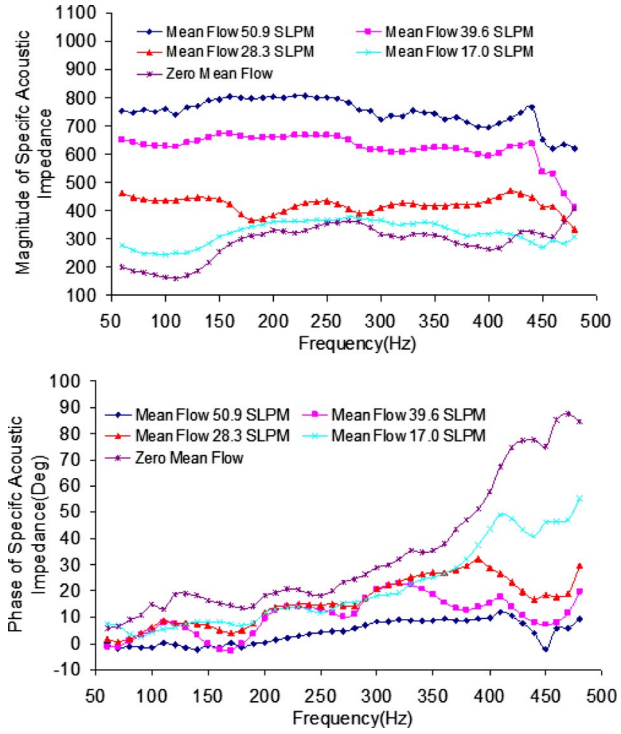

Fig. 8 Effects of mean flow on specific acoustic impedance (forcing input amplitude of 1.0 V)

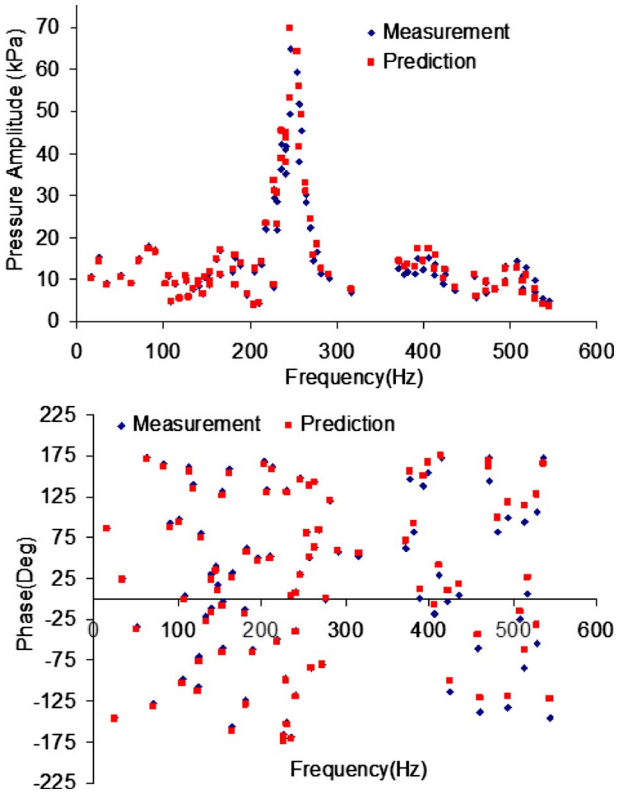

Fig. 9 Measurements versus prediction for dynamic pressure 0.04 m upstream of the fuel nozzle. The mean fuel pressure is 138 kPa. The sound speed is taken as 1100 m/s. Three pressure transducers are installed at 1.04 m, 0.57 m, and 0.04 m upstream of the fuel nozzle, respectively.

decrease in magnitude is less straightforward. This might be associated with acoustic streaming, which arises from viscosity and higher-order acoustics. Matta et al. [11] reported that sound-generated mean velocity along the speaker centerline can be up to 0.7 m/s, which is zero without speaker actuation. An analysis by Eckart [12] shows that the irrotational acoustic motion generates vorticity as a second-order effect, and the vortical motion will approach a steady state. The effect is somewhat similar to increased flow rates across an orifice plate at approximately the same pressure drop, resulting in smaller magnitude in acoustic impedance.

5.3 Effects of Mean Flow. Figure 8 shows the specific acoustic impedance at different mean flow rates with the same forcing input amplitude of 1.0 V. At larger flow rates, say, at 50.9 SLPM and 39.6 SLPM, the phases of the acoustic impedance are below 10 deg, indicating the resistive feature of the fuel injector. At the same forcing frequency, the phase lag decreases with the mean flow rate. At zero mean flow, the phase lag reaches almost 90 deg above 450 Hz. The magnitude of the acoustic impedance increases with mean flow. For a throttle valve working at low frequency or quasisteady states, the impedance is roughly proportional to the square root of the pressure drop.

6 Discussion

The developed method can be used to determine the acoustic velocity or mass flux along the fuel tubing, not necessarily immediately upstream of the fuel nozzle. In addition, it can be used to determine the acoustic velocity and mass flux in an air duct, such as the mixing tube of a gas turbine engine. Different from the traditional two-microphone method [4], which determines the acoustic velocity at the middle location between the two microphones, the present method allows the acoustic velocity, the acoustic mass flux, and the specific acoustic impedance to be determined along the fuel tubing or the air duct.

In gas turbine engines, a section of fuel tubing is immersed inside the compressed hot air; thus the sound speed will be higher than the other parts. Accuracy in determination of the instantaneous fuel flow rate can be improved by assuming a representative temperature for the hot section, and then linking this section with tubing outside the plenum, based on the continuity of acoustic pressure and flux. Accuracy may be further improved by considering several subsections.

Structural vibrations affect fuel pressure measurements, which is especially true if the pressure amplitude is small. In our experiments, fuel tubing is tightly fixed to a damping table using vibration-damping clamps.

The developed method can be extended to determine the instantaneous fuel flow rate out of a liquid fuel nozzle. In fact, we are more interested in determining liquid fuel modulations than gaseous fuel modulations. The sound speed of liquid fuel is a function of pressure, temperature, fuel species, wall elasticity, and bubbles. The sound speed in liquid hydrocarbons typically increases with pressure and wall elasticity, and decreases substantially with temperature and bubbles. The sound speed is usually above 1000 m/s at room temperature. In the presence of large pressure drop across a fuel nozzle, as is usually the case for liquid fuel injectors, acoustic impedance will be essentially resistive. Then it is possible to determine the instantaneous mass flow rate from pressure measurements at only one location upstream of the fuel nozzle. Figure 9 compares pressure measurements with prediction at 4.0 cm upstream of a single-point macrolaminated liquid fuel nozzle. Pressure is measured at three locations, and the sound speed of 1-decene is taken as 1100 m/s. The difference between measurements and prediction is less than 6% in amplitude and within 6 deg in phases. We find that even without accounting for nonlinear acoustic effects and viscous shear stresses, the developed method can well predict large-amplitude pressure oscillations up to 30% below 300 Hz. Detailed results are reported in Ref. [13].

7 Conclusions

A method is developed for accurate determination of the instantaneous fuel flow rate out of a gaseous fuel injector, which is based on 1D linear acoustic wave theory and pressure measurements at two locations upstream of the fuel injector. This method is advantageous to the traditional two-microphone method. With that, the acoustic velocity determination is not limited to the middle location of the two microphones.

Because of the 3D hydrodynamic effects and acoustics/vortex interactions, the acoustic mass flux immediately upstream of a fuel injector is not well defined. However, the instantaneous mass flux can be determined from a control volume approach. Numerically, the determined instantaneous mass flux is equal to the virtual "acoustic mass flux" immediately upstream of the fuel injector.

The specific acoustic impedance is determined by multiple factors, such as the oscillation frequency, pressure oscillation amplitude, and mean flow. With zero mean flow, the fuel injector behaves more like a reactive element at higher frequency and more like a resistive element at lower frequency. With increasing mean flow, the fuel injector behaves like a resistive element even at higher frequency. At larger mean flow, the magnitude of acoustic impedance increases, which is similar to the characteristics of a throttle valve working at low frequency.

The developed method can be extended to determine the instantaneous fuel flow rate out of a liquid fuel injector. The errors between pressure measurements and predictions are within 6% in amplitude and within 6 deg in phases. Even without accounting for nonlinear acoustic effects and viscous shear stresses, the developed method can well predict large-amplitude pressure oscillations up to 20% below 300 Hz.

The developed method has potential applications in gas turbine engines, where neither pressure sensors nor hot wires can be installed immediately upstream the fuel injectors. However, complexities in fuel manifolds and tubing branching should be considered according to Ref. [14].

Acknowledgment

Support from the NASA Glenn Research Center under Grant No. NNX07C98A, "Active Combustion Control for Low-Emission Combustors," is gratefully acknowledged. Dr. Clarence Chang is the project manager. This project is also supported by the U.S. Air Force Office of Scientific Research under Grant No. FA9550-07-1-0451, "Advanced Thermally Stable Coal-Based Jet Fuels."

Nomenclature

A and B = complex amplitude of the downstream- and upstream-propagating acoustic waves

A_t = internal flow area of the fuel tubing, m^2

$\bar{c}$ = mean sound speed, m/s

F = acoustic oscillation frequency, Hz

$k=\omega/\bar{c}$ = acoustic wave number

$\dot{m}_i'(t)$ = acoustic mass flux at the upstream boundary of the control volume

$\dot{m}_e'(t)$ = the instantaneous mass flux out of a fuel injector

$\bar{\dot{m}}$ = mean fuel flow rate out of a fuel injector

$M=\bar{u}/\bar{c}$ = mean flow Mach number

M_c = mass of fuel within the control volume

$\tilde{P}(x,t)$ = complex dynamic pressure

$\tilde{P}_0(x,t)$, $\tilde{P}_1(x,t)$, and $\tilde{P}_2(x,t)$ = complex pressure immediately upstream of a fuel nozzle and at two upstream locations, respectively

$p_c'(t)$ = acoustic pressure at x_c

$\tilde{R}$ = specific acoustic impedance

$\mathrm{Re}(\cdots)$ = the real part of a complex quantity

$\bar{u}$ = mean velocity, m/s

$\tilde{U}_c(t)$ = complex acoustic velocity at x_c, m/s

x_c = the upstream boundary of the control volume used for mass flux determination, m

$\bar{\rho}$ = mean density, kg/m^3

ν = kinematic viscosity, m^2/s

ω = fuel modulation frequency, Hz

References

[1] Cummings, A., 1984, "Acoustic Nonlinearities and Power Losses at Orifices," AIAA J., **22**(6), pp. 786–792.

[2] Hersh, A. S., and Rogers, T., 1975, "Fluid Mechanical Model of the Acoustic Impedance of Small Orifices," , AIAA Conference Paper AIAA-1975-495, pp. 75–495.

[3] Howe, M. S., 1980, "The Dissipation of Sound at an Edge," J. Sound Vib., **70**(3), pp. 407–411.

[4] Waser, M. P., and Crocker, M. J., 1984, "Introduction to the Two-Microphone Cross-Spectral Method of Determining Sound Intensity," Noise Control Eng. J., **22**(3), pp. 76–85.

[5] Chu, B. T., and Kovasnay, L. S. G., 1958, "Nonlinear Interactions in a Viscous, Heat Conducting, Compressible Gas," J. Fluid Mech., **3**, pp. 494–514.

[6] Stenzler, J. N., Lee, J. G., Deepe, J. M., and Santavicca, D. A., 2004, "Fuel Transfer Function Measurements in Modulated Liquid Jets," ASME 2004 International Mechanical Engineering Congress and Exposition, Paper No. IMECE2004-60673, pp. 31–40.

[7] Hoffman, J. A., 1999, "Mass-Related Properties of Transient Sprays," Ph.D. thesis, University of Wisconsin-Madison, Madison, WI.

[8] Barooah, P., Anderson, T. J., and Cohen, J. M., 2003, "Active Combustion Instability Control With Spinning Valve Actuator," ASME J. Eng. Gas Turbines Power, **125**, pp. 925–932.

[9] Yi, T., and Gutmark, E. J., 2007, "Dynamics of a High Frequency Fuel Actuator and Its Applications for Combustion Instability Control," ASME J. Eng. Gas Turbines Power, **129**, pp. 648–654.

[10] Kinsler, L. E., Frey, A. R., Coppens, A. B., and Sanders, J. V., 2000, *Fundamentals of Acoustics*, 4th ed., Wiley, New York.

[11] Matta, L. M., Zhu, C., Jagoda, J. A., and Zinn, B. T., 1996, "Mixing by Resonant Acoustic Driving in a Closed Chamber," J. Propul. Power, **12**(2), pp. 366–370.

[12] Eckart, C., 1948, "Vortices and Streams Caused by Sound Waves," Phys. Rev., **73**(1), pp. 68–76.

[13] Yi, T., and Santavicca, D. A., 2009, "Flame Transfer Functions and Their Applications to Combustion Control," ASME Paper No. GT2009-60181.

[14] Munjal, M. L., 1986, *Acoustics of Ducts and Mufflers With Application to Exhaust and Ventilation System Design*, Wiley, New York.

Gilles Bourque
Rolls-Royce Canada,
Montreal, H9P 1A5, Canada

Darren Healy

Henry Curran

Department of Chemistry,
National University of Ireland,
Galway, Ireland

Christopher Zinner

Danielle Kalitan

Department of Mechanical, Materials, and
Aerospace Engineering,
University of Central Florida,
Orlando, FL 32816

Jaap de Vries

Christopher Aul

Eric Petersen
Department of Mechanical Engineering,
Texas A&M University,
College Station, TX 77843

Ignition and Flame Speed Kinetics of Two Natural Gas Blends With High Levels of Heavier Hydrocarbons

High-pressure experiments and chemical kinetics modeling were performed to generate a database and a chemical kinetic model that can characterize the combustion chemistry of methane-based fuel blends containing significant levels of heavy hydrocarbons (up to 37.5% by volume). Ignition delay times were measured in two different shock tubes and in a rapid compression machine at pressures up to 34 atm and temperatures from 740 K to 1660 K. Laminar flame speeds were also measured at pressures up to 4 atm using a high-pressure vessel with optical access. Two different fuel blends containing ethane, propane, n-butane, and n-pentane added to methane were studied at equivalence ratios varying from lean (0.3) to rich (2.0). This paper represents the most comprehensive set of experimental ignition and laminar flame speed data available in the open literature for $CH_4/C_2H_6/C_3H_8/C_4H_{10}/C_5H_{12}$ fuel blends with significant levels of C2+ hydrocarbons. Using these data, a detailed chemical kinetics model based on current and recent work by the authors was compiled and refined. The predictions of the model are very good over the entire range of ignition delay times, considering the fact that the data set is so thorough. Nonetheless, some improvements to the model can still be made with respect to ignition times at the lowest temperatures and for the laminar flame speeds at pressures above 1 atm and at rich conditions. [DOI: 10.1115/1.3124665]

1 Introduction

Fuel-flexible gas turbine engines are presently of interest to the power generation and combustion research communities because variations in fuel composition are expected to increase. Such variations can be due to dissimilarities in the fuel source itself or to the advent of alternative fuels currently being developed at a fast pace. Varying fuel compositions of primary interest herein are the result of heavier hydrocarbons present in a methane-based fuel [1]. The additional hydrocarbons reside in the fuel blend as an additive or extender to a conventional fuel; as a fuel component already present in the fuel blend for various reasons; or as a fuel in its own right. One important physical parameter characterizing the chemistry of a fuel blend is its ignition delay time. This delay time is both a fundamental parameter for the development of detailed kinetics mechanisms and a practical constraint for premixed combustion. For example, residence times for premixed fuel-air compositions need to be below the mixture's autoignition time at a given temperature and pressure [2].

Additionally, the unsteady flame stretch and strain, related to the Markstein length and the Strouhal number, are known to play important roles in flame dynamics [3]. Since the Markstein length is markedly different for the different hydrocarbon species present in natural gas, the chemical kinetics modeling of the effect of natural gas composition on flame characteristics is important to understanding the flame dynamics leading to thermoacoustic instability in gas turbine combustion systems. Flame stretch is related to laminar flame speed, a fundamental parameter of a given mixture composition, stoichiometry, temperature, and pressure [4].

In a recent paper, the authors used a chemical kinetics mechanism to explore the ignition delay time and flame speed variations for a few specific natural gas blends at practical engine conditions [1]. Several studies have been performed in the past for methane-based fuel blend ignition [5–12], but most of these were at relatively low pressures and dealt with relatively small levels of hydrocarbon additives. More recently, the authors have been studying the effect of hydrocarbons on methane ignition in both shock tubes and rapid compression machines (RCMs) [13–18]. While the laminar flame speed of pure methane can be considered well known [19–22], there are few studies with laminar flame speed measurements of methane blends, particularly at elevated pressures and for 20% or more heavy hydrocarbons present in the fuel mixture [1]. Further details on related studies from the literature are presented in Refs. [1,13].

This paper addresses the topic of fuel-flexible natural gas combustion and extends the work presented in Ref. [1] to include an extensive combination of experimental data and kinetics modeling for natural gas blends with relatively large levels of heavy hydrocarbons. Table 1 presents the three target mixtures of interest, with mixtures NG2 and NG3—the two with less than 82% methane—being the focus of the present study. Ignition experiments from two different types of facilities, shock tube, and rapid compression machine, were performed at pressures between 1 atm and 30 atm for a range of temperatures between approximately 700 K and 1600 K. Details on the experiments and the corresponding results are presented and compared with a new chemical kinetics model

Contributed by the International Gas Turbine Institute of ASME for publication in the JOURNAL OF ENGINEERING FOR GAS TURBINES AND POWER. Manuscript received April 4, 2008; final manuscript received May 22, 2008; published online October 30, 2009. Review conducted by Dilip R. Ballal. Paper presented at the ASME Turbo Expo 2008: Land, Sea and Air (GT2008), Berlin, Germany, June 9–13, 2008.

Table 1 Mixture compositions in percent volume

Species	NG1 (%)	NG2 (%)	NG3 (%)
CH_4	98.125	81.25	62.5
C_2H_6	1.000	10.00	20.0
C_3H_8	0.500	5.00	10.0
nC_4H_{10}	0.250	2.50	5.0
nC_5H_{12}	0.125	1.25	2.5

designed specifically for methane-based fuel blends containing hydrocarbons with as many as five carbon atoms. High-pressure laminar flame speed experiments were also performed for NG2 and NG3, the results of which are presented below and compared with the predictions of the chemical kinetics model. No study was found in the literature that has covered such a thorough range of conditions, data type, mixture composition, and detailed kinetics modeling for natural gas blends, as presented in this paper.

2 Chemical Kinetics Model

The detailed chemical kinetic model is based on the hierarchical nature of hydrocarbon combustion mechanisms containing the H_2/O_2 submechanism, together with the CO/CH_4 and larger hydrocarbon submechanisms and is similar to, but not identical to that published in our previous work on methane/propane mixtures [14]. Some changes have been made and these are discussed here. We have adopted the rate constant of Hessler [23] for $H+O_2 \rightarrow O+OH$, but this has had little effect on the predictions. You et al. [24] recently reported on the rate constant for $CO+HO_2$, and we have adopted their value.

Recently, Srinivasan et al. [25] studied the reaction $CH_4+O_2 \rightarrow CH_3+HO_2$, and using both experimental results and calculations provided a rate constant in the temperature range 1655–1822 K. Jasper et al. [26] calculated a rate constant expression for $CH_3+HO_2 \rightarrow CH_3O+OH$, which we have also adopted. The rate constant expression for $C_2H_6+H \rightarrow C_2H_5+H_2$ was taken from GRI-MECH 3.0 [27].

Moreover, sensitivity analysis has shown that for the prediction of ignition delay times for methane, ethane, in particular, and propane fuels are very sensitive to the rate constant for the decomposition of ethyl radicals to ethylene and H atoms. We have adopted the rate constant expression recommended in GRI-MECH 3.0 [27], which is approximately a factor of 2 slower than the rate constant in our previous paper [14].

Rate constants for the C4 and C5 submechanisms are based on the reaction rate rules presented in the work on the primary reference fuels published by Curran et al. [28,29]. In particular, the reaction rate rules specified in the iso-octane paper are those used here. The mechanism comprises 289 species and 1580 reactions.

Other minor changes have been made to the mechanism, but the preceding description details the most significant changes. A full listing of the mechanism together with thermochemical parameters and transport data are available on the NUI Galway combustion chemistry website.[1]

The Premix program from CHEMKIN [30] was used to simulate the adiabatic freely propagating laminar flame. At temperatures greater than about 1000–1250 K, depending on the pressure, addition of alkyl radicals to molecular oxygen is no longer important, with β-scission and isomerization of fuel alkyl radicals dominating the oxidation process. Thus, in simulating flame speed measurements we generated a "high-temperature" mechanism from the full detailed mechanism described above by removing the low-temperature chemistry, i.e., $iC_4H_9O_2$ radicals and their subsequent low-temperature reactions are not included in the flame speed simulations.

Also, no species diffusion is included in the simulation. Verification of this assumption on a subset of the results showed no noticeable effect on the final results. Gradient and curvature parameters were set to values on the order of 0.1 to ensure appropriate flame zone resolution and the insensitivity of the resulting laminar flame speed to these parameters.

3 Ignition Delay Times

Presented in this section are the methods and results for the measurement of ignition delay times. Brief overviews of the shock-tube and RCM apparatuses are given first, followed by a detailed summary of the resulting data. The measured ignition times are compared with the predictions of the kinetics model, and shock-tube data and RCM data are shown on the same plots when overlapping data sets are available.

3.1 Apparatus and Procedure. Two high-pressure shock-tube facilities were employed for the experiments detailed herein. Key features of the shock tube of the first facility are a driven section having a length of approximately 10.7 m (35 ft) and an inner diameter of 16.2 cm with a driver section 3.5 m in length and inner diameter of 7.62 cm. The shock tube of the second facility has a driven section with an inner diameter of 15.24 cm and a length of 4.72 m with a diver section 4.93 m long and inner diameter of 7.62 cm.

Both shock-tube facilities are configured for optimum test conditions behind reflected-shock waves, and both possess the capability for reflected-region pressures on the order of 100 atmospheres with untailored experimental test times approaching 3 ms. Conditions in the quiescent region behind the reflected shock are determined by one-dimensional shock relations and the incident-shock velocity. The velocity of the incident shock is obtained by use of timer counters (Fluke PM 6666) linked to a series of sequential pressure transducers (PCB 113) at locations in the shock tube near the endwall of the driven section.

The presence of chemical reactions in the reflected-shock region is detected by pressure transducers (PCB 134A and Kistler 603B1) and photomultiplier tubes (Hamamatsu 1P21) located at the endwall of the driven section and at a sidewall location 1 cm from the endwall. For optical diagnostics of CH^* chemiluminescence, CaF_2 windows are installed at both the sidewall and endwall locations, and the emission past each window is focused through a 430 ± 5 nm bandpass filter onto photomultiplier tubes mounted in custom-made hardware. Data acquisition is handled by GAGESCOPE data acquisition boards and software with sampling rates of at least 1 MHz per channel and 14 bit resolution. Further details on the experimental hardware, physical layout, auxiliary components, and diagnostics of the first shock-tube facility are presented in Ref. [31] and of the second shock-tube facility in Ref. [32].

The NUI Galway rapid compression machine has a twin-opposed piston configuration, which has been described previously by Affleck and Thomas [33], resulting in a fast compression time of approximately 16 ms. Creviced piston heads are used to improve the postcompression temperature distribution in the combustion chamber [34]. Full details of the machine are provided in a recent work performed on propane oxidation at high pressures and low temperatures [35].

Experiments were carried out at a compression ratio, defined as the ratio between the volume before compression and at the end of compression, of approximately 10:1. The "effective" compression ratio is lower using argon compared with nitrogen as diluent gas due to its higher thermal diffusivity. In order to vary the compressed gas temperature, T_C, the proportions of the diluent gases (N_2, Ar) were varied to alter the overall heat capacity of the fuel and "air" mixture. In addition, an electrothermal digitally controlled heating blanket surrounds the combustion chamber such

[1] http://c3.nuigalway.ie/naturalgas2.html.

Table 2 RCM ignition delay time data for NG2

T_C (K)	p_C (atm)	τ_{ign} (ms)	ϕ
848	29.56	144.00	0.5
841	28.57	148.00	
896	29.06	95.80	
892	28.66	91.70	
926	27.67	57.60	
925	28.24	53.60	
925	29.11	46.52	
984	29.16	13.29	
984	29.14	12.99	
1047	29.37	3.98	
1049	29.53	3.96	
985	19.19	31.66	
985	19.21	37.67	
984	19.14	33.35	
1039	19.23	7.90	
1041	19.35	8.23	
1096	19.00	2.79	
1096	19.04	3.29	
1021	9.21	48.10	
1026	9.37	46.32	
1080	9.21	9.73	
1073	9.03	9.23	
1126	9.29	3.96	
1130	9.40	4.11	
739	29.83	212.8	1.0
741	30.15	185.0	
780	29.54	145.5	
781	29.68	146.3	
816	27.37	145.0	
817	26.38	152.1	
852	27.89	146.0	
850	28.82	127.0	
857	29.61	106.0	
857	29.54	110.0	
912	29.04	34.8	
908	28.86	50.6	
938	28.45	21.9	
989	28.18	21.3	
908	19.30	129.4	
909	19.27	129.2	
938	18.04	60.9	
939	18.90	73.6	
940	18.99	65.6	
991	18.96	9.5	
989	19.10	9.4	
1046	18.95	3.6	
1047	19.00	3.8	
984	9.26	42.8	
979	9.34	21.4	
1036	9.53	11.2	
1040	9.41	11.21	

that the initial temperature may be varied up to a maximum operating temperature of 393 K. In this way, compressed gas temperatures in the range 680–1050 K were studied.

Pressure-time data were measured using a pressure transducer (Kistler 603B) and transferred via an amplifier to an oscilloscope where they were recorded. The ignition delay time, defined as the time from the end of compression to the maximum rate of pressure rise during ignition, was measured using two vertical cursors on the oscilloscope. In general, we found that the ignition delay times were reproducible to within 10% of one another at each T_C, Table 2. The compressed gas pressure was measured using two horizontal cursors.

The primary experimental data comprised of the pressure-time record, but it was more practical to assimilate and present the results in terms of the overall dependence of ignition delay on the compressed gas temperature, Table 2.

Heat losses are always a consideration in performing RCM experiments, becoming increasingly important when ignition delay times become longer. Thus, each experiment is simulated starting with the initial temperature, pressure and mixture composition, and the appropriate compression ratio chosen such that the simulated compressed gas pressure matches that measured experimentally. The constant-volume portion of the experiment is simulated as an adiabatic expansion, such that the simulated pressure profile again reproduces the experimental measurement. For a more detailed discussed of this modeling approach please see the propane work of Gallagher et al. [35].

3.2 Ignition Results. An extensive database of ignition delay times was obtained for the NG2 and NG3 fuel blends in air. For the shock-tube measurements, the undiluted fuel-air mixtures produced very clear pressure increases at the onset of ignition for every experiment. The pressure increases were indicative of strong ignition events and are similar in appearance to those presented in Refs. [13,14]. For such pressure traces, the definition of ignition delay time is unambiguous, providing uncertainties in the definition of ignition delay time of less than 10% and typically on the order of only a few percent for ignition times greater than about 50 μs. Although sidewall pressure and emission traces were also obtained, the endwall traces were used exclusively to define the ignition delay times presented in Table 3 because ignition occurs first at the endwall and also because ignition at a sidewall location appears accelerated because of the strong ignition wave that forms at the endwall and moves away from it. The CH^* chemiluminescence data corroborated the ignition times obtained from the pressure data, and no pre-ignition or early emission was seen for the range of conditions of the shock-tube experiments herein.

The analysis of the RCM data provided in Table 2 is as described above, and the definition of ignition delay time is similar to that described previously [35]. In short, the ignition time was defined at the inflection point between the test pressure achieved after compressing the mixture and the steep rise in pressure at the time of ignition.

Overall, the breadth of the conditions for the ignition delay time data set is quite extensive, covering a combined range between the RCM and shock-tube experiments from 739 K to 1667 K and from 0.7 atm to 33.9 atm. In general, the RCM data cover the lower-temperature range, while the shock-tube data cover the higher-temperature range. Fuel-to-air equivalence ratios (ϕ) of 0.3, 0.5, 1.0, and 2.0 were tested for both fuel mixtures. Each series of data within a similar grouping of pressure was compared with predictions from the chemical kinetics model described above. These calculations were performed using the Hydrodynamics, Chemistry and Transport (HCT) program [36] at conditions of constant volume and constant internal energy to model the pressure increase due to reaction.

Results for both shock-tube and RCM experiments are available for the NG2 blend for ϕ=0.5 and 1.0, shown in Figs. 1 and 2, respectively. For the lean results in Fig. 1, the RCM and shock-tube data align nicely for common pressures. Notable also is the good agreement between model and data over most of the temperature range. At the lowest temperatures for the 20 atm and 30 atm RCM data, the model underpredicts slightly the ignition delay times, but nevertheless the model reproduces the nonlinear trends seen in the data at the lowest temperatures and highest pressures. Similar trends are seen in Fig. 2 for the stoichiometric data among the two techniques and the model predictions.

Further comparisons between model and data for NG2 are shown in Figs. 3 and 4. For the leanest case, ϕ=0.3 in Fig. 3, the agreement between the model and shock-tube data is good, but some improvements can still be made at 8 atm and 30 atm. At the rich ϕ=2.0 condition in Fig. 4, the agreement between model and data is quite good, particularly at 15 atm.

Shock-tube ignition delay time data for NG3 are shown in Figs.

Table 3 Shock-tube ignition delay time data for NG2 and NG3

T (K)	p (atm)	τ_{ign} (μs)	ϕ
	Natural gas blend 2		
1099	18.6	1489	2.0
1173	17.4	768	
1263	15.8	395	
1434	13.3	86	
1549	11.9	39	
1151	8.0	2328	
1259	6.9	806	
1372	6.1	311	
1458	5.6	150	
1547	4.9	73	
1289	1.6	2199	
1374	1.5	854	
1398	1.4	676	
1434	1.3	469	
1511	1.2	241	
1594	1.1	119	
1667	1.0	74	
1051	33.9	1485	1.0
1107	30.6	930	
1206	29.3	373	
1362	25.4	93	
1131	8.4	2378	
1230	8.5	895	
1290	7.4	481	
1389	6.7	162	
1518	5.8	58	
1328	0.9	1268	
1373	0.9	637	
1426	0.8	287	
1469	0.7	157	
1533	0.7	84	
1121	19.3	1755	0.5
1194	18.4	800	
1278	18.0	314	
1351	16.9	129	
1444	15.6	53	
1157	8.6	1976	
1227	8.3	896	
1324	8.0	253	
1384	7.6	106	
1434	7.0	62	
1297	1.0	1196	
1325	1.0	732	
1342	1.0	671	
1360	0.9	501	
1426	0.9	237	
1441	0.8	146	
1504	0.8	67	
1106	32.4	1739	0.3
1185	31.1	780	
1278	29.7	213	
1331	28.7	95	
1413	26.2	46	
1163	8.6	1978	
1242	8.2	752	
1301	7.8	319	
1379	7.5	85	
1427	6.9	55	
1252	1.1	2022	
1287	1.0	996	
1323	1.0	529	
1357	1.0	386	
1370	1.0	293	
1431	0.9	144	
1500	0.9	84	
	Natural gas blend 3		
1019	20.2	1915	2.0
1045	19.6	1500	
1101	18.2	878	
1209	17.0	344	
1317	15.2	146	
1401	14.5	69	
1477	12.6	37	
1104	8.2	2126	
1139	8.1	1381	
1189	7.8	864	
1282	7.6	361	
1334	6.7	245	
1440	6.4	94	
1508	5.3	54	
1285	1.6	1055	
1320	1.6	948	
1388	1.4	446	
1482	1.4	221	
1555	1.2	107	
1604	1.1	78	
995	34.8	1944	1.0
1047	33.2	1074	
1114	31.9	541	
1212	30.2	205	
1319	26.9	84	
1170	8.5	1037	
1249	7.6	445	
1361	6.7	126	
1470	6.3	58	
1299	0.9	1008	
1311	0.9	766	
1265	0.8	1478	
1358	0.8	507	
1378	0.9	348	
1421	0.8	214	
1446	0.8	158	
1475	0.8	101	
1530	0.7	63	
1064	20.8	2168	0.5
1126	19.7	1107	
1192	18.5	535	
1310	16.8	139	
1369	15.6	65	
1467	14.6	20	
1146	8.7	1454	
1263	8.3	306	
1349	7.7	102	
1428	6.9	29	
1228	1.0	1695	
1268	1.0	899	
1298	1.0	498	
1306	0.9	517	
1356	0.9	266	
1411	0.9	135	
1084	33.7	1494	0.3
1131	33.0	913	
1178	30.7	557	
1279	29.8	138	
1354	27.0	58	
1152	8.7	1428	
1236	8.4	497	
1257	6.2	397	
1315	8.1	120	
1403	7.4	45	
1472	6.9	21	
1212	0.9	1410	
1219	1.0	1570	
1250	1.0	882	
1274	0.9	685	
1282	1.0	464	
1293	1.0	372	
1296	0.8	418	
1346	1.0	172	
1353	0.9	173	

Table 3 (*Continued.*)

Table 3 (*Continued.*)

T (K)	p (atm)	τ_{ign} (μs)	ϕ
1366	0.9	110	
1370	0.8	105	
1381	0.9	103	
1444	0.9	47	

5–8. Again, the agreement between model and experiment is very good over the whole range of temperature, pressure, and stoichiometry. The agreement is noticeably best for the stoichiometric and rich mixtures (Figs. 7 and 8), but some improvements can be made for the leaner mixtures (Figs. 5 and 6) at pressures around 1 and 8 atm. With such a wide range of available data, cross comparisons can be made between data groupings to gauge the effect of stoichiometry and mixture composition. Such comparisons are made in Sec. 3.3.

3.3 Discussion. General trends regarding the effect of fuel-to-air equivalence ratio on the ignition delay time can be seen by plotting several results for different ϕ but for the same fuel mixture and average pressure. Figure 9(*a*) presents both RCM and shock-tube ignition-time results for NG2 at an average pressure near 10 atm. A higher pressure is represented in Fig. 9(*b*), which displays data for NG2 at an average pressure around 20 atm. Note that the data in Figs. 9(*a*) and 9(*b*) represent equivalence ratios ranging from 0.5 up to 2.0. With this range in mind, one result that can be taken from the comparisons is that the variation in ϕ does not seem to have as much of an effect on τ_{ign} as changes in pressure do (as seen in Figs. 1–8). This minimal lack of sensitivity to ϕ holds over the entire range of temperatures, from about 700 K to 1600 K for both pressures in Fig. 9. For example, a factor of

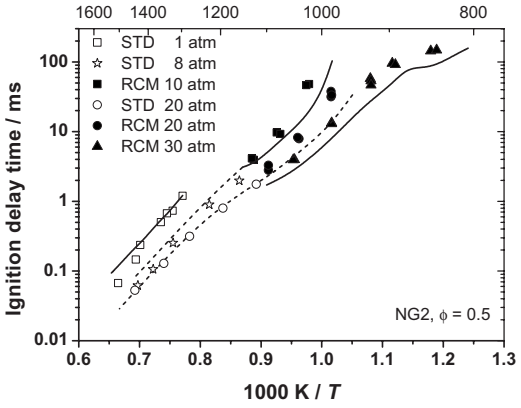

Fig. 1 Effect of pressure for NG2 mixture, ϕ=0.5 in air. Points are experimental results, and lines are model simulations. Dashed lines correspond to data at 8 atm and 20 atm.

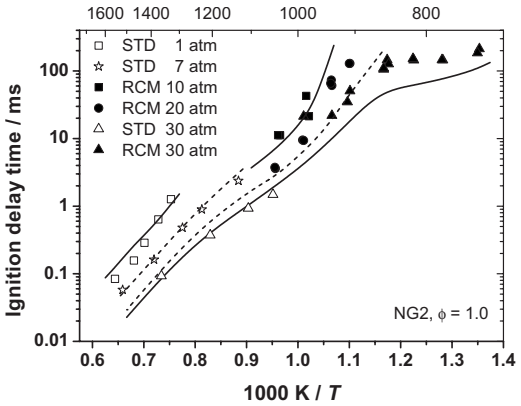

Fig. 2 Effect of pressure for NG2 mixture, ϕ=1.0 in air. Points are experimental results, and lines are model simulations. Dashed lines correspond to *P*=7 and 20 atm.

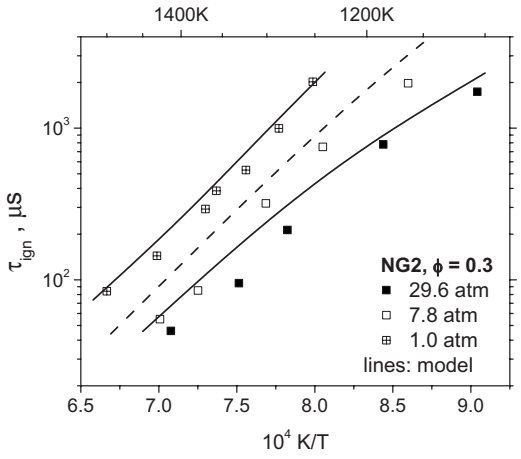

Fig. 3 Shock-tube ignition data and comparison to model for NG2, ϕ=0.3

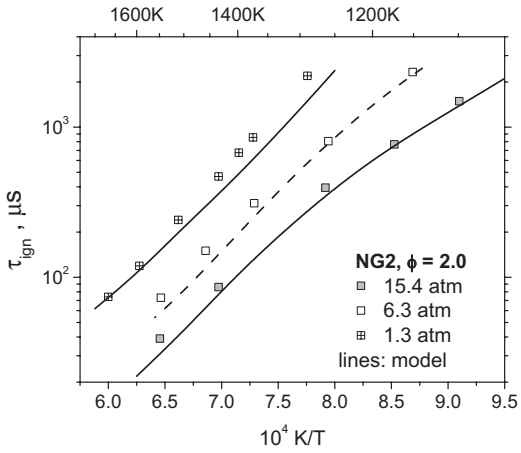

Fig. 4 Shock-tube ignition data and comparison to model for NG2, ϕ=2.0

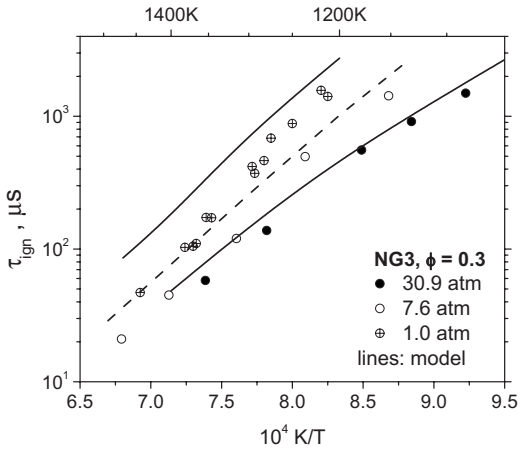

Fig. 5 Fuel-lean ignition delay time data from the shock-tube experiments and comparison to model for NG3, ϕ=0.3; dashed line: 7.6 atm

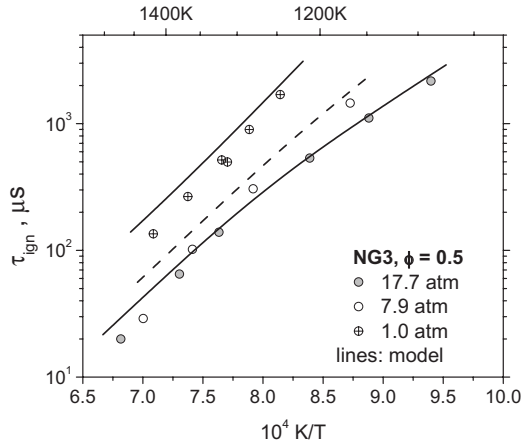

Fig. 6 Lean ignition delay time data from the shock-tube experiments and comparison to model for NG3, ϕ=0.5

4 change in ϕ from 0.5 to 2.0 at about 1400 K in Fig. 9(*b*) results in a change in ignition time of less than 50%. Conversely, at 1400 K for the same NG2 blend in Fig. 4, a factor of 4 change in pressure results in a change in τ_{ign} of about 200%.

Figures 9(*a*) and 9(*b*) also highlight the importance of the point of transition from low-to high-temperature kinetics; at low temperatures, fuel-rich mixtures are faster to ignite relative to fuel-lean mixtures, while lean mixtures ignite faster than rich mixtures at higher temperatures. At 10 atm, Fig. 9(*a*), the experimental data show that this point of transition occurs around 1212 K, while at 20 atm, Fig. 9(*b*), this transition also occurs but shifts to the higher temperature of 1250 K. This transition from low-to high-temperature kinetics is accurately reproduced by the kinetic mechanism in both figures. Moreover, because these experiments are measured close to and at the point of transition, there is observed a very small dependence on equivalence ratio for all three mixtures.

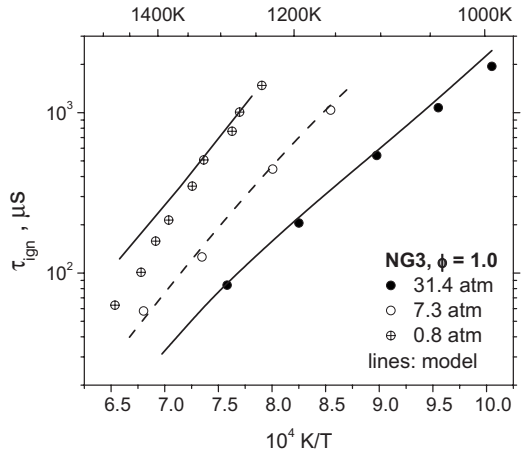

Fig. 7 Stoichiometric ignition delay time data from the shock-tube experiments and comparison to model for NG3, ϕ=1.0

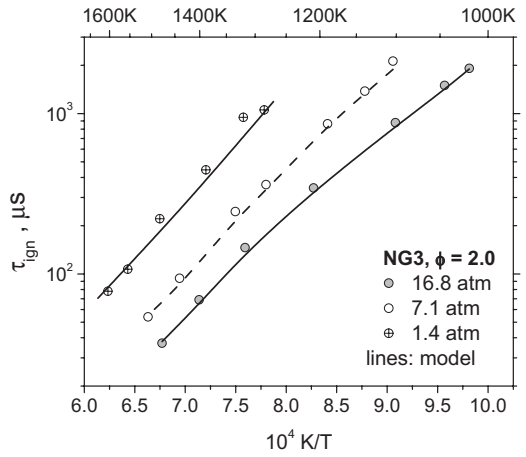

Fig. 8 Fuel-rich ignition delay time data from the shock-tube experiments and comparison to model for NG3, ϕ=2.0

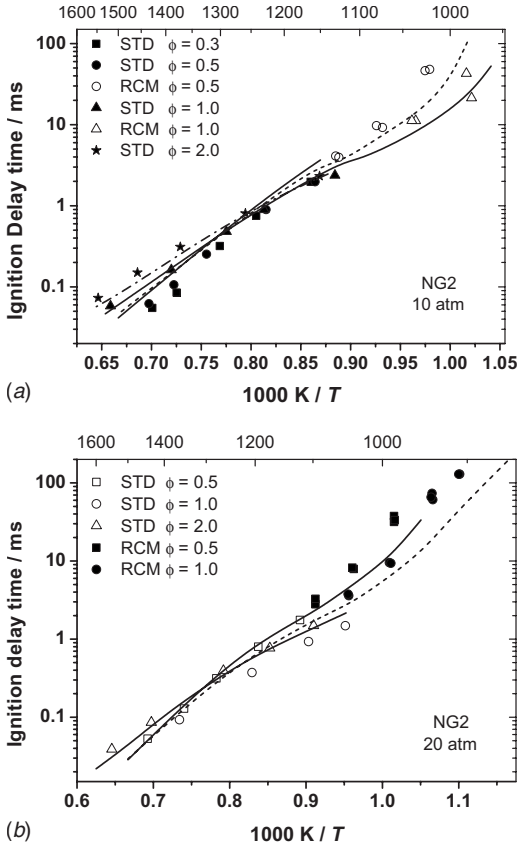

Fig. 9 Effect of equivalence ratio for the NG2 mixture using both shock-tube and RCM data. Points are experimental results, and lines are model simulations. Dashed lines correspond to ϕ=1.0.(*a*) Pressure≈10 atm. (*b*) Pressure≈20 atm.

Also with regard to the lower-temperature behavior, Figs. 1 and 2 show the effect that higher-order hydrocarbons have on ignition delay times; particularly in the RCM data at 30 atm, a region of reduced reactivity is observed in the temperature range 850–900 K at ϕ=0.5 (Fig. 1) and in the temperature range 720–850 K at ϕ=1.0 (Fig. 2). This "negative dependence" or at least zero dependence on temperature is due to the characteristic low- and intermediate-temperature chemistry associated with the larger hydrocarbons (C_3H_8, C_4H_{10}, and C_5H_{12}) present in the mixture, in which alkyl radicals from the fuel add to molecular oxygen and undergo intramolecular isomerization reactions, which lead to chain branching and/or propagation processes and which is responsible for the characteristic and complex negative temperature coefficient behavior associated with alkane fuels.

As seen in earlier studies on methane-based ignition [5–13], the addition of heavier hydrocarbons tends to have an accelerating effect on ignition. The results of the present study also show this trend. Figure 10 displays shock-tube ignition delay times comparing NG2 to NG3 at average pressures of 1 atm (Fig. 10(*a*)) and 30 atm (Fig. 10(*b*)). Also shown in Figs. 10(*a*) and 10(*b*) are calcu-

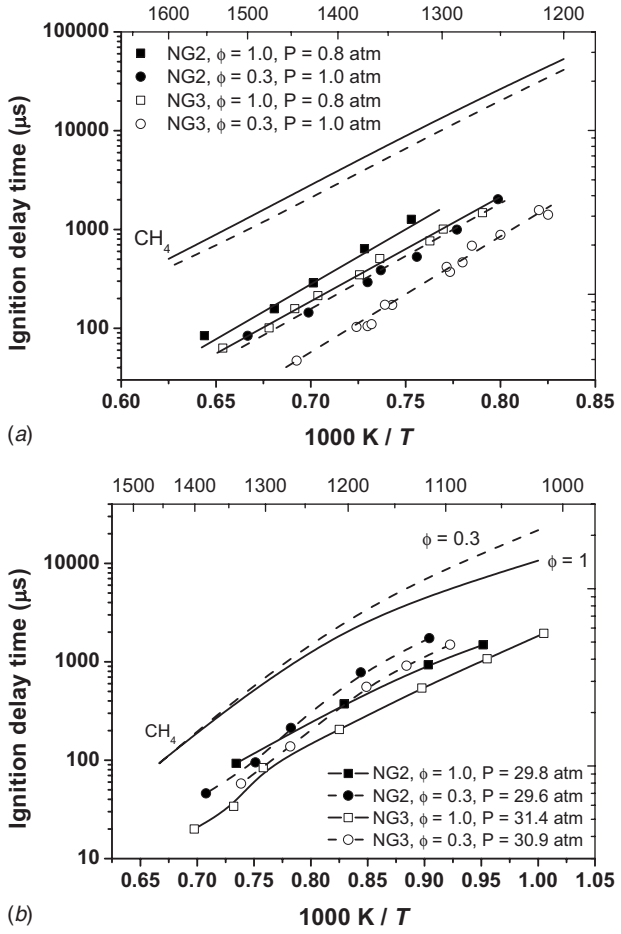

Fig. 10 Effect of mixture composition using shock-tube ignition delay time data. Points are experimental results; lines through data points are best fit lines, for clarity in deducing the trends; lines representing pure methane are model calculations. Solid lines correspond to ϕ=1.0, and dashed lines correspond to ϕ=0.3. (*a*) Pressure≈1 atm. (*b*) Pressure ≈30 atm.

lated ignition delay times for a pure methane fuel to highlight the relative effect of the heavier hydrocarbons. Each plot also shows two different equivalence ratios (0.3 and 1.0). The results in Fig. 10 indicate that, as expected, the NG3 blend, containing a greater amount of higher hydrocarbons than NG2, leads to faster ignition. This conclusion appears to hold over the entire range of ϕ, T, and P represented in Fig. 10. When compared with pure methane, the ignition of the NG2 and NG3 fuel blends are faster by a factor of 5 or more. Note, however, the somewhat diminished effect between NG2 and NG3 as compared with the much larger difference in ignition between the pure methane fuel and NG2.

One general trend evident in the data is that at higher temperatures and lower pressures, lean mixtures tend to ignite faster than rich mixtures, while at lower temperatures and higher pressures, the opposite is true. This trend is evident in the plots in Fig. 9 that show comparisons of equivalence ratio over a wide range of temperature. Figure 10 provides other stark examples; in Fig. 10(*a*), the conditions are near 1 atm, and the lean mixtures ignite faster (ϕ=0.3 compared with ϕ=1.0). In Fig. 10(*b*) at a higher pressure near 30 atm, it is the ϕ=1.0 mixtures that have the faster ignition when compared with ϕ=0.3. Increased fuel at lower temperatures and higher pressures actually contributes more to the chain branching than an increase in fuel concentration at higher temperatures.

At the lower temperatures (and higher pressures) throughout the negative coefficient regime, the alkyl radicals formed from the fuel add to molecular oxygen generating alkylperoxyl radicals (RO_2). These radicals then undergo an intramolecular isomerization reaction to generate a hydroperoxyl-alkyl radical (QOOH). At low temperatures, this radical adds to molecular oxygen generating a peroxyl-alkylhydroperoxide radical (O_2QOOH), which undergoes an intramolecular isomerization reaction and ultimately yields two reactive hydroxyl radicals and an alkoxyhydroperoxide radical. Thus, at low temperatures this process generates three reactive radicals from one fuel alkyl radical, with the fuel alkyl radical concentration being the rate determining parameter.

As the temperature increases, propagation reactions of the hydroperoxyl-alkyl radicals (QOOH) become competitive with the addition to molecular oxygen (which leads to chain branching), and thus fuel reactivity decreases leading to negative temperature coefficient behavior.

4 Laminar Flame Speeds

As mentioned above, laminar flame speed is a key parameter for gauging the effect of fuel variations on the coupling between the chemistry and diffusion. Laminar flame speed can also be tied to the Markstein length and flame dynamics via the flame stretch and strain. Presented in this section are details on the experiment used to obtain the flame speed for the NG2 and NG3 mixtures (Table 1), followed by the measured results and their comparison to the detailed kinetics model.

4.1 Experiment. All experiments were conducted in an AL7075 cylindrical bomb with an inner diameter of 30 cm and internal length of 36.2 cm. The walls are 3.18-cm thick. Both ends contain a fused quartz window of 20.3 cm diameter and 6.3-cm thick. More detail on the experimental setup is given in Ref. [37]. Both pressure and temperature are constantly monitored during the experiment, and the pressure signals are stored in a 14-bit, 5-MHz data acquisition board. The experiments are conducted behind a protective blast wall, and four pneumatic ball valves allow for remote operation of the apparatus. The vessel is rated up to 300 bars, and rupture disks are installed for overpressure protection.

A Z-type Schlieren setup, as described by Settles [38], is used for monitoring the freely propagating flames. Two $f/8$ 15.2-cm diameter mirrors in combination with a mercury light source are used for the Schlieren setup. A circular knife edge in the form an adjustable aperture is used instead of the conventional vertical "flat" knife edge techniques. It can be shown that this gives a more uniform flame front for axisymmetric phenomena [37]. The flame propagation is captured using a high-speed digital camera (Cooke Corp. PCO 1200 hs) with a frame rate of around 2000 fps.

Ignition of the mixture is accomplished by using a combination of an automotive ignition coil, a capacitor, and a constant-current power supply. In this way, the ignition energy can be minimized for each individual mixture. Two copper electrodes leave a spark gap of less the 1 mm.

Experiments were conducted at initial pressures up to 4 atm for methane, NG2, and NG3 over equivalence ratios of 0.7–1.3. The mixtures were created using partial pressures in a separate mixing tank similar to that described by Ref. [31]. This homogeneous mixture in the tank could be used for conducting several experiments depending on the initial pressure required. Prior to each run, the flame speed vessel was evacuated to less than 50 mTorr before being filled with the required mixture. The mixture was then allowed to cool down from the compression heating until the temperature in the vessel was within 0.5°C of the room temperature, which was typically at 25°C. The methane experiments were repeated at least five times and averaged per data point, and the NG2 and NG3 mixtures were repeated three to four times and then averaged.

Each experiment was initiated by sending a signal to the ignition system, the digital oscilloscope, and the digital camera. The

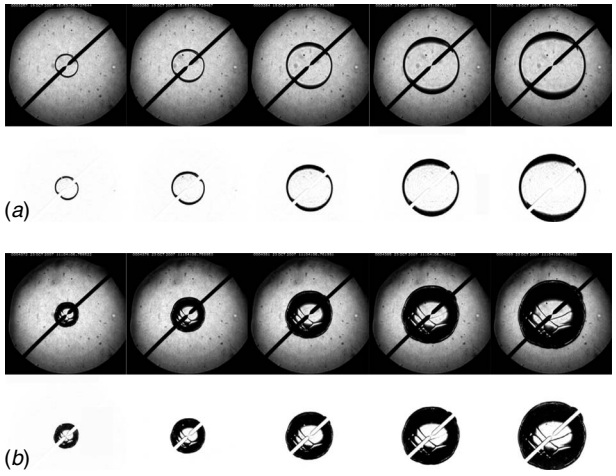

Fig. 11 Schlieren photographs of NG2/air with and without background subtraction, ϕ=1.0; frame width is 12 cm. (*a*) Pressure=1 atm. (*b*) Pressure=4 atm.

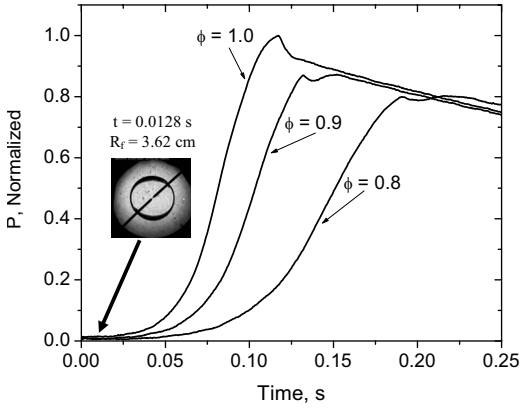

Fig. 12 Pressure histories of CH_4/air mixtures for equivalence ratios of 0.8, 0.9, and 1.0; P_i=1 atm, T_i=298 K. All images used in the data reduction are taken before significant pressure rise.

camera is then manually stopped, and the images containing the flame propagation are saved. Flame radius versus time is obtained from the stored images by using special image-tracking software [39]. Radii less than 0.5 cm were discarded to avoid any potential spark disturbances.

Note that the optical components described herein allow for a large aperture (>10 cm). For low-pressure experiments, the full 0.5–5 cm radius range can be utilized. For higher-pressure experiments where wrinkles were observed, a radius of up to 2.5 cm was used. This limiting radius compares well against other studies conducted at similar pressures.

Figures 11(*a*) and 11(*b*) show the flame propagation of NG2 for 1 atm and 4 atm, respectively. For both cases, the images are shown as recorded and then the initial flameless image is subtracted, leaving just the flame. It can be seen in Fig. 11(*b*) that there are spark- or electrode-induced wrinkles on the surface of the flame. It was shown by Rozenchan et al. [40] that self-similar propagation of such wrinkles suggests that the linear relation between flame speed and flame stretch still holds. Since it can be seen that a new wrinkle is being formed between R=3.0 and 3.5 cm, the radius was only used up to 2.5 cm for this study for elevated pressures, as mentioned above. Cell cracking was not observed in this study. The O_2/N_2 ratio was always 21/79, and the dilution level (i.e., the Lewis number) was never changed herein, but will possibly be necessary in the future for experiments conducted at initial pressures higher than 4 atm.

It is important to show that the pressure rise during the experiments is negligible during the collection of the flame images. The decrease in flame speed at higher pressures would indicate an artificial decrease in Markstein length (flame speed versus flame stretch dependency) over the period that flame speed is recorded during a pressure increase. Figure 12 shows the pressure traces recorded for CH_4/air for three different equivalence ratios (0.8, 0.9, and 1.0). The position of the flame relative to the pressure is also shown. It can be seen that the pressure rise is negligible during the collection of the data.

The proposed linear relationship between flame speed and flame stretch [41–43] was used herein to obtain the unstretched flame speed

$$S_b = S_b^0 - L_b\alpha \tag{1}$$

where S_b is the stretched flame speed, S_b^0 is the unstretched flame speed, L_b is the burned Markstein length, and α is the flame stretch defined by

$$\alpha = \frac{1}{A}\frac{dA}{dt} = \frac{1}{4\pi R^2}\frac{d(4\pi R^2)}{dt} = \frac{2}{R}\frac{dR}{dt} \tag{2}$$

Equation (1) can be integrated to obtain Eq. (3)

$$R = S_b^0 t - 2L_b \ln(R) + \text{const} \tag{3}$$

This equation can then be used to obtain the unstretched flame speed and the Markstein length through linear regression. This approach is preferred over using finite difference to obtain the instantaneous flame speed, since small perturbations in flame radius can cause major changes in slope. Using the linear regression method averages out this problem.

4.2 Flame Speed Results. As mentioned above, three different mixtures, CH_4, NG2, and NG3, were used over equivalence ratios from 0.7 to 1.3 at 1 atm. Pressure dependency of the NG2 mixture was also obtained for pressures of up to 4 atm. All data are compared against the kinetics model described above and are used to compare with the ignition delay time data. All initial temperatures were 298 ± 1 K. The experimental results can be found in Table 4.

As validation of the experimental technique and the laminar flame speed results, the CH_4 results can be compared with the established literature since the laminar flame speeds for methane at 1 atm are very well known. A convenient way of doing this is to compare the measured data for pure methane with the prediction of the GRI 3.0 chemical kinetics mechanism [27]. This particular mechanism was validated using the methane flame speed database and has been shown to replicate the measured results very well. The present data for methane at 1 atm are shown in comparison to the accurate predictions of GRI 3.0 in Figs. 13(*a*) and 13(*b*). As seen in these figures of S_L versus the equivalence ratio, the agreement between the present data and GRI 3.0 is excellent.

Figure 13(*a*) shows the burning velocity of CH_4 and NG2 for equivalence ratios of 0.7–1.3 at 1 atm. It can be seen that the NG2 mixture shows a slight acceleration over the whole range of equivalence ratios with a minimum effect at stoichiometric conditions. From the model, the difference in predicted burning velocity between CH_4 and NG2 is minimal in the fuel-lean region, and the two predictions diverge when the mixtures become more fuel rich. The model slightly overpredicts the flame speed for lean methane flames and agrees well with lean NG2 flames. For rich flames, the model underpredicts the experimental results for both the pure methane as the NG2 flames, where the effect is less profound for the later.

Figure 13(*b*) shows the burning velocity of CH_4 and NG3 mixtures at 1 atm. The experimental results indicate that the effect of the higher level of higher-order hydrocarbons (38.75% of the total fuel) has a marginal effect in the fuel-lean regime as compared

Table 4 Experimental results for laminar flame speed, S_L, for CH_4, NG2, and NG3; T_i=298 K

CH_4/air, P=1 atm	
ϕ	S_L (cm/s)
0.7	15.0
0.8	23.7
0.9	30.0
1	35.1
1.1	34.7
1.2	31.3
1.3	24.7

NG2/air, P=1 atm	
ϕ	S_L (cm/s)
0.7	17.1
0.9	31.2
1.1	37.2
1.2	35.6
1.3	28.0

NG3/air, P=1 atm	
ϕ	S_L (cm/s)
0.7	19.2
0.8	25.8
0.9	31.4
1	36.0
1.1	38.0
1.2	36.1
1.3	30.2

NG3/air, ϕ=1.0	
P (atm)	S_L (cm/s)
1.0	36.1
1.5	32.0
1.8	31.0
2.0	30.1
2.4	28.4
2.5	28.2
4.0	24.4

with the NG2 experimental results. However, for fuel-rich mixtures, the burning velocity is higher than that recorded for the pure CH_4 flames as well as for the NG2 flames. The model shows similar behavior as for the NG2 mixture, where the agreement under lean conditions is acceptable, and where the model deviated for the experimental results for rich conditions for both the pure CH_4, as well as the NG3 mixture.

The burning velocity of NG2 is plotted against pressure in Fig. 14 for pressures between 1 atm and 4 atm. The predicted burning velocity for stoichiometric CH_4 by GRI 3.0 [27] is also plotted, as well as the model prediction of the NG2 and NG3 mixtures using the present kinetics model. It can be seen that the experimental results show a burning velocity that is slightly higher than the prediction of CH_4 by GRI 3.0. The current model underpredicts the flame speed for the NG mixture and shows burning velocities that are slightly less than the predicted CH_4 burning velocities. The model prediction of the NG3 mixture is slightly faster than the NG2 mixture.

5 Discussion

Given the increasing importance of fuel flexibility for power generation applications, the present study is especially important for the gas turbine and combustion communities for several reasons: (1) a comprehensive database of ignition delay times that cover a wide range of stoichiometry, temperature, and pressure

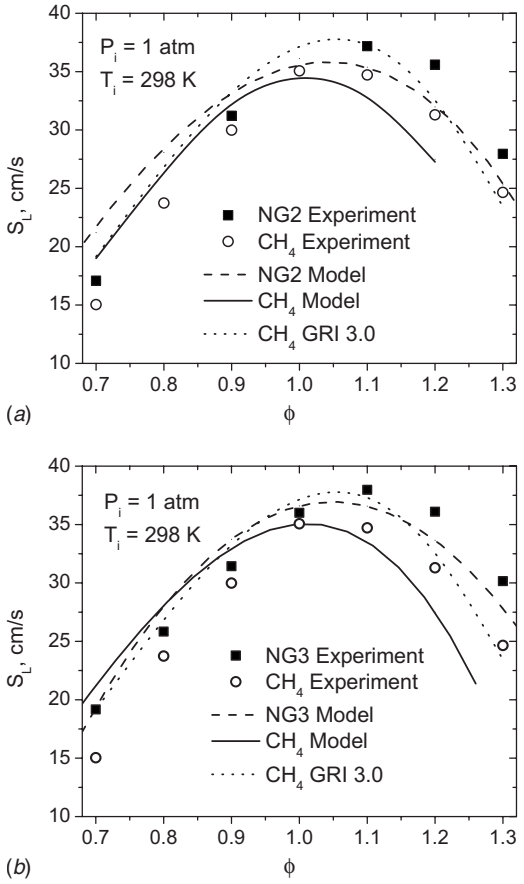

Fig. 13 Measured laminar burning velocities and comparison to model predictions for P_i=1 atm, T_i=298 K. (*a*) Methane and NG2 in air. (*b*) Methane and NG3 in air.

was produced; (2) a detailed chemical kinetics model that does a remarkable job over such a comprehensive range of conditions was presented; (3) high-pressure laminar flame speed results are also available for a similar range of fuel blend composition and stoichiometry; (4) a range of methane-hydrocarbon blends including methane concentrations as low as 62.5% by volume was explored; and (5) two experimental ignition techniques—shock tube and rapid compression machine—were combined to provide a full range of temperatures from about 700 K to 1600 K at engine pressures.

As seen in the ignition delay time results in Figs. 1–8, the strong ability of the kinetics model to reproduce the correct trends

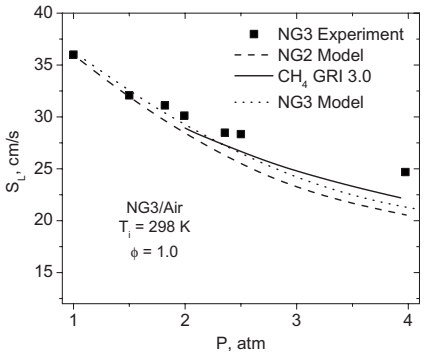

Fig. 14 Pressure dependence of the laminar burning velocity for NG2 experiments and comparison to model for CH_4, NG2, and NG3. ϕ=1.0, T_i=298 K.

both qualitatively and in absolute magnitude cannot be overstated, particularly when one considers the range of mixtures and conditions considered. The model seems to be best at stoichiometric and rich conditions, even for pressures as high as 30 atm. Nonetheless, the same figures point out some areas for improvement. For example, at the lowest temperatures, the model tends to underpredict the ignition times by as much as a factor of 2 or more. Other improvements can be made at the leanest conditions examined at the lower pressures, Figs. 5–7. One area of kinetic interest not covered by the present study is the effect of ethane and other hydrocarbons for extreme levels of them in the fuel blend, i.e., for methane contents between 60% and 0% by volume. Additional work in the area of methane-hydrocarbon kinetics would also include sensitivity analyses over the range of conditions herein, including the regions of lesser agreement between model and data, to determine the dominant reactions and pathways.

For the laminar flame speed results, the quantitative agreement between model and experiment is not as good as for the ignition times, although the basic trends with composition, pressure, and ϕ are captured. The disagreement is seen in Figs. 13 and 14, particularly at the richer conditions and at pressures greater than 1 atm. This disagreement is not too surprising, however, since the present model was tuned mostly using the ignition delay time experiments and not with the current S_L results. Note that the GRI-MECH 3.0 predictions for the pure methane case are actually better on the rich side than the present model. Since flame speeds depend not only on the chemical kinetics but also on the diffusive properties of the reactive mixtures; a careful assessment of the transport data utilized in the present model should be made in light of the results herein.

A comprehensive sensitivity analysis to identify what needs to be changed in the present mechanism to obtain better agreement between model and data is currently underway in the authors' laboratories. The results of this analysis along with the improved kinetics mechanism will be presented in a future paper.

Finally, future S_L experiments should include a wider range of pressure. However, care should be taken when moving to higher pressures since at pressures above about 4 atm in the present experiments, instabilities start to form, leading to wrinkling of the flame and inevitably faster flame speeds due to the corresponding increase in turbulence. Wrinkling of the flame front at elevated pressures can be mitigated by altering the Lewis number of the mixture (by adding different dilution gases to the fuel-air mixture). Higher-temperature experiments are also needed but will require heating of the facility to higher initial temperatures, T_i. Due to its relation to flame dynamics, additional work should concentrate on the Markstein length and its sensitivity to fuel composition.

6 Summary

Experiments and kinetics modeling were performed for two methane-based fuel blends containing relatively large levels of higher-order hydrocarbons (ethane, propane, n-butane, and pentane). The experiments included ignition delay times from shock tubes and a rapid compression machine, as well as laminar flame speed measurements from a high-pressure vessel with optical access. Conditions representative of gas turbine engines were emphasized, including pressures from 0.7 atm to 33.9 atm for undiluted fuel-air mixtures over a wide range of equivalence ratios (0.3–2.0). The combination of shock tube and rapid compression machine allowed ignition delay times to be obtained over a range of temperatures from 739 K to 1667 K.

The ignition delay time results compare favorably with the detailed kinetics model over a wide range of conditions, including pressures on the order of 30 atm and for the fuel-rich conditions. Additionally, the shock-tube and rapid compression machine results are complementary. As expected, the fuel blend with the larger percentage of higher-order hydrocarbons produced the faster ignition, and the ignition seems to depend more on the pressure than on the fuel-air stoichiometry. Some areas for improvement to the kinetics model were identified.

Laminar flame speeds for both natural gas blends, as well as a baseline pure methane fuel, were obtained at 1 atm initial pressure over a range of equivalence ratios from 0.7 to 1.31. In general, the flame speeds for the fuel blends were smaller than for the pure methane results, ranging from about 10% at lean conditions to as much as 40–50% for rich mixtures. At 1 atm, the kinetics model tends to agree well with the measured flame speeds on the lean side but underpredicts the flame speed for rich mixtures. A pressure excursion up to 4 atm was done for a stoichiometric fuel-air mixture, with S_L decreasing with increasing pressure. The model tended to under predict S_L by as much as 25% at 4 atm. Suggestions for future flame speed research for methane-hydrocarbon blends were also presented.

Acknowledgment

The work herein was sponsored primarily by Rolls-Royce Canada and in part by the National Science Foundation under Contract No. CBET-0832561. Additional support provided by The Aerospace Corporation. The assistance of Benjamin Corbin, Alexander Barrett, and Matthew Davis (UCF) in the laboratory is appreciated.

References

[1] Bourque, G., Healy, D., Curran, H., Simmie, J., de Vries, J., Antonovski, V., Corbin, B., Zinner, C., and Petersen, E., 2007, "Effect of Higher-Order Hydrocarbons on Methane-Based Fuel Chemistry at Gas Turbine Pressures," ASME Paper No. GT2007-28039.

[2] Lieuwen, T., McDonell, V., Petersen, E., and Santavicca, D., 2008, "Fuel Flexibility Influences on Premixed Combustor Blowout, Flashback, Autoignition, and Stability," ASME J. Eng. Gas Turbines Power, **130**, p. 011506.

[3] Lieuwen, T., 2003, "Modeling Premixed Combustion-Acoustic Wave Interactions: A Review," J. Propul. Power, **19**, pp. 837–846.

[4] Bradley, D., Hicks, R. A., Lawes, M., Sheppard, C. G. W., and Woolley, R., 1998, "The Measurement of Laminar Burning Velocities and Markstein Numbers for Iso-Octane–Air and Iso-Octane–n-Heptane–Air at Elevated Temperatures and Pressures in an Explosion Bomb," Combust. Flame, **115**, pp. 126–144.

[5] Higgin, R. M. R., and Williams, A., 1969, "A Shock-Tube Investigation of the Ignition of Lean Methane and n-Butane Mixtures With Oxygen," Proc. Combust. Inst., **12**, pp. 579–590.

[6] Crossley, R. W., Dorko, E. A., Scheller, K., and Burcat, A., 1972, "The Effect of Higher Alkanes on the Ignition of Methane-Oxygen-Argon Mixtures in Shock Waves," Combust. Flame, **19**, pp. 373–378.

[7] Eubank, C. S., Rabinowitz, M. J., Gardiner, W. C., Jr., and Zellner, R. E., 1981, "Shock-Initiated Ignition of Natural Gas-Air Mixtures," Proc. Combust. Inst., **18**, pp. 1767–1774.

[8] Zellner, R., Niemitz, K. J., Warnatz, J., Gardiner, W. C., Jr., Eubank, C. S., and Simmie, J. M., 1983, "Hydrocarbon Induced Acceleration of Methane-Air Ignition," Prog. Astronaut. Aeronaut., **80**, pp. 252–272.

[9] Spadaccini, L. J., and Colket, M. B., III, 1994, "Ignition Delay Characteristics of Methane Fuels," Prog. Energy Combust. Sci., **20**, pp. 431–460.

[10] Naber, J. D., Siebers, D. L., Di Julio, S. S., and Westbrook, C. K., 1994, "Effects of Natural Gas Composition on Ignition Delay Under Diesel Conditions," Combust. Flame, **99**, pp. 192–200.

[11] Griffiths, J. F., Coppersthwaite, D., Phillips, C. H., Westbrook, C. K., and Pitz, W. J., 1990, "Auto-Ignition Temperatures of Binary Mixtures of Alkanes in a Closed Vessel: Comparisons Between Experimental Measurements and Numerical Predictions," Proc. Combust. Inst., **23**, pp. 1745–1752.

[12] Huang, J., and Bushe, W. K., 2006, "Experimental and Kinetic Study of Autoignition in Methane/Ethane/Air and Methane/Propane/Air Mixtures Under Engine-Relevant Conditions," Combust. Flame, **144**, pp. 74–88.

[13] Petersen, E. L., Hall, J. M., Smith, S. D., de Vries, J., Amadio, A. R., and Crofton, M. W., 2007, "Ignition of Lean Methane-Based Fuel Blends at Gas Turbine Pressures," ASME J. Eng. Gas Turbines Power, **129**, pp. 937–944.

[14] Petersen, E. L., Kalitan, D. M., Simmons, S., Bourque, G., Curran, H. J., and Simmie, J. M., 2007, "Methane/Propane Oxidation at High Pressures: Experimental and Detailed Chemical Kinetic Modeling," Proc. Combust. Inst., **31**, pp. 447–454.

[15] Petersen, E. L., and de Vries, J., 2005, "Measuring the Ignition of Fuel Blends Using a Design of Experiments Approach," AIAA Paper No. 2005-1165.

[16] de Vries, J., and Petersen, E. L., 2005, "Design and Validation of a Reduced Test Matrix for the Autoignition of Gas Turbine Fuel Blends," ASME Paper No. IMECE2005-80040.

[17] de Vries, J., and Petersen, E. L., 2007, "Autoignition of Methane-Based Fuel Blends Under Gas Turbine Conditions," Proc. Combust. Inst., **31**, pp. 3163–3171.

[18] Healy, D., Dooley, S., Curran, H. J., Petersen, E., Simmons, S., Kalitan, D., Bourque, G., and Simmie, J. M., 2006, "A Rapid Compression Machine Study of Natural Gas Mixtures," Work in Progress Poster 4E-05: 31st International Symposium on Combustion, Heidelberg, Germany, Aug. 6–11.
[19] Eschenbach, R. C., and Agnew, J. T., 1958, "Use of a Constant-Volume Bomb Technique for Measuring Burning Velocity," Combust. Flame, **2**, pp. 273–285.
[20] Agrawal, D. D., 1981, "Experimental Determination of Burning Velocity of Methane-Air Mixtures in a Constant Volume Vessel," Combust. Flame, **42**, pp. 243–252.
[21] Egolfopoulos, F. N., Cho, P., and Law, C. K., 1989, "Laminar Flame Speeds of Methane-Air Mixtures Under Reduced and Elevated Pressures," Combust. Flame, **76**, pp. 375–391.
[22] Savarianandam, V. R., and Lawn, C. J., 2006, "Burning Velocity of Premixed Turbulent Flames in the Weakly Wrinkled Regime," Combust. Flame, **146**, pp. 1–18.
[23] Hessler, J. P., 1998, "Calculation of Reactive Cross Sections and Microcanonical Rates From Kinetic and Thermochemical Data," J. Phys. Chem. A, **102**, pp. 4517–4526.
[24] You, X., Wang, H., Goos, E., Sung, C.-J., and Klippenstein, S. J., 2007, "Reaction Kinetics of $CO+HO_2 \rightarrow$ Products: Ab Initio Transition State Theory Study With Master Equation Modeling," J. Phys. Chem. A, **111**, pp. 4031–4042.
[25] Srinivasan, N. K., Michael, J. V., Harding, L. B., and Klippenstein, S. J., 2007, "Experimental and Theoretical Rate Constants for $CH_4+O_2 \rightarrow CH_3+HO_2$," Combust. Flame, **149**, pp. 104–111.
[26] Jasper, A. W., Klippenstein, S. J., and Harding, L. B., 2007, "Theoretical Rate Coefficients for the Reaction of Methyl Radical and Hydroperoxyl Radical and for Methyl-Hydroperoxide Decomposition," private communication.
[27] Smith, G. P., Golden, D. M., Frenklach, M., Moriarty, N. W., Eiteneer, B., Goldenberg, M., Bowman, C. T., Hanson, R. K., Song, S., Gardiner, W. C., Jr., Lissianski, V. V., and Qin, Z., http://www.me.berkeley.edu/gri_mech/.
[28] Curran, H. J., Gaffuri, P., Pitz, W. J., and Westbrook, C. K., 1998, "A Comprehensive Modeling Study of n-Heptane Combustion," Combust. Flame, **114**, pp. 149–177.
[29] Curran, H. J., Gaffuri, P., Pitz, W. J., and Westbrook, C. K., 2002, "A Comprehensive Modeling Study of Iso-Octane Oxidation," Combust. Flame, **129**, pp. 253–280.
[30] Kee, R. J., Rupley, F. M., Miller, J. A., Coltrin, M. E., Grcar, J. F., Meeks, E., Moffat, H. K., Lutz, A. E., Dixon-Lewis, G., Smooke, M. D., Warnatz, J., Evans, G. H., Larson, R. S., Mitchell, R. E., Petzold, L. R., Reynolds, W. C., Caracotsios, M., Stewart, W. E., Glarborg, P., Wang, C., and Adigun, O., 2001, "PREMIX: A Program for Modeling Steady, Laminar, One-Dimensional Premixed Flames," Reaction Design, Inc., San Diego, CA.
[31] Petersen, E. L., Rickard, M. J. A., Crofton, M. D., Abbey, E. D., Traum, M. J., and Kalitan, D. M., 2005, "A Facility for Gas- and Condensed-Phase Measurements Behind Shock Waves," Meas. Sci. Technol., **16**, pp. 1716–1729.
[32] Aul, C. J., de Vries, J., and Petersen, E. L., 2007, "New Shock-Tube Facility for Studies in Chemical Kinetics at Engine Conditions," Eastern States Fall Technical Meeting of the Combustion Institute, Charlottesville, VA, Oct. 21–24.
[33] Affleck, W. S., and Thomas, A., 1969, "An Opposed Piston Rapid Compression Machine for Preflame Reaction Studies," Proc. Inst. Mech. Eng., Part H: J. Eng. Med., **183**, pp. 365–385.
[34] Brett, L., MacNamara, J., Musch, P., and Simmie, J. M., 2001, "Simulation of Methane Autoignition in a Rapid Compression Machine With Creviced Pistons," Combust. Flame, **124**, pp. 326–329.
[35] Gallagher, S. M., Curran, H. J., Metcalfe, W. K., Healy, D., Simmie, J. M., and Bourque, G., 2008, "A Rapid Compression Machine Study of the Oxidation of Propane in the Negative Temperature Coefficient Regime," Combust. Flame, **153**, pp. 316–333.
[36] Lund, C. M., and Chase, L., 1995, "HCT-A General Computer Program for Calculating Time-Dependent Phenomena Involving One-Dimensional Hydrodynamics, Detailed Chemical Kinetics and Transport," Lawrence Livermore National Laboratory, Report No. UCRL-52504.
[37] De Vries, J., Corbin, B., and Petersen, E. L., "Construction of a High Pressure Flame Speed Facility," unpublished.
[38] Settles, G. S., 2006, *Schlieren and Shadowgraph Techniques*, 1st ed., Springer, Heidelberg, Germany.
[39] Klimek, R., and Wright, T., 2006, "Spotlight-8 Image Analysis Software," Report No. NASA/TM-2006-214084.
[40] Rozenchan, G., Zhu, D. L., Law, C. K., and Tse, S. D., 2002, "Outward Propagation, Burning Velocities, and Chemical Effects of Methane Flames Up to 60 atm," Proc. Combust. Inst., **29**, pp. 1461–1469.
[41] Markstein, G. H., 1964, *Non-Steady Flame Propagation*, Pergamon, New York.
[42] Dowdy, D. R., Smith, D. B., Taylor, S. C., and Williams, A., 1990, "The Use of Expanding Spherical Flames to Determine Burning Velocities and Stretch Effects in Hydrogen/Air Mixtures," Proc. Combust. Inst., **23**, pp. 325–332.
[43] Brown, J. M., McLean, I. C., Smith, D. B., and Taylor, S. C., 1996, "Markstein Lengths of CO/H2/Air Flames Using Expanding Spherical Flames," Proc. Combust. Inst., **26**, pp. 875–881.

Emission Characteristics of a Premixed Cyclic-Periodical-Mixing Combustor Operated With Hydrogen-Natural Gas Fuel Mixtures

Jochen R. Brückner-Kalb[1]
e-mail: brueckner-kalb@mytum.de

Michael Krösser

Christoph Hirsch

Thomas Sattelmayer

Lehrstuhl für Thermodynamik,
Technische Unversität München,
Garching D-85748, Germany

*The concept of the cyclic periodical mixing combustion process (Kalb, and Sattelmayer, 2004, "Lean Blowout Limit and NO_x-Production of a Premixed Sub-ppm-NO_x Burner With Periodic Flue Gas Recirculation," Proceedings of the ASME Turbo Expo 2004, Paper No. GT2004-53410; Kalb, and Sattelmayer, 2006, "Lean Blowout Limit and NO_x-Production of a Premixed Sub-ppm-NO_x Burner With Periodic Recirculation of Combustion Products," ASME J. Eng. Gas Turbines Power, **128**(2), pp. 247–254) for the extension of the lean blowout limit had been implemented in an atmospheric experimental combustor for testing with both external perfect (Brückner-Kalb, Hirsch, and Sattelmayer, 2006, "Operation Characteristics of a Premixed Sub-ppm NO_x Burner With Periodical Recirculation of Combustion Products," Proceedings of the ASME Turbo Expo 2006, Paper No. GT2006-90072) and technical (Brückner-Kalb, Napravnik, Hirsch, and Sattelmayer, 2007, "Development of a Fuel-Air Premixer for a Sub-ppm NO_x Burner," Proceedings of the ASME Turbo Expo 2007, Paper No. GT2007-27779) premixing of reactants. It had been tested with natural gas and has now been tested with a mixture of 70%$_{vol}$ of hydrogen and 30%$_{vol}$ of natural gas (98% CH_4) as fuel. With natural gas the NO_x emissions are unaffected by the limited technical premixing quality, as long as the air preheat is in the design range of the premixers (Brückner-Kalb, Napravnik, Hirsch, and Sattelmayer, 2007, "Development of a Fuel-Air Premixer for a Sub-ppm NO_x Burner," Proceedings of the ASME Turbo Expo 2007, Paper No. GT2007-27779). Then, for adiabatic flame temperatures of up to 1630 K NO_x emissions are below 1 ppm(v) with CO emissions below 8 ppm(v) in the whole operation range of the test combustor (15% O_2, dry). With the "70%$_{vol}H_2 - 30\%_{vol}CH_4$" mixture the NO_x emissions increase by nearly one order of magnitude. Then, NO_x emissions below 7 ppm(v) (15% O_2, dry) are achieved for adiabatic flame temperatures of up to 1600 K. They approach the 1 ppm(v) level only for flame temperatures below 1450 K. CO emissions are below 4 ppm(v). The reason for the increase in the NO_x emissions is the higher reactivity of the mixture, which leads to earlier ignition in zones of still elevated unmixedness of reactants near the premixer-injector exits. This effect was investigated by chemical reactor network simulations analyzing a pressure effect and an additional chemical effect of hydrogen combustion on NO_x formation.* [DOI: 10.1115/1.3124789]

1 Introduction: Diluted Combustion for Emission Reduction

The most effective primary measure for the abatement of NO_x emissions from combustion systems is the reduction in peak temperatures in the combustion process. Therefore, lean-premixed aerodynamically stabilized burners have been used in gas turbines, as both the effect of excess air as thermal ballast and a high premixing quality of the reactants lead to reduced flame temperatures. Thus, lean-premixed combustion has the potential of minimizing NO_x emissions below 1 ppm(v) (15% O_2, dry), if the premixing quality is adequate and the adiabatic flame temperature is limited to approximately 1600 K. Yet this is not possible with aerodynamically stabilized burners because their stability limit or even lean blowout (LBO) limit usually lie in the range between 1700 K and 1750 K. For this reason, another concept of lean-premixed combustion is necessary to achieve this goal. The combustion process used in this study belongs to the class of processes known as *diluted combustion* [1], *moderate or intense low-oxygen dilution* (MILD) *combustion* [2,3], or *flameless combustion* [4,5].

The basic effect of these processes is that adiabatic mixtures of preheated fresh reactants and hot (even inert) dilution gas self-ignite reasonably quickly even at relatively low combustion temperatures [6]. The admixed diluent may be recirculated combustion products [1,3,5] or highly preheated, oxygen-depleted air (*high temperature air combustion* (HiTAC)) [7,8]. Dilution can be rather high, if the combustor wall temperature is maintained above the self-ignition limit of the employed mixture. If, additionally, incompletely burnt combustion products are used for dilution, the radicals OH, O, and H are delivered in this way to the fresh reactants, shortening their ignition delay time [6]. This effect is exploited in the *cyclic periodical mixing combustion process* (CP-MCP) that is used in this work.

[1]Corresponding author.

Contributed by the International Gas Turbine Institute of ASME for publication in the JOURNAL OF ENGINEERING FOR GAS TURBINES AND POWER. Manuscript received April 9, 2008; final manuscript received April 23, 2008; published online October 30, 2009. Review conducted by Dilip R. Ballal. Paper presented at the ASME Turbo Expo 2008: Land, Sea and Air (GT2008), Berlin, Germany, June 9–13, 2008.

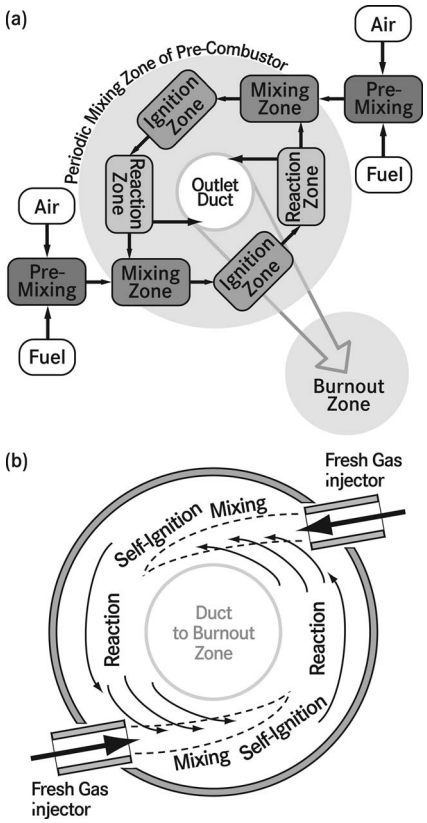

Fig. 1 The cyclic periodical mixing combustion process: (*a*) block diagram of the subprocesses and (*b*) schematic of the flow field in the precombustor

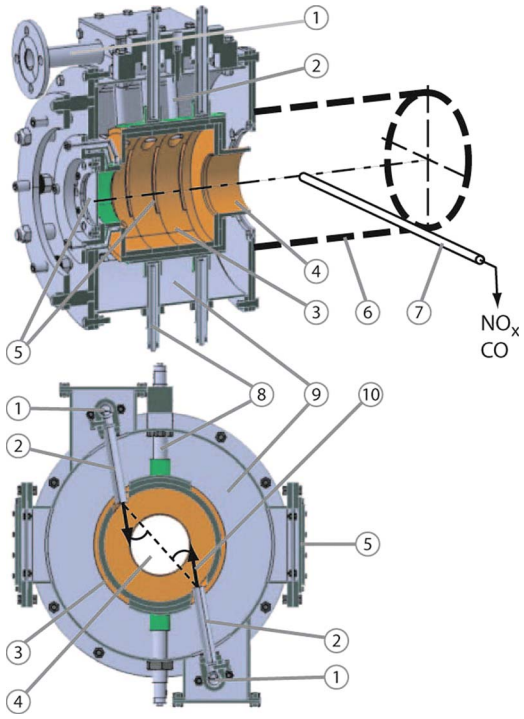

Fig. 2 Cut-away view of the precombustor test rig: (1) fresh mixture or air supply tube, (2) injector tubes, (3) precombustor liner, (4) duct to burnout combustor, (5) optical access, (6) burnout combustor, (7) suction probe, (8) air-cooled liner support, (9) void space filled with insulating material, and (10) fresh mixture injection direction

1.1 The Cyclic-Periodical Mixing Combustion Process and the Test Combustor. The conceptual basis of the steady CPMCP is the quasitangential injection of premixed fresh mixture through segmented injectors into a cylindrical flow reactor, where an inner swirling flow develops. This swirling flow leads to a strong interaction of the fresh gas jets and local, partially, or fully burnt combustion products from upstream reaction zones. Thus it produces the following spatially periodic patterns:

- mixing of fresh reactants with hot products,
- subsequent gradual self-ignition in the hot zones of the shear layers between the product gas flow and the fresh gas jets, where the reactants are diluted, and
- reaction to a certain degree of burnout before the next mixing zone is reached,

as depicted in Fig. 1. The CPMCP is implemented in a precombustor, which is followed downstream by a burnout section (Fig. 1), because if the residence time of the reacting mixture between two mixing processes is limited for the minimum required for stable operation, the gases leaving the precombustor will not yet be fully burnt.

The design of the CPMCP test combustor has been described in more detail previously [9]. The inner diameter of the precombustor (3, Fig. 2) is 220 mm, its inner length 200 mm. In order to generate a cyclone type flow in the precombustor the cylindrical connecting duct (4, Fig. 2) between the precombustor and the CO-burnout section (6, Fig. 2) comprises a nozzle with a 115 mm inner diameter. The burnout section, which is only schematically shown, is a cylindrical tube of 220 mm inner diameter and 355 mm length. The precombustor liner (3, Fig. 2) is made of sintered SiC with a maximum application temperature of 1900 K, which allows for high wall temperatures and together with thermal insulation (9, Fig. 2) limits thermal losses of the combustion to nearly adiabatic conditions.

The two opposite rows of three injector tubes (2, Fig. 2) each are inclined by 30 deg (10, Fig. 2) with respect to the radial direction of the cylindrical combustor. This value of inclination was found to be optimum [9]. The swirl number of the flow leaving the precombustor exceeds the minimum value required to generate a recirculating zone along the combustor axis. The high swirl design is a basic requirement, as it allows proper control of the residence time distribution in the precombustor.

For the study with perfectly premixed reactants a mixing stage located far upstream was used. The mixture was then fed to the supply tubes (1, Fig. 2). In the case of technical premixing, gas turbine compatible fuel-air premixers have been implemented directly into each of the six fresh gas injector tubes (2, Fig. 2, inner diameter d_I=20 mm). The design of these vortex-premixer injectors (VPMIs) has been described in Ref. [10] and is shown schematically in Fig. 3. The VPMI is based on a delta-wing vortex generator that generates a pair of large-scale secondary vortices in the main air flow. The fuel is injected through one orifice of diameter d_O into the shear layer between the two counter-rotating vortices, and then is quickly dispersed and down-mixed to the molecular level because of the high turbulence level.

All exhaust gas measurements have been made using a water-cooled suction probe (7, Fig. 2) located in the burnout zone, 140 mm downstream of the precombustor exit nozzle. Thus, the measured emission characteristics represent the entire process because burnout is already complete at the probe position.

1.1.1 The Exhaust Gas Analysis Equipment. The NO_x emissions have been measured by a chemiluminescence detector having a lower detection limit of 0.1 ppm(v) and a measurement uncertainty of $\Delta\chi_{NO_x} = \pm 0.1$ ppm(v) in the 0–10 ppm(v) range of

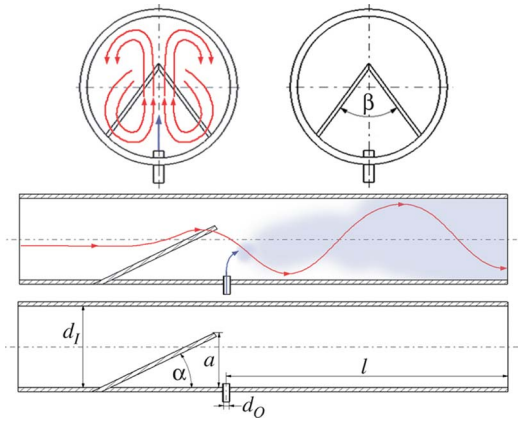

Fig. 3 Schematic drawing of the vortex-premixer injector [10]

the instrument [11]. The measurement data were corrected for the quenching efficiencies of other components in the sample gas, which would bias the results [12]. The CO emissions are measured by an infrared absorption detector having a measurement uncertainty of $\Delta\chi_{CO} \approx \pm 1$ ppm(v). All emission data were corrected to 15% oxygen in the dry exhaust gas.

The CO_2 and O_2 content of the exhaust gas was measured by an infrared absorption detector and a detector exploiting the paramagnetism of the O_2 molecule, respectively. From this data the fuel equivalence ratio was determined, and together with the air preheat temperature, the adiabatic equilibrium flame temperature T_{ad} was calculated by the EQUIL code [13] of the CHEMKIN-II software package [14] using the GRI-MECH 3.0 [15] reaction mechanism. The uncertainty of this procedure is typically $\Delta T_{ad} \approx \pm 15$ K.

1.2 Emission Characteristics of Perfectly Premixed Operation With Fuel Natural Gas. In the CPMCP test combustor a substantial extension of the regime of stable combustion in the lean regime was achieved, such that even for natural gas (CH_4 content: 98%$_{vol}$) with its high LBO temperature reliable operation with adiabatic flame temperatures of 1550 K and below and NO_x emissions below 1 ppm(v) (15% O_2, dry) has been demonstrated [9,10]. If the test combustor is operated with perfect premixing of reactants (by an external premixer) within its whole operation range the adiabatic flame temperature T_{ad} is the only relevant parameter for NO_x formation, as had been found earlier for lean perfectly premixed natural gas combustion [16]. According to Steele et al. [17] an Arrhenius best fit function has been obtained from the measured mole fractions χ_{NO_x} of NO_x in the exhaust gas (for 1500 K $< T_{ad} <$ 1850 K). Thus, the χ_{NO_x} (as ppm(v) at 15% O_2, dry) can be expressed by

$$\frac{\chi_{NO_x}}{\text{ppm(v)}} = 3.184 \times 10^5 \exp\left(-\frac{20{,}486\ \text{K}}{T_{ad}}\right) \quad (1)$$

as a function of T_{ad} [18]. The corresponding global activation energy of NO_x formation is 170 kJ/mol (in contrast to 318 kJ/mol of the rate-limiting step in the Zeldovich mechanism [19]), which shows that the thermal mechanism does not play a relevant role in the CPMCP at these low flame temperatures [17].

At the same time when NO_x emissions are reduced below 1 ppm(v), CO emissions also remain in a low range of below 8 ppm(v) (15% O_2, dry) in the whole operation range of the test combustor at atmospheric pressure. For example, at T_{ad} = 1600 K, CO emissions lie in the range 0.5 ppm(v) $< \chi_{CO} <$ 3.0 ppm(v) with the clear trend that both higher air preheat temperatures and lower mixture mass flow rates lead to lower χ_{CO}. The seemingly occurrence of subequilibrium χ_{CO} can be explained by heat losses of the exhaust gas in the burnout combustion chamber, where the sample gas is collected, which shifts the equilibrium χ_{CO} to distinctly lower values (Le Châtelier's rule) [18].

The CO emissions of the atmospheric CPMCP test combustor are very low, though the combustion temperature is low, which is expected to reduce the CO oxidation rate. But the corresponding elementary reaction

$$CO + OH \rightleftharpoons CO_2 + H \quad (2)$$

has a very low activation energy in forward direction, so that even at flame temperatures of 1500 K, the Arrhenius exponential term is approximately unity [19]. The well-known temperature effect on the CO oxidation rate is due to the strong temperature sensitivity of the OH concentration [19]. And one of the principles of the CPMCP is to provide elevated OH concentrations in the mixing and reaction zones for the stabilization of the combustion. Furthermore, the mean residence time in the precombustor is relatively high, and the higher pressure in gas turbine combustors will further decrease the CO emissions of the CPMCP because the higher particle density overcompensates the decreasing OH mole fraction and leads to a higher CO oxidation rate.

Combustion of hydrogen-natural gas fuel mixtures means a further decrease in CO emissions, as on one hand the fraction of C-species in the fuel decreases, and on the other hand the H_2 reactions may generate higher radical mole fractions like that of OH [20,21], which increase the forward rate of Reaction (2). This is also the reason why emissions of unburned hydrocarbons are not an issue. Therefore, the results presented subsequently concentrate on NO_x emissions abatement and operational flexibility.

2 Emission Characteristics of Technically Premixed Operation With Fuel Natural Gas

Before analyzing the emissions characteristics obtained with hydrogen-natural gas mixtures a brief review of the NO_x emissions from technically premixed (using the VPMI) natural gas combustion shall be given first. Figure 4(*a*) shows emission data already presented before in Ref. [10], which were achieved with the VPMI fuel orifice diameter d_O=2.5 mm. For the high air preheat operating points, the VPMI momentum flux ratio $j = (\rho_{fuel} \cdot v_{fuel}^2)/(\rho_{air} \cdot v_{air}^2)$ is near its optimum $j \approx 1$, for which the VPMI premixing performance is optimal [10]. Then the NO_x emissions are identical (within measurement uncertainty) with the emissions obtained with perfect premixing that are described by Eq. (1). Only for low air preheat temperature, where $j > 5$, χ_{NO_x} clearly increases. But there are two effects that keep this increase quite low [10,18]. First, the low preheat temperature means that more hot combustion products need to be admixed to the reactants in order to reach a mixture temperature leading to quick self-ignition, thus shifting the ignition zone away from the VPMI exit and increasing the effective premixing flow length, which compensates partly the worse VPMI performance. Second, high mixture mass flow rates $\dot{m}$ and therefore higher bulk velocities also lead to a shift in ignition zones with the same positive effect on NO_x emissions.

Figure 4(*b*) shows that in addition to the momentum flux ratio j, the injection hole diameter d_O has to be chosen carefully for good VPMI performance. With d_O=3.2 mm $\chi_{NO_x} < 1$ ppm(v) (15% O_2, dry) is not achieved in the analyzed operation range; although for most operating points, especially with medium air preheat, $j \approx 1$ is valid. Compared to d_O=2.5 mm the NO_x emissions increase by nearly one order of magnitude. The extension of the LBO limit to T_{ad}=1350 K is due to the bad VPMI performance

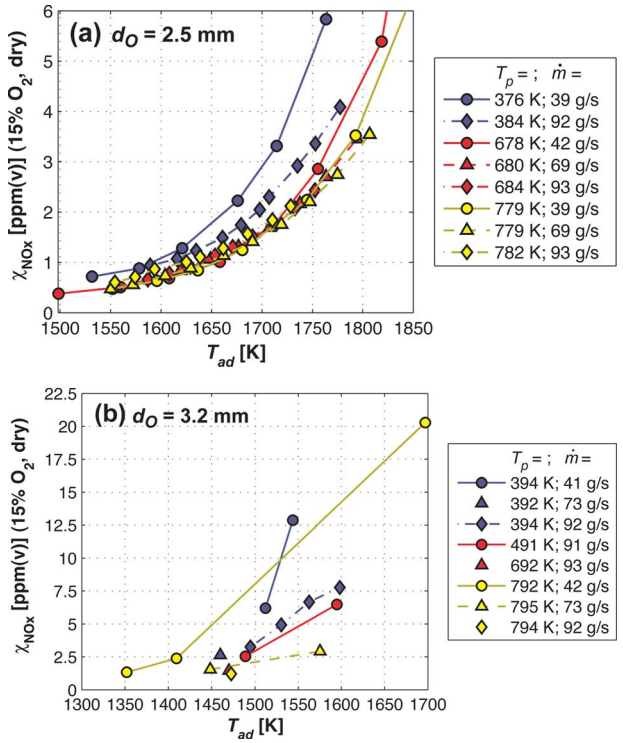

Fig. 4 NO_x emissions with natural gas as fuel for (*a*) d_O =2.5 mm (d_O/d_I=0.125) and (*b*) d_O=3.2 mm (d_O/d_I=0.160)

leading to local flame temperature peaks, for which effective values of 200–300 K above mean T_{ad} are derived with Eq. (1) from χ_{NO_x}.[2]

The conclusion is that for optimal VPMI operation in the CPMCP test combustor, d_O=2.5 mm (d_O/d_I=0.125) has to be chosen.

3 Emission Characteristics of Technically Premixed Operation With Hydrogen-Natural Gas Fuel Mixtures

The experiments with hydrogen-natural gas fuel mixtures have been conducted in order to evaluate the CPMCP test combustor's ability to cleanly burn more reactive fuels. The higher reactivity of these mixtures in comparison to natural gas results on one hand from the higher reactivity of hydrogen itself, which is evident in (even by orders of magnitude) lower ignition delay times [22] or higher flame velocities [19]. On the other hand, the ignition delay is reduced for the hydrocarbon part of the mixture, and the oxidation rate increases with the higher radical content due to the H_2 combustion [20,21]. Thus, relatively small fractions of H_2 can increase reactivity substantially [23], so that ultimately the LBO limit is shifted toward a lower T_{ad} [24,25].

These changes in reaction kinetics alter also the reaction zone structure: Compared to natural gas flames the flames become more and more compact and shorter with increasing H_2 addition [24,26], and in flameless combustion processes the reaction zone is shifted toward the fresh gas injectors [27]. This means that in the case of imperfectly premixed reactants, ignition and reaction already happen in regions of still elevated reactant unmixedness, where higher local flame temperatures produce more NO_x. This overcompensates the reduction in Fenimore–NO_x, which is due to the lower hydrocarbon radical content in the reacting mixture [20]. All in all, it can be expected that with increasing H_2 content

[2]This behavior could be used for the replacement of the pilot burner by additional annular fuel passages around the optimized VPMI fuel orifices, which would allow low-emissions operation in low part load.

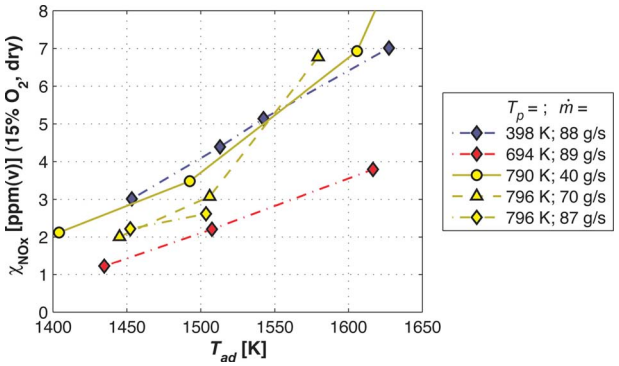

Fig. 5 NO_x emissions with the "70%$_{vol}H_2$–30%$_{vol}CH_4$" fuel mixture for d_O=2.5 mm

in the fuel mixture, the adiabatic flame temperature has to be reduced in order to keep the NO_x emissions constant. This effect has been found experimentally before [27].

In this study mainly a mixture of 30% natural gas (98% CH_4) and 70% hydrogen (volumetric) has been used as fuel. According to Burmberger [28], combustion characteristics, such as laminar flame speed and critical chemical time scale, correspond to technically relevant synthesis gases from coal or biomass gasification (e.g., "35%$_{vol}$CO–45%$_{vol}H_2$–20%$_{vol}CO_2$" or "35%$_{vol}$CO –27%$_{vol}H_2$–13%$_{vol}CH_4$–19%$_{vol}CO_2$–6%$_{vol}C_3H_8$").

The NO_x emissions obtained with the fuel mixture at various operating points are plotted in Fig. 5. For these experiments the VPMI fuel orifice diameter d_O=2.5 mm was used (therefore, Fig. 5 has to be compared with Fig. 4(*a*) for natural gas). This value of d_O provides also in this case optimal VPMI performance because the d_O/d_I ratio is still optimal, and for the investigated high-air-preheat operating points (at lower T_{ad} than with natural gas) the values of j remain in the vicinity of unity (Fig. 6). Now $\chi_{NO_x} \approx 1$ ppm(v) (15% O_2, dry) is achievable only for $T_{ad} < 1450$ K. There seems to be an optimum of the air preheat temperature T_p; with T_p=694 K the NO_x emissions are noticeably lower than those at operating points with T_p=796 K at the same mixture mass flow rate. The reason for this effect remains unclear because it did not appear in other experiments that are not presented here. The positive effect of higher mixture mass flow rates on the premixing quality—leading to lower NO_x emissions—partly occurs now also for high air preheat (Fig. 5), where it did not appear with the fuel natural gas (Fig. 4(*a*)). Interestingly, the NO_x formation

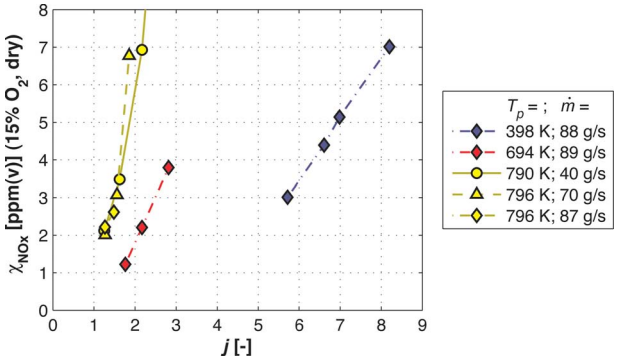

Fig. 6 NO_x emissions with the 70%$_{vol}H_2$–30%$_{vol}CH_4$ fuel mixture for d_O=2.5 mm, plotted against the VPMI momentum flux ratio

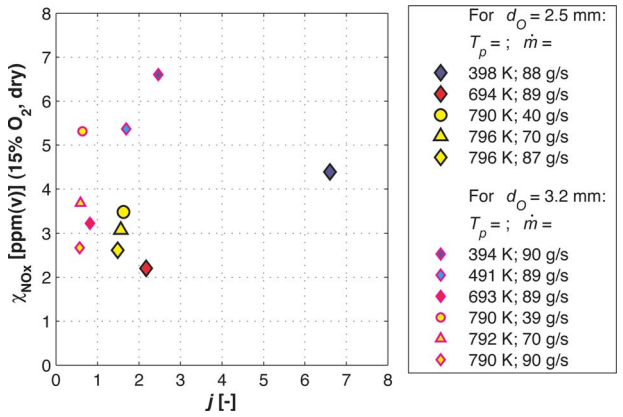

Fig. 7 NO_x emissions with the 70%$_{vol}H_2$–30%$_{vol}CH_4$ fuel mixture at $T_{ad}\approx1500$ K for $d_O=2.5$ mm and $d_O=3.2$ mm, plotted against the VPMI momentum flux ratio

increase due to the H_2 addition to the fuel is not higher than the increase due to the use of the nonoptimal VPMI fuel orifice with natural gas (see Fig. 4(*b*)).[3]

Neglecting any chemical effect of the H_2 reactions on the NO_x formation, Eq. (1) implies an effective temperature for NO_x production between 200 K and 300 K above the adiabatic equilibrium temperature of the reactant mixture. But, as will be shown later, at atmospheric pressure there seems to be a clear chemical effect due to the H_2 addition. Nevertheless, this analysis gives the correct trend and shows that ignition and reaction occur in regions of elevated unmixedness of reactants.

In order to analyze the effects influencing the premixing process the NO_x emissions are plotted against the VPMI momentum flux ratio $j=(\rho_{fuel}\cdot v_{fuel}^2)/(\rho_{air}\cdot v_{air}^2)$ in Fig. 6. The majority of operating points with high air preheat lies in the region around $j\approx1$, which is optimal for the premixing quality [10]. Nevertheless, the NO_x emissions of the operating points with low air preheat ($T_p=398$ K, $\dot{m}=88$ g/s), which lie with $j>5.5$ far from the VPMI optimum, are little different from the emissions for $T_p=790$ K and $\dot{m}=40$ g/s (compared to Fig. 5). The reason for this behavior is that with low air preheat, greater amounts of hot combustion products need to be mixed to the fresh reactants for quick ignition. This, together with the higher mixture mass flow rate, leads to a shift in the reaction zones in the downstream direction away from the injector ports. This compensates at least partly for the worse VPMI performance because the effective premixing flow length before ignition increases.

In order to show the influence of the VPMI fuel orifice diameter on the premixing quality, the NO_x emissions of some operating points at $T_{ad}\approx1500$ K obtained with either $d_O=2.5$ mm or $d_O=3.2$ mm are presented in Fig. 7. The behavior is completely different from natural gas, whereas with natural gas the increase in d_O led to an increase in χ_{NO_x} by almost one order of magnitude, here changes are much smaller. As the reason for this difference can be found only in the fuel properties, it seems that the higher diffusivity of H_2 in air accelerates the mixing process to an extent that, at least for $j\approx1$ and high mass flow rates, the effect of the nonoptimal fuel orifice diameter is compensated. However, a decrease in the mass flow rate or an increase in j leads to a stronger increase in χ_{NO_x} with $d_O=3.2$ mm than with $d_O=2.5$ mm. Under these circumstances the inferior VPMI premixing performance with larger d_O cannot be compensated any more.

[3]Furthermore, some tests have been conducted with higher hydrogen content: With a 90%$_{vol}H_2$–10%$_{vol}CH_4$ fuel mixture and $d_O=2.5$ mm, the NO_x emissions keep below 6 ppm(v) (15% O_2, dry) for $T_{ad}\leq1520$ K.

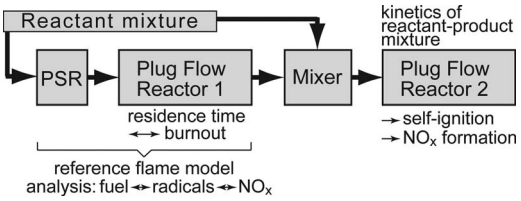

Fig. 8 Schematic of the chemical reactor network used for the analysis of fuel-dependent self-ignition kinetics and chemical effects on NO_x formation

4 Chemical Reactor Network Analysis

The chemical reactor network used for the analysis of the influence of the fuel mixture and the pressure on both self-ignition kinetics and NO_x formation was described earlier in greater detail [6,29]. It consists of two adiabatic stages (Fig. 8). The first is a combination of a perfectly stirred reactor (PSR) [30] (minimized so that ignition just occurs and thus acts as an artificial ignition zone) and a subsequent plug flow reactor (PFR) [31], where the variation in the residence time delivers combustion products of various burnout. This PSR-PFR combination is additionally used as a reference model of a turbulent premixed flame [32] for the study of chemical effects on NO_x formation depending on the fuel mixture. At the beginning of the second stage, first-stage products with specified burnout are instantaneously perfectly mixed with fresh reactants; then the self-ignition kinetics of the obtained mixture is simulated in the subsequent second PFR.

The simulations have been conducted with the CHEMKIN-II software package [14] and the GRI-MECH 3.0 reaction mechanism [15]. Although this mechanism has been optimized and validated only for natural gas combustion, it can be expected that it yields the correct trends for natural gas-hydrogen mixtures because the reactions of hydrogen are an important subset of natural gas combustion. Natural gas has been modeled as methane.

4.1 Variation of Self-Ignition Kinetics With Fuel and Pressure. The self-ignition delay times have been calculated for the fuels natural gas and the hydrogen-natural gas mixture at $T_{ad}=1600$ K, $T_p=700$ K, and pressures of 0.1 MPa and 2.0 MPa.

Figures 9(*a*) and 9(*b*) show the self-ignition times obtained in the second stage of the chemical reactor network for natural gas, which had been presented in more detail before [6,29]. They are plotted for various degrees of product burnout against the mole fraction χ_{prod} of combustion products (from the first stage) in the self-igniting reactant-product mixture. In order to obtain various burnout products, they are extracted from the first PFR (see Fig. 8) at characteristic time steps: just after the PSR exit; when the maximum of the OH radical mole fraction is reached; when the difference between this OH maximum and the OH equilibrium value is decayed to 80%–20%; when good burnout is achieved ($\chi_{CO}=1.5\cdot\chi_{CO,equilibrium}$); and when burnout is complete (see legend in Fig. 9).

For $p=0.1$ MPa the influence of the products' radical concentration on the self-ignition time is obvious (Fig. 9(*a*)); the effect of product temperature deficiency is relevant only for the case of minimal product burnout (PSR exit). At a high pressure of $p=2.0$ MPa (Fig. 9(*b*)), the ignition performance is practically independent of the product burnout: the effect of elevated radical concentration compensates the temperature deficit of incompletely burnt products. For achieving a constant ignition delay time now the admixing of a definitely lower amount of products is sufficient than for $p=0.1$ MPa and medium or good product burnout.

With the fuel mixture the ignition performance is clearly different. For $p=0.1$ MPa and $p=2.0$ MPa (Figs. 9(*c*) and 9(*d*)) definitely lower products fractions χ_{prod} are necessary for quick ignition than for methane, and the dependence of the self-ignition time on the product burnout is limited only to the minimum burn-

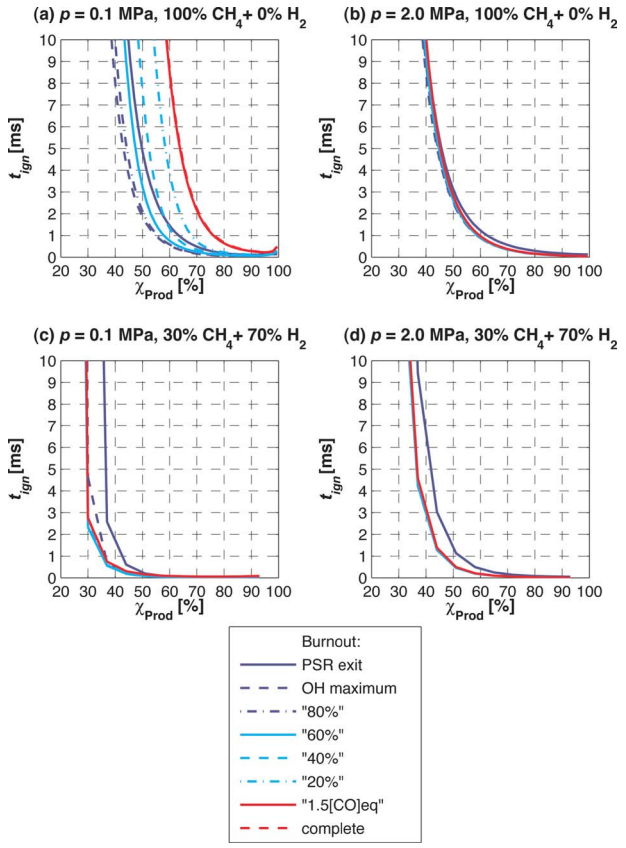

Fig. 9 Self-ignition time of mixtures of reactants with certain amounts of hot combustion products of various burnout for different fuels and pressures (T_{ad}=1600 K, GRI-MECH 3.0 [15])

out case because of the high temperature deficit there. Interestingly, the values of χ_{prod} needed at high pressure to achieve self-ignition within 1 ms are by nearly one-third higher than for atmospheric pressure.

Simulations with lower hydrogen content showed that H_2 addition always leads to better ignition performance, and this effect increases with increasing H_2 content in the fuel. The adverse effect of pressure on the ignition performance is also stronger with higher H_2 content [18].

The trends found in the simulations with the idealized chemical reactor network lead to the following conclusions concerning the NO_x emissions of a technically premixed CPMCP combustor operated with hydrogen-natural gas fuel mixtures. First, H_2 addition to natural gas leads to higher reactivity of the mixture, which means that admixing lower amounts of hot products is sufficient for quick ignition. Therefore, ignition occurs after a reduced mixing zone length, where reactant unmixedness is still higher—producing more NO_x. Second, it is important to know the effect of elevated pressure in gas turbine combustors on this shift in the ignition zone and thus on the NO_x emissions. On one hand, higher pressure increases reaction rates due to increased volumetric concentrations of species, but, on the other hand, radical concentrations are reduced by up to two orders of magnitude from p =0.1 MPa to p=2.0 MPa. Here the simulations show that, especially for higher H_2 content in the fuel, the ignition performance at high pressure becomes worse than at atmospheric pressure. This means that at high pressure more hot combustion products need to be admixed and higher mixture temperatures need to be reached in order to achieve the same self-ignition delay time. Therefore, the effective premixing length is increased, and it can be expected that the CPMCP gas turbine application will not emit more NO_x than the test combustor.[4]

4.2 Chemical Effect on NO_x Formation. Finally, it is interesting to analyze the effect of radical concentration changes due to varying H_2 mole fraction χ_{H_2} in the fuel mixture on NO_x formation, which is obtained from the first PSR-PFR combination of the reactor network (Fig. 8) acting as reference flame model. Figures 10(*a*) and 10(*b*) show for three different pressures and varying χ_{H_2} the changes of the maximum O and OH mole fractions relative to the corresponding natural-gas-only reference values at T_{ad} =1600 K (T_p=700 K). At atmospheric pressure a considerable increase is apparent at smaller χ_{H_2} than at higher pressure, where the increase occurs only between 70% and 90% H_2 content in the fuel.

These radicals are important for the thermal (O and OH), the N_2O (O), and the NNH (O) mechanisms of NO_x formation. In Fig. 10(*c*) the corresponding relative changes in NO_x emissions are displayed. These changes are due to chemical changes in the combustion of the different fuels, as the simulations assume perfectly premixed reactants. It is obvious that the simulated NO_x emissions correlate well with the maximum O and OH mole fractions. The values in Figure 10(*c*) are obtained when the burnout criterion $\chi_{CO}=1.5\cdot\chi_{CO,equilibrium}$ is fulfilled in the PFR, but any choice of residence time between 2 ms and 30 ms (and above) gives practically the same result. These simulations with GRI-MECH 3.0 [15] predict for the fuel mixture at atmospheric pressure nearly twice the NO_x emissions than for natural gas combustion. This chemical effect accounts for a considerable share of the experimentally found NO_x emissions increase, although the above-mentioned reduction in premixing length is the dominating effect. These results are consistent with earlier studies, like Ref. [24], where for p=0.5 MPa and $\chi_{H_2}=20\%_{vol}$ no chemical effect was found.

The measurements at atmospheric pressure together with the chemical kinetics modeling indicate that for fuel mixtures with less than $70\%_{vol}$ H_2 very low NO_x emissions can be expected for the pressures of gas turbine combustors.

5 Conclusions

Fuel flexibility of the atmospheric CPMCP test combustor, which had been optimized for clean natural gas combustion, was demonstrated: stable combustion with high H_2 content in the fuel is possible with relatively low NO_x and very low CO emissions.

For operation with *natural gas* and the optimal configuration of the vortex-premixer injectors, there is no pronounced sensitivity of the NO_x emissions on the limited VPMI premixing quality, as long as the mean adiabatic flame temperature is kept below 1600 K and the deviation of the momentum flux ratio j from unity is not too large ($1<j<6$). The reason for this behavior is the additional mixing process between the VPMI exit and the ignition of the mixture.

For operation with the *hydrogen-natural gas* ($70\%_{vol}$:$30\%_{vol}$) *mixture* and the optimal VPMI configuration, the NO_x emissions increase, compared to natural gas combustion, by almost one order of magnitude: for $T_{ad}<1600$ K values of χ_{NO_x} below 7 ppm(v) (15% O_2, dry) are obtained. NO_x emissions of 1 ppm(v) are approached only for $T_{ad}<1450$ K. The reason for this behavior is the higher reactivity of the fuel mixture, which ignites already in regions of still elevated unmixedness of reactants near the VPMI exit.

[4]In case the early ignition in regions of too high unmixedness at high pressures turns out to be problematic, the ignition delay could be increased by the addition of water vapor to the reactants, because H_2O as collision partner enhances in particular at high pressure a three-body chain break reaction reducing the radical concentration [34].

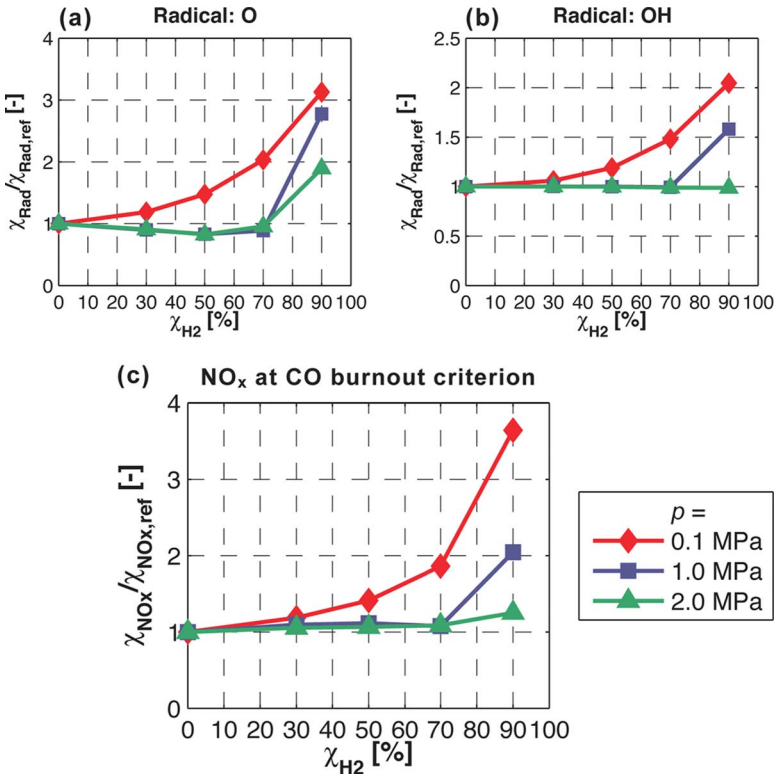

Fig. 10 Relative changes of (*a*) O, (*b*) OH, and (*c*) NO_x mole fractions with the hydrogen content in the fuel mixture and the pressure (T_{ad}=1600 K, GRI-MECH 3.0 [15])

Chemical reactor network simulations indicate that elevated pressure does not add to this trend of "early" ignition that causes the increase in NO_x emissions. A chemical effect of H_2 combustion that increases NO_x formation is present: In the simulations it is substantial for atmospheric pressure, but appears at higher pressures only for high H_2 content in the fuel mixture.

6 Outlook

The development of vortex-premixer injectors has been an important step toward the technical application of the CPMCP. VPMIs are gas turbine compatible fuel-air premixers based on a low-pressure-loss vortex generator for implementation in the precombustor injector tubes [10]. For injector tubes with an inner diameter of d_I=20 mm, the ratio of the fuel orifice diameter d_O and d_I has an optimum value at d_I/d_O=0.125. The optimal value of the momentum flux ratio is $j \approx 1$. VPMIs have been optimized for gas turbine relevant air preheat temperatures, so that with *natural* gas as fuel and high air preheat NO_x emissions below 1 ppm(v) and CO emissions below 8 ppm(v) (15% O_2, dry) are achieved for adiabatic flame temperatures between 1550 K and 1630 K.

Therefore, the cyclic-periodical-mixing combustor has a good application potential in small or medium-size gas turbines such as recuperated microgas turbines or industrial gas turbines for decentralized cogeneration of power and heat. In these cases, low temperature combustion, like the CPMCP, does not adversely affect the gas turbine efficiency because the maximum allowable turbine inlet temperature is low enough.

Experiments show that the implementation of the CPMCP in an air-cooled all-steel combustor is feasible, as long as the liner temperature is kept above the self-ignition temperature of the reactants. This is due to a certain radial temperature stratification leading to subadiabatic wall temperatures even in the well-insulated test combustor. Therefore, a CPMCP application is viable and seems to be prepared to fulfill the requirements of, e.g., the *California Senate Bill SB 1298*, corresponding to emissions of $\chi_{NO_x} < 1$ ppm(v) and $\chi_{CO} < 3$ ppm(v) (15% O_2) for a microgas turbine of 25% efficiency [33], if natural gas is used as fuel.

The achievement of the long-term objective of using hydrogen-containing fuel mixtures with sub-ppm NO_x emission levels requires further R&D work on efficient and safe fuel-air premixing systems.

Acknowledgment

The authors wish to thank Mr. Udo Glückert for his assistance in conducting the experiments.

Nomenclature

Latin Letters

d_I = inner diameter of VPMI injector tube
d_O = fuel orifice diameter in VPMI
j = momentum flux ratio in VPMI
$\dot{m}$ = fresh mixture mass flow rate
p = pressure
T_{ad} = adiabatic equilibrium flame temperature
T_p = air preheat temperature
v = velocity

Greek Letters

$\Delta\ldots$ = measurement uncertainty
χ = mole fraction
ρ = density

Subscripts

prod = combustion products
rad = radicals

ref = reference value

References

[1] Milani, A., and Saponaro, A., 2001, "Diluted Combustion Technologies," The IFRF Electronic Combustion Journal, February, p. 200101.

[2] Cavaliere, A., and de Joannon, M., 2004, "Mild Combustion," Prog. Energy Combust. Sci., **30**, pp. 329–366.

[3] de Joannon, M., Matarazzo, A., Sabia, P., and Cavaliere, A., 2006, "Mild Combustion in Homogeneous Charge Diffusion Ignition (HCDI) Regime," 31st Symposium (International) on Combustion, Combustion Institute.

[4] Milani, A., and Wünning, J., 2002, "What is Flameless Combustion?," IFRF Online Combustion Handbook, Combustion File No. 171.

[5] Wünning, J. A., and Wünning, J. G., 1997, "Flameless Oxidation to Reduce Thermal NO-Formation," Prog. Energy Combust. Sci., **23**, pp. 81–94.

[6] Kalb, J. R., and Sattelmayer, T., 2006, "Lean Blowout Limit and NO_x-Production of a Premixed Sub-ppm-NO_x Burner With Periodic Recirculation of Combustion Products," ASME J. Eng. Gas Turbines Power, **128**(2), pp. 247–254.

[7] Tsuji, H., Gupta, A. K., Hasegawa, T., Katsuki, M., Kishimoto, K., and Morita, M., 2002, *High Temperature Air Combustion. From Energy Conservation to Pollution Reduction*, CRC, Boca Raton, FL.

[8] Gupta, A. K., 2000, "Flame Characteristics and Challenges With High Temperature Air Combustion," *Proceedings of the International Joint Power Generation Conference*, Paper No. IJPGC2000-15087.

[9] Brückner-Kalb, J. R., Hirsch, C., and Sattelmayer, T., 2006, "Operation Characteristics of a Premixed Sub-ppm NO_x Burner With Periodical Recirculation of Combustion Products," ASME Paper No. GT2006-90072.

[10] Brückner-Kalb, J. R., Napravnik, C., Hirsch, C., and Sattelmayer, T., 2007, "Development of a Fuel-Air Premixer for a Sub-ppm NO_x Burner," ASME Paper No. GT2007-27779.

[11] ECO PHYSICS AG, 1997, User's Manual for CLD 700 EL ht., Munich, Germany.

[12] Gärtner, F. J., 1982, "Vergleich der Bildung von Stickstoffoxid in Methanol-Luft-und Kohlenwasserstoff-Luft-Flammen," Ph.D. thesis, Technische Hochschule Darmstadt, Darmstadt.

[13] Lutz, A. E., Kee, R. J., and Miller, J. A., 1998, "Equil: A CHEMKIN Implementation of STANJAN for Computing Chemical Equilibria," Sandia National Laboratories, Sandia Technical Report No.

[14] Kee, R. J., Miller, J. A., and Jefferson, T. H., 1989, "CHEMKIN: A General Purpose, Problem-Independent, Transportable, Fortran Chemical Kinetics Code Package," Sandia National Laboratories, Sandia Technical Report No. SAND80-8003 UC-4.

[15] Smith, G. P., Golden, D. M., Frenklach, M., Moriarty, N. W., Eiteneer, B., Goldenberg, M., Bowman, C. T., Hanson, R. K., Song, S., Gardiner, W. C., Lissianski, V. V., and Qin, Z., 1999, "GRI-MECH 3.0," http://www.me.berkeley.edu/gri_mech/.

[16] Leonard, G., and Stegmaier, J., 1994, "Development of an Aeroderivative Gas Turbine Dry Low Emissions Combustion System," ASME J. Eng. Gas Turbines Power, **116**, pp. 542–546.

[17] Steele, R. C., Tonouchi, J. H., Nicol, D. G., Horning, D. C., Malte, P. C., and Pratt, D. T., 1998, "Characterization of NO_x, N_2O, and CO for Lean-Premixed Combustion in a High-Pressure Jet-Stirred Reactor," ASME J. Eng. Gas Turbines Power, **120**, pp. 303–310.

[18] Brückner-Kalb, J. R., 2007, "Sub-ppm-NO_x-Verbrennungsverfahren für Gasturbinen," Ph.D. thesis, Lehrstuhl für Thermodynamik, Technische Universität München, Garching.

[19] Warnatz, J., Maas, U., and Dibble, R. W., 2001, *Combustion. Physical and Chemical Fundamentals, Modeling and Simulation, Experiments, Pollutant Formation*, 3rd ed., Springer Verlag, Berlin.

[20] Naha, S., Briones, A. M., and Aggarwal, S. K., 2005, "Effects of Fuel Blends on Pollutant Emissions in Flames," Combust. Sci. Technol., **177**, pp. 183–220.

[21] Derudi, M., Villani, A., and Rota, R., 2007, "Sustainability of Mild Combustion of Hydrogen-Containing Hybrid Fuels," Proc. Combust. Inst., **31**, pp. 3393–3400.

[22] Therkelsen, P., Mauzey, J., McDonell, V., and Samuelsen, S., 2006, "Evaluation of a Low Emission Gas Turbine Operated on Hydrogen," ASME Paper No. GT2006-90725.

[23] Sabia, P., Fierro, S., Cavaliere, A., de Joannon, M., and Tregrossi, A., 2005, "Hydrogen Addition Effect on Instabilities of Methane Mild Combustion in a Well-Stirred Flow Reactor," 28th Combustion Meeting: Combustion and Urban Areas, Combustion Institute.

[24] Griebel, P., Boschek, E., and Jansohn, P., 2006, "Flame Stability and NO_x Emission Improvements Due to H_2 Enrichment of Turbulent, Lean Premixed, High-Pressure, Methane/Air Flames," The Future of Gas Turbine Technology-Third International Conference, Paper No. ID S4 T2/1.

[25] Boschek, E., Griebel, P., and Jansohn, P., 2007, "Fuel Variability Effects on Turbulent, Lean Premixed Flames at High Pressures," ASME Paper No. GT2007-27496.

[26] Tomczak, H.-J., Benelli, G., Carrai, L., and Cecchini, D., 2002, "Investigation of a Gas Turbine Combustion System Fired With Mixtures of Natural Gas and Hydrogen," The IFRF Electronic Combustion Journal, Article No. 200207.

[27] Lückerath, R., Meier, W., and Aigner, M., 2007, "FLOX Combustion at High Pressure With Different Fuel Compositions," ASME Paper No. GT2007-27337.

[28] Burmberger, S., 2004, "Einfluss der Brennstoffzusammensetzung auf die reaktionskinetischen Parameter von Vormischflammen," Diploma thesis, Lehrstuhl für Thermodynamik, TUM, Munich.

[29] Kalb, J. R., and Sattelmayer, T., 2004, "Lean Blowout Limit and NO_x-Production of a Premixed Sub-ppm-NO_x Burner With Periodic Flue Gas Recirculation," ASME Paper No. GT2004-53410.

[30] Glarborg, P., Kee, R. J., Grcar, J. F., and Miller, J. A., 1988, "PSR: A Fortran Program for Modeling Well-Stirred Reactors," Sandia National Laboratories, Sandia Technical Report No. SAND86-8209 UC-4.

[31] Lutz, A. E., Kee, R. J., and Miller, J. A., 1988, "Senkin: A Fortran Program for Predicting Homogeneous Gas Phase Chemical Kinetics With Sensitivity Analysis," Sandia National Laboratories, Sandia Technical Report No. SAND87-8248.

[32] Sattelmayer, T., Polifke, W., Winkler, D., and Doebbeling, K., 1998, "NO_x-Abatement Potential of Lean-Premixed GT Combustors," ASME J. Eng. Gas Turbines Power, **120**, pp. 48–58.

[33] Phi, V. M., Mauzey, J. L., McDonell, V. G., and Samuelsen, G. S., 2004, "Fuel Injection and Emissions Characteristics of a Commercial Microturbine Generator," ASME Paper No. GT2004-54039.

[34] Sabia, P., Schiesswohl, E., de Joannon, M. R., and Cavaliere, A., 2006, "Numerical Analysis of Hydrogen Mild Combustion," Turk. J. Eng. Environ. Sci., **30**, pp. 127–134.

Flame Transfer Functions for Liquid-Fueled Swirl-Stabilized Turbulent Lean Direct Fuel Injection Combustion

Tongxun Yi[1]
e-mail: tzy1@psu.edu

Domenic A. Santavicca

Department of Mechanical and Nuclear Engineering,
Pennsylvania State University,
University Park, PA 16802

Heat release rate responses to inlet fuel modulations, i.e., the flame transfer function (FTF), are measured for a turbulent, liquid-fueled, swirl-stabilized lean direct fuel injection combustor. Fuel modulations are achieved using a motor-driven rotary fuel valve designed specially for this purpose, which is capable of fuel modulations of up to 1 kHz. Small-amplitude fuel modulations, typically below 2.0% of the mean fuel, are applied in this study. There is almost no change in FTFs at different fuel-modulation amplitudes, implying that the derived FTFs are linear and that the induced heat release rate oscillations mainly respond to variations in the instantaneous fuel flow rate rather than in the droplet size and distribution. The gain and phases of the FTFs at different air flow rates and preheat temperatures are examined. The instantaneous fuel flow rate is determined from pressure measurements upstream of a fuel nozzle. Applications of the FTF to modeling and control of combustion instability and lean blowout are discussed.
[DOI: 10.1115/1.3157101]

1 Introduction

Combustion instability and lean blowout are major technical challenges for both gas-fueled and liquid-fueled dry-low-emission (DLE) combustion [1–3]. Combustion instability refers to the self-excited, large-amplitude, limit-cycle thermoacoustic oscillations caused by positive feedback between pressure and heat release rate. Strong pressure pulsations shorten an engine's life due to enhanced heat transfer, lower combustion efficiency, exacerbate NO_x emissions, generate noise pollutions, and may even cause instrumentation failures. Lean blowout (LBO) refers to partial or global flame quenching when the equivalence ratio is decreased below certain thresholds. As the equivalence ratio approaches the lean flammability limits, a combustor's resistance to external disturbances or small deviations from the equilibrium points is considerably weakened [4]. Thus, a small external disturbance in the inlet turbulence, the fuel composition, the fuel flow rate, and/or the air flow rate may quench the flame. LBO necessitates expensive shutdown and restarting procedures for land-based gas turbines, and represents a major safety hazard for aircraft engines.

The underlying mechanisms for combustion instability and LBO are fundamentally different, but they both make engines unable to operate in an efficient, safe, and environment-friendly manner at lean conditions. Model-based control design is a standard approach for control engineers and theorists. First-principle low-order models provide valuable insight into the underlying mechanisms, but their accuracy critically depends on the assumptions and simplifications [5]. The measured flame transfer functions (FTFs), i.e., heat release responses to inlet air and/or fuel modulations, provide an accurate description of combustion dynamics around the working conditions where they are derived.

The FTF is determined by both the intrinsic dynamics of a specific combustor and the manner in which dynamic fuel is introduced into and dispersed inside the reacting flow field. To minimize the amount of fuel modulations required, it is desirable for the FTF to have as large a gain as possible. This can only be achieved by maximizing the conversion of modulated fuel flow rate to modulated heat release rate. In gas turbine combustors, the heat release zone lies along the swirling shear layer outside the recirculating vortex breakdown. Because of flow field inhomogeneities and the convective time delay, the spatially and temporally coherent fuel modulations exiting the fuel nozzle become spatially dispersed and temporally less coherent as they are transported downstream, which lowers the FTF gain. The situation becomes even worse for longer flames. Droplet size also plays a role in the resulting FTFs. Yu and Wilson [6] noticed that the critical fuel flux, i.e., the minimum fuel modulations required to attenuate combustion instability, depends on the droplet size. Smaller droplet size reduces the heating and evaporation time, and enhances the control effectiveness. This observation is consistent with the proposition that the dynamic evaporation process may play an important role in liquid-fueled combustion instability [7]. Droplet size and distribution can be measured using phase Doppler particle analyzer (PDPA), Malvern sizers, combined Mie-scattering/planar laser-induced fluorescence (PLIF), and other means. However, this is out of the scope of the present study.

This paper is organized as follows. First, the experimental setup, including the combustion rig, optical setup, and the high-frequency rotary valve, is described. Second, a method for determining the instantaneous fuel flow rate out of a fuel nozzle is presented. This method is based on acoustic wave theory and pressure measurements upstream of the fuel nozzle. Third, the FTFs at different air flow rates and preheat temperatures are reported. At last, we discuss potential applications of FTFs to combustion analysis and control, including combustion instability and lean blowout.

2 Experiment Setup

Figure 1 shows the combustion rig, optical setup, and the rotary fuel valve. Preheated air enters a quartz combustion chamber, which is 0.10 m in diameter and 0.30 m in length, through a 30 deg radial-entry swirler. The exit diameter of the swirler is 3.56 cm. Pressure drop across the air swirler varies with the air

[1]Corresponding author.

Contributed by the International Gas Turbine Institute of ASME for publication in the JOURNAL OF ENGINEERING FOR GAS TURBINES AND POWER. Manuscript received March 20, 2009; final manuscript received March 22, 2009; published online November 11, 2009. Review conducted by Dilip R. Ballal. Paper presented at the ASME Gas Turbine Technical Congress and Exposition, Orlando, FL, June 8–12, 2009.

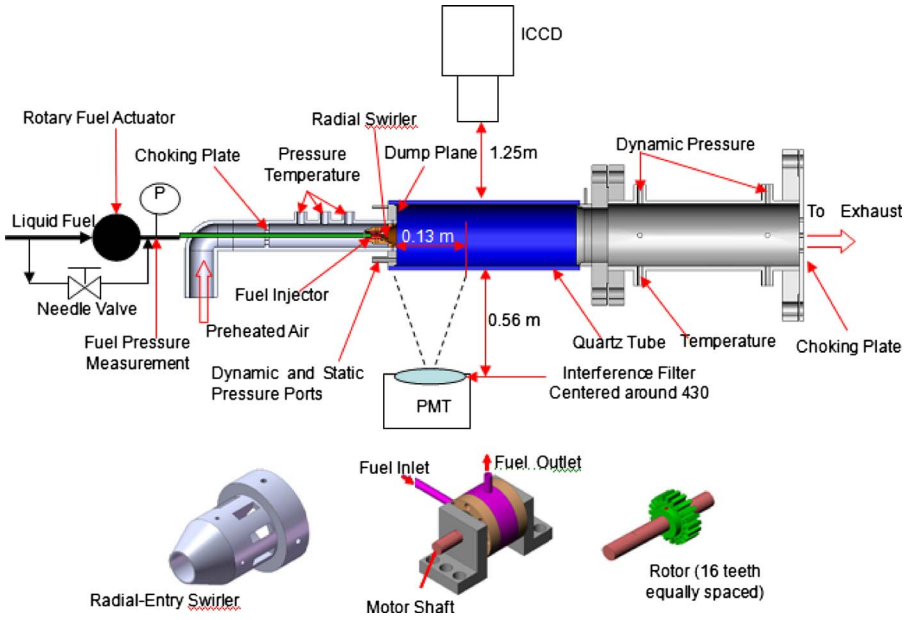

Fig. 1 The combustion rig, optical setup, and the rotary fuel actuator

flow rate and preheat temperature, but it is within 5% for all results reported here. 1-Decene or Jet-A is injected into the swirling air flow 0.02 m upstream of the dump plane using a single-point macrolaminated fuel nozzle (2.5 GPH) from Parker Hannifin. The dump plane refers to the solid surface between the swirler exit and the quartz combustion chamber. With a pressure drop of 689 kPa across the fuel nozzle, the droplet Saunter mean diameter (SMD) is less than 10 μm [8]. The air flow rate is measured using a vortex flowmeter from Omega, Stamford, CT, and the measurement uncertainty is within 1% of reading. A photomultiplier tube (PMT) (H7732-10 from Hamamatsu Photonics, Bridgewater, NJ) featured with an interference bandpass filter (~430 nm or ~307 nm with full width half minimum (FWHM) of 10 nm) is used for global chemiluminescence measurements. Generally speaking, chemiluminescence should not be assumed proportional to the instantaneous heat release rate. Probably the proportionality only exists in the weakly turbulent or the wrinkled flamelet region and in the absence of equivalence ratio variations and strong acoustic oscillations [9]. However, the instantaneous chemiluminescence intensity reflects the dynamics of the air consumption rate, the equivalence ratio, the flame temperature, and acoustic motions, thus it can be used as a valuable indicator of heat release dynamics. The PMT is placed 0.06 m downstream of the dump plane and 0.56 m away from and perpendicular to the quartz chamber. The PMT viewing area is within 0.13 m downstream of the dump plane. Time scale analysis shows that the droplets evaporation time is smaller than the convection time. Thus before the droplets are transported to the flame front, they may have been fully evaporated. In addition, from Fig. 1 one can see that high-speed air enters the diverging swirler through eight radial-entry slots, mixes with fine droplets, recombines into one stream, and suddenly expands at the dump plane. Expectedly, droplet/air entrainment and fuel/air mixing are extremely fast, and a rather homogeneous mixture of fuel vapor and air may form upstream of the major heat release zone. Thus combustion in the present rig mainly occurs in the lean premixed mode [9].

Fuel modulations are achieved using a motor-driven rotary fuel valve designed specially for this purpose. The fuel-modulation frequency is determined by the number of rotor teeth and the motor rotating speed. Liquid fuel is stored in a 19-l stainless steel tank and pressurized with N_2 at 1378 kPa. The mean fuel flow rate is measured using a linear flow meter, and the measurement uncertainty is within 5% of reading. The mean fuel flow rate is controlled using a needle valve. The rotary valve is located 0.46 m upstream of the fuel nozzle. A 0.8-l accumulator is located 0.2 m upstream of the rotary valve. Two Sensotec pressure transducers (sensitivity 172 kPa/V and uncertainty 0.25% of reading) capable of working up to 2 kHz are installed 0.29 m and 0.45 m upstream of the fuel nozzle, respectively. A bypass flow passage is installed parallel to the rotary fuel valve, and fuel-modulation amplitude is controlled by varying fuel splits between the rotary fuel valve and the bypass passage. The fuel-modulation ratio, which is defined as the ratio of the root-mean-square (rms) to mean fuel line pressure, can be greater than 30% up to 750 Hz and greater than 15% up to 1 kHz.

3 Determination of the Instantaneous Fuel Flow Rate

The instantaneous fuel flow rate out of a fuel injector is an important parameter for combustion instability analysis and control. Unsteady fuel flow rates introduced into a combustor can be caused by both self-excited pressure pulsations and fuel modulations. Because of the harsh environments and limited space inside the plenum, pressure immediately upstream of the fuel nozzle cannot be measured. Pressure measurements at some points upstream of the fuel nozzle may differ considerably in both amplitude and phases from those immediately upstream of the fuel nozzle. A literature survey shows that accurate determination of the instantaneous fuel flow rate has not been well addressed. In this study, we determine fuel modulations based on acoustic wave theory and pressure measurements at two locations upstream of the fuel nozzle. This method is an extension of a method for determining fuel flow rate modulations out of a gaseous fuel nozzle [10]. Although the mathematical formulations are essentially the same for the two methods, two major differences exist. First, the speed of sound for liquid fuel is typically above 1000 m/s [11], which is much higher than that of gaseous fuel. In addition, in order to improve atomization quality, pressure drop across a liquid-fueled pressure-swirl nozzle is typically much higher than that across a gaseous fuel injector. Thus a liquid-fueled pressure-swirl can be accurately modeled as a purely resistive element, but a gaseous fuel nozzle may not be. In the case of small-amplitude fuel modulations, the flow pattern across the fuel

nozzle can be assumed invariant, thus perturbations in the instantaneous fuel flow rate can be determined as

$$\frac{\dot{m}_f'}{\bar{\dot{m}}_f} = \frac{p_0(t)}{2\overline{\Delta P}} = \frac{\mathrm{Re}(\tilde{P}(0,t))}{2\overline{\Delta P}} \tag{1}$$

In the case of large-amplitude fuel modulations, in particular, at high frequency, the 1D nonlinear wave equation accounting for nonlinear acoustics and viscous shear stress should be used. Solutions to nonlinear wave equations are less straightforward than those to linear waves. A simple method for validating the linear acoustic assumption is to install a pressure transducer at another location in the fuel line and to compare the measured pressure with the linear prediction. It is found that, even without accounting for nonlinear acoustics and viscous shear stress, the developed method can well predict large-amplitude pressure oscillations of up to 20% below 300 Hz, and the prediction error is within 6% in amplitude and within 6 deg in phases [10].

4 Flame Transfer Functions

The FTF can be defined in multiple forms, such as,

$$W_m(s = i\omega) = \mathrm{CH}^*(s)/P_m(s) \tag{2}$$

$$W_0(s = i\omega) = \mathrm{CH}^*(s)/P_0(s) \tag{3}$$

where $\mathrm{CH}^*(s)$, $P_m(s)$, and $P_0(s)$ refer to the Laplace transform of the overall CH^* chemiluminescence intensity, pressure measurements 0.29 m upstream of the fuel nozzle, and fuel pressure immediately upstream of the fuel nozzle, respectively. The relationship between $P_m(s)$ and $P_0(s)$ can be determined from the acoustic wave equations as follows [11]:

$$W_N = \frac{P_m(s)}{P_0(s)} = \frac{\tilde{A}e^{-is(x_m/\bar{c})} + \tilde{B}e^{is(x_m/\bar{c})}}{\tilde{A} + \tilde{B}} = \frac{\tilde{A}/\tilde{B}e^{-is(x_m/\bar{c})} + e^{s(x_m/\bar{c})}}{\tilde{A}/\tilde{B} + 1} \tag{4}$$

At a fuel flow rate of 1.4 g/s, $\tilde{A}/\tilde{B}$ is determined as 1.80. The magnitude of W_N consistently decreases with frequency from unity at 0 Hz to 0.65 at 600 Hz, and the phase lead consistently increases with frequency from zero at zero frequency to 20.5 deg at 600 Hz. During fuel modulations, the mean fuel flow rate is maintained constant by adjusting the opening of a needle valve and the forcing frequency is varied from 10 Hz to 1 kHz in about 10 Hz increments. During these measurements the variations in the mean fuel pressure and the CH^* chemiluminescence intensity are found to be within 1.5%. The sampling frequency is 5 kHz, and the data length is 8 s. The data are decomposed into eight segments, and fast Fourier transform (FFT) analysis is performed for each second. Without explicit denotation, FTFs are the average of the results for the eight data segments.

Figure 2 shows the amplitude and phase of the measured flame transfer function $W_0(s)$ of up to 1 kHz. The FTF amplitude consistently increases up to 600 Hz, peaks around 750 Hz, and then drops. However, different trends are observed between 600 Hz and 660 Hz. This is caused by relatively strong acoustic responses to fuel modulations within this frequency range. The blocking ratio for the inlet and exit of the combustion chamber is 88% and 95%, respectively. Thus the combustion chamber can be considered as acoustically closed at both ends. Note that the blocking ratio is defined as the ratio of the solid surface area that air cannot flow through to the total sectional area normal to the air-flowing direction. The blocking ratio is zero downstream of the quartz tube except at the exit of the combustion chamber where a choking plate is installed. The one-wave-mode acoustic frequency of the combustion chamber is around 630 Hz. Without the baffle plates, self-excited combustion instability occurs around 630 Hz, with an amplitude of up to 12 kPa. Although the baffle plates significantly enhance acoustic damping, relatively large-amplitude

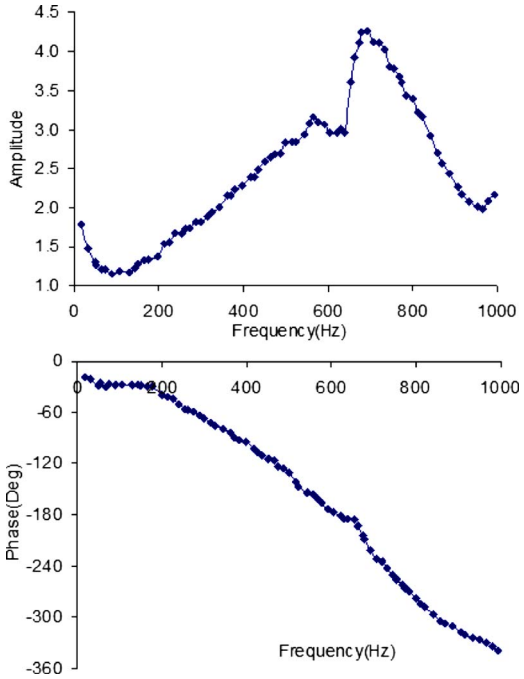

Fig. 2 Flame transfer function $W_0(s)$. The mean fuel pressure is 453 kPa, the air flow rate is 66.7 g/s, the equivalence ratio is 0.34, and the preheat temperature is 473 K. The fuel-modulation ratio is typically below 2.0%. The combustor is fueled with 1-Decene.

acoustic oscillations still occur with fuel modulations around this resonant frequency. This, in fact, implies that the measured FTFs between 600 Hz and 660 Hz are no longer open-loop transfer functions. The present paper's focus is on open-loop transfer functions below 600 Hz. Within this frequency range, forcing-induced acoustic oscillation intensities are small. For these experiments, the ratio of the complex amplitude $\tilde{A}/\tilde{B}$ is determined as 1.80. The gain of W_N consistently decreases with frequency of up to 0.65 at 600 Hz, while the phase lead consistently increases with frequency of up to 20.5 deg at 600 Hz.

4.1 Signal-to-Noise Ratio. The measured fuel pressure and CH^* chemiluminescence intensity are inevitably contaminated by electrical noises, external disturbances, and quantization errors. CH^* chemiluminescence intensity is intrinsically of broadband or stochastic nature, because of the wide range of spatial and temporal scales in flame/turbulence interactions. For reliable FTFs to be developed, fuel-modulation-induced chemiluminescence oscillations must be stronger than the background noise, i.e., the signal-to-noise ratio (SNR) must be sufficiently high. In our experiments, a SNR above 20 dB can be achieved with a fuel-modulation ratio larger than 0.5%.

4.2 Repeatability and Nonlinearity. The measured FTF is repeatable not only within the same sequence of experiments (limited by the requirements on paper length, results are not shown) but also among experiments conducted at different days (see Fig. 3). Even in the presence of self-excited large-amplitude combustion oscillations (up to 12 kPa in amplitude) around 640 Hz, the FTF at frequencies below 600 Hz is almost the same as those shown in Fig. 3. Strong repeatability in the FTF implies that a meaningful and reliable FTF has been obtained. One can see that below 600 Hz, the gain of the FTF for Jet-A is almost the same as that for 1-Decene, while above 320 Hz the phase difference slightly increases with frequency of up to 15 deg at 600 Hz. Since the droplets evaporation is not the limiting process, differences in FFTs between Jet-A and 1-Decene are associated with chemical kinetics. Jet-A has a considerable amount of hydrocarbons, which

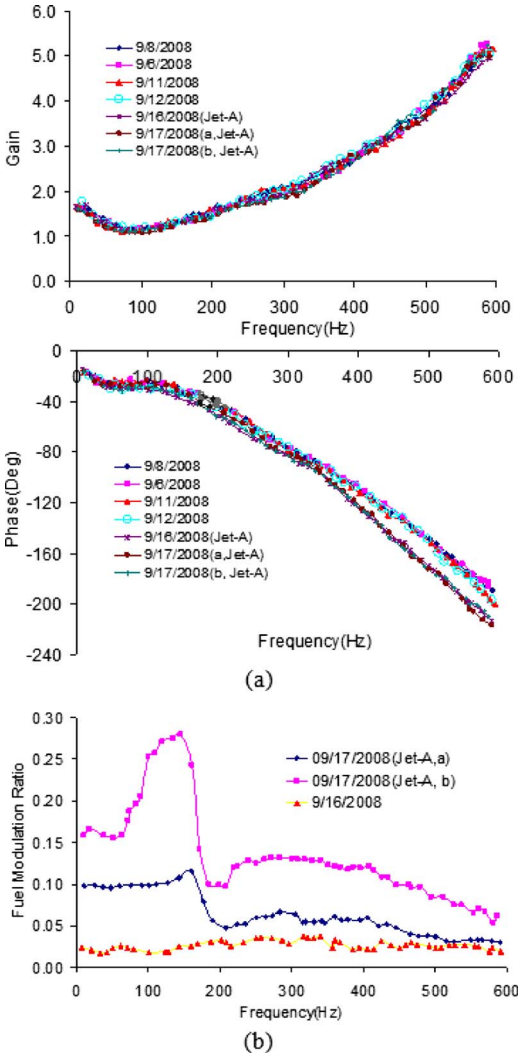

Fig. 3 (*a*) Flame transfer function $W_m(s)$ measured at different days and (*b*) the fuel-modulation ratio. The mean fuel pressure is 453 kPa, the air flow rate is 66.7 g/s, the equivalence ratio is 0.34, and the preheat temperature is 473 K. The fuel-modulation ratio is typically below 2.0%.

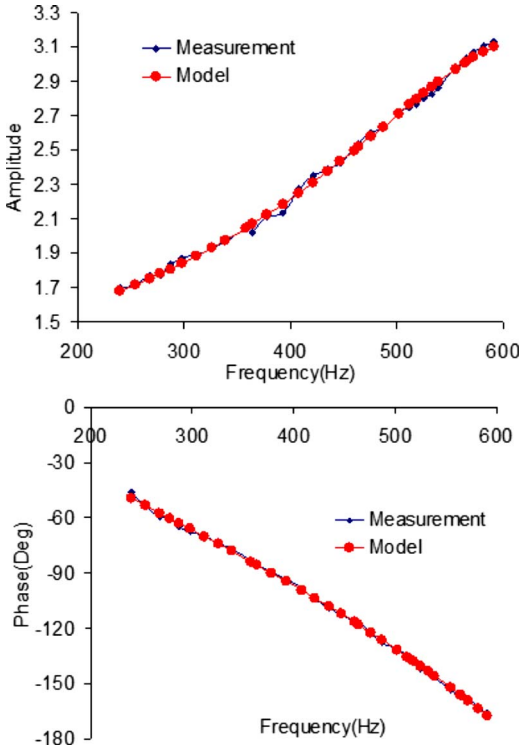

Fig. 4 Flame transfer function $W_0(s)$ versus Bode plots of the low-order model

are longer than 1-Decene. A larger hydrocarbon molecule has a larger molecular weight, so its diffusion toward the reaction zone is smaller, and the chain-initiation will require more energy. Both slow down the chemical reaction rates and the heat release responses to fuel modulations.

Possible nonlinearity in the forced flame responses is checked by examining FTFs measured at different fuel-modulation amplitudes. It is believed that the saturation thresholds, above which nonlinearity starts to appear, depend on the forcing frequency and working conditions, such as the equivalence ratio, the preheat temperature, and the air flow rates. It is found that linearity in the forced flame response is well kept, since the measured FTFs are not sensitive to the fuel-modulation ratio (see Fig. 3(*b*)).

4.3 Low-Order Modeling. The gain and phases of the measured FTF shown in Fig. 3 can be modeled by a low-order rational transfer function. Such low-order models are very convenient for combustion analysis and control. However, before the low-order models are developed, it is worthwhile to further explore system dynamics from the measured FTF.

A plateau appears in phases of the FTF between 50 Hz and 200 Hz. This is mainly because within this frequency range, forcing cycles are much longer than the time scales of fuel convection, evaporation, and chemical kinetics, as shown in Ref. [9]. The flatness in phases below 200 Hz implies the smallness of time delay in the forced flame responses. Phase lag associated with a pure time-delay unit is proportional to frequency, and the gain is unity. Since the time delay is small, the phase lag should be associated with nontime-delay units, such as a rational transfer function. Rational transfer functions allow both the gain and phases to vary continuously with frequency, which are very convenient for stability analysis and control. A low-order model is developed from the measured $W_0(s)$ from 240 Hz to 600 Hz,

$$W(z^{-1}) = \frac{\mathrm{CH}^*(z^{-1})}{P_0(z^{-1})} = \frac{-0.4213z^{-2} + 1.604z^{-3} - 1.147z^{-4}}{1 - 1.952z^{-1} + 1.525z^{-2} - 0.5222z^{-3}} \quad (5)$$

As shown in Fig. 4, the low-order model (5) closely matches the measured FTF in both amplitude and phases. The differences are less than 0.5% in amplitude and within 0.5 deg in phases. The FTF measured on September 12, 2008 are used for model development here. The measured FTF is decomposed into two data segments. One segment is used for model development, and the other one is used for validation. The time delay is identified as only one tap, i.e., 0.2 ms. The sampling frequency is 5 kHz. Small time delay greatly facilitates combustion analysis and control.

4.4 FTFs at Different Air Flow Rates (the Same Fuel Flow Rate). Figure 5 shows the flame transfer function $W_0(s)$ at three air flow rates, 58.4 g/s (ϕ=0.39), 66.7 g/s (ϕ=0.34), and 75.1 g/s (ϕ=0.30), respectively. The fuel flow rate is the same, 1.4 g/s. The air flow rate affects the FTF in two ways. First, it modifies the velocity field, the flame structure, droplets dispersion, fuel/air mixing, and the residence time (τ) and second, at the same fuel flow rate, the equivalence ratio is lower at a higher air flow rate, which slows down chemical kinetics, fuel evaporation, and so on. The increase in phase lag at lower flame temperature can be explained by larger time scales of evaporation (τ_V) and chemical kinetics (τ_c). At an air flow rate of 75.1 g/s, there is no plateau in phases below 200 Hz, which is different from that at 66.7 g/s and 58.4 g/s. This is because, at an air flow rate of 75.1 g/s (ϕ

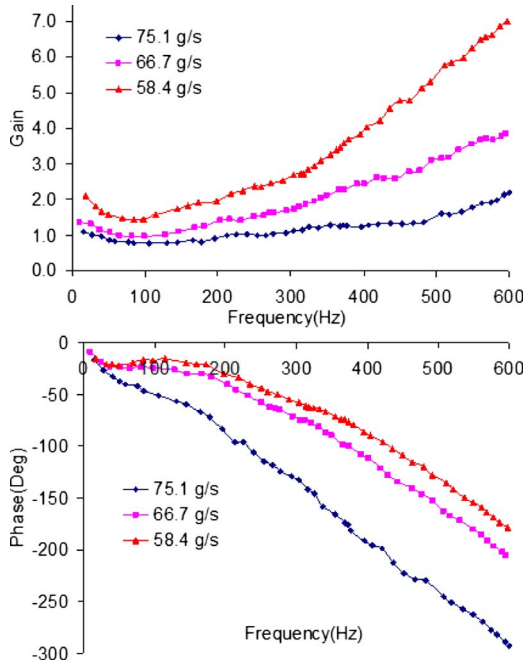

Fig. 5 Flame transfer function $W_0(s)$ at different air flow rates. The fuel-modulation ratio is typically below 2.0%, the preheat temperature is 473 K, and the fuel flow rate is 1.4 g/s.

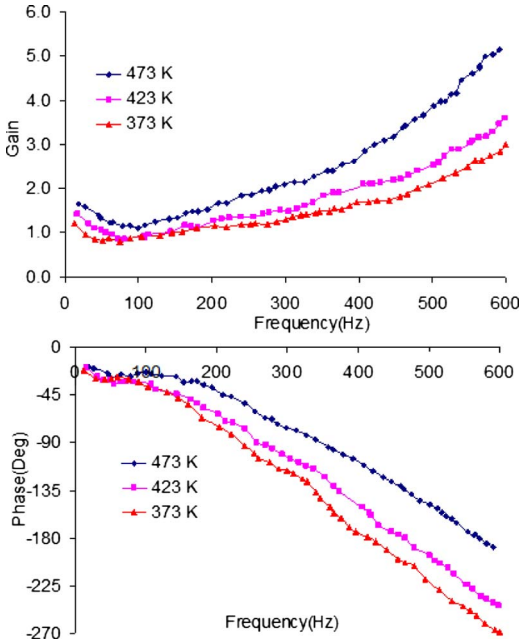

Fig. 6 Flame transfer function $W_m(s)$ at different preheat temperature. The air flow rate is 66.7 g/s, and the equivalence ratio is 0.31.

=0.30), the time scales of evaporation and chemical kinetics have considerably increased, and become comparable with the forcing cycle. Different from the phases, root-cause analysis of the gain decrease at lower flame temperature is less straightforward. For spray flames, the Damköhler number D_a can be defined as $D_a = \tau/(\tau_c + \tau_V)$. The residence time decreases almost linearly with the air flow rate, but the time scales of evaporation and chemical kinetics increase almost exponentially. With a small D_a or a large strain rate, the spray may not have enough time to evaporate, and chemical kinetics is slower at lower flame temperature. This is equivalent to a larger inertia in system dynamics. At lower flame temperature, the flame just cannot respond to fuel modulations as fast as at higher flame temperature, which inevitably results in smaller gain in the FTF. In the present experiments, the frequency responses are linear in terms of the fuel-modulation ratio but nonlinear to the flame temperature. This can be seen from the increasing differences in the FTF above 350 Hz among different air flow rates. The nonlinearity of the FTF to the flame temperature is not surprising, since both evaporation and chemical kinetics are highly nonlinear functions of the flame temperature.

4.5 FTFs at Different Preheat Temperature. The effects of preheat temperature and the equivalence ratio on forced flame responses are essentially similar, since they affect the flame temperature in the same direction. Note that at higher preheat temperature, the air velocity at the swirler exit is higher, which enhances droplet evaporation and fuel/air mixing. Figure 6 shows the flame transfer function $W_m(s)$ at the preheat temperature of 473 K, 423 K, and 373 K, respectively. The air flow rate is 66.7 g/s, and the equivalence ratio is 0.31. At the same air flow rate, the air velocity is larger at higher preheat temperature, thus the residence time decreases, but the time scales of evaporation and chemical kinetics decreases even further. Then the flame becomes more responsive to fuel modulations, resulting in larger gain and a smaller phase lag in the FTF. The FTF is nonlinear in terms of the preheat temperature, which is most obvious for fuel modulations above 400 Hz. From Figs. 5 and 6, one can see that the effects of the equivalence ratio and preheat temperatures on the forced flame responses are essentially similar.

5 Applications of FTFs

The FTF can be directly used for analysis and control of combustion instability and LBO. Active control of both phenomena can be achieved using small-amplitude fuel modulations, employing the same control hardware and fuel actuators. However, several major differences exist between combustion instability control and LBO control. First, combustion instability is linearly unstable. But near-LBO combustion dynamics is linearly stable. Stable combustion cannot be maintained at all if the equivalence ratio drops below certain thresholds. Second, because combustion instability is linearly unstable, the fuel actuator should keep working to prevent acoustic pressure from regaining energy, even after the initial strong pressure pulsations have been suppressed. However, for LBO control, no further fuel actuations are required after the initial deviations from the equilibrium points have been diminished. Third, combustion instability is temporally and spatially coherent and occurs around the acoustic resonant frequency. But near-LBO combustion dynamics are typically much less coherent and usually occur below 200 Hz. This implies that for LBO control, the actuator bandwidth and time delay associated with fuel convection, evaporation, and chemical kinetics may not be major technical challenges.

Stability enhancement of near-LBO combustion using a simple linear-quadratic-Gaussian (LQG) feedback controller has been numerically demonstrated in Ref. [4]. Such feedback controllers can also be designed based on the measured FTFs. Since an aeroengine has to operate within a large range of working conditions, stable adaptive controllers, which have superior robust stability and control performance, are promising. The measured near-LBO flame transfer functions have no unstable zeros, no unstable poles, and even negligibly small time delay, thus adaptive robust controller can be easily worked. Besides the liquid-fueled lean direct fuel injection (LDI) combustors, the developed control strategy can also be used for gas-fueled combustion, such as syngas- and natural-gas-fueled combustion. Because of variations in feedstocks, the ratio of H_2/CO in syngas can change from 0.33 to 40, and the concentration of water vapor can vary from 0% to 40% [12]. This will impose significant challenges to stable combustion in particular at very lean conditions. Near-LBO combustion dynamics may exhibit persistent low-frequency oscillations [13,14]

or undergo partial or global quenching without showing much oscillatory behavior. Both situations can be handled by the proposed feedback controllers.

6 Conclusions

A method for determining the instantaneous fuel flow rate out of a liquid fuel nozzle is developed, which is based on acoustic wave theory and pressure measurements upstream of the fuel nozzle. Repeatability and linearity in the measured FTF are demonstrated. The derived FTF is not sensitive to variations in the fuel-modulation amplitude. Low-order models in the form of a rational transfer function are developed from the measured gain and phases, which can be conveniently used for combustion analysis and control. Effects of the equivalence ratio and preheat temperature on the FTF are examined. The phase lag decreases with flame temperature and the gain increases. Heat release rate responses are linear in terms of the fuel-modulation amplitude, but nonlinear in terms of the flame temperature. Applications of the FTF to combustion control, including combustion instability and lean blowout, are discussed.

Acknowledgment

Support from NASA Glenn under Grant No. NNX07C98A, "Active Combustion Control for Low-Emission Combustors," is gratefully acknowledged. Dr. Clarence Chang is the project manager. This project is also supported by the Air Force under Grant No. FA9550-07-1-0451, "Advanced Thermally Stable Coal-Based Jet Fuels."

Nomenclature

$\tilde{A}$ and $\tilde{B}$ = complex amplitude of acoustic waves
$\bar{c}$ = mean speed of sound, m/s
D_a = the Damköhler number
i = complex symbol
$k=\omega/\bar{c}$ = wave number
$\dot{m}'(t)$ = fuel modulations, kg/s
$\bar{\dot{m}}_f$ = the mean fuel flow rate out of a fuel injector, kg/s
$\tilde{P}(0,t)$ = the estimated complex dynamic pressure immediately upstream of the fuel nozzle, Pa
$p_0(t)$ = the estimated dynamic pressure immediately upstream of the fuel injector, Pa
$p_m(t)$ = dynamic pressure measured at 0.29 m upstream of the fuel injector, Pa
$s=i\omega$ = symbol of the Laplace transform
$W_N(s)$ = the transfer function between pressure measurements and pressure immediately upstream of a fuel nozzle
x_m = a pressure measurement location, 0.29 m upstream of the fuel nozzle, m
z = symbol of Z transform
ϕ = equivalence ratio
$\mathrm{Re}(\ldots)$ = the real part of a complex quantity
$\overline{\Delta P}$ = mean pressure drop across a fuel nozzle, Pa
ω = angular frequency, radians/s
τ = the residence time, s
τ_c = the time scale of chemical kinetics, s
τ_V = the evaporation time of droplets, s

Abbreviation

ICCD = intensified charge-coupled device

References

[1] DeLaat, J. C., and Chang, C. T., 2003, "Active Control of High Frequency Combustion Instability in Aircraft Gas-Turbine Engines," NASA Report No. TM-2003-212611.
[2] Kiel, B. V., 2001, "Review of Advances in Combustion Control, Actuation, Sensing, Modeling, and Related Technologies for Air Breathing Gas Turbines," AIAA Paper No. 2001-481.
[3] Richards, G. A., Straub, D. L., and Robey, E. H., 2003, "Passive Control of Combustion Dynamics in Stationary Gas Turbines," J. Propul. Power, **19**(5), pp. 795–810.
[4] Yi, T., and Gutmark, E. J., 2009, "Stability and Control of Lean Blowout in Chemical Kinetics—Controlled Combustion Systems," Combust. Sci. Technol., **181**(2), pp. 226–244.
[5] Yang, V., 1995, *Liquid Rocket Engine Combustion Instability* (Progress in Aeronautics and Astronautics), American Institute of Aeronautics and Astronautics, Inc., Washington, DC, Vol. 169, Chap. 1.
[6] Yu, K. H., and Wilson, K. J., 2002, "Scale-Up Experiments on Liquid-Fueled Active Combustion Control," J. Propul. Power, **18**(1), pp. 53–60.
[7] Duvvur, A., Chiang, C. H., and Sirignano, W. A., 1996, "Oscillatory Fuel Droplet Vaporization: Driving Mechanism for Combustion Instability," J. Propul. Power, **12**(2), pp. 358–365.
[8] Engineers at Parker Hannifin Corp, 2008, private communication.
[9] Yi, T., and Santavicca, D. A., 2009, "Flame Spectra of a Liquid-Fueled Swirl-Stabilized LDI Combustor," AIAA Paper No. 2009-0985.
[10] Yi, T., and Santavicca, D. A., 2009, "Determination of the Instantaneous Fuel Flow Rate Out of a Fuel Injector," AIAA Paper No. 2009-0987.
[11] SAE, 2004, *Handbook of Aviation Fuel Properties*, 3rd ed., SAE World Headquarters, Warrendale, PA.
[12] Moliere, M., 2002, "Benefiting From the Wide Fuel Capability of Gas Turbines: A Review of Application Opportunities," ASME Paper No. 2002-GT-30017.
[13] Muruganandam, T. M., Nair, S., Scarborough, D., Neumeier, Y., Jagoda, J., Lieuwen, T., Seitzman, J., and Zinn, B., 2005, "Active Control of Lean Blowout for Turbine Engine Combustors," J. Propul. Power., **21**(5), pp. 807–812.
[14] Yi, T., and Gutmark, E. J., 2007, "Real-Time Prediction of Incipient Lean Blowout in Gas Turbine Combustors," AIAA J., **45**(7), pp. 1734–1739.

A Sparse Estimation Approach to Fault Isolation

S. Borguet
e-mail: s.borguet@ulg.ac.be

O. Léonard
e-mail: o.leonard@ulg.ac.be

Turbomachinery Group,
University of Liège,
1 Chemin des Chevreuils,
4000 Liège, Belgium

Least-squares-based methods are very popular in the jet engine community for health monitoring purposes. In most practical situations, the number of health parameters exceeds the number of measurements, making the estimation problem underdetermined. To address this issue, regularization adds a penalty term on the deviations of the health parameters. Generally, this term imposes a quadratic penalization on these deviations. A side effect of this technique is a relatively poor isolation capability. The latter feature can be improved by recognizing that abrupt faults impact at most one or two component(s) simultaneously. This translates mathematically into the search for a sparse solution. The present contribution reports the development of a fault isolation tool favoring sparse solutions. It is very efficiently implemented in the form of a quadratic program. As a validation procedure, the resulting algorithm is applied to a variety of fault conditions simulated with a generic commercial turbofan model. [DOI: 10.1115/1.3156815]

Keywords: gas-path analysis, fault isolation, sparse estimation, quadratic programming

1 Introduction

[1]Predictive maintenance aims at scheduling overhaul actions on the basis of the actual level of deterioration of the engine. The benefits are improved operability and safety, as well as reduced life cycle costs. Generating reliable information about the health condition of the gas turbine is therefore a requisite and has been the subject of intensive research in the community.

In this paper, *module performance analysis* is considered. Its purpose is to detect, isolate, and quantify the changes in engine module performance, described by so-called health parameters, on the basis of measurements collected along the gas path of the engine [1]. Typically, the health parameters are correcting factors on the efficiency and the flow capacity of the modules (fan, low pressure compressor (lpc), high pressure compressor (hpc), high pressure turbine (hpt), and low pressure turbine (lpt)), while the measurements are intercomponent temperatures, pressures, shaft speeds, and fuel flow.

As far as timescale is considered, alterations in engine health can be split into two groups. On the one hand, *gradual deterioration*, due to erosion or fouling for instance, occurs during normal operation of the engine and affects all major components at the same time. On the other hand, *accidental events*, caused for instance by hot restarts or foreign/domestic object damage, impact one or two component(s) at a time and occur infrequently.

Marinai et al. proposed in Ref. [2] a detailed survey of the spectrum of techniques that have been investigated to solve the diagnosis problem. They divided the methodologies into two groups. The first one encompasses optimal estimation techniques such as weighted least-squares [3], Kalman filters [4], or genetic algorithms [5]. The second set gathers approaches relying on artificial intelligence (AI) such as artificial neural networks [6], bayesian belief networks [7], or fuzzy logic [8]. One of the major conclusions of the review is that AI-based methods deliver better performance for accidental events, essentially because of their classification nature. Indeed, the continuum of solutions is approximated with a limited number of cases. On the contrary, estimation techniques are more suited to the assessment of progressive, distributed degradation, and are known to spread localized faults over several components.

This adverse effect, generally termed *smearing* in the literature, see Ref. [9], is due to the very nature of the estimation problem. In this framework, the health parameters are obtained by minimizing the squared Euclidian distance between model predictions and measurements taken on the engine (so-called residuals), resulting in the celebrated least-squares method. In practical situations, the number of unknown health parameters exceeds the number of available measurements, making the estimation problem underdetermined. As a workaround, *regularization* adds a penalty term on the deviations of the health parameters to the least-squares criterion in order to drive the algorithm to a particular solution. A common choice for the regularization term is the squared deviations of the parameters with respect to prior values. Nonetheless, a side effect of this technique is that large variations in the parameters, which are typical of abrupt faults, are too heavily penalized. This explains the poor isolation capability of optimal estimation techniques.

Grodent and Navez [10] tackled this deficiency by using a regularization term that lowers the penalty on large deviations of the health parameters, hence improving fault isolation. The authors have used a similar formulation to derive a diagnosis tool robust against sensor faults, see Ref. [11].

A further step to enhanced fault isolation can be taken by recognizing that abrupt events involve only a limited number of health parameters, which translates mathematically into the search for a *sparse solution*. Basically, the regularization term is again tweaked in order to favor a solution with many naught terms. Problems characterized by sparsity are encountered in many scientific fields such as compressed sensing [12], linear regression [13], or source localization [14] to name a few. Reference [15] provides a good review of various algorithms looking for sparse solutions. Moreover, it is shown in Ref. [16] that one flavor of the sparse estimation problem can be cast as a quadratic programming (QP) problem for which efficient solvers are available.

In the present contribution, this quadratic programming approach is adopted to derive a fault isolation tool favoring sparse solutions. As a validation procedure, the resulting algorithm is applied to a variety of fault conditions simulated with a generic commercial turbofan model.

[1]A Domestic object damage is caused by an element of the engine (e.g., part of a blade) that breaks off and strikes a downstream flow-path component.

Contributed by the International Gas Turbine Institute of ASME for publication in the JOURNAL OF ENGINEERING FOR GAS TURBINES AND POWER. Manuscript received March 19, 2009; final manuscript received March 19, 2009; published online November 4, 2009. Review conducted by Dilip R. Ballal. Paper presented at the ASME Gas Turbine Technical Congress and Exposition, Orlando, FL, June 8–12, 2009.

2 Description of the Method

The scope of this section is to provide the mathematical foundation of the fault isolation tool based on sparse estimation. First, the model relating the observations to the health parameters is described. A short background on linear least-squares is then presented, and the root cause of its poor concentration capability is underlined. Finally, sparse estimation is introduced as an appropriate framework to address this issue.

2.1 The Engine Performance Model. One of the master pieces of the gas-path analysis approach is a simulation model of the engine. Considering steady-state operation of the engine, these simulation tools are generally nonlinear aerothermodynamic models based on mass, energy, and momentum conservation laws applied to the engine flow-path. Equation (1) represents such an engine model where $\mathbf{u}$ is the variable defining the operating point of the engine (e.g., fuel flow, altitude, and Mach number), $\mathbf{w}$ are the aforementioned health parameters, and $\mathbf{y}$ are the gas-path measurements.

$$\mathbf{y} = \mathcal{G}(\mathbf{u}, \mathbf{w}) \tag{1}$$

In the frame of performance diagnostics, the model is rarely used in the previous form stated by Eq. (1). Indeed, the quantity of interest is the difference between the actual engine health condition and a reference one represented by baseline values $\mathbf{w}^{\mathrm{bl}}$. Assuming a linear relationship between the measurements and the health parameters, as well as fixed operating conditions, the model is reformulated according to Eq. (2).

$$\mathbf{y} = \mathbf{G}\mathbf{w} \tag{2}$$

where

$$\mathbf{G} = \frac{\partial}{\partial \mathbf{w}} \mathcal{G}(\mathbf{u}, \mathbf{w})\big|_{\mathbf{w}=\mathbf{w}^{\mathrm{bl}}} \tag{3}$$

is the influence coefficient matrix (ICM) of the engine model around the health condition $\mathbf{w}^{\mathrm{bl}}$. With some abuse of notation, $\mathbf{y}$ and $\mathbf{w}$ are now deviations of the measurements and the health parameters from their values at the linearization point.

A random variable $\boldsymbol{\epsilon} \in \mathcal{N}(\mathbf{0}, \mathbf{R}_{\mathbf{y}})$, which accounts for sensor inaccuracies and modeling errors is added to the deterministic linearized model (2) in order to reconcile the observed measurements and the model predictions. Equation (4) is therefore termed the statistical model.

$$\mathbf{y} = \mathbf{G}\mathbf{w} + \boldsymbol{\epsilon} \tag{4}$$

The statistical model can further be scaled to a linear system with a noise distribution $\tilde{\boldsymbol{\epsilon}} \in \mathcal{N}(\mathbf{0}, \mathbf{I})$ provided that the covariance matrix $\mathbf{R}_{\mathbf{y}}$ is positive definite. The scaled model is given by

$$\tilde{\mathbf{G}} = (\sqrt{\mathbf{R}_{\mathbf{y}}})^{-1}\mathbf{G} \tag{5}$$

where the scaling factor takes into account the relative accuracy of each sensor.

2.2 Least-Squares Estimation and the Smearing Effect. The estimation of the health parameters is basically an inverse problem, which is routinely solved with the celebrated (weighted) least-squares algorithm. In that framework, the health parameters are obtained by minimizing the squared Euclidian norm of the residuals.

$$\hat{\mathbf{w}} = \arg\min_{\mathbf{w}} \left\{ \frac{1}{2} \tilde{\boldsymbol{\epsilon}}^T \tilde{\boldsymbol{\epsilon}} \right\} = \arg\min_{\mathbf{w}} \left\{ \frac{1}{2} (\tilde{\mathbf{y}} - \tilde{\mathbf{G}}\mathbf{w})^T (\tilde{\mathbf{y}} - \tilde{\mathbf{G}}\mathbf{w}) \right\}$$
$$= (\tilde{\mathbf{G}}^T \tilde{\mathbf{G}})^{-1} \tilde{\mathbf{G}}^T \tilde{\mathbf{y}} \tag{6}$$

Note that in Eq. (5), the relative accuracy of each sensor is embedded in the scaled model $\tilde{\mathbf{G}}$. In the case of a Gaussian distribution of the error $\tilde{\boldsymbol{\epsilon}}$, the least-squares approach coincides with the maximum likelihood criterion. In that probabilistic point of view, the estimated health parameters are the most probable ones given the observed data.

However in most practical situations the number n of unknown health parameters outweighs the number m of available measurements. The estimation problem is said to be underdetermined. The matrix $\tilde{\mathbf{G}}^T\tilde{\mathbf{G}}$ is not full-ranked and cannot be inverted.

To overcome this issue, information has to be added in the definition of the estimation problem. This operation is called regularization, and typically it can be seen as a set of soft constraints on the health parameters. A very common regularization scheme for underdetermined least-squares problems consists of adding a quadratic penalization on the deviations of the health parameters. As a result, the algorithm is driven toward the optimal solution that lies in the neighborhood of the baseline values. The shape of the neighborhood is specified by the elements of the symmetric, positive definite matrix $\mathbf{Q}$.

$$\hat{\mathbf{w}} = \arg\min_{\mathbf{w}} \left\{ \tfrac{1}{2} (\tilde{\mathbf{y}} - \tilde{\mathbf{G}}\mathbf{w})^T (\tilde{\mathbf{y}} - \tilde{\mathbf{G}}\mathbf{w}) + \tfrac{1}{2} \mathbf{w}^T \mathbf{Q}^{-1} \mathbf{w} \right\}$$
$$= (\tilde{\mathbf{G}}^T \tilde{\mathbf{G}} + \mathbf{Q}^{-1})^{-1} \tilde{\mathbf{G}}^T \tilde{\mathbf{y}} \tag{7}$$

The choice of a quadratic function for the regularization term allows an analytic relation to be worked out, which is one reason for its popularity. Equation (7) can also be interpreted from a probabilistic standpoint as the Bayesian approach to estimation. In the present case, both the measurements and the health parameters are considered as Gaussian random variables and the computed solution maximizes the posterior probability distribution of the parameters (see Ref. [1] for additional details).

These developments explain the smearing effect that is observed with the usual least-squares technique. Indeed, due to the quadratic penalization on the parameter deviations, solutions involving small variations of numerous health parameters have a lower cost than solutions characterized by large deviations in a few health parameters. As a result, the algorithm has the tendency to spread the effect of localized faults over several components.

2.3 Favoring Sparsity in the Estimation Process. As underlined in Sec. 2.2, regularization helps solve underdetermined problems by artificially improving their mathematical conditioning. An adequate selection of the regularization term is hence of paramount importance and should be made in accordance with the structure of the expected solution.

Short timescale faults impact only a limited number of health parameters, which means that many elements in the vector of health parameter deviations are equal to zero. Such a pattern is termed sparse. It should therefore be possible to enhance the concentration capability of a least-squares-based algorithm by introducing a regularization term that favors sparsity.

A first possible formulation of the sparse estimation problem is to look for the solution having the smallest number of nonzero components [17], which can be thought of as an ideal measure of sparsity, this writes

$$\min_{\mathbf{w}} \left\{ \tfrac{1}{2} (\tilde{\mathbf{y}} - \tilde{\mathbf{G}}\mathbf{w})^T (\tilde{\mathbf{y}} - \tilde{\mathbf{G}}\mathbf{w}) + \lambda \|\mathbf{w}\|_0 \right\} \quad \lambda > 0 \tag{8}$$

where $\|\mathbf{w}\|_0$ is the ℓ_0 quasinorm that is equal to the number of nonzero elements in vector $\mathbf{w}$. The scalar parameter λ sets the tradeoff between least-squares fit of the data and sparsity in the solution.

Note that other definitions of sparse estimation are conceivable. For instance one could look for the solution of a given sparsity p that minimizes the data misfit. This formulation would also involve the ℓ_0 quasinorm, now as an equality constraint, in the optimization problem

$$\min_{\mathbf{w}} \left\{ \tfrac{1}{2} (\tilde{\mathbf{y}} - \tilde{\mathbf{G}}\mathbf{w})^T (\tilde{\mathbf{y}} - \tilde{\mathbf{G}}\mathbf{w}) \right\} \quad \text{subject to } \|\mathbf{w}\|_0 = p \tag{9}$$

While its mathematical expression looks incredibly simple, the sparse estimation problem (8) is quite burdensome to solve in

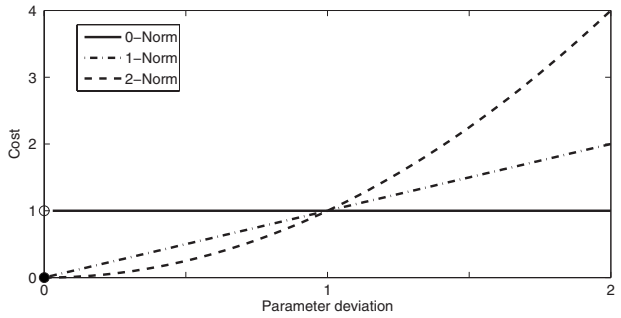

Fig. 1 Comparison of the penalty induced by different norms

practice. Indeed, the presence of the term $\|\mathbf{w}\|_0$ makes the problem combinatorial. The optimal solution can only be obtained by means of an exhaustive search, which rapidly becomes unmanageable in typical applications.

2.4 A Convex Approximation to Sparse Estimation. Different strategies have been developed in order to approximate the optimization problem (8), see for instance Ref. [18] for a short review, and make its computation tractable. Among them, the so-called relaxation approach has enjoyed a reasonable level of success and is elected here. Basically, the idea is to replace the ℓ_0 quasinorm with a suitable ℓ_p-norm (see Appendix A for the definition of the ℓ_p-norm). It can be shown that any ℓ_p-(pseudo) norm promotes sparsity provided $p \leq 1$. Besides, the ℓ_1-norm has the considerable advantage to turn the resulting optimization problem into a convex one, admitting a global optimum.

Figure 1 shows the penalty induced by three different norms for a positive deviation of a scalar parameter.[2] For the ℓ_0 quasinorm, the penalty has a unit value as soon as the parameter deviation differs from zero. In that way, large deviations have no higher cost than smaller ones. It can be seen that the ℓ_1-norm is the convex function of lowest order that places a unit penalty on unit coefficients and sets the cost to zero for naught coefficients. The ℓ_2-norm used in the classical regularized least-squares provides the same costs as the ℓ_1-norm for zero and unit deviations, but it penalizes much more large deviations and somewhat less small deviations. From this sketch, it becomes clear that the ℓ_1-norm provides the natural convex relaxation of the ℓ_0 quasinorm. On the other hand, the ℓ_2-norm is totally inappropriate for favoring sparsity.

Thus, the convex relaxation to Eq. (8) is

$$\min_{\mathbf{w}} \left\{ \tfrac{1}{2}(\tilde{\mathbf{y}} - \tilde{\mathbf{G}}\mathbf{w})^T(\tilde{\mathbf{y}} - \tilde{\mathbf{G}}\mathbf{w}) + \lambda\|\mathbf{w}\|_1 \right\} \quad \lambda > 0 \tag{10}$$

where the sparsity measure $\|\mathbf{w}\|_0$ has been replaced with the ℓ_1-norm of the parameter deviations. The scalar parameter λ plays a similar role as in Eq. (8) in the sense that it balances the least-squares data fit and the sparsity prior. There are three remarkable values for this parameter:

- if $\lambda = 0$, the optimization problem (10) boils down to the classical underdetermined least-squares and the set of solutions is convex
- if $\lambda = 0^+$, that is λ positive and arbitrarily close to zero, the solution is attained at the point(s) in the previous set having least ℓ_1-norm
- if $\lambda \geq \|\tilde{\mathbf{G}}^T\tilde{\mathbf{y}}\|_\infty$, the optimum is $\hat{\mathbf{w}} = \mathbf{0}$

See Ref. [17] for a proof of the last two items. So, as λ increases, the quality of the least-squares fit degrades while the solution becomes sparser. This parameter shall consequently be tuned by the user to reach optimal performance.

[2]The graph is symmetric with respect to the ordinate axis.

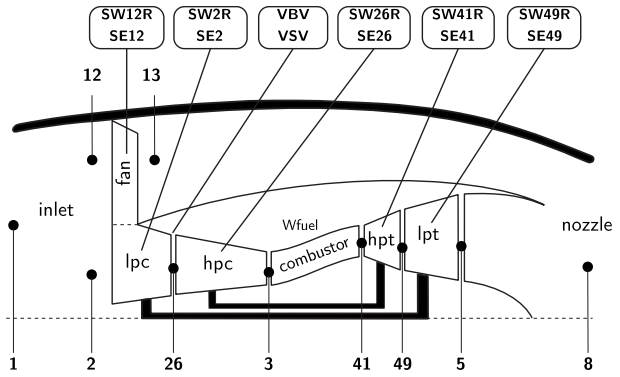

Fig. 2 Turbofan layout with station numbering and parameter location

To better understand the influence of λ on the solution, it is worth taking a look at the dual formulation of Eq. (10) which writes

$$\min_{\mathbf{w}}\{\|\tilde{\mathbf{G}}\mathbf{w}\|_2^2\} \quad \text{subject to} \quad \|\tilde{\mathbf{G}}^T(\tilde{\mathbf{y}} - \tilde{\mathbf{G}}\mathbf{w})\|_\infty \leq \lambda \tag{11}$$

For the interested reader, the conversion from primal to dual form is reported in Ref. [19].

In the dual formulation, the constraint states that, at the solution, the residuals $\tilde{\mathbf{y}} - \tilde{\mathbf{G}}\hat{\mathbf{w}}$ are such that their correlation with the columns of $\tilde{\mathbf{G}}$ never exceeds λ. As a matter of fact, λ allows to tune the maximum magnitude of these correlations. When processing noisy data, it is advised in Ref. [17] to set λ to the standard deviation of the noise, which is equal to one for the scaled system.

As shown in Ref. [16], the optimization problem (10) can be converted into a quadratic program (see Appendix B or Ref. [20]). To this end, the vectors $\mathbf{w}$ and $|\mathbf{w}|$ are replaced with their positive and negative parts

$$\begin{cases} \mathbf{w} = \mathbf{w}^+ - \mathbf{w}^- \\ |\mathbf{w}| = \mathbf{w}^+ + \mathbf{w}^- \end{cases} \quad \text{with} \quad \begin{cases} \mathbf{w}^+ = \max(\mathbf{w}, \mathbf{0}) \\ \mathbf{w}^- = \max(-\mathbf{w}, \mathbf{0}) \end{cases} \tag{12}$$

Note that the operator $\max(\mathbf{v}, \mathbf{0})$ compares each element of vector $\mathbf{v}$ to zero.

This rather simple change in variables leads to the quasi-unconstrained quadratic program (13), which is coded in MATLAB and solved with the package MINQ by Neumaier [21] dedicated to this particular type of optimization problem.

$$\min_{\mathbf{w}^+,\mathbf{w}^-} \left\{ \frac{1}{2}[\tilde{\mathbf{y}} - \tilde{\mathbf{G}}(\mathbf{w}^+ - \mathbf{w}^-)]^T[\tilde{\mathbf{y}} - \tilde{\mathbf{G}}(\mathbf{w}^+ - \mathbf{w}^-)] + \lambda \mathbf{1}^T(\mathbf{w}^+ + \mathbf{w}^-) \right\}$$
$$\text{subject to} \begin{cases} \mathbf{w}^+ \geq \mathbf{0} \\ \mathbf{w}^- \geq \mathbf{0} \end{cases} \tag{13}$$

where $\mathbf{1}$ is a column vector of appropriate dimensions with all elements equal to one.

3 Application of the Method

3.1 Engine Layout. The application used as a test case is a high bypass ratio, mixed-flow turbofan. The engine performance model has been developed in the frame of the OBIDICOTE[3] project, and is detailed in Ref. [22]. A schematic of the engine is sketched in Fig. 2, where the location of the health parameters and the station numbering are also indicated.

[3]A Brite/Euram project for onboard identification, diagnosis, and control of turbofan engine.

Table 1 Gas-path instrumentation (uncertainty is three times the standard deviation)

Label	Description	Uncertainty
$P13$	fan outlet total pressure	±100 Pa
$T13$	fan outlet total temperature	±2 K
$P3$	hpc outlet total pressure	±5000 Pa
$T3$	hpc outlet total temperature	±2 K
N_{lp}	low pressure spool speed	±6 rpm
N_{hp}	high pressure spool speed	±12 rpm
$T5$	lpt exhaust total temperature	±2 K

A total of 12 health parameters is considered. Ten of them are usual efficiency and flow capacity factors for the turbomachinery components. The last two represent deviations with respect to the nominal schedule of the variable geometry devices, namely variable stator vanes and blow-off valves. They model either a fault on the sensed actuator position or a fault on the actuator itself (e.g., mechanical failure).

The sensor suite selected to perform the engine diagnostics is representative of the instrumentation available onboard contemporary turbofan engines and is detailed in Table 1 where the nominal accuracy of each sensor is also reported.

3.2 Fault Case Generator. The assessment of the fault isolation capability of the sparse estimation tool is performed with simulated data. The operating point is representative of cruise conditions, and is randomly selected in the envelope defined in Table 2. The engine is run at a prescribed fuel flow.

The fault cases are picked up from the library summarized in Table 3, which is inspired from Ref. [23]. Each faulty condition impacts either one single turbomachinery component or one of the variable geometry devices. Component faults involve alterations in both the efficiency SEi and flow SWiR correcting factors. The magnitude f_m and coupling factor f_r for these faults are uniformly distributed in the intervals quoted in Table 3 and relate to the health parameters according to

$$1\text{-SE}i = \frac{f_m}{\sqrt{1+f_r^2}} \quad \text{and} \quad (1\text{-SW}i\text{R}) = f_r \cdot (1\text{-SE}i) \tag{14}$$

where 1 is the baseline value of the efficiency and flow factors (see Nomenclature).

For compressors SWiR and SEi vary in the same direction (as for fouling), while for turbines they vary in opposite directions (as for erosion).

Table 2 Envelope of the control parameters

Name	Units	Lower bound	Upper bound
Fuel flow	kg/s	0.350	0.360
Altitude	kft	33	37
Mach	-	0.78	0.82
ΔT_{ISA}	K	−10	+10

Table 3 List of considered fault types

Component	Magnitude f_m (%)	SW/SE ratio f_r
fan	1–5	0.5–2.0
lpc	1–5	0.5–2.0
hpc	1–5	0.5–2.0
hpt	1–5	−0.5 to −2.0
lpt	1–5	−0.5 to −2.0
vbv	1–5	/
vsv	1–5	/

The variable bleed valves behind the lpc (vbv) and variable stator vanes on the hpc (vsv) system faults are implemented as true off-schedule deviations. The uniformly distributed magnitude for these fault types is reported here as some kind of severity index, for sake of simplicity. A unit value corresponds to a small modification with respect to the nominal setting (e.g., only a slight mistuning of the vsv), while a value of five hints at a deep malfunction (e.g., fully open vbv).

The sparse estimation tool performs a snapshot-type analysis of the data. In an attempt to mimic the onboard archival of engine data, the snapshots are generated in the following ways.

1. Select a random operating condition and fault condition from the distributions specified in Tables 2 and 3.
2. Run the engine model to generate 25 samples.
3. Add Gaussian noise, whose magnitude is specified in Table 1, to the noise-free simulated measurements.
4. Average the readings and store them in the database.

For the present study, 1000 occurrences of each fault type have been generated resulting in a database of 7000 conditions to be analyzed with the sparse estimation tool. Such a number allows a rather decent coverage of the fault pattern for each component (both in magnitude and coupling factor).

3.3 Isolation Logic and Selected Metrics. The output of the sparse estimation tool are the health parameter deviations obtained by solving the optimization problem (13). Although very detailed, these results are in a not so convenient form to automatically assess the metrics described below.

In order to determine the faulty component/system, the following isolation logic is applied. The magnitude of each fault type is computed from the estimated deviations of the health parameters. For the turbomachinery components, the magnitude is defined as the l_2-norm of the efficiency and flow deviations; for the actuators, the magnitude is simply the absolute value of the deviation. The component/actuator with the largest magnitude is deemed as the faulty one.

The present work is focused on the isolation part of the diagnosis problem. Two metrics, recommended in Ref. [23], have been selected appropriately to assess the discrimination ability of the sparse estimation tool. For sake of completeness, the metrics are briefly introduced below.

The first metric is the classification confusion matrix (CCM). It is a square matrix, whose dimension is equal to the number of fault types N_f. In the most general form, the no-fault type can be included as well. It is however not the case here as the emphasis is put not on fault detection, but on fault isolation. The elements on the main diagonal reflect correct classification. Each column gives an overview of how the true occurrences of a given fault type (e.g., lpc) are affected to the various fault types by the algorithm. As a by-product of this matrix, the percent correctly classified (PCC) for a given fault type is defined as the ratio of the number of correct classifications to the total number of occurrences for the said type (which amounts to 1000 here).

The second metric is the *kappa coefficient* κ, defined as

$$\kappa = \frac{N_{cc} - N_{exp}}{N_{tot} - N_{ec}} \tag{15}$$

where N_{cc} is the number of correctly classified cases, N_{tot} is the total number of cases, and N_{ec} is the number of cases expected correct by chance.

$$N_{cc} = \sum_{i=1}^{N_f} \text{CCM}_{i,i} \quad N_{tot} = \sum_{i=1}^{N_f} \sum_{j=1}^{N_f} \text{CCM}_{i,j}$$

Table 4 Classification confusion matrix and percent correctly classified (PCC)-sparse estimation

	fan	lpc	hpc	hpt	lpt	vbv	vsv
fan	1000	0	0	0	0	0	0
lpc	0	870	2	0	0	0	1
hpc	0	0	716	0	0	0	7
hpt	0	0	0	1000	0	0	0
lpt	0	0	0	0	1000	0	0
vbv	0	0	0	0	0	1000	0
vsv	0	130	282	0	0	0	992
PCC	100	87	71.6	100	100	100	99.2

$$N_{\text{ec}} = \sum_{i=1}^{N_f} \left\{ \left(\sum_{j=1}^{N_f} \frac{\text{CCM}_{i,j}}{N_{\text{tot}}} \right) \cdot \sum_{j=1}^{N_f} \text{CCM}_{i,j} \right\}$$

The kappa coefficient conveniently summarizes the content of the confusion matrix into a single scalar and can be interpreted as a measure of an algorithm's ability to correctly classify a fault, which takes into account the expected number of correct classifications occurring by chance. The upper bound on κ is one, which means that the algorithm achieves perfect classification.

4 Results

The database of 7000 fault conditions has been processed with the sparse estimation tool, and with the classical least-squares estimator (7) for comparative purpose. The regularization parameter λ in Eq. (13) has been set to the recommended value of one. The total cpu time for processing the whole database amounts to 3 min on a current desktop computer.

Tables 4 and 5 report the classification confusion matrix for the sparse algorithm and for the usual least-squares, respectively. The true and predicted fault states are, respectively, on the horizontal and vertical axes. The percentages of correctly classified cases for each fault type are quoted in the last line of the tables.

From the PCC figures of Table 4, it can be concluded that the overall isolation capability of the sparse estimation tool is quite good. All occurrences of fan, hpt, lpt and vbv faults are indeed correctly classified. The PCC of vsv faults reaches 99.2%, which is almost perfect too. The discrimination of lpc and hpc faults is slightly worse, with PCCs of, respectively, 87% and 71.6%. Although the basic estimation problem is quite ill-posed, with five more health parameters than measurements, the addition of the sparsity constraint to the least-squares data fit allows an accurate isolation over a wide range of fault magnitudes and coupling factors.

On the other hand, the usual least-squares method has a much worse isolation capability, as can be seen from the PCCs of Table 5. Due to their good observability, fan and hpt faults enjoy a correct classification rate of 100%. The PCCs for the other turbomachinery components are between 10% and 20% lower than

Table 5 Classification confusion matrix and PCC-least-squares estimation

	fan	lpc	hpc	hpt	lpt	vbv	vsv
fan	1000	40	4	0	3	152	0
lpc	0	688	284	0	0	113	181
hpc	0	161	602	0	0	0	331
hpt	0	0	0	1000	220	229	0
lpt	0	111	0	0	777	0	0
vbv	0	0	0	0	0	506	0
vsv	0	110	0	0	0	0	488
PCC	100	68.8	60.2	100	77.7	50.6	48.8

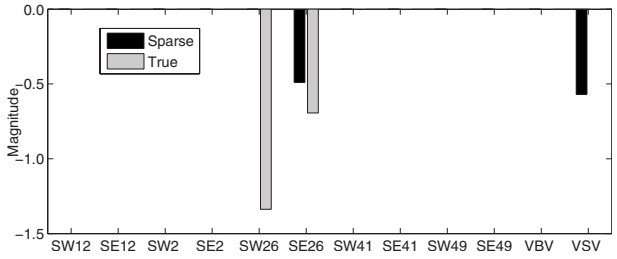

Fig. 3 Sparse estimate of a hpc fault

their corresponding values obtained with the sparse algorithm. The situation of the system faults is even worse, with only roughly one occurrence over two correctly isolated.

The kappa coefficients for the sparse tool and for the classical least-squares method have a value of 0.930 and 0.677, respectively. The lower value of the least-squares estimator comes from the lower number of total correct classifications (sum of the diagonals terms of the matrix), but also from the population of terms outside the main diagonal. Indeed, in a given column of the CCM, the larger the number of nonzero terms, the more random the fault is associated to a class by the algorithm. This effect is taken into account in the computation of the kappa coefficient.

Looking in more detail at the CCM in Table 4, 13% of lpc faults are erroneously assigned to a vsv malfunction. This percentage rises to 28 in the case of hpc faults. On the other hand, an anecdotal number of vsv faults are reported as compressor module faults. In some way, those results are not so surprising. Indeed, the border is quite thin between the impact of a compressor module fault and a system fault, particularly for the duet hpc-vsv as exposed below.

Figure 3 depicts the situation for one of the erroneously isolated hpc faults. The health parameter values, on the vertical axis, are expressed as percent deviations from baseline values for the efficiency and flow factors, and as the severity index for the system faults. Black bars are related to the solution provided by the sparse algorithm, light gray ones to the true fault condition.

First, it can be seen that the computed solution is in fact a sparse one as only 2 parameters out of 12 show nonzero deviations. If the alteration of the hpc efficiency is effectively captured with a reasonable accuracy, the modification of the hpc flow capacity is believed to be a vsv problem by the sparse algorithm. Given that the deviation on the vsv is larger than the combined one on the hpc, the previously described isolation logic declares the vsv as the faulty component/system.

The confusion between the hpc flow factor SW26R and the vsv parameter made by the sparse algorithm can be easily understood by observing Fig. 4. It shows the variation in each measurement, quoted in number of sensor's standard deviation, for a 1% change in SW26R (black bars) and a vsv malfunction of severity 0.5 (light gray bars). The value of the severity index for the vsv malfunction has been chosen so that the maximal deviation is of comparable magnitude for both parameters.

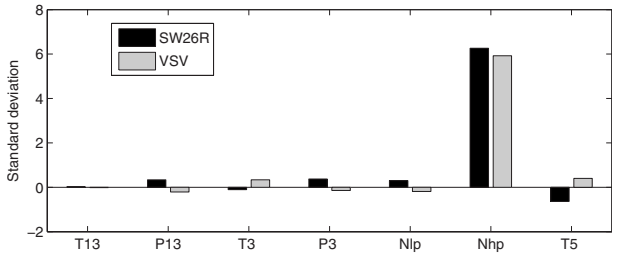

Fig. 4 Signatures of SW26R and VSV on the sensors

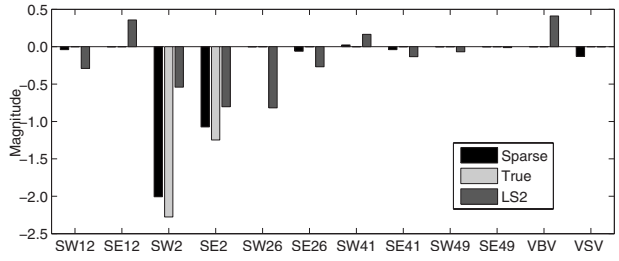

Fig. 5 Comparison of the sparse and usual least-squares solutions for an lpc fault

From the graph, it is obvious that the signature of SW26R is highly similar to the one of vsv for that level of fault magnitude. In both cases, only one sensor reading, namely the high spool speed N_{hp}, undergoes a significant deviation. Consequently, it is very hard to distinguish between these two parameters in the case of faults of small magnitude. The true loss in SW26R is preferentially affected to vsv as the same deviation in the sensors is achieved for a fault severity of half the value it would have in the case of SW26R. Part of the criterion of the sparse algorithm penalizes in fact the l_1-norm of the parameter deviations.

To conclude the review of the results, Fig. 5 compares the solutions obtained with the usual least-squares method in Eq. (7), abbreviated LS2 below (dark gray bars) and the sparse algorithm (black bars) for an lpc fault (light gray bars).

The first thing to point out is the quite different pattern of the LS2 and sparse solutions. The sparse solution and the true fault have their nonzero components at the same locations and with the same signs, so that the fault is clearly concentrated on the lpc. The estimated magnitudes are slightly lower than the actual ones. This results from the effect of the measurement noise, but also illustrates the tradeoff between fitting the data and achieving a sparse solution.

The solution computed in Eq. (7) shows the typical spread over multiple parameters of a localized fault. Among all the parasitic deviations, the one on SW26R is of the same order of magnitude as the one on the two parameters of the lpc. As a consequence, if it is not known a priori that the fault impacts only one component, a combined degradation of both the lpc and the hpc can be suspected.

5 Discussion

The analysis of the results has illustrated the superiority of the sparse estimation tool versus the usual least-squares estimator as far as fault isolation is concerned. Considering fault quantification, the example discussed in Fig. 5 shows a relatively good match although a complementary assessment is required before drawing a general conclusion. Fault quantification could also result from a two-pass procedure: first isolate the faulty component with the sparse estimation tool (i.e., select the correct subset of health parameters involved in the fault), and second estimate the deviations for this subset of parameters with the pure least-squares criterion (6).

It should also be kept in mind that both algorithms have been applied on simulated data, which are always "better looking" than true operational data. In the remainder of this section, additional ideas that may lead to further developments of the proposed methodology are discussed.

The first point concerns the definition of the sparse estimation problem. The optimization variables in Eq. (13) represent the positive and negative parts of the health parameter deviations. In the original formulation, inequality constraints force the optimization variables to be non-negative, in accordance with their definition (12). On a side note, it is worth noting that it doesn't prevent the health parameter deviations to be negative as they are computed as the difference between the positive and negative parts. The size of the optimization problem could be reduced by taking into account that some health parameters vary in a preferential direction. For instance, efficiencies are not expected to improve when a fault occurs. This additional knowledge can be implemented by setting the positive part of these parameters equal to zero. Concerning the objective function, it might be interesting to introduce in some way a coupling between efficiency and flow factors of a given component. Indeed, most of the component faults involve a combined alteration of their health parameters. The expected effect of this modification would be to improve the separability between SW26R and vsv.

A second interesting development of the sparse estimation tool consists in extending its coverage to sensor malfunctions. This encompasses both the gas-path and the operating condition instrumentation. This extension will further increase the sparse nature of the solution vector. The algorithm should also be validated on fault cases involving two turbomachinery components (e.g., combined fault on the fan and the lpc). The isolation logic should be modified accordingly to take into account these additional fault classes in order to correctly evaluate the CCM and kappa coefficient.

The sparse estimation tool is dedicated to the isolation and quantification of short timescale faults. Throughout this paper, it has been implicitly assumed that an auxiliary detection logic which triggers the sparse estimation tool is available. The handling of gradual deterioration is another concern in the development of a complete solution for performance monitoring of jet engines. The authors have presented in a previous contribution [24] an adaptive Kalman filter, which actually deals with the tracking of long timescale degradation and the detection of abrupt events. A third possibility for future work is therefore the combination of the fault isolation tool presented here with the adaptive Kalman filter.

6 Conclusion

In this contribution, an algorithm for engine fault isolation has been developed in the framework of sparse estimation. It relies on the minimization of a criterion which combines least-squares fit of the data and sparsity in the solution. It is efficiently implemented in the form of a quadratic problem, leading to a limited computational burden. Moreover, tuning of the algorithm is limited to the selection of a single parameter for which sound guidelines are available.

An interesting feature of the present isolation tool is that it does not require the setup of a predefined bank of accidental faults, but makes better use of prior knowledge about the structure of localized faults to enhance its ability to concentrate them. The performance of the sparse algorithm has been assessed in terms of classification confusion matrix and kappa coefficient from the processing of a large variety of component and system faults that may occur on a commercial turbofan engine.

Nomenclature

$\hat{\cdot}$ = estimated value
$\tilde{\cdot}$ = scaled value
bl = baseline value
m = number of measurements
n = number of health parameters
N = rotational speed
Pi = total pressure at station i
SEi = efficiency factor of the component whose entry is located at section i (baseline value: 1.0)
SWiR = flow capacity factor of the component whose entry is located at section i (baseline value: 1.0)
Ti = total temperature at station i
$\mathbf{u}$ = vector of control parameters
$\mathbf{w}$ = vector of health parameters

$\mathbf{y}$ = vector of measurements
$\boldsymbol{\epsilon}$ = vector of measurement noise
λ = regularization parameter
$\mathcal{N}(\mathbf{m},\mathbf{R})$ = a Gaussian probability density function with mean $\mathbf{m}$ and covariance matrix $\mathbf{R}$

Appendix A: Definition of the ℓ_p-Norm

For any real number $p \geq 1$ and a real-valued vector $\mathbf{w}$ with n elements, the ℓ_p-norm is defined as

$$\|\mathbf{w}\|_p = \left(\sum_{i=1}^{n} |\mathbf{w}_i|^p \right)^{1/p} \tag{A1}$$

in particular, the ℓ_2-norm is the well-known Euclidian norm

$$\|\mathbf{w}\|_2 = \sqrt{\sum_{i=1}^{n} |\mathbf{w}_i|^2} = \sqrt{\mathbf{w}^T\mathbf{w}} \tag{A2}$$

and the ℓ_1-norm can be expressed as

$$\|\mathbf{w}\|_1 = \left(\sum_{i=1}^{n} |\mathbf{w}_i| \right) = \mathbf{1}^T|\mathbf{w}| \tag{A3}$$

where 1 is a column vector of appropriate dimensions with all elements equal to one.

The formula is also valid for $0 < p < 1$, but the resulting function does not define a norm strictly speaking because it violates the triangle inequality. Taking the limit $p \to \infty$ yields the uniform norm and taking the limit $p \to 0$ yields the ℓ_0 quasinorm.

Appendix B: Elements of Quadratic Programming

A quadratic programming problem is a problem in which the objective function is quadratic and the constraint functions are linear. The problem is to find a solution vector $\mathbf{x}_{\text{opt}}$ to

$$\min_{\mathbf{x}} f(\mathbf{x}) = \tfrac{1}{2}\mathbf{x}^T\mathbf{A}\mathbf{x} + \mathbf{b}^T\mathbf{x}$$

$$\text{subject to} \quad \begin{cases} \mathbf{c}_i^T\mathbf{x} = d_i, & i \in E \\ \mathbf{c}_i^T\mathbf{x} \geq d_i, & i \in I \end{cases} \tag{B1}$$

where E and I are, respectively, the sets of equality and inequality constraints.

If the Hessian matrix $\mathbf{A}$ is positive semidefinite, $\mathbf{x}_{\text{opt}}$ is a global optimum. If $\mathbf{A}$ is positive definite, $\mathbf{x}_{\text{opt}}$ is moreover unique. These results follow from the convexity of the objective function.

References

[1] Volponi, A. J., 2003, *Foundation of Gas Path Analysis (Part I and II)* (von Karman Institute Lecture Series), von Karman Institute, Rhode-Saint-Genèse, Belgium.
[2] Marinai, L., Probert, D., and Singh, R., 2004, "Prospects for Aero Gas-Turbine Diagnostics: A Review," Appl. Energy, **79**, pp. 109–126.
[3] Doel, D. L., 1994, "An Assessment of Weighted-Least-Squares-Based Gas Path Analysis," ASME J. Eng. Gas Turbines Power, **116**, pp. 336–373.
[4] Volponi, A., DePold, H., Ganguli, R., and Daguang, C., 2003, "The Use of Kalman Filter and Neural Network Methodologies in Gas Turbine Performance Diagnostic: A Comparative Study," ASME J. Eng. Gas Turbines Power, **125**, pp. 917–924.
[5] Wallin, M., and Grönstedt, T., 2004, "A Comparative Study of Genetic Algorithms and Gradient Methods for RM12 Turbofan Engine Diagnostics and Performance Estimation," ASME Paper No. GT2004-53591.
[6] Ogaji, S. O. T., and Singh, R., 2002, "Advanced Engine Diagnostics Using Artificial Neural Networks," IEEE International Conference on Artificial Intelligence Systems, ICAIS, pp. 236–241.
[7] Romessis, C., and Mathioudakis, K., 2006, "Bayesian Network Approach for Gas Path Fault Diagnosis," ASME J. Eng. Gas Turbines Power, **128**(1), pp. 64–72.
[8] Eustace, R., 2008, "A Real-World Application of Fuzzy Logic and Influence Coefficients for Gas Turbine Performance Diagnostics," ASME J. Eng. Gas Turbines Power, **130**, p. 061601.
[9] Provost, M. J., 1994, "The Use of Optimal Estimation Techniques in the Analysis of Gas Turbines," Ph.D. thesis, Cranfield University, Bedforshire, UK.
[10] Grodent, M., and Navez, A., 2003, *A Robust Parameter Identification Approach for Engine Health Monitoring and Diagnosis* (von Karman Institute Lecture Series), von Karman Institute, Rhode-Saint-Genèse, Belgium.
[11] Borguet, S., and Léonard, O., 2008, "A Sensor-Fault-Tolerant Diagnosis Tool Based on a Quadratic Programming Approach," ASME J. Eng. Gas Turbines Power, **130**, p. 021605.
[12] Donoho, D., 2006, "Compressed Sensing," IEEE Trans. Inf. Theory, **52**(4), pp. 1289–1306.
[13] Larsson, E., and Selen, Y., 2007, "Linear Regression With a Sparse Parameter Vector," IEEE Trans. Signal Process., **55**(2), pp. 451–460.
[14] Malioutov, D., Cetin, M., and Willsky, A., 2005, "A Sparse Signal Reconstruction Perspective for Source Localization With Sensor Arrays," IEEE Trans. Signal Process., **53**(8), pp. 3010–3022.
[15] Jokar, S., and Pfetsch, M., 2007, "Exact and Approximate Sparse Solutions of Underdetermined Linear Equations," Zentrum für Informationstechnik, Berlin, ZIB Report No. 07-05.
[16] Fuchs, J. J., 2004, "Recovery of Exact Sparse Representations in the Presence of Noise," IEEE International Conference on Acoustics, Speech and Signal Processing, Vol. 2, pp. 533–536.
[17] Fuchs, J. J., 2004, "On Sparse Representations in Arbitrary Redundant Basis," IEEE Trans. Inf. Theory, **50**, pp. 1341–1344.
[18] Tropp, J., 2004, "Just Relax: Convex Programming Methods for Subset Selection and Sparse Approximation," ICES, University of Texas, Report No. 0404.
[19] Fuchs, J. J., 2001, "On the Application of the Global Matched Filter to DOA Estimation With Uniform Circular Arrays," IEEE Trans. Signal Process., **49**(4), pp. 702–709.
[20] Fletcher, R., 2000, *Practical Methods of Optimization*, Wiley, New York.
[21] Neumaier, A., 1998, MINQ—General Definite and Bound Constrained Indefinite Quadratic Programming, http://www.mat.univie.ac.at/neum/software/minq.
[22] Stamatis, A., Mathioudakis, K., Ruiz, J., and Curnock, B., 2001, "Real-Time Engine Model Implementation for Adaptive Control and Performance Monitoring of Large Civil Turbofans," ASME Paper No. 2001-GT-0362.
[23] Simon, D. L., Bird, J., Davison, C., Volponi, A. J., and Iverson, R. E., 2008, "Benchmarking Gas Path Diagnostic Methods: A Public Approach," ASME Paper No. GT2008-51360.
[24] Borguet, S., and Léonard, O., 2009, "A Generalized Likelihood Ratio Test for Adaptive Gas Turbine Performance Monitoring," ASME J. Eng. Gas Turbines Power, **131**, p. 011601.

Rakesh K. Bhargava
Foster Wheeler USA Corporation,
585 North Dairy Ashford,
Houston, TX 77079

Michele Bianchi
DIEM,
Università di Bologna,
viale Risorgimento 2,
40136 Bologna, Italy

Stefano Campanari
Department of Energy,
Politecnico di Milano,
Via Lambruschini 4,
20156 Milano, Italy

Andrea De Pascale

Giorgio Negri di Montenegro

Antonio Peretto

DIEM,
Università di Bologna,
viale Risorgimento 2,
40136 Bologna, Italy

A Parametric Thermodynamic Evaluation of High Performance Gas Turbine Based Power Cycles

This paper discusses the gas turbine performance enhancement approach that has gained a lot of momentum in recent years in which modified Brayton cycles are used with humidification or water/steam injection, termed "wet cycles," or with fuel cells, obtaining "hybrid cycles." The investigated high performance cycles include intercooled steam-injected gas turbine cycle, recuperated water injection cycle, humidified air turbine cycle, and cascaded humidified advanced turbine cycle, Brayton cycle with high temperature fuel cells (molten carbonate fuel cells or solid oxide fuel cells), and their combinations with the modified Brayton cycles. Most of these systems, with a few exceptions, have not yet become commercially available as more development work is required. The results presented show that the cycle efficiency achievable with the aforementioned high performance systems can be comparable or better than a combined cycle system, a currently commercially available power generation system having maximum cycle efficiency. The main emphasis of this paper is to provide a detailed parametric thermodynamic cycle analysis, using uniform design parameters and assumptions, of the above mentioned cycles and discuss their comparative performance including advantages and limitations. The performance of these cycles is also compared with the already developed and commercially available gas turbines without water/steam injection features, called "dry cycles." In addition, a brief review of the available literature of the identified high performance complex gas turbine cycles is also included in this paper.
[DOI: 10.1115/1.3155782]

Keywords: wet cycles, dry cycles, GT-FC hybrid cycles, parametric analysis

1 Introduction

Since the early stages of its advent, the gas turbine (GT) energy system has undergone a dramatic evolution process leading to the current level of cycle efficiency values of about 42% in the simple Brayton cycle configuration, particularly for the large size aeroderivative machines (e.g., Rolls-Royce Trent 60 and GE LM6000) [1]. Figure 1 shows two key GT design parameters, cycle pressure ratio (β) and turbine inlet temperature (TIT), of some selected and commercially available simple cycle gas turbines. The two solid lines, obtained through a parametric analysis of simple Brayton cycle by Bhargava et al. [2] and included in Fig. 1, show cycle pressure ratio variation corresponding to maximum specific work and maximum cycle efficiency. In addition, iso-efficiency contours are also shown in Fig. 1 to indicate comparative cycle efficiency of various selected gas turbines. This chart shows that a large number of existing heavy-duty gas turbines have been designed to optimize specific work in order to maintain low overall pressure ratio with some compromise in the cycle efficiency.

Several modifications to the simple Brayton cycle have been proposed since the early development of gas turbines in order to further improve its thermodynamic performance and some of which are actually implemented in industrial gas turbines, as is evident from the most recently presented review by Bhargava et al. [2]. In general, two approaches have been used in the gas turbine industry to improve Brayton cycle performance. One approach includes increasing TIT and β, but it is quite capital intensive requiring extensive research and development work, advancements in cooling (of turbine blades and hot gas path components) technologies, high temperature materials and coatings, and NO_x reducing methods. The second approach involves modifying the Brayton cycle. However, this second approach did not become very popular because of the development of high efficiency GT based combined cycle power generation systems during the 1970s in spite of their high initial capital cost. The various modified GT cycles, either implemented or analyzed and/or discussed in literature, can be divided into three main categories: (1) dry cycles, (2) wet cycles, and (3) fuel cell (FC) based hybrid GT cycles.

"Dry cycles" consist of GT based power cycles where only the external air and combustion gases are used as the operating fluid undergoing thermodynamic transforms inside the GT. Some examples of dry cycles studied and/or constructed include recuperated (REC) Brayton, intercooled (IC) Brayton, intercooled recuperated (ICR) Brayton, reheat (RH) Brayton, below ambient gas turbine (BAGT), and their combinations [3–8]. A comprehensive parametric and comparative thermodynamic performance analysis of the aforementioned dry cycles, with consistent assumptions and for varying technology levels (indicated by the value of TIT), has been recently carried out by Bhargava et al. [2], and the results of their study for TIT=1300°C, a TIT value representative of the technology for large industrial gas turbines of the 1990s, are presented in Fig. 2. As shown in Fig. 2, the simple Brayton cycle performance can be significantly improved in terms of the overall cycle efficiency (η_{el}) and the net specific work (w_{el}) by means of complex dry cycle solutions, provided a practical design is accomplished in terms of the overall cycle pressure ratio (β).

The study by Bhargava et al. [2] also showed that the ICR cycle could achieve maximum cycle efficiency of approximately 48% (at β=10, specific work of 407 kJ/kg, and TIT of 1300°C) making it a highest performing dry cycle (see Fig. 2). It must be mentioned that the results presented in Fig. 2 are found compat-

Contributed by the International Gas Turbine Institute of ASME for publication in the JOURNAL OF ENGINEERING FOR GAS TURBINES AND POWER. Manuscript received January 12, 2009; final manuscript received March 30, 2009; published online November 4, 2009. Review conducted by Dilip R. Ballal. Paper presented at the ASME Turbo Expo 2008: Land, Sea and Air (GT2008), Berlin, Germany, June 9–13, 2008.

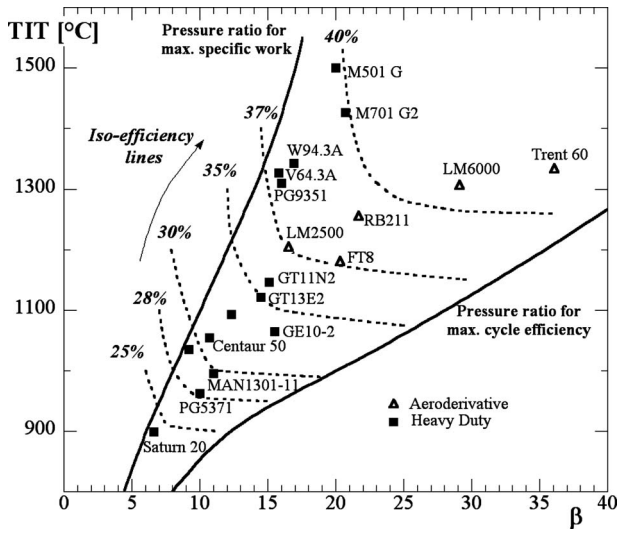

Fig. 1 Cycle efficiency, TIT, and β of simple cycle existing gas turbines

ible with some of the commercially available GTs with modified Brayton cycles [2]. It must also be mentioned that dry cycles have been the topics of discussion in many text books and GT handbooks [9–11].

A new class of GT cycles, termed "wet cycles" [10], can be obtained by introducing water and/or steam in the air/gas streams with the aim to obtain increased specific work in the turbine section and to accomplish higher cycle efficiency values through effective energy transfer to and from the system. A very comprehensive review of the available literature on the wet cycles (also called humid or evaporative GT cycles) has been recently carried out by Jonsson and Yan [12]. This family of GT cycles, originating from the early development of steam-injected gas turbine (STIG) or Cheng cycle [13–15], includes intercooled steam-injected gas turbine (ISTIG) cycle, recuperated water injected (RWI) cycle, humid air turbine (HAT) cycle, and their variants. All of these modified GT cycles, evaluated in this paper, are based on some of the dry cycle technologies (e.g., intercooling, recuperation, and reheat) with the addition of water in the air/gas stream, accomplished in different ways and in different sections of the GT engine.

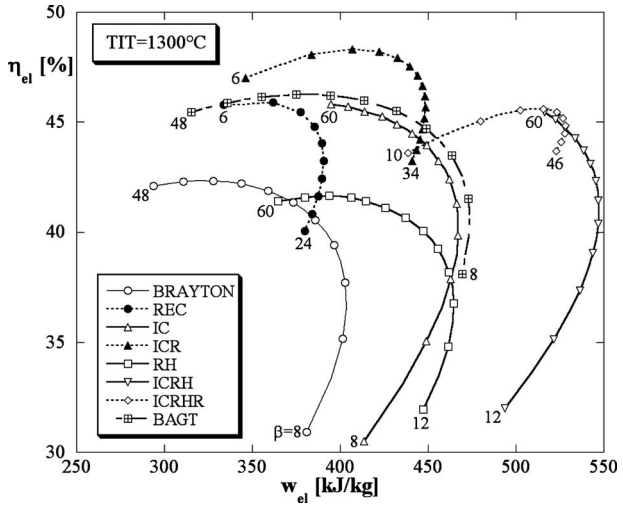

Fig. 2 Performance of selected GT dry cycles—effects of cycle pressure ratio on efficiency and specific work for a fixed TIT value of 1300°C (2370°F)

Table 1 Selected high performance GT cycles

Wet cycles	Hybrid cycles
RWI	SOFC+GT
ISTIG	SOFC+REC
HAT	SOFC+ICR
CHAT	MCFC+GT

Moreover, other high performance GT cycles have been recently proposed with advancements in the research and development work on FC energy systems. In particular, GT-FC "hybrid" cycles developed and/or under development are briefly reviewed here, considering some of the most promising configurations where a GT cycle is integrated with high temperature fuel cells, solid oxide fuel cells (SOFCs), or molten carbonate fuel cells (MCFCs), operating under pressurized conditions or in an atmospheric "externally fired" configuration. Most of these solutions are presently in a precommercialization or an early development stage.

The importance of advanced wet cycles and GT-FC hybrid cycles relies in their potential to achieve extremely high cycle efficiency values, significantly above dry cycles and compatible (or exceeding for the case of GT-FC hybrid cycles) with the existing gas-steam combined cycle technology.

In this paper, a detailed parametric thermodynamic performance analysis on wet and GT-FC hybrid cycles, identified as high performance cycles, is presented in terms of commonly used performance parameters, such as cycle efficiency and specific power. The performance results are compared for different wet cycles, GT-FC hybrid cycles, and some selected dry cycles, identifying significant achievable performance gains. It must be mentioned that economic aspects, an important consideration in the selection of a suitable configuration, of the discussed GT based power cycles are not included in this paper.

2 Selected High Performance GT Cycles: A Brief Overview

This section presents briefly the current understanding of the identified high performance GT cycles, most of which have not been currently implemented except some prototype development, and few pilot laboratory installations. Nevertheless, considerable amount of the research and development work and studies have been made in the last 15+ years describing potential gains achievable with these cycles. The selected high performance GT cycles investigated in our study are listed in Table 1.

2.1 RWI Gas Turbine Cycle. The RWI cycle, first investigated by El-Masri [16] and later further studied by Chiesa et al. [17], basically consists of a modified ICR gas turbine in which liquid water is injected in the air stream prior to entering the recuperator (REC) and the subsequent combustor, as shown in a flow schematic of the cycle used in our study (Fig. 3). The cycle water, later mixing with the air stream, is preheated in the intercooler (IC1) and in an economizer (ECO), which recovers heat from the GT exhaust gases.

Figure 3 shows also the qualitative *T-s* diagram of the cycle (note that the numbering used in the *T-s* diagram corresponds to the key flow conditions identified in the cycle layout; also, this approach of presenting *T-s* diagram has been used for various cycles discussed in this paper).

The water injection in the RWI cycle helps reducing the problem associated with the "dry" recuperated cycle wherein, the thermodynamic benefit due to heat recovery at the REC heat-exchanger is limited due to strong differences in thermal

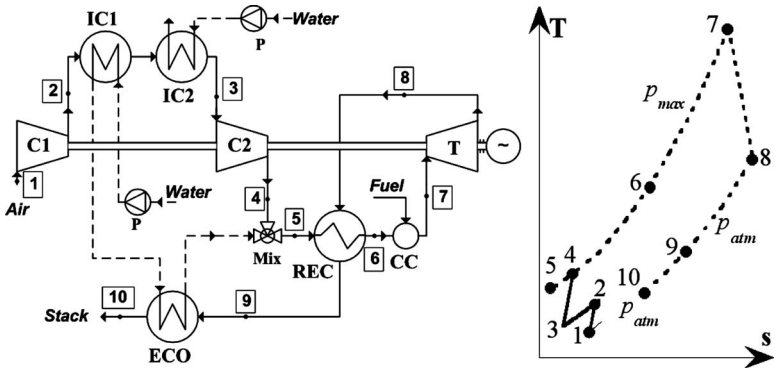

Fig. 3 RWI cycle layout and *T-s* diagram

capacities of the two counterflowing fluids at the REC heat-exchanger: Air from the compressor is cold and reduced in flow by the cooling flow rates, while the flue gas from the turbine is hot and with flow increased by the cooling streams. This large heat-capacity imbalance between the REC streams in the case of ICR cycle is partially recovered in the RWI cycle due to injection of the preheated water, which increases the flow and the specific heat of the cold-side REC inlet stream. Thus, this approach allows increasing the cycle mass flow and improves the heat-capacity imbalance between the REC streams resulting in increased power output and efficiency.

Some key advantages and limitations of the RWI cycle and of other wet cycles investigated in our study are summarized in Table 2.

2.2 ISTIG Cycle. Several variants of the STIG cycle, including intercooled, reheat, and their combinations, have been investigated by different authors (Larson and Williams [13], Rice [15], and Macchi et al. [18,19]). Among these variants, the intercooled steam-injected cycle is considered here as the high performance solution. The ISTIG cycle layout using one-pressure level (1PL) HRSG analyzed in our study and the corresponding *T-s* diagram are shown in Fig. 4. Based on the available literature, the advantages and limitations of the ISTIG cycle including its comparison with the other wet cycles can be seen in Table 2.

2.3 HAT Cycle. The HAT cycle (also called evaporative gas turbine cycle), initially analyzed by Rao and Joiner [20], is characterized by the employment of an evaporation tower (also called saturator) to fully saturate the air stream with water heated through the use of energy extracted within the cycle. In particular, the HAT system typically adopts the ICR Brayton cycle concept, as in the RWI cycle discussed earlier, combined with mixing hot water with the air stream in the saturator positioned upstream of the combustor. The saturator and the HAT cycle performances

Table 2 Comparative advantages and limitations of the examined wet cycles

Cycle	Advantages	Limitations
RWI	- Injected water mixed with air stream increases turbine power output compared with dry ICR cycle [16] - Heat recovery in REC and ECO - Smaller cooling tower than in ICR cycle for the same final IC discharge temperature - Improved thermal capacity imbalance between hot/cold streams of REC	- Water consumption increases with respect to the dry ICR cycle - Higher plant complexity than simple cycle due to increased number of heat-exchangers - Entropy losses in the mixing process (larger than in the HAT cycle adopting the saturator) [17]
ISTIG	- IC provides lower compression power and higher efficiency than in the STIG cycle [13] - Increase in power output with respect to IC cycle [19] - Very large β values not required as in STIG+RH cycle [18] - GE offers LMS100 (with 112.2 MW, η_{el}=52.8% at ISO conditions)—no commercial installation yet	- Needs HRSG: added complexity and increased GT back pressure - Issues of STIG cycles (combustor corrosion, flame stability, CO emissions, etc.) limit the value of steam-to-air ratio [19] - Multi-PL-HRSG: more complex and lower efficiency [19]
HAT	- Large increase in water mass admissible (more than 20% of the air mass flow in dry cycle) and power increase [17] - Lower irreversible heat losses than in RWI cycle due to gradual evaporation inside the SAT [17] - Efficiency comparable with CC without the use of HRSG and associated auxiliary systems [21]	- Increased plant complexity due to many heat-exchangers [22] - Turbine/compressor flow mismatch: Redesign of turbine section is needed, if an existing dry GT is used [17] - The optimum cycle pressure significantly higher than the CC system[21]
CHAT	- Better part-load and start-up characteristics, lower performance degradation over ambient temperature, and reduced NO_x emission than CC and simple cycle GT [23,24] - More easy to implement in existing machines than HAT [23,24] - Capital investment 15–20% lower than similar size CC system	- Plant complexity - Problems of RH: high inlet temperature and lower oxygen in the second combustor - The optimum cycle pressure higher than other cycles and significantly higher than the CC system [25]

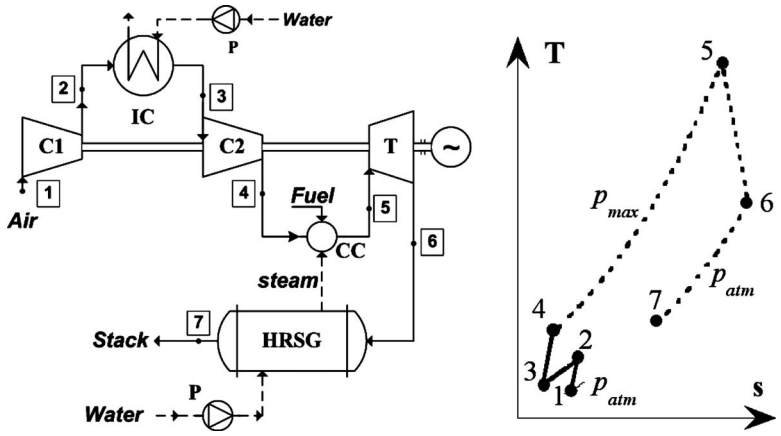

Fig. 4 ISTIG cycle layout and *T-s* diagram

have been described and modeled by several authors [17,21,22]. The countercurrent multistage water-air mixing taking place inside the saturator, with gradual water evaporation occurring under limited temperature terminal difference, allows reducing the irreversible heat losses due to the mixing process compared with the other solutions (see Table 2 for comparative advantages and limitations of the HAT cycle with the other wet cycles).

The HAT cycle plant layout analyzed in this paper is shown in Fig. 5, with its *T-s* diagram.

2.4 CHAT Cycle. The CHAT cycle is a further evolution of the HAT cycle, basically consisting of a HAT cycle combined with a reheat process. This concept, originally introduced and analyzed by Nakhamkin et al. [23], consisted in a two-shaft gas turbine system: The power-shaft (low pressure system) derived its components from an existing single shaft industrial GT (Westinghouse W501F and W501D); whereas, the power-balanced second shaft (high pressure system) utilized existing industrial compressor and expander technologies available from Dresser-Rand. Their analysis showed that with TITs of 871°C (1600°F) and 1400°C (2552°F) for HPT and LPT, respectively, the proposed CHAT plant could achieve a net cycle efficiency of 54.7% with capital cost of 15–20% lower than a similar size combined cycle plant. In a later study to examine the potential to improve performance of the CHAT plant, Nakhamkin et al. [24] analyzed a system with TITs of 1149°C (2100°F) and 1394°C (2540°F), for HPT and LPT, respectively, and noted that net efficiency of 59.2% could be achieved.

A detailed parametric study of the CHAT cycle by Facchini et al. [25] using a similar cycle layout as proposed by Nakhamkin et al. [23] revealed some interesting results: There exists an optimum value of pressure ratio for LP and IP compressors; for an optimum pressure ratio of IPC and a given pressure ratio of LPC, cycle efficiency remains almost constant over a wide range of total cycle pressure ratio; the maximum cycle efficiency close to 58% could be achieved using the same value of TIT=1350°C (2460°F) for both the HPT and LPT; and the gain in cycle efficiency due to increased value of TIT for HPT was relatively smaller above TIT=871°C (1600°F) mainly because of efficiency penalty associated with the blade cooling flow requirements.

The CHAT plant layout with its *T-s* diagram, used for the present study, is shown in Fig. 6, and its advantages and limitations compared with the other wet cycles are provided in Table 2.

2.5 Fuel Cell-Gas Turbine Hybrid Cycles. Several FC-GT hybrid cycles have been proposed in literature in recent years, where high temperature fuel cells (SOFC or MCFC) are integrated with a simple or modified Brayton cycle. The proposed configurations are generally based on a GT cycle (with simple, recuperated, intercooled, or reheat cycle) where the FCs "substitute" the combustor, oxidizing the fuel and generating electricity, and produce a hot gas stream, which is expanded in the turbine section for generating power [26,27]. The FCs may work under pressurized conditions (receiving hot and pressurized air from the compressor) [27–29] or at atmospheric pressure, exchanging heat with the GT

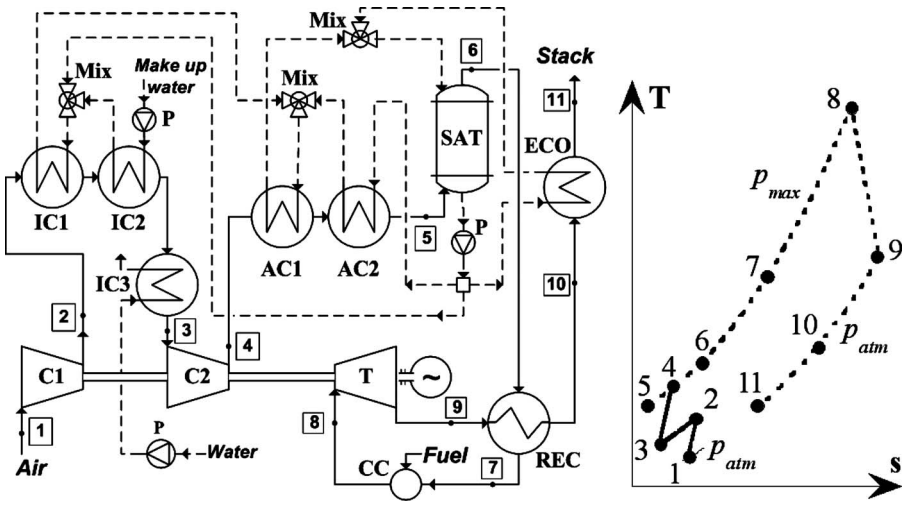

Fig. 5 HAT cycle layout and *T-s* diagram

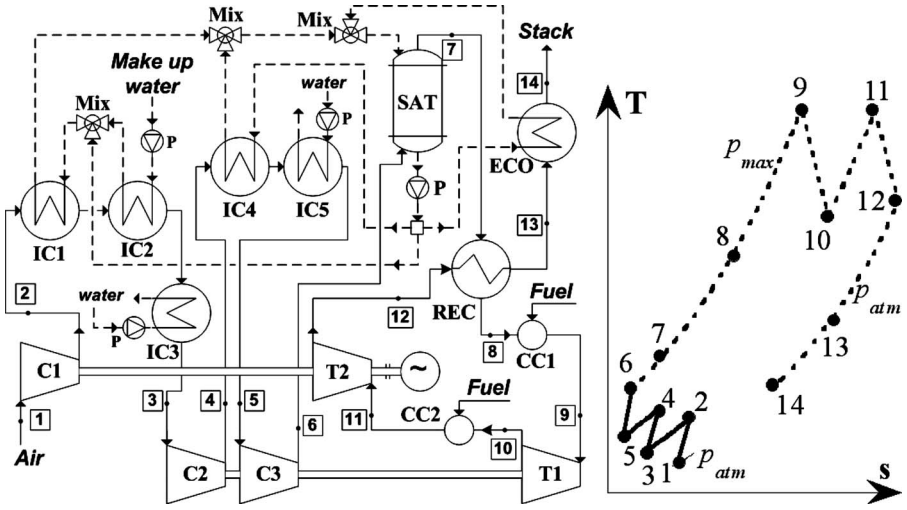

Fig. 6 CHAT cycle layout and *T-s* diagram

cycle through a heat-exchanger [30]. Furthermore, the FCs may operate with a single stage oxidation process or in a multistage arrangement, enhancing the fuel and air utilization factor [31]. Finally, the cycle may include a heat recovery bottoming cycle (steam or ammonia as a working fluid) to further increase the electrical efficiency [27,29]. For the purpose of this work, the focus is on the selection of representative hybrid configurations as reported in Table 1. The selection reflects the conceptual configurations adopted in some of the very few existing prototype plants, where the FC-GT hybrid technology has been demonstrated with small power capacity systems [26,30,31].

In all cases, it is considered to operate with natural gas as fuel, exploiting the possibility to carry out internal reforming within the FC module. The SOFC module features an internal arrangement, which includes anode recirculation (which provides steam for the reforming reaction), exhaust combustion of the spent fuel, and air preheating, as discussed in detail in Ref. [32]. As far as the SOFC hybrids are concerned, a first-of-a-kind SOFC+GT plant of this kind has been tested by Siemens-Westinghouse at a 220 kW scale and about 55% efficiency [26], while up to 1 MW plants are in a development stage by Rolls-Royce [33].

Figure 7 shows the conceptual scheme, analyzed in this study, and a *T-s* diagram of a simple GT cycle integrated with a SOFC. The recuperated GT cycle with a SOFC (see Fig. 8) follows the same conceptual principle, with the substitution of the air preheater with a recuperator, working with gas turbine exhausts as a heat source [26,32,34]. The last SOFC cycle considered here includes the integration of the fuel cells with the ICR GT cycle (SOFC+ICR) [27]. Some key characteristics of various GT-hybrid cycles reviewed from literature and investigated in this study are summarized in Table 3.

In all cases, auxiliary combustors may be added, depending also on the cycle pressure ratio, in order to increase the temperature at the FC inlet or at the GT inlet (the addition of a combustor may be required to adapt the gas cycle operating conditions to those required by existing GTs, as well as to increase the power output of the turbine, which is a less expensive power cycle component, thus decreasing the plant specific cost; the additional combustor may also be required during startup or for load regulation of the system). However, since combustion is a process featuring high exergy losses, the impact of including an auxiliary combustor in the energy balance is generally negative from the point of view of the overall cycle efficiency [27,35]. For this reason, this solution is not considered as a possible design option in this work. Consequently, the gas turbine TIT can be kept below the maximum temperatures (e.g., below 900–950°C) tolerable by the state-of-the-art materials and requiring no cooling for hot gas path components.

Similar concepts are applied to a recuperated GT cycle with atmospheric MCFC (see Fig. 9), having several differences relating to the distinctive peculiarities of MCFCs, as described in Table 3. This MCFC cycle layout has been experimented by Fuel Cell Energy and IHI at few hundred-kilowatt scale [30,36,37],

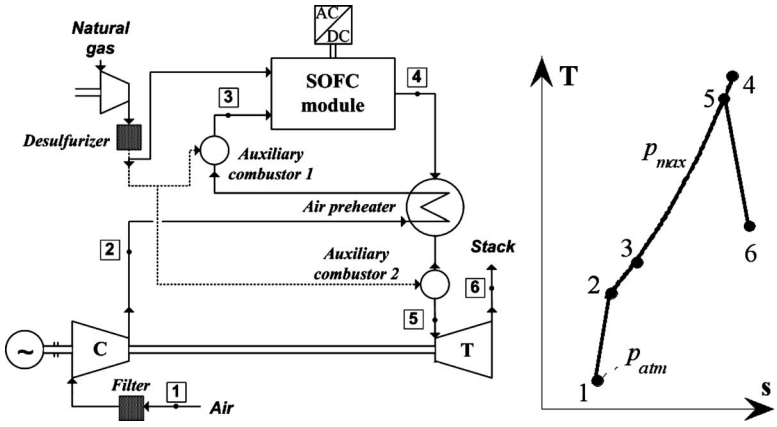

Fig. 7 SOFC+GT cycle layout and *T-s* diagram

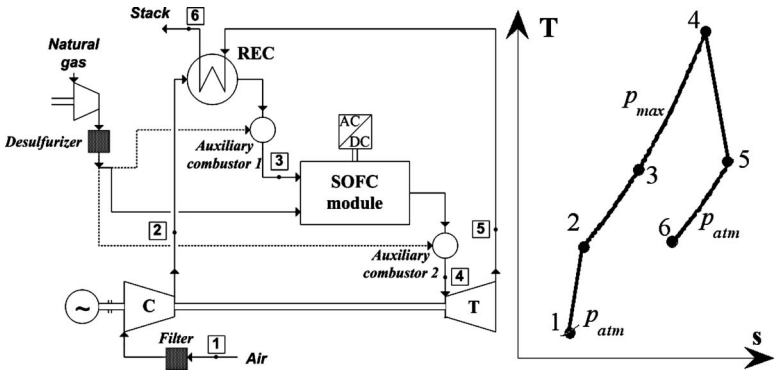

Fig. 8 SOFC+REC cycle layout and *T-s* diagram

Table 3 Characteristics of the examined hybrid cycles

Cycle	Characteristics
SOFC+GT (Fig. 7)	- Compressed air is preheated using FC exhaust gases - The high temperature air preheater is a critical component (materials and thermal duty) - Fuel is preheated by exhaust gas (not shown in the figure)
SOFC+REC (Fig. 8)	- REC recovers heat from TG exhaust gas - REC can be a critical component for thermal stress, but operates at lower temperature than in SOFC+GT air heater - First demonstrated hybrid concept: 220 kW plant by Siemens-Westinghouse [26] - Rolls-Royce proposed a mixing chamber instead of the REC, recycling a fraction of exhaust gas [33]
SOFC+ICR	- Layout of Fig. 8 with addition of IC - IC reduces not only compression work but also temperature of airflow sent to the FC - May require air preheater, which adds complexity - Auxiliary combustor can be used to increase air temperature, but the efficiency drops [27]
MCFC+GT (Fig. 9)	- MCFC requires CO_2 at the cathode (via recirculation) - MCFC is fed with steam and natural gas and spent fuel at the FC outlet react with air in a catalytic burner - Air preheated by FC exhaust and in a heat-exchanger - TG section works with pure air as "externally fired" - Very low β values required [35] - Demonstrated in few prototypes [30,36,37]

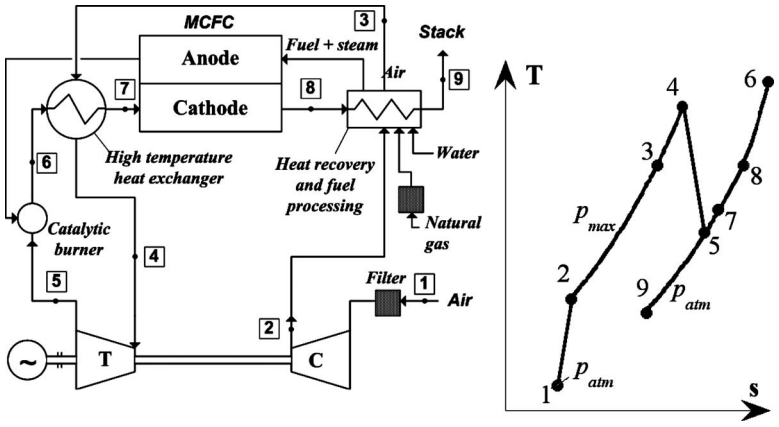

Fig. 9 MCFC+GT cycle layout and *T-s* diagram

Table 4 Gas turbine technology cases

GT Tech. level	TIT (°C)	No. of cooled stages[a]	Compressor polytropic efficiency	Turbine polytropic efficiency
A	1500	3	0.91	0.89
B	1300	2	0.90	0.89
C	1100	1	0.87	0.88

[a]In case of CHAT cycle, single stage HPT is considered cooled.

while other system arrangements (not discussed here for simplicity) rely on a pressurized and recuperated cycle as proposed by Ansaldo Fuel Cells for a 500 kW scale [31,35], showing the potential to reach very high overall cycle efficiencies, ranging around 55–60% with cycle pressure ratio of 3–7.

3 Simulation Procedures and Assumptions

Different turbine technology levels, defined in terms of TIT value, polytropic efficiency of compressor, and expander sections of a GT and blade cooling configurations, have been considered in the parametric investigation as reported in Table 4. In particular, three GT technology levels have been considered: (1) Level A—next generation and large power rating gas turbines, (2) Level B—gas turbine technology introduced in the 1990s, and (3) Level C— gas turbine technology introduced in the 1980s and earlier.

In our parametric analysis, the polytropic efficiency values of GT components (compressor and turbine) are chosen according to the work of Consonni and Macchi [38]. The cooling air mass flow rates for rotor blades and nozzles of each cooled turbine stage are calculated, assuming film-cooled blades and considering stage inlet hot gas and coolant air temperature, following the work of El-Masri [39]. It must be noted that based on the available literature, TIT of 870°C (1600°F) is considered limit for a noncooled turbine stage with uncoated blades [11]. Therefore, cooled turbine stages are considered for the three technology levels examined in our study. The stage loading values of the cooled turbine stages have been selected according to the recent investigation on the thermodynamic performance of dry cycles by Bhargava et al. [2].

Table 5 lists the main common input data assumed for the parametric study. All GT cycles have been analyzed with inlet air conditions corresponding to the ISO ambient conditions (1.013 bars, 15°C, and 60% relative humidity).

In order to simulate the high performance GT cycles considered in this study, reasonable and consistent assumptions for the key design parameters of the specific components are necessary. The assumed values of the required parameters for each high performance cycle are given in Table 6.

A brief description on the assumptions listed in Table 6 is given below.

3.1 RWI Cycle. The cycle layout, discussed earlier and shown in Fig. 3, follows the work of Chiesa et al. [17]. For the RWI cycle, the LPC pressure ratio (β_{LPC}) is chosen equal to 2.5, a value providing optimum efficiency for the IC cycle, following the work of Bettocchi et al. [40]. The injected water mass flow is equal to 10% of the inlet air mass flow, close to the condition of optimum cycle efficiency according to the study of Chiesa et al. [17]. The intercooler IC2 is sized such that the air temperature of 35°C is achieved at the inlet to the high pressure compressor (HPC). It must be mentioned that the scheme for the RWI cycle used in our study differs compared with the work of El-Masri [16] as it relates to the use of two intercoolers to meet the air temperature requirements of 35°C at the exit of IC2. The pressure of injected water, into the mixer or evaporative after-cooler (shown by thermodynamic state 5 in Fig. 3), is fixed at 30% more than the air pressure at the HPC discharge.

Table 5 Common input data

Parameter	Value	Unit
Fuel LHV	47,500	kJ/kg
Combustion efficiency	0.99	—
Generator, mech. loss and auxiliaries efficiency	0.98	—
Inlet pressure losses	1.0	kPa
Outlet pressure losses	1.0	%
Pressure drop through combustors	3.0	%
Effectiveness of ECO and REC heat-exchangers	90	%
External water inlet temperature	30	°C

Table 6 Input data for the examined "wet" cycles

Parameter	Value
Input data for RWI	
LPC pressure ratio	2.5
Injected water mass flow	10% of inlet air
Injected water pressure	130% of $p_{EX\ HPC}$
Water temperature at inlet to IC1 and IC2	15°C
Intercooling final air temperature	35°C
Δp_{IC}, Δp_{REC}, and Δp_{ECO}	3.0%
Effectiveness of IC1 heat-exchanger	90%
Input data for ISTIG	
LPC pressure ratio	2.5
IC and HRSG water inlet temperature	15°C
Intercooling final air temperature	35°C
Injected steam maximum pressure	130% of $p_{EX\ HPC}$
Second level pressure for 3LP HRSH	15 bars
Third level pressure for 3LP HRSH	4.0 bars
HRSG final ECO subcooling	5°C
HRSG minimum VAP pinch point	14°C
HRSG SH effectiveness	90%
Δp_{HRSG} and Δp_{IC}	3.0%
Input data for HAT	
LPC pressure ratio	5.0
Effectiveness of IC1, IC2, AC1, and AC2	90%
Water temperature at inlet to IC2 and IC3	15°C
Intercooling final air temperature	35°C
ΔT_{SAT}	60°C
Δp_{REC}	3.0%
Δp_{IC1}, Δp_{IC2}, Δp_{IC3}, Δp_{AC}, and Δp_{AC2}	1.5%
Δp_{SAT}	1.0%
Input data for CHAT	
LPC pressure ratio	7.0
IPC pressure ratio	5.0
Effectiveness of IC1, IC2, and IC4	90%
IC3 and IC5 outlet air temperature	35°C
IC2, IC3, and IC5 water inlet temperature	15°C
ΔT_{SAT}	60°C
Δp_{IC1}, Δp_{IC2}, Δp_{IC3}, Δp_{IC4}, and Δp_{IC5}	1.5%
Δp_{SAT}	1.0%
Δp_{REC}	3.0%

3.2 ISTIG Turbine Cycle. For simulating the ISTIG cycle, a flow schematic shown earlier in Fig. 4, the LPC, and the intercooling section design parameters are chosen in line with the RWI cycle as described above. For the present study, a single pressure level HRSG is considered. The value of steam injection pressure is chosen equal to 130% of the combustor inlet gas pressure.

3.3 HAT Cycle. For the HAT cycle, simulations have been carried out with a β_{LPC} value of 5.0, a value providing maximum cycle efficiency for wide ranging values of TIT in accordance to the study of Chiesa et al. [17]. Similar to the analysis of RWI cycle, the intercooler IC3 is sized to achieve air temperature of 35°C at the HPC inlet. The saturator is sized such that the tem-

Table 7 Fuel cell technology cases

FC Tech. level	Cell voltage, V_C (V)	Fuel utilization factor, U_f	Air utilization factor, U_a
A	0.75	0.85	0.30
B	0.70	0.80	0.25
C	0.65	0.75	0.20

perature difference between the water inlet temperature and the gas outlet temperature for various cases is 60°C. The water mass flow rate at the saturator outlet is equally divided into three streams directed toward the ECO, AC2, and the IC1. A cycle layout used in our study is shown in Fig. 5.

3.4 CHAT Cycle. For the CHAT cycle simulation, pressure ratio values for the LPC and the IPC are 7 and 5, respectively, in line with the optimum values found by Facchini et al. [25]. Moreover, the expansion ratio of the HPT has been adjusted in order to match the compressors power used by IPC and HPC, thus making the HP-shaft a power-balanced shaft. A cycle layout used in our study is shown in Fig. 6.

3.5 Fuel Cell-Gas Turbine Hybrid Cycles. As typically happens in FC+GT hybrid cycles, the FC is largely the primary power generating component of the cycle, producing 70–80% of the overall power output. In such cases, it is more interesting to investigate the effects of a variation in the FC key operating parameters rather than parameters affecting the performance of the GT components. For this reason, we have fixed here the compressor and turbine (uncooled) polytropic efficiency corresponding to the values of the GT technology level B as given in Table 4, while the combinations of FC parameters shown in Table 7 are investigated herein. Although SOFC and MCFC typically have different operating parameters (for instance, SOFCs may feature higher fuel utilization—defined as the ratio between oxidized hydrogen mass flow and the equivalent hydrogen mass flow available at the cell inlet, taking into account the internal reforming reactions—and lower cell voltages), a common set of parameters has been chosen to allow a uniform comparison highlighting thermodynamic advantages of the different power cycles.

For the case of the MCFC cycle, as discussed below, air utilization factor (U_a), defined as a ratio between oxygen mass flow consumed by the FC electrochemical reactions and the oxygen total mass flow available, has been adjusted to keep appropriate temperature conditions at the cathode inlet.

In all GT-hybrid cycle's simulation, the pressure drop in the high temperature heat-exchangers is 3% of the inlet pressure, while it is set to 1% at the FC anode and cathode side. The electrical efficiency in the dc/ac conversion is set to 96%.

The parametric analyses for RWI, ISTIG, HAT, and CHAT cycles have been performed, using a commercial simulation program (GATECYCLE™, version 5.22) for thermal power systems. This simulation analysis uses lumped-model approach, which allows modeling of each individual component (compressor, turbine, intercoolers, aftercoolers, recuperator, economizer, saturator, etc.) of a given cycle based on the user-defined input conditions and conservation laws (mass and energy balance) and subsequently obtains key performance parameters of the cycle.

The performances of the fuel cell-GT hybrid cycles have been calculated with a modular simulation code, named GS and developed at Politecnico di Milano, which has been already tested on a large variety of complex gas-steam and fuel cell cycles [41,42].

4 Results of Simulated High Performance Cycles

In this section, a review of the results obtained with simulation of the investigated high performance GT cycles is presented. Besides comparing the performance of each cycle for different technology levels, results are also compared with the corresponding dry cycles including performance of the commercially available gas turbines and the published results, wherever available.

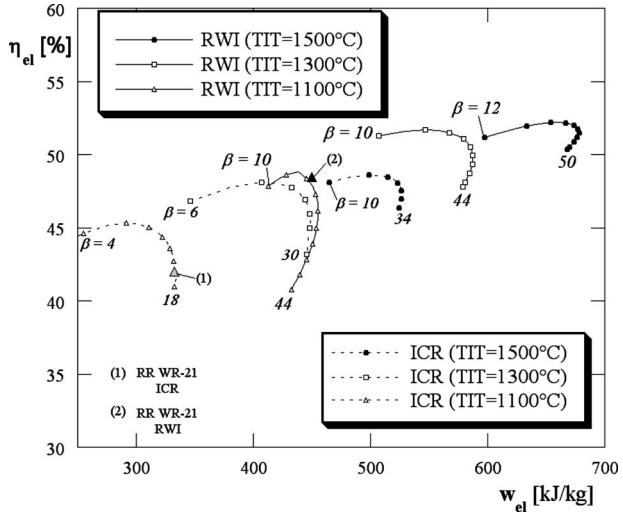

Fig. 10 Efficiency versus specific work for RWI cycle and comparison with ICR cycle

While discussing the calculated performance of wet cycles examined in this study, for each performance curve for a specific value of TIT lower and upper limits of β values investigated are shown in the presented figures.

4.1 Results for RWI Cycle. The simulation results, if compared with the ICR cycle (highest performing dry cycle) performance for the three technology levels and as presented in Fig. 10, clearly show a significant increase in both η_{el} and w_{el} for the RWI cycle. The maximum cycle efficiency achievable with the RWI cycle is approximately 52% compared with 49% for the ICR cycle at TIT=1500°C.

The obtained results show that if the RWI concept is applied to the existing ICR gas turbine, Rolls-Royce model WR-21 (having η_{el} value of 41.7%, with β=16 and TIT value around the considered GT technology level C), a gain in efficiency up to around 47% could be obtained, while power output increases by about one-third (see Fig. 10).

4.2 Results for ISTIG Cycle. For this cycle, the effect of a TIT change from 1100°C to 1500°C leads to a maximum increase in η_{el} from about 46% to nearly 54% as shown in Fig. 11. It is evident that the maximum efficiency values are obtained with β values in the range 25–40 for the three TIT values considered, these values being larger than the cycle pressure ratios providing maximum efficiency for the RWI cycle. For a given TIT value, the specific work value decreases with increase in the cycle pressure ratio, as the amount of steam produced in the HRSG is reduced due to lower temperature and residual energy content of the gas at the turbine outlet.

The ISTIG cycle is compared with the nonintercooled STIG and IC cycles in Fig. 11 for TIT=1300°C: In this case, the maximum value of ISTIG efficiency is 5% higher than the IC cycle, but the gain in efficiency is less than 1% compared with the STIG cycle maximum efficiency value.

The simulated results of the ISTIG cycle agree with the manufacturer's reported performance [7] of the existing intercooled gas turbine, GE Model LMS100, which can also be operated with steam injection. This aeroderivative engine, with a β value of 42 and a declared firing temperature of 1380°C, is rated for 7509 Btu/kWh of heat rate (β_{el}=45%) and 99 MW of output power (w_{el}=475 kJ/kg) in dry IC cycle configuration at ISO conditions (see Fig. 11); when operated in ISTIG mode [7], the gas turbine produces 112.2 MW (w_{el}=540 kJ/kg) with a heat rate value of

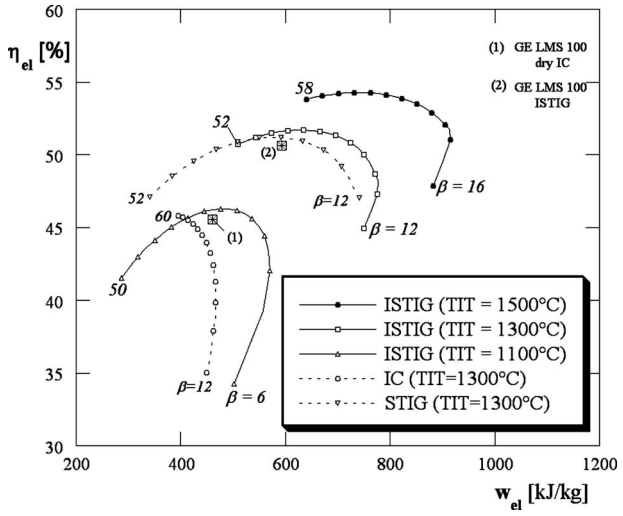

Fig. 11 Efficiency versus specific work for ISTIG cycle and comparison with IC and STIG cycles for TIT=1300°C

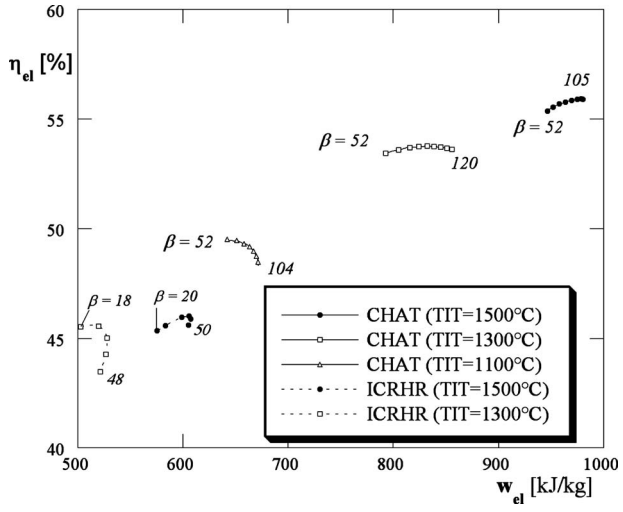

Fig. 13 Efficiency versus specific work for CHAT cycle and comparison with ICRHR cycle

6845 Btu/kWh (η_{el}=50%) at ISO conditions. The performance points of GE LMS100 with and without steam injection are shown as points (1) and (2), respectively, in Fig. 11: The slight difference between these points and the calculated values of efficiency for TIT=1300°C is probably due to uncertainty in actual TIT values and polytropic efficiencies.

4.3 Results for HAT Cycle. The HAT cycle exhibits an efficiency gain with respect to ICR cycle up to 5% while the specific work increase is about 200–300 kJ/kg (see Fig. 12). The numerical results obtained for the HAT cycle, show the possibility to achieve cycle efficiency values up to 56% for the most advanced turbine technology (TIT=1500°C) examined.

In particular, the highest performances are obtained with β in the range 30–40 (typical of an aeroderivative GT compressor) for TIT=1500°C; in case of lower β value (e.g., 16), typical of a heavy-duty GT, the calculated cycle efficiency remains still higher than 55%.

The values of cycle efficiency obtained in our study are consistent with values reported by different authors in literature: Chiesa et al. [17] calculated values of efficiency up to 57% for the HAT system with TIT=1500°C and β=48, and up to 55% for TIT =1250°C and β=27–30; a study by Yadav et al. [43] showed cycle efficiency of 56% for a TIT=1527°C at β=40 for their HAT system. Studies conducted at Pratt & Whitney [44] to evaluate implementation of HAT cycle on the existing gas turbines revealed the following: Cycle efficiency of more than 58% could be achieved for a modified P&W FT4000 aeroderivative intercooled GT (with TIT=1490°C and β=58.7); whereas, cycle efficiency of around 53% was achievable with the implementation of HAT cycle on a P&W FT8 gas turbine (with TIT=1350°C and β=24.2).

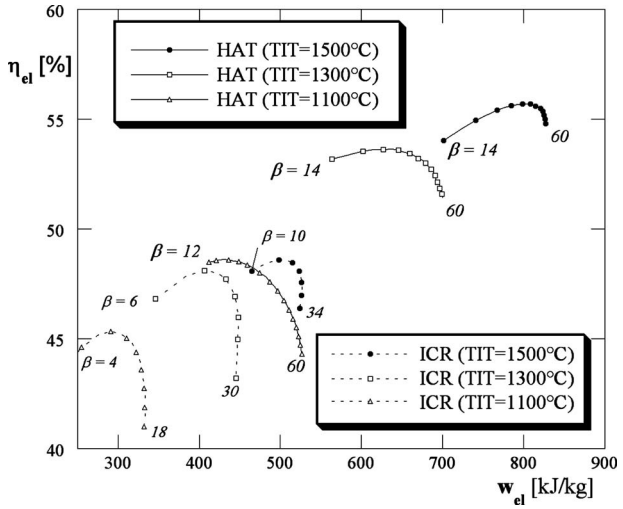

Fig. 12 Efficiency versus specific work for HAT cycle and comparison with ICR cycle

4.4 Results for CHAT Cycle. The CHAT cycle allows obtaining thermodynamic performance similar to the HAT cycle regarding the efficiency values, but with a remarkable improvement in terms of specific work. As shown in Fig. 13, the maximum η_{el} values are close to 56% for the case of TIT=1500°C while the maximum w_{el} values can be up to 1000 kJ/kg. The presented results have been obtained with very large pressure ratio values (ranging between 50 and 100). These high values of overall pressure ratios, as discussed earlier, are required to meet the assumed optimum values of 7 and 5 for LPC and IPC sections, respectively. The increase in specific work for the CHAT cycle with respect to the HAT cycle is due to the synergic effects of the increased cycle pressure ratio and the adoption of reheating.

The calculated CHAT cycle's performance data compare well with the results obtained by Wolk et al. [45], where the investigations of the CHAT cycle applied to some existing turbines were carried out: In particular, it was shown that by modifying a GE 6FA machine with a global pressure ratio of 65 and a maximum TIT value of about 1370°C, a cycle efficiency of about 54% could be obtained. In comparison, simple cycle GE 6FA has an efficiency of about 34% (indicating 20% increase). Whereas, for a smaller aeroderivative Roll-Royce Avon gas turbine with the CHAT cycle implementation and with a limited TIT level (about 900°C), a total efficiency of about 45% could be obtained compared with the simple cycle efficiency of approximately 28%.

The values of efficiency and specific work of the intercooled reheat recuperated (ICRHR) cycle (similar from the thermodynamic point of view to a dry version of the CHAT cycle) are also provided in Fig. 13 for comparison purposes, for the cases of TIT=1500°C and TIT=1300°C. The performance gain of the CHAT cycle is remarkable both in terms of β_{el} (an advantage of up to 10%) and w_{el} (gaining about 300–350 kJ/kg); this gain can be mainly associated with the larger mass flows, resulting due to humidification of air prior to combustion, expanding in the turbine sections.

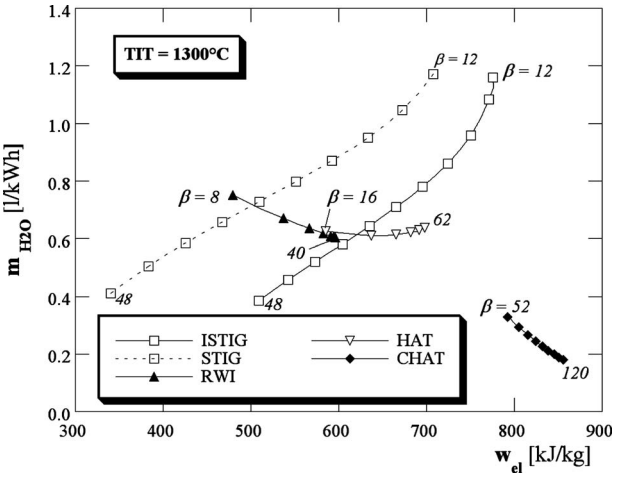

Fig. 14 Variation of injected water flow rate for wet cycles

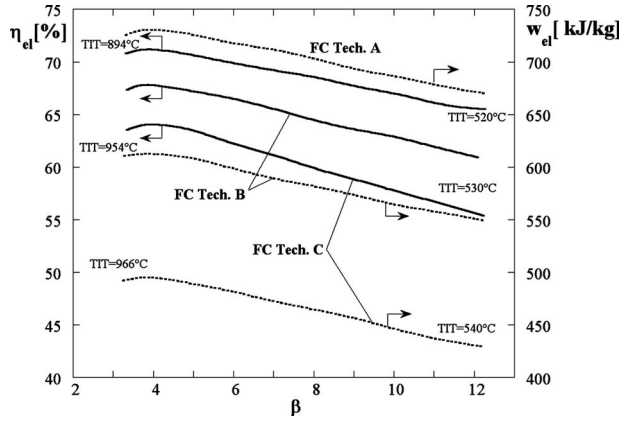

Fig. 16 Efficiency and work output for the SOFC+ICR GT cycle. TIT indications are referred to both efficiency and work output for each FC Tech. case.

A comparison of injected water flow rate normalized with the net power output (m_{H_2O}), for the examined wet cycles with TIT =1300°C, shows some interesting results (Fig. 14): The ISTIG cycle requires 30–40% less water than the STIG cycle to obtain the same specific work; whereas, the HAT cycle provides larger specific work than the RWI cycle with a similar amount of water ingestion; and the CHAT cycle requires less amount of injected water per unit of power compared with all the other wet cycles.

The effect of β on the normalized amount of water is also shown in Fig. 14. The value of m_{H_2O} decreases with the increase in cycle pressure ratio for most of the considered cycles: For example in the RWI case, the water mass flow is kept constant but the work increases with β. In the ISTIG case (where m_{H_2O} can achieve values larger than in the other cycles, up to 1.2 l/kWh), the turbine exhaust gas temperature decreases with increase in cycle pressure ratio and the amount of steam produced in the HRSG is decreased.

4.5 Fuel Cell-GT Hybrid Cycle Results. The effects of pressure ratio and TIT on a FC based hybrid cycle utilizing a simple Brayton cycle for the three FC technology levels listed in Table 7 and shown in Fig. 15(*a*) are the same as for the simple Brayton cycle, namely, increase in efficiency and specific work with the increased overall pressure ratio. However, the fuel cell-GT hybrid cycles exhibit very high performances in terms of electrical efficiency (ranging from 55% to over 70%), especially when adopting the highest FC Tech. level. The estimated performance further shows higher efficiency levels achievable with FC Tech. A compared with the other two technologies investigated, because of higher values of fuel utilization factor and air utilization factor.

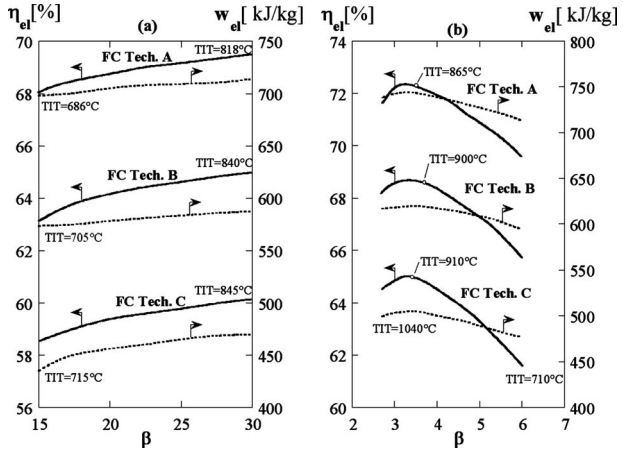

Fig. 15 Efficiency and work output as a function of pressure ratio for the SOFC+GT simple cycle (*a*) and for the SOFC +REC cycle (*b*). TIT indications are referred to both efficiency and work output for each FC Tech. case.

The calculations also show (charts not included) that GT power output share ranges from ≅25% (FC Tech. C) to 16% (FC Tech. A) with respect to the total power output, due to higher heat generation of the less efficient fuel cell case (FC Tech. C), which allows a higher power generation by the bottoming gas cycle.

The cycle requires the adoption of a heat-exchanger working at very high temperature and pressure on both sides (the air preheater in Fig. 7), with a high thermal duty. The maximum gas temperatures on the hot side exceed 1000°C, requiring the use of advanced ceramic materials. Moreover, high temperature fuel cells being a rather low power density device and needing large volumes, the selection of high operating pressures is very demanding in terms of designing the required pressure vessels.

Results for the SOFC+REC GT cycle, which on the contrary does not require high pressure ratios, are shown in Fig. 15(*b*) (for cycle layout, see Fig. 8). The recuperated cycle reaches an exceptionally high 72% electrical efficiency (scenario FC Tech. A), with an average of 3% advantage compared with the simple GT cycle based hybrid under the same FC technology scenario. The recuperator works with limited maximum gas temperatures on the hot side (≅600°C). Also in this case the maximum efficiency corresponds to maximum specific work; the GT power output share at the optimized pressure ratio ($\beta \cong 3.5$) ranges from 31% (FC Tech. C) to 19% (FC Tech. A) with respect to the total power output. Another advantage of the recuperated hybrid cycle compared with the simple cycle hybrid is the use of low cycle pressure ratio systems mainly due to recuperation effect requiring low compressor discharge temperature.

The gas turbine TIT remains below 910°C at optimized conditions, while it tends to increase at very low pressure ratios, above the possibility of an uncooled operation. Similarly to the case of Fig. 15(*a*), the highest TITs are found for FC Tech. C and the lowest for FC Tech. A: In both cases, this behavior can be explained considering that a higher efficiency FC (FC Tech. A) generates electricity releasing a lower amount of heat to the exhaust gases.

Figure 16 shows the results obtained by adopting an ICR cycle with a SOFC. The effect is a reduction in the compression work, leading to slightly higher optimized pressure ratios ($\beta \cong 4$), but also a reduction in the temperature of the airflow going to the fuel cell. For this reason, depending on the cycle pressure ratio, it is

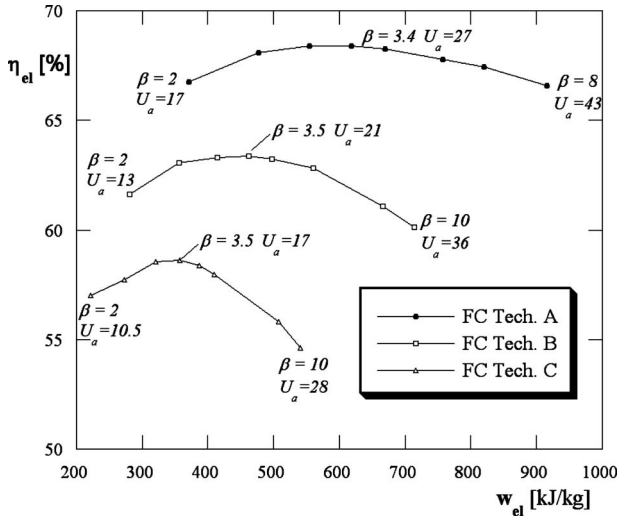

Fig. 17 Efficiency and work output for the MCFC+GT hybrid cycle

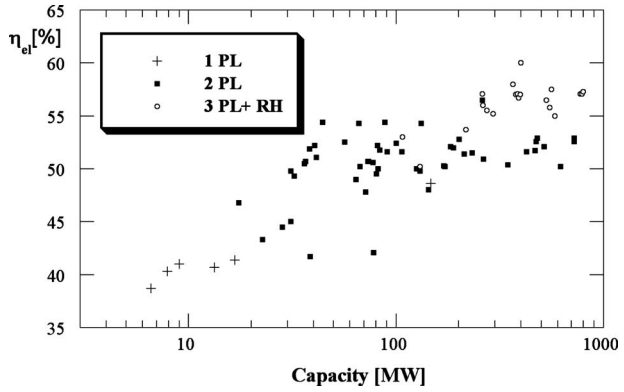

Fig. 18 Commercially available CC power plants with different HRSG arrangements (1PL: one-pressure level; 2PL: two-pressure level; and 3PL+RH: three-pressure level with reheating)

necessary to preheat the airflow using both a recuperator and a high temperature air preheater, with the drawbacks discussed for the case of the simple cycle and the addition of higher pressure losses.

Globally, the cycle does not show significant performance advantages over the recuperated cycle. The GT power output share at the optimized pressure ratio is somewhat lower, ranging from 29% (FC Tech. C) to 17% (FC Tech. A) with respect to the total power output.

Figure 17 shows the results for the hybrid cycle with atmospheric MCFC and simple cycle GT (see cycle layout in Fig. 9). The analysis is carried out at variable pressure ratios as for the previous cases, but the cycle arrangement and the effects on the FC operating conditions are completely different (but consistent with the results reported earlier by Campanari et al. [35]). The pressure ratio of the GT cycle influences the gas temperature at the FC cathode inlet (which shall be kept at about 600°C) in several ways, changing the temperature (i) at the air heater cold side, (ii) at the combustor inlet, and (iii) at the air heater hot side. The simulation is then carried out adjusting the air utilization factor U_a of the FC to keep the desired cathode inlet conditions.

The cycle analysis in this case shows a different optimized condition for efficiency and work output.

The maximum efficiency does not reach the 70% value as estimated for the SOFC-GT hybrid cycles and is limited to 68.4% in FC Tech. A for a pressure ratio of 3.4, with air utilization of 27%. In the other cases, FC Tech. B and FC Tech. C, the optimized pressure ratio is approximately constant, with decreasing air utilization. The maximum achievable efficiency drops to 58.5% in scenario FC Tech. C; the change in efficiency moving from Tech. C to A is higher with respect to the cases of the best SOFC cycles, due to the higher share of FC power on the overall energy balances.

The specific work reaches 670 kJ/kg at maximum efficiency (FC Tech. A), versus 740 kJ/kg for the best SOFC cycle (Fig. 15). The maximum specific work output of the MCFC is, however, much higher when moving on the right side of Fig. 17, reaching 920 kJ/kg at U_a=43%, with a 1.8% lower efficiency (66.6%).

The maximum specific work is higher also in cases B and C, although with a larger loss (3–4%) with respect to the maximum efficiency condition.

The GT power output share at the optimized pressure ratio ($\beta \cong 3.5$) ranges from 18% (FC Tech. C) to 14% (FC Tech. A) with respect to the total power output of the hybrid cycle. The values are lower than those found for SOFC cycles, and the MCFC holds a heavier role on the overall energy balances, due to the lower FC operating temperature and the lower thermodynamic quality of the heat transferred to the GT cycle.

4.6 Comparison of High Performance Cycles. To discuss the comparison of high performance cycles, the first performance of combined cycles having the highest cycle efficiency is examined. Figure 18 presents the cycle efficiency of commercially available combined cycle (CC) systems with HRSG at 1–3 pressure levels [1].

In particular, in the range of power generation capacity up to 300 MW, i.e., the market segment of heavy-duty GT engines, the most widespread CC technology is the two-pressure-level (2PL), while the triple pressure reheat (3PL+RH) arrangement is competitive in a range of larger power. Therefore, the 2PL based CC arrangement has been considered in this study as the reference case with which high performance GT cycles examined in this paper will be compared. Also for the FC-GT cycles, even if the sizes of a few existing prototypes are typically lower than 1 MW, the expected target size is of the order of magnitude of 10–100 MW, still comparable with 2PL CC.

The main hypothesis of the bottoming cycle adopted for CC calculations is shown in Table 8 and the key design parameters of the gas turbine components (polytropic efficiencies, TIT, cooling method, etc.) are consistent with the assumed values for simple and complex cycles. For each GT design, the HRSG high pressure level has been varied, in order to maximize the η_{el} values, while the high and low pressure steam temperatures have been determined by the fixed values of SH effectiveness.

The performances of the optimized combined cycles for the three GT technology levels as a function of the cycle pressure ratio, as shown in Fig. 19, reveal the following: As expected, maximum cycle efficiency (approximately 57%) is achieved with TIT=1500°C; and maximum levels of cycle efficiency and specific work are achievable at low value of cycle pressure ratio, the

Table 8 Assumptions for the CC simulations

HRSG VAPs' pinch points	14°C
HRSG final ECOs' subcooling	5°C
Effectiveness of low pressure SH	0.8
Effectiveness of high pressure SH	0.9
Δp_{HRSG}	3%
Condensing pressure	0.05 bar
High pressure steam turbine efficiency	0.9
Low pressure steam turbine efficiency	0.8
Low pressure level steam pressure	4.0 bars
Deaerator pressure	1.2 bars

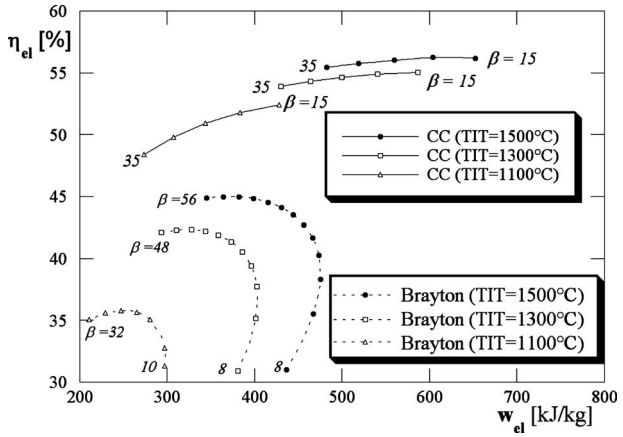

Fig. 19 Efficiency versus specific work for 2PL CC and comparison with Brayton

main features for which CC systems became popular since the 1970s. For comparison, calculated performance results of the simple Brayton cycle for the three GT technology levels are also included in Fig. 19 clearly indicating higher levels of performance for the combined cycle compared with the simple GT cycle.

Figure 20 presents a comparison of the investigated most performing GT based power cycles in terms of efficiency and specific work for the best GT Tech. A (TIT=1500°C) and the highest performing FC Tech. A. To show benefits of the high performance cycles investigated in our study, parametric performance data for the simple Brayton cycle and the most efficient dry cycle, ICR, are included in Fig. 20.

The comparative performance clearly shows potentials of achieving significantly higher cycle efficiency (about 71%) with FC-GT hybrid cycles as shown in Fig. 20. Among the wet cycles, CHAT technology shows competitive performance with the combined cycle technology with significantly higher specific work. As discussed earlier, among many advantages with the CHAT cycle, the CHAT system can be developed at a lower cost than the combined cycle as reported by Nakhamkin et al. [24] and Wolk et al. [45].

Figure 21(*a*) presents the performance comparison for the GT Tech. level B and FC Tech. B. The trends are similar to those observed in Fig. 20 except that performance levels are lower.

For the GT Tech. B and FC Tech. B, the effect of the overall

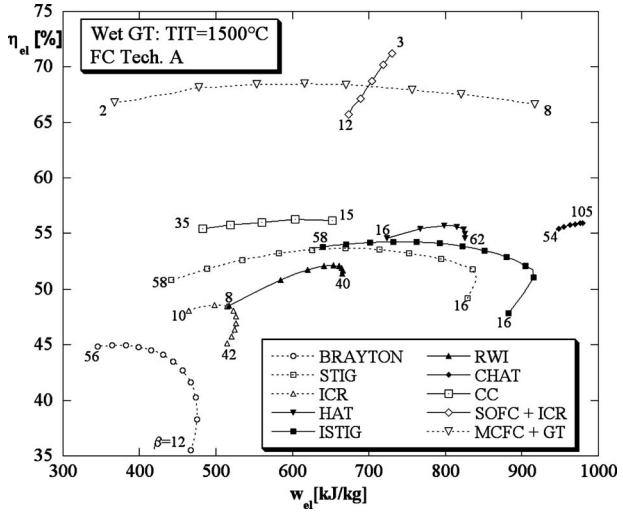

Fig. 20 Comparison of examined cycles with selected dry cycles and CC (TIT=1500°C)

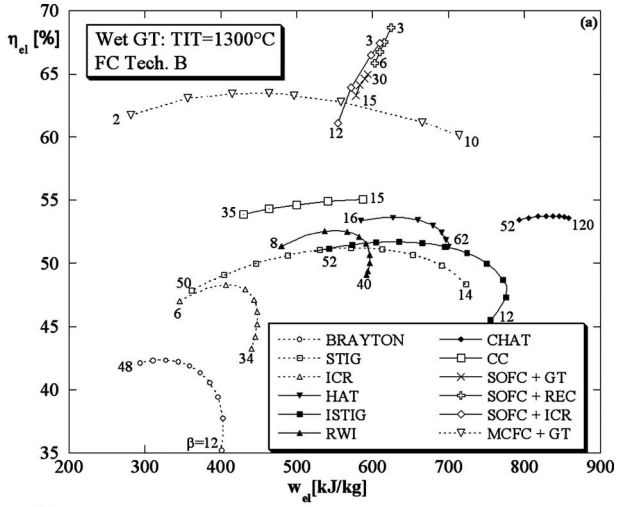

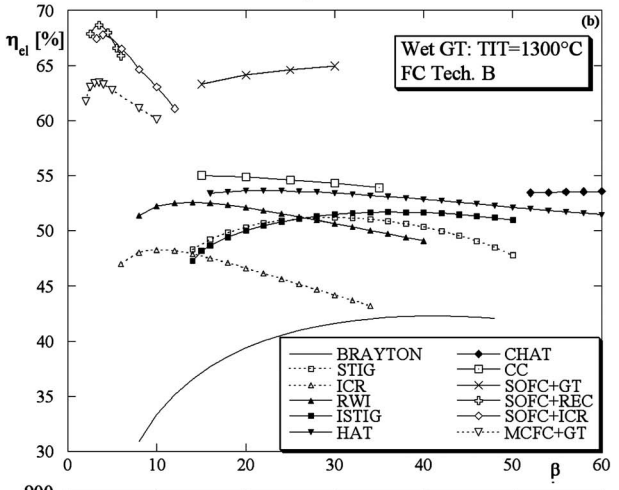

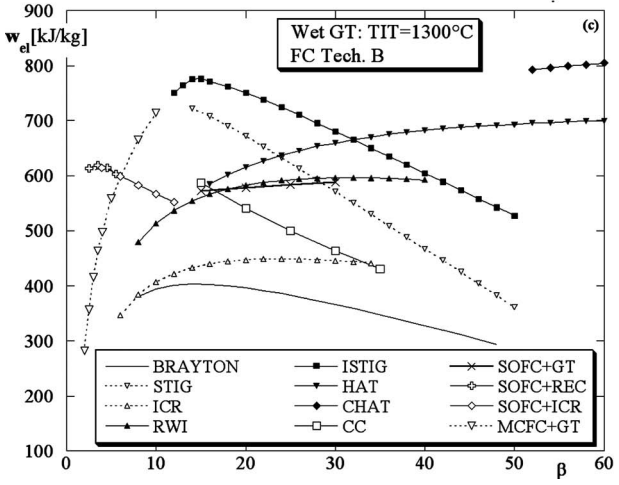

Fig. 21 Comparison of examined cycles with selected dry cycles and CC (TIT=1300°C): (*a*) efficiency versus specific work, (*b*) effect of β on efficiency, and (*c*) effect of β on specific work

cycle pressure ratio on efficiency and specific work for various cycles examined in this paper are shown in Figs. 21(*b*) and 21(*c*), respectively. Maximum values of cycle efficiency can be obtained with β in the range 5–10 by means of FC based cycles, with β in the range 10–20 with ICR, and RWI and CC and with β larger than 20 for Brayton, STIG, ISTIG, HAT, and CHAT cycles. The results presented in Figs. 21(*b*) and 21(*c*) clearly show that a significant increase in specific work with low value of cycle pres-

Table 9 Comparison of optimum performance data for examined high performance cycles with selected "dry" cycles: (case of wet GT TIT=1300°C and FC Tech. B)

	Point of max η_{el}				Point of max w_{el}			
	β	η_{el} (%)	w_{el} (kJ/kg)	m_{H_2O} (l/kWh)	β	η_{el} (%)	w_{el} (kJ/kg)	m_{H_2O} (l/kWh)
Brayton	42	42.3	320	—	14	36.6	404	—
RWI	14	52.6	554	0.650	32	50.4	596	0.604
ICR	10	48.3	407	—	24	45.7	449	—
ISTIG	36	51.7	635	0.644	15	48.2	777	1.125
STIG	30	51.2	572	0.833	12	47.0	741	1.368
HAT	24	53.6	637	0.611	60	51.5	700	0.643
CHAT	84	53.8	832	0.227	120	53.6	858	0.175
ICRHR	20	45.6	510	—	34	44.9	528	—
SOFC+GT	30	65.0	588	—	30	65.0	588	—
SOFC+REC	3.5	68.7	620	—	3.5	68.7	620	—
SOFC+ICR	4	67.8	614	—	4	67.8	614	—
MCFC+GT	3.5	63.5	464	—	10	60.1	714	—
CC (2LP)	15	55.1	587	—	15	55.1	587	—

sure ratio (about 15) and moderate efficiency (about 48%) can be achieved with the ISTIG cycle mainly due to reduced compression specific work (associated with intercooling) and increased mass flow through the turbine (steam injection effect).

The calculated results for various investigated cycles, corresponding to maximum efficiency and maximum specific work, are summarized in Table 9 for TIT=1300°C and FC Tech B. These tabulated data in combination with Fig. 21 reveal the following: The maximum efficiency values achievable are approximately between 51% and 69% for the wet and FC hybrid cycles; the CHAT cycle allows achieving increased level (more than 30%) of specific work and efficiency (2% point gain) compared with the ISTIG cycle with considerably small amount of water requirements but requiring high pressure ratio; GT-FC hybrid cycles can provide considerably higher efficiency and specific work with low levels of cycle pressure ratio compared with the combined cycle.

As far as the comparison among SOFC and MCFC hybrid cycles is concerned, it is possible to evidence the following issues.

- The thermodynamic analysis is moderately in favor of the SOFC based cycle, showing a 2–4% higher maximum efficiency (Table 9). The difference is lower than could be expected by the simple comparison of the two FC operating temperatures (1000°C versus 650°C), which would advantage the cycle with higher topping temperature.
- The SOFC-GT hybrid cycle has the advantage of a simpler configuration, namely, not influenced by the MCFC intrinsic requirements of CO_2 recirculation. The optimized pressure ratio of the more interesting solutions is similar (β =3.5–4).
- The MCFC-GT hybrid cycle may reach higher specific work when operating at higher oxidant utilization, although with a 2–4% loss with respect to the maximum efficiency condition.
- The SOFC based hybrid cycles show a higher share of GT power output on the total hybrid plant power.

Given this rather equilibrated performance comparison, the major issues that will influence the future development of MCFC and SOFC hybrid cycles are probably costs and reliability of the two technologies. Being both FCs the higher specific cost component of a hybrid power plant, the higher share of GT power could reduce the plant total cost per unit of output power.

5 Concluding Remarks

This paper has provided a detailed parametric analysis of various GT based wet and FC hybrid cycles. The presented results of the selected high performance GT cycles clearly show great potentials to improve cycle efficiency and specific work with wet and FC hybrid cycles compared with the commercially available gas turbines (simple and modified Brayton cycles). It is also seen that wet cycles could allow achieving cycle efficiency values comparable with a combined cycle, resulting in a potentially reduced installed equipment cost for future high efficiency power plants. Furthermore, this study shows that fuel cell-GT hybrid cycles have potentials to achieve cycle efficiency values much higher than 60% and significantly higher than achievable with the other investigated cycles.

Nomenclature

LHV = lower heating value (kJ/kg)
m_{H_2O} = water flow rate per unit of output power (l/kWh)
$p_{EX\ HPC}$ = high pressure compressor exit pressure
s = specific entropy (kJ/kg K)
T = temperature (°C)
U_a = air utilization factor
U_f = fuel utilization factor
V_C = fuel cell voltage (V)
w_{el} = net specific work (kJ/kg)

Greek Symbols

β = cycle pressure ratio
Δp = pressure drop (%)
ΔT_{SAT} = SAT temperature difference: water in–gas out (°C)
η_{el} = LHV cycle efficiency (%)

Acronyms

ac = after-cooler or alternate current
BAGT = below ambient gas turbine
C = compressor
CC = combustion chamber, combined cycle
CHAT = cascaded humidified advanced turbine
dc = direct current
EC = exhaust combustion
ECO = economizer
FC = fuel cell
GT = gas turbine
HAT = humid air turbine
HPC = high pressure compressor
HPT = high pressure turbine
HRSG = heat recovery steam generator
IC = inter-cooled or inter-cooler
ICR = inter-cooled recuperated

ICRH = inter-cooled reheat
ICRHR = inter-cooled reheat recuperated
IPC = intermediate pressure compressor
ISO = International Standard Organization
ISTIG = inter-cooled steam injected gas turbine
LPC = low pressure compressor
LPT = low pressure turbine
MCFC = molten carbonate fuel cell
Mix = mixer
P = pump
PL = pressure level
PR = pre-reforming
REC = recuperator or recuperated
RH = reheat
RWI = recuperated water injection
SAT = saturator
SH = superheater
SOFC = solid oxide fuel cell
STIG = steam injected gas turbine
T = turbine
TIT = turbine inlet temperature
VAP = vaporizer

References

[1] *Gas Turbine World 2004–05 GTW Handbook*, Vol. 24, Pequot, Fairfield, CT.
[2] Bhargava, R. K., Bianchi, M., De Pascale, A., Negri di Montenegro, G., and Peretto, A., 2007, "Gas Turbine Based Power Cycles—A State-of-the-Art Review," *Proceedings of the International Conference on Power Engineering-2007 (ICOPE 2007)*, Hangzhou, China.
[3] McDonald, C. F., 1999, "Emergence of Recuperated Gas Turbines for Power Generation," ASME Paper No. 99-GT-67.
[4] Takeya, K., Oteki, Y., and Yasui, H., 1984, "Current Status of Advanced Reheat Gas Turbine AGTJ-100A (Part 3) Experimental Results of Shop Tests," ASME Paper No. 84-GT-57.
[5] Eckardt, D., and Rufli, P., 2001, "Advanced Gas Turbine Technology—ABB/BBC Historical Firsts," ASME Paper No. 2001-GT-0395.
[6] McCarthy, S. J., and Scott, I., 2002, "The WR-21 Intercooled Recuperated Gas Turbine Engine-Operation and Integration Into the Royal Navy Type 45 Destroyer Power System," ASME Paper No. 2002-GT-30266.
[7] Reale, M. J., 2004, "New High Efficiency Simple Cycle Gas Turbine—GE's LMS100™," GER-4222A (06/04).
[8] Bianchi, M., Negri di Montenegro, G., Peretto, A., and Spina, P. R., 2005, "A Feasibility Study of Inverted Brayton Cycle for Gas Turbine Repowering," ASME J. Eng. Gas Turbines Power, **127**, pp. 599–605.
[9] Wilson, D. G., 1984, *The Design of High-Efficiency Turbomachinery and Gas Turbines*, MIT, Cambridge, MA, Chap. 3.
[10] Horlock, J. H., 2005, *Advanced Gas Turbine Cycles*, Elsevier Science, Oxford, UK.
[11] Boyce, M. P., 1987, *Gas Turbine Engineering Handbook*, Gulf, Houston, TX, Chap. 2.
[12] Jonsson, M., and Yan, J., 2005, "Humidified Gas Turbines—A Review of Proposed and Implemented Cycles," Energy, **30**, pp. 1013–1078.
[13] Larson, E. D., and Williams, R. H., 1987, "Steam Injected Gas Turbines," ASME J. Eng. Gas Turbines Power, **109**, pp. 55–63.
[14] Cheng, D. Y., and Nelson, A. L. C., 2002, "The Chronological Development of the Cheng Cycle Steam Injected Gas Turbine During the Past 25 Years," ASME Paper No. GT-2002-30119.
[15] Rice, I. G., 1995, "Steam-Injected Gas Turbine Analysis: Steam Rates," ASME J. Eng. Gas Turbines Power, **117**, pp. 347–353.
[16] El-Masri, M. A., 1988, "A Modified, High-Efficiency, Recuperated Gas-Turbine Cycle," ASME J. Eng. Gas Turbines Power, **110**, pp. 233–42.
[17] Chiesa, P., Lozza, G., Macchi, E., and Consonni, S., 1995, "An Assessment of the Thermodynamic Performance of Mixed Gas-Steam Cycles: Part B—Water-Injected and HAT Cycles," ASME J. Eng. Gas Turbines Power, **117**, pp. 499–508.
[18] Macchi, E., Bombarda, P., Chiesa, P., Consonni, S., and Lozza, G., 1991, "Gas-Turbine-Based Advanced Cycles for Power Generation Part B: Performance Analysis of Selected Configurations," 91-Yokohama-IGTC-72.
[19] Macchi, E., Consonni, S., Lozza, G., and Chiesa, P., 1995, "An Assessment of the Thermodynamic Performance of Mixed Gas-Steam Cycles: Part A—Intercooled and Steam-Injected Cycles," ASME J. Eng. Gas Turbines Power, **117**, pp. 489–498.
[20] Rao, A. D., and Joiner, J. R., 1990, "A Technical and Economic Evaluation of the Humid Air Turbine Cycle," Seventh Annual International Pittsburgh Coal Conference, Sept. 10–14.
[21] Stecco, S. S., Desideri, U., Facchini, B., and Bettagli, N., 1993, "The Humid Air Cycle: Some Thermodynamic Considerations," ASME Paper No. 93-GT-77.
[22] Lazzaretto, A., and Segato, F., 2001, "Thermodynamic Optimization of the HAT Cycle Plant Structure—Part I: Optimization of the "Basic Plant Configuration"," ASME J. Eng. Gas Turbines Power, **123**, pp. 1–7.
[23] Nakhamkin, M., Swensen, E., Wilson, L.M., Gaul, G., and Polsky, M., 1996, "The Cascaded Humidified Advanced Turbine (CHAT)," ASME J. Eng. Gas Turbines Power, **118**(3), pp. 565–571.
[24] Nakhamkin, M., Swensen, E. C., Scheibel, J. R., and Cohn A., 1998, "CHAT Technology: An Alternative Approach to Achieve Advanced Turbine Systems Efficiencies With Present Combustion Turbine Technology," ASME Paper No. 98-GT-143.
[25] Facchini, B., Ferrara, G., and Masi, G., 1998, "A Parametric Study of CHAT Cycle Performance: Thermodynamic and Design Features," ASME Paper No. 98-GT-166.
[26] Veyo, S., Shockling, L., Dederer, J., Giller, J., and Lundberg, W., 2000, "Tubular Solid Oxide Fuel Cell/Gas Turbine Hybrid Cycle Power Systems–Status," ASME Paper No. 2000-GT-550.
[27] Campanari, S., and Macchi, E., 1998, "Thermodynamic Analysis of Advanced Power Cycles Based Upon Solid Oxide Fuel Cells, Gas Turbines and Rankine Bottoming Cycles," ASME Paper No. 98-GT-585.
[28] Lundberg, W. L., Veyo, S. E., and Moeckel, M. D., 2001, "A High Efficiency SOFC Hybrid Power System Using the Mercury 50 ATS Gas Turbine," ASME Paper No. 2001-GT-521.
[29] Shockling, L., Veyo, S., Litzinger, K., and Lundberg, W., 2005, "Comparative Evaluation of SOFC/Gas Turbine Hybrid System Options," ASME Paper No. GT2005-68909.
[30] Ghezel-Ayagh, H., Sanderson R., and Walzak, J., 2005, "Development of Hybrid Power Systems Based on Direct Fuel Cell/Turbine Cycle," ASME Paper No. GT2005-69119.
[31] Marcenaro, B., Ferrari, E., and Torazza, A., 2004, "Series 2TW MCFC Power Plant, First of a Kind," Fuel Cell 2004 International Conference and Exhibition, Lucerne, Switzerland.
[32] Campanari, S., 2000, "Full-load and Part-Load Performance Prediction for Integrated SOFC and Microturbine Systems," ASME J. Eng. Gas Turbines Power, **122**, pp. 239–246.
[33] Agnew, G., Berenyi, S., Bozzolo, M., and Moritz, R., 2005, "The Design and Integration of the Rolls-Royce Fuel Cell Systems 1MW SOFC," ASME Paper No. GT2005-69122.
[34] Campanari, S., 2004, "Parametric Analysis of Small Scale Recuperated SOFC/Gas Turbine Cycles," ASME Paper No. 2004-GT-53933.
[35] Campanari, S., Iora, P., Macchi, E., and Silva, P., 2007, "Thermodynamic Analysis of Integrated MCFC/Gas Turbine Cycles for Multi-MW Scale Power Generation," ASME J. Fuel Cell Sci. Technol., **4**, pp. 308–316.
[36] Ghezel-Ayagh, H., Daly, J. M., and Wang, Z. H., 2003, "Advances in Direct Fuel Cell/Gas Turbine Power Plants," ASME Paper No. GT2003-38941.
[37] Azegami, O., 2006, "MCFC/MGT Hybrid Generation System," R&D Rev Toyota CRDL, **41**(1), pp. 36–43.
[38] Consonni, S., and Macchi, E., 1998, "Gas Turbine Cycles Performance Evaluation," *Proceedings of the ASME COGEN-TURBO Meeting*, Montreaux, Switzerland.
[39] El-Masri, M. A., 1986, "On Thermodynamics of Gas-Turbine Cycles: Part 2—A Model for Expansion in Cooled Turbines," ASME J. Eng. Gas Turbines Power, **108**, pp. 151–159.
[40] Bettocchi, R., Cantore, G., Negri di Montenegro, G., and Moro, D., 1991, "Optimum Performance Evaluation in Multistage Intercooled Compression Gas Turbines," *Proceedings of the ASME COGEN—TURBO IGTI*, Vol. 6, pp. 235–242.
[41] Consonni, S., Lozza, G., Macchi, E., Chiesa, P., and Bombarda, P., 1991, "Gas-Turbine-Based Advanced Cycles for Power Generation Part A: Calculation Model," *Proceedings of the International Gas Turbine Conference-Yokohama 1991*, Vol. III, pp. 201–210.
[42] Chiesa, P., and Macchi, E., 2004, "A Thermodynamic Analysis of Different Options to Break 60% Electric Efficiency in Combined Cycle Power Plants," ASME J. Eng. Gas Turbines Power, **126**(4), pp. 770–785.
[43] Yadav, R., Kumar, P., Dwivedi, P. K., and Saraswati, S., 2004, "Thermodynamic Evaluation of Humidified Air Turbine (HAT) Cycles," ASME Paper No. GT2004-54098.
[44] 2002, "Humid Air Turbine Cycle Technology Development Program," Pratt & Whitney Advanced Engine Programs, Technical Progress Report No. TW-0077.
[45] Wolk, R., Nakhamkin, M., and Goldstein, H. N., 2002, "Evaluation of Cascaded Humidified Advanced Turbine (CHAT) Cycles for Natural Gas and Syngas," USDOE Turbine Power Systems Conference.

Manufacturing Optimization for Bondcoat/Thermal Barrier Coating Systems

Hans-Peter Bossmann
e-mail: hans-peter.bossmann@power.alstom.com

Sharath Bachegowda

Alexander Schnell

ALSTOM,
Brown Boveri Strasse 7,
CH-5401 Baden, Switzerland

A reliable lifetime prediction rule for bondcoat/thermal barrier coating (BC/TBC) coated parts in gas turbine operation is necessary to determine remnant service life. The specimens investigated were coated with MCrAlY plus yttria partially stabilized zirconia applied by vacuum plasma spraying and atmospheric plasma spraying processes, respectively. The performances of these laboratory specimens were statistically assessed, combining long term oxidation testing with thermal cycling, thus superimposing thermomechanical loading on the laboratory specimens to more accurately represent engine conditions. A design of experiment (DOE) approach was used for manufacturing optimization of the BC/TBC system. The life of the coating system is influenced by several manufacturing parameters such as BC thickness, BC roughness, TBC thickness, TBC porosity, and TBC stiffness. Specimens with a suitable variation in these parameters were produced to ensure a balanced test matrix of fractional factorial DOE. Based on results derived from laboratory testing the specifically tailored parts, first and second order effects of manufacturing parameters on lifetime were quantified. The findings revealed that the second order effects (the interaction of manufacturing parameters) were more important on the lifetime of the BC/TBC system than the corresponding first order effect (single parameter). For instance, the variation in BC thickness or BC roughness led to a scatter of lifetimes of 10% and 60%, respectively, whereas their interaction resulted in a scatter of lifetime of 150% for the same range of coating parameters. Further examples of such pairings are also demonstrated. Finally, a lifetime prediction for three quality classes (high, medium, and low qualities) has been demonstrated. The difference in achievable lifetime highlights the importance of manufacturing parameters in determining the life of the BC/TBC system. [DOI: 10.1115/1.3155398]

1 Introduction

Thermal barrier coatings are widely used in gas turbine (GT) hot section components such as burners, transition ducts, shrouds, blades, and vanes. The most common TBC material is MCrAlY plus yttria partially stabilized zirconia (7YSZ) because of its high temperature stability, low thermal diffusivity, and high coefficient of thermal expansion [1–10].

BC/TBC systems are typically layered structures, consisting of a ceramic topcoat and an underlying metallic MCrAlY bondcoat (Fig. 1). The main function of the TBC layer is to reduce the temperature of the base material. A large thermal gradient in the TBC is achieved through its low conductivity [1–10]. The conductivity of the coating is not only a material property but is also a function of the microstructural parameters such as porosity and microcracks [11,12].

During service, GT blades and vanes are subjected to severe temperature, stress, and strain conditions, which result in time-dependent microstructural changes of the used materials. This applies not only to the base material but also to the protective coating systems. Further the TBC layer itself undergoes some microstructural changes at high temperatures such as phase transformations and lattice parameter changes causing volume change, resulting in changed porosity [13].

For modern GT systems, a prime reliant TBC system is essential for high cooling efficiency and high firing temperatures, which would imply that the TBC system must not fail.

2 Materials and Tests

A comprehensive study into the influence of microstructural coating parameters on the lifetime of BC/TBC systems has been carried out. In order to achieve this, the manufacturing parameters were tuned using a design of experiment (DOE) approach to cover wide range of TBC porosity, TBC thickness, BC roughness, and BC thickness. A large number of blades were specifically produced within the full range of manufacturing capability. All airfoils of these blades were cut into sections. These sections had complex geometries, consisting of concave, convex, and flat surfaces. Two sections from each blade were subjected to cyclic thermal loading. The cyclic oxidation method is a proven and validated tool to determine lifetime of BC/TBC coated parts, and the same approach has been used to make the lifing tool more accurate by being able to consider coating quality.

For testing, the samples were placed in quartz boats (Fig. 2) and subjected to a 24 h thermal cycle during which they were maintained at elevated temperature for 23 h and at room temperature for 1 h. The samples were cooled at ambient conditions, imposing harsh transient thermal loading, which simulates engine start stop conditions. Typically after 15 min the samples cooled down to room temperature and were visually checked for TBC spallation and cracking.

The initiation and progress of TBC spallation were recorded with respect to cycles. In general, it was seen that TBC spallation occurred after quite a long incubation period (first delamination of TBC or spallation of a small size area), but then propagated fast to a significant size of spalled area. Initial spallation and final spallation (50% TBC loss criterion) were recorded. This was done in order to double check tendencies and eliminates misinterpretations due to operator dependent detection and interpretation problem of spallation.

Contributed by the International Gas Turbine Institute of ASME for publication in the JOURNAL OF ENGINEERING FOR GAS TURBINES AND POWER. Manuscript received April 16, 2008; final manuscript received August 15, 2008; published online October 30, 2009. Review conducted by Dilip R. Ballal. Paper presented at the ASME Turbo Expo 2008: Land, Sea and Air (GT2008), Berlin, Germany, June 9–13, 2008.

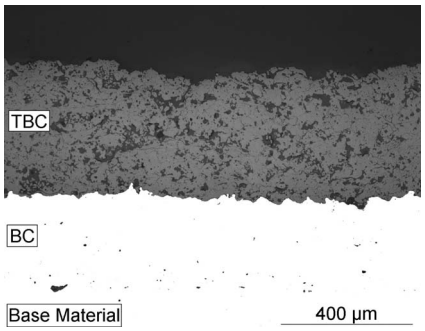

Fig. 1 Typical BC/TBC microstructure

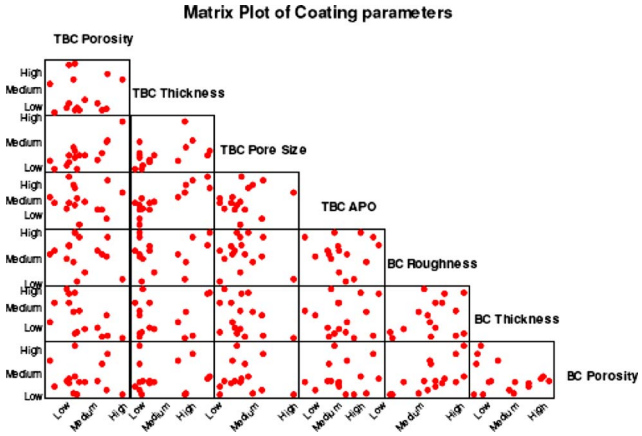

Fig. 3 Matrix plot of coating parameters

3 DOE Approach

A three-level approach was chosen to evaluate the influence of coating parameters. In this approach each microstructural coating parameter was divided into three distinct quality levels as high, medium, and low depending on their measured magnitude. An experimental study of all possible combinations of coating parameter pairings is very intensive. In order to use the minimum number of parameter combinations to extract all relevant information, a fractional factorial approach to DOE was chosen to produce a balanced test matrix.

To ensure no clustering of parameters and to ascertain if the blades produced were according to standards established in the design matrix, one section from each blade was metallographically investigated for TBC thickness, TBC porosity, TBC pore orientation, TBC pore size, BC roughness, BC thickness, and BC porosity.

The matrix plot (Fig. 3) is a guide to check the input data used in the experiment. Each box in the matrix plot needs to be read individually. Individual boxes in the matrix plot show a scatter of two microstructural coating parameters. The parameter labeled above each column represents the respective x-axis and the parameter labeled next to each row represents the corresponding y-axis.

The data points in an individual box should ideally be homogeneously scattered in order to extract any existing second order influence between the two parameters constituting that particular box. If clustering of data points occurs in one individual box, this would imply a lack of data points to extract second order influences if they would exist. However, one can already see the correlation between these two microstructural parameters that constitute that particular box.

From the matrix plot, it can be seen that the measured coating parameters do not cluster. Exceptions are noticed for TBC thickness versus TBC pore orientation, and BC roughness versus BC porosity. Also certain combinations are missing such as high BC thickness with low BC roughness.

All the measured coating parameters conformed to the established baseline for testing according to the DOE matrix. This ensures that prior to the start of the experimental effort, a suitable variation in data is available. This guarantees the identification of microstructural influences on TBC life on both first and more critically on the second order influences.

4 Results

4.1 First Order Influence of Parameters. In the first order influence of parameters, each coating parameter's influence on the life of the coating system is considered independently. The coating parameters considered for first order influence are as follows:

- bondcoat roughness
- bondcoat thickness
- bondcoat porosity
- TBC porosity
- TBC thickness
- TBC pore orientation
- TBC pore size

From the metallographic investigation of the reference section, probability plots (Fig. 4) for each parameter set, which represents the scatter of the raw data, were generated. These data were divided into three distinct regions as high (upper third of measured values), medium, and low values based on the measured magnitude from the probability plot as shown above.

Fig. 2 Arrangement of sample in quartz boats for daily cycling in the furnace

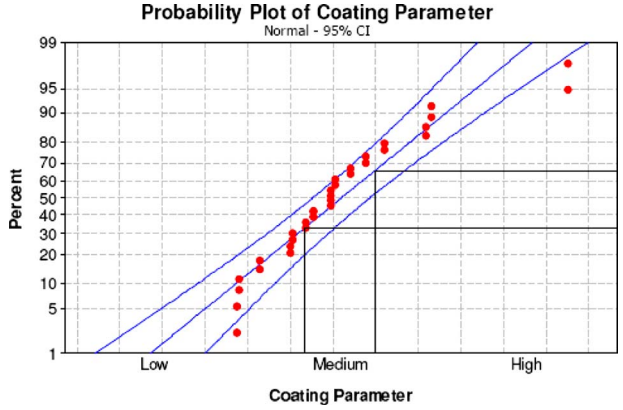

Fig. 4 Probability plot of coating parameter with high, medium, and low cutoff limits

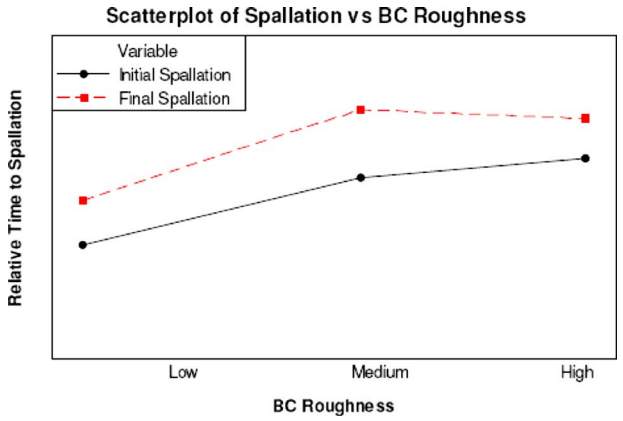

Fig. 5 Scatter plot of time to spallation versus BC roughness

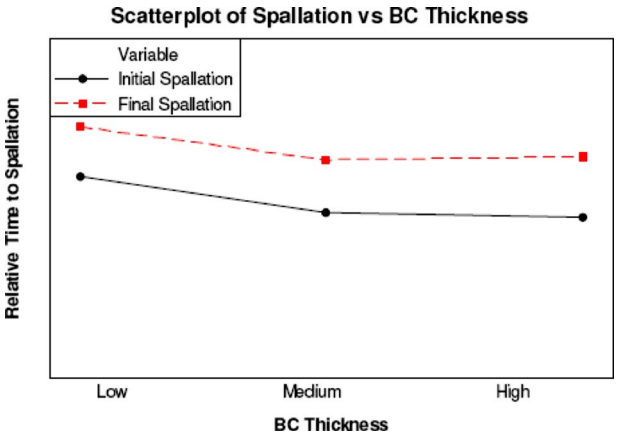

Fig. 6 Scatter plot of time to spallation versus BC thickness

The average of all the data points, which lie in one class in the probability plot, represents one data point on the first order influence plot. The three-level approach also guarantees that not just tendencies but also weighting for each parameter can be extracted. The tendencies seen in the first order influence graph need to be interpreted on a relative scale and are not with respect to any established baseline.

Bondcoat roughness. The bondcoat roughness plays a very important role in determining the lifetime of the BC/TBC system. The BC not only protects the underlying base material from oxidation but it also offers mechanical adhesion for the TBC. In the case of electron beam physical vapor deposition coatings, low BC roughness is preferred for high lifetime; however, for APS TBC systems, a rough bondcoat is preferred in order to achieve higher life as the amount of mechanical locking is increased [14]. The magnitude of benefit that can be obtained by changing the BC roughness was of interest in this section.

With an increase in BC roughness, the time to both initial and final spallations increases (Fig. 5). The increase in life with an increase in BC roughness was greater between the low and medium ranges compared with the medium and high ranges.

Bondcoat thickness. The applied BC not only acts as an anchor for the ceramic layer but also needs to be sufficiently thick to offer oxidation resistance to the base material. However, it is known that with an increase in BC thickness, the risk for crack initiation in the BC increases due to thermo-mechanical fatigue loading of the part, which is detrimental to the lifetime of the blade. An indication into the influence of BC thickness on the life of the BC/TBC system can be obtained from this campaign [15].

With an increase in the BC thickness, the time to both initial and final spallations decreases (Fig. 6). The decrease in life with an increase in BC thickness is greater between the low and medium ranges compared with the medium and high ranges.

Bondcoat porosity. The interface layer between the BC and the TBC is produced employing different manufacturing parameters to ensure higher BC roughness. As a consequence of this, the porosity of the BC layer is increased. The effect of this porous layer is analyzed in the following.

There is a very strong correlation between life of the coating and BC roughness. With an increase in the BC porosity there is an increase in the time to both initial and final spallations (Fig. 7). The correlation between an increase in BC porosity and time to spallation seems to be nearly linear.

However, it must be noted that the BC porosity is strongly correlated with BC roughness, and there could be a superposition of effects that is observed.

TBC porosity. The TBC that used industrial gas turbines is generally applied on the bondcoat using the APS process. The TBC porosity plays a critical role in determining the conductivity of the BC/TBC system and also influences the mechanical behavior of the TBC in terms of strain tolerance [16].

It was seen that with an increase in TBC porosity, the time to initial and final spallations increases (Fig. 8). The increase in time to spallation with an increase in TBC porosity seems to be more pronounced at high porosities. It could also be concluded that the initial spallation of a ceramic layer is sensitive to TBC porosity, whereas further delamination seems to be less sensitive to it.

TBC thickness. Based on the GT operating condition, the TBC layer needs to be sufficiently thick to reduce the temperature at the base material so that its mechanical integrity is not compromised. Even though a thick TBC is desirable, there are limitations on the

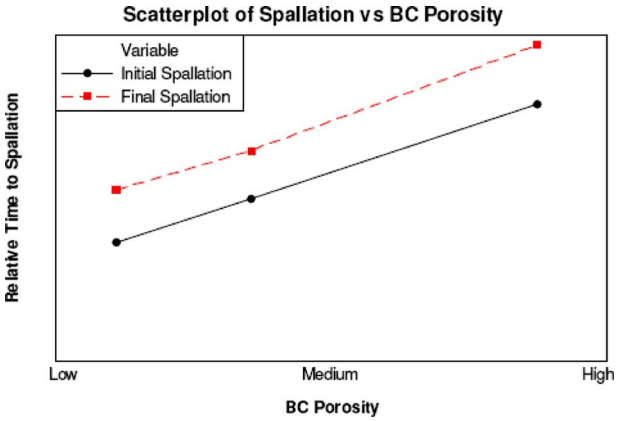

Fig. 7 Scatter plot of time to spallation versus BC porosity

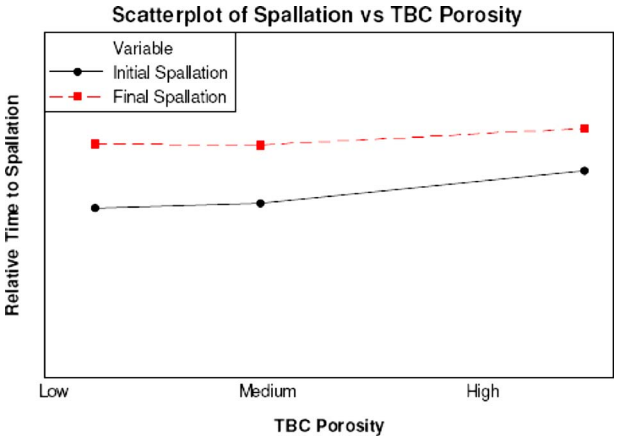

Fig. 8 Scatter plot of time to spallation versus TBC porosity

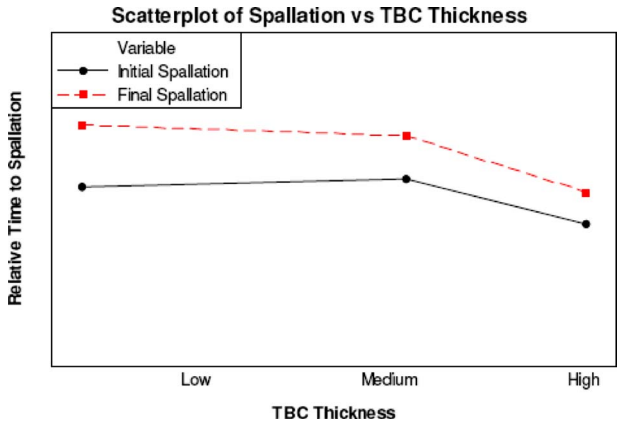

Fig. 9 Scatter plot of time to spallation versus TBC thickness

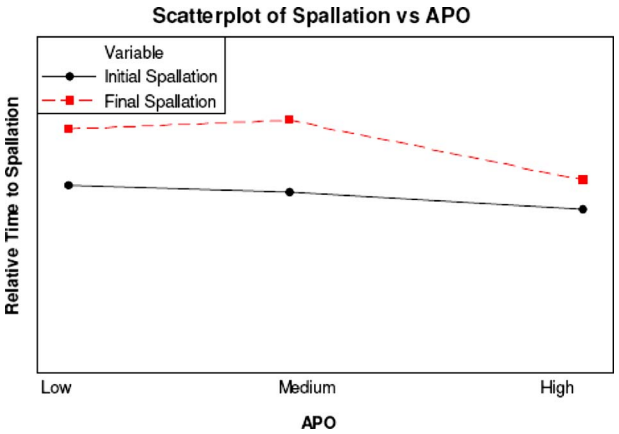

Fig. 11 Scatter plot of time to spallation versus APO

TBC thickness imposed by the mismatch in physical properties of the ceramic layer and the base material. This would imply that a thick coating is subjected to higher internal stresses, resulting in lower life of the system [17].

It was seen that with an increase in TBC thickness, the time to initial and final spallations decreases (Fig. 9). It is beneficial to have TBC with low thickness for better cyclic life of the BC/TBC system. It must be noted that the effect of the TBC thickness in the low–medium range is not so significant; however, between the medium and high ranges, TBC thickness is detrimental to the life of the system.

TBC pore orientation. The orientation of the microstructure has been expressed by average pore orientation (APO), which is defined as

$$APO = \frac{\sum A_{\text{pore}} \times \alpha_{\text{el}}}{\sum A_{\text{pore}}} \tag{1}$$

where A_{pore} is the pore area, and α_{el} is the angle of an ellipse approximating the pore shape.

Figure 10 shows the approach where one complexly shaped pore is approximated with an ellipse. The major axis of which gives the pore orientation with respect to the outer TBC surface.

As the APO gets lower, there is a tendency for higher time to initial and final spallations (Fig. 11). This means that having horizontally oriented pores in the microstructure of the TBC is more beneficial than having vertically oriented pores.

Pore size. In the microstructure of the TBC, there are pores of various sizes. There is a tendency for the microstructure to change with time and temperature, causing the smaller pores to disappear. Based on this effect, described as sintering, the coating tends to become stiffer, resulting in a reduction in the strain tolerance, which drives coating spallation. A TBC layer, which exhibits a higher porosity, contains a high amount of larger pores, which increases the resistance of the coating against sintering. Consequently high porosity is beneficial to the lifetime of the system.

However, no clear trend can be seen with respect to pore size and life of the BC/TBC system (Fig. 12).

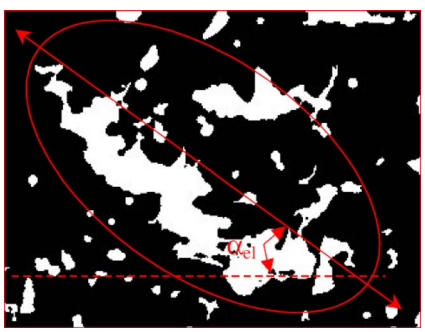

Fig. 10 Definition of "pore orientation based on an ellipse angle"

4.2 Discussion of First Order Influence of Coating Parameters. It is seen that BC roughness has a high influence on the life of the TBC; the greater the roughness, the greater the coating life; an increase in BC roughness resulted in an 80% increase in time to initial spallation and a 60% increase in time to final spallation (see Table 1).

With an increase in BC thickness, the time to initial spallation decreased by 20% and the time to final spallation decreased by 15% (see Table 2). Having a BC system with low thickness was found to be more beneficial to the life of the BC/TBC system.

There is nearly a 110% increase in time to initial and final spallations with an increase in the BC porosity (see Table 3). This showed the greatest benefit in terms of first order parameter influence.

It is also seen that with an increase in the TBC porosity, the life of the system increases. With an increase in TBC porosity, the time to initial spallation of the coating increased by 20% and the time to final spallation increased by 8% (see Table 4).

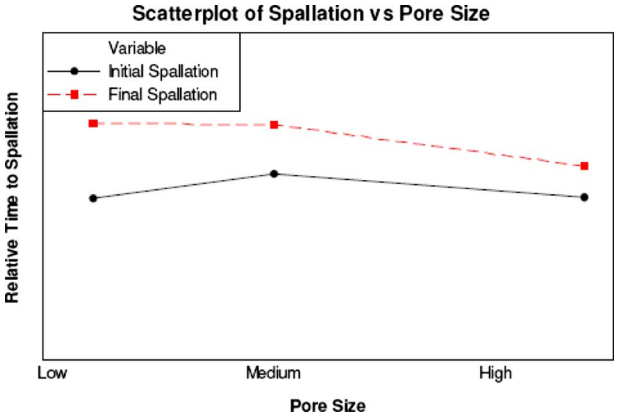

Fig. 12 Scatter plot of time to spallation versus pore size

Table 1 Influence of BC roughness

BC roughness increase over produced range	
Increase in time to spallation	80%
Increase in time to final spallation	60%

Table 2 Influence of BC thickness

BC thickness increase over production range	
Decrease in time to spallation	20%
Decrease in time to final spallation	15%

With respect to the TBC thickness, there is no significant influence of the TBC thickness on the coating life in the low to medium range; however, with an increase in TBC thickness, at the higher range, the life of the system decreases significantly (see Table 5).

Horizontally oriented pores in the microstructure are preferable to vertical pores in the system. There is an increase in time to spallation by 13% for initial spallation and 9% for final spallation as the pores become more horizontally oriented (see Table 6).

Pore size did not seem to have a significant influence on either initial spallation or final spallation (see Table 7).

4.3 Second Order Influence of Parameters. An innovative approach in order to better understand the interaction of coating parameters on the life of the coating system has been carried out. In this second order study, coating parameters were paired together. The three-level approach (high, medium, and low), which was previously used for the study of first order parameter influences, was continued. Two coating parameters were paired as high*high, high*medium, and so on to obtain up to nine sets of data points for each pair of coating parameters, and the average of each set of data points was reported to obtain up to nine points. Box plots were made taking into account only the high*high (H*H), high*low (H*L), low*high (L*H), and low*low (L*L). Surface plots were made taking into account the whole range of data points. The results for the pairing of parameters are as follows. Second order influence of BC porosity, TBC pore orientation, and TBC pore size is not discussed as these parameters are correlated with other coating parameters such as BC roughness, TBC thickness, and TBC porosity, respectively.

Table 3 Influence of BC porosity

BC porosity increase over production range	
Increase in time to spallation	110%
Increase in time to final spallation	90%

Table 4 Influence of TBC porosity

TBC porosity increase over production range	
Increase in time to spallation	20%
Increase in time to final spallation	8%

Table 5 Influence of TBC thickness

TBC thickness increase over production range	
Decrease in time to spallation	22%
Decrease in time to final spallation	28%

Table 6 Influence of TBC pore orientation

TBC APO increase over production range	
Decrease in time to spallation	15%
Decrease in time to final spallation	20%

Table 7 Influence of TBC pore size

TBC pore size increase over production range	
Decrease in time to spallation	5%
Decrease in time to final spallation	10%

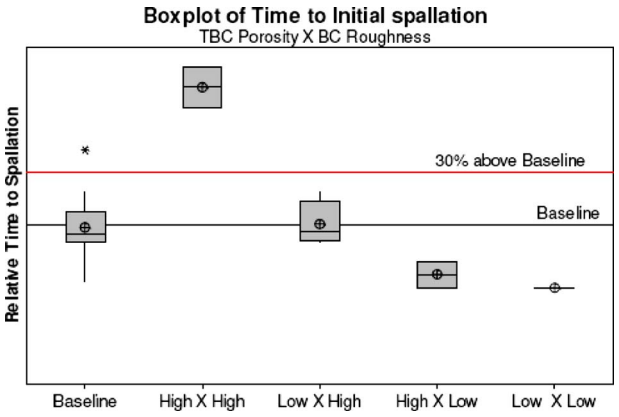

Fig. 13 Box plot of combination of TBC porosity and BC roughness

TBC porosity, BC roughness pairing. In this section, the TBC porosity and BC roughness have been paired together to study their combined influence on the life of the TBC system. From the box plot of time to spallation, it can be seen that the most favorable combination of parameters to have is high TBC porosity together with high BC roughness, whereas the worst combination of parameters was low TBC porosity in combination with low BC roughness (Fig. 13).

The surface plot offers a visualization of all cross dependencies in the investigated range. From the surface plot (Fig. 14) it can be seen that at low TBC porosity levels, with an increase in BC roughness, the life of the BC/TBC system does not change significantly; however, at high TBC porosity, with an increase in BC roughness, the life of the system increases significantly.

TBC porosity, TBC thickness pairing. In this section, the TBC porosity and TBC thickness have been paired together to study their combined influence on the life of the BC/TBC system.

From the box plot of time to spallation, it can be seen that the most favorable combination of parameters to have is high TBC porosity and low TBC thickness, whereas the worst combination of parameters was low TBC porosity and high TBC thickness (Fig. 15). However, it must be noted that the scatter for the combination of high TBC porosity and low TBC thickness is quite high. As seen from the matrix plot it was not possible to obtain enough data points to produce a surface plot.

BC roughness, TBC thickness pairing. In this section, the BC roughness and TBC thickness have been paired together to study their combined influence on the life of the BC/TBC system. From

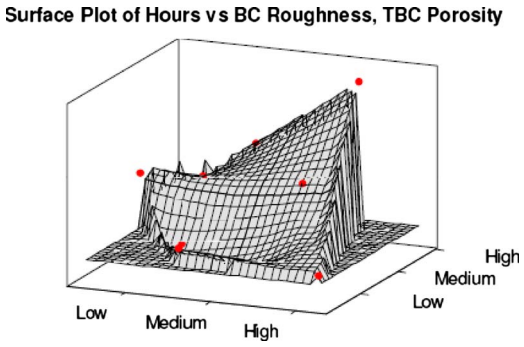

Fig. 14 Surface plot for TBC porosity and BC roughness

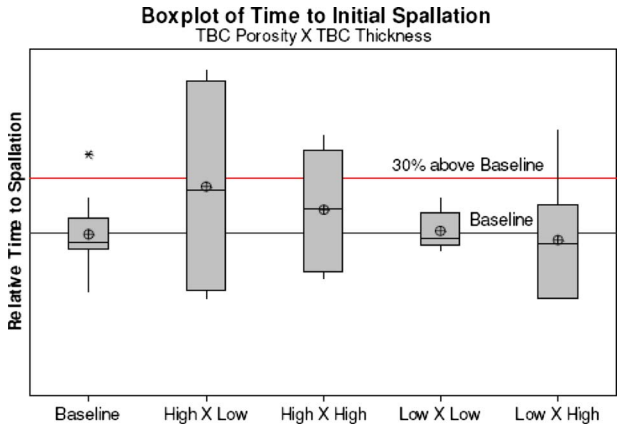

Fig. 15 Box plot of combination of TBC porosity and TBC thickness

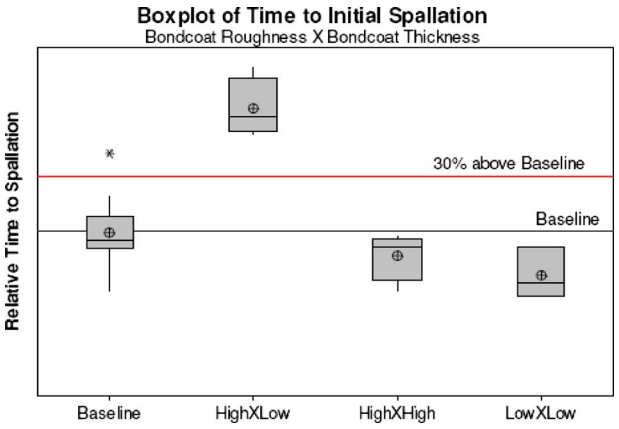

Fig. 17 Box plot of combination of BC roughness and BC thickness

the box plot of time to spallation, it can be seen that the most favorable combination of parameters to have is high BC roughness and low TBC thickness, whereas the worst combination of parameters was low BC roughness and low TBC thickness (Fig. 16).

BC roughness, BC thickness pairing. In this section, the BC roughness and BC thickness have been paired together to study their combined influence on the life of the BC/TBC system. From the box plot of time to spallation, it can be seen that the most favorable combination of parameters to have is high BC roughness and low BC thickness, whereas the worst combination of parameters was low BC roughness and low BC thickness (Fig. 17).

From the surface plot (Fig. 18), it can be seen that roughness has a more pronounced effect at low BC thicknesses than it does at high BC thicknesses. It must also be noted that the pairing of low BC roughness with high BC thickness is missing in the box plot. From the surface plot, however, it can be extrapolated that the worst combination to have would be low BC roughness with high BC thickness.

4.4 Discussion of Second Order Influence of Coating Parameters. The evaluation of second order effects revealed a clear picture of beneficial and harmful microstructural parameters.

Pairing BC roughness with TBC porosity, a difference in lifetime of +209% was found between high BC roughness and high TBC porosity and low BC roughness and low TBC porosity. Compared with current established industrial baselines, the time to spallation could be increased by 89% by applying BC roughness and TBC porosity in the high range and will be reduced by 39% when these parameters are in the low range.

Pairing BC roughness with BC thickness, a difference in lifetime of +138% was found between high BC roughness and low BC thickness and low BC roughness and high BC thickness. Compared with current established industrial baselines, the time to spallation could be increased by 76% by applying BC roughness in the upper range and BC thickness in the low range and will be reduced by 25% when these parameters are in the opposite range.

4.5 Application of Coating Parameter Influence on Lifing of BC/TBC Systems. *TBC time to failure as a function of bondcoat temperature and coating quality.* The conventionally used testing of coated parts resulted in a wide scatter of times to failure at the respective temperatures of testing. Although the reason for the scatter was explained by variations in coating microstructure, the influence of single coating microstructure parameters and the interaction between the parameters themselves was not completely understood. This resulted in a conservative approach for a prime reliant TBC system.

From experience with BC/TBC systems, we know that certain parameters are favorable toward increasing the life of the BC/TBC system: These parameters are high TBC porosity, low TBC thickness, high BC roughness, and low BC thickness. The average difference in time to spallation (life) of the optimized system as compared with the ordinary system was found to be greater than 30%. This significant increase in lifetime indicates that the study into parameter influence is not an artifact and clearly shows tendencies for improving the life of the coating system. The clear

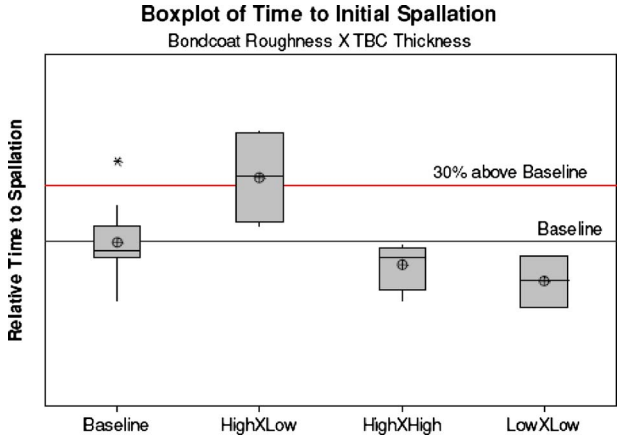

Fig. 16 Box plot of combination of BC roughness and TBC thickness

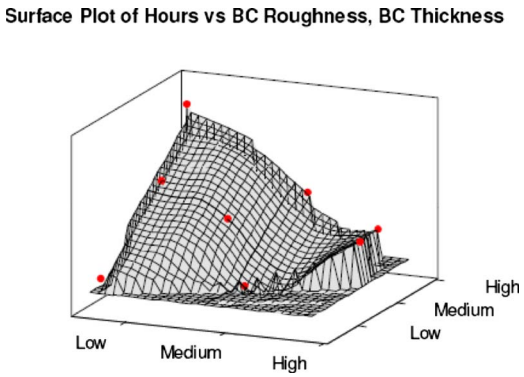

Fig. 18 Surface plot for BC thickness and BC roughness

benefit observed at the investigated temperature could be extrapolated to a wider temperature range relevant for GT operation.

5 Conclusion

The influence of coating microstructural parameters, i.e., BC roughness, BC thickness, BC porosity, TBC porosity, TBC thickness, TBC pore orientation, and TBC pore size, on the life of the BC/TBC system was established.

A DOE approach was used to extract the influence of coating parameters and their interactions on the life of the BC/TBC system.

Second order influence of coating parameters, which was not previously considered, was developed in this study. The second order influence of parameters, i.e., parameter pairing, was found to be greater than the first order influence of parameters, i.e., individual parameters on the life of the BC/TBC system.

The influence of coating parameters on the life of coating systems can be universally applied. However, it should be noted that the findings that are reported here are specific to the BC/TBC system that was investigated as a part of this study.

It is critical to avoid the ranking of the influence of coating parameters on the life of the BC/TBC system based on their first order influences.

Second order parameter influences reveal that the interaction between coating parameters plays a vital role in determining the life of the system.

It is also vital to note that the second order influence of pairing of parameters is not a cumulative effect of their first order influences but varies for each pairing.

In the same manner, it can be expected that the benefit obtained by producing a system with a combination of all optimal parameters will not be a cumulative effect of first order influences but instead will be another value.

The design of experiments approach helped clearly demonstrate influences and tendencies of coating microstructural parameters, which would have been difficult to extract without taking this approach. From the designed test matrix, it was possible to extract concrete tendencies on the first order level and more importantly on the second order level coating parameter interactions.

References

[1] Miller, R. A., 1984, "Oxidation-Based Model for Thermal Barrier Coating Life," J. Am. Ceram. Soc., **67**, pp. 517–521.

[2] DeMasi-Marcin, J. T., and Gupta, D. K., 1994, "Protective Coatings in Gas Turbine Engine," Surf. Coat. Technol., **68–69**, pp. 1–9.

[3] Hillery, R. V., 1996, *Coatings for High-Temperature Structural Materials—Trends and Opportunities*, National Academy Press, Washington, D.C.

[4] Strangman, T. E., 1985, "Thermal Barrier Coatings for Turbine Airfoils," Thin Solid Films, **127**, pp. 93–105.

[5] Wright, P. K., and Evans, A. G., 1999, "Mechanisms Governing the Performance of Thermal Barrier Coatings," Curr. Opin. Solid State Mater. Sci., **4**, pp. 255–265.

[6] Wright Mater, P. K., 1998, "Mechanisms Governing the Performance of Thermal Barrier Coatings," Mater. Sci. Eng., A, **245**, pp. 191–200.

[7] Evans, A. G., Mumm, D. R., Hutchinson, J. W., Meier, G. H., and Pettit, F. S., 2001, "Mechanisms Controlling the Durability of Thermal Barrier Coatings," Prog. Mater. Sci., **46**, pp. 505–553.

[8] Sergo, V., and Clarke, D. R., 1998, "Observation of Sub-Critical Spall Propagation of a Thermal Barrier Coating," J. Am. Ceram. Soc., **81**, pp. 3237–3242.

[9] Nicholls, J. R., 1997, "Erosion and Foreign Object Damage of Thermal Barrier Coatings," Mater. Sci. Forum, **935**, pp. 251–254.

[10] Choi, S. R., Hutchinson, J. W., and Evans, A. G., 1999, "Delamination of Multilayer Thermal Barrier Coatings," Mech. Mater., **31**, pp. 431–447.

[11] Nicholls, J. R., Lawson, K. J., Johnstone, A., and Rickerby, D. S., 2002, "Methods to Reduce the Thermal Conductivity of EB-PVD TBCs," Surf. Coat. Technol., **151–152**, pp. 383–391.

[12] Zhu, D., and Miller, R. A., 1999, "Thermal Conductivity and Elastic Modulus Evolution of Thermal Barrier Coatings Under High Heat Flux Conditions," NASA Report No. TM-1999-209069.

[13] Lee, C. H., Kim, H. K., Choi, H. S., and Ahn, H. S., 2000, "Phase Transformation and Bond Coat Oxidation Behavior of Plasma-Sprayed Zirconia Thermal Barrier Coating," Surf. Coat. Technol., **124**, pp. 1–12.

[14] Hofinger, I., Möller, J., Bobeth, M., and Raab, K., 2002, "Effect of Substrate Surface Roughness on the Adherence of NiCrAlY Thermal Spray Coatings," J. Therm. Spray Technol., **11**(3), pp. 387–392.

[15] Haynes, J. A., Ferber, M. K., and Porter, W. D., 2000, "Thermal Cycling Behavior of Plasma-Sprayed TBCs With Various MCrAlY Bond Coats," J. Therm. Spray Technol., **9**(1), pp. 38–48.

[16] Steffens, H.-D., Babiak, Z., and Gramlich, M., 1999, "Some Aspects of Thick Thermal Barrier Coating Lifetime Prolongation," J. Therm. Spray Technol., **8**(4), pp. 517–522.

[17] Wesling, K. F., Socie, D. F., and Beardsley, B., 1994, "Fatigue of Thick Thermal Barrier Coatings," J. Am. Ceram. Soc., **77**(7), pp. 1863–1868.

Effects of Coating Thickness, Test Temperature, and Coating Hardness on the Erosion Resistance of Steam Turbine Blades

Shun-sen Wang

Guan-wei Liu

Jing-ru Mao[1]
e-mail: jrmao@mail.xjtu.edu.cn

Qun-gong He

Zhen-ping Feng

Institute of Turbomachinery,
Xi'an Jiaotong University,
Xi'an 710049, P. R. China

This paper experimentally examines the influence of coating thickness, test temperature, coating hardness, and defects on the erosion resistance of boride coatings, ion plating CrN coatings, and thermal spraying coatings. The results demonstrate that the erosion rate of coating can be reduced effectively by improving coating hardness and thickness with the absence of the cracks of coating during the coating process. In comparison with thermal spraying coatings, boride coatings and ion plating CrN coatings are more suitable for protecting steam turbine blades from solid particle erosion due to higher erosion resistance. However, blades cannot be protected effectively when coating is thinner than a critical value θ_{crit}. Based on our results, it is recommended that the protective coating for the steam turbine blade should be thicker than 0.02 mm. In addition, the effect of temperature on erosion resistance of the coating is strongly dependent on the properties of transition layer between coating and substrate material. For the coating without pinholes or pores in the transition layer, the variation in erosion rate with temperature is consistent with that of uncoated substrate material. However, the erosion rate of coating descends with the elevation of test temperature when a lot of pinholes or pores are produced in the transition layer. [DOI: 10.1115/1.3155796]

Keywords: erosion, experiment, high temperature, boride coating, steam turbine

1 Introduction

Iron oxide scales exfoliated from the inner wall of the boiler tube and main steam pipe is known to cause the solid particle erosion (SPE) of steam path surfaces [1–3]. The severest erosion may be made on the control stage and the first reheat stage blades of the steam turbine, which result in the reduction in unit efficiency and the increase in maintenance cost. Since the erosion resistance of material is a function of different other parameters such as particle size, particle concentration, impingement angle, and surface hardness of material, in most cases it can be improved by providing a protective coating on the erosion-prone surfaces [4–6].

At present, boride diffusion, ion plating CrN coating, and thermal spraying coating are well-known methods to resist particulate erosion in the high pressure stages of a steam turbine. It has been reported that these coatings do increase the erosion resistance of the vanes and blades in some turbines [3,7,8], while other turbines have not demonstrated similar erosion resistance [9,10]. Coating defects and insufficient coating thickness ($\boldsymbol{\theta}$) were considered as the main causes of the failure of coated vanes. However, there is no sufficient test data about the influence of coating thickness and defects on the erosion resistance of coating, particularly for the erosion subjected to high-temperature and high-velocity particulate flows.

It is believed that erosion wear is caused via several mechanisms taking place simultaneously. As operating conditions change, the dominant erosion mechanism may also change accordingly. The working temperature of the steam turbine blades influences their erosion resistance. Although numerous studies [11–13] have been concerned with the effect of the working temperature on the solid particle erosion of bulk materials, little information is available on the coatings of steam turbine blade.

This study aims to examine effects of coating thickness and working temperature on the erosion resistance of blade coatings under special operating conditions of steam turbines. To this end, systematic erosion tests are conducted on five boride coatings, three ion plating CrN coatings, three thermal spraying coatings, and uncoated substrate materials at high temperature. The present results will be beneficial to researchers and designers in better understanding and selecting suitable coating parameters for steam turbine blades.

2 Experimental Procedures

2.1 Test Facility and Measuring Method. To examine the erosion resistance of various blade materials and coatings subjected to particulate flow, an erosion test facility was designed to provide erosion data in the range of operating temperatures and particle velocity experienced in steam turbine.

The erosion test facility consists of high-temperature gas system, particle feeding system, and erosion testing system, as illustrated in Fig. 1. Main air is heated in the combustor up to the required temperature for testing. The solid particles from a screw feeder are fed into a secondary air source and blown to a particle injector, where mixing with the high-temperature gas is taken place. The particles are heated and accelerated through a 3 m long preheating tube and an accelerating tunnel followed by impinging on the sample surface at an incidence angle ($\boldsymbol{\alpha}$) in the test section.

The test section consists of rotary device, protective casing, and top plate (Fig. 1). The incidence angle can be varied by rotating the top plate around the point R2. Four test samples are mounted

[1]Corresponding author.

Manuscript received February 24, 2009; final manuscript received April 20, 2009; published online November 4, 2009. Review conducted by Dilip R. Ballal.

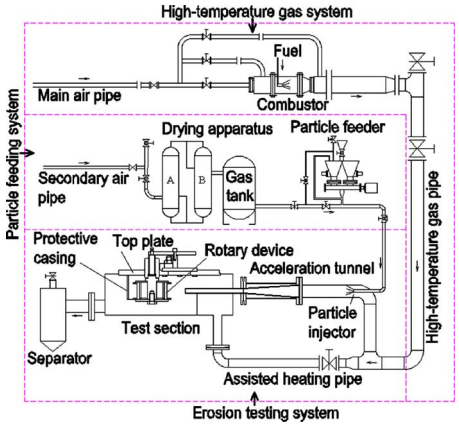

Fig. 1 Schematic of high-temperature erosion test facility

on a rotary device in the test section as illustrated in Fig. 2. However, only one sample is exposed to the high-velocity particulate flow, and other samples are protected by a protective casing. The position of the test samples can be varied by rotating the device around the point R1. Sample No. 1 is used to calibrate the test conditions. When the test temperature, the particle velocity, and the mass flow rate of the particles meet the required conditions of the erosion test, the rotary device is turned 90 deg to conduct the erosion test on sample No. 2. Then, the erosion test, in turn, is conducted on sample Nos. 3 and 4.

The incident velocity of the particles is measured using particle image velocimetry (PIV). A region of interest, covering incident particles and rebounded particles, is illuminated by the light sheet from the laser system. The charge coupled device (CCD) camera for PIV is positioned perpendicular to the laser sheet. In this paper, the statistical analysis on the velocities of solid particles near the eroded surface is performed based on a lot of PIV data. The results indicate that the uncertainty of incidence velocity and incidence angle is less than 1.5% and 1 deg, respectively.

In addition, a set of long distance microscope and CCD are used to conduct an on-line monitoring on the sample being eroded, whose spatial resolution is approximately 5–10 μm/pixel. The erosion test could be terminated at any moment based on the surface morphology of the eroded sample. For coatings, the test is terminated immediately when the initial localized erosion scar is observed.

To perform on-line measurement on the mass flow rate of particles ($\boldsymbol{R}$), the particle feeder is placed on the platform of electronic weighing scale (E-scale). The stopwatch is used to record the time interval ($\boldsymbol{t_i}$) of every beat of E-scale reading and total

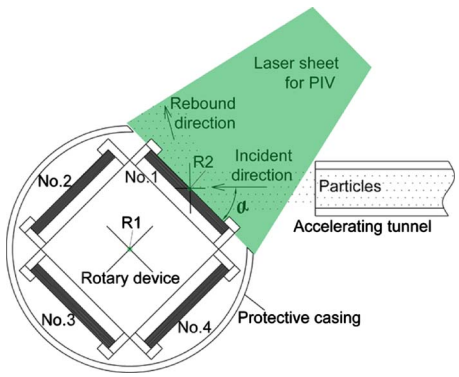

Fig. 2 Schematic of test section

Table 1 Tested boride coatings and ion plating CrN coatings

Name of coatings	Main compositions	θ (mm)	H (HV)	Substrate material
Boride coating A	FeB, Fe_2B	0.02	1400	1Cr11MoV
Boride coating B	FeB, Fe_2B	0.06	1300	1Cr11MoCo3W2
Boride coating C	FeB, Fe_2B	0.02	1400	2Cr12NiMo1W1V
Boride coating D	FeB, Fe_2B	0.08	1900	2Cr10MoVNbN
Boride coating E	FeB, Fe_2B	0.01	1400	1Cr11MoV
Ion plating A	CrN	0.02	2100	2Cr10MoVNbN
Ion plating B	CrN	0.04	2100	1Cr9Mo1VNbN
Ion plating C	CrN	0.01	2100	1Cr9Mo1VNbN

erosion time ($\boldsymbol{t}$). Hence, the mass flow rate of particles ($\boldsymbol{R}$) and the mass of the particles used per test ($\boldsymbol{m_p}$) can be determined by the following relations:

$$R = \frac{1}{n}\sum_{i=0}^{n}\frac{\Delta m}{t_i} \tag{1}$$

$$m_p = Rt \tag{2}$$

Here $\boldsymbol{\Delta m}$ is the resolution of the E-scale, and $\boldsymbol{n}$ is the beat times of E-scale reading during the erosion test. The average value of $\boldsymbol{R}$ is about 0.02 kg/min. A typical m_p is about 0.06–0.2 kg for substrate materials and 0.12–0.5 kg for coatings. The mass erosion rate ($\boldsymbol{\varepsilon_m}$) is determined by the following relation:

$$\varepsilon_m = \frac{m_1 - m_2}{m_p} \tag{3}$$

Here $\boldsymbol{m_1}$ and $\boldsymbol{m_2}$ are the mass of sample before and after the test. A precision balance of type BS224S from the Sartorius Instrument Co. of Germany, whose precision is 0.1 mg, was used to measure the value of $\boldsymbol{m_1}$ and $\boldsymbol{m_2}$. The results of the error analysis has showed that the average relative error of ε_m is about 2%, and the maximum error is about 3% in experiments.

In addition, the particle diameter is measured by the Malvern particle size analyzer. The scanning electron microscopy (SEM) of type S-2700 is used to analyze the surface morphology of the samples. The coating hardness is tested using a Vickers hardness tester.

2.2 Test Parameters. In the present study, five different blade materials were used as the substrate material of the coatings. The properties of five boride coatings and three ion plating CrN coatings are listed in Table 1. The Boride coatings were obtained at temperatures ranging from 1150 K to 1250 K by using a solid boronizing method. CrN coatings were deposited by using an arc-ion plating process.

Sheet shaped Fe_2O_3 particles with the average diameter of 0.04 mm were selected as the erodent particles, whose properties are listed in Table 2. The shape, density, size distribution, and hardness of the erodent particles are quite close to that of the particles in a steam turbine.

In this experiment, the incidence velocity of particles ($\boldsymbol{V}$) was set to be 420 m/s, consistent with the maximum particle velocity in the cascade passage of the steam turbines. The test temperature ($\boldsymbol{T}$) was varied in a range from 773 K to 883 K to simulate the operating temperatures of high-parameter steam turbine. The inci-

Table 2 Erodent particles

Fe_2O_3 (%)	Shape	ρ_p (kg/m^3)	H (HV)	d (mm)	D_{32} (mm)
>95	Irregular	4800	500	0.012–0.111	0.04

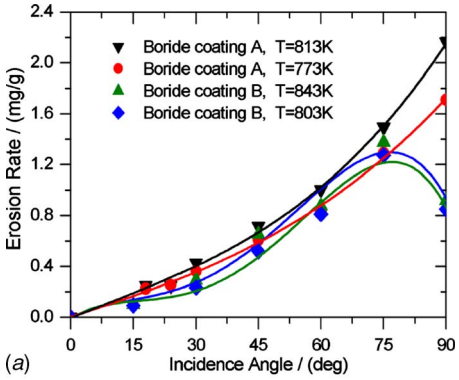

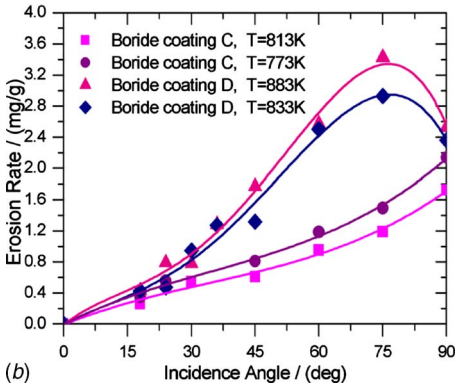

Fig. 3 The variation in erosion rate with α, T, and θ for boride coatings at a particle velocity of 420 m/s, θ=0.02 mm of boride coatings A and C, θ=0.06 mm of boride coatings B and D (the two figures need to be in the same scale (*y*-axis) so that reader can read it easily)

dence angle of particles (α) was also varied, e.g., α=15 deg, 18 deg, 24 deg, 30 deg, 36 deg, 45 deg, 60 deg, 75 deg, and 90 deg for each test temperature and sample. To save the run time for each test, a higher concentration of particulate flow than that in the steam turbines was used to erode the samples. The average mass concentration of particles is about 0.15–0.4% in the present experiment. For all that, the particulate flow is still dilute phase gas-particle flow, so the interaction among particles and the influence of particle concentration on the erosion rate of samples can be neglected.

3 Test Results

Figures 3 and 4 show the variation of erosion rate with the incident angle α for four boride coatings and two ion plating CrN coatings at different test temperatures T, respectively. These figures indicate the brittle behavior of boride coating and ion plating CrN coating, with maximum erosion rate at 75 deg or 90 deg incidence angle.

Figure 5 provides the variation in erosion rate with the incident angle α for five uncoated substrate materials, which shows the test conditions are consistent with that of coatings shown in Figs. 3 and 4. It is clear that these substrate materials exhibit a ductile erosion pattern with maximum erosion rate at 20–30 degrees incidence angle.

Comparing the erosion resistance of coatings (Figs. 3 and 4) with that of uncoated materials (Fig. 5), it can be seen that the average erosion rate of uncoated materials is more than 20 times as high as that of the coatings when the incident angle α is below 45 deg. The minimum erosion rate of the uncoated materials (at normal incidence case) is also two times higher than that of the coatings. These results indicate that boride coatings and ion plating CrN coatings can provide an excellent protection for substrate materials in the given particulate flow environment.

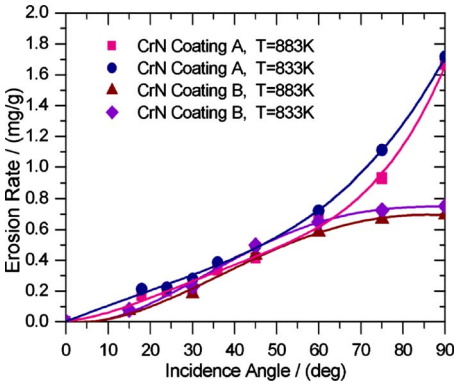

Fig. 4 The variation in erosion rate with α, Ts and θ for ion plating CrN coatings at a particle velocity of 420 m/s, θ=0.02 mm of CrN coating A, θ=0.04 mm of CrN coating B

However, it is well known that the coating with limited thickness cannot provide a permanent protection for substrate material. Besides, the life of coated material is not proportional to the thickness of coatings. As the coating thickness increases, the stress builds up and might therefore be expected to facilitate material removal, just as reported by Trezona and Hutchings [14]. In addition, considering the technical level at present, many coating defects, such as porosity, pinholes, cracks, etc. [15–17], are not completely avoidable for the brittle coating on soft substrates. It is no doubt that these defects will degrade the erosion resistance of coatings. The data shown in Figs. 3 and 4 indicate that the erosion resistance of coatings is strongly dependent on coating thickness, coating process, and test temperature besides the incidence angle

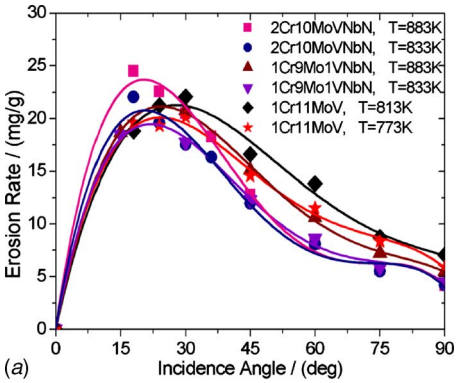

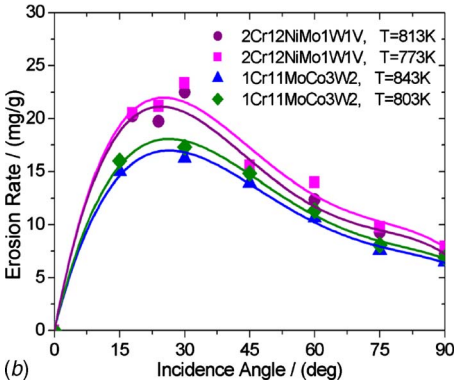

Fig. 5 The variation of erosion rate with α for five kinds of uncoated substrate materials at a particle velocity of 420m/s

and the incidence velocity of the erodent particles. The influence of V and α on the erosion rate of coatings have been discussed in many documents [3,5,18], and there is no new conclusion in this paper. The following discussion will focus on the effects of θ, T, H, and coating defects on erosion resistance.

4 Discussion

4.1 Coating Thickness. The erosion behavior of the coating is often different from that of bulk materials. As argued by Hassani et al. [19], the erosion rate of coating decreases with increasing θ. In their study, for the spherical particles with the diameter of 0.1 mm and the velocity of 84 m/s, no significant weight loss is observed when θ is above 0.008 mm. When θ is below 0.008 mm, erosion rate dramatically increases with decreasing θ. A similar observation was reported in Refs. [20,21], where surface stresses in coatings under single particle impact were investigated.

This paper focuses on the relation between the coating thickness (θ) and the erosion resistance of coatings under the erosion conditions experienced in steam turbine. A common characteristic for boride coatings and ion plating CrN coatings can be seen from Figs. 3 and 4 that the erosion rate ascends rapidly with increasing α and reaches its maximum at normal incidence (α=90 deg) when θ=0.02 mm, but the ascending trend of erosion rate is terminated at 75 deg incidence angle when $\theta>0.02$ mm. Except for boride coating D, the erosion rate of thin coating (θ=0.02 mm) is obvious higher than that of thick coatings ($\theta>0.02$ mm) at 75 deg and 90 deg incidence angles. In addition, boride coating E (θ=0.01 mm) and ion plating CrN coating C (θ=0.01 mm) are also tested at 420 m/s particle velocity. But these coatings are often entirely removed within 1–2 s so that their erosion rates could not be measured precisely.

The scanning electron microscopy and on-line monitoring system will help us understand these differences in erosion behaviors caused by θ. It is seen that a local area of the coating can be entirely removed by an individual impingement of arbitrary particle when θ is 0.01 mm, and a lot of initial erosion scars are formed in a very short time. Then these scars propagate rapidly to the whole eroded surface of coating. In this paper, this drastic erosion behavior is called the collapse erosion.

When θ=0.02 mm, samples exhibit similar collapse erosion behavior only at the incidence angle above 75 deg. However, these samples show less initial erosion scars and slower propagating rate of scars than that of coating with θ=0.01 mm. The whole process of collapse erosion was prolonged to 20–30 s. Figure 6 provides two typical SEM micrographs of ion plating CrN coatings. It can be seen that a lot of erosion scars are on the surface of ion plating CrN coating C (Fig. 6(*a*)), but only one scar is on the surface of the ion plating CrN coating A (Fig. 6(*b*)). This is because the structural stiffness of coating increases with θ, so that only a few large erodent particles are able to produce the collapse erosion on ion plating CrN coating A.

Other cases, including the boride coating B, D, and CrN coating B at any incidence angle, boride coating A, C, and CrN coating A at the incidence angle below 75 deg, show different erosion behavior from pure collapse erosion. For these cases, the erosion of coating could be divided into two stages, just as the results reported by Trezona and Hutchings [14]. Initially, the coating thickness is reduced progressively until a critical thickness θ_{crit} is reached. This stage is called lamellar erosion, whose erosion mechanism is really similar to that of brittle bulk material. But once the coating thickness is reduced to θ_{crit}, the remaining coating was quickly removed by collapse erosion. It is no doubt that the erosion rate of lamellar erosion is lower than that of collapse erosion, which results in higher erosion resistance of thick coatings ($\theta>0.02$ mm) than that of thin coating (θ=0.02 mm) at 75 deg and 90 deg incidence angles.

These results mean that the critical thickness corresponding to 420 m/s particle velocity and 75 deg or 90 deg incidence angle should be close to 0.02 mm for the boride coatings and ion plating CrN coatings. Therefore, it is recommended that the protective coating for the blade of steam turbine should be thicker than 0.02 mm.

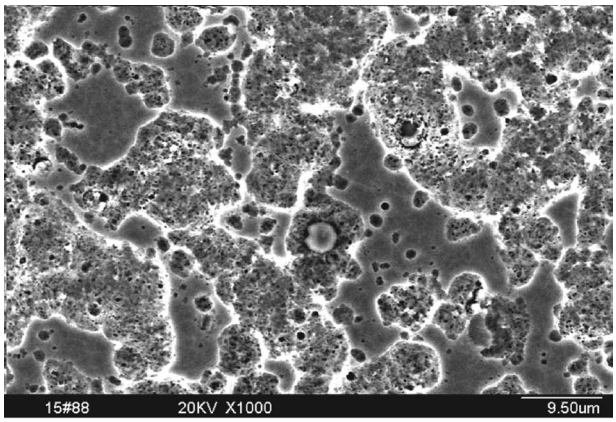

(*a*)

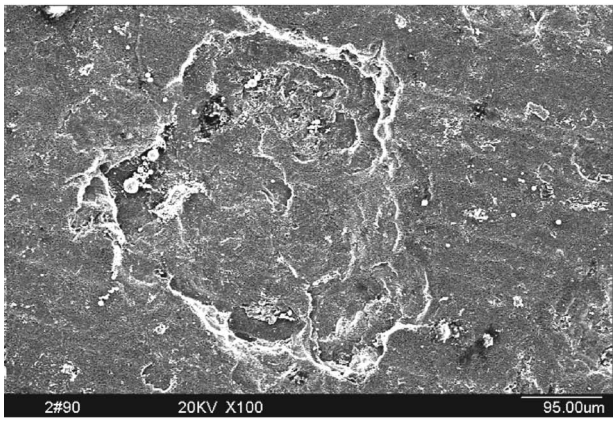

(*b*)

Fig. 6 SEM micrographs of ion plating CrN coating at 420 m/s particle velocity and 833 K test temperature; (*a*) CrN coating C, α=15 deg; (*b*) CrN coating A, α=75 deg; and (*c*) CrN coating B, α=75 deg

4.2 Coating Hardness and Surface Defects. The surface hardness (H) of sample has an important effect on crack initiation and propagation. Evans et al. [22] presented that the scale of crack is proportional to $H^{-1/4}$ based on test results. Finnie [23] stated that erosion rate is inversely proportional to the value of H. Evans and Marshall [24] showed that the force at the fracture threshold is strongly influenced by H. The erosion rate is substantially diminished below this threshold.

In this paper, boride coatings A, B, and C shows similar macrocharacteristics, which shows that their surfaces are often very compact and smooth. Figure 7(*a*) shows the surface morphology of eroded boride coating B at 15 deg incidence angle. It can be seen that a lot of black spots with the diameter of $1-2$ μm are on the surface of coatings and some large black spots are surrounded by the bright loop after the coating is eroded. The bright loop still exists even though the incidence angle is 75 deg, as shown in Fig. 7(*b*). These microcharacteristics indicate that the erosion resistance of coating near the black spots is still very high. At present, there is no obvious evidence of these black spots, which degraded the erosion resistance of coatings.

An attempt to further improve the life of coating has been made by increasing θ and H. However, the test result is not as ideal as expected. It can be seen from Figs. 3(*a*) and 3(*b*) that the erosion rate of boride coating D is two to three times higher than that of

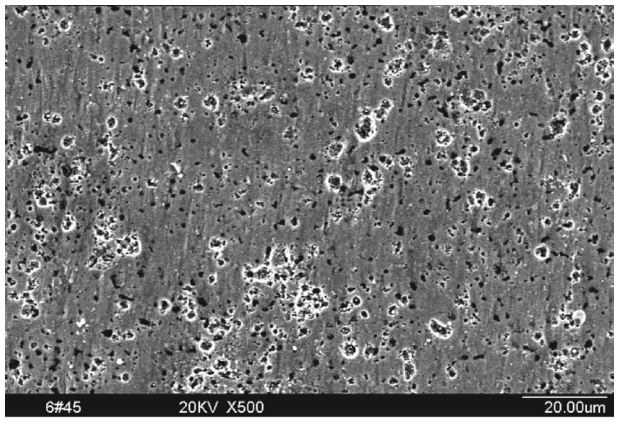

(*a*)

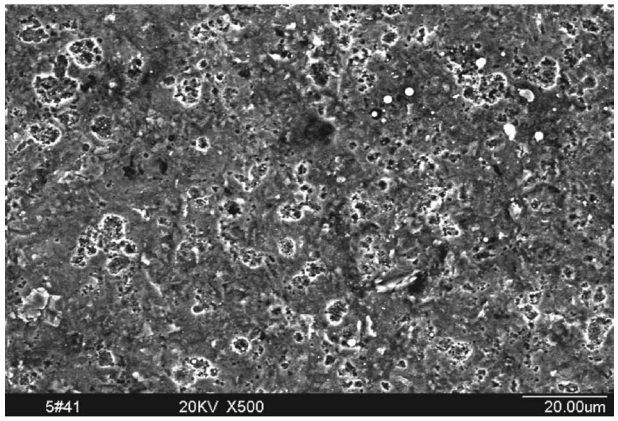

(*b*)

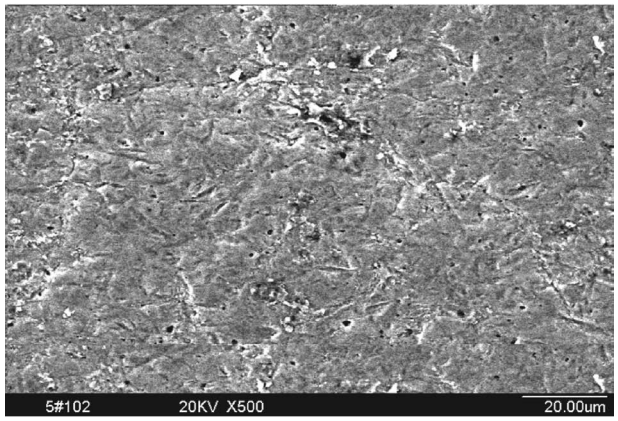

(*c*)

Fig. 7 SEM micrographs of boride coatings at 420 m/s particle velocity; (*a*) boride coating B, α=15 deg, *T*=843 K; (*b*) boride coating B, α=75 deg, *T*=843 K; and (*c*) Boride coating D, α =75 deg, *T*=883 K

boride coating B although the Vickers hardness of boride coating D is up to 1900 HV. Figure 7(*c*) shows the SEM micrographs of eroded boride coating D at 75 deg incidence angle. Obviously, some cracks are formed during boride diffusion, and the erosion scars are mainly concentrated on the edge of the original crack. These characteristics suggest that the coating defects, particularly cracks, degrade the erosion resistance of coating.

For this case, cracks are caused by the improvement of $\boldsymbol{\theta}$ and $\boldsymbol{H}$. This is because the hardness of boride coating is determined by the relative content of Fe_2B and FeB. The crystal of FeB is harder than Fe_2B, but its strong brittle-fracture trend often result in cracks. In addition, as the coating thickness increases, the stress builds up and might therefore facilitate the crack initiation and propagation. Therefore, it is necessary to control the hardness of boride coating below 1400 HV for reducing the brittle-fracture trend of coating.

However, no macroscopic crack is formed on the surface of ion plating CrN coating even though its hardness is up to 2100 HV. This is because a lot of pinholes in the transition layer between CrN layer and substrate material, as shown in Fig. 6(*a*), have released partly the internal stress of coating. Although pinholes accelerate the collapse erosion, the erosion rate of CrN coating is still lower than that of boride coating because of higher surface hardness.

Based on above discussions, not all defects have the same contribution to degrading the erosion resistance of coating. However, Improving coating hardness and thickness can effectively reduce the erosion rate of coating with the absence of the cracks of coating during the coating process.

4.3 Test Temperature. The effect of temperature on the erosion resistance of bulk materials has been studied by Gat and Tabakoff [11]. They presented that whether erosion increases or decreases as the test temperature increases depends on the ratio ($\boldsymbol{T_h}$) between the test temperature and the melting temperature of material. At $\boldsymbol{T_h} > 0.5$, the erosion resistance increases as the test temperature increases, while the inverse change trend of erosion resistance with temperature is shown at $\boldsymbol{T_h} < 0.3$. However, these results could not be used to predict the erosion behavior of coating. This is because the erosion resistance of coating is strongly dependent on the interaction among substrate material, coating, and their transition layer. In addition, the thermal stress caused by the difference in thermal expansion coefficient between coating and substrate material have some contributions to the erosion rate of coating.

The effect of temperature on the erosion rate of boride coatings and CrN coatings can be seen from Figs. 3 and 4. Boride coatings A and D show a descending erosion resistance as the test temperature increases, but other coatings, including boride coating B, boride coating C, and two kinds of CrN coatings, show inverse trend.

In addition, the effect of temperature on the erosion rate of uncoated substrate materials can be seen from Fig. 5. The materials of 1Cr11MoV, 1Cr12Mo, and 1Cr9Mo1VNbN show an increase in erosion rate with the enhancement of test temperature. However, for the materials of 1Cr11MoCo3W2 and 2Cr12NiMo1W1V, the tungsten element in alloys has improved the red hardness and high-temperature strength, which results in a decrease in erosion rate with increasing temperature.

These results indicate that the variation in erosion rate with temperature for boride coatings is consistent with that of uncoated substrate material. This means that the properties of substrate material have a significant effect on the erosion behavior of boride coatings. However, the substrate material does not show similar effect on the CrN coatings. This is because iron boride and soft substrate materials interlace each other in the transition layer for boride coating, so that the effect of the test temperature on substrate materials can be well transferred to the iron boride layer. However, the communication between CrN coating and their substrate material is cut off by a lot of pinholes, just as shown in Fig. 6(*a*). Meanwhile, the hardness of solid particles often declines with increasing temperature. Therefore, it is easy to understand that the erosion rates of CrN coatings always decrease with the ascending temperature.

In order to further confirm the above analysis, some erosion tests have been conducted on three kinds of thermal spraying coatings, which the results are shown in Fig. 8. Their chemical compositions $\boldsymbol{\theta}$ and $\boldsymbol{H}$ are listed in Table 3. It is seen that the erosion rate of detonation spraying Cr_3C_2 coating and supersonic spraying Cr_3C_2 coating decreases as the test temperature increases, while

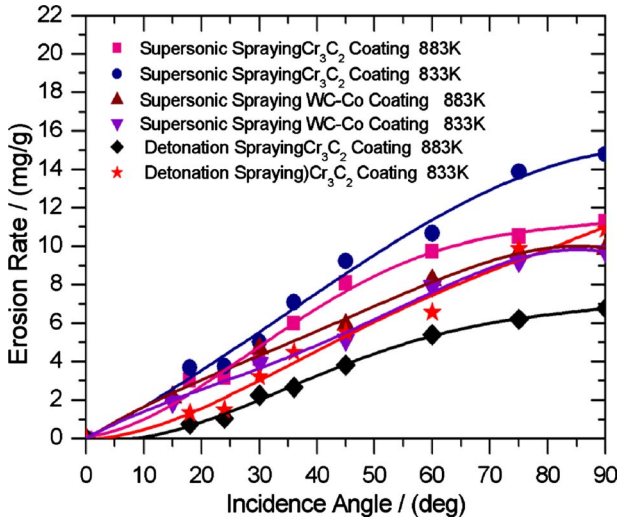

Fig. 8 The variation of erosion rate with α for three thermal spraying coatings at a particle velocity of 420 m/s

the erosion rate of supersonic spraying tungsten carbide and cobalt (WC-Co) coating increases with ascending temperature. Furthermore, Fig. 9 provides the SEM morphology of eroded coatings. Similar pinholes and pores as that of CrN coatings are seen in Cr_3C_2 coating. However, for WC-Co coating, coarse WC grain is adhered directly to substrate material by soft binder cobalt, so that no pinhole is formed in the WC-Co coating. Therefore, WC-Co coating shows similar erosion behavior as boride coating. In addition, it can be seen from Fig. 8 that the erosion rates of thermal spraying coatings are far higher than that of ion plating CrN coatings and boride coatings.

In general, the effect of temperature on the erosion resistance of coating is strongly dependent on the properties of transition layer between coating and substrate material. For the coating without pinholes or pores in the transition layer, the variation in erosion rate with temperature is consistent with that of uncoated substrate materials. However, the erosion rate of coating descends with the elevation of test temperature when a lot of pinholes or pores are produced in the transition layer.

5 Conclusions

This paper has studied the effect of coating thickness, test temperature, coating hardness, and defects on the erosion resistance of coatings for steam turbine blade. A set of erosion test facility was designed and systematic erosion tests are conducted on five boride coatings, three ion plating CrN coatings, three thermal spraying coatings, and uncoated substrate materials at high temperature. The following conclusions may be made.

(1) In comparison with thermal spraying coatings, boride coatings and ion plating CrN coatings are more suitable for protecting steam turbine blades from solid particle erosion due to higher erosion resistance.

Table 3 Tested thermal spraying coatings

Name of coatings	Main composition	θ (mm)	H (HV)	Substrate material
Supersonic spraying WC-Co coating	WC-Co	0.3	1300	1Cr9Mo1VNbN
Supersonic spraying Cr_3C_2 coating	Cr_3C_2	0.2	1100	2Cr10MoVNbN
Detonating spraying Cr_3C_2 coating	Cr_3C_2	0.2	1200	2Cr10MoVNbN

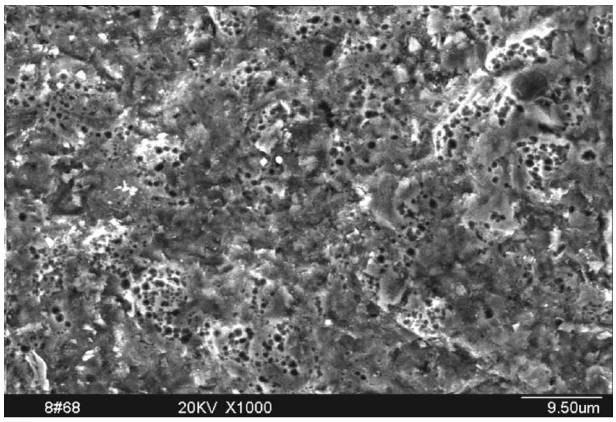

(*a*)

(*b*)

Fig. 9 SEM micrographs of thermal spraying coatings at 420 m/s particle velocity and 833 K test temperature; (*a*) detonation spraying Cr_3C_2 coating, α=90 deg; and (*b*) supersonic spraying WC-Co coating, α=90 deg

(2) When coating is thinner than a critical value θ_{crit}, the hard coatings cannot provide effective protection to substrate materials. The critical thickness corresponding to 420 m/s particle velocity and 75 deg or 90 deg incidence angle should be close to 0.02 mm for the boride coatings and ion plating CrN coatings. Based on our results, it is recommended that the protective coating for the blade of steam turbine should be thicker than 0.02 mm.

(3) Improving coating hardness and thickness can effectively reduce the erosion rate of coating with the absence of the cracks of coating during the coating process. According to our results, it is necessary to control the hardness of boride coating below 1400 HV for reducing the brittle-fracture trend of coating.

(4) The effect of temperature on the erosion resistance of coating is strong dependent on the properties of transition layer between coating and substrate material. For the coating without pinholes or pores in the transition layer, the variation in erosion rate with temperature is consistent with that of uncoated substrate material. However, the erosion rate of coating descends with the elevation of test temperature when a lot of pinholes or pores are produced in the transition layer.

Acknowledgment

The authors would like to thank for the financial support of National Natural Science Foundation of China (NSFC) (Contract No. 50476051) and NSFC Fund for Creative Research Groups (Contract No. 50521604).

Nomenclature

α = incidence angle of particles on sample, deg
d = particle diameter, mm
D_{32} = Sauter mean diameter of particles, mm
H = surface hardness of samples, HV
m_p = mass of the particles used per test, kg
m_1 = mass of sample before erosion test, g
m_2 = mass of sample after erosion test, g
ρ_p = density of particles, kg/m^3
θ = coating thickness, mm
θ_{crit} = critical coating thickness, mm
ε_m = mass erosion rate, g/kg
V = incidence velocity of particles, m/s
R = mass flow rate of particles, kg/min
T = test temperature, K
T_h = ratio between the test temperature and the melting temperature of material

References

[1] Hamed, A., Tabakoff, W., and Wenglarz, R., 2006, "Erosion and Deposition in Turbomachinery," J. Propul. Power, **22**(2), pp. 350–360.
[2] Mann, B. S., 1999, "Solid-Particle Erosion and Protective Layers for Steam Turbine Blading," Wear, **224**(1), pp. 8–12.
[3] Oka, Y. I., Yoshida, T., Yamada, Y., Yasui, T., and Hata, S., 2007, "Evaluation of Erosion and Fatigue Resistance of Ion Plated Chromium Nitride Applied to Turbine Blades," Wear, **263**(1–6), pp. 379–385.
[4] Dai, L. P., Yu, M. Z., and Dai, Y. P., 2007, "Nozzle Passage Aerodynamic Design to Reduce Solid Particle Erosion of a Supercritical Steam Turbine Control Stage," Wear, **262**(1–2), pp. 104–111.
[5] Tabakoff, W., and Shanov, V., 1995, "Erosion Rate Testing at High Temperature for Turbomachinery Use," Surf. Coat. Technol., **76–77**(1–3), pp. 75–80.
[6] Wang, S. S., Liu, G. W., Mao, J. R., and Feng, Z. P., 2007, "Experimental Investigation on the Solid Particle Erosion in the Control Stage Nozzles of Steam Turbine," *Proceedings of the ASME Turbo Expo 2007*, Vol. 6, pp. 713–721.
[7] Kawagishi, H., Kawasaki, S., Ikeda, K., Yamamoto, M., and Watanabe, O., 1990, "Protective Design and Boride Coating Against Solid Particle Erosion of First-Stage Turbine Nozzles," Advances in Steam Turbine Technology for Power Generation, **10**, pp. 23–29.
[8] Qureshi, J. I., and Tabakoff, W., 1988, "Influence of Coating Processes and Process Parameters on Surface Erosion Resistance and Substrate Fatigue Strength," Surf. Coat. Technol., **36**(1–2), pp. 433–444.
[9] Ortolano, R. J., 1985, *Resisting Steam Turbine Abrasion Damage by Using Surface Improvement Systems*, ASME, New York/IEEE, New York.
[10] Kramer, L. D., Qureshi, J. I., Rousseau, R. A., and Ortolano, R. J., 1983, *Improvement of Steam Turbine Hard Particle Eroded Nozzles Using Metallurgical Coatings*, ASME, New York/IEEE Power Engineering, New York/ASCE, New York.
[11] Gat, N., and Tabakoff, W., 1980, "Effects of Temperature on the Behavior of Metals Under Erosion by Particulate Matter," J. Test. Eval., **8**(4), pp. 177–186.
[12] Shanov, V., Tabakoff, W., and Singh, R. N., 2002, "CVD Diamond Coating for Erosion Protection at Elevated Temperatures," J. Mater. Eng. Perform., **11**(2), pp. 220–225.
[13] Tabakoff, W., and Hamed, A., 1988, "Temperature Effect on Particle Dynamics and Erosion in Radial Inflow Turbine," ASME J. Turbomach., **110**(2), pp. 258–264.
[14] Trezona, R. I., and Hutchings, I. M., 2001, "Resistance of Paint Coatings to Multiple Solid Particle Impact: Effect of Coating Thickness and Substrate Material," Prog. Org. Coat., **41**(1–3), pp. 85–92.
[15] Lathabai, S., Ottmuller, M., and Fernandez, I., 1998, "Solid Particle Erosion Behaviour of Thermal Sprayed Ceramic, Metallic and Polymer Coatings," Wear, **221**(2), pp. 93–108.
[16] Wheeler, D. W., and Wood, R. J. K., 2001, "High Velocity Sand Impact Damage on CVD Diamond," Diamond Relat. Mater., **10**(3–7), pp. 459–462.
[17] Wood, R. J. K., 2007, "Tribo-Corrosion of Coatings: A Review," J. Phys. D: Appl. Phys., **40**(18), pp. 5502–5521.
[18] Tabakoff, W., 1999, "Protection of Coated Superalloys From Erosion in Turbomachinery and Other Systems Exposed to Particulate Flows," Wear, **233–235**, pp. 200–208.
[19] Hassani, S., Bielawski, M., Beres, W., Martinu, L., Balazinski, M., and Klemberg-Sapieha, J. E., 2008, "Predictive Tools for the Design of Erosion Resistant Coatings," Surf. Coat. Technol., **203**(3–4), pp. 204–210.
[20] Bielawski, M., and Beres, W., 2007, "Fe Modelling of Surface Stresses in Erosion-Resistant Coatings Under Single Particle Impact," Wear, **262**(1–2), pp. 167–175.
[21] Hassani, S., Klemberg-Sapieha, J. E., Bielawski, M., Beres, W., Martinu, L., and Balazinski, M., 2008, "Design of Hard Coating Architecture for the Optimization of Erosion Resistance," Wear, **265**(5–6), pp. 879–887.
[22] Evans, A. G., Gulden, M. E., and Rosenblatt, M., 1978, "Impact Damage in Brittle Materials in the Elastic-Plastic Response Regime," Proc. R. Soc. London, Ser. A, **361**(1706), pp. 343–365.
[23] Finnie, I., 1960, "Erosion of Surfaces by Solid Particles," Wear, **3**(2), pp. 87–103.
[24] Evans, A. G., and Marshall, D. B., 1980, "Wear Mechanisms in Ceramics," Fundamentals of Friction and Wear of Materials, papers presented at the 1980 ASM Materials Science Seminar, pp. 439–452.

Role of Platinum in Thermal Barrier Coatings Used in Gas Turbine Blade Applications

H. M. Tawancy

Luai M. Al-Hadhrami

Center for Engineering Research,
Research Institute,
King Fahd University of Petroleum and Minerals,
P.O. Box 1639,
Dhahran 31261, Saudi Arabia

Current technology of thermal barrier coating systems used in gas turbine blade applications relies on the use of a metallic bond coat, which has a twofold function: (i) it develops a thin layer of aluminum oxide enhancing the adhesion of the ceramic top coat and (ii) it provides an additional resistance to oxidation. It was the objective of this study to develop an understanding of the role of platinum in bond coats of the diffusion-type deposited on a nickel-based superalloy. Two Pt-containing bond coats were included in the study: (i) a platinum-aluminide and (ii) a bond coat formed by interdiffusion between an electroplated layer of platinum and the superalloy substrate. In both cases, the top ceramic coat was yttria-stabilized zirconia. For reference purposes, a simple aluminide bond coat free of Pt was also included in the study. Thermal exposure tests at 1150°C with a 24 h cycling period at room temperature were used to compare the coating performance. Microstructural features were characterized by various electron-optical techniques. Experimental results indicated that Pt acts as a "cleanser" of the oxide-bond coat interface by decelerating the kinetics of interdiffusion between the bond coat and superalloy substrate. This was found to promote selective oxidation of Al resulting in a purer Al_2O_3 scale of a slower growth rate increasing its effectiveness as "glue" holding the ceramic top coat to the underlying metallic substrate. However, the exact effect of Pt was found to be a function of the state of its presence within the outermost coating layer. Of the two bond coats studied, a surface layer of Pt-rich gamma prime phase ($L1_2$ superlattice) was found to provide longer coating life in comparison with a mixture of $PtAl_2$ and beta phase. This could be related to the effectiveness of gamma prime phase as a sink for titanium minimizing its detrimental effect on the adherence of aluminum oxide. [DOI: 10.1115/1.3156814]

1 Introduction

Although the application of thermal barrier coatings as surface protection systems for gas turbine blades allows the turbine entry temperature to be increased by as much as 100–150°C [1,2]; adhesion to the metallic substrate remains to be an issue, e.g., Ref. [3]. A typical coating system consists of: (i) an outer ceramic layer about 200–250 μm in thickness (usually zirconia stabilized by 8 wt % yttria) acting as a thermal insulator and is known as the top coat and (ii) an intermediate metallic layer known as the bond coat, which varies in thickness from about 30–50 μm (diffusion-type coating) to 150–250 μm (overlay-type coatings). It is the primary function of the bond coat to develop a thin tenacious layer of aluminum oxide (Al_2O_3) about 1 μm in thickness to act as "glue" holding the top coat to the substrate. This is achieved by a pre-oxidation heat treatment prior to application of the topcoat [2]. Another important function of the bond coat is to provide an additional resistance to oxidation and hot corrosion. During subsequent exposure at elevated temperatures, the thickness of initial oxide layer increases at a rate determined by the structure and properties of the bond coat for a given superalloy substrate. The newly formed oxide is commonly referred to as thermally grown oxide.

Although it was shown that the exact failure mechanism of the coating system is a function of the processing technique (low-pressure plasma spraying versus electron-beam physical vapor deposition) [1], most of the evidence point out that the adhesion between the thermally grown oxide and bond coat plays a dominant role in determining the life of the coating life, e.g., Refs. [3–14]. However, another contributing factor was shown to be surface rumpling of the bond coat [15–17], which is known to occur in thin-film materials [18].

Earlier studies of nickel-based alloy systems [19–21] and coatings [22–25] protected by Al_2O_3 had demonstrated that the addition of Pt could improve the protective nature of the oxide scale. Therefore, this study was carried out to determine the effect of Pt on the performance of thermal barrier coating systems deposited on a nickel-based superalloy. Three bond coats of the diffusion-type were included in the study: (i) a conventional simple aluminide for comparative purposes, (ii) a platinum-aluminide, and (iii) a modified platinum bond coat consisting of a mixture of γ'- and γ-phases. For all bond coat coats, the top coat consists of a layer of yttria-stabilized zirconia deposited by the technique of electron-beam physical vapor deposition on the same superalloy substrate.

2 Procedure

All coatings included in this study were deposited on a single crystal nickel-based superalloy in the form of rods about 8 mm in diameter. Its nominal composition in wt % is Ni–9.5Co–6.5Ta–6.5W–6.2Cr–5.5Al–2.9Re–1.0Ti–0.8Mo–0.1Hf. The simple aluminide coating (nominal Al content of 25 wt %) was applied by the pack cementation process. Rods of the alloy were first grit blasted and then placed in an air tight retort containing a powder mixture of aluminum and a halide activator. The assembly was heated for 4 h at 1000°C to promote diffusion. Platinum aluminizing to produce a nominal Pt and Al contents of 55 wt % and 25 wt %, respectively, was carried out by first electroplating a 6–8 μm thick layer of Pt on the alloy surface followed by diffusion and aluminizing treatments. Processing was carried out by inward diffusion pack and CVD. A Pt bond coat was developed by

Manuscript received March 19, 2009; final manuscript received April 12, 2009; published online November 5, 2009. Review conducted by Dilip R. Ballal.

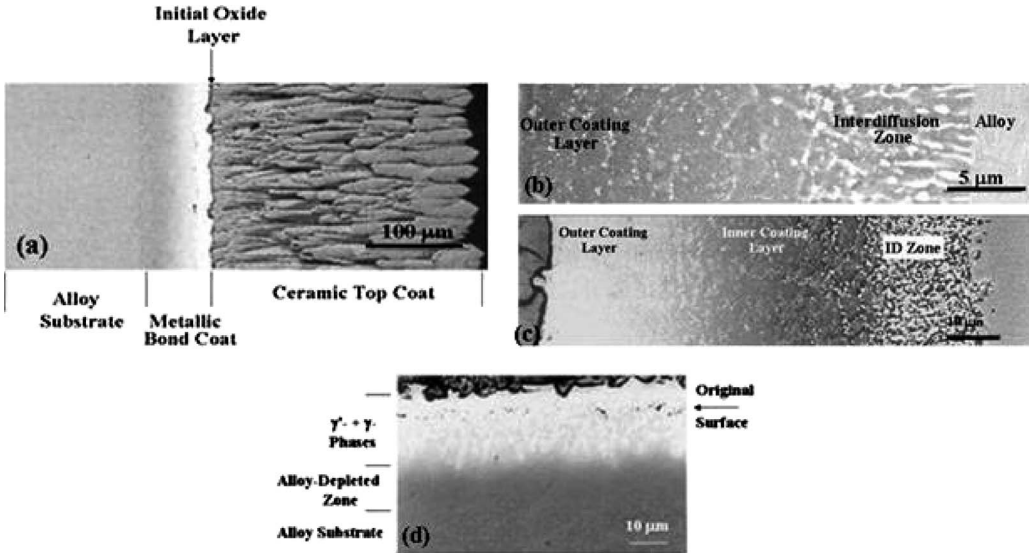

Fig. 1 Backscattered electron images illustrating characteristic microstructural features of the coating systems in the heat-treated condition: (*a*) an example derived from the system containing the Pt-aluminide bond coat to illustrate the microstructure along a cross-section of the top coat and into the superalloy substrate showing the initial oxide layer, (*b*) microstructure along a cross-section of the simple aluminide bond coat, (*c*) microstructure along a cross-section of the Pt-aluminide bond coat, and (*d*) microstructure along a cross-section of the Pt bond coat

electroplating about 10 μm thick layer of Pt on the alloy surface. The final microstructures of the three bond coats (about 40 μm in thickness) with a thin surface layer of Al_2O_3 (about 1 μm in thickness) were developed by an interdiffusion heat treatment of 4 h at 1150°C in air. Subsequently, a layer of the ceramic top coat top coat (ZrO_2+8 wt %Y_2O_3) about 250 μm in thickness was applied by the EB-PVD technique [2]. Henceforth, this is referred to as the heat-treated condition.

Rod samples were oriented at about 30 deg to the evaporation source and rotated about their longitudinal axis to ensure a uniform coating thickness. The coating chamber was evacuated to about 2 Pa. All samples were preheated to 970°C. Deposition was carried out at a rate of about 1 μm/s. Thermal exposure tests at 1150°C in still air with a 24 h cycling period at room temperature were used to evaluate the relative lives of the three coating systems as well as the thermal stability of each bond coat. Additional thermal exposure tests were carried out at 1000°C and 1050°C to study the kinetics of interdiffusion between each bond coat and the superalloy substrate.

Various techniques including scanning electron microscopy, transmission electron microscopy, microchemical analysis by energy dispersive X-ray spectroscopy, and X-ray diffraction were used to characterize the microstructure. Samples for scanning electron microscopy and microchemical analysis were examined in the as-polished condition. Qualitative wavelength dispersive spectroscopy was used to distinguish refractory transition metals particularly W, Ta, and Re. To observe the oxide phase by transmission electron microscopy (TEM) parallel to the plane of oxidation, thin foils were prepared by a standard technique consisting of electropolishing and ion beam thinning. First, oxidized specimens were electropolished on the metal side approaching the oxide-metal interface until perforation occurred. Electropolishing was carried out in a solution of 30% nitric acid in methanol maintained at about −20°C. This was followed by ion beam thinning at 5 kV. Samples used for TEM work were free of the top coat.

3 Results and Discussion

3.1 Coating Microstructure in the Heat-Treated Condition. Figure 1 summarizes characteristic microstructural features qualitatively representative of the coating systems in the heat-treated condition. As shown in the example of Fig. 1(*a*), the top ceramic coat had the typical columnar structure produced by EB-PVD. Also, Fig. 1(*a*) shows that the initial layer of Al_2O_3 developed by the bond coat prior to the deposition of the top coat had an average thickness of about 1 μm. Figure 1(*b*) shows the microstructure of the simple aluminide bond coat typical of that produced by inward diffusion. The coating consisted of: (i) an outer fine-grained layer β-NiAl containing substrate elements in solid solution and a fine dispersion of α-Cr particles, (ii) an intermediate layer of coarse grained β-NiAl containing substrate elements in solid solution as well as particles of the ternary NiCrW σ-phase, and (iii) an inner interdiffusion zone consisting of a mixture of MC-type carbide particles and *s*-phase dispersed in a matrix of β-NiAl.

Figure 1(*c*) shows a typical microstructure of the Pt-aluminide coating. As reported in an earlier study [5], the outer Pt-rich layer consisted of a fine dispersion of $PtAl_2$ in a matrix of β-NiAl. Similar, the simple aluminide coating, the intermediate layer consisted of β-NiAl. However, both layer were relatively free of secondary precipitates particularly α-Cr, which is known to degrade the protective nature of Al_2O_3 [26]. Qualitatively, the structure of the interdiffusion zone was similar to that corresponding to the simple aluminide coating.

A characteristic microstructure of the Pt bond coat is shown in Fig. 1(*d*). It consisted an outer layer of a dense compact γ'-phase ($L1_2$ superlattice) followed by a columnar layer of γ'-phase containing islands of γ-phase (solid solution), and an alloy-depleted zone. Detailed microchemical analysis showed that the surface layer of Pt-rich γ'-phase acted as an effective sink for Ti, which is known to degrade the adherence of Al_2O_3 by forming TiO_2 particles near the oxide-metal interface [27]. Similar to Ti, Ta was also found to be partitioned to the γ'-phase as expected. In comparison with the simple aluminide coating, the surface of the Pt-aluminide coating was relatively free of refractory transition metals (W, Ta, and Re) as demonstrated in the wavelength dispersive X-ray spectra of Fig. 2. Although in the case of the Pt bond coat, Ta was detected at the surface, it was partitioned to the γ'-phase. These results indicated that the structures developed by Pt had

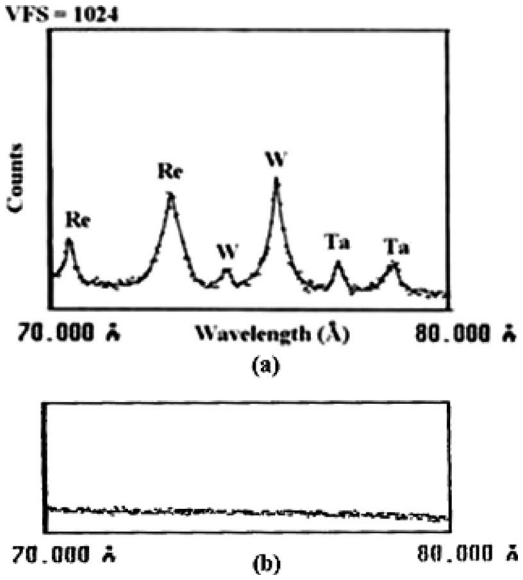

Fig. 2 Wavelength dispersive X-ray spectra illustrating the effect of Pt on the composition of the bond coat surface in the heat-treated condition (as-polished condition): (*a*) spectrum derived from the surface of the simple aluminide bond coat showing the presence of refractory transition metals, (*b*) spectrum derived from the Pt-aluminide bond coat showing the surface to be relatively free of transition metals

higher diffusional stability limiting the outward diffusional transport of refractory transition metals from the superalloy substrate into the coating particularly W and Re. Similar to the case of α-Cr, these elements are known to have adverse effects on the protective nature of Al_2O_3 [26].

The above effects of Pt on the structure and composition of the bond coat were reflected on the oxidation behavior, thermal stability characteristics, and coating performance as demonstrated later. However, it is shown that the exact effect of Pt is a function of the state of its presence in the outer coating layers.

3.2 Comparative Coating Performance. Figure 3 shows comparative performance of the three coating systems included in the study as determined from thermal exposure tests at 1150°C with a 24 h cycling period at room temperature. Failure was indicated by the onset of macroscopic spallation of the top coat. For all three types of bond coats, spallation of the top coat was found to occur by loss of adhesion between the thermally grown and underlying bond coat as further explained later.

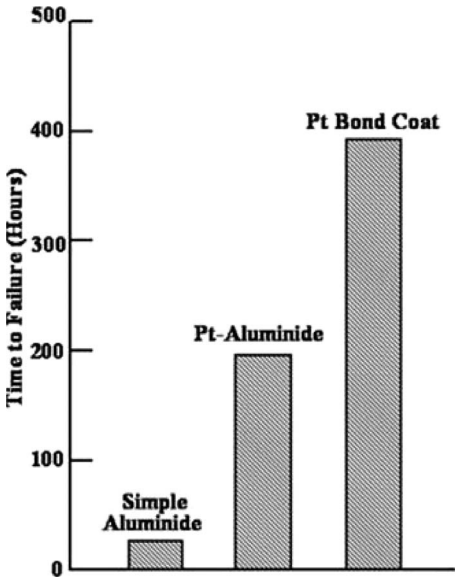

Fig. 3 Effect of the type of bond coat on the performance of thermal barrier coating systems at 1150°C with a 24-h cycling period at room temperature

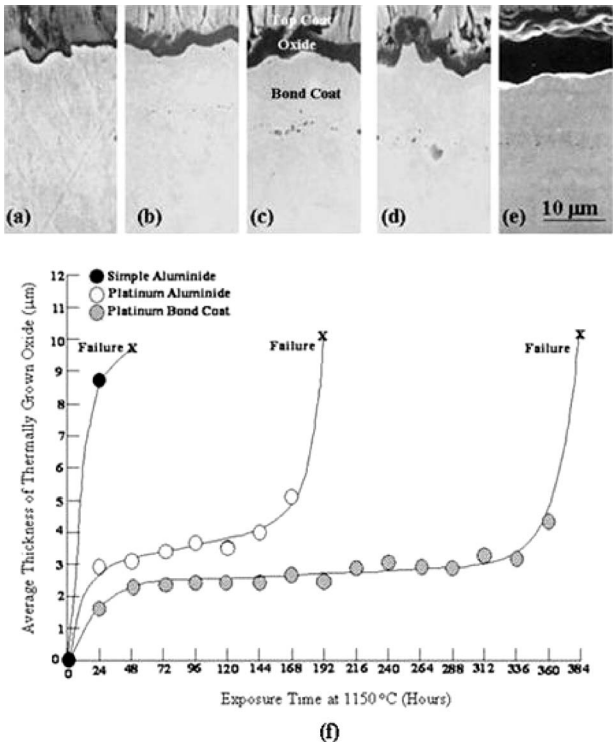

Fig. 4 Oxidation properties of the bond coats: (*a*)–(*e*) secondary electron images exemplifying the progressive thickening of the thermally grown oxide on the Pt-aluminide bond during thermal exposure at 1150°C (0 h, 24 h, 72 h, 120 h, and 168 h of exposure, respectively) eventually leading to localized decohesion between the oxide and the bond coat, and (f) comparative thickening rates of the thermally grown oxide

It was observed that both the Pt and Pt-aluminide bonds had substantially outperformed the simple aluminide. However, as can be seen, the Pt bond coat provided a considerably better performance in comparison with the Pt-aluminide. This indicated that the beneficial effect of Pt is a function of the state of its presence in the bond coat. Variations in coating performance, as shown in Fig. 3 could be explained in terms of differences in oxidation properties and thermal stabilities of the bond coats as demonstrated below.

3.3 Oxidation Properties. Noting that the ceramic top coat is transparent to oxygen, oxidation of the bond coat during exposure at elevated temperatures resembles the case of direct exposure to the environment. To differentiate between the initial oxide layer developed to enhance adhesion of the top coat (Fig. 1), and the new oxide formed during subsequent exposure at elevated temperatures, the latter is referred to as thermally grown oxide. As an example, Figs. 4(*a*)–4(*d*) show the progressive thickening of the initial oxide layer of the Pt-aluminide bond coat as a function of exposure time at 1150°C. This is followed by localized decohesion of the oxide, as shown in Fig. 4(*e*), and eventually complete spallation of the top coat. A qualitatively similar behavior was observed for the aluminide and Pt bond coats. Figure 4(*f*) illustrates the thickening rate of the thermally grown oxide at 1150°C for the three bond coats. It is evident from these results that a one-to-one correspondence exists between the life of the coating

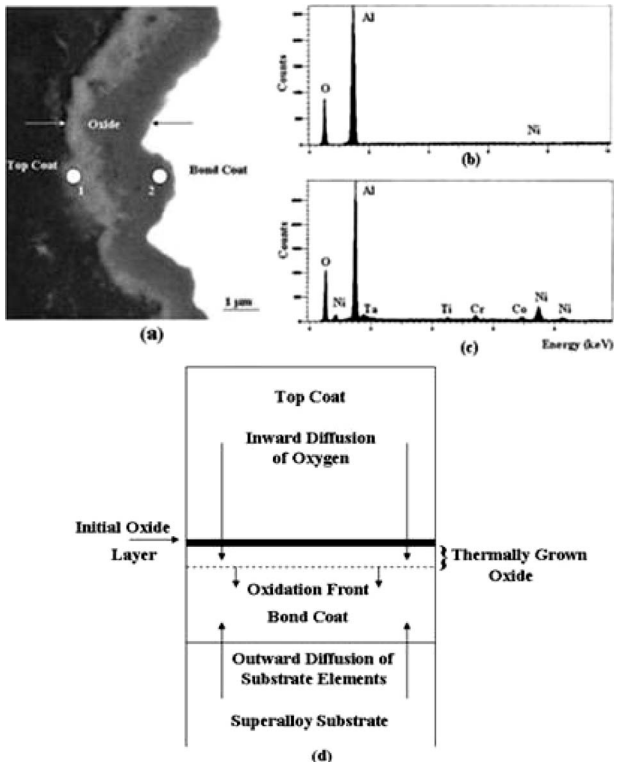

Fig. 5 An example derived from the Pt bond coat to illustrate the growth mode of the thermally grown oxide, (*a*) backscattered electron image of along a cross-section of the coating after 216 h of exposure at 1150°C, (b) an energy dispersive X-ray spectrum illustrating the elemental composition of the oxide layer near the top coat (region 1 in (*a*)), (c) an energy dispersive X-ray spectrum illustrating the elemental composition of the oxide layer near the bond coat (region 2 in (*a*)), and (*d*) a schematic illustrating the growth mode of the thermally grown oxide

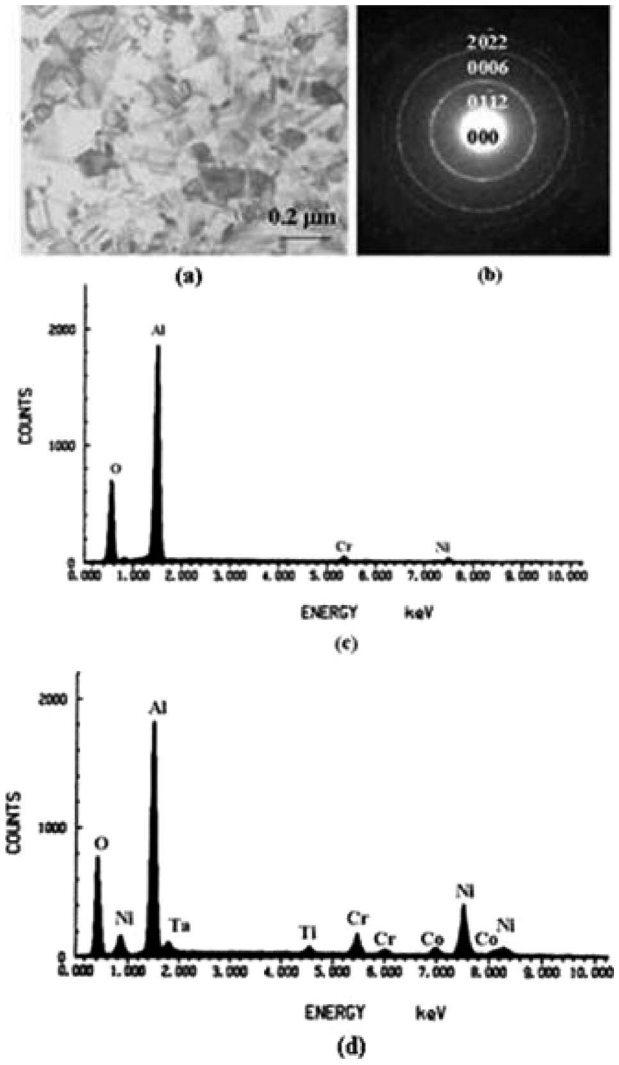

Fig. 6 Analysis of the oxide phase near the oxide bond coat interface after 96 h of exposure at 1150°C: (*a*) bright-field TEM image showing representative grain structure of the oxide developed by the Pt and Pt-aluminide and bond coats, (*b*) corresponding selected-area diffraction pattern indexed in terms of the structure of α-Al_2O_3, (*c*) energy dispersive X-ray spectrum showing the elemental composition of the oxide developed by the Pt bond coat, and (*d*) energy dispersive X-ray spectrum showing the elemental composition of the oxide developed by the Pt-aluminide bond coat

system (Fig. 3) and the oxidation resistance of the respective bond coat.

Detailed microchemical analysis of the interfacial oxide layer separating the bond coat from the top coat indicated that for all bond coats, the thermally grown oxide was developed by inward movement of the initial oxide-bond coat interface. This was suggested by the observed variation in composition of the oxide near the bond coat in comparison with oxide near the top coat, as shown in the example of Fig. 5. Near the top coat (Fig. 5(*a*)), the oxide phase was observed to be relatively free of alloy substrate elements, as shown in Fig. 5(*b*). In contrast, the oxide phase near the bond coat contained relatively high concentrations of substrate elements (Fig. 5(*c*)). Therefore, it is possible to envision the growth mode of the thermally grown oxide as depicted in the schematic of Fig. 5(*d*).

The above results indicated that the service life of the thermal barrier coating system is critically dependent on the "cleanliness" of the oxide-bond coat interface. It is expected that a higher diffusional stability of the bond coat would contribute to more selective oxidation of Al resulting in a purer thermally grown oxide of a slower growth rate and better adherence (Fig. 6). This is demonstrated in the results of TEM/STEM analysis of the thermally grown oxide developed by the Pt and Pt-aluminide bond coats. As can be seen, after a given exposure time at 1150°C, the thermally grown oxide developed by the Pt bond coat was purer (slower growth rate) in comparison with that developed by the Pt-aluminide bond coat (higher growth rate) consistent with the data shown in Fig. 4(*f*).

For both the Pt-aluminide and Pt bond coats, adhesion of the thermally grown oxide was found to be degraded by formation of Ti-rich oxide particles near the thermally grown oxide-bond coat interface as demonstrated in the example of Fig. 7. Some oxide particles were also found to contain Ta in addition to Ti. However, the process leading to the formation of Ti-rich oxide appeared to occur at a slower rate in the case of the Pt bond coat, which could be related to its higher thermal stability particularly the effectiveness of the Pt-rich γ'-phase as a sink for Ti.

3.4 Thermal Stability Characteristics. Figure 8 illustrates the effect of 48 h of exposure at 1150°C on the microstructures of the three bond coats included in the study. In the case of the simple aluminide (Fig. 8(*a*)), the coating layer became indistinguishable from the superalloy substrate reflecting its rather poor thermal stability. As shown in Fig. 8(*b*), the structure of the outer layer of the Pt-aluminide bond coat ($PtAl_2+\beta$-NiAl) became indistinguishable from the inner layer. Detailed microchemical

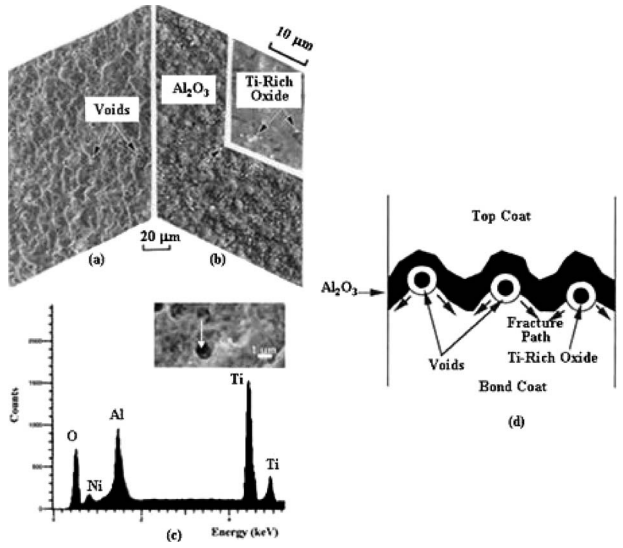

Fig. 7 An example derived from the Pt-aluminide bond coat to illustrate the role of interfacial Ti-rich oxide particles in the loss of adhesion between the thermally grown oxide and bond coat (96 h of exposure at 1150°C with a 24-h cycling period at room temperature): (*a*) secondary electron image illustrating the morphology of the bond coat surface, voids are marked by the arrows, (*b*) secondary electron image illustrating the morphology of the bottom surface of top coat covered by the thermally grown oxide containing particles of Ta- and Ti-rich oxides, (*c*) an example illustrating the presence of Ti-rich oxide particles at the bottom of voids observed in (*a*), and (*d*) a schematic illustrating decohesion of the thermally grown oxide by formation of voids around Ti-rich oxide particles at the oxide-bond coat interface

analysis showed that the outer layer was decomposed by inward diffusion of Pt and outward diffusion of Ni. However, in contrast with the simple aluminide, the interdiffusion zone remained to act as a barrier between the coating layer and superalloy substrate indicating a higher thermal stability. Although the structure of the Pt bond coat was coarsened after 48 h of exposure at 1150°C, as shown in Fig. 8(*c*), the surface layer of the Pt-rich γ'-phase maintained its stability, which could explain its higher resistance to oxidation as well as the superior performance of the respective thermal barrier coating system.

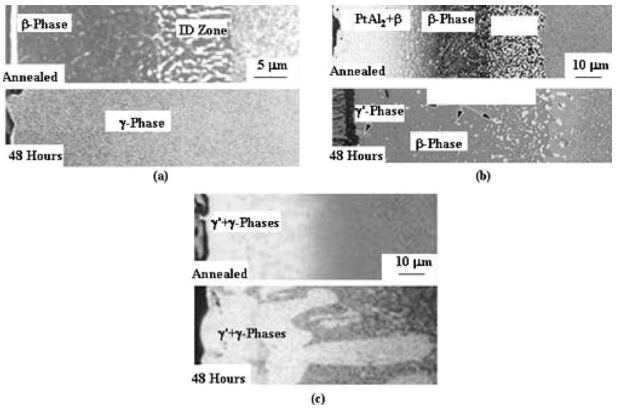

Fig. 8 Backscattered electron images illustrating comparative thermal stability characteristics of the bond coats at 1150°C as exemplified by the effect of 48 h of exposure on microstructure: (*a*) simple aluminide bond coat, (*b*) Pt-aluminide bond coat, and (*c*) Pt bond coat

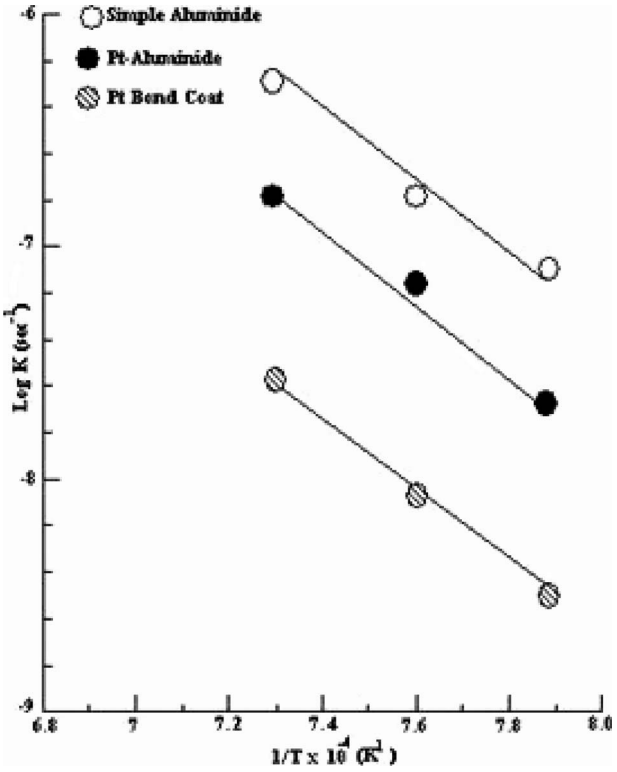

Fig. 9 Effect of temperature (*T*) on the parabolic rate constant (*K*) for interdiffusion between the superalloy substrate and various bond coats

Consistent with the above results, interdiffusion between the bond coat and alloy substrate expressed as fractional growth of the coating layer per unit time was found to occur at a slower rate in the Pt bond coat followed by the Pt-aluminide and simple aluminide, as shown in Fig. 9. As can be seen, the kinetics of interdiffusion followed a nearly parabolic rate behavior and the activation energy was nearly the same for the three bond coats (about 290 kJ/mol) suggesting that interdiffusion occurred by the same mechanism. However, since diffusion data related to intermetallic compounds is rather scarce, it was difficult to correlate the estimated activation energy with a particular diffusion mechanism.

4 Conclusion

Based on the results of this study, it could be concluded that a significant improvement in the performance of thermal barrier coatings could be achieved by the use of Pt-containing bond coats. Platinum was found to act as a cleanser of the oxide-bond coat interface by limiting outward diffusion of superalloy substrate elements detrimental to oxidation properties of the bond coat particularly Ti and refractory transition elements. This could promote the formation of purer oxide of a slower growth rate and better adherence to the substrate. However, the exact effect was found to be dependent on the state of presence of Pt within the outermost layer of the bond coat. Among the bond coats included in this study, a surface layer of Pt-rich γ'-phase is found to produce longer coating life in comparison with a mixture of $PtAl_2$ and β-NiAl.

Acknowledgment

It is a pleasure to acknowledge the continued support of King Fahd University of Petroleum & Minerals.

References

[1] Sims, C. T., 1991, "Non-Metallic Materials for Gas Turbine Engines: Are they Real," Advanced Materials and Processes, **139**(6), pp. 32–39.

[2] Lammermann, H. and Kienel, G., 1991, "Physical Vapor Deposition Coatings for Aircraft Turbine Blades," Advanced Materials and Processes, **140**(6), pp 18–23.
[3] Evans, A. G., Mumm, D. R., Hutchinson, J. W., Meier, G. H., and Petit, F. S., 2001, "Mechanisms Controlling the Durability of Thermal Barrier Coatings," Prog. Mater. Sci., **46**, pp. 505–553.
[4] Tolpygo, V., and Clarke, D. R., 2005, "The Effect of Pre-Oxidation Treatment on the Cyclic Life of EB-PVD Thermal Barrier Coatings With Platinum-Aluminide Bond Coats," Surf. Coat. Technol., **200**(5–6), pp. 1276–1281.
[5] Tawancy, H. M., UI-Hamid, A., Aboelfotoh, M. O., and Abbas, N. M., 2008, "Effect of Pt on the Oxide-to-Metal Adhesion in Thermal Barrier Coating Systems," J. Mater. Sci., **43**(9), pp. 2978–2989.
[6] Pomeroy, M. J., 2005, "Coatings for Gas Turbine Materials and Long Term Stability Issues," Mater. Des., **26**(3), pp. 223–231.
[7] Tawancy, H. M., Mohamed, A. I., Abbas, N. M., Jones, R. E., and Rickerby, D. S., 2003, "Effect of Superalloy Substrate Composition on the Performance of a Thermal Barrier Coating System," J. Mater. Sci., **38**, pp 3797–3807.
[8] Guerre, C., Remy, L., and Molins, R., 2003, "Alumina Scale Growth and Degradation Modes of a TBC System," Mater. High Temp., **20**(4), pp. 481–485.
[9] Yanar, N. M., Kim, G., Hamano, S., Petit, F. S., and Meier, G. H., 2003, "Microstructural Characterization of the Failures of Thermal Barrier Coatings on Ni-Base Superalloys," Mater. High Temp., **20**(4), pp. 495–506.
[10] Mumm, D. R., Evans, A. G., and Spitsberg, I. T., 2001, "Characterization of a Cyclic Displacement Instability for a Thermally Grown Oxide in a Thermal Barrier System," Acta Mater., **49**(12), pp. 2329–2340.
[11] Tawancy, H. M., Sridhar, N., Abbas, N. M., and Rickerby, D. S., 2000, "Comparative Performance of Selected Bond Coats in Advanced Thermal Barrier Coating Systems," J. Mater. Sci., **35**, pp. 3615–3629.
[12] Gell, M., Vaidyanathan, K., Barber, B., Cheng, J., and Jordan, E., 1999, "Mechanism of Spallation in Platinum Aluminide/Electron Beam Physical Vapor-Deposited Thermal Barrier Coatings," Metall. Mater. Trans. A, **30**(2), pp. 427–435.
[13] Tawancy, H. M., Sridhar, N., Abbas, N. M., and Rickerby, D. S., 1998, "Failure Mechanism of a Thermal Barrier Coating System on a Nickel-Base Superalloy," J. Mater. Sci., **33**, pp. 681–686.
[14] Meier, S. M., Nissley, D. M., Sheffler, K. D., and Cruse, T. A., 1992, "Thermal Barrier Coating Life Prediction Model Development," Trans. ASME: J. Eng. Gas Turbines Power, **114**, pp. 258–263.
[15] Panat, R., Hsia, K. J., and Oldham, J., 2005, "Rumpling Instability in Thermal Barrier Systems Under Isothermal Conditions in Vacuum," Philos. Mag., **85**(1), pp 45–64.
[16] Panat, R., and Hsia, K. J., 2004, "Experimental Investigation of the Bond-Coat Rumpling Instability Under Isothermal and Cyclic Thermal Histories in Thermal Barrier Systems," Proc. R. Soc. London, Ser. A, **460**(2047), pp. 1957–1979.
[17] Tolpygo, V. K., and Clarke, D. R., 2004, "On the Rumpling Mechanism in Nickel-Aluminide Coatings Part I: An Experimental Assessment," Acta Mater., **52**(17), pp. 5115–5127.
[18] Panat, R., Hsia, K. J., and Cahill, D. G., 2005, "Evolution of Surface Waviness in Thin Films Via Volume and Surface Diffusion," J. Appl. Phys., **97**(1), p. 013521.
[19] Izumi, T., and Gleeson, B., 2007, "Oxidation Resistance of Pt Containing γ-Ni+γ'-Ni_3Al Alloys," J. Jpn. Inst. Met., **71**(1), pp. 34–40.
[20] Glesso, B., Wang, W., Hayashi, S., and Sordelet, D., 2004, "Effects of Platinum on the Interdiffusion and Oxidation Behavior of Ni–Al-Based Alloys," *High Temperature Corrosion and Protection of Materials*, Vol. 6, Part 1, pp. 461–464 and Part 2, pp. 213–222.
[21] Tatlock, G. J., and Hurd, T. J., 1984, "Platinum and the Oxidation Behavior Nickel Based Superalloy," Oxid. Met., **22**(5–6), pp. 201–226.
[22] Zhang, Y., Haynes, J. A., Lee, W. Y., Wright, I. G., Pint, B. A., Cooley, K. M., and P. Liaw, K., 2001, "Effects of Pt Incorporation on the Isothermal Oxidation Behavior of CVD Aluminide Coatings," Metall. Mater. Trans. A, **32A**, pp. 1727–1741.
[23] Tawancy, H. M., Abbas, N. M., and Rhys-Jones, T. N., 1991, "Role of Pt in Aluminide Coatings," Surf. Coat. Technol., **49**, pp. 1–7.
[24] Schaffer, J., Kim, G. M., Meier, G. H., and Pettit, F. S., 1989, *The Role of Active Elements in the Oxidation Behavior of High Temperature Metals and Alloys*, E. Lang, ed., Elsevier, New York, pp. 231–270.
[25] Jackson, M. R., and Rairden, J. R., 1977, "The Aluminization of Platinum and Platinum-Coated IN-738," Metall. Trans. A, **8A**, pp. 1697–1707.
[26] Wood, J. H., and Goldman, E. H., 1987, *Superalloys II*, C. T. Sims, N. S. Stoloff, and W. C. Hagel, eds., Wiley, New York, pp. 359–384.
[27] Smialek, J. L., and Meier, G. H., 1987, *Superalloys II*, C. T. Sims, N. S. Stoloff, and W. C. Hagel, eds., Wiley, New York, pp. 293–326.

Micro Gas Turbine Recuperator: Steady-State and Transient Experimental Investigation

Mario L. Ferrari
e-mail: mario.ferrari@unige.it

Matteo Pascenti
e-mail: matteo.pascenti@unige.it

Loredana Magistri
e-mail: loredana.magistri@unige.it

Aristide F. Massardo
e-mail: massardo@unige.it

Thermochemical Power Group (TPG),
Dipartimento di Macchine, Sistemi Energetici e Trasporti (DiMSET),
Università di Genova,
Genova 16145, Italy

The aim of this work is the experimental analysis of a primary-surface recuperator, operating in a 100 kW micro gas turbine, as in a standard recuperated cycle. These tests, performed in both steady-state and transient conditions, have been carried out using the micro gas turbine test rig, developed by the Thermochemical Power Group at the University of Genova, Italy. Even if this facility has mainly been designed for hybrid system emulations, it is possible to exploit the plant for component tests, such as experimental studies on recuperators. The valves installed in the rig make it possible to operate the plant in the standard recuperated configuration, and the facility has been equipped with new probes essential for this kind of tests. A wide-ranging analysis of the recuperator performance has been carried out with the machine, operating in stand-alone configuration, or connected to the electrical grid, to test different control strategy influences. Particular attention has been given to tests performed at different electrical load values and with different mass flow rates through the recuperator ducts. The final section of this paper reports the transient analysis carried out on this recuperator. The attention is mainly focused on thermal transient performance of the component, showing the effects of both temperature and flow steps. [DOI: 10.1115/1.3156822]

Keywords: micro gas turbine, recuperator, effectiveness

1 Introduction

Since the late 1990s, microturbines have been proved to be particularly attractive for the power generation market, especially in the perspective of a widespread development of the distributed generation approach [1]. The main advantages that make microturbines preferable to Diesel engines are:

- smaller size and weight
- fuel flexibility
- lower emissions
- lower noise
- vibration-free operation
- reduced maintenance

Furthermore, this kind of machine is promising for cogenerative applications [1], and is essential for the development of innovative cycles, such as hybrid systems [2], humid cycles [3,4], or externally fired cycles [5,6].

Since microturbine technology needs to reach electrical efficiency values of at least 30% [7] or higher to penetrate the power market, the use of a recuperated cycle is mandatory. For this reason, heat recovery exchangers today, not widely used in large power plants for their earlier bulky size, poor reliability, and high cost, are designed and developed with more interest.

The new compact heat recovery exchangers for microturbine applications called primary surface recuperators, began to appear in the late 1970s in Germany [8], where a new compact metallic recuperator module was built with the potential for continuous automated process manufacturing [8]. Based on this earlier work, heat exchanger specialists have studied and designed different recuperator concepts [9] with the aim to:

- increase recuperator performance [10]
- reduce the number of parts
- use low-cost manufacture processes
- increase recuperator flexibility
- achieve a better machine/recuperator integration level
- develop new materials (i.e., for superalloy or ceramic recuperators [11])

The primary-surface recuperators are produced in different geometries, depending on the applications and space availability [10]. While several thousand recuperators are built with an annular core geometry of 30 kW and 60 kW microturbines, a platular or cube shaped core is chosen, where there is no close coupling between the rotating machinery and the recuperator (e.g., for a 100 kW unit). Today, a new geometry called spirally wrapped is being developed in Belgium, and is showing good performance, especially with laser-welded seal technology development [12].

There are several recuperators, available today on the market, tested and produced for different microturbine manufacturers. For instance, Caterpillar and Solar Turbines, USA, produced significant quantities of compact primary-surface recuperators in both platular and annular form [13]. They have shown good performance, reliability, and structural integrity.

Even if several works have been published on micro gas turbine recuperators, focusing the attention on theoretical performance curves [10,14] or on technology development [8–10,12,15,16], the published experimental wide campaigns are poor, probably for company data protection reasons. Also, when the aim of the work is the presentation of experimental tests (e.g., in Ref. [17]), the results show only few steady-state operative points, close to design conditions. For this reason, at the University of Genova, the micro gas turbine test rig [18] developed by TPG has been exploited for an extensive experimental analysis on recuperator performance. This is a primary-surface (cube geometry) recuperator located inside the power case of the Turbec T100 machine [19]. So, the recuperator has been tested not in a heat exchanger test rig, but in a real operative configuration, working in a commercial recuperated 100 kWe machine.

Contributed by the International Gas Turbine Institute of ASME for publication in the JOURNAL OF ENGINEERING FOR GAS TURBINES AND POWER. Manuscript received March 19, 2009; final manuscript received March 24, 2009; published online November 5, 2009. Review conducted by Dilip R. Ballal. Paper presented at the ASME Gas Turbine Technical Congress and Exposition, Orlando, FL, June 8–12, 2009.

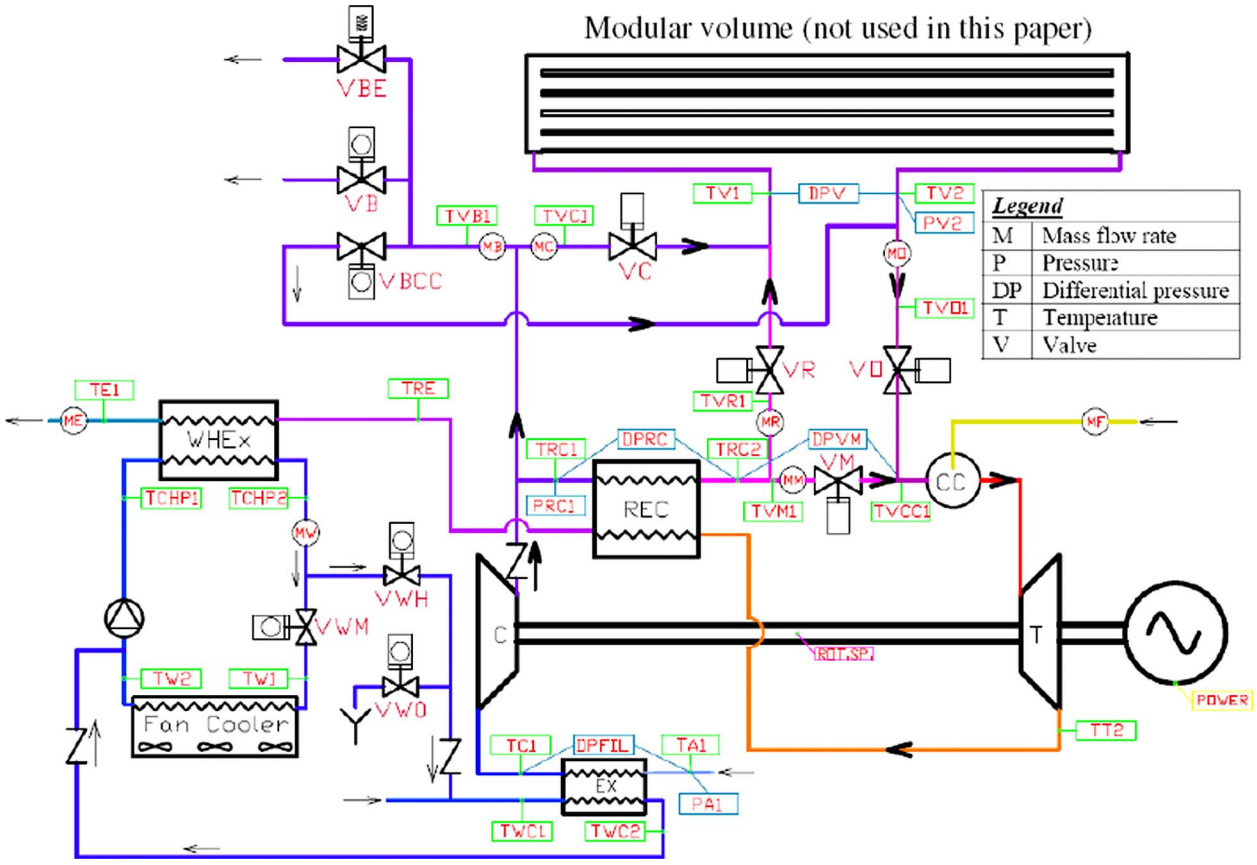

Fig. 1 Plant layout and instrumentation (the complete legend for transducers is reported in Ref. [19])

The attention is mainly focused on recuperator effectiveness, showing the heat exchanger performance, with the machine operating in stand-alone configuration or connected to the electrical grid. The tests have been carried out at different electrical load values and with different mass flow rates, studying the recuperator in the widest range of operative conditions.

This paper also shows a significant further improvement with respect to previous publications, reporting transient experimental results on this kind of heat exchanger.

2 Test Rig Layout

The test rig described in detail in previous works [19,20] was designed and built as a hybrid system emulator. It is based on the coupling of a commercial recuperated micro gas turbine with a modular volume (Figs. 1 and 2). This volume, not included in the tests reported in this paper, is located between the recuperator outlet and combustion chamber inlet, to study different fuel cell sizes and technologies.

The machine is a Turbec T100 PHS Series 3 [21]. It is equipped to operate in stand-alone configuration, or connected to the electrical grid with an apt safety interconnection panel. Its control system works at constant rotational speed in stand-alone mode or at constant TOT when the machine operates connected to the electrical grid. This micro gas turbine consists of a complete module for power generation (100 kWe at nominal conditions, N =70,000 rpm, β=4.45 at a TIT of 950°C, that is, 1223.15 K), a heat exchanger located downstream of the recuperator outlet (hot side) for cogenerative applications, and two battery packages for the startup phase, when the machine is in stand-alone mode.

The commercial power unit has been modified for the volume coupling, as described in Ref. [19]. For this reason, the original piping has been substituted with four pipes for the external connections. At the compressor outlet, a check valve has been introduced to prevent damages due to possible surge conditions, and, between this valve and the recuperator inlet, a T-joint has been introduced to connect a recuperator bypass line (Fig. 1). However, the original combustor and its fuel system have been exploited in their standard configuration, as in a commercial machine.

The coupling between the machine and the volume is carried out by a set of thermally insulated connection pipes, as shown in Fig. 1. They are equipped with pneumatic gate valves (for VM, VR, VO and VC of Fig. 1) to have the lowest possible additional pressure drops, and with additional length pipes to get the highest precision in the flow measurement [18]. The plant is equipped with a cold bypass to connect the volume directly to the compressor, and with a bleed line [19] equipped with an electrical globe valve (VB of Fig. 1). These pipes are essential for changing the

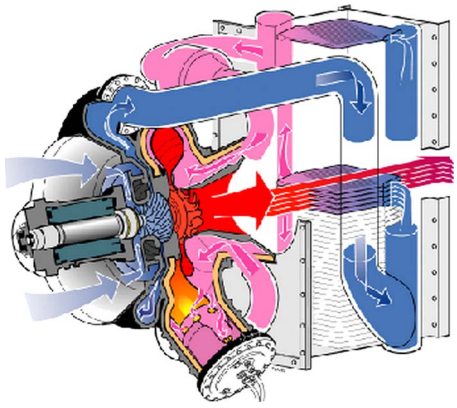

Fig. 2 Recuperator and mGT flow details (courtesy by Turbec)

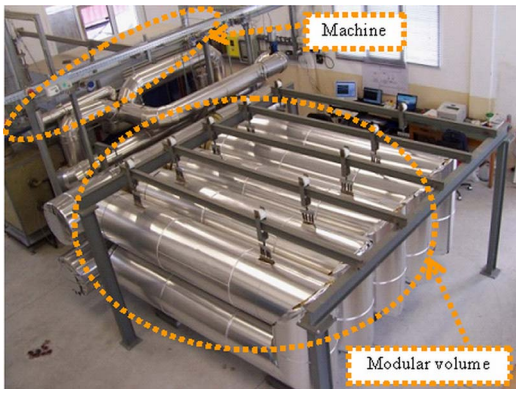

Fig. 3 Test rig picture (volume side)

recuperator mass flow rate with high flexibility, as performed in several tests reported in this paper. A bleed emergency valve (VBE of Fig. 1) has been included to prevent surge during emergency shutdown, and an additional pneumatic globe valve (VBCC of Fig. 1) has been introduced to connect the compressor outlet directly to the combustor inlet, bypassing both recuperator and volume.

The modular volume has been designed for fuel cell emulation tests, as shown in Ref. [20]. It is composed of two collector pipes that are connected at the recuperator outlet and the combustor inlet, respectively, and five module pipes that are connected to both collectors (Fig. 3). Since the volume is not used in this work (VO fully closed during all tests), no detailed volume description is reported here (see Ref. [20] for further details).

In comparison of the layout presented in previous works [18,20], the test rig here has been improved with the installation of a water fan cooler, located outside of the laboratory. It is based on three 0.7 kW electrical fans, used to cool the water that is coming from the water heat exchanger (WHEx) of Fig. 1, and to operate in closed circuit conditions, a 1.5 kW pump has been installed. Furthermore, a new water system has been designed and installed to control the machine compressor inlet temperature. This is composed of three air/water heat exchangers, installed at the machine air intakes (Fig. 4), and connected to the water system; moreover, it has been equipped with three controlled electrical valves (VWM, VWH, and VWO of Fig. 1). The compressor inlet air can be cooled (opening VWO) by means of cold water from the supply system, and heated (by closing VWM, and opening VWH) by means of the hot water coming from the machine cogeneration system (WHEx). Currently, the maximum cooling performance depends on the supply water temperature (about 22°C in summer, that is 295.15 K), while the only constraint on the heating performance is the maximum compressor inlet air temperature for the machine cooling system that is 40°C (313.15 K). However, in an ongoing work, it is planned to connect an absorber cooler to the system to study trigeneration options, and use the cold flow produced for lower compressor inlet temperature generation. In comparison to the layout reported in Refs. [18,20], additional thermocouples and a water mass flow meter have been installed (as reported in Fig. 1). While the thermocouples have the same accuracy as the previous ones (see Ref. [18] for details), the new mass flow meter has an accuracy of ±4% (Table 1). It is important to highlight the installation of a new thermocouple at the compressor inlet (TC1) used for the control system, and also, at the recuperator outlet (TRE), for temperature measurement at the hot side outlet of this heat exchanger.

Table 1 New probes in addition to the transducers shown in Table 1 of Ref. [19]

Mass flow rates			
Name	Location	Probe type	Accuracy (%)
MW	Water main line	Magnetic meter	±4
Pressures			
Name	Location	Probe type	Accuracy (%)
DPFIL	Machine intake	Differential	±1
PV2	Volume outlet	Absolute	±1
Temperatures			
Name	Location	Probe type	Accuracy (K)
TC1	Compressor inlet	Thermocouple	±2.5
TRE	Recuperator outlet	Thermocouple	±2.5
TCHP1	WHEx inlet	Thermocouple	±2.5
TCHP2	WHEx outlet	Thermocouple	±2.5
TW1	Cooler inlet	Thermocouple	±2.5
TW2	Cooler outlet	Thermocouple	±2.5
TWC1	EX inlet (water)	Thermocouple	±2.5
TWC2	EX outlet (water)	Thermocouple	±2.5

The acquisition and control system, developed with the LabVIEW™ software, and as already presented in Ref. [20], is coupled with the standard software of the machine. The machine/acquisition interface system has been enhanced to have in the LabVIEW™ software, all the machine signals necessary for performance calculation (e.g., the recuperator effectiveness). However, the safe operation of the machine is assured (also in the final test rig layout) through its own control system by Turbec, Italy.

Three new proportion integral (PI) control systems have been introduced for compressor inlet temperature control and TOT control through the machine load (only for the micro gas turbine stand-alone configuration). Figure 5 shows the compressor inlet temperature controller that is used for cooling operations. The difference between the set point and the TC1 value is the input of a PI controller, optimized for the VWO fractional opening calculation that controls the cold water mass flow rate for cooling. Figure 6 is the control system diagram used for compressor inlet heating. This second PI controller manages both VWH and VWM fractional opening signals (from 0 to 1). When the PI output is x, VWH is opened at $(x^*100)\%$ FO and VWM is closed at $[(1-x)^*100]\%$ FO. Figure 7 shows the TOT control system for

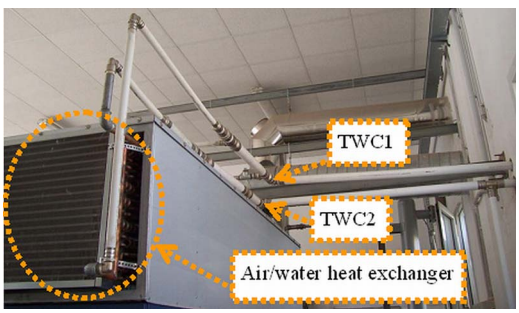

Fig. 4 Air/water heat exchanger with water pipes for compressor inlet temperature control

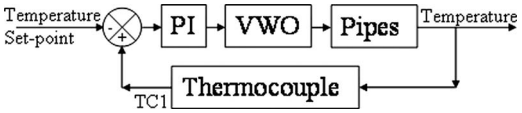

Fig. 5 Compressor inlet temperature control system scheme for cooling operations (see Fig. 1 for nomenclature)

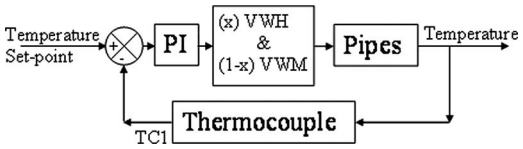

Fig. 6 Compressor inlet temperature control system scheme for heating operations (see Fig. 1 for nomenclature)

stand-alone applications. The difference between the set point and the *TT*2 signal is the input of a slow response PI controller that is used to manage the electrical load, to obtain the required TOT value by means of the machine control system that manages the fuel valves.

3 Steady-State Analysis

The experimental results reported here have been produced on the recuperator (Figs. 2 and 8) of the TPG test rig, with the machine working in its standard recuperated layout (VM fully open, and VR, VO, VC, and VBCC fully closed). Considering the significant influence of the ambient temperature on recuperator performance, the compressor inlet temperature control system has been used to maintain this temperature at a fixed value of 28°C (301.15 K, with maximum errors of ±0.2 K during all the tests). This temperature value has been chosen to provide enough flexibility to perform tests at the same temperature in every season. The recuperator steady-state tests were carried out in different mGT operative conditions (grid connected, or stand-alone configuration).

3.1 Electrical Grid-Connected Configuration. These steady-state tests were carried out with the machine connected to the electrical grid to measure recuperator performance at different mass flow rates. In fact, in this configuration, the machine control system operates at constant TOT (called here as *TT*2, which is maintained at 645°C, that is 918.15 K), and changes the rotational speed (and the air mass flow rate) by changing the electrical load. For surge prevention reasons, the machine controller does not allow steady-state tests to be conducted with less than 20 kW of electrical load.

$$\varepsilon = \frac{TRC2 - TRC1}{TT2 - TRC1} \tag{1}$$

Figure 9 shows the recuperator effectiveness (defined in Eq. (1) because in the tests reported in this paper, the cold flow is always the recuperator lowest capacitance flow) performed at different loads, that means, different air mass flow rates (measured with

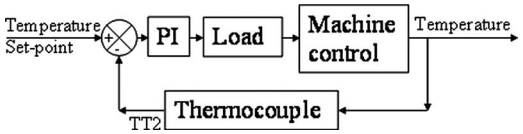

Fig. 7 Turbine outlet temperature control system scheme (see Fig. 1 for nomenclature)

Fig. 8 Primary-surface recuperators ready to be installed in T100 machines (courtesy of Turbec)

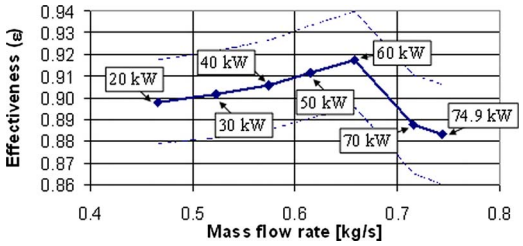

Fig. 9 Machine connected to the electrical grid: steady-state recuperator effectiveness (compressor inlet temperature fixed at 301.15 K)

ME of Fig. 1). While the continuous line connects the effectiveness values, calculated through recuperator boundary temperatures measured during the tests, the dotted lines show the accuracy values for this performance parameter. Since the effectiveness values are calculated by using temperature measurements with a ±2.5 K accuracy, it is possible to exploit the error theory [22] to calculate an accuracy around ±2%,during these tests performed at maximum TOT, i.e., 918.15 K. As shown in previous theoretical works [7,10], starting from the maximum flow, it is possible to see an effectiveness increase (from 0.883 to 0.918) while the mass flow rate decreases, and an effectiveness peak followed by a decrease. However, this final decrease is not as evident as it is in Ref. [10]. In fact, the substantial effectiveness decrease at low mass flow rates is not measured by these tests because, to avoid unstable condition risks, the machine control system does not enable steady-state tests at less than 20 kW (under 0.47 kg/s). The slight decrease (from 0.918 to 0.898) is clearly shown in the figure. Theoretical calculations are currently under development at TPG, and their initial comparison with experimental data is shown and discussed in Ref. [23].

Figure 10 shows the recuperator boundary temperatures measured during this test at the same load values reported in Fig. 9, and used for the effectiveness calculation of Fig. 9. While the TOT (called *TT*2 in Fig. 10, using Fig. 1 nomenclature) is maintained constant by the machine control system, the compressor outlet temperature (*TRC*1) increases with the load and mass flow rate increase, due to a rotational speed increase. The hot side recuperator outlet temperature (TRE) shows the same behavior because, since the mass flow rate increases, the recuperator heat flux decreases for the *TRC*1 increase. For this reason, the hot side cooling effect decreases, generating the TRE increase. This figure also reports the recuperator average outlet temperature on the cold side (*TRC*2) that does not show similar significant variations. However, its trend (an approximate 15 K variation) is the most evident cause of the effectiveness trend.

3.2 Stand-Alone Configuration. Several steady-state tests have been carried out with the machine operating in stand-alone mode. The recuperator effectiveness, calculated using the tem-

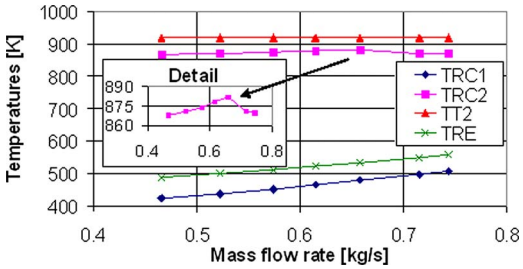

Fig. 10 Machine connected to the electrical grid: steady-state recuperator boundary temperatures (see Fig. 1 for nomenclature)

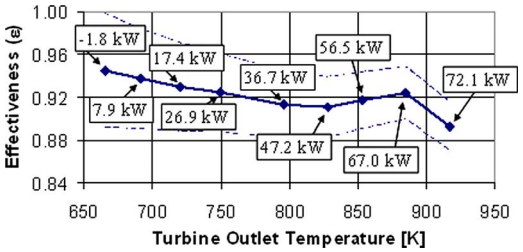

Fig. 11 Machine in stand-alone configuration: steady-state recuperator effectiveness (compressor inlet temperature fixed at 301.15 K)

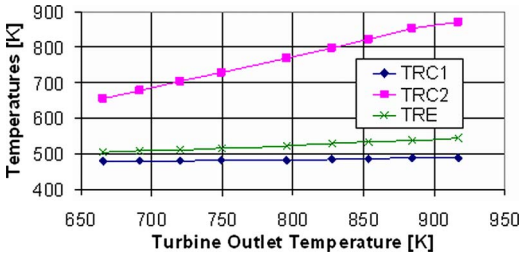

Fig. 12 Machine in stand-alone configuration: steady-state recuperator boundary temperatures (see Fig. 1 for nomenclature)

perature measurements taken during these tests, is shown in Fig. 11, versus the TOT values instead of the mass flow rate. Since in this configuration, the machine operates at constant rotational speed, the mass flow rate difference between different electrical load tests is very small, depending on compressor map behavior (see Ref. [18] for details). On the other hand, the TOT variation, from idle to full load condition, is extremely significant, especially in terms of the recuperator performance. Even if it is not possible to compare these experimental data with theoretical results (in previous theoretical works, e.g., Refs. [7,10], the recuperator effectiveness trend is used to be reported versus the mass flow rate), these tests are extremely essential for plant improvement and model validation [23] in stand-alone operations.

The tests reported in Fig. 11 were carried out at different electrical load values, fixed or defined through the resistor bank. The load value fixed at the resistor bank inverter was set at 0 kW, 10 kW, 20 kW (since in this case a complete analysis is possible even at very small loads), 30 kW, 40 kW, 50 kW, 60 kW, 70 kW, and 75 kW, respectively, during each test (now the maximum power is no longer 100 kW, not even at the ISO ambient temperature, for the machine modifications shown in the rig layout paragraph). Figure 11 shows the net electrical power produced during the tests, which is a bit lower than the command for resistor bank control logic and battery recharge reasons. It is noteworthy that the net electrical power value in idle conditions (zero load bank power) is negative, instead of zero, because the machine generates about 1.8 kW for battery recharge reasons. While the recuperator effectiveness is high (about 0.945) during low temperature conditions (idle conditions), an almost decreasing behavior is produced increasing the load and temperatures. This is essentially due to an increase in the maximum temperature difference ($TT2-TRC1$) on the recuperator, which generates an increase in the temperature difference along the whole thermal exchange surface. At full load, the effectiveness value is similar to that reported for the grid-connected configuration tests at 96.5% of the nominal machine speed. The difference is definitely inside the measurement accuracy discussed in the previous paragraph. In Fig. 11 (as in Fig. 9), the dotted lines show the maximum error band on this parameter, calculated with the error theory [22]. Since thermocouples have an accuracy of ± 2.5 K, regardless of temperature, it is possible to evaluate high error band values (about $\pm 6\%$) at low temperature (e.g., idle). When the temperature is increased, the accuracy increases up to approximately $\pm 2\%$.

Figure 12 shows the recuperator boundary temperatures measured during these tests in stand-alone mode. They were used for the effectiveness calculation, and reported versus the TOT values. The main effect of the increase with the electrical load was the recuperator outlet temperature increase on the cold side. In comparison with the *TRC*1 and the TRE behavior in Fig. 10, in this case, the temperature increase is less significant (especially for *TRC*1). This is due to the rotational speed that, during these tests, was maintained constant (in steady-state conditions) by the machine control system. For this reason, the compressor outlet pressure, and, as a consequence, the temperature increase is lower than in the grid-connected case.

A second set of steady-state tests were carried out in stand-alone configuration with different values of bleed mass flow rates, using the VB valve to discharge a part of the compressor flow directly to the machine stack. These tests were conducted using the TOT control system (see Fig. 7), changing the electrical load to maintain the TOT at its maximum value (around 645 °C, i.e., 918.15 K). Figure 13 shows the effectiveness values calculated with temperature measurements at different bleed flow values. The mass flow rate reported in Fig. 13 as the *x*-axis is the mass flow rate through the recuperator ducts (when the bleed mass flow rate increases, the recuperator mass flow rate decreases). The cited figure also shows the measurement accuracy that in these tests, is almost constant around $\pm 2\%$, because the temperature variations at the recuperator boundaries between different tests is less than 20 K (see the *TRC*2 of Fig. 14). The effectiveness value at maximum mass flow rate (VB fully closed) is similar to the values at maximum TOT reported in Fig. 11. The difference (under 0.5%) is within the error band of the temperature measurement accuracy. The effectiveness trend is similar to the behavior reported in Fig. 9 for the tests carried out with the machine connected to the electrical grid. Also in this case, the recuperator flow decrease generates an effectiveness increase until reaching a maximum value, followed by a gradual decrease. The difference between the Fig. 9 and Fig. 13 effectiveness values (the maximum in Fig. 13 is closer to the maximum mass flow rates values) is mainly due to the

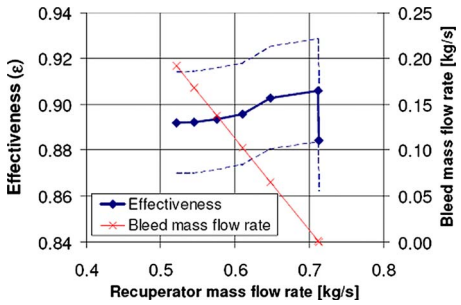

Fig. 13 Machine in stand-alone configuration with different bleed mass flow rates: steady-state recuperator effectiveness (compressor inlet temperature fixed at 301.15 K)

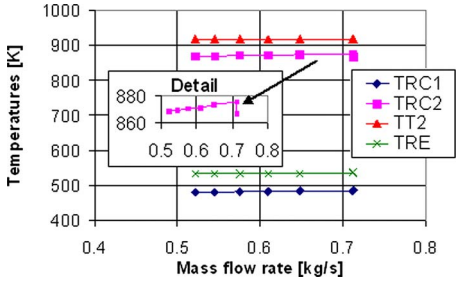

Fig. 14 Machine in stand-alone configuration with different bleed mass flow rates: steady-state recuperator boundary temperatures (see Fig. 1 for nomenclature)

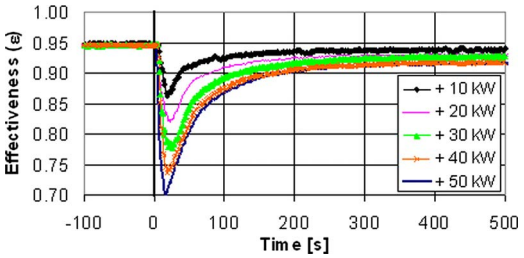

Fig. 15 Machine in stand-alone configuration: transient recuperator effectiveness

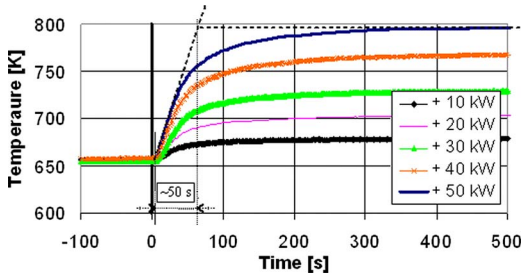

Fig. 16 Machine in stand-alone configuration: transient recuperator outlet temperature (cold side)

different compressor outlet temperatures. While in the grid-connected tests the compressor outlet temperature (*TRC*1) increases with the mass flow rate increase (due to the increase of the rotational speed), in latter tests in stand-alone mode the *TRC*1 (see Fig. 14) is almost constant (the mass flow rate increase is produced by closing the VB valve).

4 Transient Analysis

Further experimental results were carried out to study recuperator performance in transient conditions. These tests are extremely significant not only in terms of the cycle performance, but also regarding component life and recuperator interaction with the control system or additional plant components (e.g., fuel cells). As in the steady-state tests, the compressor inlet temperature control system was used to maintain this temperature at a fixed value of 301.15 K (no significant oscillations are produced at this temperature during the transient property changes). For these tests, the stand-alone configuration was chosen because the resistor bank makes it possible to do load steps (more significant in terms of plant response), while in grid-connected conditions, the load is gradually ramped up by the machine control system to the set point value [21].

4.1 Load and Temperature Steps. Figure 15 shows the dynamic recuperator effectiveness values calculated from the temperatures measured at the recuperator boundaries. For readability reasons, the accuracy band is not reported in this figure, but it can be obtained from Fig. 11. The dynamic performance of the instrumentation is fully discussed in Ref. [19] for the whole test rig. However, the probes used for the measurements reported in this paper have a time response constant that can be considered negligible for plant level tests, operating with an acquisition sample time of 1 s.

These tests have been performed with different load increase steps. Starting from 0 kW, the load command to the resistor bank inverter has been set to 10 kW, 20 kW, 30 kW, 40 kW, and 50 kW, respectively, generating load increase steps from 0 kW power, during each test. While the initial and final values of recuperator effectiveness are the steady-state values reported in Fig. 11 (showing the net electrical power output in correspondence to the bank loads), the transient behavior of the effectiveness is due to the temperature trends over time. The initial decrease, that is more significant for higher load step values, is due to the fast TOT (called *TT*2 in the graphs, in accordance with Fig. 1 nomenclature) increase, coupled with the thermal delay in the *TRC*2 values. This is caused by the recuperator thermal capacitance that generates a delay in the *TRC*2 increase. Then, Fig. 15 shows the effectiveness increase up to the steady-state values reported in Fig. 11.

Figure 16 shows the recuperator outlet temperature (cold side, *TRC*2) during these transient tests. This temperature has a dead time delay of about 10 s, followed by an increase trend up to the new steady-state value (see Fig. 12). The time constant of this transient phenomenon (the time necessary to reach about the 63% of the variation) is about 50 s, as shown in Fig. 16 for the 50 kW load step case.

The same *TRC*2 performed with the 50 kW load step increase is reported in Fig. 17, with all the other recuperator boundary temperatures measured during this test. As an example of temperatures measured during these transient tests, Fig. 17 shows the TOT increase, followed by the *TRC*2 increase (affected by the thermal capacitance delay). Since the machine controller maintains the rotational speed constant, the compressor outlet temperature increase (*TRC*1) is almost negligible (just about 4 K due to the compressor outlet pressure increase).

4.2 Mass Flow Rate Steps. Several mass flow rate steps were carried out on the recuperator, operating FO steps on the bleed valve (VB). Since, in stand-alone mode, the machine works at constant rotational speed, the recuperator mass flow rate can be changed only by discharging a part of the compressor flow directly to the machine stack (through the bleed valve). Starting from the lowest recuperator mass flow rate point of Fig. 13, different closing 2.5% steps were made on the VB, from an initial value of about 15%, down to 0% (i.e., VB fully closed). During these tests, the TOT value was controlled through the machine load, using the controller reported in Fig. 7 to maintain its initial value (around 918.15 K).

While the steady-state results obtained in this configuration were already shown in Figs. 13 and 14, here, the attention is focused on the recuperator transient behavior, showing the test data obtained when closing the VB valve with a 2.5% step.

Figure 18 shows the fractional opening values generated after the closing step command, and their effect on the recuperator mass flow rate increase. The net electrical power output (Fig. 19) is increased by the controller (through the load bank), to have the fuel increase necessary to maintain constant the TOT value. Furthermore, Fig. 19 shows the recuperator effectiveness values, calculated with the temperatures measured during this test. Since the mass flow rate variation is very fast at both recuperator sides (flow variation characteristic time: less than 1 s), the effectiveness transient behavior is due to the temperature trends reported in Fig. 20.

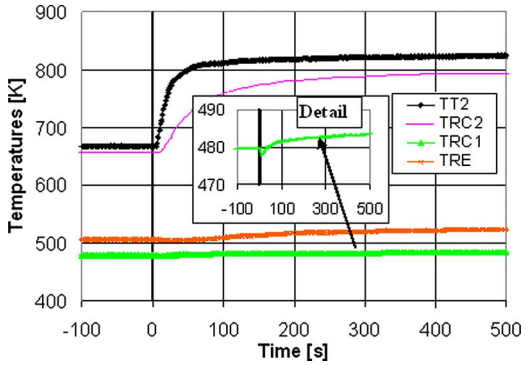

Fig. 17 Machine in stand-alone configuration: transient recuperator boundary temperatures after a +50 kW load step (see Fig. 1 for nomenclature)

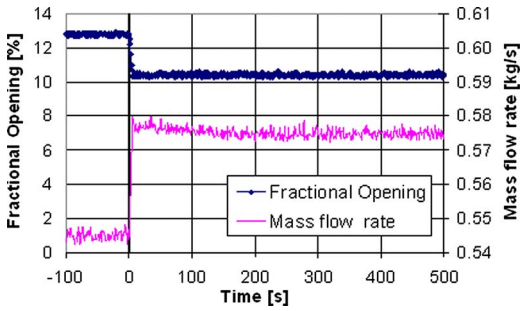

Fig. 18 Machine in stand-alone configuration with different bleed mass flow rates: bleed valve fractional opening and recuperator mass flow rate in transient conditions

The initial effectiveness increase is generated by the initial TOT (*TT*2 in Fig. 20) decrease coupled with the *TRC*2 decrease delay due to recuperator thermal capacitance. Then, the effectiveness decreases down to its initial value for the *TRC*2 decrease. Finally, for the gradual *TT*2 increase up to its initial value (TOT controller activity), the effectiveness goes toward its steady-state value reported in Fig. 13 for the 0.575 kg/s mass flow rate. The *TRC*1 and the TRE temperature variations are almost negligible during this test for an insignificant compressor outlet pressure variation.

5 Summary

The micro gas turbine test rig developed by TPG at the University of Genova was used to perform a wide-ranging experimental analysis on the primary-surface recuperator, typically used as a component of the Turbec T100 machine. Since the original commercial machine does not allow this kind of measurement to be taken, it has been developed an apt test rig equipped with all the necessary probes and valves used to manage the recuperator flow. An extensive experimental campaign was carried out to produce data, useful for the recuperator design, improvements, and theoretical model validation. Since such experimental data on recuperators have been inadequate in previously published works, the data presented in this paper are essential for the validation of off-design and transient models (as well as real-time approaches).

The main research activities and results presented in this paper are the following points.

- The test rig was enhanced with the installation of a water circuit for compressor inlet temperature control, and the acquisition and control system of the rig was equipped with new PI controllers. Considering the significant influence of the ambient temperature on recuperator performance, the compressor inlet temperature control system was used to maintain this temperature at a fixed value during all the tests.
- Further probes were introduced in the rig for the tests reported in this paper.
- A new TOT controller was developed for the mass flow rate step tests carried out on the recuperator.
- Steady-state tests were performed in both grid-connected and stand-alone modes, exploiting the compressor inlet temperature controller.
- The recuperator performance is discussed to illustrate the accuracy band obtained on the effectiveness calculation in different operating conditions.
- The transient tests conducted in stand-alone mode have been included in this work, focusing the attention on the recuperator effectiveness values.
- The effects of different load steps are reported in this work to show the recuperator effectiveness and boundary temperatures.
- A mass flow rate step test is discussed in terms of recuperator transient performance.

Besides the additional development and tests on the rig that were already planned and presented in Ref. [18], the recuperator performance will be tested in various plant configurations. In an ongoing work, it is planned to connect an absorber cooler to the system to study trigeneration options, and use the cold flow produced for lower compressor inlet temperature generation. This option will be extremely useful to expand the operating conditions to be considered for tests, to measure the recuperator performance in both steady-state and transient modes, and with different plant layout configurations.

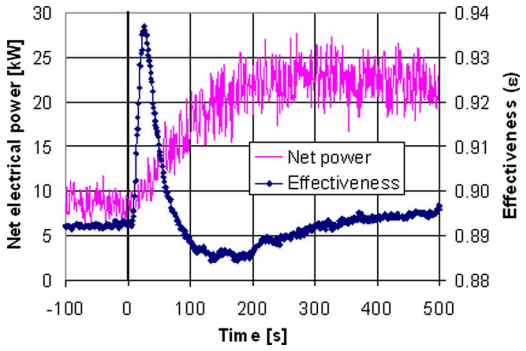

Fig. 19 Machine in stand-alone configuration with different bleed mass flow rates: net electrical power and recuperator effectiveness in transient conditions

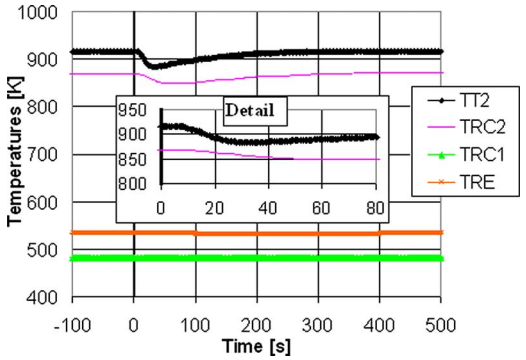

Fig. 20 Machine in stand-alone configuration with different bleed mass flow rates: recuperator boundary temperatures in transient conditions (see Fig. 1 for nomenclature)

Acknowledgment

The authors would like to thank Alessandro Sorce, Master Student at TPG, for his support on the graphical development of Fig. 1. This work was funded by LARGE-SOFC European Integrated Project No. 019739, coordinated by VTT of Finland.

Nomenclature

C	=	compressor
CC	=	combustion chamber
EX	=	exchanger
REC	=	recuperator
SOFC	=	solid oxide fuel cell
T	=	turbine
WHEx	=	water heat exchanger

Variables

FO	=	fractional opening (%)
N	=	rotational speed (rpm)
TIT	=	turbine inlet temperature (K)
TOT	=	turbine outlet temperature (K)

x = PI signal of Fig. 6

Greek Symbols

β = compression ratio

ε = recuperator effectiveness

References

[1] Kesseli, J., Wolf, T., Nash, J., and Freedman, S., 2003, "Micro, Industrial, and Advanced Gas Turbines Employing Recuperators," ASME Paper No. GT2003-38938.

[2] Roberts, R. A., Brouwer, J., Liese, E., and Gemmen, R., 2005, "Development of Controls for Dynamic Operation of Carbonate Fuel Cell-Gas Turbine Hybrid Systems," ASME Paper No. 2005-GT-68774.

[3] Pedemonte, A. A., Traverso, A., and Massardo, A. F., 2008, "Experimental Analysis of Pressurised Humidification Tower for Humid Air Gas Turbine Cycles. Part A: Experimental Campaign," Appl. Therm. Eng., **28**, pp. 1711–1725.

[4] Parente, J., Traverso, A., and Massardo, A. F., 2003, "Saturator Analysis for an Evaporative Gas Turbine Cycle," Appl. Therm. Eng., **23**, pp. 1275–1293.

[5] Traverso, A., Massardo, A. F., and Scarpellini, R., 2006, "Externally Fired Micro-Gas Turbine: Modelling and Experimental Performance," Appl. Therm. Eng., **26**, pp. 1935–1941.

[6] Elmeegard, B., and Qvale, B., 2002, "Analysis of Indirectly Fired Gas Turbine for Wet Biomass Fuels Based on Commercial Micro Gas Turbine Data," ASME Paper No. GT2002-30016.

[7] McDonald, C. F., 1996, "Heat Recovery Exchanger Technology for Very Small Gas Turbines," Int. J. Turbo Jet Engines, **13**, pp. 239–261.

[8] Foerster, S., and Kleeman, M., 1978, "Compact Metallic and Ceramic Recuperators for Gas Turbines," ASME Paper No. 78-GT-62.

[9] McDonald, C. F., 2000, "Low-Cost Compact Primary Surface Recuperator Concept for Microturbines," Appl. Therm. Eng., **20**, pp. 471–497.

[10] McDonald, C. F., 2003, "Recuperator Considerations for Future High Efficiency Microturbines," Appl. Therm. Eng., **23**, pp. 1453–1487.

[11] McDonald, C. F., 2005, "Ceramic Recuperator and Turbine—The Key to Achieving a 40 Percent Microturbine," ASME Paper No. GT2005-68644.

[12] Antoine, H., and Prieels, L., 2002, "The ACTE Spiral Recuperator for Gas Turbine Engines," ASME Paper No. GT2002-30405.

[13] Ward, M. E., Holman, L., 1992, "Primary-Surface Recuperator for High Performance Prime-Mover," SAE Paper No. 920150.

[14] Holman, J. P., 1997, *Heat Transfer*, 8th ed., McGraw-Hill, New York.

[15] Traverso, A., and Massardo, A. F., 2005, "Optimal Design of Compact Recuperators for Microturbine Application," Appl. Therm. Eng., **25**, pp. 2054–2071.

[16] McDonald, C. F., Massardo, A. F., Rodgers, C., and Stone, A., 2008, "Recuperated Gas Turbine Aeroengines, Part I: Early Development Activities," Aircraft Engineering and Aerospace Technology, **80**(2), pp. 139–157.

[17] Lagerström, G., and Xie, M., 2002, "High Performance & Cost Effective Recuperator for Micro-Gas Turbines," ASME Paper No. GT2002-30402.

[18] Ferrari, M. L., Pascenti, M., Magistri, L., and Massardo, A. F., 2007, "A General Purpose Test Rig for Innovative Cycles Based on a 100 kWe Micro Gas Turbine," International Gas Turbine Congress, Tokyo, Japan, Paper No. IGCT2007-TS-015.

[19] Pascenti, M., Ferrari, M. L., Magistri, L., and Massardo, A. F., 2007, "Micro Gas Turbine Based Test Rig for Hybrid System Emulation," ASME Paper No. GT2007-27075.

[20] Ferrari, M. L., Pascenti, M., Magistri, L., and Massardo, A. F., 2008, "Emulation of Hybrid System Start-Up and Shutdown Phases With a Micro Gas Turbine Based Test Rig," ASME Paper No. GT2008-50617.

[21] 2002, Turbec T100 Series 3, Installation Handbook.

[22] Young, H. D., 1962, *Statistical Treatment of Experimental Data: An Introduction to Statistical Methods*, McGraw-Hill, New York.

[23] Ghigliazza, F., Traverso, A., Pascenti, M., and Massardo, A. F., 2009, "Micro Gas Turbine Real-Time Modeling: Test Rig Verification," ASME Paper No. GT2009-59124.

Comparison of Three Microturbine Primary Surface Recuperator Alloys

Wendy J. Matthews
Capstone Turbine Corporation,
Chatsworth, CA 91311

Karren L. More

Larry R. Walker

Oak Ridge National Laboratory,
Oak Ridge, TN 37831

Extensive work performed by Capstone Turbine Corporation, Oak Ridge National Laboratory, and various others has shown that the traditional primary surface recuperator alloy, type 347 stainless steel, is unsuitable for applications above 650°C (~1200°F). Numerous studies have shown that the presence of water vapor greatly accelerates the oxidation rate of type 347 stainless steel at temperatures above 650°C (~1200°F). Water vapor is present as a product of combustion in the microturbine exhaust, making it necessary to find replacement alloys for type 347 stainless steel that will meet the long life requirements of microturbine primary surface recuperators. It has been well established over the past few years that alloys with higher chromium and nickel contents than type 347 stainless steel have much greater oxidation resistance in the microturbine environment. One such alloy that has replaced type 347 stainless steel in primary surface recuperators is Haynes Alloy HR-120 (Haynes and HR-120 are trademarks of Haynes International, Inc.), a solid-solution-strengthened alloy with nominally 33 wt % Fe, 37 wt % Ni and 25 wt % Cr. Unfortunately, while HR-120 is significantly more oxidation resistant in the microturbine environment, it is also a much more expensive alloy. In the interest of cost reduction, other candidate primary surface recuperator alloys are being investigated as possible alternatives to type 347 stainless steel. An initial rainbow recuperator test has been performed at Capstone to compare the oxidation resistance of type 347 stainless steel, HR-120, and the Allegheny Ludlum austenitic alloy AL 20–25+Nb (AL 20–25+Nb is a trademark of ATI Properties, Inc. and is licensed to Allegheny Ludlum Corporation). Evaluation of surface oxide scale formation and associated alloy depletion and other compositional changes has been carried out at Oak Ridge National Laboratory. The results of this initial rainbow test will be presented and discussed in this paper. [DOI: 10.1115/1.3157094]

1 Introduction

[1]A primary surface recuperator (PSR) is a counter flow heat exchanger with a core manufactured from thin corrugated metallic foils. The addition of a PSR, used to recover the heat energy of exhaust gas by preheating combustion air, can almost double the thermal efficiency of a small gas turbine such as the Capstone MicroTurbine [1]. A large number of PSR designs have been investigated over the years, with Capstone opting to use an all-welded annular PSR. This robust annular design, used on both the Capstone C30 and C65 MicroTurbines, has a significant impact on the microturbine thermal efficiency [2]. The all-welded annular PSR design has proven to be resistant to fatigue cracking due to thermal and pressure cyclings.

When the PSR was first introduced as a microturbine component, type 347 stainless steel (347SS) was the material of choice. This Niobium-stabilized grade of 300 series stainless steel provided a good combination of creep and oxidation resistance with relatively low direct raw material cost. As PSRs were put into production and began to accumulate significant operating exposure, stability issues associated with the 347SS were discovered. Creep damage in certain applications resulted in blockage of the hot gas flow through the recuperator, causing reduced recuperator effectiveness [3]. In other applications, accelerated rates of oxidation were observed in the PSR thin foil material leading to blockage of flow channels (due to excessively thick oxide scale) and to complete oxidation of the PSR foils, which both result in reduced PSR effectiveness [3–5].

At the same time, extensive laboratory research was being carried out to characterize the effect of water vapor on the oxidation rate of 347 stainless steel and other recuperator alloys. A number of researchers have shown that at operating temperatures in excess of ~600°C (~1110°F), small amounts of water vapor will significantly increase the rate of oxidation of chromia-forming stainless steels such as 347SS, resulting in what is sometimes referred to as accelerated attack (AA) [6–11]. The increased rate of oxidation leads to an increased rate of Cr-depletion at the foil surface, which in turn leads to breakaway oxidation. Breakaway oxidation is also referred to as chemical failure and is specifically identified as mechanically induced chemical failure (MICF) when it occurs in this temperature regime [12]. MICF occurs once the Cr-depletion occurring across the thickness of the foil has reached a level below the critical Cr-concentration required to maintain and reform a healing chromia-scale. The effect of water vapor on the oxidation rate of 347SS was an important discovery, since newer generation microturbines operate with turbine-exit temperature (TET) or PSR inlet temperature above 650°C (~1200°F). The Capstone C65 has a PSR inlet temperature of ~666°C (~1230°F) with ~3–4 vol % water vapor (as a product of combustion) in the turbine exit gas.

At the same time that the effects of water vapor on the oxidation rate of 347SS were being evaluated, alternative materials with greater oxidation resistance were also being developed and characterized [13–15]. Studies have shown that increasing the amount of Cr and/or Ni present in an alloy will prevent or greatly reduce

[1]MicroTurbine is a registered trademark of Capstone Turbine Corporation.

Contributed by the International Gas Turbine Institute of ASME for publication in the JOURNAL OF ENGINEERING FOR GAS TURBINES AND POWER. Manuscript received March 19, 2009; final manuscript received March 23, 2009; published online November 5, 2009. Review conducted by Dilip R. Ballal. Paper presented at the ASME Gas Turbine Technical Congress and Exposition, Orlando, FL, June 8–12, 2009.

Table 1 Typical chemical composition of HR-120, AL 20–25 +Nb, and 347SS (wt %)

Element	HR-120 (N08120) [21]	AL 20–25+Nb [17]	347SS (S34700) [22]
Ni	37.0	25.5	10.5
Cr	25.0	20.5	18.0
Mn	0.7	1.0	2.00[a]
C	0.05	0.08	0.08[a]
Cu	–	–	0.75[a]
Si	0.6	–	1.00[a]
S	–	–	0.030[a]
Al	0.1	–	–
Nb	0.7	0.4	0.95
Mo	2.5[a]	1.5	0.75[a]
P	–	–	0.040[a]
W	2.5[a]	–	–
Co	3.0[a]	–	–
N	0.20	0.1	–
B	0.004	–	–
Fe	As balance (~33 wt %)	As balance (~50 wt %)	As balance (~66 wt %)

[a]Maximum

the rate of accelerated attack [16,17]. Alumina-forming austenitic alloys are also being investigated as possible alternatives to 347SS [18].

Based on the published results of various researchers, and the extensive characterization of 347SS field-operated Capstone PSRs, the material used to manufacture the Capstone C65 PSR was changed to Haynes alloy HR-120 [19,20]. While the HR-120 PSR performs exceptionally well, and has shown no signs of AA after extensive long-term elevated temperature exposures, the alloy is significantly more expensive than 347SS. The higher cost is primarily due to the much higher Cr and Ni content of HR-120. The Allegheny Ludlum (AL) austenitic alloy AL 20–25+Nb has been proposed as a lower cost alternative to HR-120. AL 20–25 +Nb contains more Cr and significantly more Ni than 347SS, though the content of both elements is not as high as that of HR-120. The chemical compositions of HR-120, AL 20–25+Nb, and 347SS are given in Table 1. It is anticipated that the oxidation resistance of AL 20–25+Nb will be lower than HR-120, but significantly higher than that of 347SS.

In an effort to better understand the oxidation resistance of AL 20–25+Nb when compared with HR-120 and 347SS, Capstone manufactured a "rainbow" PSR from the three alloys. This rainbow PSR was subjected to an elevated temperature cyclic test, and samples were removed for analysis at Oak Ridge National Laboratory (ORNL). This paper presents the results of the post-exposure characterization of the surface oxide scale and associated alloy depletion and other compositional changes that have occurred in all three alloys tested. It is not the intent of this paper to develop a life prediction model for any of the alloys examined, but to provide a direct comparison between the three alloys after exposure to identical operating conditions.

2 Experimental Procedure

2.1 PSR Core Production. The heart of the PSR is the counter flow heat exchanger core, as shown in Fig. 1. Capstone Turbine Corporation has been manufacturing 347SS PSR cores since 2001 (C30 and original C60) [2], and HR-120 PSR cores since 2005 (C60/C65 replaced 347SS) [20,23]. A number of complex manufacturing steps are involved in the production of a PSR core.

Cold-rolled ~80 μm (3.2 mils) thick foil in the bright annealed condition is formed into what is called the fin-fold, which is a wavy corrugated pattern [5,19,20]. Individual aircell sheets, comprised of both fin-folded and crushed regions, are fabricated after subjecting the fin-folded stock material to crushing and trimming operations. These sheets, known as the primary sheets, are made with a slight offset in the fin-fold pattern resulting in "A" and "B" primary sheets. Various spacer bars are welded together with the two primary sheets to create an individual aircell, as shown in the inset of Fig. 1. The aircells are bent into a curved shape and ~165–170 aircells are stacked together for welding to become the PSR core. The turbine exit gas flows between the aircells of the PSR core, preheating the compressor discharge air flowing inside the aircells before it exits to the combustor.

Fig. 1 Primary surface recuperator (PSR) core with individual aircell (inset)

2.2 Rainbow PSR Engine Testing. Individual aircells were manufactured using HR-120, AL 20–25+Nb, and 347SS. A rainbow PSR core was then stacked and welded containing $\frac{1}{3}$ HR-120, $\frac{1}{3}$ AL 20–25+Nb, and $\frac{1}{3}$ 347SS aircells. A recuperator was built using this rainbow core and installed on a Capstone C65 MicroTurbine. The engine was used to perform an elevated temperature cyclic test.

The test engine ran with a TET set-point ~55C° (~100F°) above the normal operating TET set-point, resulting in an average PSR inlet temperature of ~720°C (1330°F). The cyclic testing was performed using an aggressive profile of 1 cycle/h at the elevated TET set-point with a minimum temperature drop on cool down of 500°C (~900°F) between cycles. The aggressive cycle and elevated TET set-point were chosen in an effort to accelerate the rate of oxidation experienced by the rainbow PSR core. The test engine accumulated a total of 1642 h and 1551 cycles.

Previous Capstone experience has shown that for 347SS, every cycle with a temperature drop on cool down similar to or greater than that used in the elevated TET test is equivalent to ~1.5 h of steady-state operation [5]. This means that the Equivalent Operating Hours (EOH) experienced by 347SS at the elevated TET set-point was 1642 h plus 1.5 times 1551 cycles, or ~3969 EOH. Previous experience has also shown that a 347SS PSR core operating at normal TET set-point has ~3.2 times the oxidation life of a 347SS PSR core, operating at the TET set-point used for the elevated TET testing [20]; thus, ~3969 EOH at the elevated TET set-point is considered to be equivalent to ~12,700 EOH for 347SS at normal operating TET set-point.

3 Results

Once the elevated TET cyclic test was completed, the rainbow core was removed from the PSR. Sections were cut from the hot turbine-exit gas-inlet side of the core. Samples of HR-120, AL 20–25+Nb, and 347SS aircells were examined using electron-probe microanalysis (EPMA). The ORNL JEOL JXA-8200 Combined Microanalyzer, equipped with both wavelength and energy

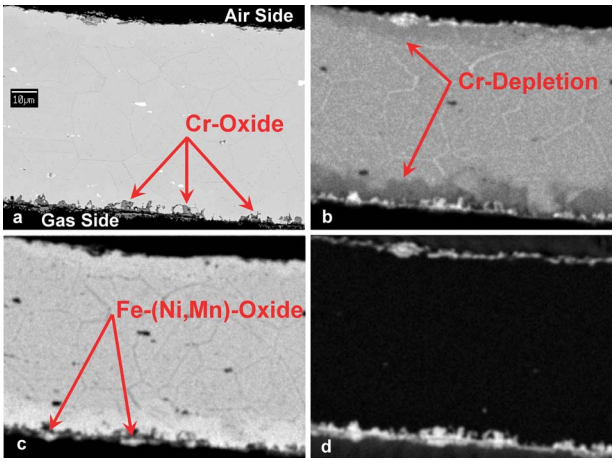

Fig. 2 HR-120 sample from rainbow PSR: (*a*) BSE image, (*b*) Cr map, (*c*) Fe map, and (*d*) O map

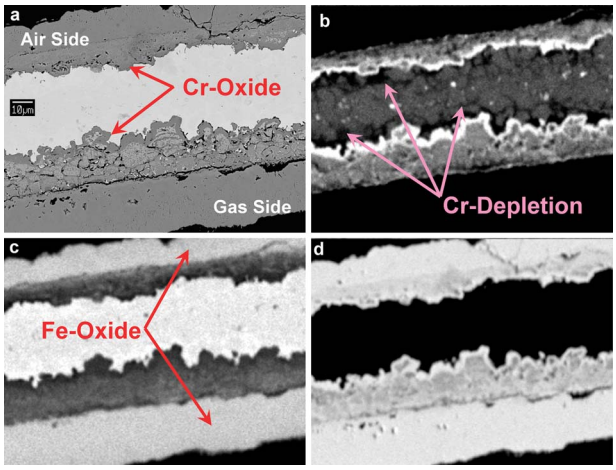

Fig. 4 347SS sample from rainbow PSR: (*a*) BSE image, (*b*) Cr map, (*c*) Fe map, and (*d*) O map

dispersive spectrometers (W/EDS), was used to perform microstructural and compositional characterization of the rainbow PSR core samples.

With reference to the samples removed from actual PSR core aircells, the inside of the aircell (exposed to compressor air) is called the "air side" and the outside of the aircell (exposed to exhaust gas) is called the "gas side." All figures shown are labeled to identify the air side and the gas side of the image.

Cross section samples were prepared from the hot gas inlet side of the engine-exposed rainbow PSR aircells, with samples being taken from both the crushed and fin-folded regions of the aircells. All of the samples were examined with the same types of analyses being performed from both regions of the aircells. The oxidation damage was more severe in the crushed region for all of the samples. The crushed region corresponds to the region of highest temperature exposure at the recuperator inlet and thus, all data presented herein are for samples from the crushed regions.

3.1 Qualitative Analysis. Elemental maps for each of the HR-120, AL 20–25+Nb, and 347SS samples were acquired using W/EDS and are shown in Figs. 2–4, respectively. These maps provide a relative measure of the difference in the extent of surface oxidation and Cr-depletion experienced by the HR-120, AL 20–25+Nb, and 347SS elevated TET aircells from the rainbow PSR core, after identical engine-exposure conditions. Higher relative concentrations of the element being mapped are indicated by the brighter regions of the images.

Figure 2(*a*) is a backscatter electron (BSE) image of the location chosen for element mapping on the HR-120 sample. As has been shown in previous analyses [19,20,23], a thicker, Cr-rich oxide scale has formed on the gas side of the foil (bottom of image). Figures 2(*b*)–2(*d*) are element maps showing the distribution of Cr, Fe, and O.

The element maps in Fig. 2 show a very thin Cr-oxide layer on both the air and gas sides of the sample. The gas side of the sample also has a thin outer layer of Fe–(Ni,Mn) oxide. Cr-depletion is occurring below the oxide scale on the gas side of the sample. The extent of Cr-depletion appears to be consistent within the grains and along the grain boundaries of the HR-120 material, i.e., there does not appear to be any selective Cr-depletion occurring along the grain boundaries. Such nonselective Cr-depletion has been observed on several long-term elevated TET HR-120 samples [23] and on field-operated PSR cores [24]. Work is ongoing to establish a correlation between the oxidation damage experienced at the elevated TET set-point and that at the normal operating TET set-point.

Figure 3(*a*) is a BSE image of the AL 20–25+Nb sample, and Figs. 3(*b*)–3(*d*) are element maps showing the distribution of Cr, Fe, and O.

The element maps in Fig. 3 show a very thin Cr-oxide layer on both the air and gas sides of the sample. The gas side of the sample also has a relatively thin intermittent outer layer of Fe-oxide in the form of small nodules similar to those observed on the AL 20–25+Nb material examined by other researchers [15,25]. Cr-depletion is occurring below the oxide scale, primarily on the gas side of the sample, and selectively along grain boundaries to a depth of ~1/3 of the thickness of the foil sample.

Figure 4(*a*) is a BSE image of the 347 SS sample, with element maps for Cr, Fe, and O shown in Figs. 4(*b*)–4(*d*). These maps indicate a thick, multicomponent oxide scale present on both the air and gas sides of the sample, typical of the accelerated attack observed in 347SS PSRs [5,20].

The innermost oxide layer, immediately adjacent to the region of Cr-depletion, is predominantly Cr-rich oxide, while the thick outermost oxide scale is Fe-oxide, typical of the nodules that form upon breakdown of the Cr-rich layer and spread across the outer surface [5]. A further oxide layer, between the Cr-rich and Fe-rich oxides, contains Cr, Fe, and Ni. Cr-depletion extends through the thickness of the sample, selectively along the grain boundaries. The thick multicomponent oxide scale on both the air and gas sides of the 347SS sample is typical of the AA that has been

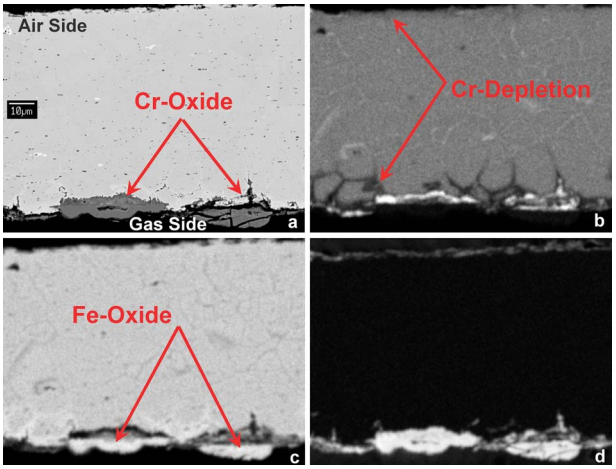

Fig. 3 AL 20–25+Nb sample from rainbow PSR: (*a*) BSE image, (*b*) Cr map, (*c*) Fe map, and (*d*) O map

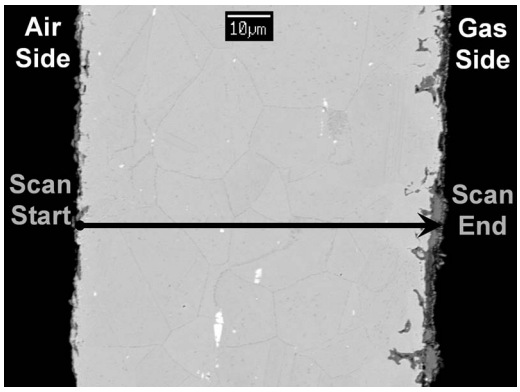

Fig. 5 HR-120 profile scan location

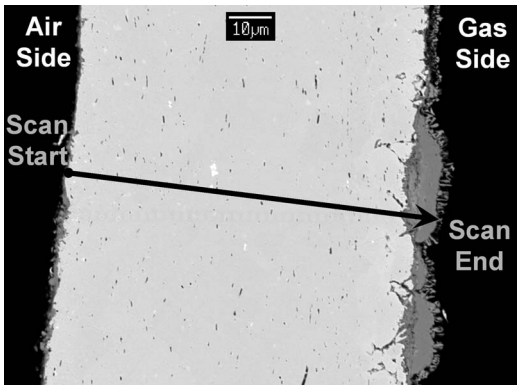

Fig. 7 AL 20–25+Nb profile scan location

observed in 347SS PSRs [5,20]. The extent of Cr-depletion visible is very similar to that measured for a 12,400 EOH 347SS sample [5].

3.2 Quantitative Analysis. Compositional analyses of the three alloys include estimates of Cr-loss from the starting (bulk) Cr-reservoir. Methods for predicting the extent of Cr-loss in thin foil sections based on chromium volatilization rates have been proposed and developed [26]; however, these require measurement of mass change over time, making them impractical for use with samples removed from field-exposed PSRs. In this work, the starting Cr contents of the HR-120, AL 20–25+Nb, and 347SS are based on the nominal compositions given in Table 1, i.e., 25.0 wt %, 20.5 wt %, and 18.0 wt %, respectively. Estimation of the amount of Cr-loss from the starting Cr-reservoir is based on the amount of the starting foil thickness consumed by oxidation, and the depth and level of Cr-depletion. This procedure for estimating the Cr-loss from the starting reservoir has been described elsewhere [5,23]. While this method is somewhat simplistic, it has proven sufficient for purposes of alloy comparison and component life prediction [5,23].

A BSE image of a typical profile scan location for the HR-120 sample is shown in Fig. 5, and the corresponding element profile scan for Cr, Fe, Ni, and O is shown in Fig. 6. The various measurements indicated that this sample has experienced ~4.4% Cr-loss from the starting Cr-reservoir to ~23.9 wt % Cr, that is, it retained 95.6% of the original starting Cr content.

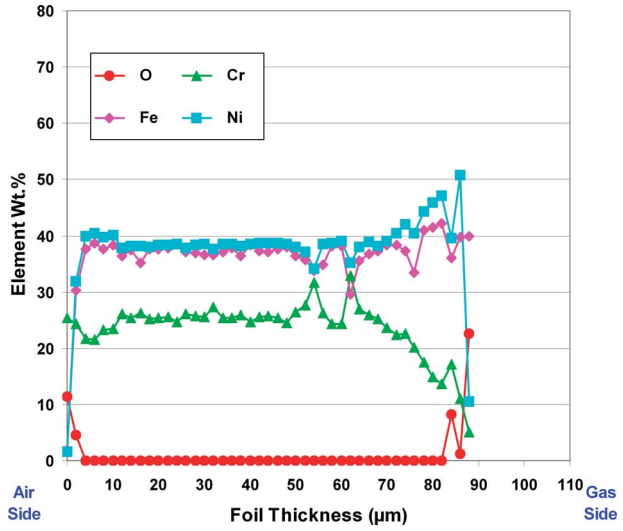

Fig. 6 HR-120-EPMA O, Cr, Fe, and Ni profiles

Figures 7 and 8 are the BSE image and element profile scan, respectively, for the AL 20–25+Nb sample. This sample experienced ~8.9% Cr-loss from the starting Cr-reservoir, resulting in a net Cr level of ~18.7 wt %, or ~91.1% of the original starting Cr content.

Similar data for the 347SS sample are shown in Figs. 9 and 10, and indicate a Cr-loss from the starting Cr-reservoir of ~51% to ~8.8 wt % Cr. Previous analyses have shown that once the Cr

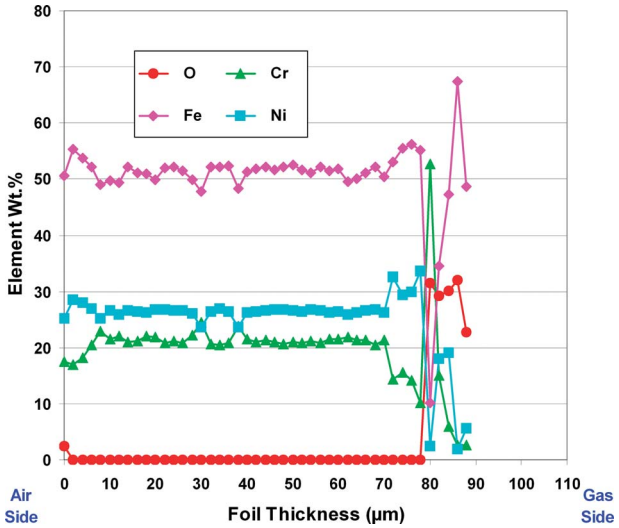

Fig. 8 AL 20–25+Nb: EPMA O, Cr, Fe, and Ni profiles

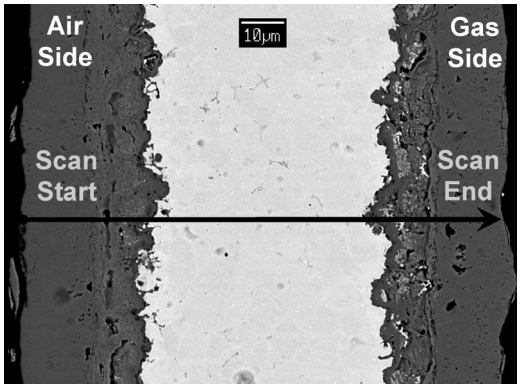

Fig. 9 347SS profile scan location

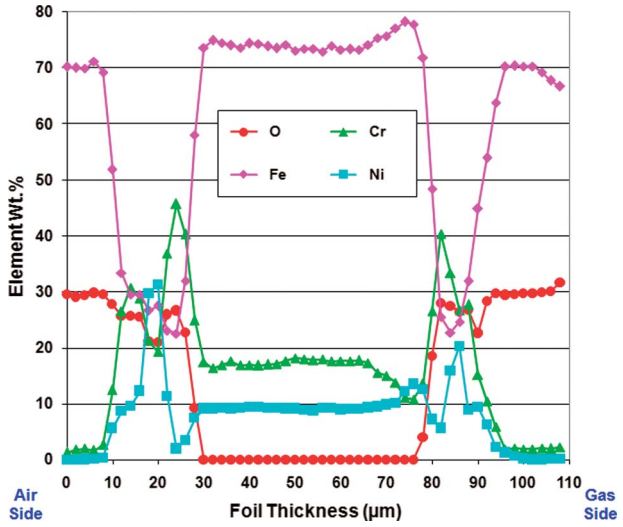

Fig. 10 347SS-EPMA O, Cr, Fe, and Ni profiles

level in 347SS is depleted to below ~11–13 wt %, breakaway oxidation occurs with rapid consumption of the foil [5].

A comparison of the post-exposure Cr profiles of the three PSR alloys examined is shown in Fig. 11. The profiles are for the full foil thickness between the oxide layers and include the Cr-depleted layers. It is clearly observed that a significant amount of the starting 347SS foil thickness has been lost to oxidation, since the Cr profile covers only ~46 μm (~1.8 mils) of material. In addition, the thickness of the foil that still retains approximately the starting nominal Cr content (18 wt %) is only ~16 μm (~0.6 mils). The HR-120 and AL 20–25+Nb profiles show similar Cr-depletion depths and similar thicknesses of foil retaining the starting nominal Cr content, but it is clear that the HR-120 retains significantly more Cr than the AL 20–25+Nb. The higher Cr retention of the HR-120 foil is directly related to the much higher starting nominal Cr content. It should be noted that the Cr-depletion along the grain boundaries of the AL 20–25+Nb has not been accurately captured by the Cr profiles shown in Fig. 11.

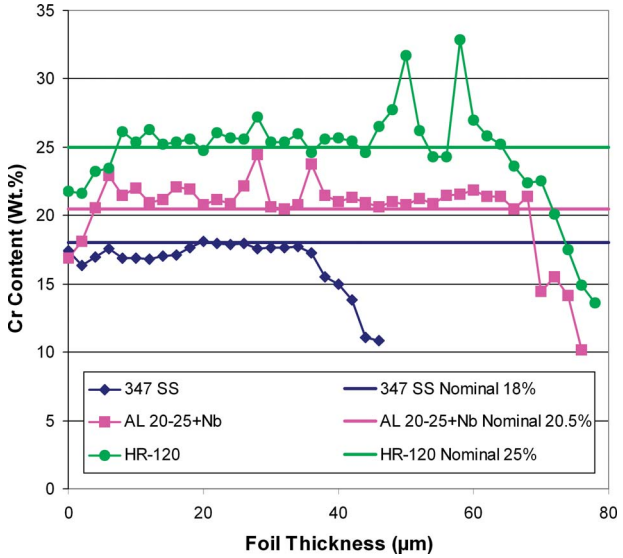

Fig. 11 Comparison of postexposure Cr profiles of HR-120, AL 20–25+Nb, and 347SS

Table 2 Total Cr-loss from bulk starting reservoir and remaining Cr content

Material	Total Cr-loss from starting reservoir (%)	Remaining foil Cr content (wt %)
HR-120	4.4	23.9
AL 20–25+Nb	8.9	18.7
347SS	51.0	8.8

4 Summary

The elevated TET cyclic rainbow test has provided a direct comparison of three PSR alloys: 347SS, AL 20–25+Nb, and HR-120. The 347SS experienced excessive oxidation, with breakaway oxidation either occurring or imminent, while the HR-120 alloy exhibited minimal oxidation damage. The AL 20–25+Nb alloy experienced significantly less oxidation damage than 347SS, though its resistance was not as great as HR-120. The comparative oxidation resistance of the three alloys was characterized by estimating the total Cr-loss during the test; the results are summarized in Table 2.

The onset of accelerated attack in 347SS is generally signaled by the formation of Fe-oxide nodules, which ultimately leads to breakaway oxidation [6,8,9,16]. Fe-rich oxide nodule formation apparently is associated with surface exposed Cr-depleted grain boundaries, or to localized Cr_2O_3 evaporation and/or rapid Fe diffusion through the Cr-rich oxide [5,15]. In service, 347SS PSRs have exhibited Fe-oxide nodule formation after relatively short times of less than 2000 h [5]. With an estimated 12,700 EOHs for the 347SS foil in this rainbow test, the sample progressed well beyond the Fe-oxide nodule formation phase.

Fe-oxide nodule formation did not occur on the HR-120 samples, nor has nodule formation been observed in any of the HR-120 samples analyzed to date [23,24]. The lack of nodule formation on HR-120 samples may be due to a number of factors: (i) the higher Ni content of HR-120 may be impeding or preventing nodule formation, (ii) the presence of both Ni and Mn in the outward growing Fe-rich oxide also may slow down or eliminate nodule formation (347SS PSR samples, with much lower Ni content, all developed an outward growing Fe-oxide that did not contain Ni or Mn [5,23]), and (iii) nonselective Cr-depletion observed in these and in previously characterized HR-120 samples [23] may also play a role in the prevention of Fe-oxide nodule formation. Since analysis of laboratory-exposed HR-120 samples indicated that nodule formation occurred at locations of grain boundary Cr-depletion [15], the lack of preferential grain boundary Cr-depletion in engine-exposed HR-120 PSR foils may also be a contributing factor.

Fe-oxide nodule formation was observed on the AL 20–25+Nb rainbow samples, and has been observed by other researchers [15,25], although the rate of growth of such nodules on this alloy apparently slows after initial formation [27]. In this study, Fe-oxide nodules on AL 20–25+Nb appeared to form over regions of Cr-oxide and Cr-depleted grain boundaries. These samples also exhibited selective Cr-depletion along the grain boundaries, similar to the behavior of 347SS, but not as extensive.

Breakaway oxidation is the greatest concern for PSR life. The length of time that the PSR foil retains sufficient Cr content to continue to form and reform the protective oxide layer, thereby healing any flaws at the oxide surface, will determine the PSR operating life. Once the Cr content in the PSR foil falls below this critical value, extremely rapid (breakaway) oxidation will occur. Previous analyses have shown that the critical Cr content below, which breakaway oxidation will occur in 347SS, is ~11–13 wt %. The Cr levels in the 347SS samples from this test fell below this critical Cr content, and breakaway oxidation en-

sued. The critical Cr content for a 20Cr-25Ni austenitic stainless steel, similar to AL 20–25+Nb, has been shown to be ~16 wt % [12,25,27]. The AL 20–25+Nb samples from this test had 18.7 wt % Cr remaining and no breakaway oxidation was observed. The critical Cr content for HR-120 is unknown, but is likely to be similar to that of AL 20–25+Nb. The HR-120 samples from this test retained 23.9 wt % Cr, and showed no sign of breakaway oxidation.

The estimates of total Cr-loss summarized in Table 2 suggest that in this test the rate of loss of Cr from AL 20–25+Nb was approximately twice that for HR-120, suggesting that AL 20–25 +Nb may provide only half the oxidation life of HR-120 in the PSR application. Additional testing in the microturbine environment under service conditions is necessary to provide confirmation of these life estimates.

Acknowledgment

Part of this research was sponsored by the Assistant Secretary for Energy Efficiency and Renewable Energy, Office of Freedom-CAR and Vehicle Technologies, as part of the High Temperature Materials Laboratory User Program, Oak Ridge National Laboratory, managed by UT-Battelle, LLC, for the U.S. Department of Energy under Contract No. DE-AC05-00OR22725.

References

[1] Kang, Y., and McKeirnan, R., 2003, "Annular Recuperator Development and Performance Testing for 200 kW Microturbine," ASME Paper No. GT2003-38552.
[2] Treece, B., Vessa, P., and McKeirnan, R., 2002, "Microturbine Recuperator Manufacturing and Operating Experience," ASME Paper No. GT-2002-30404.
[3] Rakowski, J. M., Stinner, C. P., Lipschutz, M., and Montague, J. P., 2004, "The Use and Performance of Oxidation and Creep-Resistant Stainless Steels in an Exhaust Gas Primary Surface Recuperator Application," ASME Paper No. GT2004-53917.
[4] Lara-Curzio, E., More, K. L., Maziasz, P. J., and Pint, B. A., 2004, "Screening and Evaluation of Materials for Microturbine Recuperators," ASME Paper No. GT2004-54254.
[5] Matthews, W. J., More, K. L., and Walker, L. R., 2007, "Accelerated Oxidation of Type 347 Stainless Steel Primary Surface Recuperators Operating Above 600°C," ASME Paper No. GT200-27190.
[6] Pint, B. A., and Peraldi, R., 2003, "Factors Affecting Corrosion Resistance of Recuperator Alloys," ASME Paper No. GT2003-38692.
[7] Rakowski, J. M., 2001, "The Oxidation of Austenitic Stainless Steel Foils in Humidified Air," ASME Paper No. 2001-GT-0360.
[8] Pint, B. A., Swindeman, R. W., More, K. L., and Tortorelli, P. F., 2001, "Materials Selection for High Temperature (750°–1000°C) Metallic Recuperators for Improved Efficiency Microturbines," ASME Paper No. 2001-GT-0445.
[9] Pint, B. A., More, K. L., and Tortorelli, P. F., 2002, "The Effect of Water Vapor on Oxidation Performance of Alloys Used in Recuperators," ASME Paper No. GT-2002-30543.
[10] Rakowski, J. M., 2003, "The Oxidation of Metal Alloy Foils in the Presence of Water Vapor," ASME Paper No. GT2003-38059.
[11] Pint, B. A., and More, K. L., 2004, "Stainless Steels With Improved Oxidation Resistance for Recuperators," ASME Paper No. GT2004-53627.
[12] Evans, H. E., Donaldson, A. T., and Gilmour, T. C., 1999, "Mechanisms of Breakaway Oxidation and Application to a Chromia-Forming Steel," Oxid. Met., **52**(5/6), pp. 379–401.
[13] Maziasz, P. J., Pint, B. A., and Swindeman, R. W., 2003, "Selection, Development and Testing of Stainless Steels and Alloys for High-Temperature Recuperator Applications," ASME Paper No. GT2003-38762.
[14] Maziasz, P. J., Pint, B. A., Shingledecker, J. P., More, K. L., Evans, N. D., and Lara-Curzio, E., 2004, "Austenitic Stainless Steels and Alloys With Improved High-Temperature Performance for Advanced Microturbine Recuperators," ASME Paper No. GT2004-54239.
[15] Pint, B. A., 2005, "The Effect of Water Vapor on Cr Depletion in Advanced Recuperator Alloys," ASME Paper No. GT2005–68495.
[16] Pint, B. A., and Rakowski, J. M., 2000, "Effect of Water Vapor on the Oxidation Resistance of Stainless Steels," NACE Corrosion 2000, Orlando, FL, NACE Paper No. 00-59.
[17] Rakowski, J. M., Stinner, C. P., Bergstrom, D. S., Lipschutz, M., and Montague, J. P., 2005, "Performance of Oxidation and Creep Resistant Alloys for Primary Surface Recuperators for the Mercury 50 Gas Turbine," ASME Paper No. GT2005-68313.
[18] Pint, B. A., Shingledecker, J. P., Brady, M. P., and Maziasz, P. J., 2007, "Alumina-Forming Austenitic Alloys for Advanced Recuperators," ASME Paper No. GT2007-27916.
[19] Matthews, W. J., Bartel, T., Klarstrom, D. L., and Walker, L. R., 2005, "Engine Testing of an Advanced Alloy for Microturbine Primary Surface Recuperators," ASME Paper No. GT2005-68781.
[20] Matthews, W. J., 2006, "Additional Engine Testing of an Advanced Alloy for Microturbine Primary Surface Recuperators," ASME Paper No. GT2006-90068.
[21] Haynes International Inc., 1992, "Haynes HR-120 Alloy," Alloy Brochure H-3125B.
[22] SAE International, "Steel, Corrosion and Heat Resistant, Sheet, Strip, and Plate 18Cr–0.5Ni–0.80Cb (SAE 30347) Solution Heat Treated, UNS S34700," Aerospace Material Specification, AMS 5512.
[23] Matthews, W. J., More, K. L., and Walker, L. R., 2008, "Long-Term Microturbine Exposure of an Advanced Alloy for Microturbine Primary Surface Recuperators," ASME Paper No. GT2008-50037.
[24] Capstone Turbine Corporation, Confidential and Proprietary Internal Correspondence.
[25] Rakowski, J. M., Stinner, C. P., Lipschutz, M., and Montague, J. P., 2007, "Environmental Degradation of Heat-Resistant Alloys During Exposure to Simulated and Actual Gas Turbine Recuperator Environments," ASME Paper No. GT2007-27949.
[26] Young, D. J., and Pint, B. A., 2006, "Chromium Volatilization Rates From Cr_2O_3 Scales Into Flowing Gases Containing Water Vapor," Oxid. Met., **66**, pp. 137–153.
[27] Rakowski, J. M., Stinner, C. P., Lipschutz, M., and Montague, J. P., 2008, "Environmental Degradation of Heat-Resistant Alloys During Exposure to Simulated and Actual Gas Turbine Recuperator Environments," ASME Paper No. GT2008-51336.

Nonlinear Dynamic Analysis and Experiment Verification of Rotor-Ball Bearings-Support-Stator Coupling System for Aeroengine With Rubbing Coupling Faults

G. Chen[1]
College of Civil Aviation,
Nanjing University of Aeronautics and Astronautics,
Jiangsu, Nanjing, 210016, P.R.C.
e-mail: cgzyx@263.net

C. G. Li
e-mail: lichenggang606@126.net

D. Y. Wang

Strength and Vibration Technique Center,
Shenyang Aeroengine Research Institute,
Liaoning, Shenyang, 110015, P.R.C.

In this paper, a new rotor-ball bearings-support-stator coupling system dynamic model with rubbing coupling faults is established for practical aeroengine. In the model, the rubbing fault is modeled, the stator motion is considered, the flexible support and squeeze film damper are established, and the nonlinear factors of ball bearing, such as the clearance of the bearing, the nonlinear Hertzian contact force between balls and races, and the varying compliance vibration because of the periodical variety of the contact position between balls and races, are modeled. The numerical integral method is used to obtain the system responses, the effect of support stiffness on rotor responses is studied using a vibration amplitude-rotating speed plot, and the characteristics of the rubbing fault is analyzed using a 3D cascade plot. An aeroengine tester with a stator is established to carry out the rubbing fault experiments, the simulation results from the rotor-ball bearings-support-stator coupling model are compared with the experimental results, and the consistency of the results show fully the effectiveness of the new rotor-ball bearings-support-stator coupling model with rubbing fault. [DOI: 10.1115/1.2940355]

1 Introduction

Usually, the rotor of an aeroengine is supported on the stator by way of bearings, and the stator is supported on the foundation. In order to reduce the rotor vibration and adjust the rotor's critical rotating speed, a flexible support and a squeeze film damper (SFD) are often used between the bearing and the bearing housing. Therefore their motions are affected by each other, and the rotor-ball bearings-support-stator coupling system is formed. With aeroengine performance improving continuously, in order to improve the thrust/weight ratio and increase the structural efficiency, researchers are trying to improve the geometric configuration of the structure to make full use of the material's characteristics. One of the most important methods is to reduce the clearance between the rotor and the stator, and seal structures (such as zirconia, honeycomb structure, etc.) are adopted on the rotor and the stator to obtain the least clearance between them, so that the possibility of rotor-to-stator rubbing is greatly increased. Rotor-stator rubbing will widen the rotor-stator clearance, aggravate the wear of the bearings, break the blades off, and break the engine down. Usually, the rubbing is a twinborn fault, which is caused by imbalance, misalignment, pedestal looseness, oil-film whirling and so on; therefore it possesses the typical characteristics of a coupling fault. Presently, increasing researchers started gradually to study the rubbing coupling faults [1–5]. In Refs. [2–4], the characteristics of rubbing-pedestal looseness coupling faults were studied, and in Ref. [5], the response characteristics of a rotor system with rubbing and crack were analyzed. At present, the studies of multifault coupling dynamic model with rubbing fault mainly aim at sliding bearings; however, ball bearings are widely used in aeroengine, and therefore, it is of great significance to establish a detailed model of ball bearings in an aeroengine rotor system. In recent years, the multifault coupling rubbing fault dynamic models supported on ball bearings have also rapidly developed, and many valuable results have been obtained. Reference [6], aimed at an aeroengine rotor experimental rig, established a rotor-ball bearings-stator model: but in this model, the modeling of ball bearings was too simple and some nonlinear factors were not thought into, such as the stiffness variety and the clearance of ball bearings; in addition, flexible support and a SFD between bearings and bearing housings were not considered in detail in Ref. [6]. Therefore, aiming at the rotor-bearing system of practical aeroengine, this paper will establish a new rotor-ball bearings-support-stator coupling system dynamic model. In the model, the nonlinear contact force, the periodic variety of total stiffness, and the clearance of ball bearing are fully considered. In the coupling model, a dynamic model with imbalance and rubbing coupling fault is established, and the nonlinear characteristics of this system are studied in detail. Finally, an aeroengine rotor tester with a stator is designed to carry out the rubbing fault experiments, and the simulation results from rotor-ball bearings-support-stator coupling model are compared with the experimental results in order to verify the effectiveness of the new rotor-ball bearings-support-stator coupling model with rubbing coupling fault.

2 Rotor-Ball Bearings-Support-Stator Coupling System With Imbalance-Rubbing Coupling Fault

Figure 1 is the sketch map of the rotor-ball bearings-support-stator coupling system dynamic model with imbalance and rubbing coupling faults. The two ends of this rotor are supported on the same ball bearings. The rubbing fault between the rotor and the stator is considered. When the rotor rotates, its lateral bending

[1]Corresponding author.

Manuscript received November 26, 2007; final manuscript received May 5, 2008; published online October 15, 2009. Review conducted by Patrick S. Keogh.

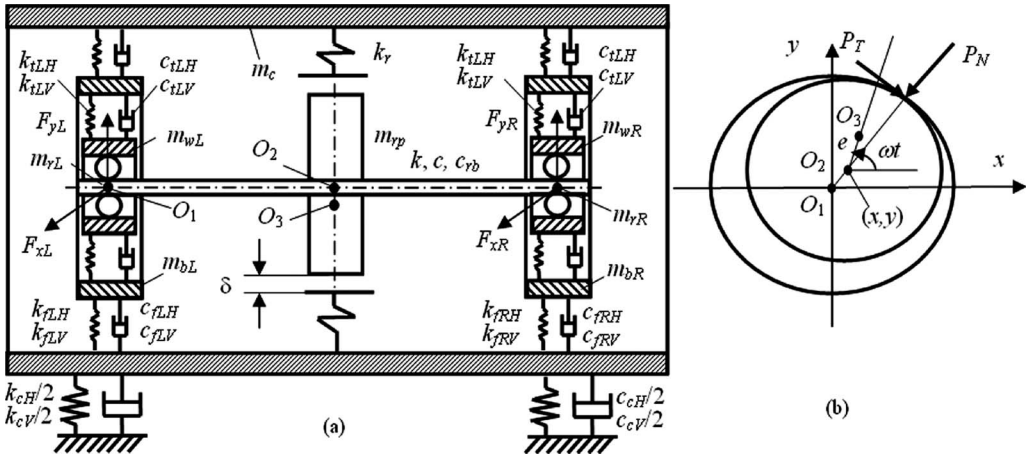

Fig. 1 Rotor-ball bearings-support-stator coupling model with imbalance and rubbing coupling faults

vibration is excited due to its mass imbalance, and once the vibration displacement exceeds the clearance between the rotor and the stator, the rotor-to-stator rubbing fault appears.

The explanations of symbols in Fig. 1 are shown in the Nomenclature. According to Newton's second law, the system differential equations are obtained as follows:

$$m_{rp}\ddot{x}_{rp} + k(x_{rp} - x_{rR}) + k(x_{rp} - x_{rL}) + c\dot{x}_{rp} = P_x + m_{rp}e\omega^2 \cos \omega t$$

$$m_{rp}\ddot{y}_{rp} + k(y_{rp} - y_{rR}) + k(y_{rp} - y_{rL}) + c\dot{y}_{rp} = P_y + m_{rp}e\omega^2 \sin \omega t - m_{rp}g$$

$$m_{bR}\ddot{x}_{bR} + k_{fRH}(x_{bR} - x_c) + c_{fRH}(\dot{x}_{bR} - \dot{x}_c) + k_{tRH}(x_{bR} - x_{wR}) + c_{tRH}(\dot{x}_{bR} - \dot{x}_{wR}) = 0$$

$$m_{bR}\ddot{y}_{bR} + k_{fRH}(y_{bR} - y_c) + c_{fRH}(\dot{y}_{bR} - \dot{y}_c) + k_{tRH}(y_{bR} - y_{wR}) + c_{tRH}(\dot{y}_{bR} - \dot{y}_{wR}) = -m_{bR}g$$

$$m_{bL}\ddot{x}_{bL} + k_{fLH}(x_{bL} - x_c) + c_{fLH}(\dot{x}_{bL} - \dot{x}_c) + k_{tLH}(x_{bL} - x_{wL}) + c_{tLH}(\dot{x}_{bL} - \dot{x}_{wL}) = 0$$

$$m_{bL}\ddot{y}_{bL} + k_{fLH}(y_{bL} - y_c) + c_{fLH}(\dot{y}_{bL} - \dot{y}_c) + k_{tLH}(y_{bL} - y_{wL}) + c_{tLH}(\dot{y}_{bL} - \dot{y}_{wL}) = -m_{bL}g$$

$$m_{rR}\ddot{x}_{rR} + k(x_{rR} - x_{rp}) + c_{rb}\dot{x}_{rR} - F_{xbR} = 0$$

$$m_{rR}\ddot{y}_{rR} + k(y_{rR} - y_{rp}) + c_{rb}\dot{y}_{rR} - F_{ybR} = -m_{rR}g$$

$$m_{rL}\ddot{x}_{rL} + k(x_{rL} - x_{rp}) + c_{rb}\dot{x}_{rL} - F_{xbL} = 0$$

$$m_{rL}\ddot{y}_{rL} + k(y_{rL} - y_{rp}) + c_{rb}\dot{y}_{rL} - F_{ybL} = -m_{rL}g$$

$$m_{wR}\ddot{x}_{wR} + k_{tRH}(x_{wR} - x_{bR}) + c_{tRH}(\dot{x}_{wR} - \dot{x}_{bR}) + F_{xbR} = 0$$

$$m_{wR}\ddot{y}_{wR} + k_{tRH}(y_{wR} - y_{bR}) + c_{tRH}(\dot{y}_{wR} - \dot{y}_{bR}) + F_{ybR} = -m_{wR}g$$

$$m_{wL}\ddot{x}_{wL} + k_{tLH}(x_{wL} - x_{bL}) + c_{tLH}(\dot{x}_{wL} - \dot{x}_{bL}) + F_{xbL} = 0 m_{wL}\ddot{y}_{wL} + k_{tLH}(y_{wL} - y_{bL}) + c_{tLH}(\dot{y}_{wL} - \dot{y}_{bL}) + F_{ybL} = -m_{wL}g$$

$$m_c\ddot{x}_c + k_{cH}x_c + c_{cH}\dot{x}_c + k_{fRH}(x_c - x_{bR}) + k_{fLH}(x_c - x_{bL}) + c_{fRH}(\dot{x}_c - \dot{x}_{bR}) + c_{fLH}(\dot{x}_c - \dot{x}_{bL}) = -P_x$$

$$m_c\ddot{y}_c + k_{cH}y_c + c_{cH}\dot{y}_c + k_{fRH}(y_c - y_{bR}) + k_{fLH}(y_c - y_{bL}) + c_{fRH}(\dot{y}_c - \dot{y}_{bR}) + c_{fLH}(\dot{y}_c - \dot{y}_{bL}) = -P_y - m_cg \quad (1)$$

The model of rubbing force. Supposing that r is the radial relative displacement between the rotor disk and the stator, and $r = \sqrt{(x_{rp}-x_c)^2+(y_{rp}-y_c)^2}$. When $r < \delta$, rubbing does not appear, namely, $P_x = P_y = 0$. When $r \geqslant \delta$, rubbing takes place. Supposing that the friction force obeys the Coulomb friction law, and there is always a relative motion between the rotor and the stator, then

$$P_N = k_r(r - \delta)$$
$$P_T = fP_N \quad (2)$$

where k_r is the rubbing contact stiffness and f is the dynamic friction coefficient. The rubbing force components in the X and Y directions are, respectively,

$$P_x = k_r(1 - \delta/r)[-(x_{rp} - x_c) + f(y_{rp} - y_c)]$$
$$P_y = k_r(1 - \delta/r)[-(y_{rp} - y_c) - f(x_{rp} - x_c)] \quad (3)$$

Ball bearing model. The ball bearing consists of an inner race, an outer race, rolling balls, and cages; the outer race acts on the inner race by rolling balls, and their interaction force is a restoring force, which is generated by the contact deformation between balls and races. In the rotor-ball bearing system, usually, the outer race of the ball bearing is fixed to the bearing housing and the inner race is rigidly fixed to the rotating shaft. When the ball bearing works, with the contact position between balls and races periodically varying, the total stiffness and compliance of the bearing will periodically vary, and the varying compliance (VC) of the bearing is a parametric excitation of a rotor-balling bearing coupling system, finally, a so-called VC vibration is generated. VC vibration is an inherent vibration; it always exists even if the bearing is new and does not have any fault.

Figure 2 is a sketch map of a ball bearing model, which makes reference to Refs. [7] and [9]. The excitations of the ball bearing come from two aspects: one is the rotor imbalance, and the other is the continuous periodic change of the total stiffness of the bearing, which is a parametric excitation.

In the ball bearing model, it is supposed that the balls are equispaced between the inner race and the outer race, and the contact angle of bearing is considered as zero. v_{outer} is the tangent velocity of the contact point between the ball and the outer race, v_{inner} is the tangent velocity of the contact point between the ball and the inner race, ω_{outer} is the rotating angular velocity of bear-

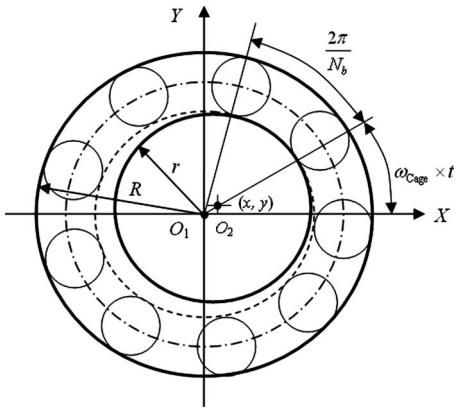

Fig. 2 A sketch map of ball bearing model

ing's outer race, ω_{inner} is the rotating angular velocity of bearing's inner race, R_o is the radius of the outer race, and r_i is the radius of the inner race. Therefore

$$v_{\text{outer}} = \omega_{\text{outer}} R_o \quad v_{\text{inner}} = \omega_{\text{inner}} R_i \tag{4}$$

The tangent velocity of the cage (the center of the ball) is given by

$$v_{\text{cage}} = (v_{\text{outer}} + v_{\text{inner}})/2$$

Because the outer race of the ball bearing is fixed to a rigid support, $v_{\text{outer}}=0$. Therefore,

$$v_{\text{cage}} = v_{\text{inner}}/2 = (\omega_{\text{inner}} R_i)/2$$

Therefore, the angular velocity of the cage is given by

$$\omega_{\text{cage}} = \frac{v_{\text{cage}}}{(R_o + R_i)/2} = \frac{(\omega_{\text{inner}} R_i)/2}{(R_o + R_i)/2} = \frac{\omega_{\text{inner}} R_i}{(R_o + R_i)} \tag{5}$$

Because the inner race is fixed to the shaft, $\omega_{\text{inner}}=\omega_{\text{rotor}}$. If N_b is the number of balls, then VC frequency can be given by

$$\omega_{VC} = \omega_{\text{cage}} N_b = \omega_{\text{rotor}} \left(\frac{R_i}{R_o + R_i} N_b \right) = \omega_{\text{rotor}} BN \tag{6}$$

where

$$BN = \frac{R_i}{R_o + R_i} N_b$$

Obviously, the number BN depends on the bearing size.

Supposing the angle location of the jth ball is θ_j, which is given by $\theta_j=\omega_{\text{cage}}t+(2\pi/N_b)(j-1)$, $j=1,2,\ldots N_b$, x and y are, respectively, vibration displacements of the center of the inner race in the X and Y directions, and r_0 is the bearing clearance, the normal contact deformation between the jth ball and races is given by

$$\Delta r_j = x \cos\theta_j + y \sin\theta_j - r_0 \tag{7}$$

According to the nonlinear Hertzian contact theory, the contact force f_j between the ball and the race due to the rolling contact can be gotten. At the same time, because the ball at an angular location θ_j can only give rise to a normal positive restoring force f_j, f_j must be greater than zero. Therefore, only when $\Delta r_j > 0$ can the contact force appear. By introducing the Heaviside function $H(x)$, whose definition is

$$H(x) = \begin{cases} 1, & x > 0 \\ 0, & x \le 0 \end{cases}$$

f_j can be obtained as follows:

$$\begin{aligned} f_j &= C_b[\Delta r_j]^{3/2} \\ &= C_b(x\cos\theta_j + y\sin\theta_j - r_0)^{3/2} H(x\cos\theta_j + y\sin\theta_j - r_0) \end{aligned} \tag{8}$$

where C_b is the Hertzian contact stiffness and it has relation with the contact material and shape. The components of f_j in the X and Y directions are

$$f_{jx} = C_b(x\cos\theta_j + y\sin\theta_j - r_0)^{3/2} H(x\cos\theta_j + y\sin\theta_j - r_0)\cos\theta_j \tag{9}$$

$$f_{jy} = C_b(x\cos\theta_j + y\sin\theta_j - r_0)^{3/2} H(x\cos\theta_j + y\sin\theta_j - r_0)\sin\theta_j$$

Therefore, the bearing forces generated by the ball bearing are given by

$$\begin{aligned} F_x &= \sum_{j=1}^{N_b} f_{jx} = \sum_{j=1}^{N_b} C_b(x\cos\theta_j + y\sin\theta_j - r_0)^{3/2} \\ &\quad \times H(x\cos\theta_j + y\sin\theta_j - r_0)\cos\theta_j \\ F_y &= \sum_{j=1}^{N_b} f_{jy} = \sum_{j=1}^{N_b} C_b(x\cos\theta_j + y\sin\theta_j - r_0)^{3/2} \\ &\quad \times H(x\cos\theta_j + y\sin\theta_j - r_0)\sin\theta_j \end{aligned} \tag{10}$$

Therefore, the bearing forces in Fig. 1 can be given by as follows:

(1) when $x=x_{wR}-x_{rR}$, $y=y_{wR}-y_{rR}$, then $F_{xbR}=F_x$, $F_{ybR}=F_y$
(2) when $x=x_{wL}-x_{rL}$, $y=y_{wL}-y_{rL}$, then $F_{xbL}=F_x$, $F_{ybL}=F_y$

Initial parameters. In this paper, the initial parameters of the rotor system are chosen as follows: $m_{rR}=m_{rL}=4.0$ kg, $m_{rp}=32.1$ kg, $c_{rb}=1050$ N s/m, $c=2100$ N s/m, $k=2.5\times10^7$ N/m, $e=0.01$ mm, $m_c=50$ kg, $m_{bL}=m_{bR}=20$ kg, $k_{fLH}=k_{fLV}=k_{fRH}=k_{fRV}=7.5\times10^6$ N/m, $c_{fLH}=c_{fLV}=c_{fRH}=c_{fRV}=2100$ N s/m, $k_{tLH}=k_{tLV}=k_{tRH}=k_{tRV}=2.5\times10^6$ N/m, $c_{tLH}=c_{tLV}=c_{tRH}=c_{tRV}=1050$ N s/m, $k_{cH}=k_{cV}=2.5\times10^9$ N/m, $c_{cH}=c_{cV}=2100$ N s/m, and $k_r=2.5\times10^7$ N/m, and $\delta=0.01$ mm.

The JIS6306 ball bearing of Ref. [7] is chosen as the ball bearing in this paper, and its parameters are listed in Table 1.

In order to study fully the dynamic behavior of the rotor-ball bearings-support-stator coupling system with imbalance and rubbing coupling faults, the system dynamic responses need to be obtained. There are many methods to obtain the periodic solution of the nonlinear system, but the numerical methods are the most efficient approaches to study the quasiperiodic and chaos phenomena. Because of the very strong nonlinearity of the rotor-ball bearings-support-stator coupling system with rubbing coupling faults, the Runge–Kutta–Fehlberg method [8] is used to solve differential equations and obtain the responses of the rotor-ball bearings-support-stator coupling system.

Table 1 The main parameters of the JIS6306 ball bearing

Radius of the outer race R (mm)	Radius of the inner race r (mm)	Number of balls N_b	Contact stiffness C_b (N/m$^{3/2}$)	Bearing clearance r_0 (μm)	BN
63.9	40.1	8	13.34×10^9	5	3.08

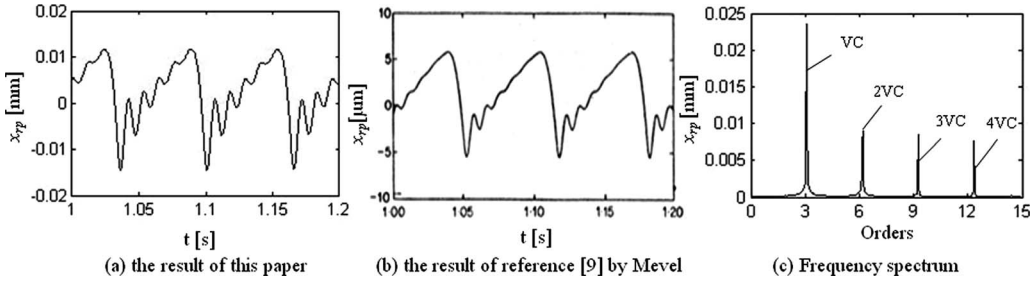

Fig. 3 The rotor response in the *X* direction at rotor disk (300 rpm)

3 Dynamics Analysis of the Rotor-Ball Bearings-Support-Stator Coupling System With Imbalance-Rubbing Coupling Fault

3.1 Model Verification. In Ref. [9], a dynamic model of an unbalanced rotor supported on ball bearings, which are subject to a constant vertical radial load, was established by Mevel, and the sixth order Runge–Kutta-Fehlberg method was used to obtain the responses of the rotor. In this paper, the same ball bearing as in Ref. [9] is used, the effect of the rotor imbalance and the vertical radial load on the bearing is considered, and the rotor responses of the rotor-ball bearings-support-stator coupling system are obtained by Runge–Kutta–Fehlberg method. Figures 3(*a*) and 4(*a*) are, respectively, the vibration displacements in the *X* and *Y* directions at disk at the rotating speed of 300 rpm; Figs. 3(*b*) and 4(*b*) are, respectively, the vibration displacements in the *X* and *Y* directions at rotor disk at the rotating speed of 300 rpm in Ref. [9] by Mevel. Obviously, their time wave forms and periods are very similar, and the difference of the vibration amplitude is due to the different rotor parameters.

The excitations of the unbalanced rotor supported on the ball bearing come from two aspects: one is the rotating frequency excitation from imbalance, and the other is the VC frequency excitation from the periodic variety of bearing stiffness. When the rotating speed is very low, unbalanced force is very weak, and the VC vibration, because of the periodic variety of the bearing stiffness, can be observed clearly; hereinto, the frequency of VC vibration is *BN* times of rotating frequency, and in this paper, the value of *BN* is 3.08 (according to Table 1). From Figs. 3(*a*), 3(*b*), 4(*a*), and 4(*b*), it can be seen that the motions in the *X* and *Y* directions are periodic, and the ball passage frequency (VC frequency) is shown clearly. When a ball leaves the load zone, and the rotor falls and contacts the next ball, in this progress, the transient oscillations appear and disappear quickly. From the frequency spectra of signals, such as in Figs. 3(*c*) and 4(*c*), it can be seen that the rotor vibration represents the VC frequency (the ball passage frequency) and its multiple harmonic components. The study of Fukata et al. [7] shows that when the rotating speed is far from the two critical rotating speeds in the *X* and *Y* directions, the motion is periodic and represents the ball passage frequency and its multiple harmonic components. Apparently, the result of this paper accords with the conclusion.

3.2 Effect of System Support on Dynamic Characteristics of Rotor. The rotating speed of the modern aeroengine is commonly over 10,000 rpm, and some minitype aeroengine can reach 40,000–50,000 rpm. For such engines with a high rotating speed, it is very important to maintain the structure integrality and the reliability of engine; moreover, the vibration and stability of the rotor-supporting system are often the sticking point of faults. The design practice of engine indicates that the malfunctions of whole-engine vibration, which come from the rotor-supporting system, had already become a great key technology problem in the process of engine development; therefore, it is very important to accurately design and analyze the dynamic characteristics of the rotor-support system and adopt proper measures of reducing vibration [10].

The rotor of the modern aeroengine of high rotating speed commonly adopts the design of a flexible shaft so that the rotating speed is over the critical rotating speed. For this rotor, adopting proper measures such as reducing the imbalance of rotor, falling critical rotating speed, and increasing damping can reduce rotor vibration. However, when the whole structure design of the aeroengine has been already determined, it is very difficult to adjust the critical rotating speed by way of changing the structure of the rotor system such as the diameter of the shaft and the distance between supports. The most efficient and feasible method is to adopt a flexible support. In fact, some types of modern aeroengine have already adopted the flexible support and SFD to reduce aeroengine vibration.

The purposes of adopting flexible support in the rotor-supporting system are mostly as follows: (1) to change the stiffness of flexible support, adjust, and control the critical rotating speed in order to meet the design requirements of system critical rotating speed; (2) to change the distribution of the rotor-support system's strain energy to meet the requirements of design rules; and (3) to use the distortion of flexible support and the inherent resistance of the material to absorb vibration energy and reduce

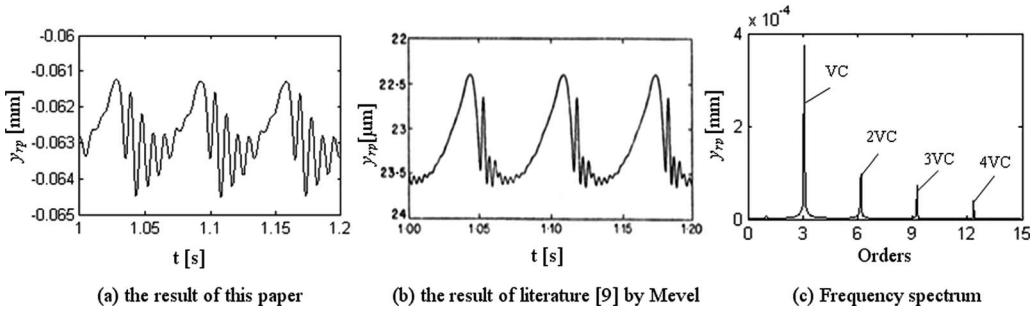

Fig. 4 The rotor response in the *Y* direction at rotor disk (300 rpm)

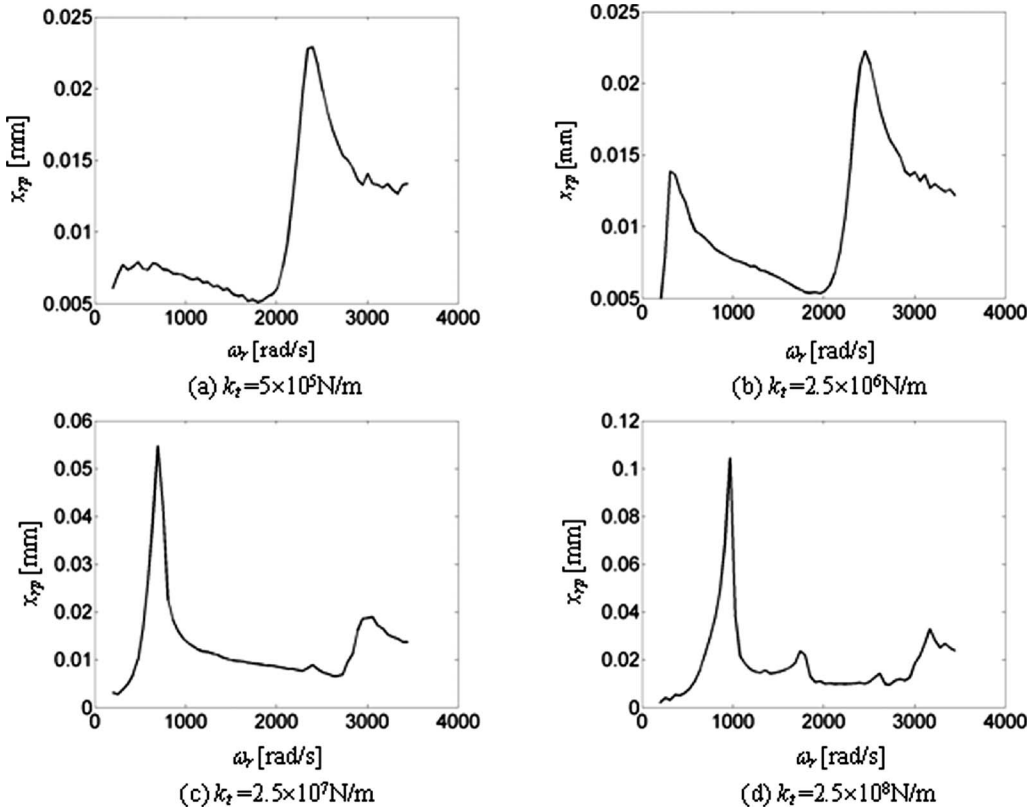

Fig. 5 Vibration amplitude-rotating speed plots of rotor responses under different support stiffnesses

vibration.

In this paper, the support's stiffness of system is supposed as $k_{tLH}=k_{tLV}=k_{tRH}=k_{tRV}=k_t$. The rotor responses under various supports stiffnesses are obtained. Figures 5(*a*)–5(*d*) are, respectively, the vibration amplitude-rotating speed plots of rotor responses under different support stiffnesses; hereinto, the vibration amplitude-rotating speed plot is obtained through calculating the vibration amplitude of the steady response for each rotating speed; in the plot, the *X* coordinates and the *Y* coordinates denote, respectively, the rotating speed and the corresponding vibration amplitude.

From Fig. 5, it can be seen that (1) when the support stiffness is lower than the stiffness of the shaft, two resonance peaks appear in the rotor response. In other words, the rotor has two critical rotating speeds, the lower one corresponds to rigid body motion, and the higher one corresponds to the first order bending critical rotating speed of the rotor. In Figs. 5(*a*) and 5(*b*), the support stiffness is, respectively, lower 50 and 10 times than the shaft stiffness. (2) When the support stiffness is higher than the stiffness of the shaft, such as in Figs. 5(*c*) and 5(*d*), it means that the support of the rotor is rigid, only one resonance peak appears in rotor responses, and the rotor's critical rotating speed corresponds to the first order bending natural frequency. From Figs. 5(*a*)–5(*d*), it can be seen that adopting a flexible support can increase the bending critical rotating speed of a rotor at which the vibration of the rotor is very great, and disastrous accident can happen. The bending critical rotating speed of a rotor with flexible support corresponds to the second critical rotating speed, namely, $\omega_{cr2}=2500$ rad/s, and it is about 1.5 times higher than the first bending critical rotating speed of the rotor with rigid support, namely, $\omega_{cr1}=1000$ rad/s. At the same time, it can be seen that the resonance response of the rotor with flexible support is much lower than that with rigid support. This result shows that adopting a flexible support can not only make the rotor rotating speed avoid the rotor bending critical rotating speed efficiently but also reduce rotor vibration at the critical rotating speed. The numerical simulation calculation in this paper clearly shows these results.

3.3 Characteristics Analysis of Rubbing Fault. With the development of aviation technique and continual improvement of the performance of aeroengine, researchers try to reduce the clearance between the rotor and the stator, but this method increases the probability of rotor-to-stator rubbing. The physical phenomena caused by rubbing, such as friction, impact, structure stiffness changing, and so on, can affect normal mechanical motion and change the balance force and the dynamic stiffness of the system, so that the engine efficiency falls down, prodigious normal force and tangent force appear in the rotor system, and enormous vibration and noise are caused. Finally, the aeroengine can be destroyed in few seconds, and a disastrous accident can occur. The aeroengine rotor-to-stator rubbing fault has a very complicated evolvement process, and presently, it has become a greatly difficult problem of engine design, and has produced serious effects on aeroengine performance and reliability. Therefore it is urgent to understand the generating process, to find out the characteristics of rotor-stator rubbing, and to analyze the mechanism of the rubbing malfunction for effectively avoiding rubbing and quickly diagnosing the reasons, positions, and characters of rubbing fault.

In this paper, a new rotor-ball bearings-support-stator coupling system dynamic model is established. By way of numerical simulation, the responses of imbalance and rubbing coupling faults are obtained. Table 2 lists the computational conditions.

Through analyzing the cascade plots of rotor responses above, the following results can be obtained.

(1) When the rotating speed is lower than the critical rotating speed, rubbing excites more abundant multiple harmonic components (1*X*, 2*X*, and so on), but the fractional harmonic components are very difficult to be excited by rub-

Table 2 The computational conditions

No. of figures	Support stiffness k_t (N/m)	Rubbing stiffness k_r (N/m)
Fig. 6(*a*)	2.5×10^7	0
Fig. 6(*b*)	2.5×10^7	2.5×10^7
Fig. 6(*c*)	2.5×10^6	2.5×10^7
Fig. 6(*d*)	2.5×10^8	2.5×10^7
Fig. 6(*e*)	2.5×10^7	1.25×10^8
Fig. 6(*f*)	2.5×10^7	5×10^6

bing. In a high rotating speed range over the critical rotating speed, many fractional harmonic components start to appear when rubbing happens, but the multiple harmonic components (1*X*, 2*X*, and so on) are very few. The three dimensional cascade plots in Fig. 6(*b*) validate the rotor-stator rubbing fault characteristics in Ref. [11] qualitatively; namely, when the rotor rotating speed is lower than the critical rotating speed, the partial rubbing mainly excites the multiple harmonic components of 1*X*, 2*X*, and so on, and when the rotor rotating speed is close to *n* times of the critical rotating speed, the $1/n$ fractional harmonic components can appear.

(2) When the system adopts a flexible support, the multiple harmonic and fractional harmonic components caused by rubbing are much less. Apparently, as compared with rigid support, the chaos phenomena caused by rubbing fault also greatly decrease. Thus it can be seen that adopting flexible support can effectively increase the system stability. This is also the reason that few chaos phenomena can be observed in the operating process of a practical aeroengine. From Figs. 6(*b*)–6(*d*), this conclusion can be found out.

(3) Figure 6(*e*) is the cascade plot of rotor responses; hereinto, the rubbing stiffness k_r is 1.25×10^8 N/m. When the rotor rotating speed is 1500 rad/s, the time wave form, the frequency spectra, and the Poincaré map of the rotor responses are shown in Fig. 7. From Fig. 7, a continual frequency spectrum appears in the frequency spectrum, and messy points come forth in the Poincaré map. These phenomena indicate that the rotor motion runs into chaos. Therefore, a bigger rubbing stiffness can excite more multiple and fractional harmonic components, and finally result in more chaos; oppositely, a lower rubbing stiffness can give birth to much less multiple and fractional harmonic components, and the chance that the system appears chaotic will also be greatly reduced, as shown in Figs. 6(*c*) and 6(*f*).

4 Experiment Verification and Analysis

4.1 Aeroengine Rotor Tester. In order to simulate the rotor vibration of a real aeroengine, an aeroengine rotor tester is designed and manufactured. By comparison to the real aeroengine, the tester has these features as follows: (1) its size is one-third of real aeroengine and its shape is similar to the stator of engine; (2) its internal structure is simplified: the core machine is simplified as the 0-2-0 support structure, which is a rotor with two disks supported on two bearings, and the outsides of two bearings have no other disks, and the support stiffness is adjustable in order to adjust the dynamic characteristics of the system; the multistage compressor is simplified as a single-stage disk structure; the compressor blade is simplified as the inclined plane shape; (3) its shaft is solid and rigid and its maximal rotating speed is 7000 rpm; and

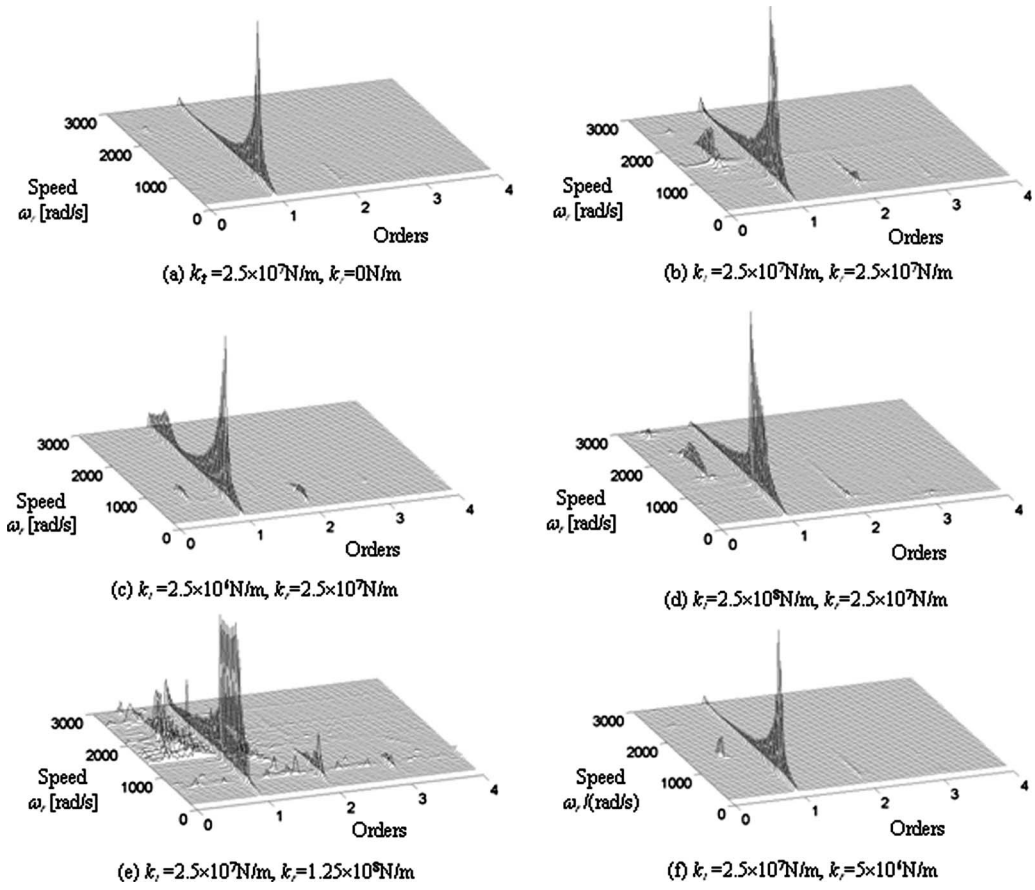

Fig. 6 Cascade plot of rotor response

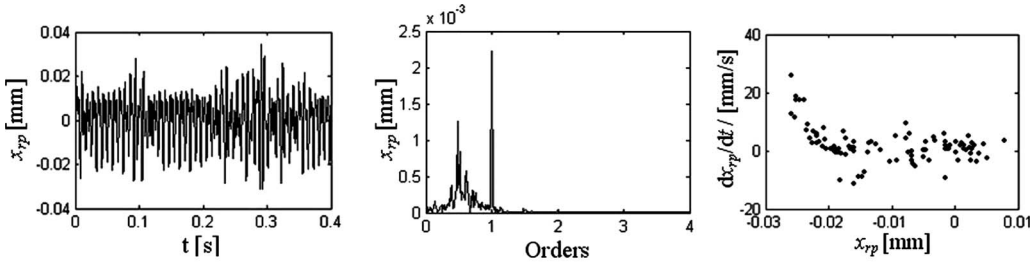

(a) time response plot (b) frequency spectra plot (c) Poincaré plot

Fig. 7 Time wave form, frequency spectrum, and Poincaré map of the rotor response at a rotating speed of 1500 rad/s (k_t=2.5×10^7 N/m, k_r=1.25×10^8 N/m)

(4) the rotor is driven by a motor, and the flame flask is canceled. Therefore, the aeroengine rotor tester becomes a single-rotor system model, and its full-scale photo is shown in Fig. 8(*a*) and its section drawing is shown in Fig. 8(*b*).

The whole engine rotor tester is mainly composed of a demonstrative model, installation platform, electromotor, foundation platform, and lubricating system. The tester can display and simulate some typical faults, which usually appear in practical aeroengine: (1) rubbing between turbine blades and stator (including point rubbing, local rubbing, and slight or severe rubbing), (2) rubbing between the sealing labyrinth, (3) bearing damage, (4) misalignment between the former and the latter support, and (5) the effect of support stiffness on the vibration characteristics.

4.2 Vibration Testing System of the Aeroengine Rotor-Tester. The rotor tester is driven by an electromotor. Considering that the electromotor shaft is difficult to keep in alignment with the shaft of rotor tester, a soft connection is adopted between the two shafts. The rotating speed can be obtained by way of detecting the pulse number of the eddy current transducer, which is installed at Testing Point 1, and the rotor fault signals in the *X* and *Y* directions, are picked up, respectively, by four eddy current transducers, which are installed at Testing Points 2 and 3. The fault analog signal is enlarged first by a preamplifier, and then is sampled and quantified into digital signals by the USB-14054 data acquisition instrument; finally, the digitals are sent into PC. The vibration testing system of the aeroengine rotor tester is shown in Fig. 9.

4.3 Comparing Experimental Results With Simulation Results. Figure 10(*a*) is the cascade plot of a rotor imbalance-rubbing coupling fault response, which is obtained by the rotor-ball bearings-support-stator coupling system dynamics model. Figure 10(*b*) is the cascade plot of the rotor response, which is obtained by way of the rubbing test of the aeroengine rotor tester. From Fig. 10, it can be seen that the simulation results and experimental results all show the phenomena of multiple harmonic frequency components 2*X*, 3*X*, and so on, when a rubbing fault occurs. In Ref. [12], the same experimentation phenomena are also obtained by making use of the aeroengine rotor tester, which is the same as the one used in this paper.

Because the rotating speed of this tester can only reach 7000 rpm, the rotating speed is lower than the first critical rotating speed; therefore fractional harmonic frequency components cannot be observed. The accordance of the experiment and simulation results validates to a certain extent the effectiveness of the new rotor-ball bearing-support-stator coupling system dynamics model with rubbing coupling fault established in this paper.

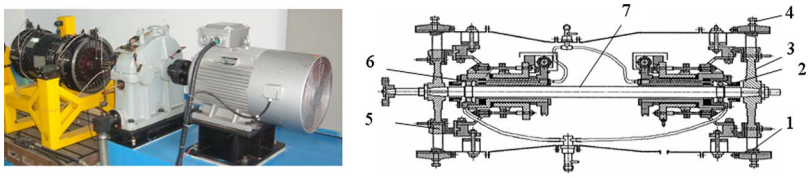

(a) Photo of the aero-engine rotor tester (b) Section drawing of the aero-engine rotor tester

1-rubbing ring, 2-ball bearing, 3- turbine disk, 4-bolt for deforming rubbing ring, 5- disk of compressor, 6-ball bearing, 7-shaft

Fig. 8 The aeroengine rotor tester

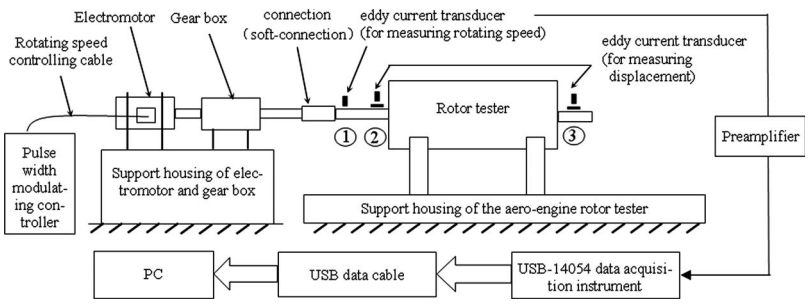

Fig. 9 The vibration testing system of the aeroengine rotor tester

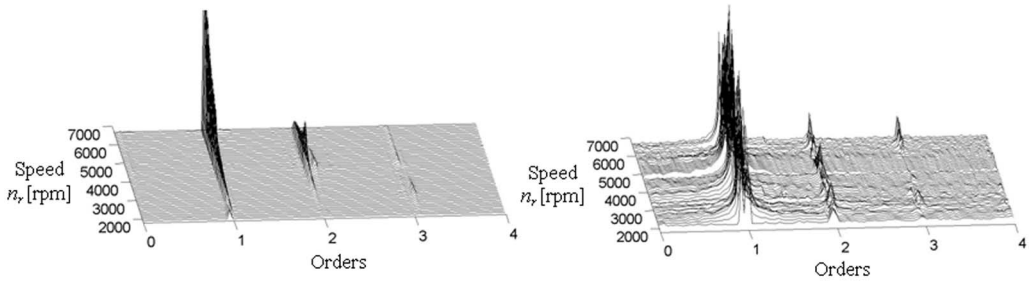

Fig. 10 The cascade plot of rotor rubbing fault response

5 Conclusions

In this paper, a new rotor-ball bearings-support-stator coupling system dynamics model with imbalance-rubbing coupling fault for practical aeroengine is established. In the new coupling model, the flexible support and the stator motion are considered; the nonlinear factors of ball bearings are considered such as the VC vibration because of the varying support stiffness of ball bearings, nonlinear Hertzian contact force, and ball bearing clearances the imbalance and rubbing faults of the rotor are fully considered in the rotor system. Finally, the Runge–Kutta–Felhberg method with varying steps is used to compute responses of the system.

The simulation results show that adopting a flexible support can not only make the rotating speed avoid the rotor bending critical rotating speed effectively but also reduce rotor vibration at the critical rotating speed in effect. These results accord with the vibration rules of real aeroengine.

The simulation results show that when the rotating speed is lower than the critical rotating speed, the rubbing fault can cause multiple harmonic frequency components; hereinto, the 2*X* frequency component is greater; when the rotating speed is higher than the critical rotating speed, the rubbing fault can excite fractional harmonic frequency components. These results have very important significance for identifying the rubbing fault effectively.

Increasing the support flexibility, the multiple and fractional harmonic frequency components are much less, and as compared with the rigid support, the chaos phenomena caused by the rubbing fault is also greatly reduced.

An aeroengine rotor tester and signal testing system are designed, the rubbing fault tests are carried out, and the rubbing response, which come from rotor tester and rotor-ball bearings-support-stator coupling model, is compared with the experimental result. Finally, the accordance of the experiment and simulation result validates the correction of the new rotor-ball bearing-support-stator coupling model with rubbing coupling fault.

Acknowledgment

The author is very grateful to his master graduate students F. M. Li, H. L. Zhou, and X. Y. Li who did the translation and data collection work for this paper. The work is supported by the National Science Foundation of China (Grant No. 50705042) and the Aviation Science Funds of China (Grant No. 2007ZB52022).

Nomenclature

x_{rp}, y_{rp} = the x and y components of displacement of rotor at disk

x_{rR}, y_{rR} = the x and y components of displacement of rotor at right bearing

x_{rL}, y_{rL} = the x and y components of displacement of rotor at left bearing

x_{bR}, y_{bR} = the x and y components of displacement of right bearing housing

x_{bL}, y_{bL} = the x and y components of displacement of left bearing housing

x_{wR}, y_{wR} = the x and y components of displacement of outer race of right bearing housing

x_{wL}, y_{wL} = the x and y components of displacement of outer race of left bearing housing

x_c, y_c = the x and y components of displacement of stator

m_c = the stator mass

m_{rp} = the rotor equivalent mass at disk

m_{rL}, m_{rR} = the rotor equivalent masses at the left and the right bearings (usually, $m_{rL}=m_{rR}$)

m_{wL}, m_{wR} = the outer race masses of the left and the right ball bearings (usually, $m_{wL}=m_{wR}$)

m_{bL}, m_{bR} = the masses of the left and the right bearing housings (usually, $m_{bL}=m_{bR}$)

k_r = the rubbing contact stiffness

k, c, c_{rb} = the stiffness of the shaft, the damping of rotor at disk, and the damping of rotor at bearings

k_{tLH}, k_{tLV} = the horizontal and the vertical stiffness of flexible support between the left outer race of ball bearing and the left bearing housing

c_{tLH}, c_{tLV} = the horizontal and the vertical damping of SFD between the left outer race and the left bearing housing

k_{tRH}, k_{tRV} = the horizontal and the vertical stiffness of flexible support between the right outer race of ball bearing and the right bearing housing

c_{tRH}, c_{tRV} = the horizontal and the vertical damping of SFD between the right outer race and the right bearing housing

k_{fLH}, k_{fLV} = the horizontal and the vertical support stiffness between the stator and the left bearing housing

c_{fLH}, c_{fLV} = the horizontal and the vertical support damping between the stator and the left bearing housing

k_{fRH}, k_{fRV} = the horizontal and the vertical support stiffness between the stator and the right bearing housing

c_{fRH}, c_{fRV} = the horizontal and the vertical support damping between the stator and the right bearing housing

k_{cH}, k_{cV} = the horizontal and the vertical support stiffness between the stator and the foundation

c_{cH}, c_{cV} = the horizontal and the vertical support damping between the stator and the foundation

O_1, O_2, O_3 = the geometric center of bearing, the geometric center of rotor, and the rotor's center of mass

δ = the clearance between the rotor disk and the stator

e = the eccentricity of mass

F_{xbL}, F_{ybL} = the supporting force components in X and Y directions at the left bearing

F_{xbR}, F_{ybR} = the supporting force components in X and Y directions of at the right bearing
P_T, P_N = the tangent and the normal rubbing forces
f = the dynamic friction coefficient
v_{outer} = the tangent velocity of the contact point between the ball and the outer race
v_{inner} = the tangent velocity of the contact point between the ball and the inner race
ω_{outer} = the rotating angular velocity of bearing outer race
ω_{inner} = the rotating angular velocity of bearing inner race
v_{cage} = the tangent velocity of the cage (the center of the ball)
ω_{cage} = the angular velocity of the cage (the center of the ball)
ω_{VC} = the varying compliance frequency
ω_{rotor} = the rotating speed of rotor
R_o = the radius of outer bearing race
R_i = the radius of inner bearing race
N_b = the number of bearing balls
BN = the bearing number
r_0 = the bearing clearance
θ_j = the angular position of the jth ball in the ball bearing
Δr_j = the normal contact deformation between the jth ball and races
C_b = the Hertzian contact stiffness constant

References

[1] Wen, B. C., Wu, X. H., and Han, Q. K., 2004, *The Nonlinear Dynamics Theory and Experiments of Rotating Mechanism With Faults*, Science Press, Beijing, pp. 149–151 (in Chinese).
[2] Muszynska, A., and Goldman, P., 1995, "Chaotic Responses of Unbalance Rotor Bearing Stator Systems With Looseness or Rubs," Chaos, Solitons Fractals, **5**(9), pp. 1683–1704.
[3] Liu, Y. F., Zhao, M., and Zhu, H. J., 2002, "The Study on the Chaos Characteristics of Rotor With Rubbing and Pedestal Looseness Faults," Journal of Vibration and Shock, **21**(4), pp. 36–38 (in Chinese).
[4] Luo, Y. G., Li, Z. F., Liu, C. L., and Wen, B. C., 2003, "Study on Nonlinear Behavior of Rotor System With Pedestal Looseness and Rubbing Faults," China Mechanical Engineering, **14**(14), pp. 1224–1226 (in Chinese).
[5] Li, Z. P., Luo, Y. G., Yao, H. L., and Wen, B. C., 2003, "Dynamics of Rotor-Bearing System With Coupling Faults of Crack and Rub-Impact," Chinese Journal of Applied Mechanics, **20**(3), pp. 136–140 (in Chinese).
[6] Yuan, H. Q., Wen, B. C., Wamg, D. Y., and Liu, S. L., 2003, "Nonlinear Dynamic Properties of Rolling Bear-Rotor-Stator Box with Local Rubbing," Journal of Northeastern University (Natural Science), **24**(3), pp. 244–247 (in Chinese).
[7] Fukata, S., Gad, E. H., and Kondou, T., 1985, "On the Radial Vibration of Ball Bearings (Computer Simulation)," Bull. JSME, **28**, pp. 899–904.
[8] Jiang, J. F., Hu, L. J., and Tang, J., 2004, *Numerical Analysis and MATLAB Experimentation*, Science Press, Beijing, pp. 149–151 (in Chinese).
[9] Mevel, B., and Guyader, J. L., 1993, "Routs to Chaos in Ball Bearing," J. Sound Vib., **162**(3), pp. 471–487.
[10] Aeroengine Design Manual Compiling Committee, 2000, *Aeroengine Design Manual (19th part): Rotor Dynamics and Whole-Engine Vibration*, Aviation Industry Press, Beijing, pp. 208–226 (in Chinese).
[11] Chen, Y. S., Tian, J. Y., Jin, Z. W., and Ding, Q., 1999, "Theory of Nonlinear Dynamics and Applied Techniques of Solving Irregular Operation of a Large Scale Gas Turbine in a Comprehensive Way," China Mechanical Engineering, **10**(9), pp. 1063–1067 (in Chinese).
[12] Gao, Y. L., Li, Y., and Wang, D. Y., 2002, "Experimental Investigation of Rotor-to-Casing Rubbing Fault," Aeroengine, **4**, pp. 16–21 (in Chinese).

Onset of $\frac{1}{2}X$ Vibration and Its Prevention

John J. Yu
GE Energy,
1631 Bently Parkway South,
Minden, NV 89423
e-mail: john.yu@ge.com

This paper discusses real cases on three different machines where subsynchronous vibration occurred suddenly at a frequency exactly equal to one-half ($\frac{1}{2}X$) of the operational speed of 3600 rpm. In two cases, vibration amplitude increased from around 2 mils (51 μm) pp to over 12 mils (305 μm) pp, causing the machine to trip unexpectedly. The $\frac{1}{2}X$ vibration was even sustained during shutdown at speed below 3600 rpm after trip. Unlike other reported experimental results, shaft orbit measured by proximity probes was fairly circular and dominantly composed of the $\frac{1}{2}X$ component without significant components at multiple orders of the $\frac{1}{2}X$. The onset of the subsynchronous $\frac{1}{2}X$ vibration was sometimes triggered by changes in bearing lube oil temperature and supply pressure, which would typically be believed to be caused by oil whirl that could occur at close to the $\frac{1}{2}X$ frequency. An upward shift in shaft centerline plot was observed to occur prior to the onset of the subsynchronous vibration. The $\frac{1}{2}X$ vibration was successfully prevented by changing bearing clearance or adjustment of bearing oil temperature and supply pressure. Parametric excitation analysis on $\frac{1}{2}X$ vibration is also given in this paper. The main purpose of this paper, unlike previously published papers on analytical or experimental results, is to show shaft orbital and centerline plots as well as spectrum data due to the $\frac{1}{2}X$ vibration, including effects of operating conditions in real rotating machines.
[DOI: 10.1115/1.3155794]

1 Introduction

In rotating machines, unlike synchronous 1X vibration, which can often be reduced through balance, subsynchronous vibration can sometimes be difficult in finding its root-cause and means to prevent it. Amplitude of subsynchronous vibration that occurs due to an instability issue can often go beyond the danger level to trip the machine.

Subsynchronous vibration at a frequency of around but just below one-half of the rotational speed is sometimes called *half-frequency whirl* [1] due to fluid-induced instability in bearings or seals. Muszynska in 1986 [2] demonstrated whirl frequency of around but just below $\frac{1}{2}X$ through both analytical and experimental approaches. Though numerical simulation from a nonlinear fluid bearing force model in a recent paper by Shen et al. in 2006 [3] seems to indicate a possible $\frac{1}{2}X$ vibration, many other analytical and experimental results such as those by Crandall in 1990 [4] and Childs in 1993 [5] in addition to Ref. [1] do not support the notion of the exact $\frac{1}{2}X$ whirl due to fluid-induced instability. In real rotating machines, if oil whirl occurs, its whirl frequency is generally lower than $\frac{1}{2}X$ due to axial flow out of the bearing, which is inevitable to some extent due to oil film pressure. Reference [1] listed oil whirl frequency range from 0.35X to 0.47X.

It is believed that the exact $\frac{1}{2}X$ vibration is caused by parametric excitation due to nonlinear or step-changing stiffness within the shaft orbit. It is often confused with oil whirl, as indicated in Ref. [1]. The mechanism of the exact $\frac{1}{2}X$ vibration is totally different from that of just below 0.5X oil whirl. The formal is often associated with bearing looseness or rub. Ehrich in 1966 [6] published his observation of exact $\frac{1}{2}X$ vibration in an aircraft gas turbine engine, and also called it as subharmonic vibration to distinguish it from general subsynchronous vibrations. Bently in 1974 [7] demonstrated his experimental results of this fractional frequency and named "normal-tight" and "normal-loose" conditions. Childs in 1982 [8] published some analytical work to explain Bently's work [7]. Muszynska in 1984 [9] presented partial rub experimental results with shaft orbit shape "8" containing the $\frac{1}{2}X$ component. Eisenmann et al. in 1997 [10] showed a case history of the $\frac{1}{2}X$ vibration due to loose bearing housing in an 11,520 rpm machine where an about 1 mil (25 μm) pp $\frac{1}{2}X$ component appeared along with a 1.5 mil (38 μm) pp 1X component.

This paper presents vibration data and plots of the $\frac{1}{2}X$ vibration in real rotating machines running at 3600 rpm where the vibration reached 12 mils (305 μm) pp, far exceeding the 1X component. Unlike those published results, which often show elliptical 8 shape orbits, the current data show fairly circular shaft orbits. It is found that changes in bearing oil temperature and supply pressure can actually trigger the $\frac{1}{2}X$ vibration. These changes are typically believed to possibly trigger oil whirl or whip. The paper also demonstrates effective diagnostic tools as well as corrections on how to prevent the $\frac{1}{2}X$ vibration.

It should be noted that the confusion might occur in assessing a source of subsynchronous vibration in real rotating machines. Relatively small difference between vibrations exactly at or less than $\frac{1}{2}X$ points out totally different root-causes.

2 Case History 1

This is a 3600 rpm steam turbine generator with rated power output of 25 MW. The turbine and the generator are each supported by two journal bearings, numbered in order from the turbine to the generator. The machine train is viewed from the turbine toward the generator and therefore is considered to be rotating in the counterclockwise direction. Both the steam turbine and the generator vibrations are measured by XY pairs of noncontacting proximity probes mounted at 45 deg left (Y-probe) and 45 deg right (X-probe) from Bearing 1 to 4. Its machine train diagram is shown in Fig. 1. The data in this case were presented by using Bently Nevada™ ADRE® SXP software.

Contributed by the International Gas Turbine Institute of ASME for publication in the JOURNAL OF ENGINEERING FOR GAS TURBINES AND POWER. Manuscript received March 16, 2009; final manuscript received April 13, 2009; published online November 4, 2009. Review conducted by Dilip R. Ballal. Paper presented at the ASME Turbo Expo 2009: Power for Land, Sea and Air.

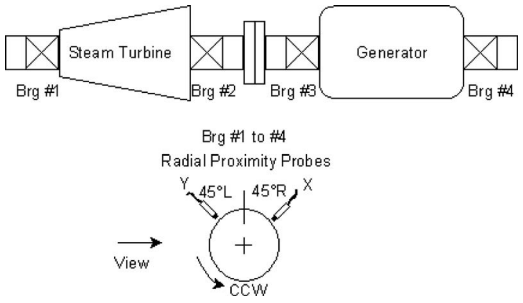

Fig. 1 Machine train diagram for Case History 1

After reaching 3600 rpm, the machine was running at approximately 2 MW. During the initial 20 min after reaching 3600 rpm, vibration level was around 2 mils (51 μm) pp or below at all bearings. Figure 2 shows direct (broad-band), $\frac{1}{2}X$, and $1X$ vibration trend plots at Bearing 3Y-probe from time 16:27:09 after reaching 3600 rpm. The vibration was mainly composed of the $1X$ component without the $\frac{1}{2}X$ component during the initial 20 min. Though vibration remained almost constant during this period of time, shaft centerline or journal position at Bearing 3 (axial groove bearing) shifted significantly to the upright as shown in Fig. 3.

At time 16:46:39, approximately 20 min after reaching 3600 rpm, shaft centerline had a rise of about 2–3 mils (51–76 μm) toward approximately 45 deg right at Bearing 3. Then the $\frac{1}{2}X$ vibration started to occur, as shown in Fig. 2. This change was also observed in orbital plots measured by a pair of X- and Y-probes at Bearing 3, as shown in Figs. 4(a) and 4(b).

The $\frac{1}{2}X$ vibration kept increasing while the $1X$ component remained fairly the same. The shaft centerline also kept moving toward the left. At approximately 16:52:59, direct amplitude predominantly composed of the full-blown $\frac{1}{2}X$ vibration reached the trip level of 12 mils (305 μm) pp at Bearing 3Y-probe (see Fig. 4(c)). Therefore the machine tripped and its speed dropped below 3600 rpm. However, the $\frac{1}{2}X$ vibration level did not stop increasing immediately. At 16:53:02 when speed dropped to 3573 rpm, the $\frac{1}{2}X$ vibration reached the highest level of 12.9 mils (328 μm) pp where the shaft centerline reached the far left. At 16:53:14 when speed dropped to 3466 rpm, the vibration is still around 12 mils (305 μm) pp, as shown in Fig. 4(d). High vibration was also observed at Bearing 4 (outboard bearing of the generator), and its highest $\frac{1}{2}X$ component reached 9 mils (229 μm) pp. However, no significant change in vibration at turbine bearings was observed. The $\frac{1}{2}X$ component at Bearings 1 and 2 was only 1 mil (25 μm) pp or less.

As speed deceased further, the $\frac{1}{2}X$ vibration started to diminish. Shaft centerline also moved toward the right. At approximately 16:53:37 when speed dropped to 3299 rpm, the $\frac{1}{2}X$ vibration totally disappeared, as shown in Fig. 2.

Figure 5 shows a waterfall plot measured by Y-probe at Bearing 3 prior to the onset of $\frac{1}{2}X$ vibration. Subsynchronous components around 1800 cycles per minute (cpm) were observed before the high $\frac{1}{2}X$ vibration occurred. These very low level components, most likely due to suppressed whip, indicate a natural frequency of the rotor-bearing system near 1800 cpm or half of the running speed.

Figure 6 shows its spectrum plot when full-blown $\frac{1}{2}X$ developed. The vibration was dominantly composed of the $\frac{1}{2}X$ component, not accompanied by significant components at multiple orders of the $\frac{1}{2}X$. Orbital plots in Figs. 4(c) and 4(d) also demonstrate the exact $\frac{1}{2}X$ component by two fixed Keyphasor® dots that do not move as the orbit repeats itself.

After the machine shutdown, Bearing 3 was inspected for any abnormality and damage. It was found that the bearing diametrical clearance was 0.005 in. (127 μm) higher than its specification. A crack on the bearing surface was also observed as shown in Fig. 7, most likely due to vibration impact of the journal against the bearing wall.

This oversized and damaged bearing was then replaced with a new one. Since then no $\frac{1}{2}X$ vibration has occurred. Direct or broad-band vibration level at Bearing 3 has been steady at less than 2 mils (51 μm) pp at all operating conditions.

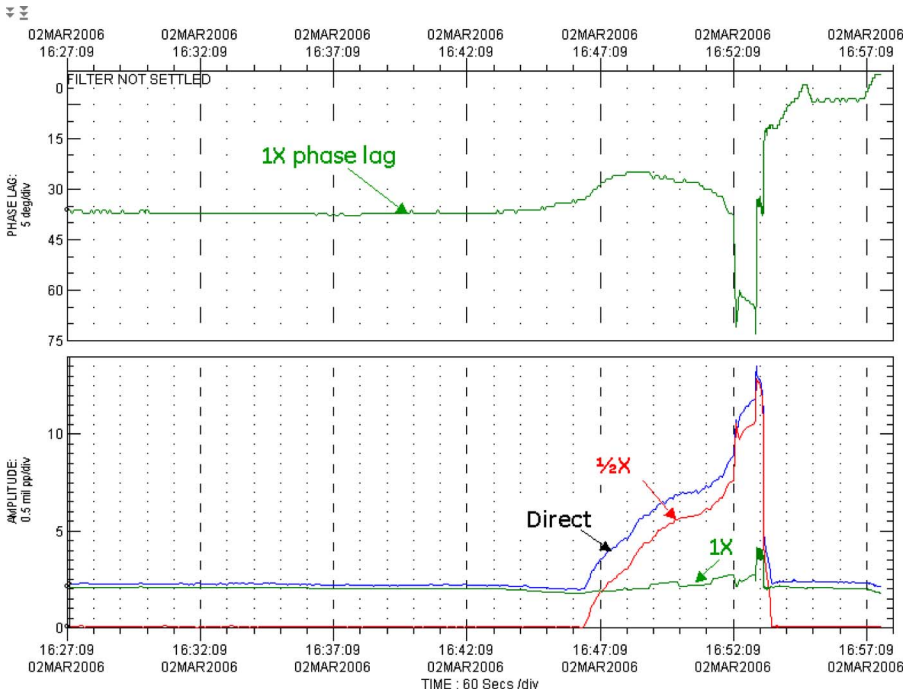

Fig. 2 Direct, $\frac{1}{2}X$, and $1X$ vibration trend plots at Bearing 3Y-probe

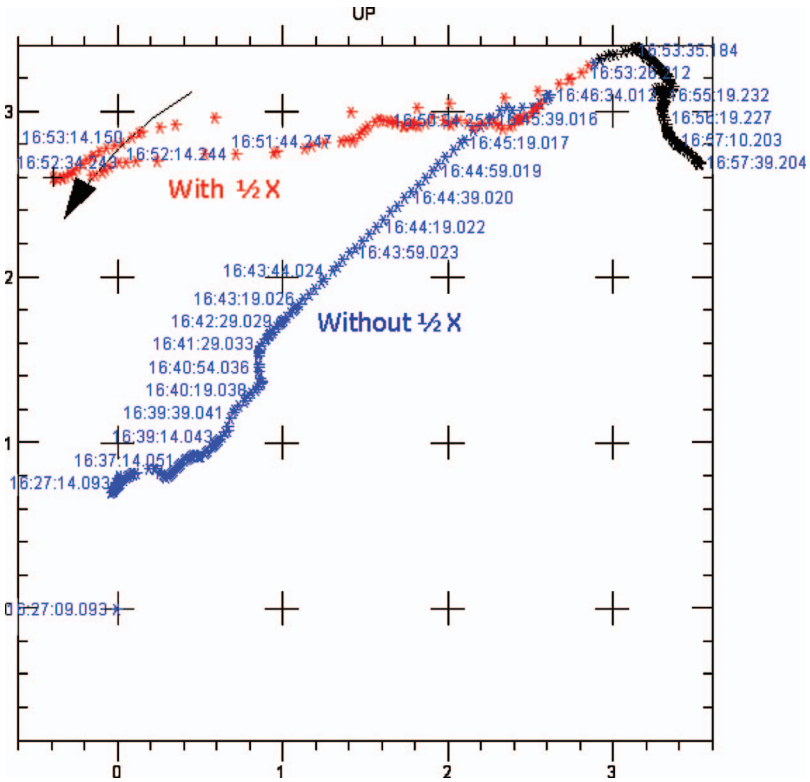

Fig. 3 Shaft centerline plot at Bearing 3

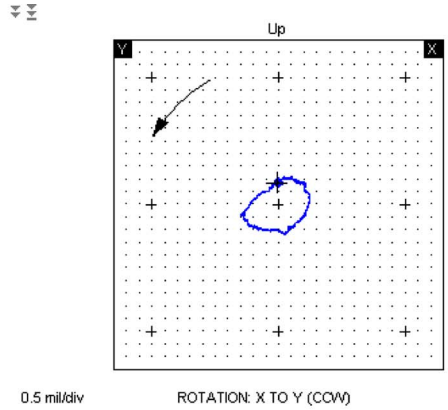

(a) Normal orbit without ½X vibration at 16:46:34

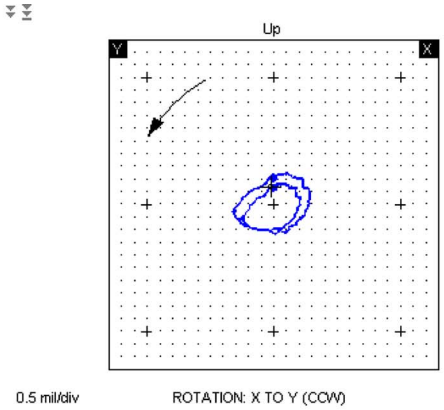

(b) Starting ½X vibration at 16:46:39

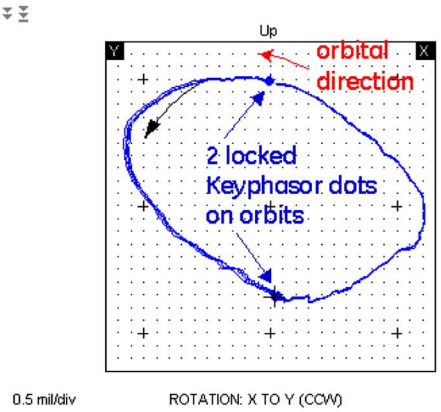

(c) Full-blown ½X vibration at 16:52:59

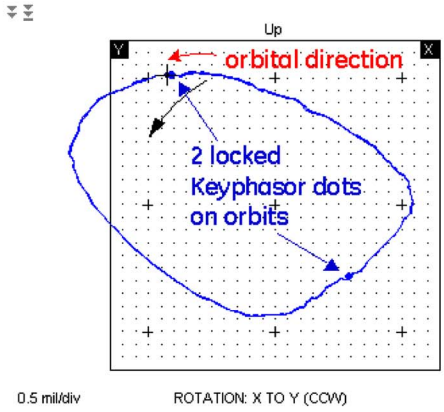

(d) Maintaining ½X vibration at 3466 rpm at 16:53:14

Fig. 4 Orbital plots at different stages at Bearing 3

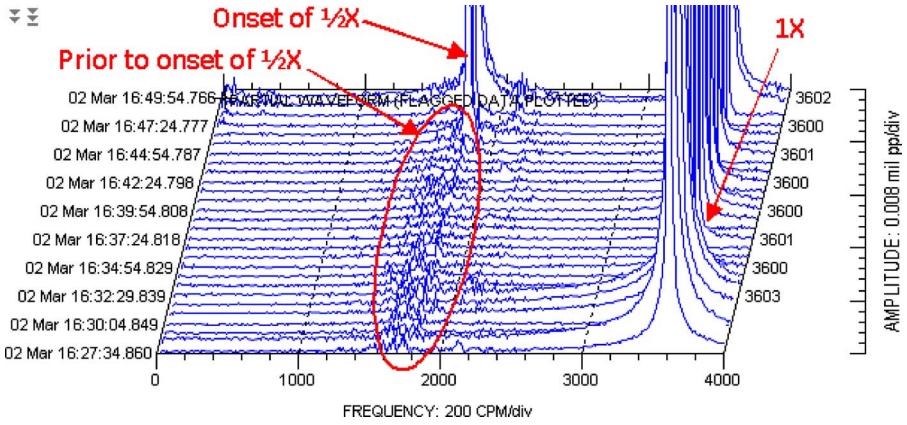

Fig. 5 Waterfall plot measured by Bearing 3 *Y*-probe showing subsynchronous components around 1800 cpm prior to onset of the full-blown $\frac{1}{2}X$ vibration

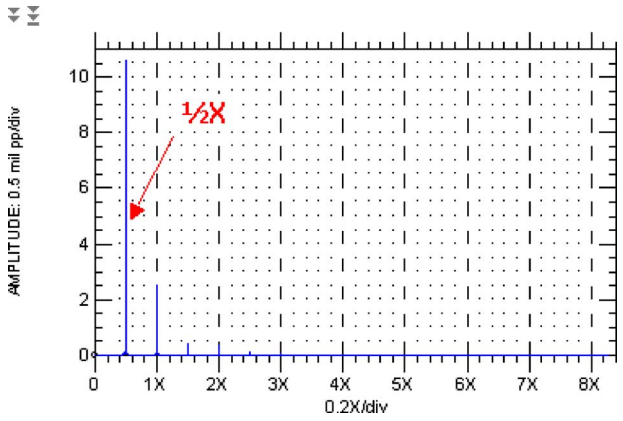

Fig. 6 Spectrum plot measured by Bearing 3 *Y*-probe when full-blown $\frac{1}{2}X$ vibration developed (primarily $\frac{1}{2}X$ component without significant harmonics)

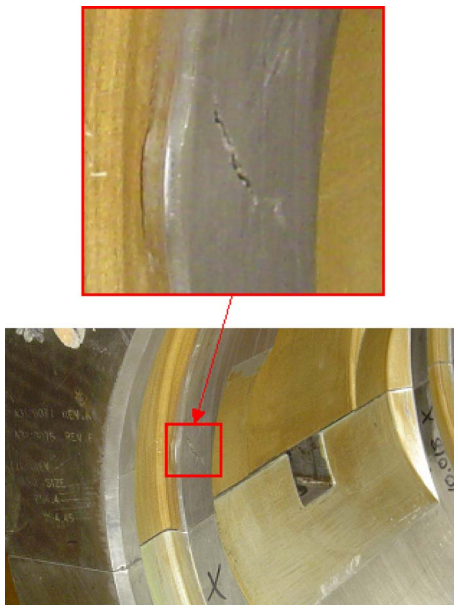

Fig. 7 Damage on Bearing 3 surface

3 Case History 2

In this case history, $\frac{1}{2}X$ vibration occurred on a rated 7.5 MW steam turbine generator made by an original equipment manufacturer (OEM) different from that in Case History 1. Its machine train diagram is shown in Fig. 8. The turbine and the generator are supported by Bearing 1 (axial groove bearing), Bearing 2 (elliptical bearing with clearance of 0.023 in. in horizontal direction versus 0.013 in. in vertical direction), and Bearing 3 (axial groove bearing). The data in this case were presented by using Bently Nevada ADRE® for Windows™.

The machine was reported to have had high vibration excursion for many years when power output increased to over 3 MW. Figure 9 shows high vibration excursion at Bearing 2*X*-probe when power output increased to 3.6 MW. The vibration was predominantly composed of the $\frac{1}{2}X$ component. At time 14:38 when power output increased to 3.6 MW, direct amplitude suddenly increased from 3.3 mils (84 μm) pp to 6.9 mils (175 μm) pp. The $\frac{1}{2}X$

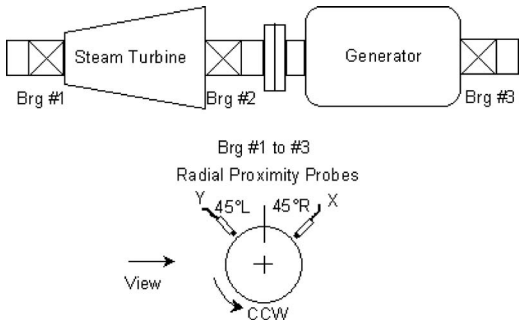

Fig. 8 Machine train diagram for Case History 2

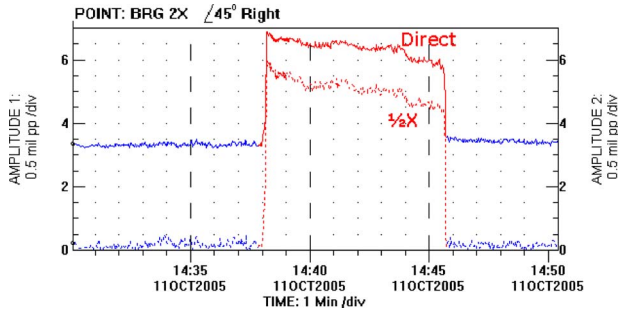

Fig. 9 $\frac{1}{2}X$ vibration occurred when power output increased to 3.6 MW

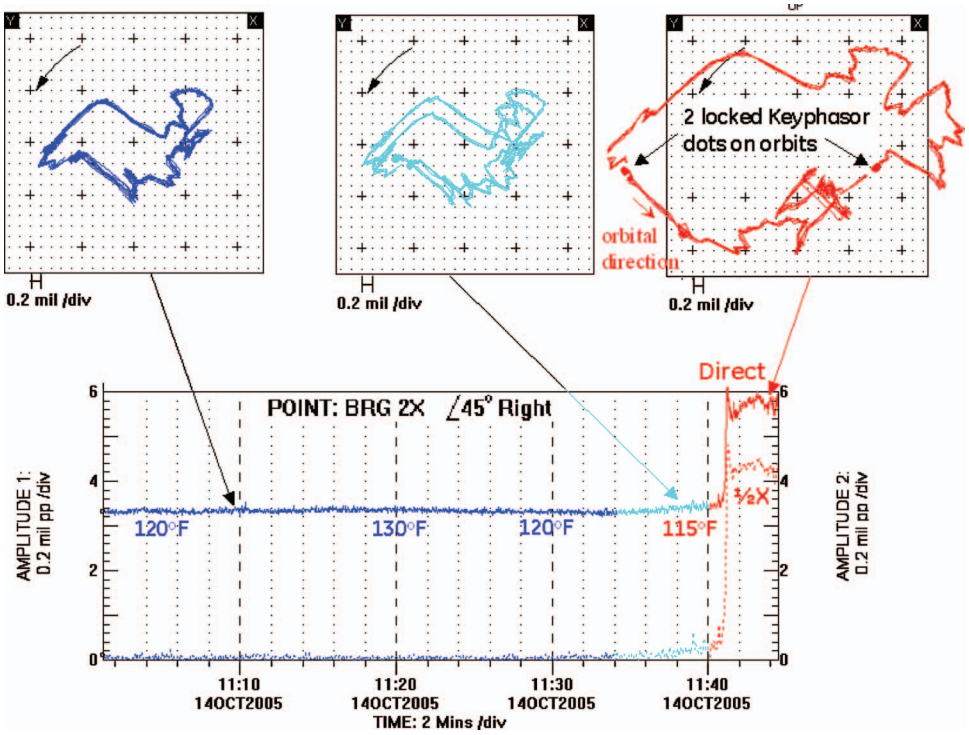

Fig. 10 $\frac{1}{2}X$ vibration occurred when oil temperature dropped to 115°F

component was increased from almost zero level to 6.0 mils (152 μm) pp at Bearing 2*X*-probe. The corresponding $\frac{1}{2}X$ vibration amplitudes at Bearings 1 and 3*X*-probes reached approximately 1 mil (25 μm) pp and 4.5 mils (114 μm) pp, respectively. Power output was then reduced to get rid of the subsynchronous vibration. However, when power output decreased to 3.0 MW at around 14:40, vibration still remained high. At around 14:44 when power output reduced to 1.5 MW, direct amplitude was still around 6 mils (152 μm) pp at Bearing 2. Vibration did not return to the previous normal level until power output decreased to 1.0 MW at around 14:45. Had the subsynchronous vibration frequency not been exactly $\frac{1}{2}X$, steam whirl might have been considered as a possible root-cause.

The effects of bearing oil temperature on the subsynchronous vibration were examined while keeping oil supply pressure at around 11.5 psi (gauge) and power output at around 2.2 MW. Oil temperature was kept at 120°F in the beginning, and vibration was steady at around 3.3 mils (84 μm) pp measured by Bearing 2*X*-probe, as shown in Fig. 10. When it increased to 130°F, no significant change in vibration was observed. However, when oil temperature decreased to 115°F, vibration excursion occurred, as shown in Fig. 10. As indicated in both orbital and trend plots at time 11:43:29, the vibration was predominantly composed of the $\frac{1}{2}X$ component. The two Keyphasor® dots were locked into the same spots on orbit during eight shaft revolutions. The $\frac{1}{2}X$ component reached 4.3 mils (109 μm) pp.

Note that abrupt changes can be observed on orbits parallel to orientations of *X*- and *Y*-probes. These were due to scratches of the shaft surface in the probe-viewing area, and affected direct vibration readings as well as 1*X*, 2*X*, and higher harmonic components. However, there should be no effect on $\frac{1}{2}X$ or any other subsynchronous component. In other words, if $\frac{1}{2}X$ or any other subsynchronous component is observed, it will be considered to be real no matter shaft scratches or runout issues exist or not.

Similar changes in shaft centerline plot as those observed in Case History 1 were also observed during this test. As shown in Fig. 11, $\frac{1}{2}X$ vibration started to develop when shaft centerline had a rise of about 0.5 mil (13 μm). After full-blown $\frac{1}{2}X$ occurred, the shaft centerline moved toward the left on this counterclockwise rotation machine.

Figure 12 shows a waterfall plot during this test. Prior to the onset of full-blown $\frac{1}{2}X$ vibration, subsynchronous components around 1800 cpm were observed. These low level components, as indicated in Case History 1, were most likely due to suppressed whip or steam whirl at a natural frequency near 1800 cpm.

Figure 13 shows a zoomed spectrum plot with 3200 spectral lines when high vibration excursion occurred. The high resolution of 1.88 cpm (0.03 Hz) confirms the exactly $\frac{1}{2}X$ component as well. It was also noticed that when shaft speed varied above 3600 rpm the subsynchronous frequency also changed accordingly to track the speed. The vibration was predominantly composed of the $\frac{1}{2}X$ component. The $\frac{3}{2}X$ component only accounted for less than 10% of the $\frac{1}{2}X$ component.

After letting vibration back to normal by increasing oil temperature, the effects of oil supply pressure on the subsynchronous vibration were also examined while keeping oil temperature at

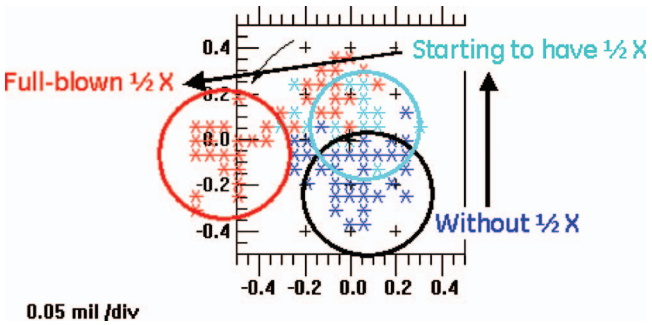

Fig. 11 Changes in shaft centerline at Bearing 2 during oil temperature variation test

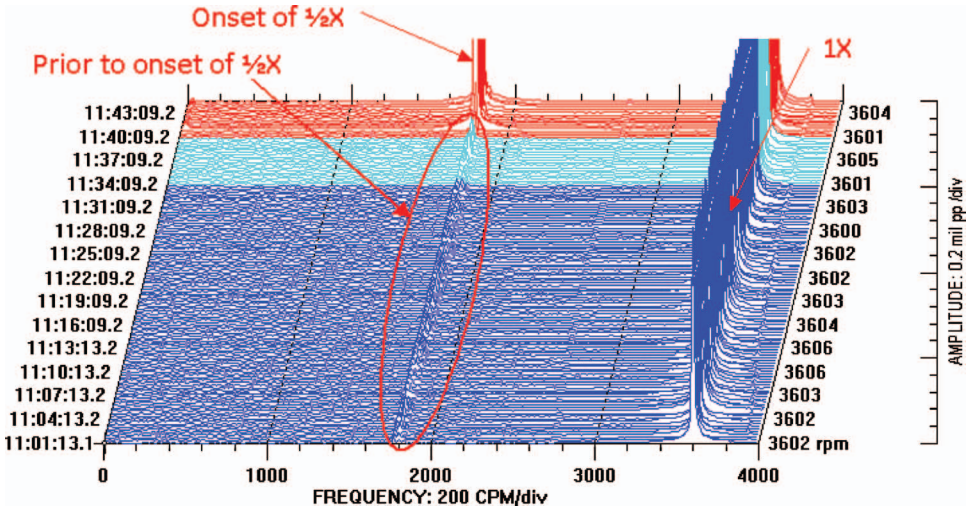

Fig. 12 Waterfall plot measured by Bearing 2*X*-probe showing subsynchronous components around 1800 cpm prior to onset of $\frac{1}{2}X$ vibration

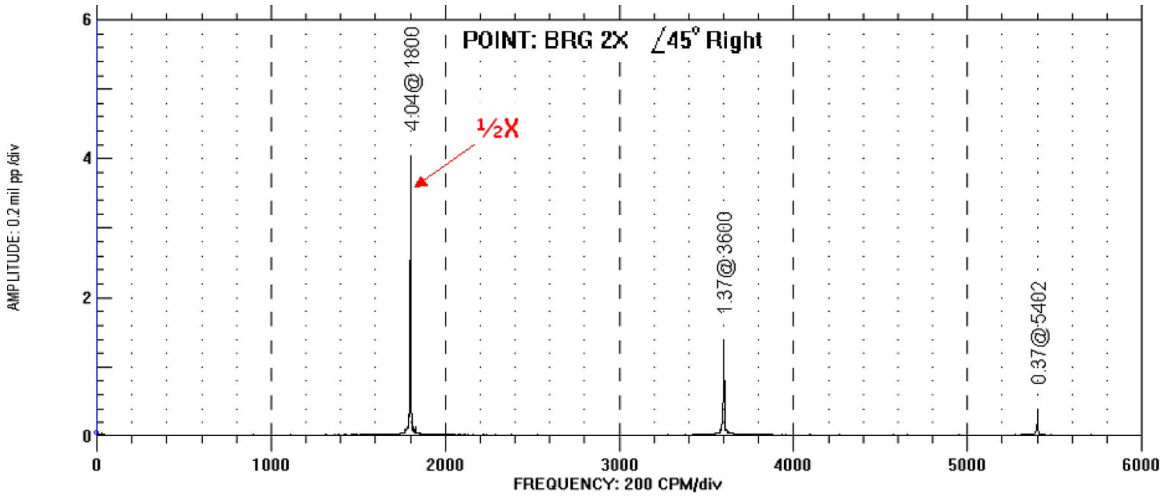

Fig. 13 Zoomed spectrum plot with frequency resolution of 1.88 cpm (0.03 Hz) when high vibration excursion occurred

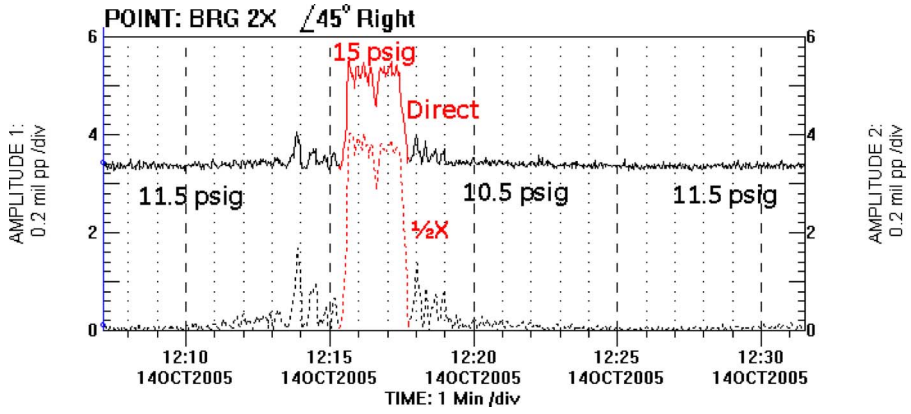

Fig. 14 $\frac{1}{2}X$ vibration occurred when oil supply pressure increased from 11.5 psi (gauge) to 15 psi (gauge)

120°F. Vibration remained steady at around 3.3 mils (84 μm) pp measured by Bearing 2*X*-probe while oil pressure increased from 11.5 psi (gauge) to 13 psi (gauge) at 12:10, as shown in Fig. 14. Oil pressure then continued to increase to 15 psi (gauge) at 12:13. 2 min later, vibration excursion occurred with the $\frac{1}{2}X$ component reaching 3.9 mils (99 μm) pp. After dropping oil supply pressure to around 10–11 psi (gauge), vibration returned to the previous normal level. Increasing oil supply pressure might have flooded the bearing. Swap in oil coolers, which resulted in an increase in oil pressure from approximately 12 psi (gauge) to 14 psi (gauge), also caused the $\frac{1}{2}X$ vibration excursion for a few minutes.

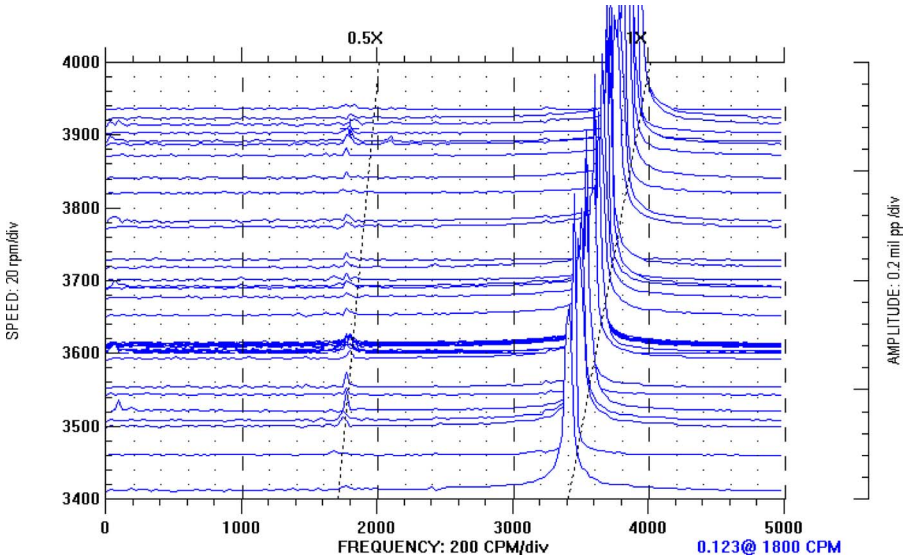

Fig. 15 Cascade plot measured by Bearing 2*X*-probe showing no vibration excursion when speed increased from 3600 rpm to 3940 rpm during overspeed test

If the vibration excursion frequency had been not exactly $\frac{1}{2}X$ during the above bearing oil temperature and pressure variation tests, oil whirl would have possibly been the root-cause. An overspeed test without power output was also performed earlier to check the possible oil whirl/whip issue. As shown in Fig. 15, no vibration excursion occurred when speed increased from 3600 rpm to 3940 rpm. Subsynchronous components around 1800 cpm were observed when speed was above 3500 rpm, but their amplitude was suppressed to a very low level. These suppressed components indicate the natural frequency of the rotor-bearing system near 1800 cpm or 30 Hz.

4 Case History 3

In the third case history, $\frac{1}{2}X$ vibration occurred on a rated 80 MW steam turbine generator made by another OEM. The steam turbine is made up of high- and intermediate-pressure (HP-IP) and low-pressure (LP) rotors, driving the 3600 rpm generator and the 1800 rpm exciter. Its machine train diagram is shown in Fig. 16. The setup of *X*- and *Y*-probes is the same as in the above-mentioned two cases. The turbine shaft rotation direction, however, is considered to be clockwise when viewed from driver to driven. The data in this case were presented by using SYSTEM1® software.

High vibration excursion occurred at Bearing 3 (plain sleeve bearing) as shown in Fig. 17. Within 2 s from 17:31:17 to 17:31:19, direct vibration amplitude measured by Bearing 3*Y*-probe suddenly increased from 3.8 mils (97 μm) pp to 13 mils (330 μm) pp. Figure 17 points to the time at 17:32:10 when over 13 mil pp amplitude was measured by the data collection system just before shutdown. Vibration of over 12 mils maintained until speed dropped to below 2944 rpm at 17:34:44.

Fairly circular forward orbits were observed for this $\frac{1}{2}X$ vibration excursion, as shown in Fig. 18 at a speed of 3600 rpm before shutdown. The corresponding full spectrum shows a predominant $+\frac{1}{2}X$ (forward) component of around 12 mils (305 μm) pp versus a $-\frac{1}{2}X$ (reverse) component of around 1.6 mils (41 μm) pp. The $\frac{3}{2}X$ amplitude was less than 1 mil (25 μm) pp for either forward or reverse component. Figure 19 shows orbit at speed of 3245 rpm during shutdown when the $\frac{1}{2}X$ vibration still existed. Vibration amplitudes at Bearing 3 reached over 15 mils (381 μm) pp at both *X*- and *Y*-probes with fairly circular forward orbits.

Figure 20 shows a waterfall plot measured by *Y*-probe at Bearing 3 prior to the onset of $\frac{1}{2}X$ vibration. Similar to the above-mentioned two cases, subsynchronous components around 1800 cpm were detected before the extremely high $\frac{1}{2}X$ vibration occurred. These low level components, probably due to suppressed oil whip or steam whirl, indicate a natural frequency of the rotor-bearing system near 1800 cpm or half of the running speed of 3600 rpm.

It was reported that diametral clearance on Bearing 3 was approximately 0.020 in. Shaft centerline plot during shutdown resulting from vibration excursion shows an approximately 0.015 in. drop from 3600 rpm to turning gear speed. This indicates that the Bearing 3 journal was staying too high within its bearing. A shaft centerline rise was also observed before the onset of $\frac{1}{2}X$ vibration.

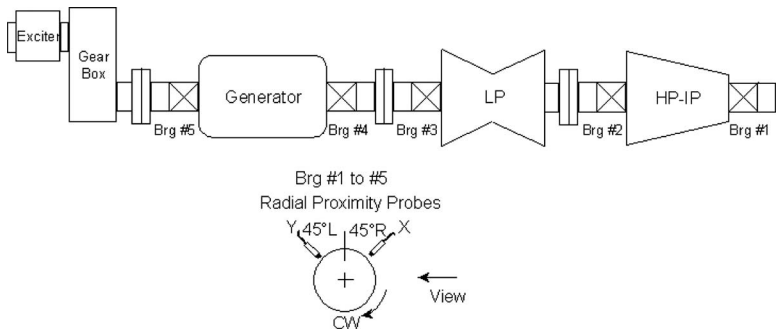

Fig. 16 Machine train diagram for Case History 3

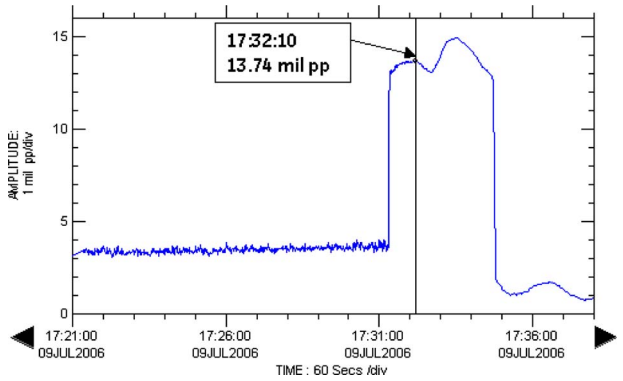

Fig. 17 Vibration excursion occurred at Bearing 3 *Y*-probe not due to 1 *X* component

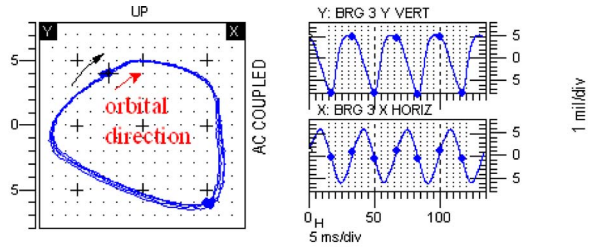

(a) Orbits and timebase

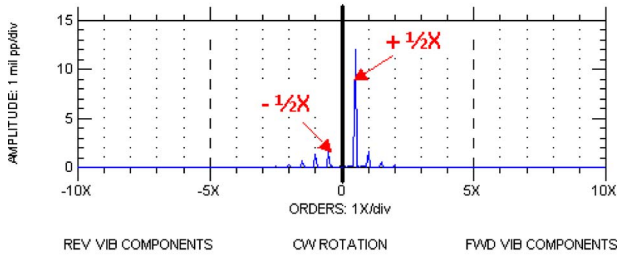

(b) Full spectrum

Fig. 18 $\frac{1}{2}X$ vibration orbits and spectrum at 3600 rpm

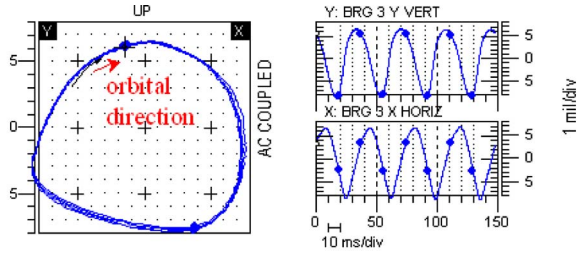

(a) Orbits and timebase

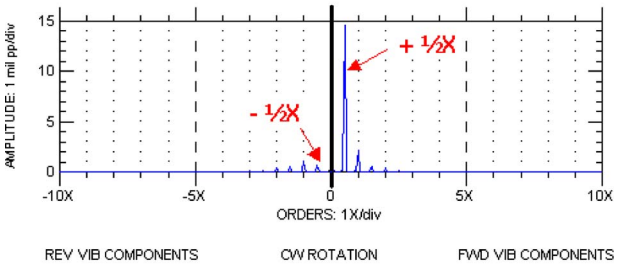

(b) Full spectrum

Fig. 19 $\frac{1}{2}X$ vibration orbits and spectrum at 3245 rpm

5 Discussions

Parametric excitation analysis of why $\frac{1}{2}X$ vibration can occur is attached in the Appendix, which includes an unstable speed region for the Jeffcott rotor model. Step-changing nonlinear stiffness function is modeled and expanded into Fourier series. The homogeneous equation of the Jeffcott rotor model is then simplified into the well-known Mathieu equation, which yields solution of instability.

As indicated in the Appendix, two conditions are needed to make this unstable $\frac{1}{2}X$ vibration possible. First, stiffness would need a step-change within a cycle or orbit of synchronous $1X$ vibration. In the above three real cases, shaft centerline had a rise prior to the full-blown $\frac{1}{2}X$ vibration. It is believed that when the journal moved upward to some point, bearing stiffness became nonlinear. In other words, on part of the orbit journey at the top,

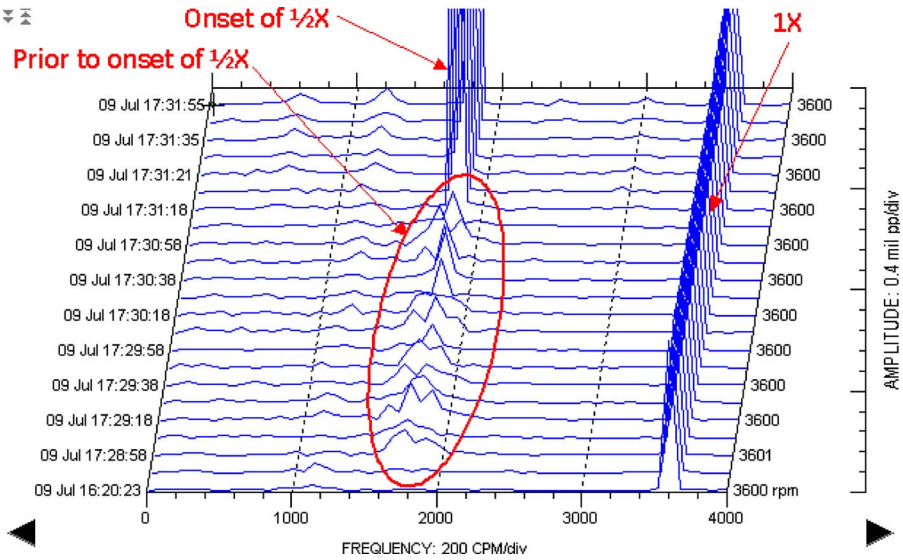

Fig. 20 Waterfall plot measured by Bearing 3 *Y*-probe showing subsynchronous components around 1800 cpm prior to the full-blown $\frac{1}{2}X$ vibration

bearing stiffness decreased from K_0 to $K_0+\Delta K$ where $\Delta K<0$ (see Appendix). An oversize bearing as shown in Case 1 is more prone to have this issue. After replacing the oversized bearing, the $\frac{1}{2}X$ vibration no longer occurred in Case 1. Managing not to let journal or shaft centerline move upward might be able to prevent step-changing stiffness and so to avoid $\frac{1}{2}X$ vibration. Second, rotor speed would have to be approximately at twice the natural frequency of the rotor-bearing system. In the above three cases, very low level subsynchronous components around 1800 cpm were observed prior to the full-blown $\frac{1}{2}X$ vibration for these 3600 rpm machines. The frequency of these subsynchronous components, most likely affected by suppressed oil whip or steam whirl, should be very close to the natural frequency of the rotor-bearing system. This fact indicates that the machine was running approximately at twice the natural frequency. Step-changing stiffness region α and level of change ΔK, as shown in Eq. (A12) in the Appendix, determine the unstable speed region that allows for $\frac{1}{2}X$ vibration. That explains why the $\frac{1}{2}X$ vibration still maintained until speed dropped to 3299 rpm in Case 1 and 2944 rpm in Case 3. For these three cases, based on shaft centerline plots, normal-loose appear to be the case. Though bearing damage was observed at the left of the bearing wall in the first case history, the impact of journal against the bearing wall apparently did not occur when the $\frac{1}{2}X$ vibration just started to occur, according to the shaft centerline plot. The impact is believed to happen when orbit became larger for the journal to touch the bearing wall, and the $\frac{1}{2}X$ vibration still maintained afterwards by having this step-changing stiffness due to partial rub.

It is very interesting to see that the $\frac{1}{2}X$ vibration can be triggered by changes in oil temperature and pressure in Case 2. Without looking at the orbits or high-resolution spectrum plots, one would believe that the high vibration excursion was oil whirl/whip. The fact of pure $\frac{1}{2}X$ vibration indicates that it was not oil whirl/whip. The decrease in bearing oil temperature caused the shaft centerline to move upward, which might have created step-changing stiffness. Changes in the bearing oil condition might have also affected damping, which contributes to the instability threshold.

For the first case, the $\frac{1}{2}X$ vibration issue was completely resolved by replacing the oversize bearing. For the second case, since the machine needed to run continuously without any outage, the $\frac{1}{2}X$ vibration was avoided by maintaining bearing oil temperature 120°F or above and oil pressure 11.5 psi (gauge) or below with power output of around 3 MW or below. For the third case, the $\frac{1}{2}X$ vibration was avoided by reducing bearing oil temperature.

6 Conclusions

Based on real case studies along with stability analysis presented in this paper, the following conclusions are stated regarding $\frac{1}{2}X$ vibration that occurred in real rotating machines.

(1) Extremely high $\frac{1}{2}X$ vibration with a fairly circular forward orbit can occur in real machines. For reported two cases, vibration amplitude increased from around 2 mils (51 μm) pp to over 12 mils (305 μm) pp.
(2) Subsynchronous components at around half of the running speed, which may be at a very low level due to suppressed oil whip or steam whirl, could be a warning sign of having potential $\frac{1}{2}X$ vibration. This indicates that one of the natural frequencies of the rotor-bearing system, usually the lowest, is around half of the running speed. Redesign of bearing might be an option to keep the resonance away from half of the running speed.
(3) Onset of $\frac{1}{2}X$ vibration was accompanied by changes in shaft centerline. As journal or shaft centerline moved upward, step-changing nonlinear bearing stiffness occurred to make parametric excitation and trigger $\frac{1}{2}X$ vibration. An oversize or less loaded bearing tends to create this situation. Control of shaft centerline movement by appropriate loading on bearing might be able to prevent nonlinear bearing stiffness and $\frac{1}{2}X$ vibration.
(4) Two conditions are required for $\frac{1}{2}X$ vibration to occur as indicated in (2) and (3). Based on shaft centerline and orbital plots, as well as on unstable speed regions, normal-loose appears to be the case for these three reported real cases, though normal-tight due to partial rub could create $\frac{1}{2}X$ vibration as well. The latter, as reported in rotor kit experiment [9], may typically form an 8 shape orbit.
(5) Vibration excursion triggered by changes in bearing oil temperature or pressure may not necessary be the oil whirl/whip issue. As demonstrated in the second case history, decreasing oil temperature or increasing oil pressure triggered pure $\frac{1}{2}X$ vibration.

Acknowledgment

The author is grateful to Robert C. Eisenmann, Sr. of GE Energy for his support of and comments on the current work.

Nomenclature

x = rotor lateral deflection in one direction
M = rotor mass
D = damping of the rotor-bearing system
$K(\Omega t)$ = time-varying stiffness of the rotor-bearing system
K_0 = original stiffness
ΔK = increased or decreased stiffness during part of the vibration cycle
α = range where ΔK occurs
k = any positive integer
m = unbalance mass
r = radius of unbalance mass
φ = phase lag of unbalance mass
Ω = rotor speed
t = time
τ = dimensionless time variable
a_n = Fourier coefficient of cosine term
b_n = Fourier coefficient of sine term
δ = coefficient in Mathieu equation
ε = coefficient in Mathieu equation (same sign as ΔK in this paper)
ω_n = original natural frequency of the rotor-bearing system

Appendix: Parametric Excitation Analysis on $\frac{1}{2}X$ Vibration

The equation of motion of the Jeffcott rotor model can be given by

$$M\frac{d^2x}{dt^2}+D\frac{dx}{dt}+K(\Omega t)x=mr\Omega^2\cos(\Omega t-\varphi) \tag{A1}$$

where x is the rotor lateral deflection in one direction, M is rotor mass, D and $K(\Omega t)$ are damping and stiffness of the rotor-bearing system, m, r, and φ are unbalance mass, radius, and phase lag, Ω is the rotor speed, and t is time.

In some circumstance, stiffness changes within each vibration cycle. It could be decreased (normal-loose) or increased (normal-tight) for part of synchronous $1X$ vibration cycle. To reflect this change in stiffness, as shown in Fig. 21, $K(\Omega t)$ can be modeled by the following periodic step-function:

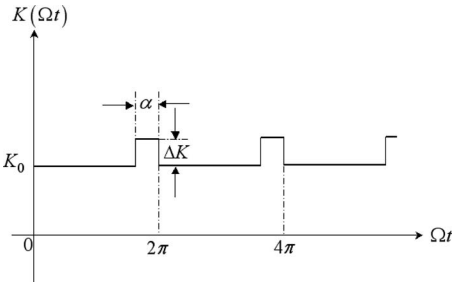

Fig. 21 Time-dependent stiffness varying within each synchronous 1*X* vibration cycle

$$K(\Omega t) = \begin{cases} K_0 & \text{for } 2(k-1)\pi \le \Omega t < 2k\pi - \alpha \\ K_0 + \Delta K & \text{for } 2k\pi - \alpha \le \Omega t \le 2k\pi \end{cases} \quad \text{(A2)}$$

where K_0 is original stiffness, ΔK is the change in stiffness, α is the range where stiffness has the change ΔK, and k can be any positive integer. Equation (A2) can be expressed as Fourier series in the following:

$$K(\Omega t) = \frac{a_0}{2} + \sum_{n=1}^{\infty} (a_n \cos n\Omega t + b_n \sin n\Omega t) \quad \text{(A3)}$$

where

$$a_n = \frac{1}{\pi}\int_0^{2\pi} K(\Omega t)\cos n\Omega t d(\Omega t)$$

$$b_n = \frac{1}{\pi}\int_0^{2\pi} K(\Omega t)\sin n\Omega t d(\Omega t)$$

Thus time-dependent stiffness $K(\Omega t)$ can be given by

$$K(\Omega t) = K_0 + \frac{\alpha\Delta K}{2\pi} + \frac{2\Delta K}{\pi}\sum_{n=1}^{\infty}\frac{\sin\dfrac{n\alpha}{2}}{n}\cos\left(n\Omega t + \frac{n\alpha}{2}\right) \quad \text{(A4)}$$

A dimensionless time variable τ is introduced as follows:

$$\tau = \tfrac{1}{2}\Omega t + \tfrac{1}{4}\alpha \quad \text{(A5)}$$

Since the homogenous solution of Eq. (A1) is of interest only to examine instability issues, the unbalance force term is neglected. To examine possible $\frac{1}{2}X$ parametric excitation due to time-dependent stiffness, case $n=1$ in Eq. (A4) is considered. Inserting Eq. (A4) with $n=1$ and Eq. (A5) into Eq. (A1) yields

$$\frac{d^2x}{d\tau^2} + \frac{2D}{M\Omega}\frac{dx}{d\tau} + (\delta + 2\varepsilon\cos 2\tau)x = 0 \quad \text{(A6)}$$

where

$$\delta = \frac{1}{\left(\dfrac{1}{2}\Omega\right)^2}\frac{K_0 + \dfrac{\alpha\Delta K}{2\pi}}{M} \quad \text{(A7)}$$

$$\varepsilon = \frac{1}{\left(\dfrac{1}{2}\Omega\right)^2}\frac{\Delta K \sin\dfrac{\alpha}{2}}{\pi M} \quad \text{(A8)}$$

To get an approximate solution of the instability region and frequency, the damping term in Eq. (A6) is neglected. Thus, Eq. (A6) is simplified into the standard Mathieu equation [11] as follows:

$$\frac{d^2x}{d\tau^2} + (\delta + 2\varepsilon\cos 2\tau)x = 0 \quad \text{(A9)}$$

The principal instability region is approximately determined by

$$|\delta - 1| < |\varepsilon| \quad \text{(A10)}$$

and the unstable solution is dominantly composed of $\cos\tau$ and $\sin\tau$ terms. As indicated in Eq. (A5), this is exactly the $\frac{1}{2}X$ vibration.

Assume that α is small. Thus $\sin(\alpha/2) \approx \alpha/2$. From Eq. (A10), the unstable speed region due to step-changing stiffness is determined by

$$2\omega_n < \Omega < 2\omega_n\sqrt{1 + \frac{\alpha\Delta K}{\pi K_0}} \quad \text{for } \Delta K > 0 \quad \text{(A11)}$$

and

$$2\omega_n\sqrt{1 + \frac{\alpha\Delta K}{\pi K_0}} < \Omega < 2\omega_n \quad \text{for } \Delta K < 0 \quad \text{(A12)}$$

where

$$\omega_n = \sqrt{\frac{K_0}{M}}$$

is obviously the original natural frequency of the rotor-bearing system. Equations (A11) and (A12) can be regarded as normal-tight and normal-loose cases, respectively.

References

[1] Ehrich, F. F., 1999, *Handbook of Rotordynamics*, Krieger, Malabar, FL.
[2] Muszynska, A., 1986, "Whirl and Whip—Rotor/Bearing Stability Problems," J. Sound Vib., **110**, pp. 443–462.
[3] Shen, G., Xiao, Z., Zhang, W., and Zheng, T., 2006, "Nonlinear Behavior Analysis of a Rotor Supported on Fluid Film Bearings," ASME J. Vibr. Acoust., **128**, pp. 35–40.
[4] Crandall, S., 1990, "From Whirl to Whip in Rotordynamics," IFToMM Third International Conference on Rotordynamics, Lyon, France, pp. 19–26.
[5] Childs, D. W., 1993, *Turbomachinery Rotordynamics: Phenomena, Modeling, and Analysis*, Wiley, New York.
[6] Ehrich, F. F., 1966, "Subharmonic Vibration of Rotors in Bearing Clearance," ASME Paper No. 66-MD-1.
[7] Bently, D. E., 1974, "Forced Subrotative Speed Dynamic Action of Rotating Machinery," ASME Paper No. 74-Pet-16.
[8] Childs, D. W., 1982, "Fractional Frequency Rotor Motion Due to Non-Symmetric Clearance Effects," ASME J. Eng. Power, **104**(3), pp. 533–541.
[9] Muszynska, A., 1984, "Partial Lateral Rotor to Stator Rubs," *Proceedings of the Third International Conference on Vibration in Rotating Machinery*, IMechE, York, UK, pp. 227–236, Paper No. C281/84.
[10] Eisenmann, R. C., Sr., and Eisenmann, R. C., Jr., 1997, *Machinery Malfunction Diagnosis and Correction: Vibration Analysis and Troubleshooting for the Process Industries*, Prentice-Hall, Englewood Cliffs, NJ.
[11] Meirovitch, L., 1975, *Elements of Vibration Analysis*, McGraw-Hill, New York.

An Experimental and Modeling Study of HCCI Combustion Using *n*-Heptane

Hongsheng Guo
W. Stuart Neill
Wally Chippior

National Research Council Canada,
1200 Montreal Road,
Ottawa, ON, K1A 0R6, Canada

Hailin Li
West Virginia University,
P.O. Box 6106,
Morgantown, WV, 26506

Joshua D. Taylor
National Renewable Energy Laboratory,
1617 Cole Boulevard,
Golden, CO 80401

Homogeneous charge compression ignition (HCCI) is an advanced low-temperature combustion technology being considered for internal combustion engines due to its potential for high fuel conversion efficiency and extremely low emissions of particulate matter and oxides of nitrogen (NO_x). In its simplest form, HCCI combustion involves the auto-ignition of a homogeneous mixture of fuel, air, and diluents at low to moderate temperatures and high pressure. Previous research has indicated that fuel chemistry has a strong impact on HCCI combustion. This paper reports the preliminary results of an experimental and modeling study of HCCI combustion using n-heptane, a volatile hydrocarbon with well known fuel chemistry. A Co-operative Fuel Research (CFR) engine was modified by the addition of a port fuel injection system to produce a homogeneous fuel-air mixture in the intake manifold, which contributed to a stable and repeatable HCCI combustion process. Detailed experiments were performed to explore the effects of critical engine parameters such as intake temperature, compression ratio, air/fuel ratio, engine speed, turbocharging, and intake mixture throttling on HCCI combustion. The influence of these parameters on the phasing of the low-temperature reaction, main combustion stage, and negative temperature coefficient delay period are presented and discussed. A single-zone numerical simulation with detailed fuel chemistry was developed and validated. The simulations show good agreement with the experimental data and capture important combustion phase trends as engine parameters are varied.
[DOI: 10.1115/1.3124667]

1 Introduction

Homogeneous charge compression ignition (HCCI) is an advanced low-temperature combustion technology. In principle, HCCI involves the auto-ignition of a homogeneous mixture of fuel, air, and diluents at low to moderate temperatures and high pressure. This approach enables the engine designer to have a high compression ratio (CR), minimize air throttling losses, and rapidly burn the fuel-air mixture near top dead center, which contributes to high thermal efficiency. Meanwhile, the burning of a homogeneous fuel-lean mixture at relatively low-temperature suppresses the formation of particulate matter (PM) and oxides of nitrogen (NO_x), the two problematic emissions from diesel engines. These desirable combustion characteristics make HCCI a potentially promising combustion mode for internal combustion engines [1,2].

HCCI was identified as a distinct combustion phenomenon in the late 1970s. Early research [3–5] investigated the potential benefits of HCCI combustion and recognized its potentially attractive characteristics for internal combustion engines. Different approaches for controlling HCCI combustion phasing have been reported [1,5–7]. Christensen et al. [8] demonstrated that HCCI combustion has a multifuel capability compared to traditional internal combustion engines. Recent experimental data available in the open literature [8–12] indicate that fuel chemistry has a strong impact on HCCI combustion. It has been recognized that there is a potential benefit to better understand the fundamentals of HCCI combustion, and, in particular, tailoring a fuel specifically for HCCI combustion [9]. HCCI combustion of both gasoline- and diesel-like fuels and their mixtures has been investigated [10–12]. In these studies, direct injection (DI) diesel engines were adopted due to the increasing interest in employing low-temperature combustion strategies for the reduction in diesel engine emissions [11]. A low-pressure port fuel injector was used in one study to atomize diesel fuels for HCCI combustion research [12].

Apart from fuel chemistry, the fuel injection system and the physical properties of the fuel affect the formation of a homogeneous fuel-air mixture and the HCCI combustion process [11,13]. The experimental results from prototype production engines, typically employing direct injection strategies, reflect the combined effects of fuel injection, fuel-air mixing, and fuel chemistry. The results obtained by different manufacturers may not be consistent due to different fuel injection hardware and combustion strategies adopted to form the homogeneous mixture and control HCCI combustion. This makes it very difficult to ascertain the fuel chemistry effects. In addition, it is very difficult to interpret some experimental data available in the open literature without detailed knowledge of the specific engine hardware and the low-temperature combustion strategy employed. However, detailed information is not always provided, particularly when economic considerations are paramount. Thus, there appears to be a need to develop a method that can be used to evaluate the low-temperature combustion of candidate HCCI fuels, while isolating the effects of the fuel injection system and fuel physical properties.

An engine research facility was constructed to focus on the fuel chemistry aspects of HCCI combustion. The effects of fuel physical properties and fuel system hardware on HCCI combustion were isolated through the adoption of an air-assist port fuel injection system. The system is able to finely atomize a variety of hydrocarbon fuels, leading to a homogeneous air/fuel mixture in the combustion chamber before significant oxidation reactions occur [10,13]. *N*-heptane, a liquid reference fuel with a low boiling point and well known chemistry was used in the current research.

Contributed by the Internal Combustion Engine Division of ASME for publication in the JOURNAL OF ENGINEERING FOR GAS TURBINES AND POWER. Manuscript received November 28, 2006; final manuscript received August 7, 2008; published online October 15, 2009. Review conducted by Christopher J. Rutland. Paper presented at the 2006 Fall Conference of the ASME Internal Combustion Engine Division (ICEF2006), Sacramento, CA, November 5–8, 2006.

Table 1 Engine specifications

Cylinder bore	82.55 mm
Stroke	114.3 mm
Displacement	611.7 ml
Connecting rod length	254 mm
Compression ratio	4.6–16
Combustion chamber	Pancake shape
Intake valve open	10°CA ATDC
Intake valve close	36°CA ABDC
Exhaust valve open	40°CA BBDC
Exhaust valve close	5°CA ATDC
Fuel system	Air-assist port fuel injection

Preliminary research has been conducted to demonstrate its capability to produce stable and repeatable HCCI combustion. In the future, this facility will be used to better understand the role of fuel chemistry in low-temperature combustion and to develop an appropriate method for rating the suitability of HCCI fuels.

Numerical simulations have been widely used to explore fuel chemistry effects on the performance of HCCI engines. Considering the relatively minor influence of physical effects such as turbulence and mixing on HCCI combustion as reported in the literature [1], single- and multizone simulations are suitable tools for exploring fuel chemistry effects on HCCI combustion [14–17], as well as to validate detailed chemical kinetic models [15]. For the current application to predict HCCI combustion phasing, there does not seem to be a requirement to develop a detailed computational fluid dynamics (CFD) model. Also, the large computational requirement for a CFD model limits the ability to implement detailed fuel chemistry, which has been demonstrated to be a critical element in HCCI research [14,15]. Of course, CFD is a useful tool for understanding engine performance and emissions, where the presence of boundary layer and crevices are of great importance.

This paper reports the preliminary results of an experimental and modeling study of HCCI combustion over a wide range of operating conditions using *n*-heptane. The experiments were designed to investigate the effects of a number of engine parameters on the combustion phasing of the low-temperature reaction (LTR) and main combustion stage (MCS), as well as to measure the negative temperature coefficient (NTC) delay period. A numerical model with detailed fuel chemistry was developed and compared to the combustion data obtained in this study. The numerical simulation was able to capture the combustion phasing trends observed during the experiments with changes in several engine parameters. Based on the experimental and numerical results, it is believed that the research engine used in this study is suitable for investigating fuel chemistry effects on HCCI combustion. In the future, the research engine will be used to evaluate the HCCI combustion behavior of real hydrocarbon fuels.

2 Experimental Apparatus and Procedure

2.1 CFR Engine. A Co-operative Fuel Research (CFR) engine was used for this research. It is a single-cylinder, variable compression ratio, four-stroke engine commonly used to evaluate the knock resistance of gasoline and the ignition quality of diesel fuels. Table 1 provides the basic specifications of the CFR engine. Figure 1 shows the schematic of the research facility.

The engine was modified from the standard ASTM setup by the addition of an air-assist port fuel injection system and other hardware and software needed for the control of critical engine parameters such as intake air temperature, air/fuel ratio (AFR), exhaust gas recirculation, and intake and exhaust back pressure.

2.2 Fuel Injection. A port fuel injector for flexible fuel vehicles was modified to provide air-assist atomization of liquid fuels. For this study, the fuel system and air-assist pressures were

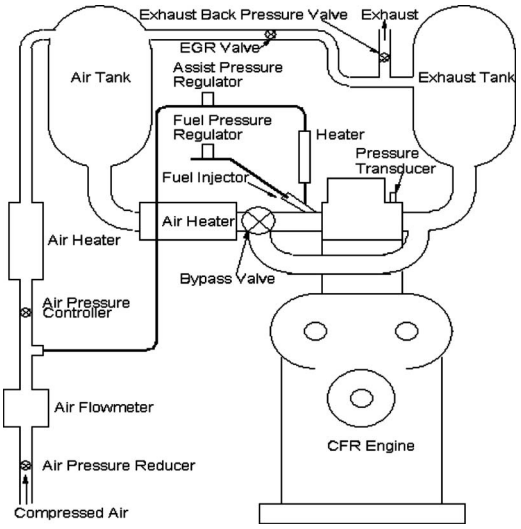

Fig. 1 Schematic of HCCI engine setup

maintained at 500 kPa and 200 kPa, respectively. The injector produces droplets with a Sauter mean diameter (SMD) of 15 μm or less with both diesel- and gasolinelike fuels under these conditions. In this research, the fuel was injected into the intake manifold during the intake stroke. A Coriolis-effect mass flow meter (Micro Motion, Model D6) was used to measure the fuel flow rate. The amount of fuel injected was controlled by adjusting the fuel injection pulse width, and feedback control was provided based on the measured fuel and air flow rates.

2.3 Intake Air and Exhaust Systems. Surge tanks were installed in the intake and exhaust systems to minimize pressure pulsations of the intake and exhaust gases, thereby improving engine operational stability and airflow measurement. The intake air was maintained at a specified temperature by precisely controlling the power supplied to a 1.5 kW heater installed after the intake surge tank. Combustion air was supplied by regulated compressed air and mixed with the desired quantity of recirculated exhaust in the intake surge tank.

The exhaust surge tank provides complete mixing of the exhaust gases before sampling for emissions analysis and recirculation into the intake manifold. A back pressure valve was installed at the exit of exhaust surge tank to create the pressure drop needed for exhaust gas recirculation (EGR) operation and to simulate the back pressure of the turbocharged engine.

The total air flow rate to the engine was measured using a mass flow meter (Sierra, model 780 Series Flat-Trak™). A portion of the air was diverted to assist in fuel atomization prior to entering the intake manifold.

2.4 Data Acquisition. The low-speed data acquisition system is based on National Instruments' PXI hardware platform. The hardware is controlled by data acquisition and control software (Sakor Technologies, Inc., DynoLAB™ PT), which provided stable control of the engine speed and load conditions, as well as critical parameters such as engine coolant and lubricating oil temperatures, intake air pressure and temperature, exhaust back pressure, fuel injection timing, and the quantity of fuel injected.

Cylinder pressure was measured with a high frequency-response piezoelectric pressure transducer (Kistler Corp., model 6121) mounted flush with the cylinder surface using the detonation transducer access port. The transducer was connected to a dual mode charge amplifier (Kistler, model 5010). An encoder fitted to the cam shaft provided a transistor-transistor logic (TTL) signal with a resolution of 0.1 deg camshaft (0.2 deg crankshaft), which was used as the data acquisition clocking pulses to acquire the pressure data and which served also as an input to the fuel and

blast air injection controlling hardware/software. The resultant pressure and crank angle signals were routed to a high-speed data acquisition system (Op-timum Power Technology, model PTrAc), also based on National Instruments' hardware.

2.5 Dynamometer. The engine was coupled to an eddy current dynamometer that absorbed engine load. A variable-speed ac motor, coupled to the dynamometer with an overdrive clutch, was used to start and motor the engine before stable HCCI combustion was initiated, as well as to maintain engine speed when HCCI combustion was unstable.

2.6 Experimental Procedure. Prior to each experiment, the lubricating oil and coolant systems were preheated by electric heaters to a temperature of 82°C. At the same time, the intake and exhaust systems were also preheated. HCCI combustion was easily initiated after the coolant, lubricating oil, and fuel/air mixture temperatures reached the desired levels. At each operating condition, the engine was run for at least 5 min or until engine operation stabilized before sampling experimental data while continually monitoring key operating parameters such as intake pressure and temperature, as well as brake power, brake specific fuel consumption (BSFC) and unburned hydrocarbon (UHC) and carbon monoxide (CO) emissions.

At each operating condition, engine performance data and critical operating parameters were collected for approximately 4 min at a sampling frequency of 1 Hz. At the same time, 500 engine working cycles were sampled, stored, and processed. The averaged cylinder pressure was analyzed to obtain the heat release and a complete set of combustion parameters such as CA50 and NTC delay period. Each cycle was analyzed individually and used to calculate statistical results such as the COV_{IMEP}. In this research, pure *n*-heptane was used as fuel.

3 Numerical Simulation

In order to predict the combustion process of the HCCI engine, a numerical model with detailed chemistry was developed to simulate the four-stroke process. The intake stroke was simulated while accounting for the presence of residual gases and fresh charge efficiency measured experimentally. The air-fuel-diluents mixture was assumed to be an ideal gas with uniform temperature, pressure, and mixture composition. If blow-by is neglected, the energy conservation equation for the working fluid at any instant in time t, from intake valve closure to exhaust valve opening, is

$$\frac{dQ}{dt} = \frac{dU}{dt} + \frac{dW}{dt} \tag{1}$$

where Q is the heat transfer to the cylinder charge, U is the total internal energy of the cylinder charge, and W is work output due to piston movement.

dW/dt is given by

$$\frac{dW}{dt} = P\frac{dV}{dt} \tag{2}$$

where P is the cylinder pressure, and V is the volume of the combustion chamber.

dQ/dt is given by

$$\frac{dQ}{dt} = -h \cdot A(T - T_w) \tag{3}$$

where A is the surface area of the combustion chamber wall, T is the mean temperature of the charge, T_w is the cylinder wall temperature that is assumed to be constant throughout the cycle, and h is the heat transfer coefficient. Traditionally, h is estimated using an empirical equation developed by Woschni [18] and Heywood [19]. The equation was derived for a propagating turbulent flame, which is obviously not the case of HCCI engine. In this research, the heat transfer coefficient was calculated using formulations derived recently by Chang et al. [20] based on spatially averaged heat flux measurements of HCCI combustion using gasoline.

dU/dt may be calculated as

$$\frac{dU}{dt} = \frac{d\sum (N_i u_i)}{dt} = \sum N_i \frac{du_i}{dt} + \sum u_i \frac{dN_i}{dt} \tag{4}$$

where N_i is the number of moles of the ith species. It changes with time as a result of a chemical reaction as follows:

$$\frac{dN_i}{dt} = V\dot{\omega}_i \tag{5}$$

where $\dot{\omega}_i$ is the production rate of the ith species and can be calculated using CHEMKIN subroutines based on the instantaneous mixture composition, temperature, and pressure. The remaining thermodynamic properties such as internal energy and specific heat capacity were also calculated using CHEMKIN with the corresponding species property data reported in the literature [21].

The presence of residual gases was also considered. The temperature and composition of the combustion products at the exhaust valve closing of the prior engine cycle was used to calculate the residual gas composition and other properties such as enthalpy of the bulk mixture of the following cycle. After adjusting the temperature and composition of the calculated residual gases, the cycle calculation was repeated until the cylinder mixture temperature from one cycle to the next varied by less than 0.5°C at the exhaust valve opening. Under normal conditions, the cylinder mixture temperature converged after three engine cycles. When the combustion process was retarded, however, it took more than five cycles to obtain a stable exhaust temperature considering the significant effect of intake temperature on HCCI combustion under such conditions.

3.1 Effective Fuel/Air Mixture Temperature. In this research, the intake air-diluent mixture temperature was measured using a thermocouple installed about 25 cm upstream of the intake valve and 5 cm upstream of fuel injector. However, the intake mixture is cooled due to fuel evaporation and then continually heated by the intake port and intake valve. Accordingly, the effective fuel/air mixture temperature entering the combustion chamber must be estimated. Following the procedure recommended in literature [22], the effective intake temperature $T_{\text{in,effective}}$ was estimated as follows:

$$T_{\text{in,effective}} = T_{\text{in,effective,base}} \cdot \frac{\dot{m}_{\text{air,base}}}{\dot{m}_{\text{air+fuel}}} \cdot \frac{M_{\text{air+fuel}}}{M_{\text{air}}} \cdot \frac{P_{\text{in}}}{P_{\text{in,base}}} \tag{6}$$

where $\dot{m}_{\text{air+fuel}}$, $M_{\text{air+fuel}}$, and P_{in} are the mass flow rate, molar mass, and pressure of intake mixture, respectively; $\dot{m}_{\text{air,base}}$, $M_{\text{air,base}}$, and $P_{\text{in,base}}$ are the mass flow rate, molar mass, and intake air pressure for the base case, respectively; and $T_{\text{in,effective,base}}$ is the effective intake temperature for the base case.

In principle, the base case can be any experimental condition for which the effective intake temperature can be accurately estimated or computed. For this study, the base case involved motoring the engine at a constant speed while maintaining the intake air and lubricating oil and coolant temperatures at 82°C. Under these conditions, heat transfer between the intake mixture and the intake port and valve is minimized and the effective fuel/air mixture temperature will be close to the intake air temperature. Figure 2 shows the variation of the effective intake mixture temperature as a function of the intake air temperature with a constant AFR. For 20°C intake air temperature, the effective intake mixture temperature was about 20°C higher than the measured intake air temperature. The effective intake mixture temperature was equivalent to the intake air temperature with an intake air temperature of 82°C, as shown in Fig. 2.

3.2 Fuel Chemistry. A detailed chemistry, consisted of 561 species and 2539 elementary reactions, was adopted to simulate the ignition process for *n*-haptane-air mixtures [21]. This is the

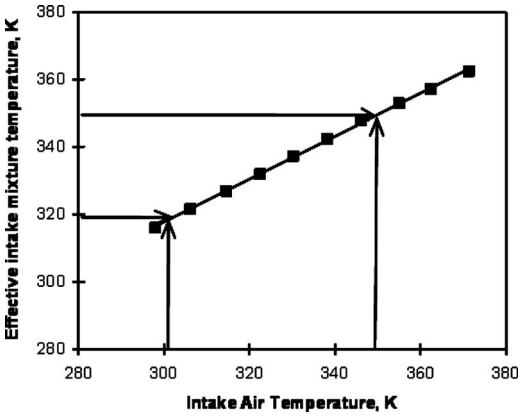

Fig. 2 Variation of effective intake mixture temperature with intake air temperature: N=900 rpm, CR=10.0, P_{in}=95 kPa, P_{exh}=104 kPa, AFR=50

most detailed chemistry for *n*-heptane [15,21] and has been shown to be suitable for HCCI engine simulations using a single-zone model [15].

3.3 Validation of Numerical Simulation. The aforementioned numerical simulation with detailed fuel chemistry was first validated against shock tube data reported in the literature [21,23]. As shown in Fig. 3, the ignition delay calculated by the model agrees well with experimental data measured under both stoichiometric and lean conditions over a range of temperatures and pressures [21,23]. This confirms that the chemistry scheme employed can simulate the *n*-heptane oxidation process and predict the ignition delay measured in a shock tube. Accordingly, this chemistry was used in this research to examine HCCI combustion. As an example, the predicted results were also compared to pressure traces generated by CHEMKIN IV, a well known commercial software package, for adiabatic HCCI combustion. The model developed produced identical cylinder pressure and temperature traces to those generated by CHEMKIN IV when heat transfer between bulk gas and engine coolant was neglected. This confirms that the numerical simulation can be used to calculate the combustion process of HCCI engine if a suitable heat transfer equation is employed.

4 Results and Discussion

Figure 4 shows a typical HCCI combustion trace using *n*-heptane. The motoring cylinder pressure is shown for comparison purposes. As reported by many other researchers, *n*-heptane

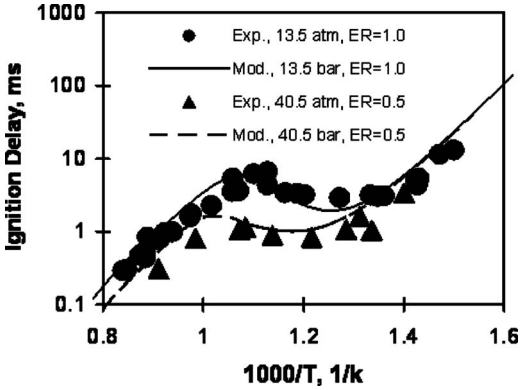

Fig. 3 Ignition delay of *n*-heptane at moderate and high pressure for both lean and stoichiometric mixtures. Experimental data were obtained from Ref. [23].

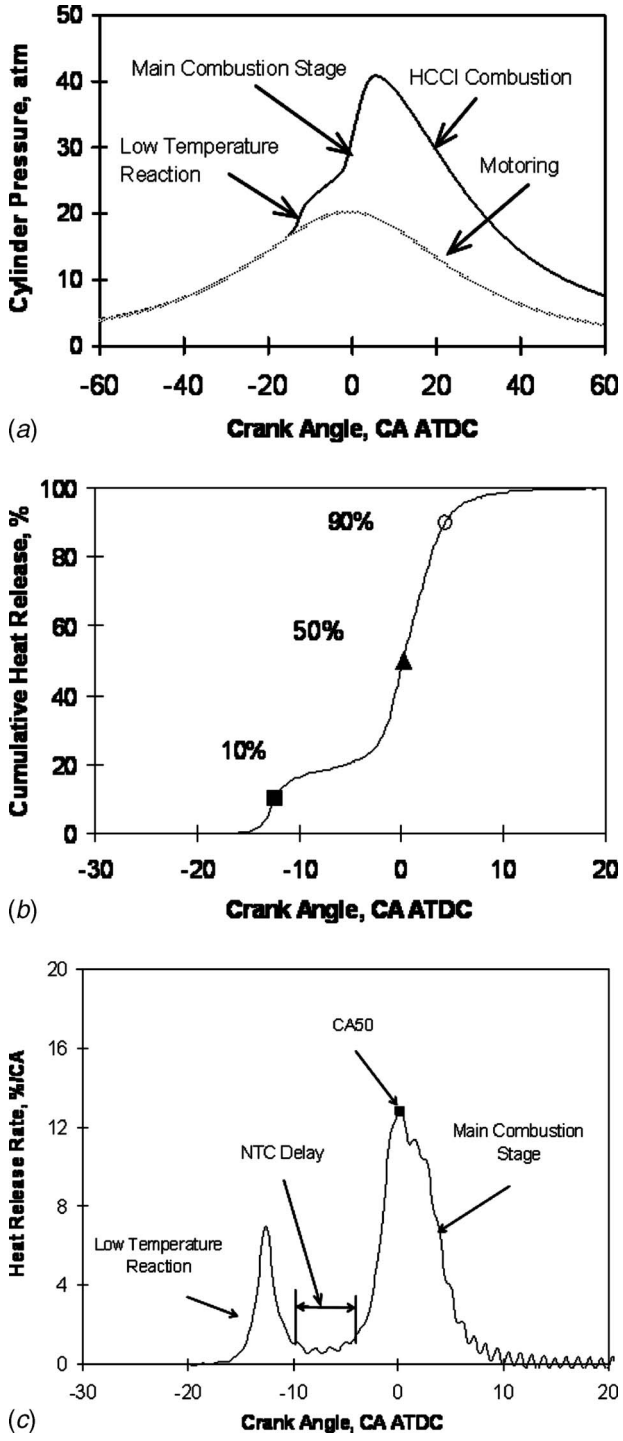

Fig. 4 Variation of (*a*) cylinder pressure (HCCI and motoring), (*b*) cumulative heat release, and (*c*) heat release rate with crank angle; CR=10, T_{in}=30°C, AFR=50, P_{in}=95 kPa

combustion is characterized by a well known two-stage oxidation process. The first stage is associated with LTRs and releases a relatively small amount of energy. The second stage associated with high temperature oxidation releases most of the energy and is considered as the MCS. In this research, the crank angle duration between the end of the LTR and the beginning of the MCS is defined as the NTC delay, as shown in Fig. 4(*c*). The heat release process was characterized by the start (10% heat release, CA10), middle (50%, CA50), and end (90%, CA90) of combustion as shown in Fig. 4(*b*). The location of 50% heat release (CA50) is

Table 2 Repeatability of HCCI engine operation (CR=10.0, T_{in} =30°C, P_{in}=95 kPa, P_{exh}=104 kPa, AFR=50)

Test No.	CA10[a]	CA50[a]	CA90[a]	IMEP (bar)	COV_{IMEP} (%)	ISFC (g/kW h)
1	−11.72	0.20	2.80	3.42	2.3	213.1
2	−12.53	0.68	5.47	3.28	2.0	221.6
3	−12.41	0.24	4.42	3.34	2.0	215.2
4	−12.53	−0.33	3.45	3.41	2.2	213. 6

[a]°CA ATDC.

generally considered to be the most important parameter that is adjusted to optimize HCCI combustion phasing. As shown in Fig. 4(*c*), CA50 is located close to the middle of the main combustion stage. For this condition, the engine produced near-zero soot emissions measured by laser-induced incandescence (Artium Technologies) and less than 2 ppm NO_x emissions (California Analytical Instruments), reflecting excellent HCCI combustion [24].

Table 2 compares the combustion process, indicated engine performance and combustion stability obtained in a series of experiments conducted over a 2 week period under the prescribed operating conditions. The data show that stable and repeatable HCCI combustion has been achieved at this operating condition. For example, the observed differences in CA10 and CA50 were within 1°CA and the coefficient of variation (COV) in the indicated mean effective pressure (IMEP) was found to be about 2%.

On the basis of these preliminary results, the experimental apparatus was used to investigate the effects of critical engine parameters on HCCI combustion. Details of the experimental matrix are provided in Table 3. The experimental results are shown in Figs. 5–11.

Figure 5 shows the effect of engine speed on HCCI combustion. Increasing engine speed tends to reduce cylinder pressure and retard the peak pressure location as shown in Fig. 5(*a*). This is due to a significantly retarded MCS, as shown in Fig. 5(*b*). The heat release rate during the MCS is also reduced with retarded combustion due to the increasing combustion chamber volume after top dead center. This leads to lower combustion chamber temperatures and a corresponding decrease in the oxidation reaction rates. However, the effect of engine speed on the LTR phase tends to be relatively weak, reflecting its strong dependence on temperature history. Increasing the engine speed delays the phasing of the MCS, primarily due to its effect on the NTC delay period. Figure 6 shows that the NTC delay increases linearly with increasing engine speed, reflecting the constant NTC delay period (in seconds) under constant AFR conditions.

Similar to spark ignition and diesel engines, the work produced by an HCCI engine is controlled by adjusting the amount of fuel supplied. Figure 7 shows the effect of AFR on cylinder pressure and heat release rate when intake air temperature was kept constant. As shown in Fig. 7(*a*), the cylinder pressure increases more rapidly and reaches its peak value at an earlier crank angle when the fueling rate is increased, which corresponds to a lower AFR. The advanced MCS combined with the enhanced heat release rate,

Table 3 Experiment matrix

Test No.	Speed (rpm)	AFR (mass)	CR	$T_{in,air}$ (°C)	P_{in} (kPa)
1	600–1400	50	10.0	40	95
2	900	43–63	10.0	40	95
3	900	50	9–16	30	95
4	900	50, 60	10.0	25–100	95
5	900	60	10.0	40	95–200
6[a]	900	20–60	10.0	40	40–95

[a]Constant fuel flow rate.

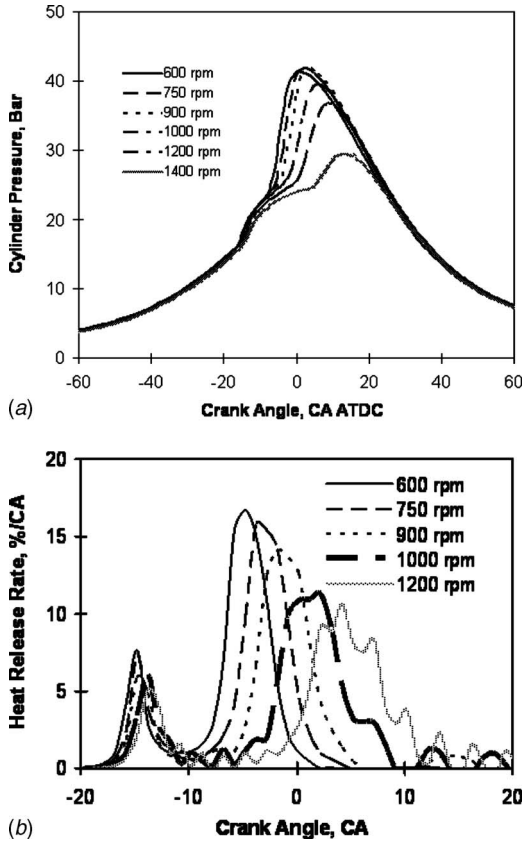

Fig. 5 Effect of engine speed on (*a*) cylinder pressure and (*b*) heat release rate: CR=10.0, AFR=50, $T_{in,air}$=40°C, P_{in}=95 kPa, P_{exh}=104 kPa

as shown in Fig. 7(*b*), contributes to this phenomenon. Similar to the effect of engine speed, AFR does not have a large influence on the phasing of the LTR, indicating a stronger dependence on mixture temperature history than on mixture composition. In comparison, increasing the AFR by reducing the fueling rate significantly retarded the phasing of the MCS. This is primarily due to the effect of leaner conditions on the NTC delay period, as shown in Fig. 8. The NTC delay increases almost linearly with increasing AFR.

The effect of turbocharging on HCCI combustion was examined at a constant AFR condition. As shown in Fig. 9, boosting the

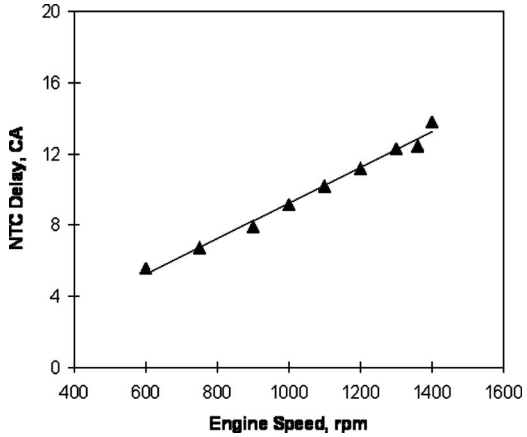

Fig. 6 Effect of engine speed on NTC delay: CR=10.0, $T_{in,air}$ =40°C, P_{in}=95 kPa, P_{exh}=104 kPa, fuel: *n*-heptane, AFR=50.

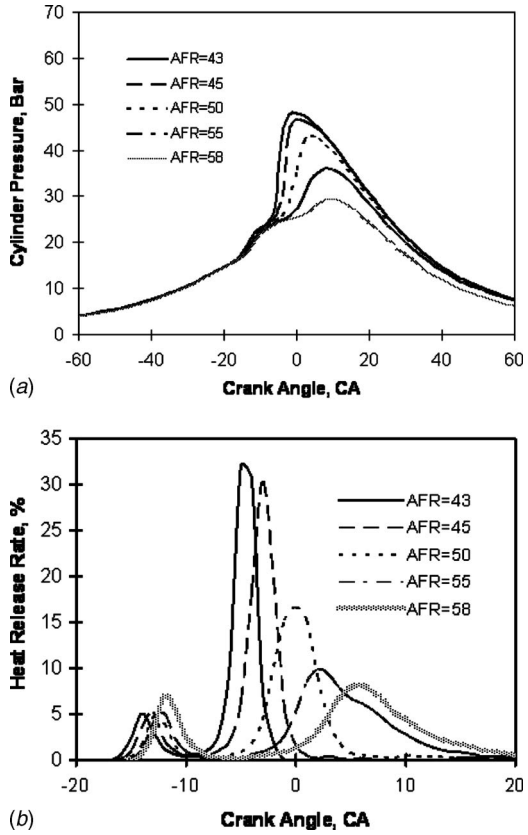

Fig. 7 (*a*) Cylinder pressure; (*b*) heat release rate. Effect of air-fuel ratio on HCCI combustion: CR=10.0, $T_{in,air}$=40°C, P_{in}=95 kPa, P_{exh}=104 kPa, N=900 rpm.

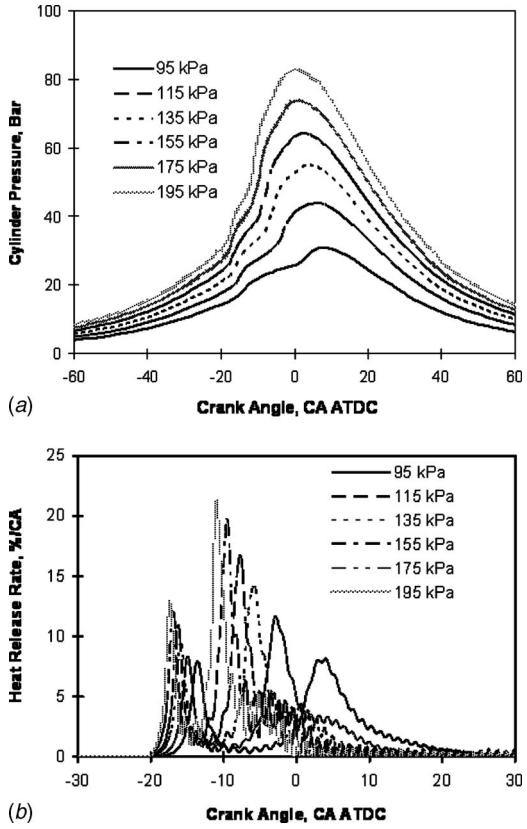

Fig. 9 (*a*) Cylinder pressure; (*b*) heat release rate. Effect of turbocharging on HCCI combustion: CR=10, $T_{in,air}$=40°C, AFR=60.0, *N*=900 rpm.

intake pressure tends to significantly increase the cylinder pressure during the compression stroke. Since the quantity of fuel injected is increased as intake pressure increases to maintain a constant AFR, the LTR stage is advanced and intensified. This leads to a shorter NTC delay period and significantly advances phasing of the MCS, as shown in Fig. 9(*b*). Figure 10 shows that increasing the intake pressure significantly reduces the NTC delay period as the intake pressure is increased from 80 kPa to 120 kPa. Boosting the intake pressure beyond 120 kPa continued to reduce the NTC delay period, but the rate of decrease in the NTC delay period was lower.

Intake temperature is the most critical and widely used engine operation parameter to control the phasing of HCCI combustion. Figure 11 shows the effect of intake temperature on HCCI combustion for a constant AFR of 50. Stable HCCI combustion was obtained for a wide range of temperatures. As shown in Fig. 11(*b*), increasing the intake temperature advances the phasing of both the LTR and MCS. The LTR heat release profiles were found to be quite similar, although they were advanced as temperature increased. However, increasing the intake temperature significantly enhances the heat release rate of the MCS. The increasingly advanced phasing of the MCS contributes to the increased heat release rate. As shown in Fig. 12, intake temperature does not have a large influence on the NTC delay period.

Figure 13 shows that increasing the compression ratio advances the combustion process and increases the peak cylinder pressures.

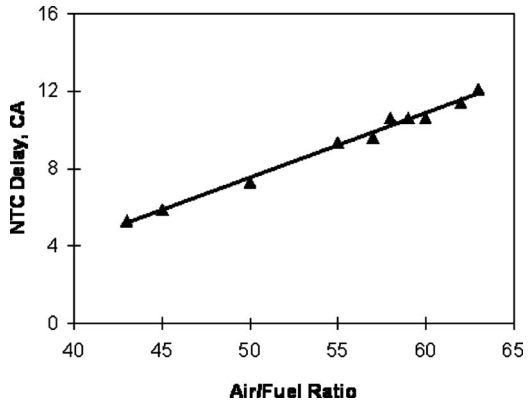

Fig. 8 Effect of air-fuel ratio on NTC delay: CR=10.0, $T_{in,air}$=40°C, P_{in}=95 kPa, P_{exh}=104 kPa, *N*=900 rpm

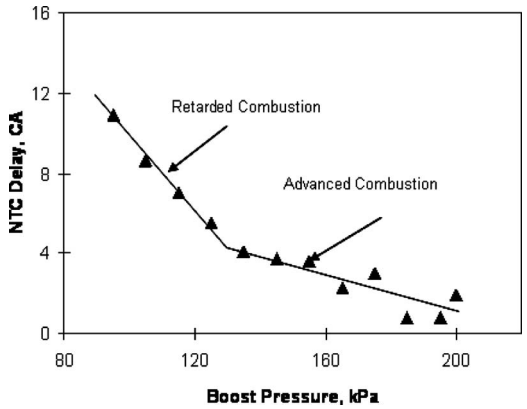

Fig. 10 Effect of turbocharging on NTC delay: CR=10, $T_{in,air}$=40°C, AFR=60.0, *N*=900 rpm

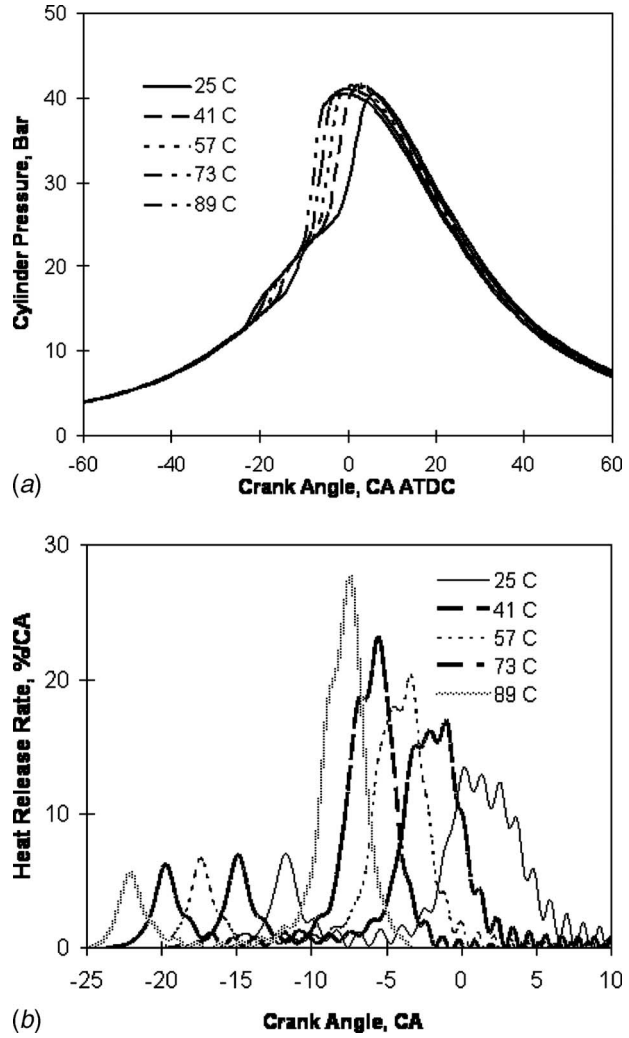

Fig. 11 (*a*) **Cylinder pressure;** (*b*) **heat release rate. Effect of intake air temperature on HCCI combustion:** N**=900 rpm, CR =10.0,** P_{in}**=95 kPa,** P_{exh}**=104 kPa, AFR=50.**

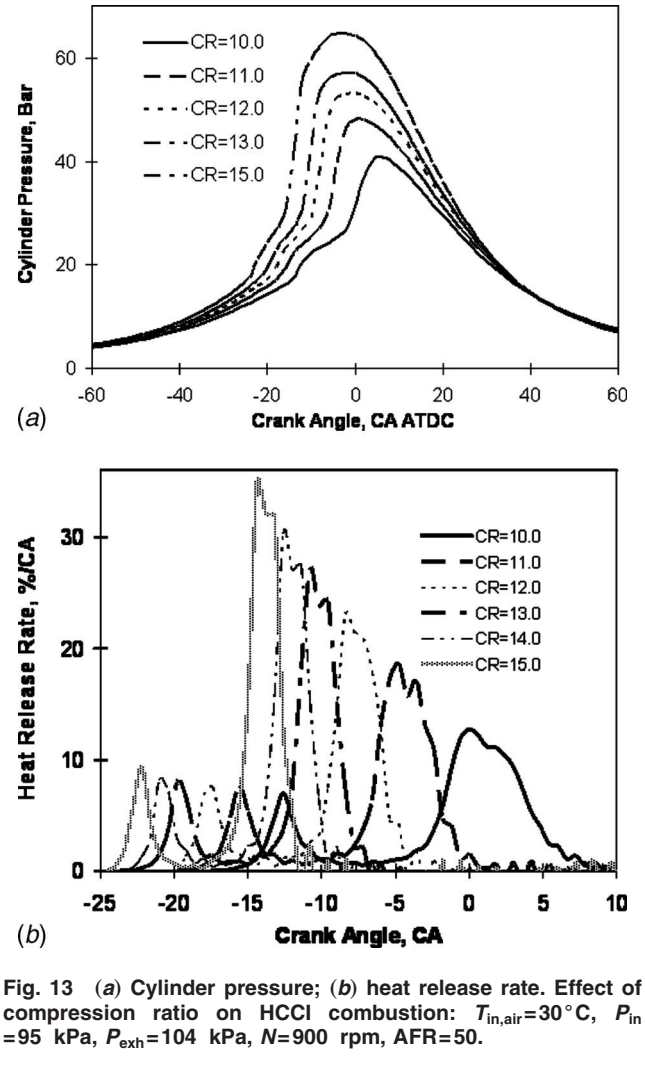

Fig. 13 (*a*) **Cylinder pressure;** (*b*) **heat release rate. Effect of compression ratio on HCCI combustion:** $T_{in,air}$**=30°C,** P_{in} **=95 kPa,** P_{exh}**=104 kPa,** N**=900 rpm, AFR=50.**

This is primarily due to the effect of increased compression temperatures and pressures as the compression ratio increases, which enhances *n*-heptane oxidation. As shown in Fig. 13(*b*), the phasing of both LTR and MCS phases were advanced with increasing compression ratio. Figure 14 shows that increasing the compression ratio from 9 to 10 dramatically decreased the NTC delay period. For a compression ratio of 11, the MCS was advanced beyond top dead center. Increasing the compression ratio beyond 11 had a negligible effect on the NTC delay period. The combustion phasing of the LTR and MSC were advanced by a comparable amount as compression ratio was increased beyond 11.

HCCI combustion tends to become unstable and incomplete when the MCS is retarded excessively. In these cases, the combustion phasing can be advanced by heating the intake mixture to a higher temperature or increasing the compression ratio. As re-

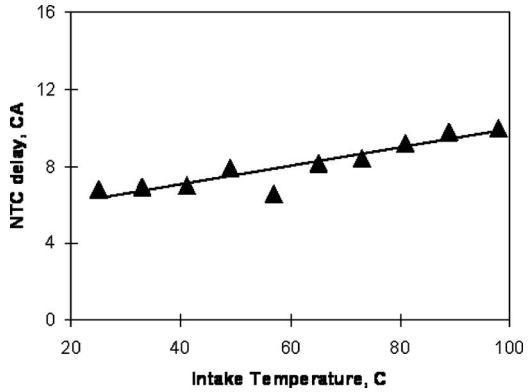

Fig. 12 Effect of intake air temperature on NTC delay: N **=900 rpm, CR=10.0,** P_{in}**=95 kPa,** P_{exh}**=104 kPa, AFR=50**

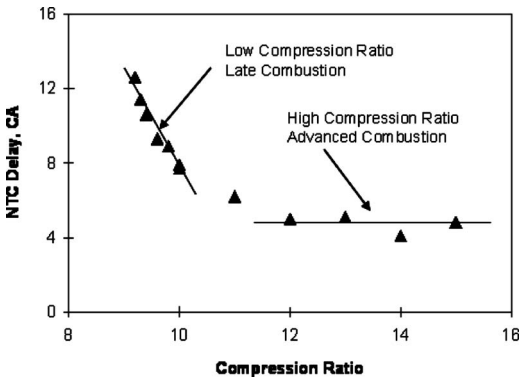

Fig. 14 Effect of compression ratio on NTC delay: $T_{in,air}$ **=30°C,** P_{in}**=95 kPa,** P_{exh}**=104 kPa,** N**=900 rpm, AFR=50**

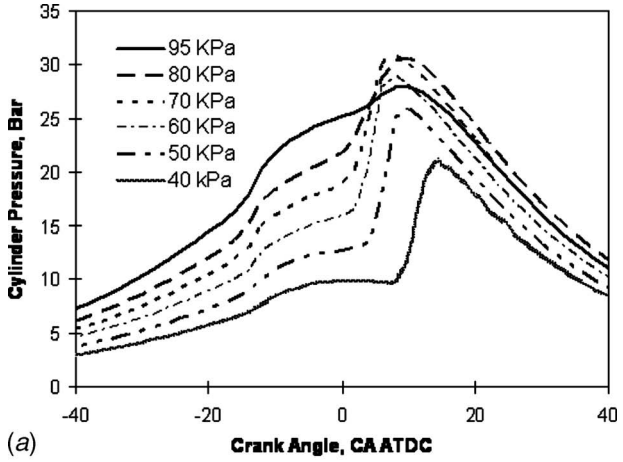

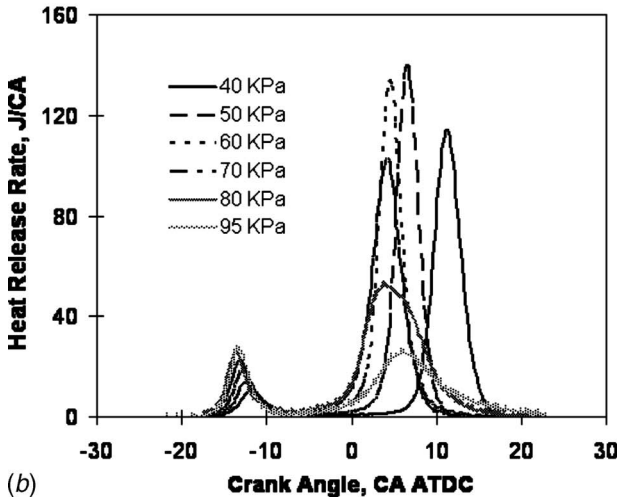

Fig. 15 (*a*) Cylinder pressure; (*b*) heat release rate. Effect of intake air throttling on HCCI combustion at constant intake fuel flow rate: N=900 rpm, CR=10.0, $T_{in,air}$=40°C, P_{exh}=104 kPa, $\dot{m}_{fuel}$=0.273 kg/h, AFR=20–60.

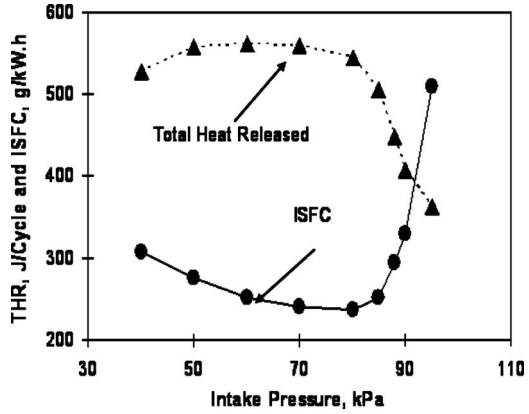

Fig. 16 Effect of throttling intake air on total heat release and indicated specific fuel consumption when intake fuel flow rate was kept constant: N=900 rpm, CR=10.0, $T_{in,air}$=40°C, P_{exh}=104 kPa, $\dot{m}_{fuel}$=0.273 kg/h, AFR=20–60

ported in the literature [25], enriching the air/fuel mixture under lean operation can enhance the oxidation reaction rates. The experiments that examined AFR effects on HCCI combustion in this study demonstrated that a relatively richer mixture helps to advance the combustion phase and accelerate the oxidation process to achieve complete combustion. Traditionally, enriching the intake mixture is achieved by injecting more fuel into the intake air. However, this same effect may also be obtained by throttling the intake air while keeping the fuel flow rate constant. Figure 15 shows the effect of intake air throttling on HCCI combustion under a constant fuel flow rate condition. Late and incomplete combustion was encountered with 95 kPa intake pressure, which is reflected by a relatively weak MCS and reduced heat release during the combustion process. Throttling the intake air enhanced the heat release during the MCS, although its effect on the combustion phasing of the LTR is relatively weak, as shown in Fig. 15(*b*). Intake air throttling can help to burn the fuel completely as indicated by the increased total heat release and reduced indicated specific fuel consumption (ISFC), as shown in Fig. 16. Throttling the intake air enables complete combustion even though the MCS occurs after top dead center. The presence of less excess air (a diluent) in the combustion chamber helps to increase the bulk gas temperature and enhance the oxidation process during the MCS. However, overthrottling the intake pressure tends to delay the MCS again. This is due to the effect of cylinder pressure on the combustion process, as well as the increasing role played by residual gases, which tends to deteriorate the oxidation process and retard the main combustion phase [26]. As shown in Fig. 16, ISFC increases when the intake pressure is overthrottled. This is due to increased pumping losses and the reduced oxidation rate associated with having a higher fraction of residual gases.

The aforementioned single-zone numerical model was used to simulate the HCCI combustion process. Figure 17 compares the predicted cylinder pressure, heat release rate, and cumulative heat release with those measured experimentally. For comparison purposes, the effective intake mixture temperature used in the simulation was adjusted such that the calculated CA50 matched experimental data. The effective intake temperature used in the numerical simulation was 350 K compared with the experimental value of 319.5 K as calculated by Eq. (6). Other researchers have reported a need to adjust the intake mixture temperature in modeling HCCI combustion. For example, Yelvington et al. [27] reported that the intake temperature adjustment was approximately 30 K in order to match the predicted phasing of the heat release with experimental data. This is likely due to the imperfect assumption of a homogeneous air/fuel mixture with uniform temperature, pressure, and reaction rate, as well as potential limitations of the fuel chemistry. The assumption of uniform and constant combustion chamber wall temperature during the whole engine cycle may also contribute to the requirement to adjust the intake mixture temperature. Intake mixture temperature adjustments have also been used in multizone models to account for nonuniformities of the mixture temperature. For example, an initial temperature difference between the core and outer boundary zones in one multizone numerical simulation was reported to be ~35 K to achieve reasonable predictions of cylinder pressure and combustion phasing [28,29].

As shown in Fig. 17, the numerical simulation was able to capture elements of HCCI combustion of *n*-heptane, particularly the phasing of the MCS. In comparison, the LTR predicted by the numerical simulation is advanced compared to the experimental data as shown in Figs. 17(*b*) and 17(*c*). A spike in the predicted heat release rate was observed during the MCS. This spike was caused by the rapid oxidation of all CO accumulated to this point in the simulation to CO_2. The conversion of CO to CO_2 is predicted to happen rapidly once the required temperature is reached because only a few reactions are involved. Rapid oxidation of CO to CO_2 has not been observed experimentally or reported in the oliterature. The assumption of uniform mixture temperature and mixture composition contributes to this overly-rapid heat release rate.

For this research, a single adjustment was made to the effective intake mixture temperature and then applied to all operating con-

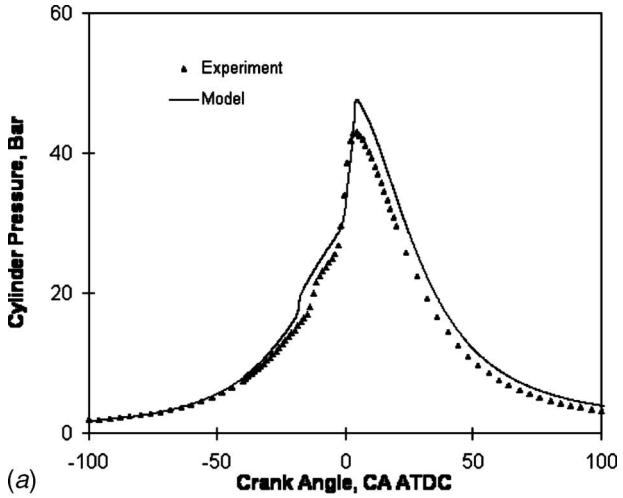

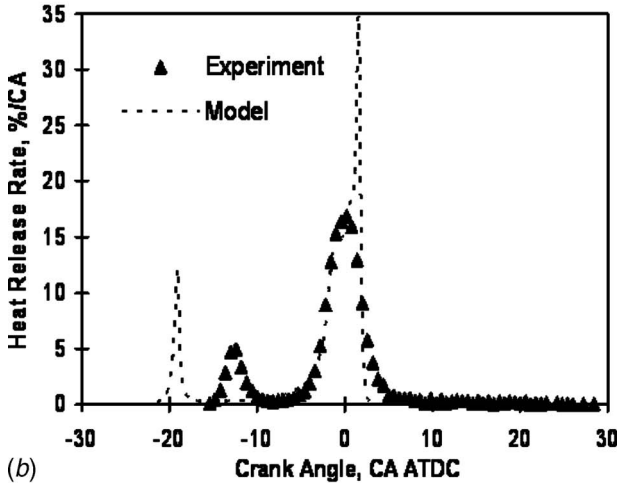

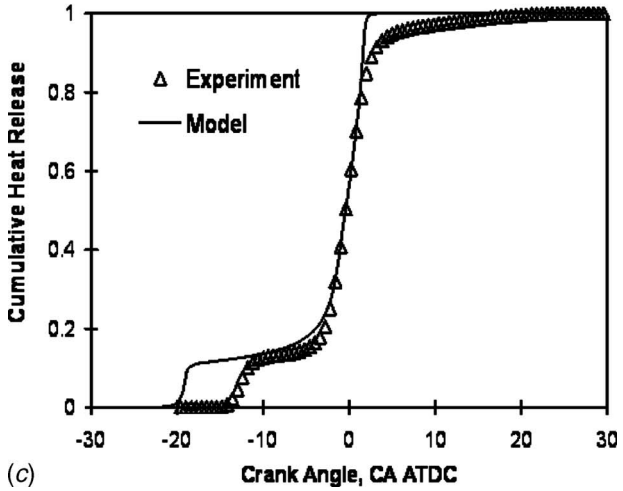

Fig. 17 Comparison of predicted (*a*) cylinder pressure, (*b*) heat release rate, and (c) cumulative heat release with experimental data: CR=10, $T_{in,air}$=30°C, AFR=50, P_{in}=95 kPa

ditions. On this basis, this model was shown to be able to capture the effect of compression ratio on the combustion phasing of HCCI combustion using *n*-heptane. Figure 18 compares the predicted CA50 with those measured experimentally for different compression ratios while keeping the AFR constant at 50. The predicted CA50 combustion phasing was found to agree well with

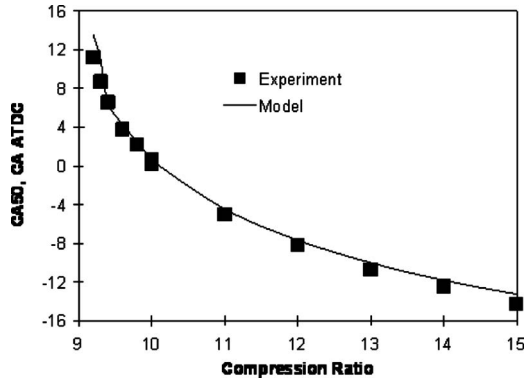

Fig. 18 Comparison of the predicted CA50 with those determined experimentally over a range of compression ratios. Operating condition is the same as Fig. 13.

the experimental measurements. It was found that CA50 retards almost linearly with decreasing CR for high compression ratios (CR > 11). However, the CA50 retards rapidly when the compression ratio is reduced below 10, reflecting an increasing sensitivity for *n*-heptane when CA50 occurs after top dead center.

Figure 19 shows that the numerical simulation is able to capture the approximately linear trend of CA50 retardation as engine speed increases.

Finally, the effect of turbocharging on CA50 may be seen in Fig. 20. For this figure, the effective intake mixture temperature in the numerical simulation was adjusted to match the experimental data when the intake pressure was 95 kPa. Figure 20 shows that the numerical simulation is able to capture the trend of advanced

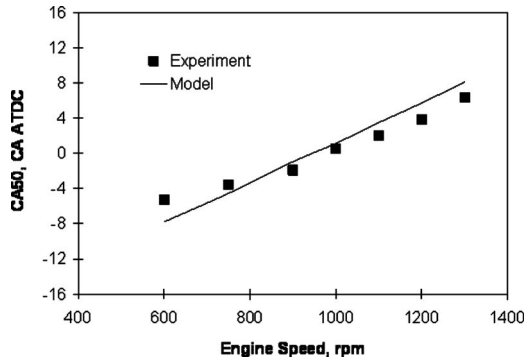

Fig. 19 Comparison of the predicted CA50 with those determined experimentally over a range of engine speeds. Operating condition is the same as in Fig. 5.

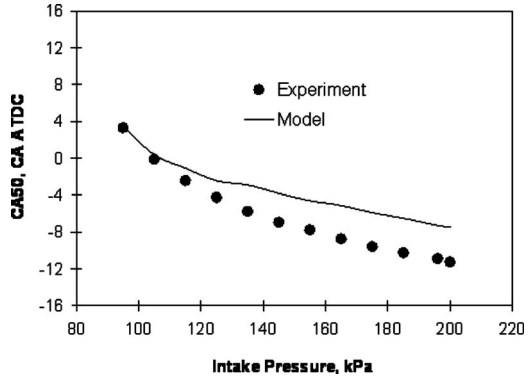

Fig. 20 Comparison of the predicted CA50 with those determined experimentally over a range of intake pressures. Operating condition is the same as in Fig. 9.

CA50 as intake pressure increases. However, the predicted CA50 is retarded relative to the experimental data at higher intake pressures. The assumption that the combustion chamber wall temperature is not a function of engine load may be responsible for this difference. Since the combustion chamber wall temperature likely increases with increasing load, incorporating a variable combustion wall temperature should improve the predictions of CA50 under turbocharged conditions.

5 Conclusions

A CFR engine was modified to investigate HCCI combustion characteristics over a wide range of operating conditions. In particular, a port fuel injection system was implemented for atomizing *n*-heptane for this study. Based on the experimental data and complementary numerical simulations of HCCI combustion, the following conclusions may be drawn.

- Increasing the intake air temperature and compression ratio advances the phasing of both the low-temperature reaction and main combustion stage. In comparison, the effects of AFR, engine speed, and turbocharging on the phasing of low-temperature reaction are relatively weak, but they significantly affect the phasing of the main combustion stage.
- The NTC delay period is a strong function of engine speed, air/fuel ratio, and intake pressure (at constant air/fuel ratio). The effect of intake temperature (at constant air/fuel ratio) on the NTC delay period is not as strong as those previously described. In comparison, the effect of compression ratio on NTC delay is negligible except for low compression ratios when the combustion phasing is very retarded.
- Throttling the intake air while keeping fuel flow rate constant tends to improve HCCI combustion when incomplete combustion is observed. It is believed that the resultant enrichment of the air/fuel mixture contributes to this desirable characteristic. However, overthrottling tends to retard the main combustion stage and deteriorate engine performance even though relatively complete combustion can still be obtained at a later combustion phasing.
- The validated numerical simulation was able to capture trends in combustion phasing variation with critical engine parameters. The calculated CA50 was found to agree well with those measured experimentally over a wide range of engine compression ratios, speeds, and intake pressures.

Acknowledgement

The financial support of the Government of Canada's PERD/AFTER and Climate Change T&II programs are gratefully acknowledged. The technical contribution of Mr. M. F. Baksh in constructing the fuel delivery system is acknowledged.

References

[1] Epping, K., Aceves, S. M., Bechtold, R. L., and Dec, J. E., 2002, "The Potential of HCCI Combustion for High Efficiency and Low Emissions," SAE Paper No. 2002-01-1923.
[2] Zhao, F., Asmus, T, Assanis, D., Dec, J., Eng, J., and Najt, P, 2003, "Homogeneous Charge Compression Ignition (HCCI) Engines: Key Research and Development Issues," Society of Automotive Engineers, Inc., SAE Paper No. PT-94.
[3] Onishi, S., Jo, S. H., Shoda, K., Jo, P. D., and Kato, S., 1979, "Active Thermo-Atmosphere Combustion (ATAC)–A New Combustion Process for Internal Combustion Engines," SAE Paper No. 790501.
[4] Noguchi, M., Tanaka, Y., Tanaka, T., and Takeuchi, Y., 1979, "A Study on Gasoline Engine Combustion by Observation of Intermediate Reactive Products During Combustion," SAE Paper No. 790840.
[5] Najt, P. M., and Foster, D. E., 1983, "Compression-Ignited Homogeneous Charge Combustion," SAE Paper No. 830264.
[6] Chen, R. and Milovanovic, N., 2001, "A Review of Experimental and Simulation Studies on Controlled Auto-Ignition Combustion," SAE Paper No. 2001-01-1890.
[7] Yang, J., Culp, T., and Kenney, T., 2002, "Development of a Gasoline Engine System Using HCCI Technology—The Concept and the Test Results," SAE Paper 2002-01-2832.
[8] Christensen, M., Hultqvist, A., and Johansson, B., 1999, "Demonstrating the Multi-Fuel Capability of a Homogeneous Charge Compression Ignition Engine With Variable Compression Ratio," SAE Paper No. 1999-01-3679.
[9] Kalghatgi, G. T., 2005, "Auto-Ignition Quality of Practical Fuels and Implication for Fuel Requirements of Future SI and HCCI Engines," SAE Paper No. 2005-01-0239.
[10] Amann, M., Ryan, T. W., and Kono, N., 2005, "HCCI Fuels Evaluations-Gasoline Boiling Range Fuels," SAE Paper No. 2005-01-3727.
[11] Ryan, T.W., Callahan, T.J., and Mehta, D., 2004, "HCCI in a Variable Compression Ratio Engine—Effects of Engine Variables," SAE Paper No. 2004-01-1971.
[12] Zhong, S., Megaritis, A., Yap, D., and Xu, H., 2005, "Experimental Investigation Into HCCI Combustion Using Gasoline and Diesel Blended Fuels," SAE Paper No. 2005-01-3733.
[13] Li, Y., Zhao, H., Brouzos, N., Ma, T., and Leach, B., 2006, "Effect of Injection Timing on Mixture and CAI Combustion in a GDI Engine With an Air-Assisted Injector," SAE Paper No. 2006-01-0206.
[14] Easley, W., Agarwal, A., and Lavoie, G. A., 2001, "Modeling of HCCI Combustion and Emissions Using Detailed Chemistry," SAE Paper No. 2001-01-1029.
[15] Naik, C., Pitz, W. J., Sjoberg, M., Dec, J. E., Orme, J., Curran, H., Simmie, J. M., and Westbrook, C. K., 2005, "Detailed Chemical Kinetic Modelling of Surrogate Fuels for Gasoline and Application to an HCCI Engine," SAE Paper No. 2005-01-3741.
[16] Xu, H., 2005, "Modelling of HCCI Engines: Comparison of Single-Zone, Multi-Zone and Test Data," SAE Paper No. 2005-01-2123.
[17] Kongsereeparp, P., Kashani, B., and Checkel, M. D., 2005, "A Stand-Alone Multi-Zone Model for Combustion in HCCI Engines," ASME ICED 2005 Fall Technical Conference, Ottawa, Canada, Sept.11–14, ASME Paper No. ICEF2005-1241.
[18] Woschni, G., 1967, "A Universal Applicable Equation for the Instantaneous Heat Transfer Coefficient in the Internal Combustion Engines," SAE Paper No. 670971.
[19] Heywood, J. B., 1988, *Internal Combustion Engine Fundamentals*, McGraw-Hill, New York.
[20] Chang, J., Guralp, O., Asanis, D., Kuo, T., Najt, P., and Rask, R., 2004, "New Heat Transfer Correlation for an HCCI Engine Derived From Measurements of Instantaneous Surface Heat Flux," SAE Paper No. 2004-01-2996.
[21] Curran, H. J., Gaffuri, P., Pitz, W. J., and Westbrook, C. K., 1998, "A Comprehensive Modeling Study of *n*-Heptane Oxidation," Combust. Flame, **114**, pp. 149–177.
[22] Sjöberg, M., and Dec, J.E., 2004, "An Investigation of the Relationship Between Measured Intake Temperature, BDC Temperature, and Combustion Phasing for Premixed and DI HCCI Engines," SAE Paper No. 2004-01-1900.
[23] Ciezki, H. K., and Adomeit, G., 1993, "Shock-Tube Investigation of Self-Ignition of n-Heptane-Air Mixtures Under Engine Related Conditions," Combust. Flame, **93**, pp. 421–433.
[24] Li, H. L., Neill, W. S., Chippior, W., Graham, L., Connolly, T., and Taylor, J. D., 2007, "An Experimental Investigation on the Emission Characteristics of HCCI Engine Operation Using n-Heptane," SAE Paper No. 2007-01-1854.
[25] Glassman, I., 1987, *Combustion*, Academic Press, New York.
[26] Peng, Z., Zhao, H., and Ladommatos, N., 2003, "Effect of Air/Fuel Ratios and EGR Rates on HCCI Combustion of n-Heptane, a Diesel Type Fuel," SAE Paper No. 2003-01-0747.
[27] Yelvington, P. E., Rallo, M. B., Liput, S., Tester, J. W., Green, W. H., and Yang, J., 2004, "Prediction of Performance Maps for Homogeneous-Charge Compression-Ignition Engines," Combust. Sci. Technol., **176**, pp. 1243–1282.
[28] Kongsereeparp, P. and Checkel, M. D., 2007, "Novel Method of Setting Initial Conditions for Multi-Zone HCCI Combustion Modeling," SAE Paper No. 2007-01-0674.
[29] Kongsereeparp, P. and Checkel, M. D., 2007, "Investigating the Effects of Reformed Fuel Blending in a Methane- or *n*-Heptane-HCCI Engine Using a Multi-Zone Model," SAE Paper No. 2007-01-0205.

Experimental Study on Effects of Nozzle Hole Geometry on Achieving Low Diesel Engine Emissions

Prashanth K. Karra

Song-Charng Kong[1]
e-mail: kong@iastate.edu

Department of Mechanical Engineering,
Iowa State University,
Ames, IA 50011

Three injectors with different nozzle geometries were tested in a multicylinder diesel engine with a high-pressure common-rail injection system. Various injection pressures were tested along with exhaust gas recirculation to achieve low NO_x and soot emissions. The injectors used in the study included a six-hole nozzle, a ten-hole nozzle, and a six-hole convergent nozzle with a K-factor of 3. All three injectors had the same flow numbers. All three injectors tested were effective in reducing NO_x and soot emissions at appropriate conditions. It was found that low temperature combustion can be achieved by using high levels of exhaust gas recirculation with late injection timings. High injection pressures significantly reduced soot emissions at conventional injection timings. The effect of injection pressure was not significant at retarded injection timings, i.e., 5 ATDC. The convergent nozzle was found to produce higher soot emissions compared with the straight-hole nozzle under the same injection conditions. Effects of the convergent nozzle on NO_x emissions and fuel consumption were not significant. The small nozzle size in the ten-hole injector can generate smaller fuel drops and lead to better atomization. The ten-hole injector appeared to have better air utilization and resulted in significant reductions in NO_x and soot emissions over a wide range of operating conditions.
[DOI: 10.1115/1.3124791]

1 Introduction

Internal combustion engines are a major consumer of fossil fuel and a significant contributor to environmental pollution. In particular, diesel engines are widely used in the transportation industry due to their high efficiency and durability. Continuing research is needed to reduce exhaust emissions to meet the emissions standards. Simultaneous reductions in emissions required by the new standards include particulate matter (PM), nitrogen oxides (NO_x), hydrocarbon (HC), and carbon monoxide (CO). The United States federal government mandated on-highway diesel engines to meet Tier 4 emissions standards by the year of 2010. The standards include a 0.268 g/kW h limit on NO_x, a 0.0134 g/kW h limit on PM, and a 0.188 g/kW h limit on nonmethane hydrocarbons (NMHC) [1]. For nonroad diesel engines with a rated power between 56 kW and 130 kW, the Tier 4 emissions standards are 0.40 g/kW h for NO_x, 0.02 g/kW h for PM, 5.0 g/kW h for CO, and 0.19 g/kW h for NMHC.

The above emissions reduction challenge is further compounded by the request of improving fuel economy by customers. Various approaches have been proposed for emission reduction while maintaining a reasonable fuel efficiency. Fuel injection is one of the most important parameters that will affect performance and emissions. Effects of fuel injection on diesel engine emissions will be discussed in this paper.

The geometry of the nozzle in an injector plays an important role in controlling diesel spray atomization and combustion. Several nozzle parameters, such as the nozzle hole diameter, the length-to-diameter ratio, and the roundness of the nozzle inlet will affect fuel atomization characteristics and combustion [2,3]. The importance of the nozzle flow and its effects on spray atomization were discussed by Bergwerk [4]. Internal flow phenomena, such as the velocity distribution inside the nozzle, turbulence, and cavitation inside the nozzle, can determine the disturbance level in the liquid jet at the nozzle exit [5–7]. These initial disturbances will affect the liquid breakup, penetration, spray evaporation, and eventually, ignition and combustion.

Nozzles with large diameters are less efficient in atomizing fuel sprays compared with those with smaller diameters. However, small nozzles require a longer injection duration which could reduce combustion efficiency [8]. High injection pressures (150–200 MPa) can reduce the injection duration of small diameter nozzles by increasing the injection velocity. As a result, high injection pressures with small nozzles are common in the modern diesel engine.

The nozzle size will influence the fuel-air mixing process and, therefore, engine performance and emissions. Pickett and Siebers [9] investigated the effects of nozzle hole diameter on soot formation in diesel engine environments. Nozzles with different hole diameters were tested in a constant-volume chamber. It was found that soot formation can be reduced as the nozzle hole diameter was reduced. Numerical modeling using detailed chemistry also revealed that soot formation can be closely related to the lift-off length of the diesel diffusion flame [10]. Meanwhile, the soot-NO_x trade-off can be overcome by using high exhaust gas recirculation (EGR) to achieve low temperature combustion.

Another important characteristic of a nozzle is the variation in the nozzle cross-sectional area along its length. This geometrical characteristic can be defined by the conicity of the nozzle which is also called the *K*-factor

$$K = 100 \cdot \frac{(D_i - D_o)}{L} \tag{1}$$

where D_i is the inlet diameter, D_o is the outlet diameter, and L is the length of the nozzle.

Various studies have showed that the variation in the nozzle geometry can produce different fuel spray characteristics [2,3,11,12]. Nurick [13] investigated the effect of nozzle inlet ge-

[1]Corresponding author.

Manuscript received May 29, 2008; final manuscript received February 15, 2009; published online November 2, 2009. Review conducted by James S. Wallace.

ometry on the nozzle flow. It was found that cavitation can be prevented by using a round-edge inlet nozzle with the ratio of inlet radius to nozzle hole diameter (R/D) larger than 0.14. Benajes et al. [14] conducted an experimental study to analyze the influence of different orifice geometries (conical and cylindrical) on the injection rate of a common-rail fuel injection system. It was found that the discharge coefficient was higher in the conical nozzle than that in the cylindrical nozzle. In addition, the flow in the cylindrical nozzle collapsed at high injection pressures due to cavitation that was not observed in the conical nozzle.

Literature on the effects of nozzle conicity on spray related issues such as cavitation and injection velocity is limited. Desantes et al. [18] tested three injector nozzles with different conicity ($K=-0.2$, 0.0, 1.1) for cavitation under different injection pressures and ambient pressures. Fuel flow rates and momentum fluxes at the nozzle exit were measured. The injection pressure was varied between 2 MPa and 160 MPa. It was found that, as the value of K-factor increased, the tendency toward cavitation was reduced [18]. Cavitation was not evident for $K=1.1$. The mass flow rate can be reduced due to cavitation at high injection pressures. The momentum flux did not change as the K-factor of the nozzle changed, i.e., cavitation did not influence the momentum flux. Hence, the exit velocity was increased to compensate for the reduced mass flow rate due to cavitation.

While the nozzle geometry influences the fuel spray behavior and mixture formation, combustion temperature also plays an important role in emissions formation. Various strategies have been proposed to reduce combustion temperature for NO_x reduction. Methods for in-cylinder control of emissions encompass EGR, air management and flexible fuel injection schemes. Particulate filters and NO_x reduction catalysts have also been tested as the aftertreatment devices. EGR has been demonstrated to reduce NO_x emissions by lowering combustion temperatures. However, soot emissions increase as the amount of EGR is increased to a moderate level. It was found that soot emissions could be reduced if a very high level of EGR was used [15]. This is because the combustion temperature is lower than the soot formation temperature, as explained by Kitamura et al. [16]. Low temperature diesel combustion was achieved by Alriksson and Denbratt [17] using high EGR (up to 60%) for various engine loads (up to 50%) and injection timings. Results indicated that appropriate levels of EGR can be used to achieve a premixed charge compression ignition (PCCI) combustion.

Despite that experiments in constant-volume chambers indicated that injectors with small nozzle holes or convergent nozzles had the potential to reduce soot emissions [9,14], there has not been actual engine testing using such injectors. Therefore, in the present study, various injectors were made, and engine tests were performed using injectors with different nozzle geometries. The objective of this study was to investigate the effect of nozzle geometry on diesel engine performance and to explore their potential to achieve simultaneous soot and NO_x reduction.

2 Experimental Conditions

In this study, injectors with different nozzle geometries and hole diameters were tested in a multicylinder turbocharged diesel engine. The detailed engine parameters are given in Table 1. The engine speed was 1400 rpm that was the engine speed to produce the peak torque. Injected fuel was 50 mg per injection per cylinder, corresponding to 50% load conditions under the current engine speed. Three injectors with different nozzle geometries were tested, as described in Table 2. The nozzles are represented with the following notation: 6X133X800. The first number represents the number of holes on the injector tip. The second number indicates the included spray angle. The third number indicates the flow number, which is in cc/min.

The present engine used an electronically controlled common-rail injection system manufactured by Denso. Fuel injection was controlled by a specialized software for the injection pressure, number of injection, fuel mass per pulse, and dwell duration. Appropriate rail pressure relief valves were used to achieve high injection pressures. The injection pressures used in this study varied between 150 MPa and 200 MPa. Note that different nozzles have different flow coefficients and thus the maximum allowable injection pressure could vary slightly.

Table 1 Specifications of the test engine

Engine	John Deere 4045 HF475 four-cylinder four-valve direct injection
Bore and stroke (mm)	106×127
Total engine displacement (L)	4.5
Compression ratio	17.0:1
Valves per cylinder intake/exhaust	2/2
Firing order	1-3-4-2
Combustion system	Direct injection
Engine type	In-line, four-stroke
Aspiration	Turbocharged
Injection system	Common rail
Piston	Bowl-in-piston

In the current engine, a direct control of the boost level was not available due to the use of the turbocharger driven by the exhaust energy. This study opted to control the fueling rate rather than the torque output considering the large number of variables to be studied. It was anticipated that EGR would alter the exhaust energy level and cause variability in related operating parameters such as boost pressure and charge temperature. In order to alleviate this problem, the intake manifold temperature was maintained at 23°C for all the conditions tested. As a result, experiments indicated that the variation in torque output and BMEP were within a reasonable range, as shown in Table 3.

The gaseous emissions were measured using a Horiba MEXA 7100DEGR emissions analyzer. The emission data recorded were CO, CO_2, NO_x, HC, O_2, and EGR CO_2. Heated sample lines were used for both HC and CO. CO and CO_2 were measured using nondispersive infrared (NDIR), HC was measured using a flame ionization detector (FID), NO/NO_2 were measured using chemiluminescent detectors, and O_2 was measured using magnetopneumatic detectors. The measured total unburned HC was methane equivalent, and the fuel to the FID was a mixture of 40% hydrogen in helium. The calibration gas to HC analyzer was propane. The smoke number was measured using an AVL 415S soot meter. The cylinder pressure was measured using a Kistler 6125B piezoelectric pressure transducer that was mounted utilizing the original glow plug hole and cooled by the coolant in the cylinder head. The signal was amplified using a Kistler 5010 charge amplifier. The cylinder pressure was measured every 0.1 crank angle degrees and averaged over 50 engine cycles. The fuel flow rate was measured using a Coriolis meter manufactured by Micromotion.

3 Results and Discussion

Results of the brake specific fuel consumption (BSFC) and emissions are presented in the units of g/kW h. The label that

Table 2 Experimental conditions for the engine runs

Engine speed	1400 rpm
Main SOI	−20–5 ATDC
EGR	0–30%
Injection pressure	150–200 MPa
Injectors	6X133X800 ($d=148$ μm) (six-hole) (baseline) 6X133X800 $K=3$ ($d=148$ μm) (six-hole convergent nozzle) 10X133X800 ($d=114$ μm) (ten-hole)
Fuel Injected	50 mg/injection/cylinder, corresponding to 50% peak torque

Table 3 Ranges of engine torque and BMEP under various injection timings (e.g., −20−+5 ATDC) for specific injectors and EGR conditions

	Baseline injector		Ten-hole injector		$K=3$ injector	
	Torque	BMEP	Torque	BMEP	Torque	BMEP
0% EGR	238 ± 10	6.64 ± 0.28	239 ± 11	6.69 ± 0.30	242 ± 14	6.75 ± 0.39
15% EGR	243 ± 13	6.77 ± 0.36	245 ± 8	6.87 ± 0.24	243 ± 12	6.78 ± 0.31
30% EGR	248 ± 5	6.84 ± 0.21	238 ± 7	6.65 ± 0.19	240 ± 11	6.72 ± 0.31

represents the data in the following figures consists of three parts. The first part is the injection pressure, the second part is the injector type, and the third part is the EGR rate. Note that in this study, the baseline injection pressure was 150 MPa. Higher injection pressures were also attempted. The maximum injection pressure for the convergent nozzle (6X133X800, $K=3$) and the ten-hole nozzle injectors was 200 MPa, while the baseline six-hole nozzle (6X133X800) injector was 180 MPa due to a lower flow coefficient. The start of injection (SOI) was varied between −20 deg and 5 deg after top-dead-center (ATDC).

Three EGR levels were tested, namely 0%, 15%, and 30%. EGR was cooled prior to mixing with the fresh intake air before entering the turbocharger. An intercooler was used to further cool the intake charge before entering the engine. The temperature at the intake manifold was maintained at 23°C regardless of the EGR levels. The use of EGR results in reduced oxygen levels in the cylinder. Note that 15% and 30% EGR will correspond to 19.3% and 17.6% oxygen molar fraction in the cylinder based on the current fuel and air flow rates conditions in this study.

3.1 0% EGR Conditions. Figures 1 and 2 show the results of NO_x and soot emissions, respectively. It can be seen that the NO_x emissions were very similar between the baseline injector and the convergent nozzle ($K=3$) injector under the same injection pressure. On the other hand, the convergent nozzle produced more soot emissions than the baseline nozzle. According to Desantes et al. [18], the convergent nozzle can reduce cavitation and increase the injection velocity. The high injection velocity may be expected to enhance fuel atomization in order to reduce soot emissions. However, the present results show an increase in soot emissions by using the convergent nozzle and thus contradicted the above expectation of soot reduction. It is suspected that cavitation may actually help with the spray atomization by creating disturbances in the liquid jet to enhance liquid breakup. Without such disturbances in the liquid jet, the high injection velocity using the convergent nozzle could cause the fuel jet to penetrate further without effective atomization. As a result, ineffective fuel-air mixing may occur and result in higher soot emissions. The study by Tamaki et al. [5] indicated that cavitation could promote liquid atomization. Nonetheless, more detailed in-cylinder diagnostics are needed for further clarifications.

Effects of the nozzle hole size were found to be important in determining emissions. The nozzle diameter was reduced from 148 μm for the six-hole baseline injector to 114 μm for the ten-hole injector. It should be noted that both injectors had the same flow number, i.e., the same injection duration. At 150 MPa injection pressure, the ten-hole injector produced the least NO_x emissions compared with the other injectors. Moreover, the ten-hole injector also produced the least soot emissions under the same injection pressure. The main reason is thought to be the better fuel atomization by using a small size nozzle. Better atomization can lead to a better mixing and more complete combustion. Exhaust temperature measurements also indicated that the ten-hole injector produced a higher exhaust temperature (~365°C) compared with that of the six-hole injector (~345°C). The higher combustion temperatures also resulted in better CO oxidization and led to a reduction in CO emissions when the ten-hole injector was used (Fig. 3).

Effects of injection pressure on NO_x and soot emissions can

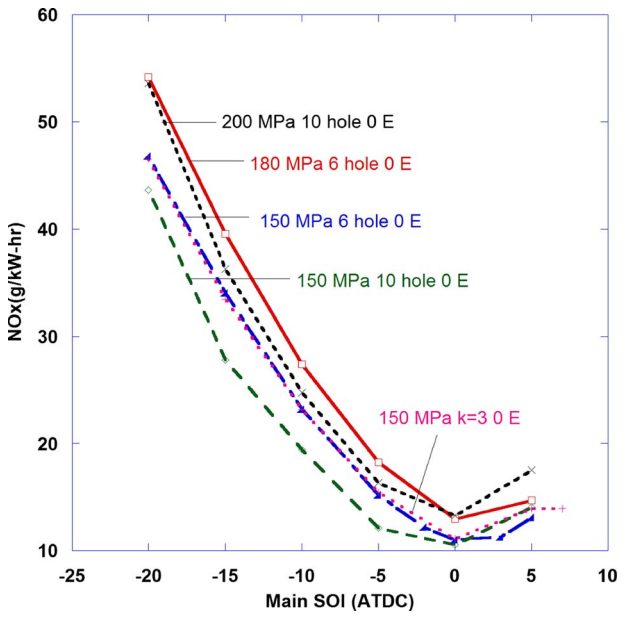

Fig. 1 NO_x emissions of all three injectors at 0% EGR with different injection pressures

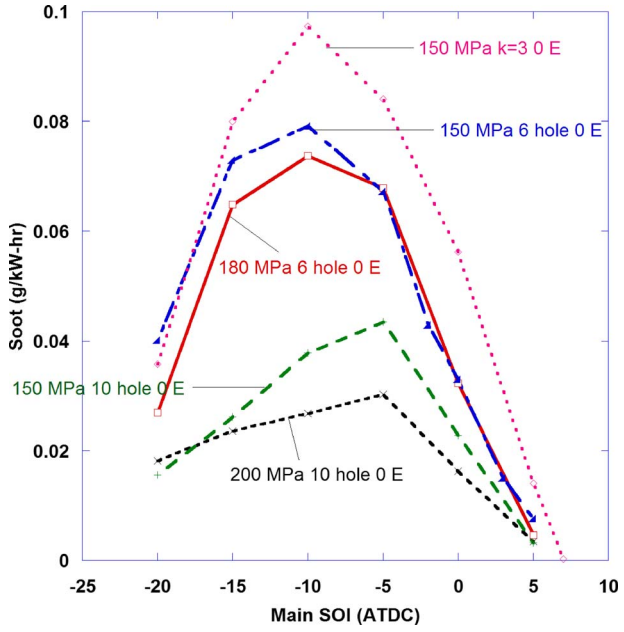

Fig. 2 Soot emissions of all three injectors at 0% EGR with different injection pressures

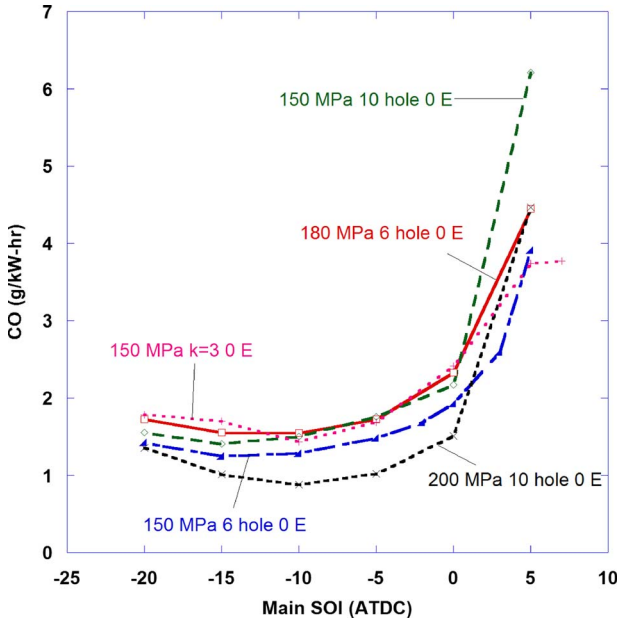

Fig. 3 CO emissions of all three injectors at 0% EGR with different injection pressures

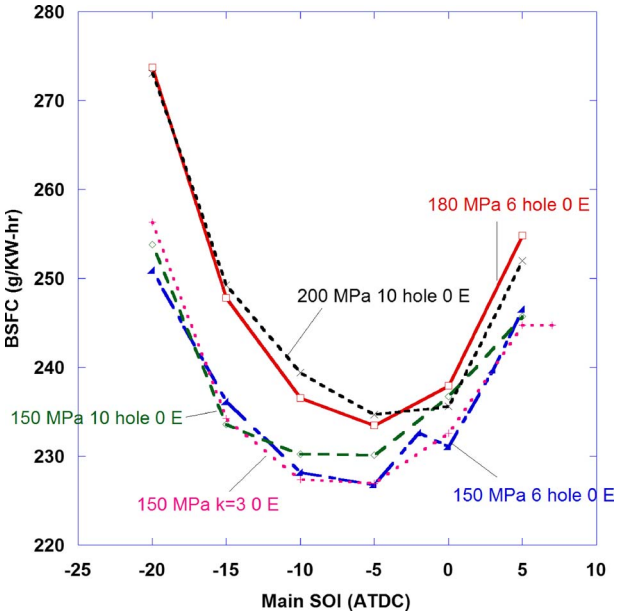

Fig. 4 BSFC of all three injectors at 0% EGR with different injection pressures

also be seen from Figs. 1 and 2. As can be seen in Fig. 1, NO_x emissions increased as the injection pressure was increased. This can be attributed to the increase in spray velocity at higher injection pressures leading to better atomization which, in turn, will lead to more rapid premixed burn and higher local combustion temperatures that will increase NO_x emissions.

At 200 MPa injection pressure, the ten-hole injector produced the least soot emissions. The low soot emissions may result from better atomization due to the high injection pressure and the enhanced fuel-air mixing due to the small nozzle hole that produced small fuel drops. Despite the significantly low soot emissions for the conventional injection timing using the ten-hole injector, the reduction in soot emissions for late injection (i.e., 5 ATDC) was not significant. The reason may be due to the fact that soot emissions were already low at the late injection timing and further reductions would be difficult.

Results of CO, BSFC, and HC emissions are shown in Figs. 3–5, respectively. As the injection pressure was increased, in general, BSFC also increased with the exception of 0 ATDC injection using the ten-hole injector. It is also noticed that the difference in BSFC is larger for early injection timing cases. It is speculated that the increase in BSFC using high injection pressure was due to the higher power consumption by the fuel pump. The difference in BSFC may also result from the detailed variations of the in-cylinder process caused by the increase in the fuel injection velocity. On the other hand, the effects of nozzle geometry on BSFC were not significant. The ten-hole injector produced less CO emissions but higher HC emissions than the six-hole injector in numerous conditions. However, a clear trend was not discernible.

From the above emissions results of using 0% EGR, it appeared that a late injection strategy (i.e., 5 ATDC) was required for simultaneous soot and NO_x reductions using the single injection scheme. However, the NO_x levels remain significantly higher than the required standards. Thus, more study on using high EGR was performed and will be discussed next.

3.2 High EGR Conditions. By comparing Figs. 1 and 6, it can be noted that NO_x emissions were significantly lower for 15% EGR than those for 0% EGR. As expected, EGR reduced NO_x emissions but increased soot emissions. From the emissions results in Figs. 6 and 7, a late SOI (e.g., 5 ATDC) was required for simultaneous soot and NO_x reductions. As in the case of 0% EGR, the NO_x emissions using the convergent nozzle did not vary significantly compared with the baseline injector at 150 MPa injection pressure. On the other hand, the convergent nozzle produced significantly higher soot emissions under traditional injection timing (i.e., from −20 ATDC to −5 ATDC) despite the fact that a higher injection pressure (200 MPa) was used.

As in the case of 0% EGR, the ten-hole injector proved to be more effective in reducing NO_x and soot emissions compared with other injectors at the same injection pressure. It is believed that the ten-hole injector can make better use of surrounding air compared with the six-hole injectors, including both the straight-hole and the convergent nozzles. Visualization of fuel spray using these injectors would be helpful in confirming the above statement.

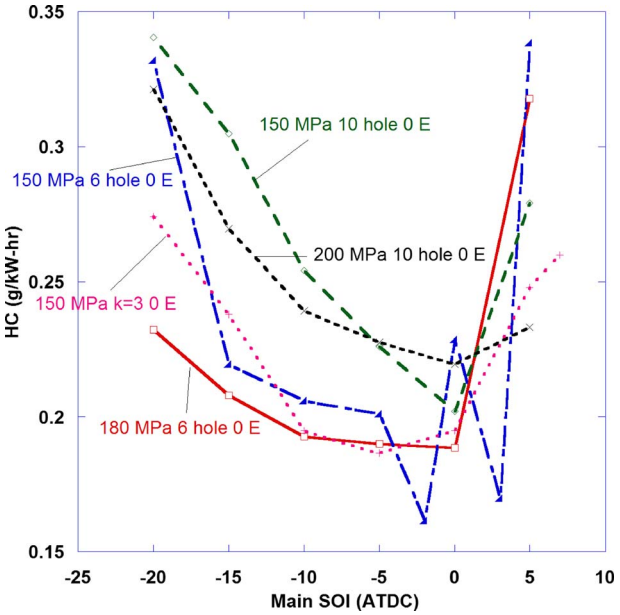

Fig. 5 HC emissions of all three injectors at 0% EGR with different injection pressures

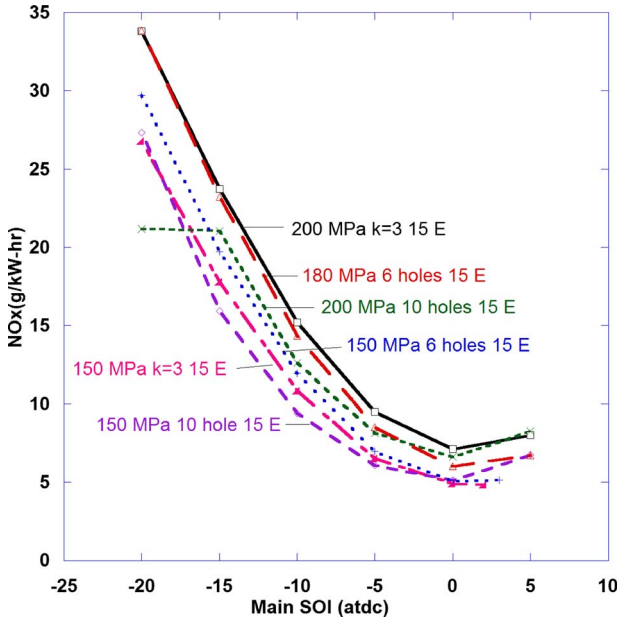

Fig. 6 NO_x emissions of all three injectors at 15% EGR with different injection pressures

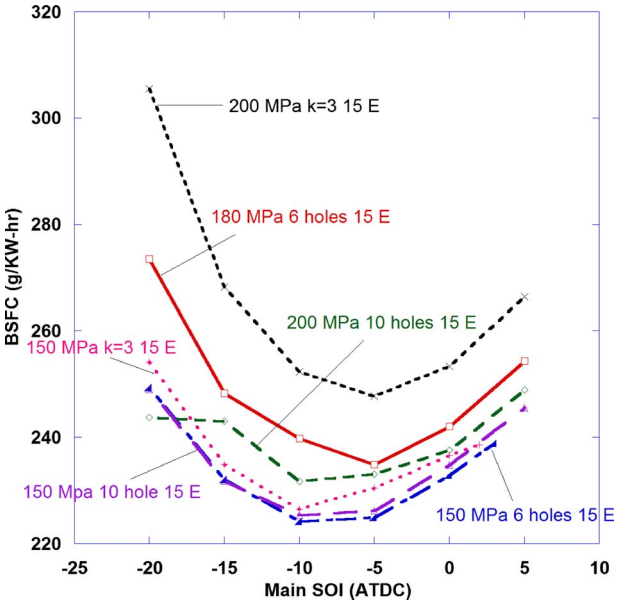

Fig. 8 BSFC of all three injectors at 15% EGR with different injection pressures

Injection pressure affected both NO_x and soot emissions for all injectors when 15% EGR was used, as in the 0% EGR conditions. NO_x increased as the injection pressure was increased. The maximum NO_x emissions were observed with the convergent nozzle at 200 MPa injection pressure. On the other hand, high injection pressures significantly reduced soot emissions for the same type of injectors. Results of BSFC, CO, and HC emissions are shown in Figs. 8–10, respectively. The fuel consumption deteriorated as the injection pressure was increased, thus being consistent with the 0% EGR conditions. The effects of nozzle geometry on CO and HC were not clear, and a definitive trend was not observed.

Further testing using 30% EGR was performed for NO_x reduction. Comparisons of Figs. 1, 6, and 11 revealed that NO_x was reduced significantly with increased EGR. With 30% EGR, NO_x levels were reduced to around 1 g/kW h at late SOI, close to the Tier 4 standard for NO_x (0.4 g/kW h). Simultaneous reductions of NO_x and soot can be achieved with high EGR, high injection pressures, and late injection timings. The present results on low soot and NO_x emissions are consistent with the findings in literature using high EGR [15–17]. Under the conventional injection timing range, NO_x emissions decrease and soot emissions increase as the injection timing is retarded. However, as the injection timing is further retarded close to TDC, the ignition delay increases allowing more time for fuel-air timing to achieve a more homogeneous mixture [15]. Additionally, combustion takes place at a lower temperature environment that can avoid the production of soot, thus resulting in smokeless diesel combustion [16]. The use of high EGR rates can further prolong ignition delay to increase time for mixing. As a result, high EGR combined with late injection can result in simultaneous reduction [17,19].

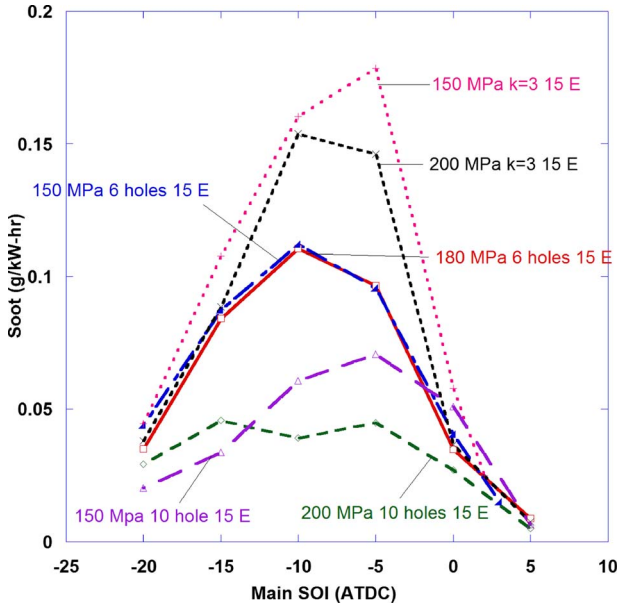

Fig. 7 Soot emissions of all three injectors at 15% EGR with different injection pressures

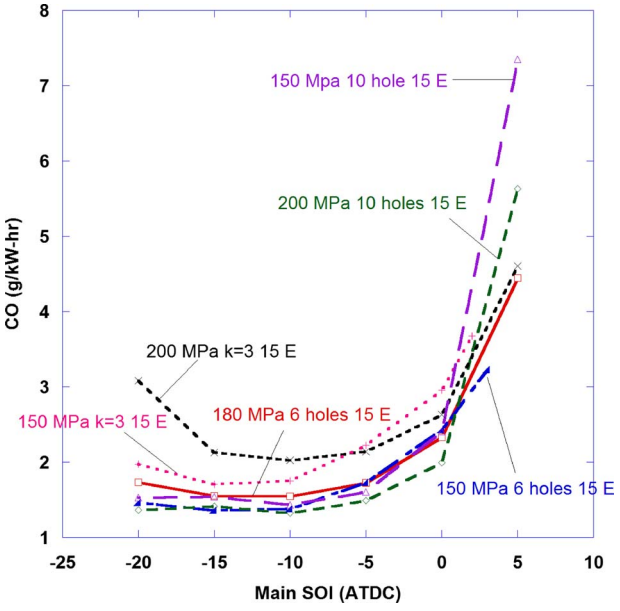

Fig. 9 CO emissions of all three injectors at 15% EGR with different injection pressures

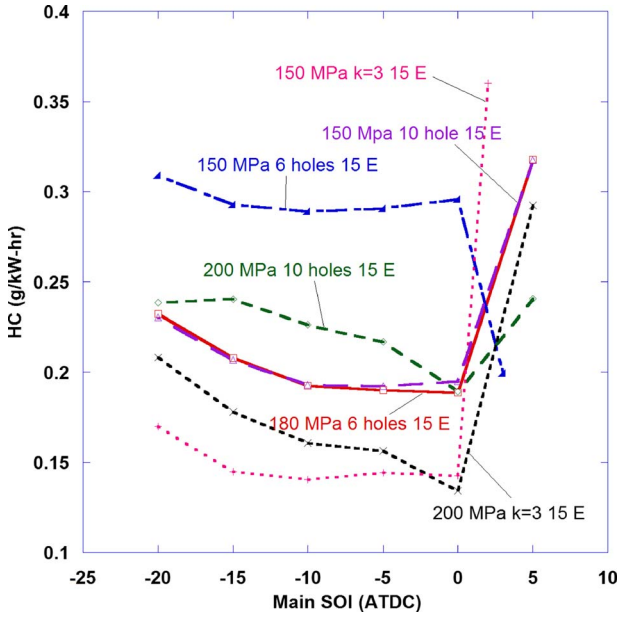

Fig. 10 HC emissions of all three injectors at 15% EGR with different injection pressures

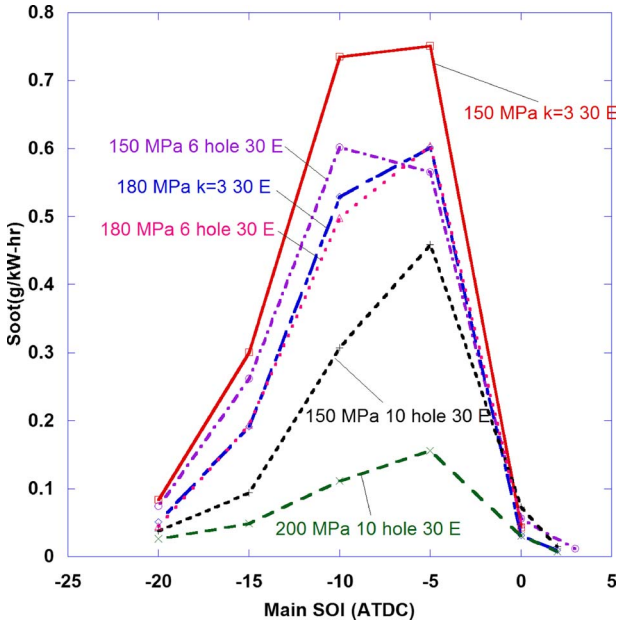

Fig. 12 Soot emissions of all three injectors at 30% EGR with different injection pressures

From Figs. 11 and 12, NO_x emissions using the convergent nozzle were comparable with the baseline injector, but soot emissions were significantly higher. It is evident that using the ten-hole injector could reduce soot emissions with very little sacrifice to NO_x emissions, in particular, for late injection timings.

The injection pressure was found to have significant effects on NO_x and soot emissions at high EGR conditions. NO_x levels increased with injection pressures while soot levels reduced for all injectors. It is interesting to observe that although the introduction of EGR reduced the oxygen available to the fuel for most of the injection timings, the BSFC did not vary noticeably between 0% and 30% EGR conditions, as can be seen from Figs. 4 and 13. The reason is that the same amounts of fuel were used and the intake charge temperatures were kept constant (i.e., 23°C) regardless of the EGR levels.

Figures 14 and 15 show the CO and HC emissions for 30% EGR. It can be readily noticed that at late injection timing (e.g., past TDC), significant CO and HC emissions were produced due to incomplete combustion. As a result, the BSFC increased significantly at late SOI. Note that the latest allowable injection timing was 3 ATDC for 30% EGR due to the low in-cylinder oxygen levels, as compared with 5 ATDC for 0% and 15% EGR conditions.

3.3 Characteristics of Low Temperature Combustion. It is of interest to investigate the global combustion characteristics of

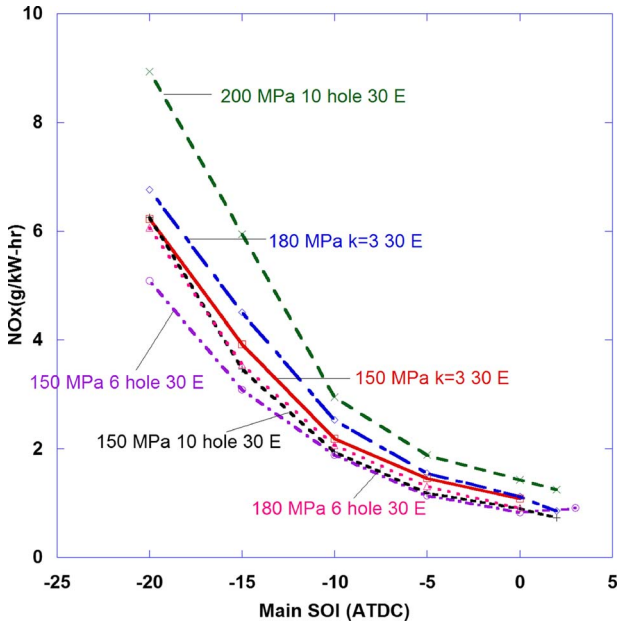

Fig. 11 NO_x emissions of all three injectors at 30% EGR with different injection pressures

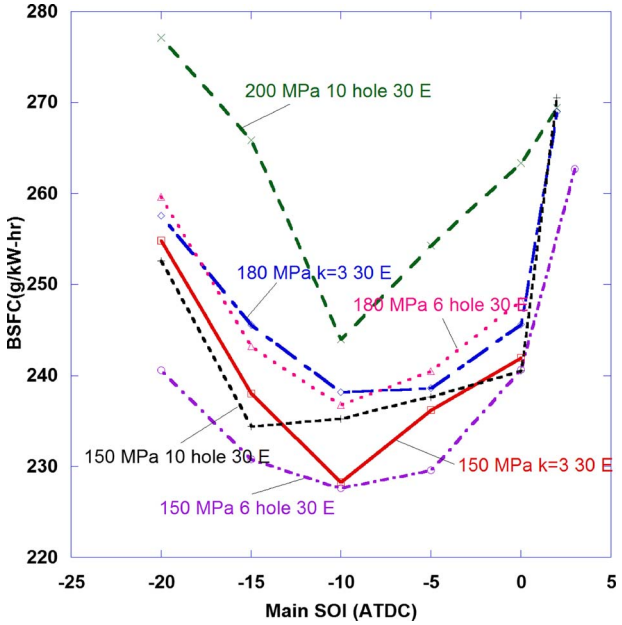

Fig. 13 BSFC of all three injectors at 30% EGR with different injection pressures

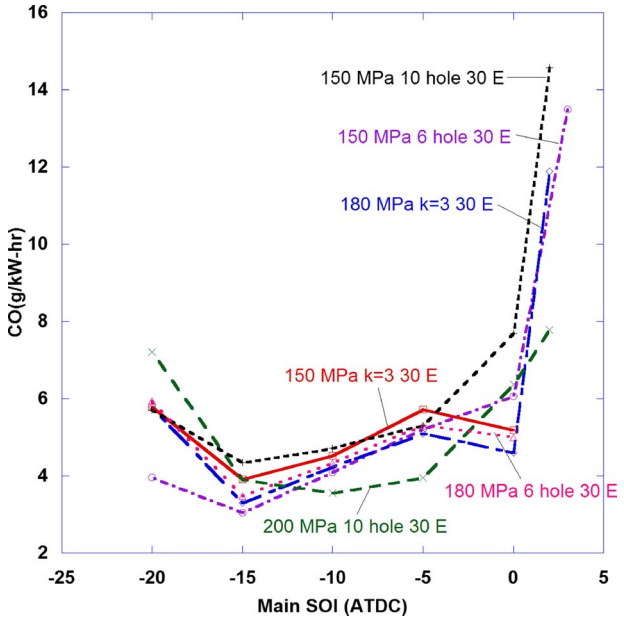

Fig. 14 CO emissions of all three injectors at 30% EGR with different injection pressures

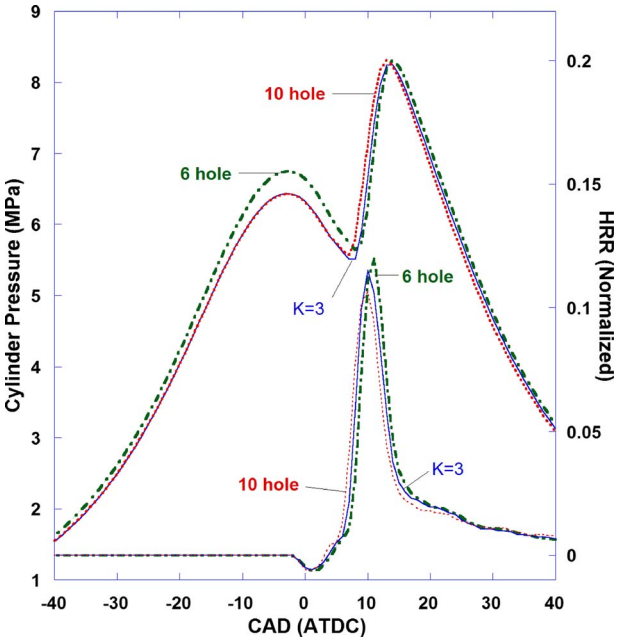

Fig. 16 Cylinder pressures and normalized heat release rate data for different injectors with 150 MPa injection pressure, 0 ATDC SOI, and 30% EGR

the high EGR, late injection cases, i.e., low temperature combustion conditions. Figure 16 shows the cylinder pressure and the normalized heat release rate data for all three injectors at 150 MPa injection pressure, 0 ATDC SOI, and 30% EGR. Note that in a production engine, the turbocharger is driven by exhaust gas and different operating conditions can result in different exhaust gas energy levels. As a result, the compression pressures at TDC differed slightly due to the use of a turbocharger to the extent that the intake boost pressure could not be directly controlled by the operator. All three injectors produced very similar combustion phasing under the same injection timings as can be seen from the heat release rate data in Fig. 16. Under these low temperature combustion conditions, the soot emissions levels using the three injectors were also similar, as seen in Figs. 17 and 18.

Figure 17 shows the effect of EGR on the cylinder pressure. As EGR was increased, the combustion temperature was reduced such that the exhaust gas energy level was also decreased. As a result, the turbo boost was reduced and caused a lower compression pressure. Note that EGR was cooled, and an intercooler was used to maintain a constant intake temperature at 23°C in the intake manifold.

Figure 18 shows NO_x and soot emissions data from all the cases tested in this study. It appears that higher EGR rates with late SOI are required for simultaneous soot and NO_x reductions using single injection. Figure 19 shows the same data set in a smaller

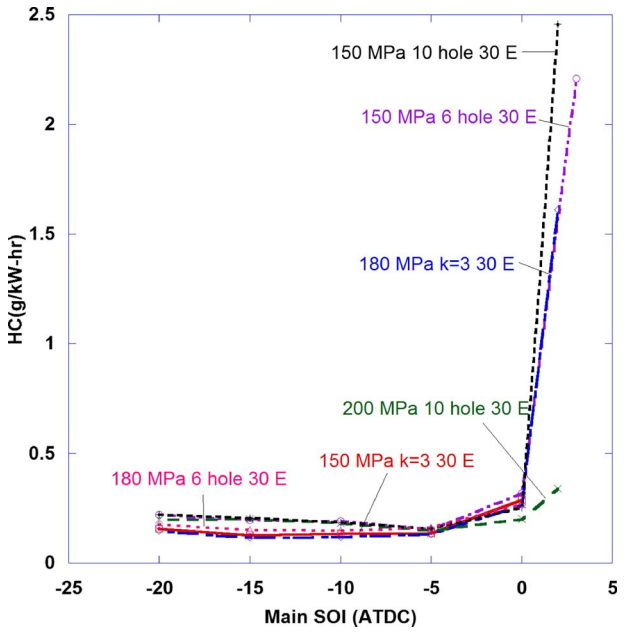

Fig. 15 HC emissions of all three injectors at 30% EGR with different injection pressures

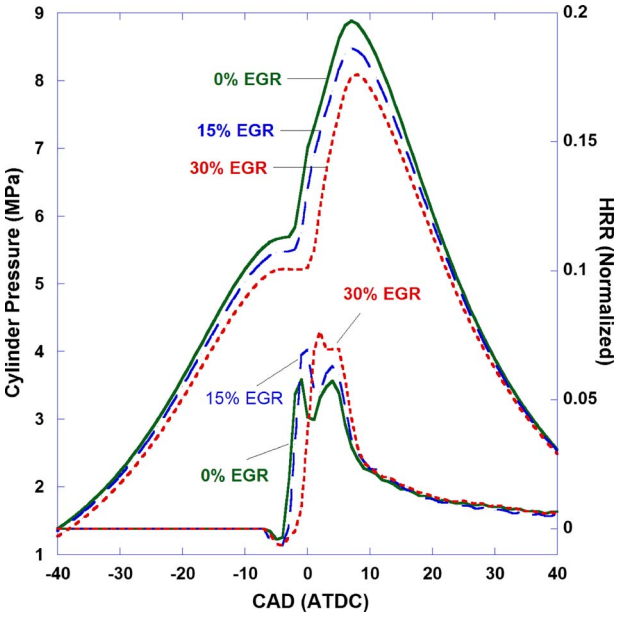

Fig. 17 Cylinder pressures of using the convergent nozzle with different EGR levels at 150 MPa injection pressure and –5 ATDC SOI

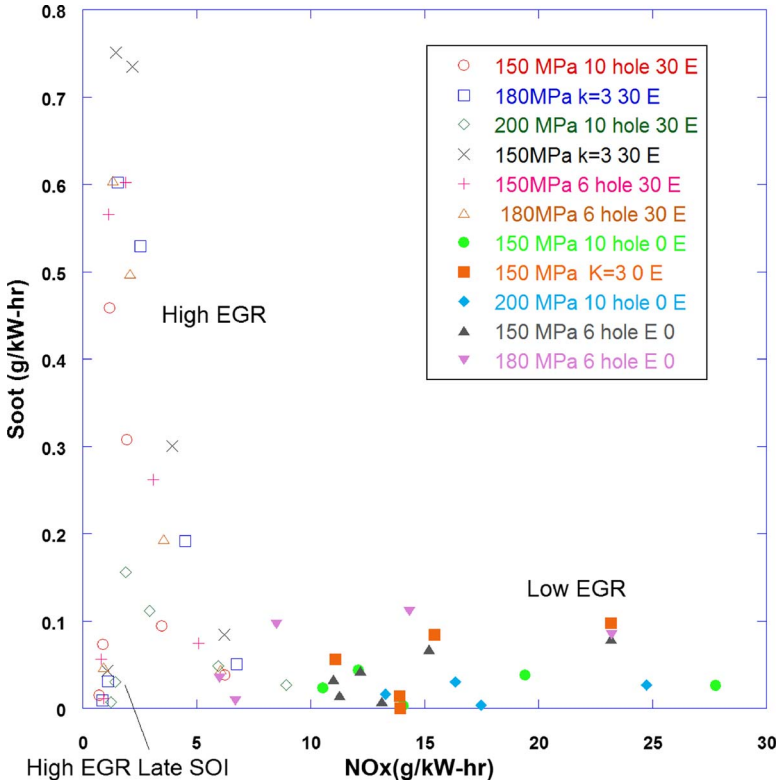

Fig. 18 Soot and NO_x emissions for all the cases tested in this study (0%, 15%, and 30% EGR for all three injectors at different injection pressures)

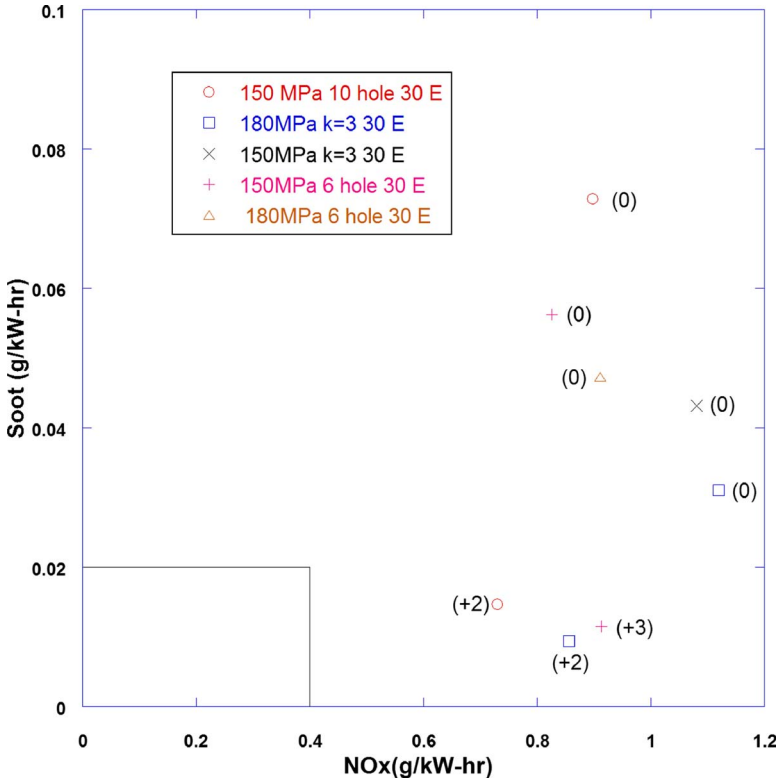

Fig. 19 Soot and NO_x emissions for selected cases that produced emission results within the scale shown. The number next to the data point is the SOI timing. The box on left bottom corner shows the Tier 4 standards for NO_x and soot emissions.

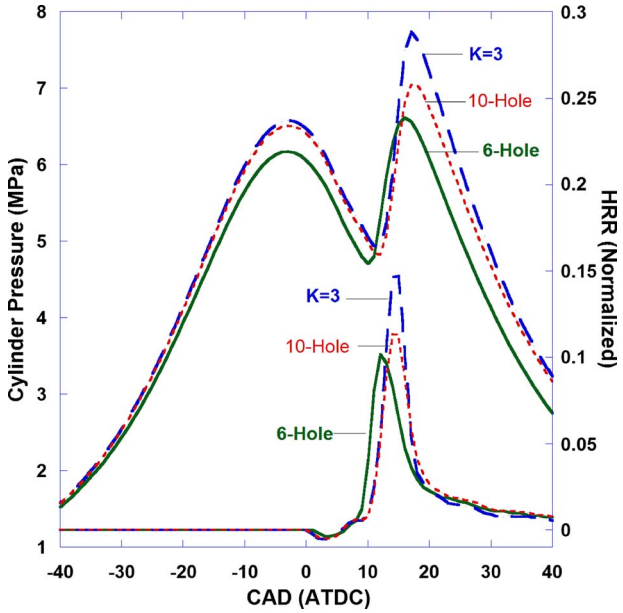

Fig. 20 Cylinder pressure and heat release rate for 30% EGR, late injection conditions (SOI=2 and 3 ATDC) that produced low soot emissions shown in Fig. 19

scale. The box at the left bottom corner indicates the Tier 4 emission requirements for the present class of engines. Among the cases that met soot regulations were the ten-hole injector using 150 MPa injection pressure with SOI at 2 ATDC, the convergent nozzle using 180 MPa injection pressure with SOI at 2 ATDC, and the six-hole injector using 150 MPa injection pressure with SOI at 3 ATDC. Despite the fact that a 30% EGR rate was used, NO_x emissions were still not within the limit of the Tier 4 standards. Further investigations are needed to create a local mixture condition that can prevent NO_x production such as using extremely high EGR or other injection schemes.

It was documented that the soot formation regime resides on the range for local equivalence ratio higher than 2 and local temperature between 1600 K and 2100 K [17]. Additionally, NO_x formation will not be a concern for local temperatures lower than 2200 K [17]. Low temperature combustion was achieved with late injection combined with high EGR to avoid the formation of soot and NO_x in the present study. Figure 20 shows the cylinder pressure and heat release rate data for the above three cases with low emissions. It can be seen that the ignition delay was relatively long, and the peak cylinder pressure was lower than those in earlier injection timings (e.g., Figs. 16 and 17). Combustion in the above three cases did not exhibit conventional premixed and diffusion burn characteristics. Instead, a largely premixed combustion was observed which is characteristic of low temperature combustion using high EGR [15,19]. On the other hand, low temperature combustion did not favor HC and CO emissions and thus the engine BSFC increased noticeably, as seen in Figs. 13–15. Various strategies, such as multiple fuel injections and boost, can be utilized to improve the combustion efficiency under these conditions [20,21].

4 Conclusions

In this study, three injectors with different nozzle geometries were tested in a multicylinder turbocharged diesel engine. Effects of nozzle geometry were investigated together with the use of high injection pressure, exhaust gas recirculation, and various injection timings. The fuel consumption, gaseous emissions, and soot emissions were measured.

The use of a convergent nozzle allowed higher injection pressures to be used due to reduced cavitation. Emissions results showed that the convergent nozzle produced higher soot emissions than the straight-hole nozzle. The possible reason is that the lack of cavitation in the convergent nozzle may have a negative effect on liquid atomization. The cylinder pressure measurements also indicated a slow combustion when the convergent nozzle was used. Effects of the convergent nozzle on NO_x emissions and fuel consumption were not significant.

The ten-hole injectors also allowed higher injection pressures to be used, as compared with the baseline six-hole injectors. The small nozzles in the ten-hole injector can produce small fuel drops for better atomization and mixing to reduce soot emissions. By using more nozzle holes, better air utilization can also contribute to the reduction in NO_x and soot emissions.

A high injection pressure was found to increase NO_x emissions but decrease soot emissions. Effects of injection pressure on soot emissions were not significant at retarded injection timings. The effect of injection pressure on NO_x emissions also decreased at high EGR rates.

Simultaneous reductions in NO_x and soot emissions were achieved by using high EGR and late injection timings to facilitate low temperature combustion. All three injectors could achieve comparable soot and NO_x emissions levels with appropriate injection conditions. Based on the overall performance, the present ten-hole injector appeared to have a better potential for achieving low soot and NO_x emissions over a wider range of injection timings and injection pressures.

Acknowledgment

The authors acknowledge the financial and equipment support of John Deere.

References

[1] U.S. EPA, 2002, "Emission Standards and Supplemental Requirements for 2007 and Later Model Year Diesel Heavy-Duty Engines and Vehicles," Paper No. 40 CFR.
[2] Su, T.F., Chang, C.T., Reitz, R.D., Farrell, P.V., Pierpont, A.D., and Tow, T.C., 1995, "Effects of Injection Pressure and Nozzle Geometry on Spray SMD and D.I. Diesel Emissions," SAE Paper No. 952360.
[3] Montgomery, D.T., Chan, M., Chang, C.T., Farrell, P.V., and Reitz, R.D., 1996, "Effect of Injector Nozzle Hole Size and Number of Spray Characteristics and the Performance of a Heavy-Duty D.I. Diesel Engine," SAE Paper No. 962002.
[4] Bergwerk, W., 1959, "Flow Pattern in Diesel Nozzle Spray Holes," Proc. Inst. Mech. Eng., **173**, pp. 655–660.
[5] Tamaki, N., Nishida, K., and Hiroyasu, H., 1998, "Promotion of the Atomization of a Liquid Jet by Cavitation in a Nozzle Hole," Proceedings of the ILASS 98, pp. 218–223.
[6] Arcoumanis, C., and Gavaises, M., 1998, "Linking Nozzle Flow With Spray Characteristics in a Diesel Fuel Injection System," Atomization Sprays, **8**, pp. 307–347.
[7] Chaves, H., Knapp, M., Kubitzek, A., and Obermeier, F., 1995, "Experimental Study of Cavitation in the Nozzle Hole of Diesel Injectors Using Transparent Nozzles," SAE Paper No. 950290.
[8] Challen, B., and Baranescu, R., 1999, *Diesel Engine Reference Book*, 2nd ed., Butterworth Heinemann.
[9] Pickett, L.M., and Siebers, D.L., 2004, "Non-Sooting, Low Flame Temperature Mixing-Controlled DI Diesel Combustion," SAE Paper No. 2004-01-1399.
[10] Kong, S.-C., Sun, Y., and Reitz, R. D., 2007, "Modeling Diesel Spray Flame Liftoff, Sooting Tendency and NO_x Emissions Using Detailed Chemistry With Phenomenological Soot Models," ASME J. Eng. Gas Turbines Power, **129**, pp. 245–251.
[11] He, L., and Ruiz, F., 1995, "Effect of Cavitation on Flow and Turbulence in Plain Orifices for High-Speed Atomization," Atomization Sprays, **5**, pp. 569–584.
[12] Knox-Kelecy, A. L., and Farrell, P. V., 1992, "Internal Flow in a Scale Model of a Diesel Fuel Injector Nozzle," SAE Paper No. 922308.
[13] Nurick, W. H., 1976, "Orifice Cavitation and Its Effects on Spray Mixing," ASME J. Fluids Eng., **98**, pp. 681–687.
[14] Benajes, J., Pastor, J. V., Payri, R., and Plazas, A. Z., 2004, "Analysis of Influence of Diesel Nozzle Geometry in the Injection Rate Characteristic," ASME J. Fluids Eng., **126**, pp. 63–71.
[15] Miles, P. C., Choi, D., Pickett, L. M., Singh, I. P., Henein, N., Rempel-Ewert, B. A., Yun, H., and Reitz, R. D., 2004, "Rate-Limiting Processes in Late-Injection, Low-Temperature Diesel Combustion Regimes," Proceedings of the THIESEL 2004 Conference, pp. 429–447.
[16] Kitamura, T., Ito, T., and Fujimoto, H., 2002, "Mechanism of Smokeless Diesel Combustion With Oxygenated Fuels Based on the Dependence of the

Equivalence Ratio and Temperature on Soot Particle Formation," Int. J. Engine Res., **3**(4), pp. 223–248.
[17] Alriksson, M., and Denbratt, I., 2006, "Low Temperature Combustion in a Heavy Duty Diesel Engine Using High Levels of EGR," SAE Paper No. 2006-01-0075.
[18] Desantes, J., Arregle, J., Lopez, J., and Hermens, S., 2005, "Experimental Characterization of Outflow for Different Diesel Nozzle Geometries," SAE Paper No. 2005-01-2120.
[19] Klingbeil, A., Juneja, H., Ra, Y., and Reitz, R. D., 2003, "Premixed Diesel Combustion Analysis in a Heavy-Duty Diesel Engine," SAE Paper No. 2003-01-0341.
[20] Keeler, B., and Shayler, P. J., 2008, "Constraints on Fuel Injection and EGR Strategies for Diesel PCCI-Type Combustion," SAE Paper No. 2008-01-1327.
[21] Kumar, R., and Zheng, M., 2008, " Fuel Efficiency Improvements of Low Temperature Combustion Diesel Engines," SAE Paper No. 2008-01-0841.

Computationally Efficient Whole-Engine Model of a Cummins 2007 Turbocharged Diesel Engine

Anup M. Kulkarni

Gregory M. Shaver[1]
Assistant Professor

School of Mechanical Engineering,
Purdue University,
West Lafayette, IN 47909
e-mail: gshaver@purdue.edu

Sriram S. Popuri
e-mail: sriram.s.popuri@cummins.com

Tim R. Frazier
e-mail: tim.r.frazier@cummins.com

Donald W. Stanton
e-mail: donald.w.stanton@cummins.com

Cummins Tech Center,
Columbus, IN 47201

This paper describes an accurate, flexible, and computationally efficient whole engine model incorporating a multizone, quasidimension combustion submodel for a 6.7-l six-cylinder turbocharged diesel engine with cooled exhaust gas recirculation (EGR), cooled air, and multiple fuel injections. The engine performance and NO_x emissions predicative capability of the model is demonstrated at 22 engine operating conditions. The only model inputs are physical engine control module "control actions," including injection rates, injection timings, EGR valve position, and variable geometry turbocharger rack position. The model is run using both "open" and "closed" loop control strategies for air/EGR path control, in both cases achieving very good correlation with experimental data. Model outputs include in-cylinder pressure and heat release, torque, combustion timing, brake specific fuel consumption, EGR flow rate, air flow rate, exhaust and intake pressure, and NO_x emissions. The model predicts engine performance and emissions with average absolute errors within 5% and 18%, respectively, of true values with "open-loop" air/EGR control, and within 5% and 11% with "closed-loop" air/EGR control. In addition, accurate prediction of the coupling of the in-cylinder combustion and emission-production processes with the boosted, cooled air/EGR gas dynamics is a key characteristic of the model. [DOI: 10.1115/1.3125316]

1 Introduction

Design optimization and control system development for modern turbocharged direct injection (DI) diesel engines with exhaust gas recirculation (EGR) and charge/EGR cooling require extensive testing and calibration. If these tasks could be conducted primarily on validated simulation models, via analysis-led design [1], of the engine and its external components (turbocharger, EGR loop, etc.), development cost and time would be substantially reduced. Furthermore, there exists an opportunity to develop cleaner and more efficient powertrain strategies through implementation of advanced combustion concepts (e.g., premixed charge compression ignition) and environmentally friendly alternative fuels in ultra-efficient diesel engines. Through computer simulation, the effect of advanced combustion strategies and alternative fuels on engine performance and pollutant formation can also be investigated on a fundamental basis, offering valuable guidelines to engine designers. However, for simulation models to compliment engine testing efforts, they should yield an acceptable level of predictiveness. Additional requirements are the flexibility to allow incorporation of different component architectures and control strategies, and computational requirements that are not prohibitively "expensive." For these reasons, an accurate, flexible, and computationally inexpensive whole engine model of a modern multicylinder medium-duty diesel engine is the goal of the present work.

1.1 Desired Model Characteristics. For whole diesel engine systems models, quasidimensional, multizone approaches [2–14] strike a very good balance between accuracy and computational cost. Studies have shown that these models are able to predict the rate of heat release and engine performance, and in many cases may also be capable of predicting NO_x emissions [2,5,7,8].

The purpose of this study was to develop an accurate, flexible, and computationally efficient model that:

(1) explicitly includes all major engine components, including:

- variable geometry turbocharger
- EGR valve
- EGR circuit with heat exchanger
- boosted charge air circuit with heat exchanger
- air/EGR mixer
- intake and exhaust manifolds
- combustion cylinders with multiple pulse injectors

(2) predicts:

- gas dynamics: EGR and air flows, pressures, and temperatures
- performance: torque, fuel consumption, and heat release
- NO_x emissions

(3) given engine control module (ECM)-dictated actuator commands:

- EGR valve position
- variable geometry turbo sliding nozzle position
- pilot, main. and post injection

As such, the desired outcome is a flexible, computationally efficient virtual engine testbed which explicitly includes all major components, and predicts both engine performance and NO_x emissions in response to real-world ECM-dictated "inputs." In other words, the goal is a model that captures the dynamic coupling between ECM control actions (injection timings and amounts, EGR valve position, and sliding nozzle variable geometry turbocharger (VGT) position) and engine performance and emissions "outputs."

Specifically, this paper describes the development, use, and

[1]Corresponding author.

Manuscript received September 12, 2008; final manuscript received January 1, 2009; published online November 2, 2009. Review conducted by Christopher J. Rutland.

validation of a steady-state quasidimensional multizone Gamma Technologies-Power [8,15,16] simulation model to achieve this. The model accurately predicts gas exchange processes, ignition, and heat release over a wide operating range without sacrificing large simulation time or computational cost. The basis of the model includes 1D compressible flow equations for gas flow through the intake and exhaust manifolds coupled with a quasidimensional, multizone predictive combustion model to simulate the diesel spray penetration, evaporation, entrainment, mixing, ignition, and combustion. The model captures the interaction between the EGR loop and VGT, and incorporates complex multipulse fuel injection. The main objective is to develop a model capable of predicting engine combustion, performance, and emissions in satisfactory agreement with the experimental data. Although the accuracy of the quasidimensional combustion model may be lower than multidimensional approaches, a significant reduction of computation time is achieved, allowing its incorporation in a whole engine system model. The software platform is also very flexible, allowing the representation of different hardware configurations, calibrations, and control strategies. In the future this fully calibrated and validated six-cylinder diesel engine model will be used as a launching point to investigate novel combustion strategies, including premixed charge compression ignition (PCCI) and alternate fuels combustion by leveraging the merits of variable valve actuation (VVA).

2 Description of the Model

The engine model was developed to give a detailed representation of all modern diesel engine components such as the intake and exhaust manifold, valves, multipulse injector, cylinders, turbocharger, and cooled EGR loop. A predictive, quasidimensional, multizone combustion submodel is used to calculate in-cylinder heat release, temperature, and species concentrations.

The intake and exhaust manifolds are modeled as multiple pipes with characteristics including diameter, length, volume, surface roughness, and bend radius. Each pipe is discretized into finite volume for better accuracy and the scalar equations of mass and energy are solved at the center, while mass flows are solved at the boundaries between them. To capture the interaction of flow through ports with arbitrary orientations, a momentum solution accounting for conservation in three dimensions is used. Discharge coefficients for 1D compressible flow through the valves are calculated from flow measurements taken on a cylinder head. The predictive combustion model "DI-Jet" (direct injection diesel jet model) [8] simulates the fuel plume from the nozzle. It is a multizone, quasidimensional model capturing the effects of fuel evaporation, mixing, ignition, and combustion. NO_x emissions are calculated using the extended Zeldovich mechanism.

The model predicts combustion in each cylinder, while taking into account the influence that exhaust gas pressure and temperature have on the EGR and turbo loops, as well as the gas exchange into and out of each cylinder. The ability to capture this coupling between in-cylinder, EGR loop, and air circuit is a critical desired characteristic of the model.

2.1 Modeling Fluid Flow. The equations for conservation of mass, energy, and momentum are used for gases in the cylinder, intake and exhaust manifolds, and EGR and VGT loops. Equations for the mass flow rates through valves are developed using a compressible, steady-state, one-dimensional, isentropic flow analysis for a restriction, where real gas flow effects are included by means of a discharge coefficient. Different effective opening areas of the EGR valve are simulated by adjusting the orifice diameter. Turbocharger maps obtained from the manufacturer are used in simulation to predict the performance of compressor and turbine.

2.2 Modeling Cylinder Combustion and Emissions. The quasidimensional, multizone combustion submodel's burn rate calculation is dependent on local temperature, fuel concentration, and oxygen concentration within each of up to 400 in-cylinder zones.

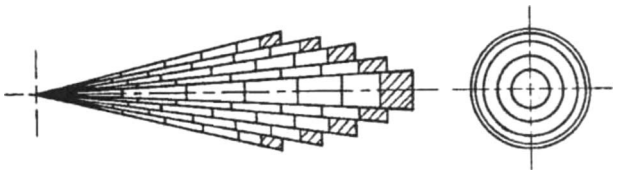

Fig. 1 Spray model in DI-jet

Fuel enters the cylinder in the form of axial slices, with each slice subdivided into five radial zones as shown in Fig. 1. Fuel is equally distributed between these five zones, and the total amount of fuel depends on the injection rate and instantaneous injection pressure specified. The injection velocity of each axial slice depends on the instantaneous injection pressure.

This modeling approach allows the emulation of complex fuel injection processes utilizing pilot, main, and post injections. When the zone is injected it is 100% liquid fuel. As the zone moves into the cylinder, it entrains air. Simultaneously, the fuel evaporates due to high in-cylinder temperature, and in so doing produces an unburned gas subzone. At this point the zone consists of liquid droplets, vaporized fuel, and entrained air as shown in Fig. 2 [17].

Since momentum of the zone is conserved, the mass of entrained air causes the velocity of the zone to decrease. As the outer zones entrain more air, their velocity decreases more rapidly and ultimately do not penetrate as far into the cylinder, resulting in a spray shape as shown in Fig. 1. Details of the submodels of fuel jet development, air entrainment, droplet evaporation, ignition, combustion, and emissions are given below [5,8].

2.2.1 Fuel Jet Development. The initial jet velocity U_i, prebreakup centerline penetration distance S, breakup time t_{br}, post breakup penetration S_{br}, droplet diameter at jet breakup D_d, and entrained air mass m_a are given as

$$U_i = C_n \left[\frac{2(p_i - p_c)}{p_{fi}} \right]^{0.5} \left(\frac{p_{fi}}{p_{fc}} \right) \tag{1}$$

$$S = U_i t \left[1 - 0.06 \times \left(\frac{t}{t_{br}} \right)^7 \right] \tag{2}$$

$$t_{br} = 0.29 \left(3 + \frac{L_n}{D_n} \right) \left(\frac{p_{fc}}{p_a} \right) \left(\frac{D_n}{U_i} \right) \tag{3}$$

$$S_{br} = U_i t_{br} [(t_{br} t)^{0.5} - 0.06] \tag{4}$$

$$D_d = 60 D_n R_e^{-0.22} W_e^{-0.31} \left(\frac{\rho_{fc}}{\rho_a} \right)^{-0.17} \tag{5}$$

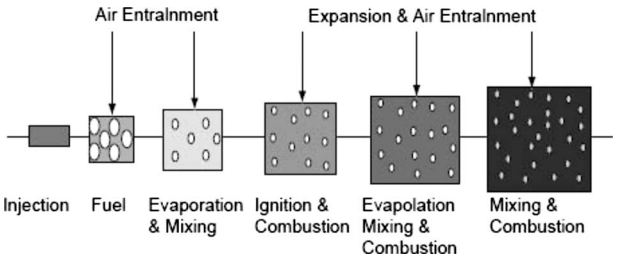

Fig. 2 Air entrainment and mixing within each zone

$$m_a = m_f \left[\frac{U_i}{\left(\frac{dS_s}{dt} \right)} - 1 \right] \tag{6}$$

where C_n is the discharge coefficient of the nozzle, p is pressure, ρ is density, C is the specific heat of fuel, Re is the Reynolds number, and We is the Weber number. For the subscripts, i is injector, c is cylinder, f is fuel, br is breakup, a is air, n is nozzle, s is swirl, and d is droplet.

2.2.2 Evaporation of Droplets. The single droplet evaporation equations used are

$$\frac{dT_l}{dt} = \frac{1}{M_l C_{pl}} \left(\Pi D_l^2 h (T_2 - T_1) + \frac{dM_l}{dt} \right) \tag{7}$$

$$\frac{dD_l}{dt} = \frac{2}{\Pi D_l^2 \rho_l} \left(\frac{dM_l}{dt} - \frac{\Pi D^3}{6} \frac{d\rho_l}{dt} \right) \tag{8}$$

$$\frac{dM_l}{dt} = -\Pi D_l^2 k \frac{Y_0 - Y_2}{(1+\xi) Y_0} \tag{9}$$

$$M_{fg} = \frac{\Pi}{6} (\rho_{lo} D_{lo}^3 - \rho_l D_l) N \tag{10}$$

where T is the temperature, M is mass, C_p is the specific heat at constant pressure, D is the droplet diameter, h is the heat transfer coefficient between burned gas and cylinder wall, k is the mass transfer coefficient, Y is the mass fraction of vaporized fuel, ξ is the flow rate ratio of air to fuel at droplet surface, N is the number of droplets in the package. Subscripts include l for liquid, 2 for bulk, 0 for surface or initial condition, and fg for vaporized fuel.

2.2.3 Ignition Delay Relation. The zonal fuel-to-air ratio is known from the mass of vapor fuel and entrained air at any given point in time. The zonal temperature is calculated by taking into account the temperature of the injected fuel, entrained air temperature, the effect of fuel vaporization, and heat transfer between zones. Once the fuel evaporates and experiences elevations in temperature and local oxygen concentration, the gaseous zone ignites according to an integrated Arrhenius ignition delay relation. This results in an additional increase in the local temperature and pressure. Subsequently injected fuel droplets then evaporate more quickly under the influence of the elevated temperature. The vaporized fuel is mixed with fresh air and combustion products, as the spray continues to burn. The ignition delay for unburnt gas subzones are modeled via equations of the form:

$$\tau = A p^{-n} \exp\left(\frac{E_A}{RT} \right) \tag{11}$$

$$\int_{t_{SI}}^{t_{SI}+\tau_{ID}} \left(\frac{1}{\tau} \right) dt = 1 \tag{12}$$

where τ_{ID} is the ignition delay or time between the start of injection and the start of detectable heat release, E_A is the apparent activation energy, R is the universal gas constant, A and n are constants depending on the fuel and airflow characteristics, t_{SI} is the time of start of injection [18].

2.2.4 NO_x Emissions Model. The products of combustion form the burned subzone. NO_x is calculated independently using the extended Zeldovich mechanism, for each burned subzone taking into account the fuel-air ratio and temperature. The integrated total of all the burned subzones gives the total cylinder NO_x. The principal reactions governing the formation of NO from molecular nitrogen and its destruction are [8,19]:

$$N + NO \leftrightarrow N_2 + O \tag{13}$$

$$N + O_2 \leftrightarrow NO + O \tag{14}$$

$$N + OH \leftrightarrow NO + H \tag{15}$$

where the forward rate constants used for the three reactions are given in Ref. [5].

2.2.5 Model Parameters and Outputs. The combustion submodel is capable of tracking up to 200 axial zones, resulting in up to 1000 total zones. Zones injected later may overtake the earlier injected zones depending on the injection pressure and rate of air entrainment.

Outputs provided by the model include in-cylinder pressure and

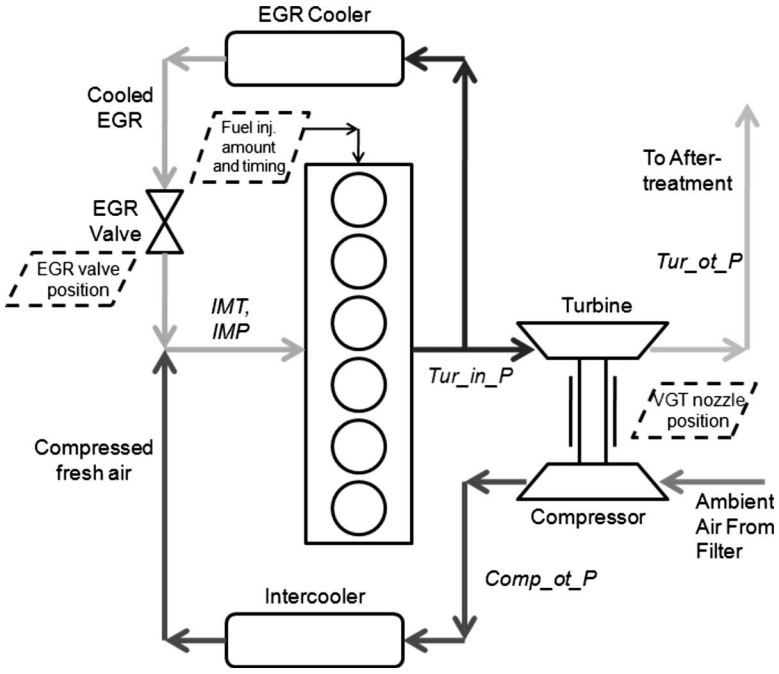

Fig. 3 Engine schematic. actuators noted with dashed lines

Table 1 Engine parameters

Parameter	Value	Units
No. of cylinders	6	-
Valves per cylinder	4	-
Bore diameter	107	mm
Stroke	124	mm
Connecting rod length	192	mm
Compression ratio	17.3	-
Intake valve opening	20 BTDC	CAD
Intake valve closing	200 ATDC	CAD
Exhaust valve opening	220 BTDC	CAD
Exhaust valve closing	20 ATDC	CAD
Intake valve diameter	29.27	mm
Exhaust valve diameter	29.4	mm

heat release, indicated mean effective pressure (IMEP), intake airflow rate, efficiency, brake specific fuel consumption (BSFC), torque, EGR flow, and turbocharger speed, all of which can be compared with measured data. In addition, the model provides details about each of the subzones which can be useful in determining the fuel impingement, zonal temperatures, and equivalence ratios. This is a very important feature especially for predicting and analyzing NO_x emissions, which are dominated by zonal temperatures and concentrations as well as time spent at elevated temperatures.

3 Model Validation

Figure 3 illustrates the configuration of a modern, high performance, low-emission Cummins six-cylinder direct injection diesel engine.

As shown, the engine is equipped with a turbocharger and a cooled EGR loop. The turbocharger consists of a compressor and a variable geometry turbine on a single shaft. By changing the position of the sliding nozzle VGT, the amount of exhaust energy utilized to drive the compressor can be modulated. Table 1 lists the main specifications of the engine. In this study, the shaded region in Fig. 4 is the area of focus. These points represent engine speeds and loads expected to be most commonly encountered in normal operation for "mid range" applications, including motor homes, school buses, shuttles, and fire trucks. Specifically, the shaded region represents the not-to-exceed (NTE) zone as specified by the United States Environmental Protection Agency (EPA) for engine emissions assessment. The United States EPA introduced not-to-exceed (NTE) emission limits as a requirement to make sure that heavy-duty engine emissions are controlled over the full range of speed and load combinations commonly experienced in use. Predicting the engine behavior in this NTE region is therefore of paramount importance.

Engine data, including in-cylinder pressure, airflow, EGR fraction, torque, fuel consumption, and exhaust NO_x, as well as pressures and temperatures at different locations were recorded at 22 different operating points in the NTE region, as shown in Table 2. Two different modeling modes were investigated.

(1) Open-loop mode, where the following were dictated to reflect the test values for these actuators:

- fuel injection shape and amount
- EGR valve position
- VGT position

(2) Closed-loop mode, where:

- fuel injection shape and amount were dictated,
  while the following were achieved via modulation of the VGT and EGR valve positions:
- target EGR flow
- target charge flow

Specifically, in the closed-loop mode, the VGT and EGR positions were modulated in a manner consistent with EGR/air-path control in modern diesel engines, to attain the target EGR fraction and charge flow. These modulations were done by trial and error, with minor changes to the positions observed in the experiments (and used in the open-loop mode).

Table 3 shows the calibration parameters for the model. Only the ignition model activation temperature and multipliers for entrainment before combustion, combustion rate, NO_x, compressor efficiency, and in-cylinder heat convection were changed from the nominal model settings. No changes were made to this calibration for different operating points. In other words, one single calibration was used across all 22 cases described in Fig. 4 and Table 2.

The model/experiment comparison for open-loop and closed-loop are summarized in the Table 4, which show the average absolute error of the model for 16 different quantities. The correlation across a large number of operating points is excellent, with average absolute errors less than 4% for the vast majority of predictions. As will be discussed further in the following, the open- and closed-loop modes show very similar results, except for the

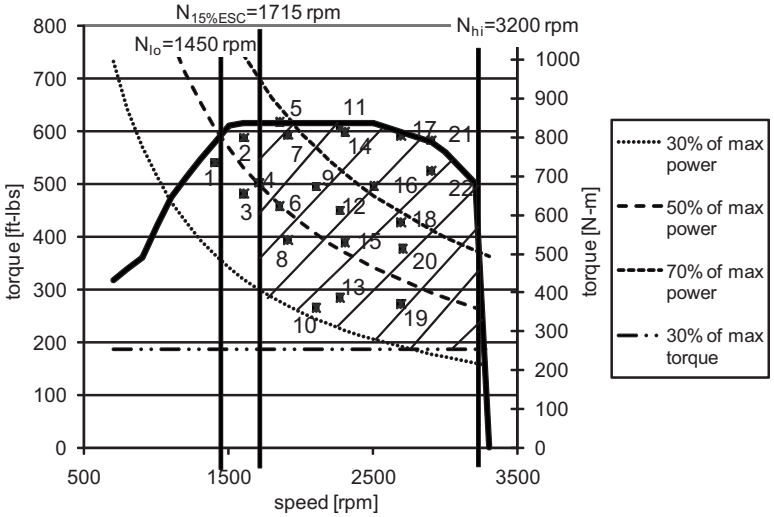

Fig. 4 Engine torque-speed map with the operating region for calibration

Table 2 Operating parameters for each of the 22 operating point. Note: some information, including pilot/main/post injection amounts and timings and common rail pressure have been suppressed for purposes of confidentiality.

Case	rpm	Total fueling (mg/stroke)	EGR vlv. equiv. dia. (mm)	VGT pos. (% open)	Dictated air flow (lb/min)	Dictated EGR fraction
1	1402	90.4	0.0	50	17.8	0.0
2	1603	99.5	0.0	54	22.8	0.0
3	1603	84.0	0.0	53	21.2	0.0
4	1705	84.4	14.8	50	21.2	12.1
5	1850	100.8	16.9	51	26.0	13.9
6	1850	77.3	17.0	52	21.3	14.5
7	1907	96.6	16.8	51	26.6	14.6
8	1907	68.1	16.9	49	20.4	18.3
9	2104	84.4	17.4	53	27.9	16.2
10	2104	53.3	23.0	53	18.5	22.7
11	2269	104.4	17.5	50	35.2	16.1
12	2269	79.3	17.7	54	29.3	16.9
13	2269	56.8	25.4	55	20.7	21.1
14	2303	102.2	17.6	51	35.5	16.0
15	2303	70.4	20.2	55	26.2	18.9
16	2502	89.2	15.9	55	35.9	13.8
17	2689	108.2	14.5	65	42.6	12.0
18	2689	82.9	16.1	64	36.6	13.1
19	2689	60.2	25.6	63	26.6	17.3
20	2702	75.1	17.3	67	32.9	13.6
21	2900	104.6	10.0	83	44.4	9.7
22	2900	100.2	10.6	77	43.9	10.2

Table 3 Model calibration parameter settings

Calibration parameters	Nominal values	Model values
Entrainment mult. before combustion	1.2	0.8
Entrainment mult. after combustion	0.5	0.5
Entrainment mult. after impingement	1.2	1.2
Combustion rate mult.	1	0.6
Droplet drag mult.	0.9	0.9
Droplet evaporation multi.	1.0	1.0
Droplet breakup length mult.	1.0	1.0
Sauter mean diameter mult.	1.0	1.0
Ignition model activation temp.	4000 K	3000 K
Ignition model combustion delay mult.	1.0	1.0
Ignition model pressure exponent	−1.25	−1.25
Overall NO_x mult.	1	1.5
Compressor mass mult.	1.0	1.0
Compressor efficiency mult.	1	0.97
Convection mult.	1	0.9

enhanced prediction of EGR fraction, intake manifold temperature, and NO_x emissions for the closed-loop mode.

3.1 Predictions for Heat Release. The model predictions for heat release rate for 4 (cases 2, 15, 19, and 22) of the 22 cases are shown in Fig. 5 for the closed-loop cases. The correlation is very good and consistent, with the accuracy for the other 18 cases (not shown). The largest observed discrepancy occurred for case 19, corresponding to the portion of the heat release curve associated with the post injection event. Case 19 has the largest post injection, 5.6% of the total fuel injected. Cases 2, 15, and 22 have 1.7%, 2.9%, and 1.2% of the total fuel in the post injection. By inspection, it was observed that cases with larger amounts of post injection where not as accurately captured as those with less. Figure 5 illustrates this point. All cases have a pilot injection, and case 1 is the only operating point to have no post injection. In summary, the in-cylinder modeling approach demonstrates good correlation with experimental heat release data for combustion cycles that include pilot, main, and post injections for post injections of up to 6% of the total fueling amount.

Also, note that while the heat release plots for the open-loop cases are not shown, there are minimal differences between the open- and closed-loop modes. Accurate prediction of heat release is of critical importance since combustion performance-related predictions, including in-cylinder pressure evolution, combustion timing, work output, torque, and brake specific consumption are driven in large part by the evolution of heat release during the conversion of fuel and oxygen to combustion products. Furthermore, accurate heat release calculations, as a summation of the heat release in each and every zone, indicates that the zonal temperature and reactant concentrations both prior to and following combustion are likely consistent with experiments, a prerequisite for accurate emissions prediction.

Table 4 Average absolute error across all 22 operating points considered in open-loop and (closed-loop)

Average absolute error (%)			
Airflow	Charge flow	A/F	Vol. eff.
3.43(3.93)	3.11(3.86)	3.28(3.75)	3.45(3.06))
EGR	NO_x	IMT	PCP
16.78(1.67)	17.63(11.00)	7.57(4.99)	3.75(4.30)
Torque	BSFC	NMEP	IMP
3.48(3.4)	3.29(3.72)	4.41(4.34)	3.55(4.13)
Tur-in-p	Tur-speed	Tur-out-p	Comp-out-p
4.65(5.99)	1.97(2.68)	4.75(4.68)	3.10(3.71)

3.2 Predictions for Airflow, Air/Fuel Ratio, and Volumetric Efficiency. Table 4 shows that the air and charge flows are well predicted by the model both in open-loop, as well as closed-loop. Good agreement for airflow coupled with a dictated fuel rate yields an accurate prediction for air-to-fuel ratio (Table 4).

The intake system inherently restricts the amount of air that can be inducted into the cylinder during one cycle. The volumetric efficiency is the metric describing the effectiveness of the induc-

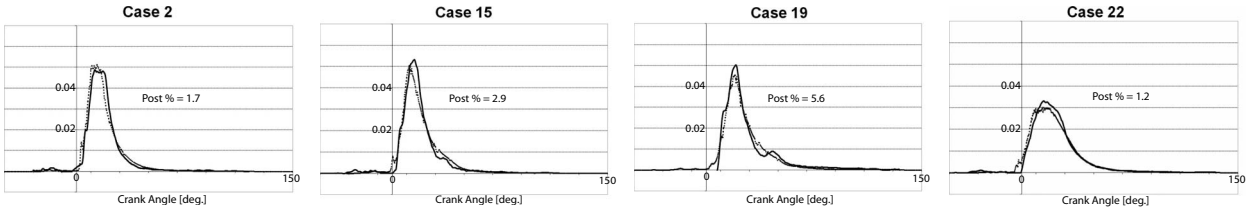

Fig. 5 Normalized apparent heat release rate for four representative cases spanning NTE region, see Fig. 4

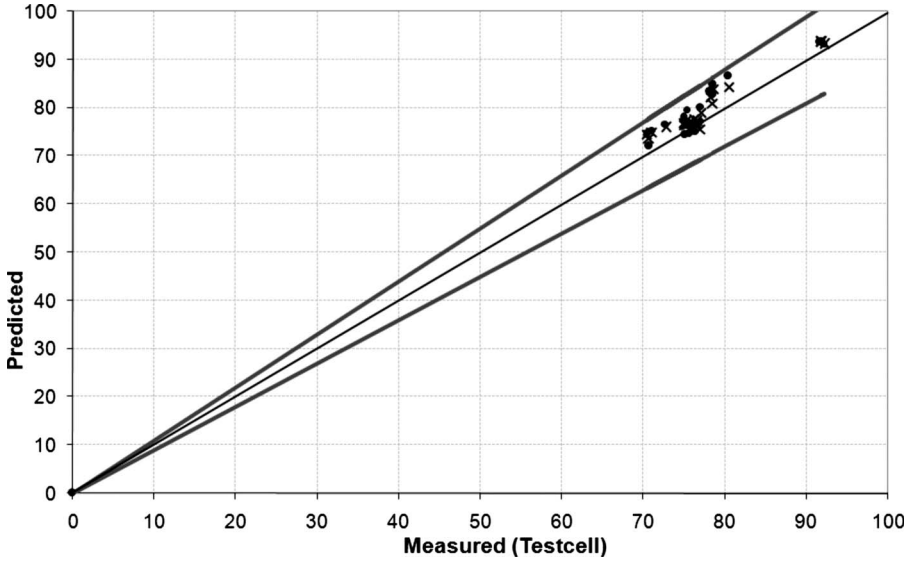

Fig. 6 Prediction for volumetric efficiency (%), ● open-loop, and × closed-loop

tion process. Figure 6 and Table 4 show excellent predictions for volumetric efficiency. Note that the two thick lines in all plots represent a ±10% deviation from the experimental values.

In summary, accurate prediction of airflow, charge flow, air-to-fuel ratio, and volumetric efficiency demonstrate the engine models effectiveness at capturing the gas exchange into the cylinders. This is of paramount importance since in-cylinder combustion process (in both reality and simulation) depends heavily on the inducted gas composition.

3.3 Predictions and Interdependence of EGR fraction, NO_x Emissions, and Intake Manifold Temperature. The model is not as accurate in predicting the EGR fraction at all points in the open-loop mode, as seen in Fig. 7. In particular, points 4, 5, and 7 show the most discrepancy with experiments in regard to EGR fraction. The most significant impact of this can be seen in the NO_x predictions, as shown in Fig. 8. The results are generally quite good, except for those points where EGR fraction predictions are significantly underpredicted, again, namely, points 4, 5, and 7. The result is overpredictions of NO_x at these points. The EGR increases the specific heat capacity of the in-cylinder gases, lowering the peak combustion temperature. To first order, NO_x formation is an exponential function of peak in-cylinder temperature. As a result, the underpredictions of EGR fraction at points 4, 5, and 7 lead to overpredictions in NO_x.

As depicted in Fig. 3, EGR flow is governed by the pressure difference between the intake and exhaust manifolds, which is significantly influenced by the in-cylinder combustion and gas dynamics in the turbocharged air circuit. Despite these complex interactions, the predicted EGR fraction follows the correct trend, while NO_x predictions are generally good at most of the operating conditions.

This inherent sensitivity of EGR flow to air/EGR path pressures, as well as the aforementioned importance of EGR fraction on NO_x, motivates the use of closed-loop control of EGR fraction in modern diesel engines. It was for this reason that the model was also run in a closed-loop mode, whereby EGR and VGT positions were modulated to achieve target values for EGR fraction and charge flow.

For the closed-loop mode, emphasis was directed at achieving the EGR fraction target while maintaining an agreeable prediction for charge flow (Fig. 7 and Table 4). As expected, a direct impact of this can be seen in the NO_x predictions as shown in Fig. 8 and Table 4. Tighter control of NO_x emissions in the closed-loop mode

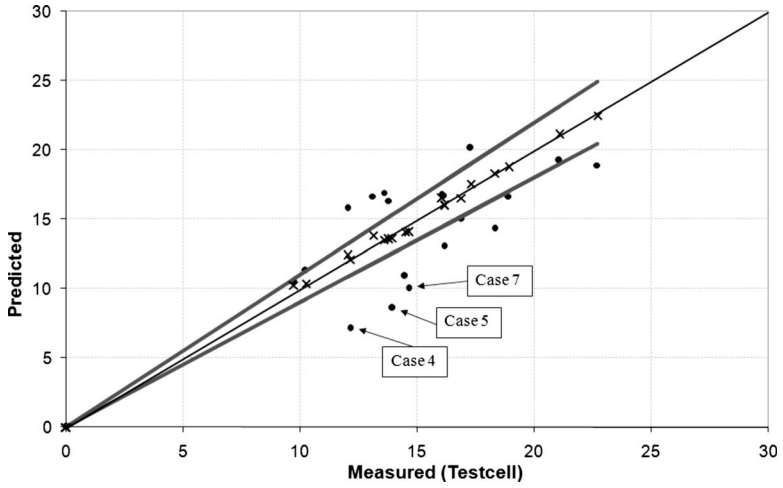

Fig. 7 Prediction for EGR fraction (%), ● open-loop, and × closed-loop

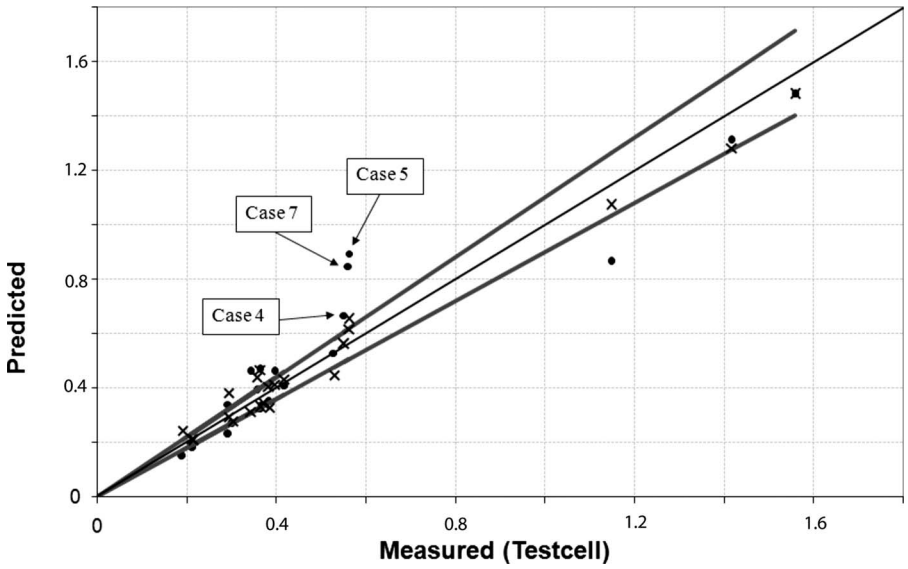

Fig. 8 Prediction for NO_x (ppm), ● open-loop, and × closed-loop. Note: actual values are suppressed due to confidentiality.

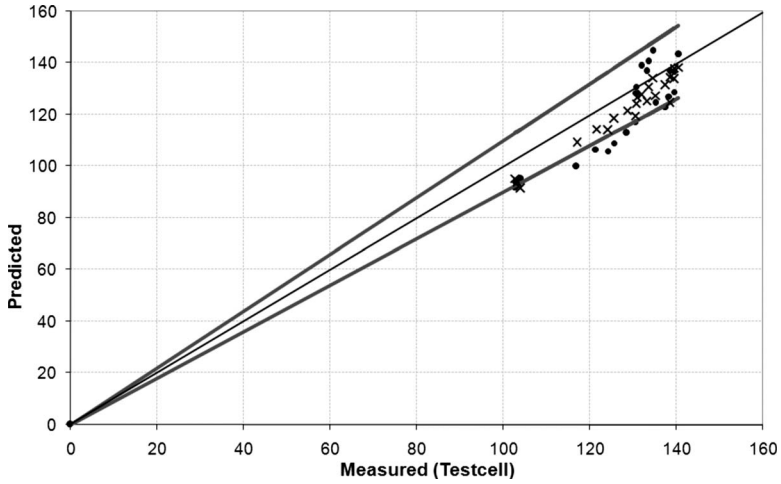

Fig. 9 Prediction for intake manifold temperature (deg F), ● open-loop, and × closed-loop

clearly indicates the importance of closing the loop on EGR fraction on an actual engine.

Predictions for intake manifold temperature are shown in Fig. 9. Since the engine incorporates EGR, the intake temperature is directly influenced by the amount of EGR. A more accurate prediction of intake temperature is therefore seen for closed-loop mode in which the EGR flow target is achieved.

3.4 Prediction of Combustion Behavior Performance. Very good correlations for key combustion performance outputs including torque, brake specific fuel consumption (BSFC, an efficiency-related metric), and peak cylinder pressure (PCP) are shown in Table 4. Net indicated mean effective pressure (NMEP, an indicated work metric) is also shown in Fig. 10.

Since torque is the most fundamental output of any prime mover, its accurate prediction is critical for any whole engine model. The ability to capture PCP is important because elevated in-cylinder pressures can cause damage if unchecked, and are directly related to combustion noise. Furthermore, efficiency, which is directly related to the BSFC and NMEP, is generally considered the most essential characteristic of a diesel engine—an attribute that clearly distinguishes diesel and spark-ignited engines. In summary, the ability to predict torque, PCP, BSFC, and NMEP accurately in a whole engine model in which only ECM-commanded actuators (pilot/main/post amount and timing, rail pressure, and EGR/VGT positions) are dictated is a key enabler for analysis-led design [1] of modern diesel engines. In order to capture the combustion performance, both the predictive combustion model and the EGR/air path-related models predicting intake manifold pressure (IMP), intake manifold temperature (IMT), and EGR fraction must be accurate. The model/experiment correlations discussed thus far and below demonstrate this.

3.5 Predictions of Temperature and Pressure in Air/EGR Paths. The accurate predictions of intake manifold pressure and temperature, as shown in Table 4, are required for capturing the in-cylinder combustion events including start of combustion, fuel burn rate, and postcombustion pressure/temperature since the intake manifold conditions provide the "initial" conditions for a combustion cycle. As noted previously, a sought after characteristic of the model is the capability to accurately capture this coupling between in-cylinder combustion and the gas exchange pro-

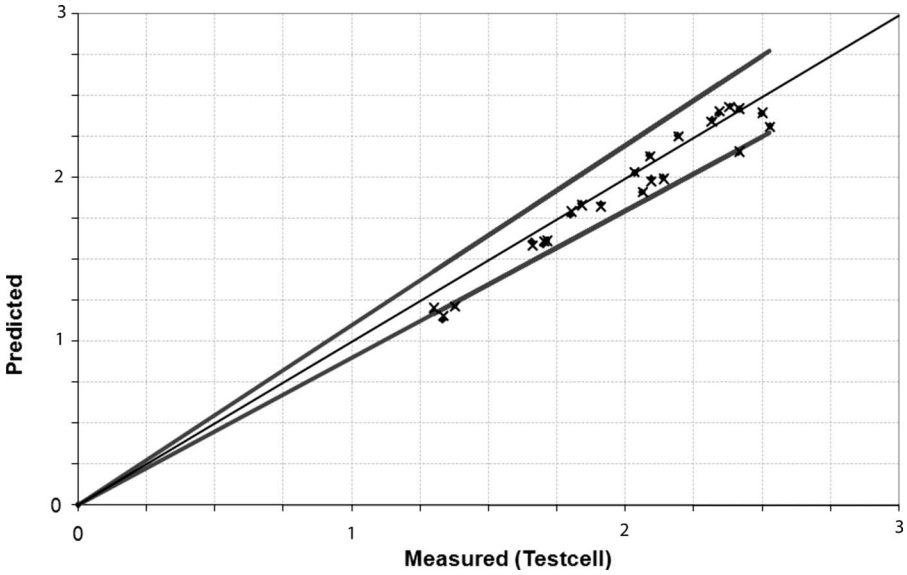

Fig. 10 Prediction for net indicated mean effective pressure, ● open-loop, and × closed-loop. Note: actual values are suppressed due to confidentiality.

cesses in the boosted air and EGR circuits.

Turbocharger turbine and compressor maps were obtained from the manufacturer and implemented in the model. The turbine inlet pressure (essentially the exhaust manifold pressure) drives the turbocharger. The turbine is coupled to the compressor that compresses the ambient intake air to the compressor outlet pressure, which drives the compressed air through the intercooler and into the intake manifold. The turbocharger-driven air boosting, therefore, dictates the intake manifold pressure, to a large extent. The turbine inlet pressure, turbine speed, and compressor outlet pressure are well predicted, as shown in Table 4.

As noted in Sec. 3.3, the EGR flow is dictated by, and very sensitive to, the difference between the intake and the exhaust manifold pressures, as well as the imposed EGR valve position. Therefore, in addition to the intake manifold pressure, the accurate prediction of the exhaust manifold pressure (e.g., the turbine inlet pressure) is also required and achieved, as shown in Table 4.

This is a key point, as neither the boosted airflow nor the EGR fraction are being directly dictated in open- or closed-loop versions of the model. Consistent with our modeling aim, the only parameters dictated on the model are fueling amount/timing, EGR valve position, and VGT position.

3.6 Model Prediction Summary. As noted previously, in the open-loop mode the fuel injection amounts/timings, EGR position, and VGT position are dictated to values equivalent to those observed on the experimental engine testbed. In the closed-loop mode, the EGR and VGT positions were modulated to achieve the experimental engine EGR fractions and charge flows. In both cases the model predicts the airflow, EGR fraction, and charge flow. In so doing, the model is quite different than the vast majority of simulation models, where one or more of these variables would be fixed and considered "boundary" or initial conditions for a closed-cycle, in-cylinder combustion model [3,4,6,20–22]. The coupling of the in-cylinder combustion and emissions-production process with the air/EGR gas dynamics is a key characteristic/requirement of the whole engine model developed here.

Furthermore, the predictions of airflow, charge flow, peak cylinder pressure, brake specific fuel consumption, net indicated mean effective pressure, torque, volumetric efficiency, and pressures/temperatures around the air/EGR paths are excellent. NO_x and intake manifold temperature predictions are fair in open-loop mode, and excellent in closed-loop mode, in which the target EGR fraction (corresponding to the experimental value) is achieved via modulation of the EGR and VGT positions. In sum, the model predicts key engine performance metrics and NO_x emissions as desired.

4 Conclusion

A computationally inexpensive, whole-engine simulation model capable of accurately predicting combustion timing, work output, fuel consumption, and NO_x emissions given only EGR position, VGT setting, and fuel rate has been developed. The main processes in the cylinder: spray penetration, droplet evaporation, air-fuel mixing, ignition, and fuel combustion are explicitly simulated with a multizone, quasidimensional combustion submodel. The approach is capable of simulating complex phenomenon including multipulse injection, turbocharging, cooled EGR, cooled boosted air, and their inherent coupling. The results are promising and show that both open- and closed-loop models are capable of predicting the heat release and NO_x emission over a wide range of operating conditions. As expected, when closed-loop control of EGR fraction and charge flow is accomplished via EGR valve and VGT modulation, the model predictions for NO_x and intake manifold temperature are improved. In summary, the flexibility and accuracy of this whole-engine modeling approach makes it attractive for engine design optimization, control development, as well as the exploration of novel engine concepts including variable valve actuation and fuel-flexible combustion, subject matter of current and ongoing efforts.

Acknowledgment

Funding for this work was provided by Cummins Inc., and the NSF GOALI program. Special thanks to Cummins Inc. for generously providing the experimental engine, technical support, fuel, and also other experimental equipment. The authors are very grateful to the following additional researchers at the Cummins Technical Center in Columbus, Indiana: Wayne Eckerle, Shankar Kumar, and Phanindra Garimella. The authors also wish to thank the Ray W. Herrick Laboratories Technical Services staff of Fritz Peacock, Bob Brown, Gil Gordon, and Frank Lee.

Nomenclature

NO_x = oxides of nitrogen
U_i = initial jet velocity
S = jet centerline penetration distance

t_{br} = jet breakup time
S_{br} = jet centerline penetration distance after breakup
D_d = droplet diameter at jet breakup
m_a = entrained air mass
C_n = nozzle discharge coefficient
p = pressure
ρ = density
C = fuel specific heat
Re = Reynolds number
We = Weber number
i = injector
c = cylinder
f = fuel
br = breakup
a = air
n = nozzle
s = swirl
d = droplet
T = temperature
M = mass
C_p = specific heat at constant pressure
D = droplet diameter
h = heat transfer coefficient between burned gas and cylinder wall
k = mass transfer coefficient
Y = mass fraction of vaporized fuel
ξ = flow rate ratio of air to fuel at droplet surface
N = number of droplets per package
1 = liquid
2 = bulk
0 = surface or initial condition
fg = vaporized fuel
τ_{id} = delay between injection and onset of combustion
E_A = apparent activation energy
R = universal gas constant
t_{si} = time at start of injection
BTDC = before top dead center
ATDC = after top dead center
CAD = crank angle degrees
A/F = air-to-fuel ratio
Tur-in-p = turbine inlet pressure
Tur-speed = turbine speed
Tur-ou-p = turbine outlet pressure
Comp-out-p = compressor outlet pressure

References

[1] Eckerle, W. A., and Stanton, D. W., 2006, "Analysis-Led Design Process for Cummins Engine Development," THIESEL.

[2] Jung, D., and Assanis, D., 2001, "Multi-Zone DI Diesel Spray Combustion Model for Cycle Simulation Studies of Engine Performance and Emissions," SAE Paper No. 2001-01-1246.

[3] Bohbot, J., Zolver, M., Klahr, D., and Torres, A., 2003, *Three Dimensional Modelling of Combustion in a Direct Injection Diesel Engine Using a New Unstructured Parallel Solver*, ICCSA, Montreal, Canada, pp. 483–492.

[4] Gao, Z., and Schreiber, W., 2001, "A Phenomenologically Based Computer Model to Predict Soot and NO_x Emission in a Direct Injection Diesel Engine," Int. J. Engine Res., **2**(3), pp. 177–182.

[5] Yoshizaki, T., Nishida, K., and Hiroyasu, H., 1993, "Approach to Low NO_x and Smoke Emission Engines by Using Phenomenological Simulation," SAE Paper No. 930612.

[6] He, Y., Lin, C-C., and Gangopadhyay, A., 2006, "Integrated Simulation of the Engine and Control System of a Turbocharged Diesel Engine," SAE Paper No. 2006-01-0439.

[7] Zhou, P., Zhou, S., and Clelland, D., 2006, "A Modified Quasi-Dimensional Multi-Zone Combustion Model for Direct Injection Diesels," Int. J. Engine Res., **7**, pp. 335–345.

[8] Morel, T., and Wahiduzzaman, S., 1996, "Modeling of Diesel Combustion and Emissions," XXVI FISITA Congress.

[9] Tan, P. Q., Deng, K. Y., and Lu, J. X., 2004, "Predicting PM Emissions From Direct Injection Diesel Engines Using a Phenomenological Model," J. Energy Inst., **77**, pp. 68–75.

[10] Cui, Y., Deng, K., and Wu, J., 2001, "A Direct Injection Diesel Combustion Model for Use in Transient Condition Analysis," Proc. Inst. Mech. Eng., Part D (J. Automob. Eng.), **215**(9), pp. 995–1004.

[11] Rakopoulos, C.D., and Hountalas, D.T., 1998, "Development and Validation of a 3-D Multi-Zone Combustion Model for the Prediction of DI Diesel Engines Performance and Pollutant Emissions," SAE Paper No. 981021.

[12] Mustafi, N. N., and Raine, R. R., 2008, "Application of a Spark Ignition Engine Simulation Tool for Alternative Fules," ASME J. Eng. Gas Turbines Power, **130**(1), p. 012804.

[13] Cerri, T., Onorati, A., and Mattarelli, E., 2008, "1D Engine Simulation of a Small HSDI Diesel Engine Applying a Predictive Combustion Model," ASME J. Eng. Gas Turbines Power, **130**(1), p. 012802.

[14] Li, H., and Karim, G. A., 2008, "Modeling the Performance of a Turbo-Charged Spark Ignition Natural Gas Engine With Cooled Exhaust Gas Recirculation," ASME J. Eng. Gas Turbines Power, **130**(3), p. 032804.

[15] Morel, T., Keribar, R., Silvestri, J., and Wahiduzzaman, S., 1999, "Integrated Engine/Vehicle Simulation and Control," SAE Paper No. 1999-01-0907.

[16] Ciesla, C., Keribar, R., and Morel, T., 2000, "Engine/Powertrain/Vehicle Modeling Tool Applicable to All Stages of the Design Process," SAE Paper No. 2000-01-0934.

[17] Yoshizaki, T., Nishida, K., and Hiroyasu, H., 2004, "Reduction of Heavy Duty Diesel Engine Emission and Fuel Economy With Multi-Objective Genetic Algorithm and Phenomenological Model," SAE Paper No. 2004–01–0531.

[18] Heywood, J. B., 1988, *Internal Combustion Engine Fundamentals*, McGraw-Hill, New York.

[19] Lavoie, G., Heywood, J., and Keck, J., 1970, "Experimental and Theoretical Investigation of Nitric Oxide Formation in Internal Combustion Engines," Combust. Sci. Technol., **1**, pp. 313–326.

[20] Chan, M., Das, S., and Reitz, R., 1997, "Modeling Multiple Injection and EGR Effects on Diesel Engine Emissions," SAE Paper No. 972864.

[21] He, Y., 2005, "Development and Validation of a 1D Model of a Turbocharged V6 Diesel Engine Operating Under Steady-State and Transient Conditions," SAE Paper No. 2005-01-3857.

[22] Singh, S., Reitz, R., Musculus, M., and Lachaux, T., 2007, "Validation of Engine Combustion Models Against Detailed In-Cylinder Optical Diagnostics Data for a Heavy-Duty Compression-Ignition Engine," Int. J. Engine Res., **8**, pp. 97–126.

A Convective Mass Transfer Model for Predicting Vapor Formation Within the Cooling System of an Internal Combustion Engine After Shutdown

Rocco Piccione
e-mail: r.piccione@unical.it

Antonio Vulcano
e-mail: alvulcano@unical.it

Sergio Bova
e-mail: s.bova@unical.it

Department of Mechanics,
University of Calabria,
87030 Arcavacata di Rende, Cosenza, Italy

In the usual liquid cooling system of an internal combustion engine a centrifugal pump is driven by the crankshaft and imposes a coolant flow, which transfers heat from the engine walls to the radiator. Therefore, as the engine is switched-off, the coolant flow also stops, while metal temperature may be particularly high after a period of high load operation; coolant vaporization in the cylinder head passages may occur in these conditions, with a pressure increase inside the cooling circuit. A numerical dynamic model was developed to predict this phenomenon, often called after-boiling among engine manufacturers. The model structure includes thermodynamic equations to compute heat transfer as well as mass transfer equations to determine the vaporized mass of the coolant, which occurs in cylinder head passages and the vapor condensation within the radiator. The developed mathematical model was validated against test data carried out on a production four-stroke spark-ignition engine, and simulation results show good agreement with experimental data. [DOI: 10.1115/1.3126262]

Keywords: heat and mass transfer, engine cooling system, cooling circuit, after-boiling, rapid shut down

1 Introduction

In designing internal combustion engine (ICE) cooling systems, one of the goals of manufacturers is to improve reliability and severe thermal-stress tests are carried out as routine during engine development. For example, when an engine is stopped after a prolonged time of high load operation and the metal temperature is particularly high, as the coolant flow stops, the coolant temperature rapidly increases and a fraction of it vaporizes. If the mass of the coolant, which vaporizes, is non-negligible, the pressure within the cooling system increases to the level that causes the opening of the radiator-cap pressure valve and part of the coolant leaks out. Engine manufacturers are interested in avoiding the occurrence of this phenomenon, which is often called after-boiling, and is much more likely to occur in small engines, which are most often operated at full load and are also shut down frequently.

This paper describes a method for modeling the thermal transient of a cooling system after a rapid shut down of the engine. The model structure includes thermodynamic equations to simulate engine heat transfer and convective mass transfer equations to predict the vaporized mass of coolant, which occurs in the cylinder head passages and the pressure evolution within the cooling circuit, after a rapid engine shut down. All model inputs are in terms of general parameters, typically known to the user. The simulation results are compared with experimental tests carried out on a production four-cylinder, MPI small spark-ignition (SI) engine, 1.2 dm^3 displacement.

2 The After Boiling Phenomenon

In previous studies [1,2] the analysis of experimental data of the after-boiling phenomenon in a small ICE. is shown in more details. Tests were carried out on a production four-stroke engine. The engine displaces 1.242 dm^3 in four in-line cylinders with a four-valve per cylinder aluminum head and a 60 kW at 5500 rpm rated power.

In the following, the more relevant aspects of the phenomenon are summarized. The engine was operated at 4000 rpm wide open throttle (WOT) for a time long enough to stabilize metal and coolant temperatures. Data were recorded for 2 min in this condition and then in 5 s the engine was brought to idle (25% throttle, 750 rpm). The idle operation was maintained for 5 s and then the engine was stopped. In addition, during the transition to idle and the idle operation, data acquisition was continued for 15 min after engine shut down.

Figure 1 shows the evolution of the coolant conditions and the temperatures at two points in the cylinder head and cylinder block. Coolant pressure and temperature during full load operation are essentially constant and so is the temperature at the different measuring points.

Starting from the time abscissa 2, during the 5 s transition to idle and the subsequent 5 s of idle operation (line *ab*, Fig. 1) coolant flow rate and pressure diminish due to the lower pump rotational speed. Coolant temperature at the engine outlet therefore rises due to a longer residence time within the engine, where some nucleate boiling of the coolant within the engine eventually occurs. Also the metal temperature of both engine head and cylinder block rapidly decreases during this period.

After engine shut down (point *b*, Fig. 1) the coolant flow rate also stops, while the head temperature is still quite high (about 150°C, well above coolant saturation temperature). Consequently, part of the coolant vaporizes within the engine head. This gives rise to a pressure increase and pushes the fluid out of the engine toward the radiator: the temperature at the engine outlet therefore increases. At the same time, the metal temperature of the head steadily diminishes while the temperature of the part of the engine block closer to the coolant entrance, after reaching a minimum,

Manuscript received October 2, 2008; final manuscript received March 25, 2009; published online November 2, 2009. Review conducted by Margaret Wooldridge.

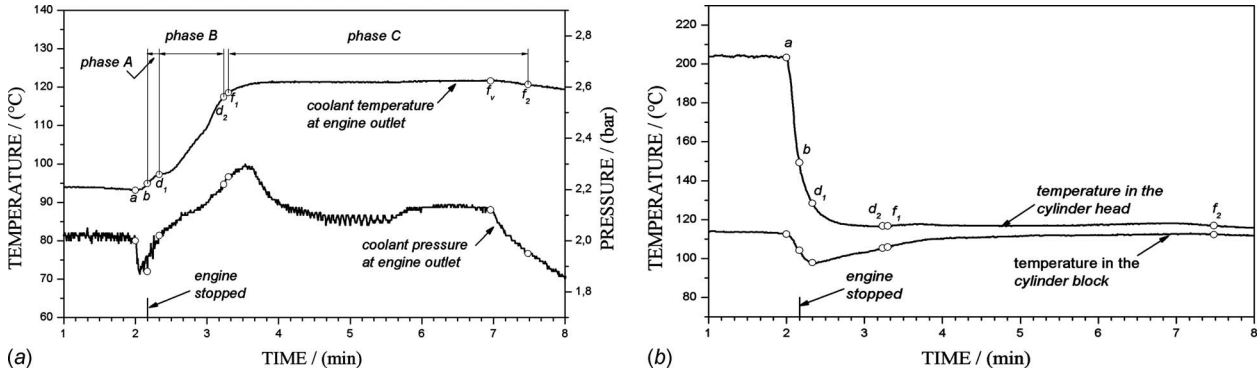

Fig. 1 (*a*) Time history of coolant pressure and temperature at engine outlet. (*b*) Temperature evolution in the cylinder block and in the engine head. Baseline case: time of idle operation 5 s; initial condition at WOT; standard length of cooling circuit.

starts to increase, as a result of conductive heat transfer from the warmer engine block parts.

Three different phases can be identified on the curves of Fig. 1.

2.1 Phase A: Air Compression. The sudden heat transfer from the high temperature head metal to the coolant contained in the cylinder head passages causes a rapid increase in coolant temperature and pressure. At the same time, a fraction of the coolant eventually vaporizes and this causes the pressure in the cooling circuit to rise above the level, which would be reached owing to heat transfer alone. In this phase, the air contained in the radiator expansion tank and in the airpockets in the cooling circuit (radiator, heater-core) is compressed to a small fraction of its initial volume. At the end of this phase (point d_1, Fig. 1), the pressure within the cooling system increases to the level, which causes the opening of the radiator-cap pressure valve (normally 2.0–2.15 bars).

2.2 Phase B: Air Leakage. As the pressure rises above the threshold value of the radiator-cap pressure valve, air in the radiator expansion tank starts to be expelled (point d_1, Fig. 1). At this stage the pressure in the cooling system still increases, mainly owing to vapor production, which occurs in the cylinder head passages. At point d_2 the air leakage phase stops and the radiator expansion tank becomes completely full of liquid.

2.3 Phase C: Coolant Leakage. At point f_1 the pressure is still above the threshold value of the radiator relief valve and the coolant starts to be expelled. At this stage the pressure within the cooling system initially increases due to vapor production. As the effect of volume reduction owing to the leaked fluid becomes predominant over the effect of vapor production, the pressure firstly stops increasing and then starts to decrease. The temperature difference between the metal and coolant now becomes negligible and no more heat transfer from the head metal to the coolant can occur during this phase. When the vapor phase reaches the radiator (point f_v, Fig. 1) a condensation of part of the vaporized mass of coolant occurs and the pressure in the cooling circuit quickly keeps diminishing due to the losses of vaporized mass. Finally, at point f_2 the pressure in the cooling circuit reaches the value which causes the closing of the radiator-cap relief valve and the coolant leakage stops. From this point the coolant cools in the form of stagnant vapor at engine outlet.

3 Model Description

A model was developed to predict the above described phenomena. The model structure includes thermodynamic equations to determine heat transfer as well as mass transfer equations to determine the vaporized mass of coolant, which occurs in cylinder head passages and the vapor losses via radiator. A radiator-cap pressure valve submodel allows the prediction of the leaked flow rate both during the air leakage phase and coolant leakage phase. The submodel interacts with the main model as the pressure in the cooling system rises above the threshold value of the radiator-cap pressure valve, allowing predictions of volume variations in the cooling circuit due to the leakage.

Model inputs include information about engine geometry (actual head mass, head material, head coolant volume, actual cylinders block mass, cylinders block material, cylinders block coolant volume), cooling system geometry (capacity of cooling circuit, capacity of radiator, capacity of radiator expansion tank), and coolant physical properties. All required inputs are in terms of general parameters, which are typically known to the user. In previous studies [2], experimental tests on the engine were used to determine thermal capacitor and resistor values both for the head and the cylinder block. Figure 2 shows an overview of the model.

3.1 Model Hypothesis. The proposed model is based on the convective mass transfer mechanism [3–8]: an individual chemical species moves from regions of high concentration to regions of low concentration. An analogy exists between heat and mass transfer: as thermal energy transfer is proportional to a temperature gradient according to Fourier's law, the diffusive mass flux of a species is related to its concentration gradient. The quantity of a species may be quantified either in terms of its mass density ρ or its molar concentration c. In the following the mass density ρ will be used.

A schematic of the thermodynamic system considered to model the phenomenon is shown in Fig. 3: it displays the part of the coolant, which is contained in the head passages and is directly heated by the hot metal surface. The system is composed of a

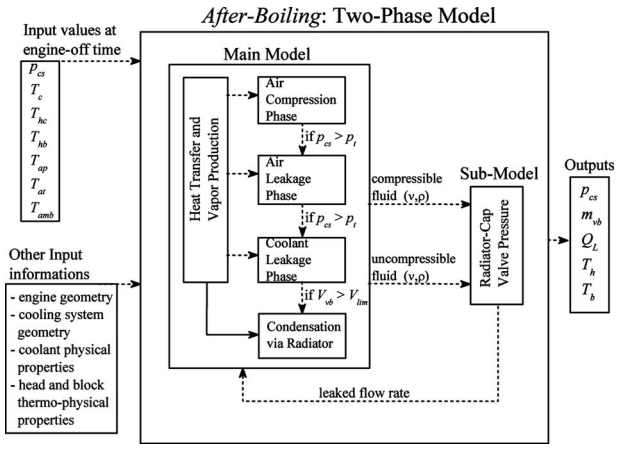

Fig. 2 Flow chart of the zero-dimensional two-phase model

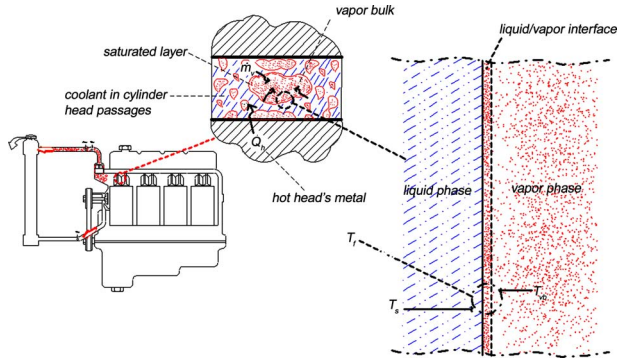

Fig. 3 Schematic representation of mass transfer process in the coolant contained in cylinder head passages of an internal combustion engine

liquid phase at a saturation temperature T_s, corresponding to the pressure in the cooling circuit, and of an overheated vapor phase at a higher temperature T_{vb}; at the vapor/liquid interface, where mass transfer occurs, saturation conditions are assumed at an unknown temperature T_i [8–10].

The vaporized mass of the coolant is computed by assuming mass diffusion from the liquid phase surface toward the vapor bulk through an interface zone (saturated vapor region) whose composition varies from saturated liquid conditions (at the liquid phase surface) to overheated vapor conditions (at vapor bulk).

The concentration gradient, which drives the diffusion is represented by the density difference between the vapor/liquid interface and the vapor bulk so that the similarity of the equations of heat convection and diffusion extends to the definition and use of the convective mass transfer coefficient, defined as

$$h_m = \dot{m}_v/(\rho_i - \rho_{vb})A_i \tag{1}$$

(the meaning of the symbols is reported at the end of the paper). By means of this coefficient the vaporized mass flux is proportional to the density difference (driving potential) between the vapor/liquid interface and the vapor bulk. Such a mechanism explains how vapor formation inside the head passages may occur even when temperature differences between the hot metal surface and the coolant are negligible and no more heat transfer, therefore, takes place. The described approach can be applied both in the case of vapor formation and in the case of vapor condensation so that in the model structure it will also be used to make predictions on vapor losses via the radiator.

3.2 Heat Transfer and Vapor Production. For the cylinder head metal, the zero-dimensional thermal power balance gives

$$\dot{Q}_h = -(\dot{Q}_{hc} + \dot{Q}_{hb} + \dot{Q}_{hr}) \tag{2}$$

where

$$\dot{Q}_h = m_h c_h (T_h^{t+\Delta t} - T_h^t)/\Delta t \tag{3}$$

$$\dot{Q}_{hc} = h_h A_{hc} (T_h^t - T_{hc}^t) \tag{4}$$

$$\dot{Q}_{hb} = C_{hb} (T_h^t - T_b^t) \tag{5}$$

while the radiation term $\dot{Q}_{hr}$ is generally negligible. In Eq. (4) T_{hc} represents the estimated saturation temperature of the liquid coolant in the head passages. Then, the head metal temperature at time $t+\Delta t$, from Eqs. (2) and (3) can be written as

$$T_h^{t+\Delta t} = T_h^t - (\dot{Q}_{hc} + \dot{Q}_{hb})\Delta t/m_h c_h \tag{6}$$

Similar to the engine head, the cylinders block metal temperature is

$$T_b^{t+\Delta t} = T_b^t + (\dot{Q}_{hb} - \dot{Q}_{bc})\Delta t/m_b c_b \tag{7}$$

The vaporized mass of coolant, which occurs in the cylinder head passages, can be determined from Eq. (1).

$$m_{vb}^{t+\Delta t} = m_{vb}^t + \overline{h_m A_i}^e (p_{sat,h} - p_{vb}^t)\Delta t/R_v T_{f,h} \tag{8}$$

The meaning of the symbols of the above equation will be explained in Sec. 4.

Finally, the energy balance for the coolant in the head passages allows one to determine the coolant temperature as

$$T_{hc}^{t+\Delta t} = T_{hc}^t + (\dot{Q}_{hc} - \dot{Q}_l)\Delta t/m_{hc} c_c \tag{9}$$

where the energy contribution associated with the vapor phase was taken into account by the latent term $\dot{Q}_l$ made explicit by Eq. (10). The vaporized mass of the coolant is negligible compared to the system global mass so that the liquid coolant mass m_{hc} can be assumed unaltered as a result of the vapor formation.

$$\dot{Q}_l = (m_{vb}^{t+\Delta t} - m_{vb}^t)\lambda/\Delta t \tag{10}$$

In an analogous way, assuming that no vapor formation occurs in the cylinder block passages we obtain

$$T_{bc}^{t+\Delta t} = T_{bc}^t + \dot{Q}_{bc}\Delta t/m_{bc} c_c \tag{11}$$

3.3 Air Compression Phase. Owing to the heat transfer from the high temperature head metal, coolant expansion in the cylinder head passages may be written as

$$\Delta V_c^t = (\rho_c^{t+\Delta t} - \rho_c^t) V_{hp}/\bar{\rho}_c \tag{12}$$

Using a first try value for the pressure in the cooling system, from the ideal gas law the bulk vapor volume $V_{vb}^{t+\Delta t}$ can be determined, where the nonideal behavior can be accounted for by using a z_v factor. Analogously, the volume of air pockets in the cooling circuit $V_{ap}^{t+\Delta t}$ can be calculated.

Finally, the volume of compressed air in the expansion tank is given by

$$V_{at}^{t+\Delta t} = V_{at}^t - \Delta V_c - (V_{vb}^{t+\Delta t} - V_{vb}^t) - (V_{ap}^{t+\Delta t} - V_{ap}^t) \tag{13}$$

Therefore, a new value of the pressure in the cooling system can be calculated as

$$p_{cs}^{t+\Delta t} \equiv m_{at}^{t+\Delta t} R_a T_{at} z_a / V_{at}^{t+\Delta t} \tag{14}$$

The above equations are then iteratively calculated to convergence.

3.4 Air Leakage Phase. As the pressure rises above the threshold value of the radiator-cap pressure valve, the air in the radiator expansion tank starts to be expelled. Thus

$$m_{at}^{t+\Delta t} = m_{at}^t - \Delta m_{at} \tag{15}$$

where Δm_{at} is the leaked air through the relief valve. Using a first try value for the pressure in the cooling system p_{cs}, from the ideal gas law with a z_a factor the air volume $V_{at}^{t+\Delta t}$ in the expansion tank can be determined. In an analogous way, the bulk vapor volume $V_{vb}^{t+\Delta t}$ in the cooling circuit can be calculated.

Finally, the volume of air pockets in the cooling circuit can be obtained from the condition

$$V_{ap}^{t+\Delta t} = V_{at}^t + V_{vb}^t + V_{ap}^t - (V_{at}^{t+\Delta t} + V_{vb}^{t+\Delta t}) \tag{16}$$

Therefore, a new value of the pressure in the cooling system, which corresponds to the new equilibrium condition can be calculated as

$$p_{cs}^{t+\Delta t} \equiv p_{ap}^{t+\Delta t} = m_{ap} R_a T_{ap} z_a / V_{ap}^{t+\Delta t} \tag{17}$$

Equations (15)–(17) are then iteratively calculated up to convergence.

3.5 Coolant Leakage Phase. In this phase the pressure is still above the threshold value of the radiator relief valve and the coolant starts to be expelled. Thus

$$m_c^{t+\Delta t} = m_c^t - \Delta m_c \tag{18}$$

where Δm_c is the leaked coolant through the relief valve. Therefore, the volume reduction is

$$\Delta V_c = \Delta m_c / \bar{\rho}_c \tag{19}$$

Using a first try value for the pressure in the cooling system, from the ideal gas law with a z_v factor the vapor bulk volume $V_{\mathrm{vb}}^{t+\Delta t}$ in the cooling circuit can be determined. In an analogous way, the volume of air pockets in the cooling circuit can be obtained from the following condition:

$$V_{\mathrm{ap}}^{t+\Delta t} = V_{\mathrm{vb}}^t + V_{\mathrm{ap}}^t - (\Delta V_c + V_{\mathrm{vb}}^{t+\Delta t}) \tag{20}$$

Therefore the pressure in the cooling system, which corresponds to the new equilibrium condition can be calculated as

$$p_{\mathrm{cs}}^{t+\Delta t} \equiv p_{\mathrm{ap}}^{t+\Delta t} = m_{\mathrm{ap}} R_a T_{\mathrm{ap}} z_a / V_{\mathrm{ap}}^{t+\Delta t} \tag{21}$$

The above equations are then iteratively calculated up to convergence of the gas volume variation (air and vapor) within the cooling circuit during the time interval Δt to the leaked coolant during the same time interval.

3.6 Vaporized Mass Losses Via Radiator. The coolant leakage through the radiator relief valve causes the vaporized mass to move from the cylinder head passages toward the radiator. As the mass of leaked coolant increases, the vaporized mass first occupies the whole external piping and then reaches the radiator; the time to reach the radiator is mainly affected by the piping cross-sectional area and piping length. In this condition, while an evaporating interface inside the cylinder head passages still exists, which causes more vapor formation, a second interface (condensing) develops inside the radiator, which causes vapor condensation.

As long as the effect of the vapor production inside the head passages is predominant on the effect of vapor losses via the radiator, the pressure level inside the cooling circuit remains above the threshold value of the relief valve and, consequently, coolant leakage still occurs. The coolant leakage phase stops when the effect of vapor condensation via the radiator becomes meaningful so that the pressure decreases and the radiator-cap valve closes.

Equations from (18)–(21) are valid also in the case of vapor condensation inside the radiator with an open radiator valve; however, to determine the total amount of vaporized coolant one must also take into account the mass of vapor condensed in the radiator. This quantity can be expressed through the following equation:

$$m_c^{t+\Delta t} = \overline{h_m A_i}^c (p_{\mathrm{vb}}^t - p_{\mathrm{sat},r}) \Delta t / R_v T_{\mathrm{vb}} \tag{22}$$

Thus, the mass of vaporized coolant will be obtained as

$$m_{\mathrm{vb}}^{t+\Delta t} = m_{\mathrm{vb}}^t + \overline{h_m A_i}^e (p_{\mathrm{sat},h} - p_{\mathrm{vb}}^t) \Delta t / R_v T_{f,h} - \overline{h_m A_i}^c (p_{\mathrm{vb}}^t - p_{\mathrm{sat},r}) \Delta t / R_v T_{f,r} \tag{23}$$

where the $p_{\mathrm{sat},r}$ term can be determined from the mean coolant temperature and the mean vapor bulk temperature inside the radiator.

3.7 Radiator Cap Model. The pressure radiator cap contains a stainless steel pressure valve spring and pressure valve (Fig. 4). The valve begins to open when the pressure within the cooling system increases to a certain level (normally 2.0–2.15 bars).

The opening of the pressure valve causes the air in the expansion tank and part of the coolant to leak out. The leaked flow rate (air and coolant) depends on the cross-sectional area of the pressure valve. This opening area is a function of the spring disk diaphragm position (Fig. 4) from the start of the valve opening position $x_{\min}$ to the maximum opening position $x_{\max}$. Considering rectangular holes, this area can be calculated as

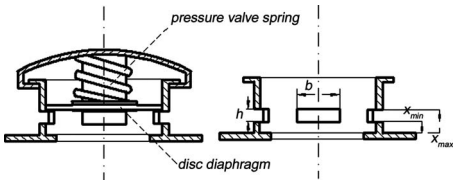

Fig. 4 Schematic representation of a radiator-cap pressure valve

$$\text{for } x \le x_{\min}, \quad A = 0$$

$$\text{for } x_{\min} < x < x_{\max}, \quad A = n_h b h$$

$$\text{for } x > x_{\max}, \quad A = n_h b h_{\max}$$

where n_h is the number of holes in the relief valve. The leaked flow rate can be formulated as

$$Q_L = C_d A \sqrt{2|p_{\mathrm{cs}} - p_{\mathrm{atm}}|/\rho} \tag{24}$$

The spring disk diaphragm position x can be obtained from the forces balance acting on the spring disk diaphragm (Fig. 4)

$$m\ddot{x} + C_v \dot{x} + kx = F_{\mathrm{fl}} - F_p + (p_{\mathrm{cs}} - p_{\mathrm{atm}}) S_d \tag{25}$$

where a constant value for the flux Force F_{fl} term was considered acceptable for the purpose of the model.

4 Experimental Evaluation of the Model Parameters

The main difficulty of the proposed approach concerns the evaluation of the term ρ_i (fluid density at liquid/vapor interface), which appears in Eq. (1). In this respect, in the last few decades several theoretical approaches have been proposed by many authors for the solution to problems dealing with mass transfer phenomena and, in particular, with the analysis and evaluation of interface conditions during a mass diffusion process [9,10]. Some authors [4–6], in many practical cases of heat and mass transfer where the liquid surface temperature may be measured, suggest for the liquid/vapor interface temperature T_i a value equal to this mean liquid surface temperature, thus assuming equilibrium thermodynamic conditions at the interface. However, for the specific case of the after-boiling phenomenon, the high variability of the interface geometric and temperature conditions makes the hypothesis of a nonequilibrium condition between the two phases more appropriate. Thus, an empirical approach similar to that suggested by Eckert and Drake [5] was preferred in the proposed model, by assuming a single temperature value T_f at the interface, averaged between the liquid/vapor interface and the vapor bulk. From this supposition by using the ideal gas law, Eckert and Drake reformulated Eq. (1) as follows:

$$\dot{m}_v = h_m A_i (\rho_i - \rho_{\mathrm{vb}}) = h_m A_i (p_i - p_{\mathrm{vb}}) / R_v T_f \tag{26}$$

assuming that the temperature differences in the field are small compared with the average absolute temperature of the thermodynamic system.

Therefore, assuming the above hypothesis, the term ρ_i represents the saturated vapor density, which corresponds to an ideal surface indefinitely near to the liquid/vapor interface at a temperature T_f, whereas p_i is the corresponding saturation pressure; moreover, as a good approximation, one can assume that the mean temperature of the considered thermodynamic system and the mean temperature of the vapor bulk are equal to the temperature T_f.

4.1 Empirical Estimation of T_f . An ad hoc test was conducted at the engine test-bed to determine experimentally the averaged value for T_f in Eq. (1). In detail, a rapid shut down test was conducted with the relief valve of radiator cap blocked (in such a way that the vaporized mass of coolant remains inside the head

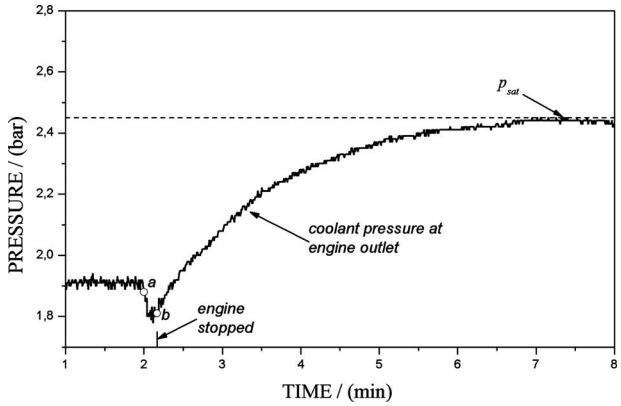

Fig. 5 Ad hoc test for determination of the averaged value for T_f: pressure evolution in the "sealed" cooling circuit (relief valve blocked)

passages instead of moving toward the external cooling circuit) and with the cooling circuit thermally insulated, so that the two-phase system can be considered closed and adiabatic. Therefore, at equilibrium the liquid/vapor mixture reaches a uniform temperature, which is equal to the mean temperature of the system at the beginning of the process.

Moreover, at equilibrium no more vapor formation can occur at the liquid/vapor interface so that from Eq. (26) one can write the following:

$$\dot{m}_v = h_m A_i (p_i - p_{vb})/R_v T_f = 0 \tag{27}$$

It follows that

$$p_i = p_{vb} = p_{cs} \equiv p_{sat} \tag{28}$$

Thus at the equilibrium the pressure in the cooling system p_{cs} is equal to the pressure p_i at the evaporating interface and to the pressure p_{vb} at the vapor bulk; this equilibrium value represents the saturation pressure of the two-phase mixture. The corresponding temperature provides the saturation temperature of the thermodynamic system: this value is averaged in the field temperature T_f between the liquid/vapor interface and the vapor bulk and, under adiabatic assumptions, can be well approximated by a constant value during the whole evolution of the after-boiling phenomenon. Thus, Eq. (26) can be reformulated as

$$\dot{m}_v = h_m A_i (p_{sat} - p_{vb})/R_v T_f \tag{29}$$

This approach allows one to quantify the concentration gradient between the liquid/vapor interface and the vapor bulk in terms of pressure differences, avoiding direct measurements of the temperature at the liquid/vapor interface, which is obviously far more complicated.

Figure 5 depicts the pressure evolution in the cooling system during the ad hoc test. At equilibrium the saturation pressure approaches the value of ~2.45 bars, which corresponds to a saturation temperature of ~140°C for a 50/50% by mass mixture of water and commercially available ethylene glycol [11].

4.2 Empirical Estimation of $h_m A_i$. The evaluation of the mass transfer coefficient is the key problem in modeling mass convection processes; this coefficient allows one to make predictions on the mass transfer from the liquid/vapor interface. In many simple problems, where the mass transfer occurs on a surface of well defined geometry, a theoretical approach can be adopted to estimate the mass transfer coefficient by solving the energy, mass, and momentum transfer governing equations; however, this is not the case of the vaporized mass of coolant, which occurs in cylinder head passages of an internal combustion engine, which is obviously far more complicated. In other practical cases a similarity exists between boundary conditions and dimensionless governing equations so that the analogy between heat and mass transfer can be employed to determine the mass transfer coefficients by solving equations such as

$$\overline{\mathrm{Sh}} = f(\mathrm{Re}, \mathrm{Sc}) \tag{30}$$

which is similar to the analogous one for heat transfer problems

$$\overline{\mathrm{Nu}} = f(\mathrm{Re}, \mathrm{Pr}) \tag{31}$$

This approach is also not useful in the specific case of the after-boiling phenomenon. An empirical approach was preferred in this case mainly owing to the complexity of boundary layer conditions and interface geometry, which make a theoretical approach inapplicable. Thus, on the basis of experimental data the combined quantity $h_m A_i$ of Eq. (29) is measurable even when h_m and A_i are not.

In detail, from the experimental data of vaporized (or condensed) mass of coolant per unit time $\Delta\dot{m}_v$, of two-phase mixture saturation pressure p_{sat}, and of vapor bulk pressure p_{vb} for n time intervals, an estimation of the mean value of the $h_m A_i$ quantity can be obtained for each phase of the after-boiling phenomenon as follows:

$$\overline{h_m A_i} = 1/n \sum_{j=1}^{n} \Delta\dot{m}_{v_j} R_v T_f/(p_{sat} - p_{vb})_j \tag{32}$$

Table 1 shows the mean value of the $h_m A_i$ quantity provided from experimental measurements at the engine test-bed for each phase of the after-boiling phenomenon.

Table 1 Mean values of the coefficient $h_m A_i$ at different stages of the after-boiling phenomenon, empirically obtained from experimental data

Phase	Evaporating interface, $\overline{h_m A_i^e}$ (m^3/s)	Condensing interface, $\overline{h_m A_i^c}$ (m^3/s)
(A) Air compression	18.2×10^{-6}	-
(B) Air leakage	42.0×10^{-6}	-
(C) Coolant leakage	20.0×10^{-6}	-
Vapor losses via radiator	4.0×10^{-6}	6.0×10^{-6}

5 Vaporized Mass Evaluation

Vaporized mass of coolant was obtained from the experimental data of the coolant pressure and temperature, of metal temperature, and from measurements of coolant and air volume distribution in the cooling circuit during each phase of the after-boiling phenomenon.

5.1 Air Compression Phase. After engine shutdown the specific volume of the coolant in the head passages rapidly varies due to the thermal soaking from hot metal. Therefore, the mass of coolant in the head passages reduces to

$$m_{c,\mathrm{hp}}^{t} = m_{c,\mathrm{hp}}^{t_0} - \Delta m_{c,\mathrm{hp}} \tag{33}$$

where $m_{c,\mathrm{hp}}^{t_0}$ is the mass of the coolant in the head passages at the initial environmental conditions; the term $\Delta m_{c,\mathrm{hp}}$ can be calculated from the specific mass of the coolant as

$$\Delta m_{c,\mathrm{hp}} = V_{\mathrm{hp}} \Delta\rho_{c,\mathrm{hp}} \tag{34}$$

The corresponding volume variation is given by

$$\Delta V_{c,\mathrm{hp}} = \Delta m_{c,\mathrm{hp}}/\bar{\rho}_{c,\mathrm{hp}} \tag{35}$$

During this phase the system is closed (no air or coolant leakage occurs through the relief valve) and air in the radiator tank is compressed either due to the coolant thermal expansion or to the

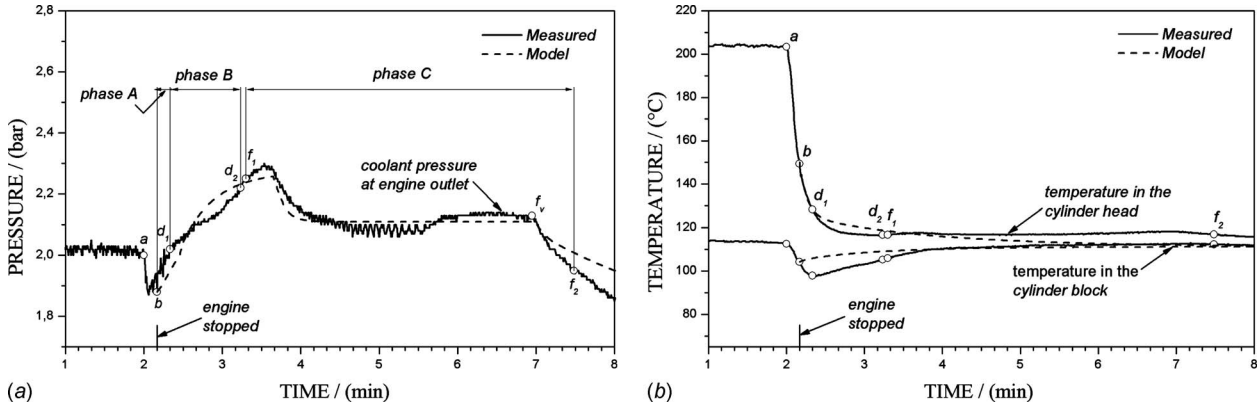

Fig. 6 Comparison of measured (solid lines) and predicted (dash lines) values: (*a*) coolant pressure and (*b*) head and cylinder block temperature

vapor formation, which starts to occur inside the head passages.

The volume of air in expansion tank V_a^t can be derived from experimental data by using the ideal gas law corrected for nonideal effects with a z_a factor.

Thus, the vapor volume can be calculated as

$$V_v^t = \Delta V_a - \Delta V_{c,\mathrm{hp}} \tag{36}$$

Finally, by the ideal gas law with a z_v factor, the corresponding vaporized mass of coolant m_v^t can be obtained.

5.2 Air Leakage Phase. During this phase air leakage through the relief valve occurs. Equation (36) is still valid. Considering air mass reduction it follows that

$$V_a^t = z_a(m_a - \Delta m_a)R_a T_a^t / p_{\mathrm{cs}}^t \tag{37}$$

where a linear leakage law is assumed between the recorded air leakage start time and end time to compute the Δm_a term, considering the short duration of the air leakage phase.

5.3 Coolant Leakage Phase. At this stage no more coolant thermal expansion occurs and no more air is present in the radiator tank. The vapor volume variation is calculated from measured data of leaked coolant as follows:

$$\Delta V_v^t = \Delta V_{c,L}^t \tag{38}$$

5.4 Experimental Uncertainty. For a known function F of n independent variables $u_1, u_2, \ldots, u_n$ the formula for computing the overall uncertainty is given by [12]

$$\Delta F = \sqrt{\left(\Delta u_1 \frac{\partial F}{\partial u_1}\right)^2 + \left(\Delta u_2 \frac{\partial F}{\partial u_2}\right)^2 + \cdots + \left(\Delta u_n \frac{\partial F}{\partial u_n}\right)^2} \tag{39}$$

where Δu_i is the uncertainty on variable u_i.

Thus, for the vaporized mass term m_v the overall uncertainty is expressed as

$$\Delta m_v = \sqrt{\left(\Delta p_{\mathrm{cs}} \frac{\partial m_v}{\partial p_{\mathrm{cs}}}\right)^2 + \left(\Delta V_v \frac{\partial m_v}{\partial V_v}\right)^2 + \left(\Delta z_v \frac{\partial m_v}{\partial z_v}\right)^2 + \left(\Delta T_v \frac{\partial m_v}{\partial T_v}\right)^2} \tag{40}$$

and according to the ideal gas law with a z_v factor

$$\frac{\Delta m_v}{m_v} = \sqrt{\left(\frac{\Delta p_{\mathrm{cs}}}{p_{\mathrm{cs}}}\right)^2 + \left(\frac{\Delta V_v}{V_v}\right)^2 + \left(\frac{\Delta z_v}{z_v}\right)^2 + \left(\frac{\Delta T_v}{T_v}\right)^2} \tag{41}$$

In the pressure error estimate calculations Δp_{cs} was ± 0.05 bar, according to the manufacturer of the transducer; ΔT_v was $\pm 15\,^{\circ}\mathrm{C}$, which corresponds to the maximum difference between the measured head metal temperature and the measured vapor phase temperature in the external cooling circuit. Δz_v contributed with a value of ± 0.02, according to vapor properties tables at the corresponding conditions of pressure and temperature [13]. Finally, ΔV_v was assumed to be equal to 50 ml, which is the smallest division of the 1000 ml graduated cylinder used for leaked coolant measurements. Applying Eq. (41), it is found that

$$\frac{\Delta m_v}{m_v} \approx \pm 11.1\%$$

6 Model Results

Model results and experimental data are compared in Figs. 6 and 7.

Figure 6 shows predicted coolant pressure at the engine outlet, head, and cylinder block temperatures as a function of time for the case of the rapid shutdown test described in paragraph 2. Predicted and experimental coolant pressures agree well in all the phases of the after-boiling phenomenon (with a mean absolute percentage error of about 1.2%), although the proposed model considers an adiabatic system so that convective heat transfer to the environment is neglected. Point f_v in Fig. 6(*a*) identifies the vapor inlet time inside the radiator. From this point, both the experimental pressure and the predicted pressure start to decrease, primarily owing to the reduction in the vaporized mass of coolant, which occurs when the vapor reaches the radiator, as observed visually through the transparent tubes at the radiator inlet. Also in this case the measured and model data agree well. The predicted curves for head and cylinder block temperatures show the same trends as the experimental data (Fig. 6(*b*)), with a mean absolute percentage error of 2.1% for the head metal temperature and of 1.4% for the cylinder block temperature.

The measured and simulated vaporized mass are shown in Fig. 7(*a*), while prediction of the coolant leaked through the relief valve is shown in Fig. 7(*b*). After point f_v of Fig. 7(*a*) both simulated vaporized mass and experimental data show a reduction due to the vapor condensation via the radiator. However, the predicted curve for vaporized mass is lower due to underestimation of the coolant leaked during the coolant leakage phase, as Fig. 7(*b*) illustrates.

It is worth pointing out that experimental vaporized mass values were not measured directly, but they were derived from other quantities (temperature, pressure, air volume, coolant volume, etc.); this yields an uncertainty in the experimental measurement of the vaporized mass itself. Predicted and experimental data of vaporized mass differ with a mean absolute percentage error of 6.3%, while the mean absolute percentage error increases to 8.6%

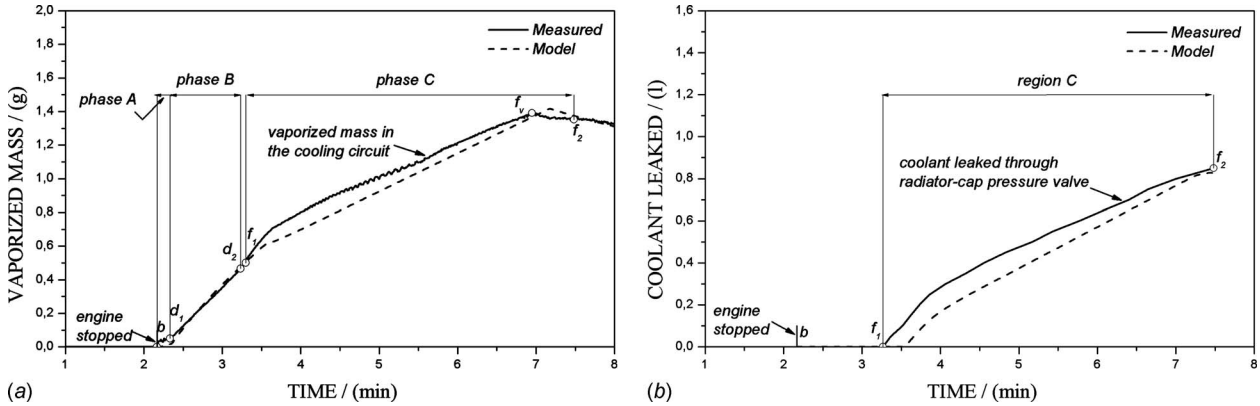

Fig. 7 Comparison of measured (solid lines) and predicted (dash lines) values: (*a*) vaporized mass in the cooling circuit and (*b*) leaked coolant

for the leaked coolant. Note that all previous values of the mean absolute percentage error (MAE%) include measurement uncertainties of the experimental apparatus.

As the h_mA product was determined experimentally for the specific engine operating conditions, a sensitivity analysis of the model to this parameter was carried out. Figure 8 reports the results of further simulations performed by increasing and decreasing the h_mA parameter by $\pm 10\%$ in each phase of the phenomenon. Since the h_mA parameter is strongly related to the rate of vapor formation according to Eq. (8), a more rapid increase in the pressure level and, consequently, a shorter duration of coolant leakage phase is expected by increasing this parameter (Figs. 8(*a*) and 8(*c*)). However, the sensitivity analysis shows that a 10% increase in the h_mA parameter yields a modest increase in the maximum pressure level reached in the cooling circuit (1.30%), of the maximum amount of vaporized coolant (0.42%) and of the maximum amount of leaked coolant (0.24%). These results are summarized in Table 2.

Table 2 also reports the incidence on the mean absolute percentage error between experimental and predicted data resulting from the variation in the h_mA parameter. The mean error reported in Table 2 was evaluated for each variable depicted in Fig. 8. From the table it is evident that both increasing or decreasing h_mA by 10% causes an increase in the mean absolute error on coolant pressure; a variation of 10% of h_mA implies a maximum MAE variation of 62% on the coolant pressure, whereas for the vaporized mass of coolant and the leaked coolant an increase in h_mA implies a reduction in MAE.

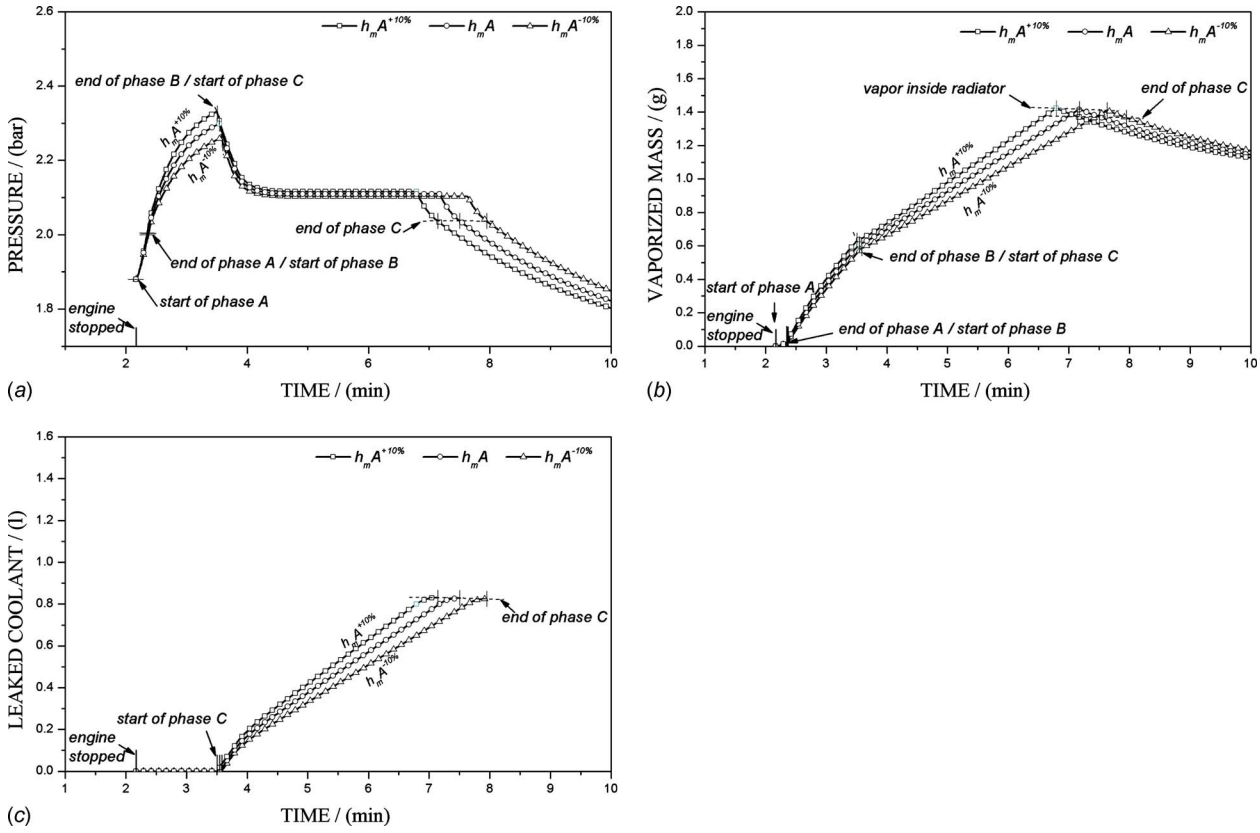

Fig. 8 (*a*) Changes in coolant pressure, (*b*) vaporized mass in the cooling system, and (*c*) leaked coolant with a 10% variation of h_mA parameter

Table 2 Mean absolute percentage error on coolant pressure, coolant vaporized mass and leaked coolant, as a result of a change of the h_mA parameter of ±10%

	$p_{cs\text{-}max}$ (bar)	$m_{vb\text{-}max}$ (g)	$V_{L\text{-}max}$ (l)	MAE%		
				p_{cs}	m_{vb}	V_L
$h_mA^{+10\%}$	2.33	1.423	0.830	1.62	3.94	6.77
h_mA	2.30	1.417	0.828	1.25	6.25	8.58
$h_mA^{-10\%}$	2.26	1.410	0.824	2.02	10.31	17.24

Another parameter that influences the model results is the saturation pressure p_{sat}, which mainly depends on the metal thermal conditions at the metal-liquid interface when the engine is shut down. The value of 2.45 bars was empirically estimated through the ad hoc test, which was used as reference case. Further simulations were then performed by using two different values of this parameter: 2.35 bars and 2.65 bars; whereas the pressure level in the cooling circuit at phase A start time and all other variables were kept constant at their baseline values. Figure 9 shows the results of these simulations. From the graph of Fig. 9(*b*) one may observe that increasing saturation pressure p_{sat} (such an occurrence may correspond to a higher thermal condition for the coolant in the head passages at the shutdown time) enhances the rate of vapor formation. The maximum amount of vaporized coolant (Fig. 9(*b*)) and of leaked coolant (Fig. 9(*c*)) does not significantly differ in the three cases. On the contrary, the maximum pressure level reached in the circuit at the end of phase B (Fig. 9(*a*)) significantly increases due to the higher rate of vaporization during phase B (Fig. 9(*b*)). As a result, a more rapid increase in coolant pressure during phase B occurs and the pressure peaks earlier. Consequently, the start of phase C is advanced whereas the duration of this phase is significantly reduced due to a more rapid coolant leakage through the relief valve (Fig. 9(*c*)).

Simulation results depicted in Fig. 10 show how the behavior of the phenomenon is affected by the coolant fluid levels in the expansion tank. Graphs of Fig. 10 were obtained by reducing the volume of air in the coolant expansion tank to 0.2 l (overfilled condition) or by increasing the volume of air to 1.0 l (underfilled condition). The saturation pressure p_{sat}, the pressure level in the cooling circuit at the phase A start time, and all other variables were kept constant at their baseline values. Increasing the volume of air in the coolant tank results in a prolonged duration of phase B (Fig. 10(*a*)). This also implies a significant increase in the amount of vaporized coolant at this stage (Fig. 10(*b*)). Although there is a higher amount of vaporized mass, the peak pressure at the end of phase B increases only moderately due to the larger volume of the circuit occupied by the vapor phase. From the graph of Fig. 10(*c*), it is clear that the start of the coolant leakage phase is retarded as the expansion tank becomes underfilled. Furthermore, by reducing the coolant level in the expansion tank the pressure curve slope both during the air compression phase (phase A) and the air leakage phase (phase B) varies due to the change in relative air volume and the initial volume (Fig. 10(*a*)).

7 Summary and Conclusions

The model described in this paper has been developed with the goal to provide a practical tool to predict the behavior of cooling system after an engine rapid shutdown. The proposed algorithm can be easily adapted to different engines. In fact, all the model inputs are in terms of general parameters, typically known to the user; while the main model parameters can be evaluated on the basis of simple ad hoc tests. The convective mass transfer mechanism has been demonstrated to predict vapor formation inside the head passages and vapor condensation inside the radiator. The simulation results were compared with experimental tests carried

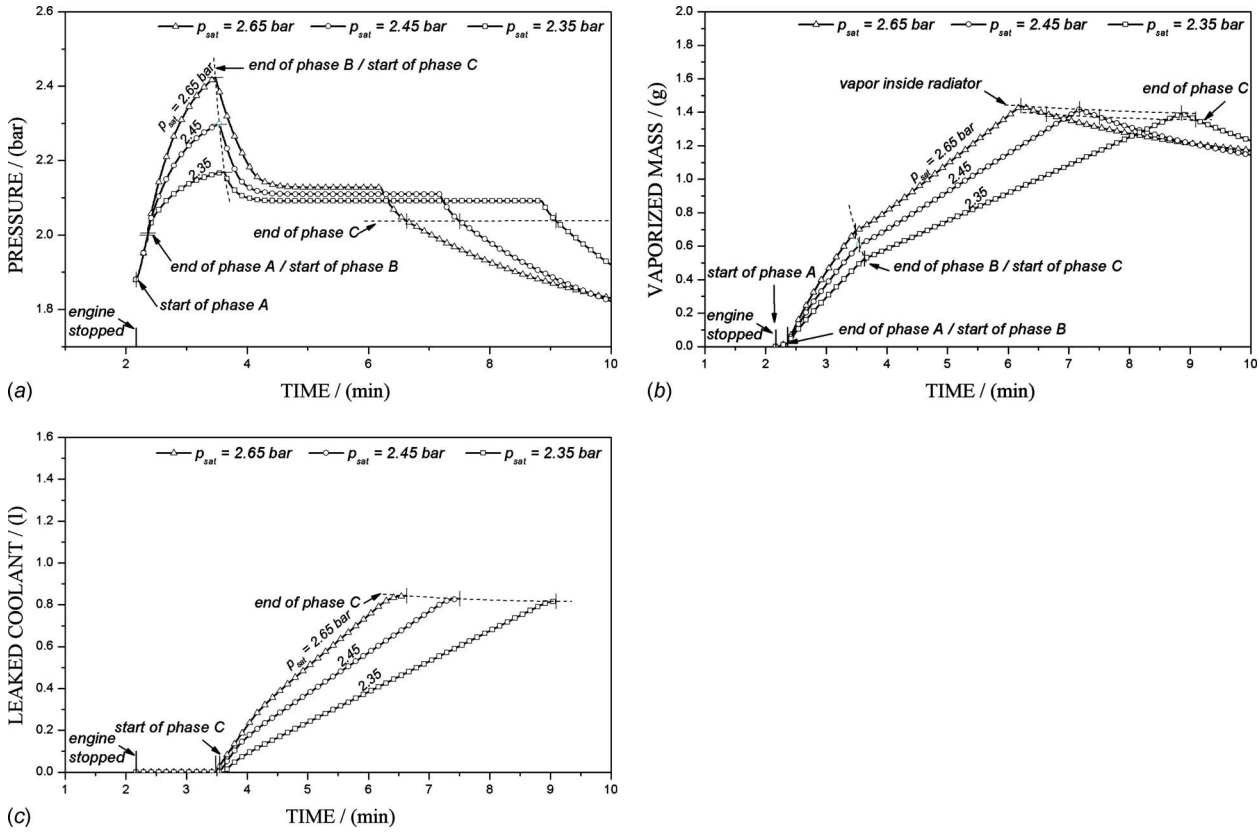

Fig. 9 (*a*) Effect of p_{sat} parameter on coolant pressure, (*b*) vaporized mass in the cooling system, and(*c*) leaked coolant

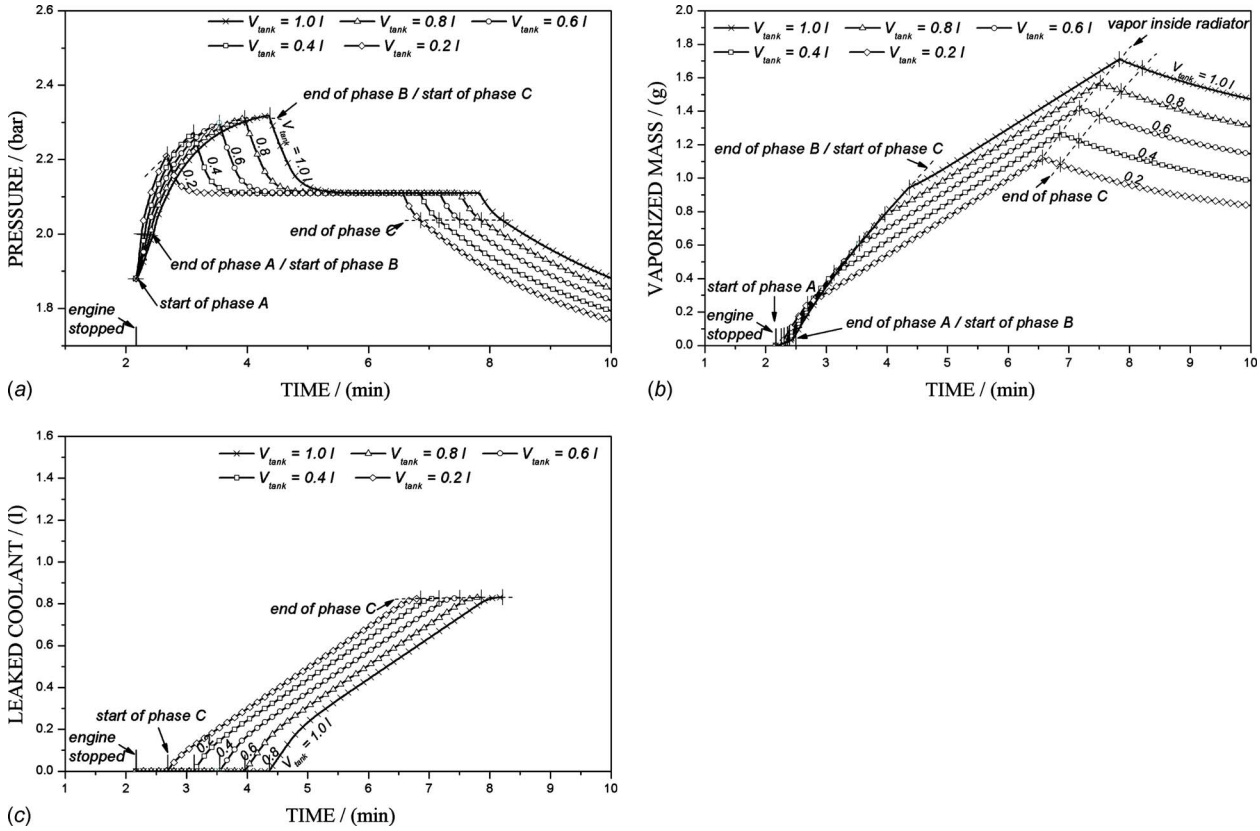

Fig. 10 (*a*) **Behavior of coolant pressure,** (*b*) **vaporized mass in the cooling system, and** (*c*) **leaked coolant for different levels of coolant fluid in the radiator expansion tank**

out on a production four-cylinder, MPI small SI engine, 1.2 dm^3 displacement operated under WOT conditions at 4000 rpm. The satisfactory agreement confirms how the mathematical model successfully predicts the experimental results. Simulations were performed to investigate the influence of parameter p_{sat} on the evolution of the pressure in the cooling circuit. A change in p_{sat} may occur as a consequence of different metal thermal conditions at the engine shutdown event, related to engine initial operative conditions. The rate of pressure increase was found to be higher by increasing p_{sat}, with a consequent reduction in the phenomenon duration. Additional simulations showed that a further factor, which significantly influences the rate of vapor formation inside the cooling circuit and, consequently, the behavior of coolant pressure, is the level of coolant fluid in the radiator expansion tank. The model requires limited computing resources and could be used, therefore, as a model-based electronic control unit (ECU) control algorithm to manage a cooling strategy after the engine shutdown by controlling an additional small electric pump.

Nomenclature

A = surface area (m^2)
C = thermal conductance (W/K)
C_d = discharge coefficient
C_v = friction coefficient
c = specific heat (J/kg K)
F = force (N)
h = heat transfer coefficient (W/m^2K)
h_m = mass transfer coefficient (m/s)
k = spring constant (kg/s^2)
m = mass(kg)
$\dot{m}$ = mass rate (kg/s)
Nu = Nusselt number
p = pressure (Pa)
Pr = Prandtl number
Q = flow rate (m^3/s)
$\dot{Q}$ = thermal power (W)
R = gas constant (J/kg K)
Re = Reynolds number
S = surface area (m^2)
Sc = Schmidt number
Sh = Sherwood number
T = temperature (°C)
t = time (s)
V = volume (m^3)
z = compressibility factor
λ = latent heat of vaporization (J/kg)
ρ = mass density or concentration (kg/m^3)
$\bar{\rho}$ = average mass density (kg/m^3)

Subscripts

a = air
ap = air in air-pockets
at = air in expansion tank
atm = atmosphere
b = cylinder block
bc = cylinder block /coolant
c = coolant
cs = cooling system
d = disc diaphragm
f = field
fl = flux
h = cylinder head
hb = head/cylinder block

hc = head /coolant or coolant inside head passages
hr = radiation from head
hp = head passages
i = interface value
j = interval
l = latent
L = leaked
p = preloading
r = radiative
sat = saturation
sat,h = saturation on the interface inside head passages
sat,r = saturation on the interface inside radiator
t = threshold
v = vapor
vb = vapor bulk

Superscripts

c = condensation
e = evaporation

References

[1] Bova S., Piccione R., Durante D. and Perrussio M., 2004, "Experimental Analysis of the After-Boiling Phenomenon in a Small I.C.E.," SAE Paper No. 2004-32-0091.

[2] Piccione, R., 2004, "Analisi Numerico-Sperimentale in Regime Transitorio del Sistema di Raffreddamento in un MCI," Ph.D. thesis, University of Calabria, Cosenza, Italy.

[3] Bova S., Piccione R., Vulcano A., 2007, "A Zero-Dimensional Two-Phase Model of the Thermal Transient of an I.C.E. Cooling System After a Rapid Switch-Off," SAE Paper No. 2006-01-2999.

[4] Bird, R. B., Stewart, W. E., and Lightfoot, E. N., 1960, *Transport Phenomena*, Wiley, New York, Chap. 16 and 21.

[5] Eckert, E. R. G., and Drake, R. M., 1959, *Heat and Mass Transfer*, McGraw-Hill, New York, Chap. 16.

[6] Incropera, F. P., Dewitt, D. P., Bergman, T. L., and Lavine, A. S., 2007, *Fundamentals of Heat and Mass Transfer*, 6th ed., Wiley, New York.

[7] Lienhard, J. H., IV, and Lienhard, V. J. H., 2001, *A Heat Transfer Textbook*, 3rd ed., Phlogiston Press, Cambridge, MA, Chap. 11.

[8] ASHRAE Handbook, 1989, Fundamentals, Chap. 5.

[9] Wang, H. S., and Rose, J. W., 2004, "Effect of Interphase Matter Transfer on Condensation on Low-Finned Tubes – A Theoretical investigation," Int. J. Heat Mass Transfer, **47**, pp. 179–184.

[10] Popov, S., Melling, A., Durst, F., and Ward, C. A., 2005, "Apparatus for Investigation of Evaporation at Free Liquid-Vapour Interfaces," Int. J. Heat Mass Transfer, **48**, pp. 2299–2309.

[11] Lee, H. S., and O'Neill, A. T., 2006, "Comparison of Boiling Curves Between a Standard S.I. Engine and a Flow Loop for a Mixture of Ethylene Glycol and Water," SAE SP-2041, pp. 157–167.

[12] Doebelin, E. O., 1990, *Measurement System. Application and Design*, McGraw-Hill, New York.

[13] Schmidt E., 1968, *VDJ–Wasserdampftafeln*, Springer-Verlag, Berlin./R. Oldenbourg, München.

Measurement of Flow Phenomena in a Lower Plenum Model of a Prismatic Gas-Cooled Reactor

Hugh M. McIlroy, Jr.
Idaho National Laboratory,
P.O. Box 1625,
Idaho Falls, ID 83415-2200
e-mail: hugh.mcilroy@inl.gov

Donald M. McEligot[1]
Professor Emeritus
University of Arizona,
Tucson, AZ 85721;
Idaho National Laboratory,
P.O. Box 1625,
Idaho Falls, ID 83415-3870

Robert J. Pink
Idaho National Laboratory,
P.O. Box 1625,
Idaho Falls, ID 83415-2209
e-mail: robert.pink@inl.gov

Mean-velocity-field and turbulence data are presented that measure turbulent flow phenomena in an approximately 1:7 scale model of a region of the lower plenum of a typical prismatic gas-cooled reactor similar to a General Atomics gas-turbine-modular helium reactor design. The data were obtained in the Matched-Index-of-Refraction (MIR) Facility at Idaho National Laboratory (INL) and are offered for assessing computational fluid dynamics software. This experiment has been selected as the first standard problem endorsed by the Generation IV International Forum. Results concentrate on the region of the lower plenum near its far reflector wall (away from the outlet duct). The flow in the lower plenum consists of multiple jets injected into a confined cross flow—with obstructions. The model consists of a row of full circular posts along its centerline with half-posts on the two parallel walls to approximate geometry scaled to that expected from the staggered parallel rows of posts in the reactor design. The model is fabricated from clear, fused quartz to match the refractive-index of the working fluid so that optical techniques may be employed for the measurements. The benefit of the MIR technique is that it permits optical measurements to determine flow characteristics in complex passages in and around objects to be obtained without locating intrusive transducers that will disturb the flow field and without distortion of the optical paths. An advantage of the INL system is its large size, leading to improved spatial and temporal resolutions compared with similar facilities at smaller scales. A three-dimensional particle image velocimetry system was used to collect the data. Inlet-jet Reynolds numbers (based on the jet diameter and the time-mean bulk velocity) are approximately 4300 and 12,400. Uncertainty analyses and a discussion of the standard problem are included. The measurements reveal developing, nonuniform, turbulent flow in the inlet jets and complicated flow patterns in the model lower plenum. Data include three-dimensional vector plots, data displays along the coordinate planes (slices), and presentations that describe the component flows at specific regions in the model. Information on inlet conditions is also presented.
[DOI: 10.1115/1.3078784]

1 Introduction

The very high temperature reactor (VHTR) is the most likely candidate for the next generation nuclear plant (NGNP). Because of the high temperature characteristic of the VHTR, it is important to be able to simulate the turbulent flow in the reactor, especially in the lower plenum in order to ensure that large temperature gradients are not present in the coolant that could adversely impact structural materials. It is recognized that to simulate the flow in the VHTR lower plenum, advanced computational fluid dynamics (CFD) codes using appropriate turbulence modeling will be necessary.

The objectives of the experimental and computational research programs conducted at the INL are (1) to build accurate, reliable numerical simulation models of important VHTR thermal-hydraulic phenomena; (2) to provide benchmark data for the assessment and improvement of thermal-hydraulic codes proposed for evaluating the VHTR designs; and (3) to begin preliminary code development and assessment tasks based on identified modeling needs and existing data.

Feasibility studies for VHTR designs will require accurate, reliable predictions of material temperatures to evaluate the material capabilities. In a prismatic VHTR, these temperatures depend on the thermal convection in the coolant channels for the core and in other important components. Unfortunately, correlations in one-dimensional system codes for gas-cooled reactors typically underpredict these temperatures, particularly in reduced-power operations and hypothesized-accident scenarios. Likewise, some turbulence models in general purpose CFD codes provide optimistic predictions in the sense that surface temperatures are typically underpredicted [1,2]. These treatments are further complicated by the nonhomogeneous power distributions with strong peaking that can occur, in addition to buoyancy, strong pressure gradients, and gas property variations in the channels (the "hot channel" issue). The U.S. Department of Energy (DOE) needs improved modeling capabilities, independent of the sometimes simplistic approaches employed by reactor vendors. These computational capabilities need, in turn, to be validated by comparison to experimental and analytical benchmark data.

McEligot et al. [3] reported six areas of thermal-hydraulic phenomena in which the application of improved CFD and system thermal-hydraulic analytical techniques can be used in the design and safety analyses of a prismatic VHTR. Several of these phenomena are pertinent to pebble bed versions of the VHTR as well. Initial studies concentrate on coolant flow distribution through the reactor core channels and mixing of hot jets in the reactor core lower plenum. These phenomena are important both in normal operation and in accident scenarios.

[1]On sabbatical leave at University of Limerick.

Manuscript received August 12, 2008; final manuscript received August 14, 2008; published online November 2, 2009. Review conducted by Dilip R. Ballal. Paper presented at the ICONE16, Orlando, FL, May 11–15, 2008.

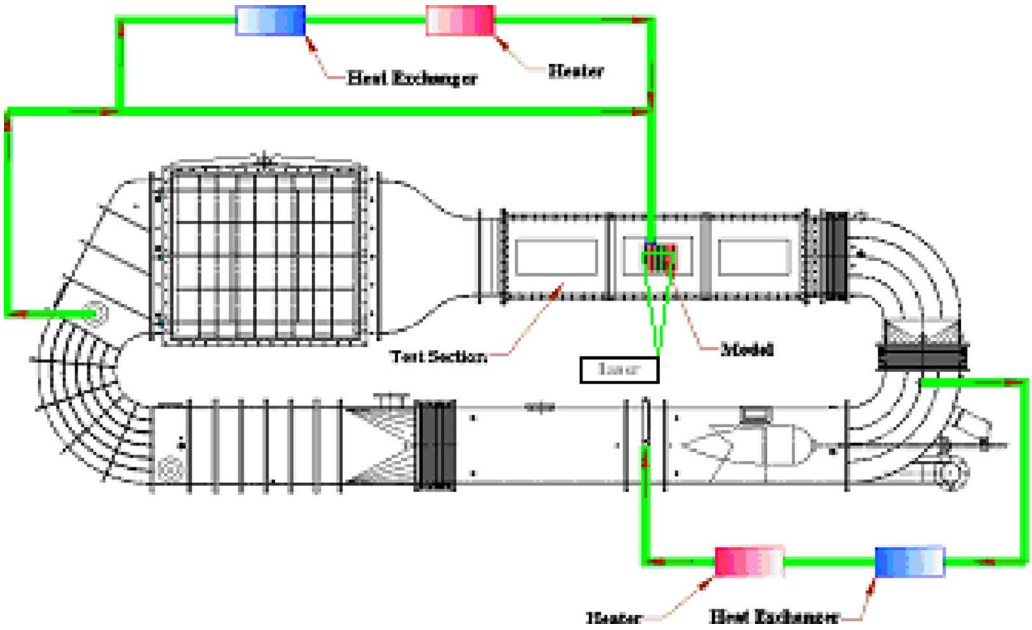

Fig. 1 MIR Facility

The general approach of the overall project is to develop new benchmark experiments for assessment in parallel with CFD and coupled CFD system code calculations for the same geometry. The velocity and turbulence fields measured in the MIR flow system will be used to assess the capabilities of the CFD codes and their turbulence models and to provide guidance in improving the models. A model of the lower plenum based on the point design of the NGNP [4] was developed and employed in this experiment.

McEligot and McCreery [5] conducted scaling studies and conceptual designs for flow and heat-transfer experiments intended to assess CFD codes and their turbulence models proposed for application to prismatic VHTR concepts. Condie et al. [6] documented the design of the present experiment to measure generic flow phenomena expected to occur in the lower plenum of a typical prismatic VHTR. The product of these efforts resulted in the fabrication and installation of a scaled model of the region of a typical VHTR lower plenum that is near the outer reflector wall away from the plenum outlet.

The objective of this paper is to document the data set that has been established as benchmark data for flow phenomena in a lower plenum model of a typical prismatic gas-cooled reactor for the validation (as defined by Roach [7]) of CFD codes.

2 Matched Index-of-Refraction Flow Facility

Velocity field measurements were taken in the MIR closed-loop flow system located at INL in Idaho Falls, Idaho (Fig. 1). Stoots et al. [8] presented a detailed review of this system. The system consists of a stainless steel closed flow loop with three polycarbonate and glass test sections. The facility can operate with water or light mineral oil as the working fluid. The working fluid for this experiment was light mineral oil that is circulated (clockwise in Fig. 1) by an axial pump powered by a 56 kW (75 hp) variable speed electric motor that can provide a maximum volumetric flow rate of approximately 0.6 m^3/s of mineral oil through the test section. This maximum volumetric flow rate corresponds to a maximum test section inlet velocity of approximately 1.7 m/s. The test section includes three chambers that are constructed of 3.8 cm thick polycarbonate supported by a stainless steel framework. Each chamber is fitted with a removable lid. The test section inside dimension is 0.61 m square and it is 2.44 m long. Both sides of each chamber of the test section are equipped with glass window inserts in the side panels to accommodate high-quality measurements with laser Doppler velocimetry (LDV) and/or particle image velocimetry (PIV) systems.

Mineral oil in the primary flow loop flows around the model for temperature control of the external surfaces of the model. The mineral oil temperature is maintained with a temperature control loop as shown in the lower right corner of Fig. 1. The temperature control loop extracts approximately 300 L/min from the primary loop flow and is pumped through a glycol-cooled heat exchanger and a 10 kW dc heater, filtered, and then re-injected into the primary flow loop. This temperature control system can maintain the fluid temperature in the test section to within $\pm 0.05\,^{\circ}C$ of the specified index-matching temperature. An additional auxiliary flow loop (shown in the upper left corner of Fig. 1), with a similar temperature control system, is used to provide fluid for the interior-model flows. Fluid is extracted from the primary flow loop and routed to a 5 kW (7 hp) pump that produces flow to the model inlet jets. To maintain the required working fluid temperature, a portion of this fluid is extracted from the auxiliary loop and routed through a parallel auxiliary temperature control loop. As in the primary temperature control loop, the mineral oil is cooled and reheated before returning to the auxiliary flow loop and into the model inlet jets. Control instrumentation includes thermistors, flow meters, data acquisition, and computer controls.

3 PIV System

Velocity field measurements were obtained with a 3D PIV system from LaVision, Inc. The 3D PIV system consists of two ImagerPro Plus digital charge-coupled device (CCD) cameras and a double-pulsed Nd:YAG (yttrium aluminum garnet) laser. The system is controlled with DAVIS 7.1 software. DAVIS is a CCD image acquisition program developed by LaVision and controlled by a LaVision dual-processor programmable timing unit (PTU). The PIV system cameras are mounted on a three-directional traverse system that is controlled by three separate electric stepping motors. The cameras can be positioned and repositioned to within 2 μm accuracy using linear stages and digital readouts at the operator's station. The spanwise laser position is also controlled with an electric stepping motor. The laser can be positioned to within 5 μm accuracy with an optical linear stage on the laser and a digital readout located at the operator's station. The PIV system laser was mounted below the test section (Fig. 1) and

Table 1 Model parameters

Properties	Value
Model length	558.80 mm
Model height	306.40 mm
Model width	104.78 mm
Channel height	217.50 mm
Channel width	53.98 mm
Post diameter	31.75 mm
Post height	217.5 mm
Jet inlet diameter	22.10 mm
Centerline distance between posts	93.50 mm
Ratio of plenum height to post diameter	6.85
Ratio of jet diameter to post diameter	0.7
Ratio of channel width to post diameter	1.7

Table 2 MIR and PIV parameters

Parameter	Re_{jet} ~4300	Re_{jet} 12~400
	MIR	
Jet No. 1 flow rate (gal/min)	11.25	32.11
Jet No. 2 flow rate (gal/min)	16.75	48.14
Jet No. 3 flow rate (gal/min)	16.75	48.14
Jet No. 4 flow rate (gal/min)	16.75	48.14
	PIV	
Pixel size	7.4 μm	7.4 μm
Interrogation window	64×64–50% overlap then 32×32–50% overlap	64×64–50% overlap then 32×32–50% overlap
Camera mode	3D cross correlation	3D cross correlation
Image acquisition method	RAM (fast)	Standard
Acquisition—No. of images	170	750

produced a vertical light sheet approximately 2 mm thick. Both of the two PIV system cameras were mounted on one side of the test section and aligned horizontally for camera views normal to the vertical light sheet.

4 Experimental Model

The model is fabricated from fused quartz and carefully positioned, located, and fixed in the test section (see Appendix A by Condie et al. [6] for detailed drawings of the model). Table 1 lists some of the key parameters of the model. Mineral oil from the auxiliary loop enters into the model jets on the top of the model via four inlet-jet elbow manifolds. The four inlet-jet flows merge in the lower plenum and flow toward the outlet (left) end of the model where the flow exits and merges with the primary loop flow. The four jet inlet flows are conditioned in the elbow manifolds to model flow characteristics expected to be present in the actual gas-cooled reactor (GCR) cooling channels that the inlet jets are simulating. Key requirements for the inlet-jet flows are that they are moderately turbulent, uniform, and contain negligible swirl. When the working fluids reach the inlet-jet elbow manifolds the flows are turned and straightened, then pass through a honeycomb, through a screen, and finally through a turbulence generator to induce expected levels of turbulence before entering the inlet jets.

5 Experimental Procedures

The main circulating pump was operated at 50 rpm to circulate the mineral oil around the exterior of the model at approximately 0.18 m/s for index-matching temperature control. The temperatures of both the primary flow loop and auxiliary flow loop were controlled with LABVIEW™ software. The temperature control system maintained the oil temperature to within $\pm 0.05\,^{\circ}C$ of the calculated index-matching temperature ($\sim 23.3\,^{\circ}C$) in the model and to within $\pm 0.03\,^{\circ}C$ of the index-matching temperature in the primary flow loop. The facility remained at a constant, steady state condition throughout the data collection periods. Temperature records for all data collection files are archived on the temperature control computer. The PIV system was operated in the 3D expert user mode. Laser power, Q-switch delays, and the time between frames of the double-image cameras (dt) were adjusted using the interactive mode in the DAVIS 3D PIV software.

In an effort to balance the requirement for high resolution data and to keep the size of data files within reasonable limits (for data processing and data storage considerations), the collection effort on the model was divided into eight regions. The lower plenum area of the model was divided into six regions and, for the higher Re_{jet} flow study, the inlet-jet area was divided into two regions (one region for Jets 1 and 2 and one region for Jets 3 and 4). Additionally, in order to collect (3D) data across the entire width of the model channel (spanwise) the laser and cameras were positioned at 23 different spanwise planes. The laser-light sheet was adjusted to a thickness of about 2 mm, which allowed for complete coverage of the model except for an area near the model walls where the laser-light sheet was blocked by O-ring seals. Therefore, each region of the lower plenum consisted of 23 PIV image files—one file for each spanwise plane. The inlet-jet regions only required 11 planes/files to cover the full width of the jets.

Because of the refractive-index difference between the air space where the cameras operated and the mineral oil where the light sheet was located, it was necessary to coordinate the movement of the two digital cameras relative to the movement of the laser-light sheet. This coordination was accomplished with a MATHCAD code. The code used the mineral oil temperature to determine the index of refraction of the mineral oil and the camera angles relative to the laser-light sheet reported by the camera calibration procedure to calculate a movement ratio for the camera movement relative to the laser-light sheet movement. This ratio was typically between 0.62 and 0.68, that is, for a movement ratio of 0.66, a 2 mm shift of the laser-light sheet required the camera support to be moved about 1.32 mm.

Table 2 summarizes the settings used on the MIR and PIV systems.

Data postprocessing of the acquired images was accomplished with DAVIS 7.1 software. The postprocessed data were then transferred from DAVIS to a secondary PC where data were organized and displayed with TECPLOT 360™ and/or MS Excel software. The total processing time exceeded 900 h of computer time and produced approximately 2 Tbytes of data.

6 Uncertainty Estimates

The objective of uncertainty analysis is to develop an understanding of the estimated experimental uncertainties in the results. For proper benchmark databases, the experimental uncertainties of all measured quantities and their propagation into the results must be obtained quantitatively. In a complicated experiment such as this, some experimental uncertainties can be expected to vary significantly with position as the local velocities vary. McEligot et al. [9] presented a detailed analysis of the experimental uncertainty estimates for this study. Table 3 is a list of some of the uncertainty estimates.

7 Experimental Results

The objective of the experimental program was to obtain velocity field measurements for CFD code assessment. To accomplish this objective the flow inside the lower plenum model was characterized with velocity-vector fields and 14 scalar quantities. McIlroy et al. [10] provided a list that defines the vector and scalar field measurements that were obtained.

Table 3 Uncertainty estimates

Parameter	Uncertainty
Pixel displacement	0.3 pixels
Timing	~0.001%
Lightsheet thickness	10%
Velocity	~0.3%–1.2%
Turbulence intensity	~1.8%
Scatter in velocity statistics	~0.4%–10%
Mean square fluctuations	~1.3%–6%
Camera position	±2 μm
Laser position	±5 μm
Image distance	±0.16 mm
Fluid temperature	±0.05°C
Fluid density	~0.2%
Dynamic viscosity	~2%
Kinematic viscosity	~0.2%
Refractive index	~0.02%
Geometry	~0.2%
Flow rates	0.5%
Reynolds numbers	1%

Since uniform time intervals were employed, the time-mean statistics are calculated from suitable arithmetic averages of the stored data.

The data set presented here is a sample of the data available for code assessment. Due to the tremendous volume of data obtained and the complicated nature of the flow, only a brief analysis is presented. Data at specific locations will be presented along with a brief description of some of the major phenomena observed in the flow.

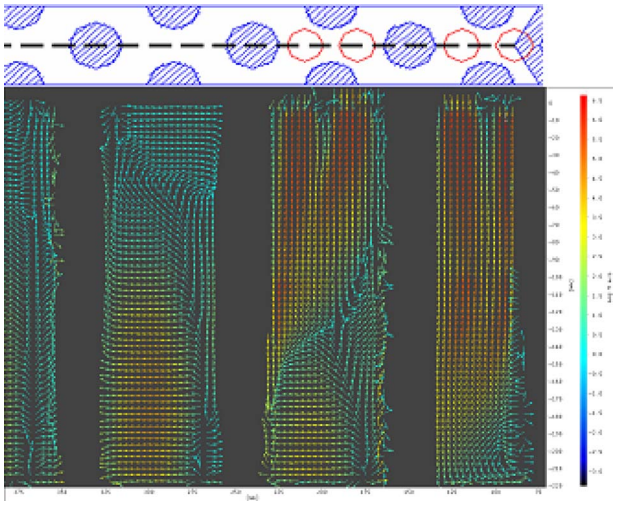

Fig. 2 Mean vector field for Re_{jet}~12,400

Figure 2 is a vector plot of the flow along the centerline of the model. The black regions between the vector groups represent the model support posts. Flow enters the model vertically from the four inlet jets located at the top-right corner of the plot and streams downward into the lower plenum where it interacts with the support posts and reflector wall, and then gradually turns toward the left and flows toward the model exit located to the left of the figure.

The dashed line in the diagram above the figure shows the location of this data plane.

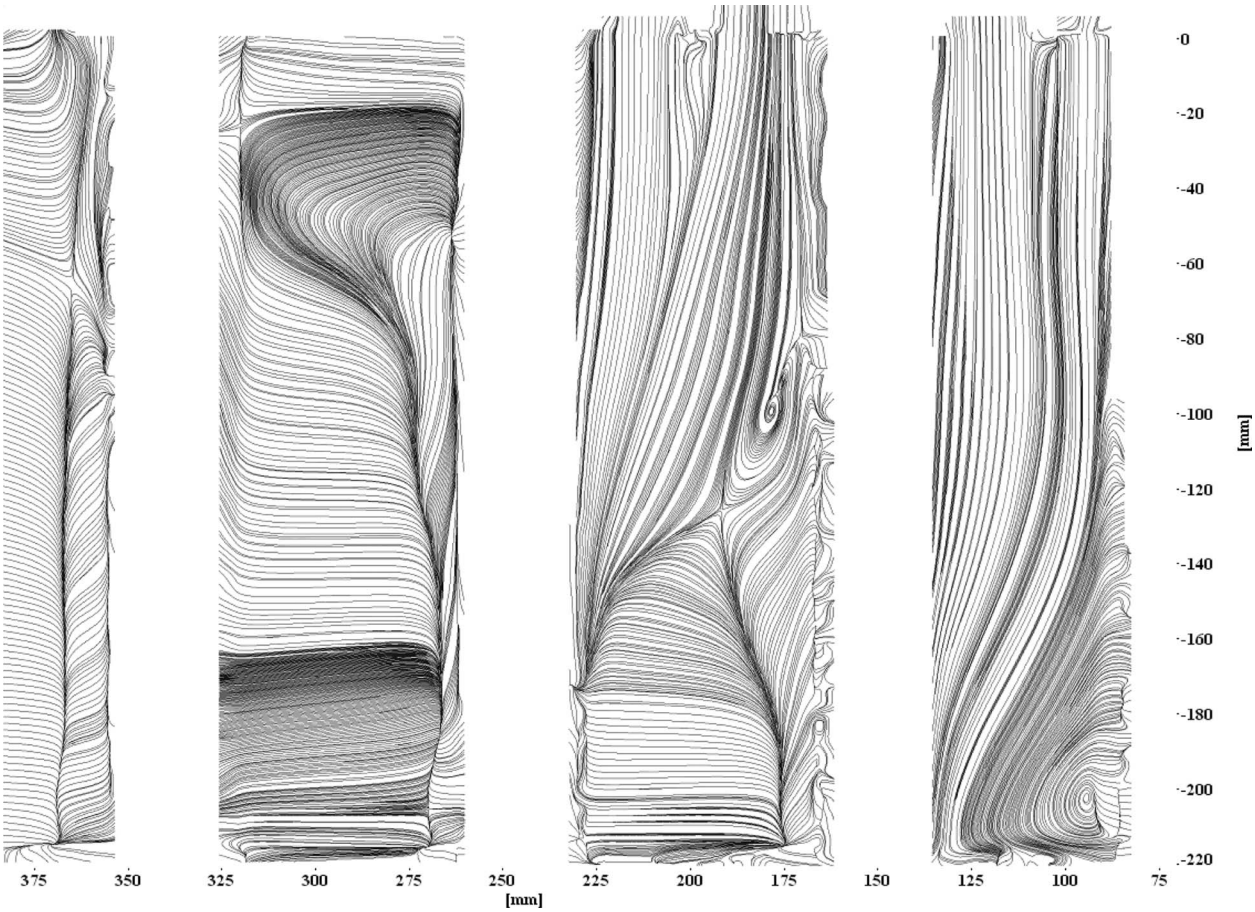

Fig. 3 Mean streamlines for Re_{jet}~12,400

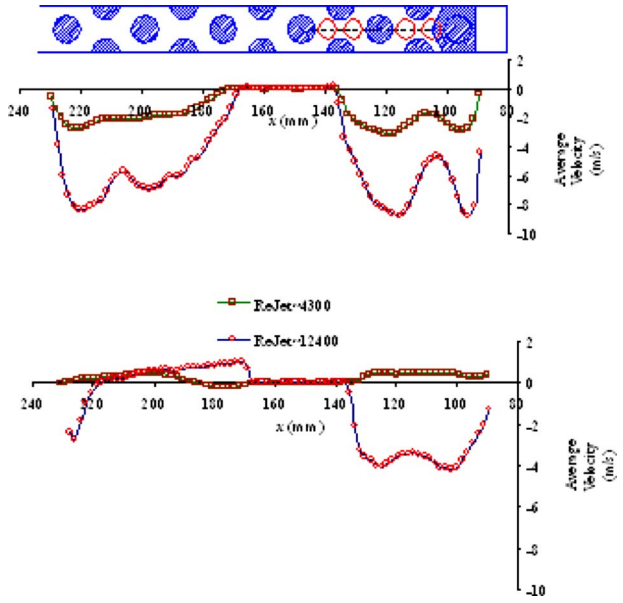

Fig. 4 Average *Vy* at *y*~−70 mm (top) and *y*~−150 mm (bottom)

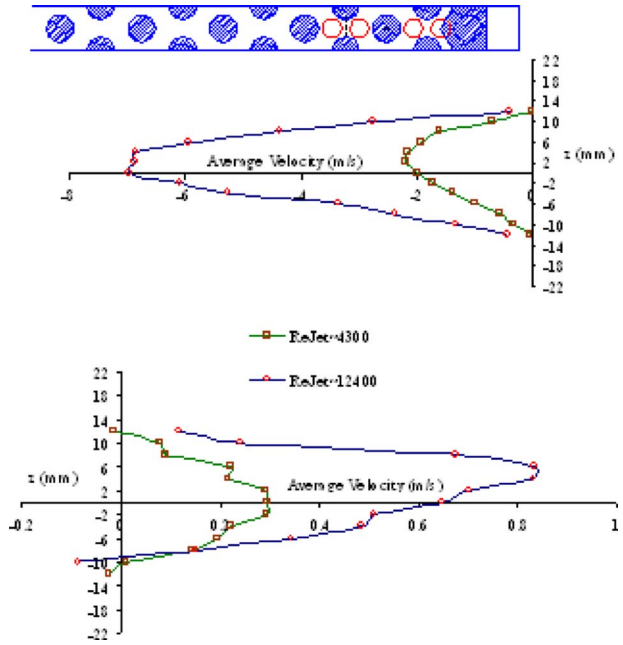

Fig. 5 Average *Vy* at *y*~−70 mm (top) and *y*~−150 mm (bottom)

Figure 3 is a streamline plot of this flow.

Three major structures are visible in Figs. 2 and 3: the recirculation zone in the lower right corner, the recirculation zone near the midheight of the model between the first two support posts, and the recirculation zone near the top of the model on the downstream side of the second and third support posts. Three secondary structures are also visible: the line of merging flow below the two downstream (left) pair of jets and just downstream of the first support post from the bottom of the model to just below the second recirculation zone noted above, the line of merging flow just downstream of the second support post, and the line of merging flow that extends along the full model height on the downstream side of the third support post.

The first recirculation zone is formed by the first pair of inlet jets and their interaction with the reflector wall, first support post, and the bottom of the model. The flows from the two jets merge quickly near the top of the model and are channeled downward between the first support post and reflector wall. As the flow approaches the bottom of the plenum the major portion of this flow turns to the left, flows around the first support post, and interacts with the flow from the second pair of jets. A small portion of this flow is forced to the right where it encounters the reflector wall and creates a recirculation zone. Some of this recirculating fluid is forced up the reflector wall where it interacts with the downward flow from the jets and is subsequently reversed and forced toward the bottom of model plenum.

The second major structure is the recirculation zone that is formed by the flow from the second pair of jets. These flows also merge near the top of the plenum and are channeled downward in the area between the first and second support posts where they interact with the flow from the first (upstream) pair of jets that has passed around the first support post. This interaction results in a portion of the flow rising up the downstream edge of the first support post, causing a second recirculation zone about half way up the downstream edge of the first support post. The remainder of the flow generates a wake behind the lower portion of the second support post and then begins to flow toward the model exit (toward the left).

The third major structure is formed as the flows from both jet pairs merge and begin to flow toward the exit and interact with the second support post. Because no fluid is entering the plenum downstream of the second support post (no inlet jets above this region, which corresponds to the central section of an annular core/plenum), the fluid flows around the second post, forms a wake, and begins to rise to fill the upper portion of the model. A portion of this flow near the top of the plenum moves to the right on the downstream side of the second support post, and then downward forming the third recirculation zone. The flows in the bottom half of the model on the downstream side of the second support post merge and move toward the model exit. The flow then moves around the third support post, merges in a wake on the downstream side of the post, and gradually flows toward the left and slightly upward as it moves toward the model exit.

Finally, a small recirculation zone is evident on the downstream side of the third support post. This flow appears to be a result of the recirculating flow on the upstream side of the post. On the downstream side of the post the upper portion of the flow moves downward until it joins the flow moving upward from the bottom of the model. These two flows merge and move around the post where they join the recirculation zone between the second and third posts.

Figure 4 displays values of average (mean) *Vy* (vertical velocity component) of a vertical data slice along the centerline of the model in the regions below the four inlet jets. The small diagram above the figure describes the spanwise location of the data slice. At the *y*~−70 mm depth, the vertical velocity under the jets (vertical momentum with no imposed crossflow) is substantial and downward. Lower in the plenum (at *y*~−150 mm), the flow under the jets in the Re_{jet} 4300 case has reversed (flows upward) and the flow in the Re_{jet} 12,400 case shows a flow reversal (upward flow) under Jets 3 and 4.

Figure 5 displays values of average (mean) *Vy* (vertical velocity component) in a spanwise line from the vertical data slice as shown in the diagram above the figure. At *y*~−70 mm depth, the vertical velocity is substantial and negative (downward) from the inlet-jet flows entering the lower plenum from Jets 3 and 4. Lower in the plenum, at *y*~−150, the vertical flow reverses and moves upward to form the lower part of a recirculation zone noted earlier.

Figure 6 displays the inlet-jet average (mean) *Vy* (vertical) velocity profiles for the Re_{jet} 12,400 case. The dashed lines represent the locations of the inlet jets. Jet No. 1 is on the left, and inlet Jets

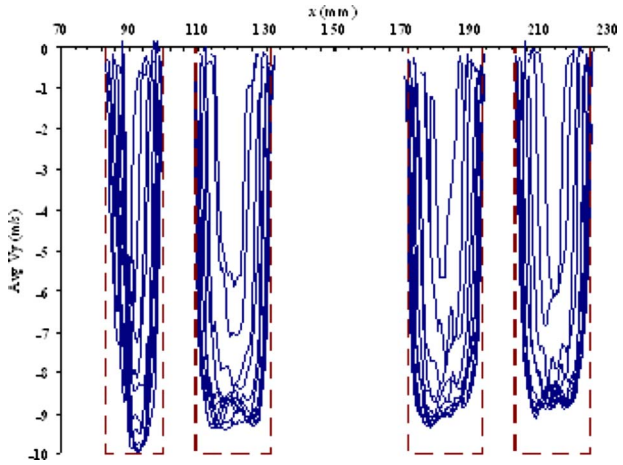

Fig. 6 Average *Vy* in inlet jets for $Re_{jet} \sim 12{,}400$ at $y \sim 11$, $-10 < z < +10$ at 2 mm intervals

2–4 are on the right. The profiles were measured at a level inside the inlet ducts 11 mm above the opening into the plenum ($y/d_{jet} \sim 0.5$ to the exit plane). The 11 velocity profiles in each inlet jet display developing, nonuniform, turbulent flow in the ducts. Jet No. 1 is smaller than the other jets because 1/3 of this jet is filled, as in a prismatic reactor, by the reflector wall model. These profiles were extracted from the raw data files using the locations of the jets from fabrication drawings and analysis of the flows close to the jet walls. It is noteworthy that results of numerical integrations using both the trapezoid rule and Simpson's rule produce an inlet volume flow rate of 169.68 gal/min, which is only 3.9% less than the volume flow rate measured by calibrated flow meters upstream of the jets. The estimated uncertainty in the measured flow rate is approximately 1% and the estimated uncertainty in the integrated flow rate is approximately 0.4–1.2%.

8 Standard Problem

A challenge of designing and licensing the VHTR is to confirm that the intended analysis tools can be used confidently to make decisions and to assure that the reactor systems are safe and meet the performance objectives of the Generation IV Program. The research and development projects at the INL will ensure that the tools used to perform the required calculations and analyses are accurate and reliable.

CFD analyses will be a major component in the analysis suite that will be required to design and license the VHTR so the reactor can operate at maximum outlet temperatures and efficiencies. Only CFD analysis tools have the capability to determine where localized hot spots will occur in the reactor and also whether or not unacceptably large thermal gradients are present.

The calculational envelope of the CFD tools used to analyze the behavior of the VHTR is defined by the scenarios and phenomena that these tools can calculate with confidence. CFD tools can only be used confidently when the results they produce have been shown to be in reasonable agreement with first-principles results, thought-problems, and data that describe the "highly ranked" phenomena inherent in all operational conditions and important accident scenarios for the VHTR. Reasonable agreement is achieved when the calculation generally lies within the uncertainty band of the data used for validation and always shows the same trends as the data and when code deficiencies are minor.

Presently, the CFD tools to be used for analyzing the VHTR are not ready to perform design and analysis, nor are they ready for licensing calculations to the standard that will be required by the VHTR. Considerable validation and, perhaps, development of the software tools is required. Additionally, practices and procedures are required for both validating and developing the necessary CFD software that are acceptable to the nuclear community.

The validation process is based on developing a set of standard problems that will populate a validation matrix for the various tools. The standard problems are defined by the Generation IV International Forum Standard Problem Committee, which defines its standard problems on the basis of comprehensive phenomena identification and ranking tables (PIRT) [11]. The standard problems, which are defined using high-quality data sets with known uncertainty bands, are the measures used to determine whether or not an analysis tool is capable of calculating the required phenomena. The members of the Standard Problem Committee are experts in the potential scenarios that are projected to be important in the VHTR.

Standard problems consist of data sets that have the following characteristics.

a. The data set describes a phenomenon, or a set of phenomena, that influences the behavior of an important figure-of-merit. That is, given that the figure-of-merit is the reactor-vessel wall temperature, which must be less than a predetermined value, then important phenomena are those that significantly influence the reactor-vessel wall temperature. Such phenomena are identified in phenomena identification and ranking studies and are documented [11]. An example of such a phenomenon is the turbulent mixing of hot exit gases in the lower plenum of the reactor vessel because hot jets with an above-average temperature may impinge on the outlet plenum wall and perhaps cause a local hot spot on the reactor-vessel wall.
b. The phenomenon given in the standard problem data set, although it may be measured in a reduced-scale system, can be scaled to the full-sized system using accepted scaling practices. The scaling studies that link the experimental apparatus and data to the full-sized system are documented in a report.
c. The standard problem data set has been shown to measure the data required to determine whether the software is capable of calculating the important phenomenon.
d. The standard problem data set has uncertainties associated with each data point.
e. The quality assurance procedures used to design the experiment, build the experiment, and conduct the experiment are consistent with NQA-1 requirements.

The experiment and results summarized in this paper are intended to assess CFD software and the experiment described herein meets the requirements identified in a–e above.

9 Concluding Remarks

The model design and MIR flow facility produced satisfactory flow conditions, as required by previous scaling studies and model design. As a result of the experiments described in this paper, the objectives of developing benchmark databases for the assessment of CFD solutions of the momentum equations, scalar mixing, and turbulence models for typical prismatic VHTR plenum geometries in the limiting case of negligible buoyancy and constant fluid properties have been met. Additionally, the data obtained from these experiments meet the requirements of a standard problem as defined.

Preliminary measurements of velocity components have been compiled for a low-power case of $Re_{jet} \sim 4300$, and detailed measurements of the flow field for the maximum achievable flow rate in the present MIR flow facility of $Re_{jet} \sim 12{,}400$ have also been completed. The data have been documented to identify and report estimated uncertainties of the measurements and have been collected into various formats suitable for release to the CFD community and others, as necessary. Future plans include distribution of instructions to obtain data sets and points of contact at the INL.

Acknowledgment

This manuscript has been authored by a contractor of the U.S. Government under DOE Contract No. DE-AC07-05ID14517. The authors also acknowledge the highly professional and timely support and assistance of Dr. Steven L. Anderson of LaVision, Inc., Professor Barton L. Smith of Utah State University, and Richard R. Schultz of INL for their assistance in this project.

References

[1] Mikielewicz, D. P., Shehata, A. M., Jackson, J. D., and McEligot, D. M., 2002, "Temperature, Velocity and Mean Turbulence Structure in Strongly-Heated Internal Gas Flows. Comparison of Numerical Predictions with Data," Int. J. Heat Mass Transfer, **45**, pp. 4333–4352.

[2] Richards, A. H., Spall, R. E., and McEligot, D. M., 2004, "An Assessment of Turbulence Models for Strongly Heated Internal Gas Flows," *Proceedings of the 15th IASTED International Conference on Modeling and Simulation Conference*, Marina Del Ray, CA, Mar. 1–3, pp. 119–124.

[3] McEligot, D. M., Condie, K. G., Foust, T. D., McCreery, G. E., Pink, R. J., Stacey, D. E., Shenoy, A., Baccaglini, G., Pletcher, R. H., Wallace, J. M., Vukoslavcevic, P., Jackson, J. D., Kunugi, T., and Satake, S.-i., 2002, "Fundamental Thermal Fluid Physics of High Temperature Flows in Advanced Reactor Systems," INEEL, NERI Program Final Report No. INEEL/EXT-2002-1613.

[4] MacDonald, P. E., Sterbentz, J. W., Sant, R. L., Bayless, P. D., Schultz, R. R., Gougar, H. D., Moore, R. L., Ougouag, A. M., and Terry, W. K., 2003, "NGNP Preliminary Point Design—Results of the Initial Neutronics and Thermal-Hydraulic Assessments," INEEL, Technical Report No. INEEL/EXT-03-00870.

[5] McEligot, D. M., and McCreery, G. E., 2004, "Scaling Studies and Conceptual Experiment Designs for NGNP CFD Assessment," INL, External Report No. INEEL/EXT-04–02502.

[6] Condie, K. G., McCreery, G. E., McIlroy, H. M., Jr., and McEligot, D. M., 2005, "Development of an Experiment for Measuring Flow Phenomena Occurring in a Lower Plenum for VHTR CFD Assessment," INL, External Report No. INL/EXT-05–00603.

[7] Roach, P. J., 1998, *Verification and Validation in Computational Science and Engineering*, Hermosa, Albuquerque, NM, p. 271.

[8] Stoots, C., Becker, S., Condie, K., Durst, F., and McEligot, D. M., 2001, "A Large-Scale Matched Index of Refraction Flow Facility for LDA Studies Around Complex Geometries," Exp. Fluids, **30**, pp. 391–394.

[9] McEligot, D. M., McIlroy, H. M., Jr., and Johnson, R. C., 2007, "Estimated Uncertainties in the Idaho National Laboratory Matched-Index-of-Refraction Lower Plenum Experiment," INL, External Report No. INL/EXT-07–13539.

[10] McIlroy, H. M., Jr., McEligot, D. M., and Pink, R. J., 2007, "Measurement of Turbulent Flow Phenomena for the Lower Plenum of a Prismatic Gas-Cooled Reactor," *Proceedings of the 12th International Meeting on Nuclear Reactor Thermal Hydraulics*, Pittsburgh, PA, Sept. 30–Oct. 4, Log No. 67.

[11] Lee, W-J., Kim, K. D., Hwang, M-K., Lim, H-S., Lee, S-W., Wei, T. Y. C., Vilim, R. B., Feldman, E. E., Pointer, W. D. R., Schultz, R. R., Bayless, P. D., and Moore, R. L., 2005, "Generation of a Preliminary PIRT (Phenomena Identification and Ranking Table) for Very High Temperature Gas-Cooled Reactors," Report No. KAERI/TR-3050/2005, INL/EXT-05-00829, ANL-GenIV-066.

Extrapolation and Curve-Fitting of Calibration Data for Differential Pressure Flow Meters

David R. Keyser
Fellow ASME
Survice Engineering Co.,
Belcamp, MD 20653

Jeffrey R. Friedman
Fellow ASME
Siemens Energy, Inc.,
Orlando, FL

Performance test codes require primary mass-flow accuracies that in many applications require laboratory quality calibration of differential pressure meters. It is also true that many performance tests are conducted at Reynolds numbers and flows well above the laboratories' capacities, and sound extrapolation methods had to be developed. Statistical curve fits and regression analyses by themselves, absent fluid-dynamic foundations, are not valid procedures for extrapolation. The ASME PTC 19.5-2004 discharge coefficient equations reproduced in this paper for nozzles, orifices, and venturis are suitable for use whenever calibration data are to be applied in a flow measurement and/or extrapolated to higher Reynolds numbers as necessary. The equations may also be used for uncalibrated differential pressure meters by using nominal values. It is necessary to note that the metering runs must be manufactured with dimensions, tolerances, smoothness, etc., and installed in strict accordance with ASME PTC 19.5 for these equations to be valid. Note that for compressible flow, the value of the expansion factor term in the PTC 19.5 equation must be the one corresponding to the published PTC 19.5 equation.
[DOI: 10.1115/1.3126778]

1 Introduction

ASME PTC 19.5-2004 [1] presents in one code the results and major details of decades of fluid-dynamic research and development of formulations for coefficients of discharge for all covered meters of this class—orifices, nozzles, and venturis. It began with early work performed in the 1980s and in the 1990s, which culminated in the formulations for nozzles and venturis developed for use in testing steam turbines. The fluid dynamics of orifice meters is more complex, and once the nozzle and venturi formulations were developed, the committee proceeded with applying dimensional analysis, boundary layer theory, and the same fundamental fluid-dynamic principles to derive the correct formulation appropriate for orifice metering as published in PTC 19.5 [1].

Authors of texts on analysis of data have warned us not to utilize standard statistical regression analysis beyond the data range. The variance (or standard deviation) of the predictor usually increases as one moves further away from the mean of the input levels [2].

Any extrapolation of laboratory data using statistical curve fits, regression analyses, or procedures that are not firmly grounded in the physics of fluid dynamics is clearly not valid.

The complete rationale and derivation of the PTC 19.5-2004 formulations are presented in this paper. Remarkably similar technology is used for fitting and extrapolating calibration data for nozzles, venturis, and orifices.

1.1 Theoretical Development. The equations for measuring flow with head class (differential pressure) meters begin with the fundamental principles of conservation of mass and conservation of energy. These equations are one-dimensional, varying only along the axis of the pipe, assuming uniform velocity and properties across the circular plane of flow. Conservation of mass in this simple form for incompressible, inviscid flow is

$$V_1 A_1 = V_2 A_2 \tag{1}$$

The conservation of energy for the same constraints is the well-known Bernoulli equation

$$P_1 + \tfrac{1}{2}\rho V_1^2 = P_2 + \tfrac{1}{2}\rho V_2^2 \tag{2}$$

Combining these two derives the well-known equation for the measurement of flow using a differential pressure device, wherein Cd is the coefficient of discharge, which accounts for viscous and other minor effects.

$$Q_v = CdV_2A_2 = CdA_2\sqrt{\frac{2}{\rho}\frac{\Delta P}{(1 - A_2^2/A_1^2)}} \tag{3}$$

This equation describes the idealized conditions wherein the velocity is uniform across the pipe at each station and the density is constant.

The equations for the coefficient of discharge are used to correct for the deviations of the velocity profile from this idealized situation. Likewise equations for the "expansion factor," most often seen as Y or ε, are used to correct for small density variations between pressure tap stations 1 and 2 when gases are flowing.

The coefficient of discharge, Cd, for nozzles and venturis depends almost entirely on the existence of a boundary layer at the downstream tap location (Eq. (2)), whereas the Cd for orifices depends on the boundary layer at the upstream tap and on the geometry of the orifice meter itself.

2 Nozzles and Venturis

Because of the fully developed velocity profile at the upstream tap and the size of the boundary layer relative to the pipe diameter, its effect on Cd may be neglected. By far, the major contribution of the boundary layer to Cd occurs at the downstream tap, for which the displacement thickness is used. The effect of the boundary layer is to subtract an annulus of flow area from the measured throat area. This causes the velocity in the throat to be increased according to Eqs. (1) and (2), which in turn causes the differential pressure to be higher than ideal. Consequently the correction factor, Cd, must reduce the value of the idealized flow.

The growth of the boundary layer for nozzles and venturis is based on that formed from the leading edge of a flat plate. For the purposes of deriving the Cd, we have identified four intervals of Reynolds numbers based on distance from the leading edge:

a. Region I. Wholly laminar: $\mathrm{Re} < 5 \times 10^5$
b. Region II. Mostly laminar, but partly turbulent, with laminar thickness greater than the turbulent contribution: $5 \times 10^5 < \mathrm{Re} < 7 \times 10^5$
c. Region III. Partly laminar and partly turbulent, with the turbulent contribution greater than the laminar contribution. The start of this region is often called "transition" in nozzle calibrations: $7 \times 10^5 < \mathrm{Re} < 10^7$
d. Region IV. Fully developed turbulent boundary layer: $\mathrm{Re} > 10^7$

For the purposes of the use of ASME throat tap nozzles, we are concerned only with Regions III and IV, with the former asymptotically becoming the latter. In fact, we insist that the nozzle not be used until the Reynolds number is comfortably into Region III.

Manuscript received December 6, 2008; final manuscript received October 17, 2008; published online November 2, 2009. Review conducted by Dilip R. Ballal.

The ASME nozzle is modeled by a flat plate wrapped into a cylinder which is one throat diameter long. In this case, the Reynolds number based on the distance from the leading edge numerically equals that based on the throat diameter. This model was first published by Hall [3] with satisfactory results. For each of the above regions, boundary layer thicknesses may be used to compute the *Cd* valid for each region. The equations for each region were taken from Schlichting [4] and developed for the coefficient of discharge. The range of Reynolds numbers for each region above is also given in Ref. [5]. At the start of Region III, the momentum boundary layer thickness must be equal for both laminar and turbulent layers. The distance taken from the leading edge is that at which a fully turbulent boundary layer would begin in order to equal the momentum thickness at the transition Reynolds number's distance, x_0. For nozzles and venturis manufactured in accordance with PTC 19.5, this Reynolds number is around 800,000. In cases of highly polished throats, this transition can be delayed up to significantly higher values. Fortunately, the Reynolds numbers during which transition occurs can be observed from the calibration data, and the nozzle or venturi should be used only at greater values.

2.1 Tap Effect. There is an additional term which is caused by the location of the downstream pressure tap inside the throat. Briefly, any hole in an aerodynamic surface creates drag. Drag is an adverse pressure opposing the flow and, in this case, it is observed as an increased pressure at the throat tap. This in turn decreases the observed differential pressure for which compensation must be made by a multiplicative value greater than unity. This semi-empirical value was determined to be 1.0054, or in other words, an upward compensation of 0.54%. The acceptable range published in PTC 6, *Steam Turbines*, about this value is 0.25%. Relative to its magnitude, the uncertainty of the "tap effect" is large, which is why such devices must be calibrated to assure sufficient accuracy.

Consequently, in the limit as the Reynolds number approaches infinity, the *Cd* becomes

$$Cd = 1.000000 + \text{tap effect} \pm U_{95\%} \tag{4}$$

Note that for a regular ASME nozzle with taps in the pipe wall, the tap effect is zero.

In the normal range of use, Regions III and IV, the equation for *Cd*, as published in PTC 19.5, is

$$Cd = -0.185\left\{R_d^{-1/5}\left[1 - \frac{361{,}239}{R_d}\right]^{4/5}\right\} + C_x = mX + b \tag{5}$$

which in this linearized form of the equation, $m=-0.185$, $b=C_x$, and the term in {} is the transformed independent variable, X.

3 Coefficient of Discharge for Orifice Metering Sections

Orifices are more complicated to model sufficiently than nozzles and venturis because, fortunately, the latter are always geometrically similar. Such is not the case for orifices. If we had standardized on one diameter ratio, β, (e.g., 0.45), then geometric similarity—which is a necessary condition for using fluid-dynamic dimensional analysis—would likewise be accomplished. However, for many good and practical reasons, this is not done. Consequently, there exists a significant range of area ratios in use, which require additional correction factors in the equation for *Cd* of orifices. In spite of the large range of area ratios successfully being used, relatively small perturbation factors included in the equation for *Cd* accurately accomplish the necessary and sufficient compensation for the geometric similarity in orifice metering sections.

When developing perturbation equations covering a small interval from a known point, the Taylor (or MacLaurin) series is the usual method of expansion from that point. The criterion for truncating all such series expansions in this work is to cease adding terms to the series when the net change in the result is smaller than $\sim 1/4$ of the experimental uncertainty of the supporting data. Any additional terms may indeed improve the "goodness of fit" statistics, but they do so primarily by fitting the equation to the "noise" and laboratory biases in these data. Consequently, the correction factor to compensate for the small geometric dissimilitude was determined to be a quadratic Taylor series in the area ratio, as shown in Eq. (6).

$$Cd = Cd_o + f'(0.04)(\beta^2 - 0.04) + f''(0.04)(\beta^2 - 0.04)^2/2\ldots \tag{6}$$

The expansion begins at the lower end of the permitted beta ratios, e.g., 0.2.

3.1 Boundary Layer Effects. The effect of boundary layers on the coefficient of discharge in orifices is opposite to what it is for nozzles and venturis because obviously there is no boundary layer in the bore of the sharp-edged orifice, but there is one at the upstream tap. The displacement boundary layer at the upstream tap effectively subtracts an annulus of flow area from the pipe and, consequently, the velocity there is higher than predicted by the one-dimensional conservation of mass (Eq. (1)). The consequence, via the Bernoulli equation, is to lower the pressure at the upstream tap and lower the differential pressure across the orifice. Therefore the boundary layer correction factor must be positive.

In this case we again use the same concept for boundary layer growth as in Hall's model nozzle, except here the "throat" is a nominal 20 diameters in length—in other words, there are ~ 20 diameters of straight pipe upstream. Using the Reynolds number based on length, it was found that the turbulent boundary layer reached the centerline of the pipe after single-digit pipe diameters, and from there downstream it transitioned to the desired, fully developed, turbulent profile. The displacement boundary layer which influences the flow measurement is in fact the laminar sublayer at the upstream tap. Therefore, the boundary layer equation for Region I is the proper one to apply to the coefficient of discharge of the orifice.

Furthermore, because of the fluid dynamics about the orifice and its vena contracta, the boundary layer affects the Euler number of the orifice's flow. The Euler number is related to the "velocity-of-approach" factor in Bernoulli's equation, and the Reynolds number derived from the boundary layer effects modifies this Euler number. Consequently, the "boundary layer factor" in its *Cd* equation is a function of both the Euler and Reynolds numbers of the flow—quite distinct from the case for nozzles and venturis and a bit more complicated. The Euler number for orifices is

$$\text{Eu} = \frac{2(P_1 - P_2)}{\rho V_2^2} = (1 - \beta^4) \tag{7}$$

The effective β flowing through an orifice is larger than the measured geometry because of the boundary layer. The boundary layer factor, F, becomes

$$F(\text{Re},\text{Eu}) = \frac{\sqrt{1-\beta^4}}{\sqrt{1 - \dfrac{\beta^4}{[1 - 30.78\ \text{Re}^{-1/2}]^2}}} - 1 \tag{8}$$

where this Re is based on the pipe diameter, not the bore diameter, in contrast to the case of nozzles and venturis.

3.2 Velocity Profile Effects. There is one more factor in the orifice *Cd* which provides a small but admissible improvement in the results with regard to the error criterion above, and that is a quadratic correction for the upstream velocity profile. The velocity-of-approach factor in the standard differential pressure meter's flow equation is derived directly from Eqs. (1) and (2), and is the area ratio term in the denominator under the radical in

Eq. (3). The fifth term in the *Cd* equation for orifices is like unto it, their product becoming the square of the one-dimensional velocity term, ϕ

$$\phi = 1/(1-\beta^4)^{1/2} - 1 \tag{9}$$

At this point in the development of the equation, we derived its correct theoretical form

$$C = C_x + a\beta^2 + b\beta^4 + d\{F(\mathrm{Eu},\mathrm{Re})\} + e\phi \tag{10}$$

The five terms each have a meaning in fluid dynamics and dynamic similarity. The first one is a starting point (which is the only one to be modified by calibration); the second and the third compensate for variations in the geometric similarity requirements of dimensional analysis; the fourth accounts for the boundary layer; and the last compensates for actual velocity profile effects.

However, this equation for *Cd* is not purely theoretical. It is half theoretical and half empirical because each of the five dimensionless coefficients ($a-e$) of each of the terms in Eq. (10) are determined by multiple-variable, linear optimal regression derived from the same base of 16,700+data on which the Reader–Harris/Gallagher/Gallagher (1998) interpolation equation for *Cd* was used [6]. Being based on the boundary layer equations of Regions III and IV above, the resulting equation is valid for pipe Reynolds numbers above ~35,000. Almost all performance testing applications of orifices are conducted well above this value; consequently no effort has been expended in applying this same concept and framework to orifice data below this value. However, no obstacle exists to prevent such an application if one were so motivated.

The method of applying the data to the form of the equation is the use of ensemble averages. There are broadly two approaches to such regression fitting of the data. The typical approach, as used in the Reader–Harris/Gallagher formulation, is to weigh each datum equally—just input all the available data and turn the statistical crank. This is appropriate in cases wherein the data are fairly evenly dispersed and only an interpolation formula is desired. In the set of data for these orifices, the Reynolds numbers' range was between 1000 and $\sim 14\times 10^6$. Consequently, the resulting formula should not be used outside that range [2,7,8]. Very often in performance testing, the requirement is for accurate, calibrated flow measurement well above the Reynolds numbers available from the existing calibration laboratories. This requirement drives the need for extrapolation of calibration data, which in turn leads to the need for a fluid-dynamic model of an orifice to be used and fitted to the calibration data in order to obtain the best possible *Cd* to use under the test's flow conditions.

In order to develop a semi-empirical model of the orifice, the method of ensemble averaging was chosen. In this method, the average of all data within a "box" of data was used to determine, statistically, the weighing coefficients of Eq. (10). The sides of the box containing the data were formed from equal increments of area ratio and equal increments of the square root of the pipe Reynolds number. The resulting average *Cd* of all the data contained in each such space is what was used for source data in the multivariable, optimal linear regression used to calculate the weighing coefficients $a-e$. The resulting uncertainties of these weighing coefficients are given in Ref. [1].

4 Method of Extrapolation of *Cd*

The advantage of a fluid-dynamic model of the orifice metering section is that one may use it with confidence well outside the range of the supporting data. That is the whole point actually of dynamic similarity analyses. Doing so with merely empirical interpolation formulas, on the other hand, is quite risky and uncertain in general, and such extrapolation should be avoided. From Ross [7], "One should not make predictions about responses at input levels that are far from those used to obtain the estimated regression line." From Holman [8], "Before trying to obtain correlations of the experimental data, the investigator should carefully review the theory appropriate to the subject and try to glean some information that will indicate the trends the results may take. Important dimensionless groups, pertinent functional relations, and other information may lead to a fruitful interpretation of the data."

Ross [7] advises that standard statistical data regression utilizing standard functions such as pure linear regression schemes are strictly to be used for predictions within the range of calibration, even with excellent variances. Holman [8] advises that, with an understanding of the physics behind the phenomena being studied, such correlations are far more meaningful and that, if the appropriate dimensionless groups and other appropriate functional relationships are applied, the interpretation of the data is far more believable. It is clear that to solve the extrapolation problem for PTCs, the discharge coefficient equations had to be developed based on fluid-dynamic theory and not based on standard statistical regression analysis.

In spite of differing step-by-step published procedures for extrapolation, the concepts of the methods for both PTC-6 throat tap nozzles and orifices are the same. Simply stated, the semitheoretical, semi-empirical curves of Eqs. (5) and (10) are moved vertically parallel to the ordinate until such "average curve" fits the calibration data the best. The consequence of this calculation is that only the lead, constant term, which represents the intercept or value of the coefficient of discharge in the limit as the Re approaches infinity, is changed. Margins are specified on the acceptable amount of such change, but only that term is modified to fit the calibration. This becomes the equation to use from the lowest Reynolds number of the calibration, through all the data, and upward through the range of performance-testing flows. Obviously in the case of the orifice, only the boundary layer term remains, since all the other terms, while kinematic in effect, are related to the geometry and become incorporated into the lead constant as a consequence of the calibration. The same is true for the nozzle calibration because the tap effect term likewise is constant.

Each of the codes, PTC 6 (Steam Turbines) and PTC 19.5 (Flow Measurement), have published detailed step-by-step procedures for fitting the calibration data to Eqs. (5) and (10), so we shall not duplicate them here. As a practical matter, however, we illustrate the concept of fitting the data and use of the equations discussed above as follows: Most spreadsheet software contains functions for calculating standard deviations of data and routines for fitting data to linear equations (optimized in the sense of least-squared error). All one need do is compare the calibration data, point by point at each Re, with the standard, uncalibrated curve published in Ref. [1]. Then

a. calculate the average of these deviations from the standard curve
b. calculate the standard deviation of these averages from the standard curve
c. adjust the lead term, C_x, using the average deviation from (a) so that the calibration curve goes through the middle of the data
d. twice the standard deviation from (b) provides the estimated random uncertainty of the calibration curve

It is important not to alter the value of the dimensionless coefficients of the one remaining Re term (e.g., −0.187 for nozzles, which is a theoretical value derived from Ref. [3]—nor the value of *d* premultiplying the term in Eq. (8) as published in PTC 19.5),

Example Problem. The essentials of the curve fitting and extrapolation are identical for nozzles, venturis, and orifices. To illustrate, the orifice calibration used is presented in Table 1. For

Table 1 Orifice calibration data (β=0.6024, D=7.496 in.)

Re	X	C uncalculated	C measured	C fitted
6.649×10^5	0.006 121 731	0.6070	0.6076	0.60 777
7.334×10^5	0.005 809 662	0.6069	0.6079	0.60 770
7.900×10^5	0.00 558 433	0.6069	0.6080	0.60 765
8.019×10^5	0.005 540 142	0.6069	0.6075	0.60 764
8.500×10^5	0.005 371 471	0.6068	0.6079	0.60 760
9.174×10^5	0.005 158 686	0.6068	0.6078	0.60 755
9.755×10^5	0.004 993 913	0.6067	0.6073	0.60 752
1.043×10^6	0.00 482 0672	0.6067	0.6076	0.60 748
1.088×10^6	0.0 047 145 640	0.6067	0.6075	0.60 745
1.171×10^6	0.004 535 693	0.6066	0.6074	0.60 741
1.229×10^6	0.004 421 961	0.6066	0.6074	0.60 739
1.294×10^6	0.004 303 998	0.6066	0.6071	0.60 736
1.358×10^6	0.004 196 485	0.6066	0.6073	0.60 734
1.424×10^6	0.004 093 528	0.6065	0.6073	0.60 732
1.483×10^6	0.004 007 545	0.6065	0.6069	0.60 730
1.539×10^6	0.003 930 687	0.6065	0.6075	0.60 728
1.568×10^6	0.00 389 256	0.6065	0.6071	0.60 727
1.664×10^6	0.003 773 743	0.6065	0.6071	0.60 724
1.738×10^6	0.003 689 141	0.6065	0.6072	0.60 723
1.791×10^6	0.003 631 886	0.6064	0.6073	0.60 721

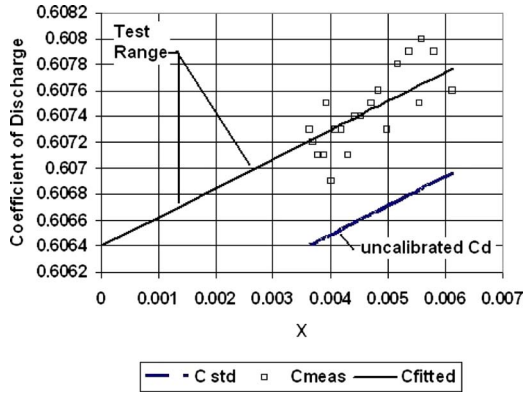

Fig. 1 Orifice data extrapolation

this β, the "standard," uncalibrated equation for this orifice would be calculated from Eq. (11) and the values of $a-e$ are published in PTC 19.5

$$Cd = 0.6056 + 0.2232 \times F(\mathrm{Eu},\mathrm{Re}) = b + mX \tag{11}$$

For the linearized form, b=0.6056, m=0.2232, and F(Eu,Re) is the independent variable.

These values are shown and plotted in Fig. 1, along with the calibration data. Note that the data all lie above the standard curve, but well within 0.25% of it. What remains is to calculate how far up this standard curve must be moved to fit the data (step (a)). From steps (b) and (d), the random uncertainty of these data is found to be $\pm$0.0004. Using the average deviation of these data from the standard curve (step c) gives the plot in Fig. 1. The equation for use with this orifice becomes

$$Cd = 0.6064 + 0.2232 \times F(\mathrm{Eu},\mathrm{Re}) \tag{12}$$

which is valid for use from the beginning of the calibration range without an upper limit of Re.

Nomenclature

A = flow area, L^2
Cd = coefficient of discharge
C_x = intercept of the curve of Cd
D = inside diameter of pipe, L
d = bore diameter, L
Eu = Euler number
F = appropriate units of force
g_c = conversion factor, L/T^2
g = local acceleration of gravity, L/T^2
L = appropriate units of length
M = appropriate units of mass
n = units conversion factor
ΔP = differential pressure, F/L
Q, q = volumetric flow, L^3/T
Re = pipe Reynolds number
Rd = Reynolds number of bore or throat
V = flow velocity, L/T
W = weighed mass, M
T = time, s

Greek

β = d/D
ε = expansibility factor for gases and vapors
ρ = density of fluid, M/L^3

References

[1] ASME Performance Test Code 19.5-2004, "Flow Measurement," an American National Standard, The American Society of Mechanical Engineers, New York.
[2] Romeijn, E., 2008, private communication.
[3] Hall, G. W., "Application of Boundary Layer Theory to Explain Some Nozzle and Venturi Peculiarities," Trans. IME, London, **173**(36) 1959, pp. 837–870.
[4] Schlichting, H., *Boundary Layer Theory*, 7th ed., J. Kestin, translator, McGraw-Hill, New York.
[5] Murdock, J. W., and Keyser, D. R., 1991, "A Method for the Extrapolation of Calibration Data of PTC 6 Throat Tap Nozzles," ASME J. Eng. Gas Turbines Power, **113**(2), pp. 233–241.
[6] ASME MFC-3M-2004, "Measurement of Fluid Flow in Pipes Using Orifice, Nozzle, and Venturi," ASME, New York.
[7] Ross, S., 2004, *Introduction to Probability and Statistics for Engineers and Scientists*, 3rd ed., Elsevier, New York, p. 347.
[8] Holman, J. P., 1978, *Experimental Methods for Engineers*, McGraw-Hill, New York, p. 82.

A Micro Gas Turbine Based Test Rig for Educational Purposes

Mario L. Ferrari
e-mail: mario.ferrari@unige.it

Matteo Pascenti
e-mail: matteo.pascenti@unige.it

Loredana Magistri
e-mail: loredana.magistri@unige.it

Aristide F. Massardo
e-mail: massardo@unige.it

Dipartimento di Macchine, Sistemi Energetici e Trasporti (DiMSET),
Thermochemical Power Group (TPG),
Università di Genova,
Genova 16145, Italy

The Thermochemical Power Group of the University of Genoa, Italy, has developed a new "Gas Turbine" laboratory to introduce undergraduate students to the Gas Turbines and Innovative Cycles course, and Ph.D.s to advanced experimental activities in the same field. In the laboratory a general-purpose experimental rig, based on a modified commercial 100 kW recuperated micro gas turbine, was installed and fully instrumented. One of the main objectives of the laboratory is to provide both students and researchers with several experimental possibilities to obtain data related to the gas turbine steady-state, transient, and dynamic performance, including the effect of interaction between the turbomachines (especially the compressor), and more complex innovative gas turbine cycle configurations, such as recuperated, humid air, and hybrid (with high temperature fuel cells). The facility was partially funded by two Integrated Projects of the EU VI Framework Program (Felicitas and LARGE-SOFC) and the Italian Government (PRIN project), and it was designed with a high flexibility approach including: flow control management, cogenerative and trigenerative applications, downstream compressor volume variation, grid-connected or stand-alone operations, recuperated or simple cycles, and room temperature control. The paper also shows, as an example of the possibilities offered by the rig, experimental data obtained by both Master and Ph.D. students. The tests presented here are essential for understanding commercial gas turbines and microturbine performance, control strategy development, and theoretical model validation.
[DOI: 10.1115/1.3157099]

Keywords: micro gas turbine, test rig, experimental lessons

1 Introduction

The development of an experimental laboratory based on a large size gas turbine for educational activities is usually not feasible at the University level, due to the cost of rig components and plant management. However, the recent microturbine (mGT) technology [1] allows wide-ranging experimental educational activities on gas turbine cycles, which considerably reduce cost.

Moreover, it is essential to provide both students and researchers with experimental tests on micro gas turbines because of their recent integration in innovative cycles, such as hybrid systems [2], humid cycles [3], and externally fired cycles [4], which are still under development. On the other hand, microturbines are a promising technology for distributed power generation and cogeneration. However, additional components generate new variables to be monitored, new risky conditions to be avoided, and require additional control devices and control systems [5]. This aspect is particularly interesting in terms of Ph.D. education and research.

The test rig, developed by Thermochemical Power Group (TPG) at the University of Genoa, is based on a commercial recuperated 100 kW micro gas turbine equipped with original-design external pipes for proper measurements and valves for flow management. These pipes were also used to connect the machine to a modular vessel located between the recuperator outlet (cold side) and the combustor inlet, designed by Ph.D. students [6] to emulate the dimensions of innovative cycle components (such as fuel cells [2,6,7], externally fired gas turbines [4], and saturators [3]).

The main capabilities of this test rig involve steady-state and transient experimental tests to be carried out by students or researchers on the following mGT plant configurations:

- simple cycle
- recuperated and partly recuperated cycle
- both simple and recuperated cycles coupled with a modular vessel for the emulation of additional component volume
- cogenerative systems

Moreover, on all these plant layouts it is possible to test the influence of the following properties, especially in transient conditions:

- ambient temperature
- volume size (downstream of the compressor)
- valve fractional opening values
- bleed mass flow rates
- grid connection or stand-alone systems

This paper shows some examples of tests carried out with the rig (using different plant layouts and operative conditions), during undergraduate course lessons [8] or by Ph.D. students.

The rig is widely used at the University of Genoa as a support for the undergraduate course titled "Gas Turbines and Innovative Cycles" (mechanical engineers), and for the course "Thermal Machines" (control engineers).

2 The Commercial Machine

The basic machine is a Turbec T100 PHS Series 3 [9] operating in stand-alone configuration or connected to the electrical grid with a suitable safety interconnection panel. It consists of a complete module for power production (100 kW at nominal conditions), a heat exchanger located downstream of the recuperator outlet (hot side) for cogenerative applications, and two battery packages for the start-up phase when the machine operates in stand-alone configuration.

The power module includes a single shaft radial machine (compressor and turbine) operating at a nominal rotational speed of 70,000 rpm (β=4.45) and a turbine inlet temperature (TIT) of 950°C, that is, 1223.15 K, a natural gas fed combustor, a primary-surface recuperator directly attached to the turbine outlet, a water cooled high speed generator, a power electronic unit (rectifier, converter, filters, and main circuit breaker), an automatic control system interfaced with the machine control panel, and the auxiliaries. The machine control system operates at constant rotational speed in stand-alone mode, whereas in the grid-connected mode,

Contributed by the International Gas Turbine Institute of ASME for publication in the JOURNAL OF ENGINEERING FOR GAS TURBINES AND POWER. Manuscript received March 20, 2009; final manuscript received May 20, 2009; published online November 11, 2009. Review conducted by Dilip R. Ballal. Paper presented at the ASME Gas Turbine Technical Congress and Exposition, Orlando, FL, Jun. 8–12, 2009.

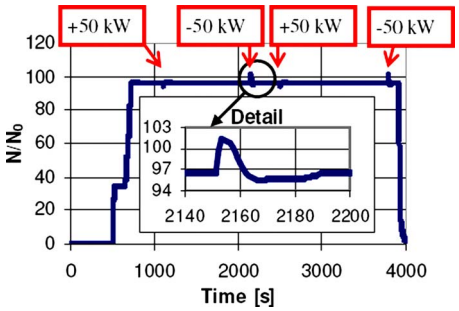

Fig. 1 Typical test data (rotational speed) in standard recuperated cycle mode

it performs a constant turbine outlet temperature (TOT) control strategy. Further details on the machine layout and instrumentation are available in Refs. [6,8–10].

The TPG laboratory was also equipped with a 100 kW resistor bank (pure resistive load) for the turbine operation in stand-alone mode. In the stand-alone mode the turbine control system maintains the rotational speed constant at the 96.5% of its nominal value [9].

The practical experience obtained by TPG researchers when installing the mGT is essential for clearly illustrating it to the undergraduate course in Gas Turbines and Innovative Cycles. Now, in addition to learning about the thermodynamic cycles and plant layouts, students can also become familiar with their materials, piping, gaskets, technology for auxiliaries, and instrumentation.

2.1 Test Example of the Machine Operating in Standard Recuperated Cycle Mode. This paragraph shows an example of the possible tests to be carried out on the machine in standard recuperated cycle mode. This kind of test is extremely useful to provide undergraduate students with experimental experience on machine behavior in both steady-state and transient conditions. For this test the stand-alone configuration was chosen because by connecting the machine to the resistor bank, it is possible to perform load steps (more significant in terms of plant response), while in grid-connected conditions the load is gradually ramped up by the machine control system to the set point value [9].

The rotational speed graph (Fig. 1) shows the machine start-up and shutdown phases (see Ref. [10] for further details), and focuses the attention on speed effects caused by electrical load steps. After the start-up phase and a brief heating period, the machine was tested while performing 50 kW load steps. The electrical load was applied and removed twice before the machine shutdown. The rotational speed oscillations caused by the load steps are clearly reported in Fig. 1. This is an essential test to provide students with experimental experience on micro gas turbines during critical phases, such as start-up, shutdown, or load changes.

3 Machine Modifications and Connection Pipes

The commercial power unit was modified for coupling with the external connection pipes used for flow measurement and management purposes. These modifications are essential for measuring all the properties necessary for cycle characterization (e.g., air mass flow rate or recuperator boundary temperatures), not available in the commercial layout of the machine. For this reason, the two pipes between the recuperator and the combustor inlet were substituted with four pipes for the external connections. Furthermore, at the compressor outlet a check valve was introduced to prevent damage and block compressor backflow if surge conditions occur during experimental tests. Between this valve and the recuperator inlet, a T-joint was introduced to have a recuperator bypass line, which is necessary for studying non-recuperated cycles or hybrid system start-up and shutdown phases [6,7].

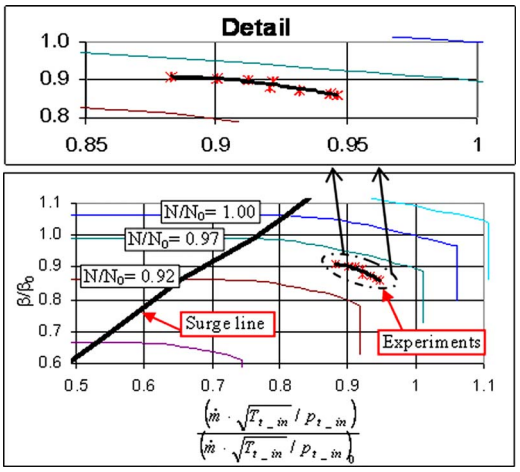

Fig. 2 Direct-line test: experimental data on compressor map obtained in stand-alone configuration

The connection pipes were designed for flow measurement performance with pitot devices. For this reason, each pitot meter is preceded by a pipe of at least 18 diameter length and followed by a minimum length pipe of 4 diameters. This layout was chosen to obtain high-precision measurements (flow uniformity). A cold bypass was included to bypass the recuperator or connect the compressor outlet directly to additional external components (e.g., the modular vessel [6] used to emulate additional component dimensions). This line (see Fig. 3) was equipped with two valves (VC and VR) to manage the flows if an additional component is connected (between VC and VR). Furthermore, a bleed line [6], equipped with a globe valve (VB), was introduced at the compressor outlet (Fig. 3) to bleed a part of the flow when operative conditions are too close to the surge region. The plant includes an additional pipe (direct line), equipped with a mass flow rate meter that directly connects the recuperator outlet to the combustor inlet (through the VM valve), as occurs in a typical recuperated cycle.

Since the machine is not designed for connection to additional components between the compressor and expander, such as external pipes (and volumes), the connection pipes were designed, using different theoretical models [6], to incur the lowest possible pressure drops between the recuperator outlet and the combustor inlet. This is necessary to prevent surge conditions and to avoid extreme reduction in machine performance. Therefore, gate valves were chosen (except in the case of the bleed line), and the pipes were designed with wide theoretical support [6].

Using a pressure probe (PRC1 in Fig. 3 located at the compressor outlet and a mass flow meter (MM in Fig. 3) located in the direct connection between the recuperator outlet and the combustor inlet (Fig. 3), it is possible to show in Fig. 2 the experimental tests at different load values reported on the manufacturer compressor map. It is the result of a typical experimental lesson for Master students running the machine at constant rotational speed. The machine start-up is carried out in stand-alone conditions, and all the operations [10] are presented to students (e.g., evacuation fan start-up, initial machine start-up, machine purge, combustor light-off, heating up phase, rotational speed ramp, and idle condition). At idle steady-state condition, the resistor bank is used to test the machine with different load values (starting from 10 kW and increasing the load with 10 kW steps up to the maximum power). Each load value is maintained constant up to steady-state temperature values. The maximum load value depends on the ambient conditions. High ambient temperatures reduce machine performance, decreasing the maximum load value. Then, a load rejection is produced providing students with the TOT and rotational speed data over time. Finally, the machine is stopped with the normal shutdown operation, as implemented by the

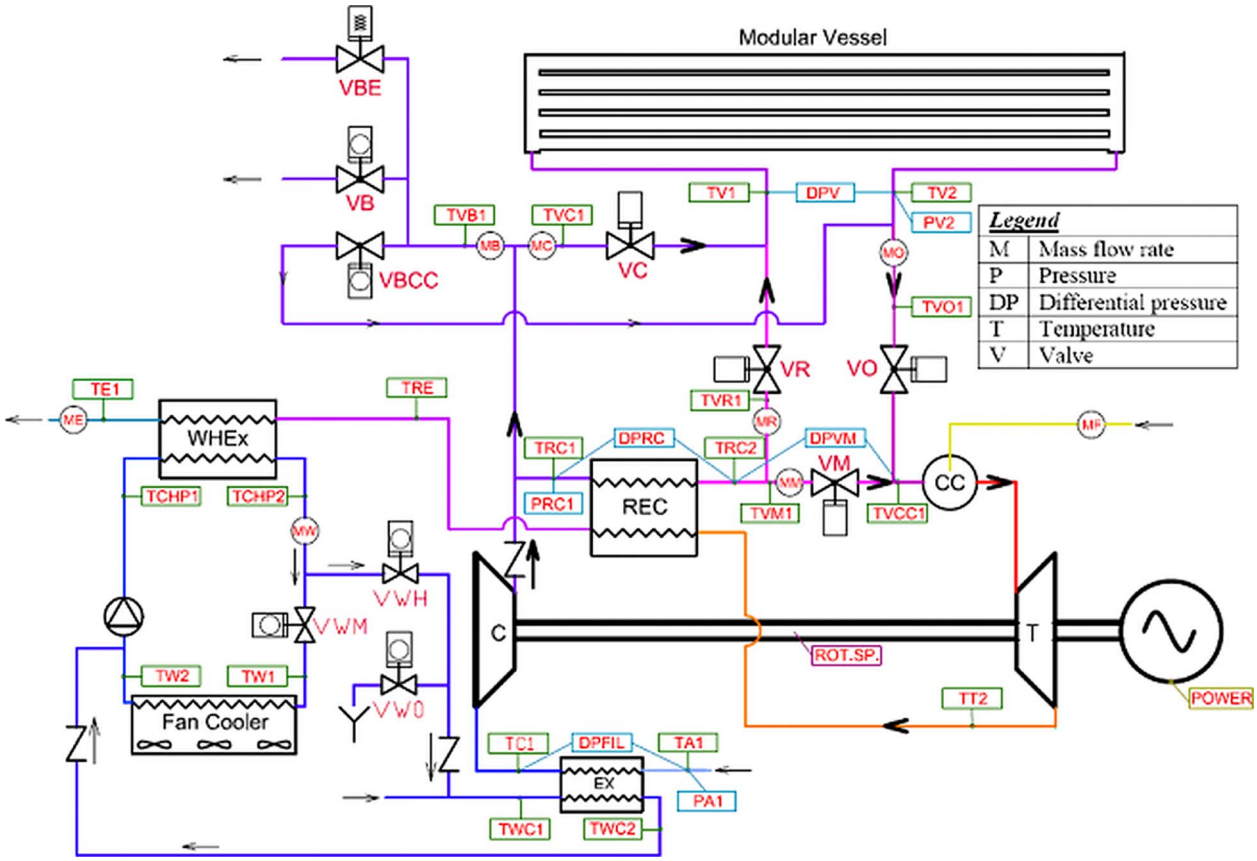

Fig. 3 Plant layout and instrumentation including the modular vessel

manufacturer in the machine control system. The experimental points reported on manufacturer compressor map (Fig. 2) are well located between the 0.97 and 0.92 curves. The slight discrepancy between the curve obtained from the manufacturer datum interpolation and the experimental one is due to the ambient temperature, which is around 25°C (298.15 K) instead of 15°C (288.15 K) and to the accuracy of probes utilized [10].

4 Machine Connected to an External Vessel

The effect of different volume sizes (between the compressor outlet and the turbine inlet) at different plant layout cycles (hybrid system, micro-HAT cycle (mHAT), and externally fired cycle) is extremely important in dynamic conditions to prevent the machine or other plant components (e.g., the fuel cell) from stress or dangerous conditions [10]. Usually, undergraduate lessons do not include details on microturbine dynamic behavior and management due to the lack of time or lack of access to experimental facilities and data. Therefore, this test rig was equipped with a modular vessel designed to provide both students and researchers with experimental tests on the coupling of the machine with different kinds of components, such as saturators, fuel cells of different layouts or technology, or additional heat exchangers (such as in an externally fired configuration). These additional components can be emulated by using the right number of vessel modules to have the real volume dimension coupled with the machine. The thermal and flow composition aspects can be emulated through the valve management [6], the coupling with real-time models [6], or the injection of additional flows (e.g., for the chemical composition emulation). These tests are essential for illustrating the Gas Turbines and Innovative Cycles undergraduate course and for developing of new Ph.D. theses in this kind of field.

The vessel, designed for a maximum temperature of about 630°C (903.15 K), is composed of two collector pipes, connected to the recuperator outlet and the combustor inlet, respectively (see Fig. 3), and five module pipes connected to both collectors. These last pipes are mounted on seams for easy removal, i.e., easy volume dimension change. Both collectors and module pipes have a nominal diameter of 350 mm, and their total length is around 43 m for a maximum volume of about 4 m^3 (the Greitzer's parameter [11] of the compressor is between about 1.0 with the minimum volume and 8.0 in maximum volume configuration, while in the original commercial layout of the machine the Greitzer's parameter of the compressor is between about 0.4 and 0.7).

A vessel outlet line equipped with a gate valve (VO) was installed, and a bleed emergency valve (VBE) was included to prevent surge during emergency shutdown. Furthermore, an additional globe pneumatic valve (VBCC) was introduced to connect the compressor outlet directly to the combustor inlet, bypassing both recuperator and vessel. Moreover, the test rig was further improved with the installation of a water fan cooler located outside the laboratory. It is based on three 0.7 kW electrical fans used to cool down the water (coming from the water heat exchanger (WHEx) of Fig. 3), and to operate in closed circuit conditions a 1.5 kW pump was installed. This is an essential improvement to provide both students and researchers with a large set of experimental data measured on a cogenerative microturbine plant to enable them to study the interaction between the power generation system and the thermal load in both steady-state and transient conditions.

A new acquisition and control system was developed with the Lab-VIEW™ software, and now it runs coupled with the machine standard software [12]. However, safe machine operation is assured, in the final test rig layout too, through its own control system by Turbec. Furthermore, the Lab-VIEW™ Web Server tool is used to manage this plant from a remote PC equipped with a general Internet access.

The test rig was equipped with additional instruments (Fig. 3) to measure the largest number of properties [10]. All additional transducers, discussed in detail in a previous work [10], are connected to a PC, through a FieldPoint™ device, and their signals are acquired via local area network (LAN) using the Lab-VIEW™ software.

5 Compressor Inlet Temperature Control

To control the machine compressor inlet temperature (Fig. 3), a water system was designed and installed. This system is essential to compare tests affected by a significant influence of the ambient temperature variation, such as the performance tests on the machine (maximum electrical power and electrical efficiency) or on the recuperator (effectiveness). This system is composed of three air/water heat exchangers installed at the machine air intakes (Fig. 3) and connected to the water system. It is equipped with three controlled electrical valves (VWM, VWH, and VWO of Fig. 3). The compressor inlet air can be cooled down (opening VWO) by means of cold water from the supply system, and heated up (closing VWM and opening VWH) by means of the hot water coming from the machine cogeneration system (WHEx). A new control system (see Ref. [13] for details) was developed to manage these valves for the required temperature generation (a constant value or a trend typical of ambient temperature variation).

5.1 Example of an Experimental Test for Student Lessons. As discussed in Ref. [13], it is extremely important to provide both students and young researchers with experimental data measured on the recuperator, especially considering that there are too few comprehensive test campaigns published on recuperator performance, probably for company data protection reasons. Since the large influence on the recuperator temperatures of the compressor inlet temperature, this new control system was used to maintain this temperature at a fixed value of 28 °C (301.15 K, with maximum errors of ±0.2 K during all the tests). These steady-state tests were carried out with the machine connected to the electrical grid to measure recuperator performance at different mass flow rate values. In fact, in this configuration the machine control system operates at constant TOT (called TT2 in Fig. 3, that is maintained at 645 °C, that is 918.15 K) and changes the rotational speed (and the air mass flow rate) with load changes.

As shown during a typical experimental lesson for Master students, after the machine start-up the 20 kW load steady-state condition is reached. Then, the test is carried out in different load conditions up to the maximum load value. Each load value is maintained constant up to steady-state temperature condition. Finally, after a load decrease down to 20 kW, the machine shutdown is carried out and presented to students. The data acquired during one of these tests can be used to calculate the recuperator effectiveness performed at different loads, i.e., different air mass flow rates (see Ref. [13] for further details).

6 Future Work

Further developments will study commercial microturbine improvements for innovative cycle applications, such as hybrid systems [6], mHAT cycles [3], or externally fired gas turbine plants [5]. Moreover, this plant will be used to develop, test, and optimize new control systems for both traditional and innovative cycles. For instance, a specific experimental activity will be devoted on a new active control system development for compressor surge prevention.

The largest number of experimental data available during the tests is also used to validate both steady-state (design and off-design) and transient (also real-time) theoretical models and to develop higher performance control systems for innovative cycle plants. At the moment, several Master and Ph.D. [14] theses are under development on this subject. Based on certain preliminary theoretical transient calculations [10], a good level of consistency can be achieved thanks to the complete knowledge of the test rig dimensions, volumes, masses, shaft inertia, thermal capacitances, and operating procedure. Such completeness is difficult to obtain in industrial plants, where details about equipment are often missing or confidential.

7 Conclusions

A new general-purpose test rig based on microturbine technology was developed at the TPG laboratory of the University of Genoa, Italy, to better underpin the undergraduate course in Gas Turbines and Innovative Cycles and the Ph.D. course in fluid machinery engineering.

The main experimental facilities developed and built for student lessons and researcher tests are as follows.

- A commercial recuperated micro gas turbine (100 kW) equipped with a hot water cogeneration unit and with the essential instrumentation to provide students with typical operation tests (start-up, shutdown, and load changes) on the machine.
- A set of external pipes connected to the machine (after suitable modifications to the component connections) for flow measurement and management. A large number of probes is used to provide both students and researchers with wide-ranging experimental data related to this kind of plants. In particular the paper reports the measured compressor map compared with the manufacturer curves.
- An apt modular vessel to test the coupling of the machine with different kinds of additional innovative cycle components, such as saturators, fuel cells of different layouts or technology, or additional heat exchangers.
- The compressor inlet temperature control devices (heat exchangers, pipes, pump, and control system) and the tests carried out on the recuperator for educational purposes.

Acknowledgment

This work has been funded by FELICITAS European Integrated Contract No. TIP4-CT-2005-516270 coordinated by Fraunhofer Institute, LARGE-SOFC European Integrated Project No. 019739, coordinated by VTT of Finland, and by PRIN 2005, National Coordinator A. F. Massardo.

Nomenclature

C	=	compressor
CC	=	combustion chamber
Ex	=	exchanger
LAN	=	local area network
mGT	=	micro gas turbine
mHAT	=	micro HAT cycle
REC	=	recuperator
SOFC	=	solid oxide fuel cell
T	=	turbine
WHEx	=	water heat exchanger

Variables

$\dot{m}$	=	mass flow rate (kg/s)
N	=	rotational speed (rpm)
p	=	pressure (Pa)
T	=	temperature (K)
TIT	=	turbine inlet temperature (K)
TOT	=	turbine outlet temperature (K)

Greek Symbols

β	=	compressor pressure ratio (total to static)

Subscripts

0	=	on design
in	=	inlet
t	=	total

References

[1] Kolanowski, B. F., 2004, *Guide to Microturbines*, Fairmont, Lilburn, GA.

[2] Magistri, L., Traverso, A., Cerutti, F., Bozzolo, M., Costamagna, P., and Massardo, A. F., 2005, "Modelling of Pressurised Hybrid Systems Based on Integrated Planar Solid Oxide Fuel Cell (IP-SOFC) Technology," Fuel Cells, **1**(5), pp. 80–96.

[3] Pedemonte, A. A., Traverso, A., and Massardo, A. F., 2008, "Experimental Analysis of Pressurised Humidification Tower for Humid Air Gas Turbine Cycles—Part A: Experimental Campaign," Appl. Therm. Eng., **28**, pp. 1711–1725.

[4] Elmeegard, B., and Qvale, B., 2002, "Analysis of Indirectly Fired Gas Turbine for Wet Biomass Fuels Based on Commercial Micro Gas Turbine Data," ASME Paper No. GT2002-30016.

[5] Schirmeister, U., and Staudacher, S., 2006, "Operational Performance Analysis of an Externally Fired Gas Turbine," ASME Paper No. GT2006-90830.

[6] Ferrari, M. L., Pascenti, M., Bertone, R., Magistri, L., 2009, "Hybrid Simulation Facility Based on Commercial 100 kWe Micro Gas Turbine," ASME J. Fuel Cell Sci. Technol., **6**, p. 031008.

[7] Tucker, D., Liese, E., VanOsdol, J. G., Lawson, L. O., and Gemmen, R. S., 2003, "Fuel Cell Gas Turbine Hybrid Simulation Facility Design," 2003 ASME International Mechanical Engineering Congress and Exposition, New Orleans, LA.

[8] Moretti, J., 2007, "Test Rig Emulator of a Hybrid System with Micro Gas Turbine," MS thesis, TPG-DiMSET, University of Genoa (in Italian).

[9] Turbec T100 Series 3, 2002, *Installation Handbook*.

[10] Pascenti, M., Ferrari, M. L., Magistri, L., and Massardo, A. F., 2007, "Micro Gas Turbine Based Test Rig for Hybrid System Emulation," ASME Paper No. GT2007-27075.

[11] Greitzer, E. M., 1976, "Surge and Rotating Stall in Axial Compressors. Part I: Theoretical Compression System Model. Part II: Experimental Results and Comparison With Theory," ASME J. Eng. Power, **98**(2), pp. 190–217.

[12] Pascenti, M., 2009, "Development, Study and Experimental Characterisation of a Hybrid System Emulator Plant," Ph.D. thesis, TPG-DiMSET, University of Genoa.

[13] Ferrari, M. L., Pascenti, M., Magistri, L., and Massardo, A. F., 2009, "Micro Gas Turbine Recuperator: Steady-State and Transient Experimental Investigation," ASME Paper No. GT2009-59172.

[14] Ghigliazza, F., Traverso, A., Pascenti, M., and Massardo, A. F., 2009, "Micro Gas Turbine Real-Time Modeling: Test Rig Verification," ASME Paper No. GT2009-59124.